

11-29-2007

# Modeling Streambed Heating in Shallow Streams

Robert Leslie Annear Jr.  
*Portland State University*

Follow this and additional works at: [https://pdxscholar.library.pdx.edu/open\\_access\\_etds](https://pdxscholar.library.pdx.edu/open_access_etds)



Part of the [Civil and Environmental Engineering Commons](#)

Let us know how access to this document benefits you.

---

## Recommended Citation

Annear Jr., Robert Leslie, "Modeling Streambed Heating in Shallow Streams" (2007). *Dissertations and Theses*. Paper 6034.

<https://doi.org/10.15760/etd.7904>

This Dissertation is brought to you for free and open access. It has been accepted for inclusion in Dissertations and Theses by an authorized administrator of PDXScholar. Please contact us if we can make this document more accessible: [pdxscholar@pdx.edu](mailto:pdxscholar@pdx.edu).

DISSERTATION APPROVAL

The abstract and dissertation of Robert Leslie Annear Jr. for the Doctor of Philosophy in Civil and Environmental Engineering were presented November 29, 2006, and accepted by the dissertation committee and the doctoral program.

COMMITTEE APPROVALS:



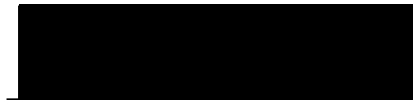
Scott A. Wells, Chair



Roy W. Koch



William Fish



Alan Yeakley



Curt Peterson  
Representative of the Office of Graduate Studies

DOCTORAL PROGRAM APPROVAL:



Scott A. Wells, Director  
Civil and Environmental Engineering Ph.D. Program

## ABSTRACT

An abstract of the dissertation of Robert Leslie Annear Jr. for the Doctor of Philosophy in Civil and Environmental Engineering presented November 29, 2006.

Title: Modeling Streambed Heating in Shallow Streams

The Oregon Department of Environmental Quality is developing Total Maximum Daily Loads to address water quality concerns and threatened and endangered species habitat requirements. Approximately 940 water body segments are listed as water quality limited for temperature in Oregon. CE-QUAL-W2 Version 3 is a two-dimensional water quality and hydrodynamic model capable of modeling rivers, reservoirs and estuaries. An important aspect of modeling stream temperature is handling the short-wave solar radiation that penetrates the water surface and impacts the streambed, which can affect water temperatures under low-flow conditions. The Bull Run River-Reservoir system is a 264 km<sup>2</sup> watershed 42 km east of downtown Portland and serves as the city's primary drinking water source. A dynamic, three-dimensional streambed heat transfer model was developed and calibrated with field data from the Lower Bull Run River and laboratory experiment data. Model results compared well to field data from bedrock and cobble substrates. The model calibration for the cobble substrate revealed the substrate interstitial water temperature played a large role in the substrate temperatures and was necessary to calibrate the model. The streambed heating model compared well with the laboratory experiments'

---

data in many cases. The model was compared to two analytical models and a one-dimensional model for various application cases and performed well.

The streambed heating model was implemented in CE-QUAL-W2 and a sensitivity analysis examined the impacts of river flows, substrate type and streamside shading. Water temperature impacts focused on daily minimum and maximum temperatures. Increased flow rates resulted in decreased water temperature impacts from streambed heating. The largest water temperature impacts occurred with the bedrock streambed with decreasing impacts once cobble was incorporated. Increased streamside shading reduced the impact of streambed heating. General guidelines were discussed when streambed heating may be an important part of the surface water heat budget.

The clear-sky solar radiation model in CE-QUAL-W2 was compared to four models and calibrated to data from 17 sites around the U.S.A. to identify improvements in predicting clear-sky solar radiation. A dynamic vegetative and topographic streamside shading model was included to more accurately simulate the effective solar radiation striking the water surface.



MODELING STREAMBED HEATING IN SHALLOW STREAMS

by

ROBERT LESLIE ANNEAR JR.

A dissertation submitted in partial fulfillment of the  
requirements for the degree of

DOCTOR OF PHILOSOPHY  
in  
CIVIL AND ENVIRONMENTAL ENGINEERING

Portland State University  
© 2007

## Dedication

The dissertation is dedicated to  
Barbara Helen and Richard Lloyd Annear  
who could not be here to see this day.

## **Acknowledgements**

I would like to thank Rich Miller, Toni Pennington, Miguel Estrada, Dr. Mark Sytsma, Kazu Sonoda, and Dr. Alan Yeakley with the Environmental Science and Resources Department and Sharon Stanton and Dr. Robert Tinnen with the Biology Department for assistance with borrowing field equipment. David Percy and Dr. Curt Peterson with the Geology Department for their efforts using ground-penetrating radar at my field site. Spencer Slominski, Mike McKillip, and Steve Speer with the Civil and Environmental Engineering Department for their help with fieldwork and designing equipment. Kyle Muramatsu and Vanessa Wells, both interns, who were invaluable with the field work. Additional thanks goes to Vanessa Wells for her assistance with the lab experiments.

Special thanks go to Stan Cioeta, Doug Bloem and Jeff Leighton with the City of Portland Water Bureau for providing access to the Bull Run watershed and assistance with fieldwork logistics and data collection.

Finally, I would also like to thank my committee members: Dr. Scott Wells, Dr. Curt Peterson, Dr. William Fish, Dr. Roy Koch, and Dr. Alan Yeakley for their time and energy reviewing my research and providing feedback. I would like to give special thanks to my advisor Dr. Scott Wells who has given me constant support and mentoring over the years. The field work was partially funded by a grant from U.S. Geological Survey, Oregon Water Resources Research Institute, through the Center for Water and Environmental Sustainability at Oregon State University.

## Table of Contents

Acknowledgements .....	ii
List of Figures .....	ix
List of Tables.....	xxii
Notation.....	xxix
Solar Formulation .....	xxix
Dynamic Shade Algorithm.....	xxxii
Streambed Heating Algorithm .....	xxxii
Meteorology .....	xxxiii
Light Attenuation .....	xxxiii
Flow Measurements .....	xxxiv
1. Introduction .....	1
1.1 Bull Run .....	2
1.2 Research Objectives .....	7
2. Literature Review .....	9
2.1 Modeling Approaches .....	10
2.2 Streambed Study Characteristics.....	16
2.3 Streambed Temperature Monitoring Approaches.....	23
2.4 Position of the Sun .....	25
2.4.1 Standard Meridian .....	25
2.4.2 Local Hour and Julian Day.....	26
2.4.3 Solar Declination.....	27

2.4.4 Equation of Time.....	30
2.4.5 Local Hour Angle.....	33
2.4.6 Solar Altitude .....	37
2.4.7 Solar Azimuth .....	38
2.4.8 Atmospheric Refraction .....	41
2.5 Extraterrestrial Solar Radiation.....	42
2.5.1 Solar Constant .....	42
2.5.2 Incoming Solar Radiation.....	43
2.6 Atmospheric Attenuation .....	44
2.6.1 Optical Air Mass and Transmittance.....	45
2.6.2 Precipitable Water Content .....	45
2.6.3 Ozone Absorption .....	47
2.6.4 Atmospheric Turbidity .....	49
2.6.5 Aerosol Absorptance .....	50
2.6.6 Atmospheric Albedo .....	51
2.6.7 Atmospheric Dust.....	51
2.6.8 Atmospheric Transmission.....	52
2.6.9 Surface Reflectivity.....	54
2.6.10 Ground-level Clear-Sky Solar Radiation .....	56
2.6.11 Cloud Cover .....	58
2.7 Thermophysical Properties of Matter.....	59
3. Field Work .....	63

3.1 Bathymetric Data .....	64
3.2 Stream Temperature Data .....	69
3.3 Streambed Temperature Data.....	71
3.3.1 Cobble Streambed Temperature Results .....	75
3.3.2 Bedrock Streambed Temperature Results .....	86
3.4 Streambed Substrate and Geology .....	92
3.4.1 Bedrock Substrate .....	93
3.4.2 Boulder/Cobble Substrate .....	98
3.5 Meteorological Data.....	103
3.6 Light Attenuation Data.....	109
3.7 Flow and Dye Study Data .....	126
3.7.1 Dye study.....	126
3.7.2 Water Level Measurements.....	130
3.7.3 Flow Measurements .....	131
3.8 Vegetative and Topographic Shade Data.....	136
3.8.1 Vegetation Data.....	136
3.8.2 Topographic Data.....	142
4. Experimental Laboratory Work .....	144
4.1 Experimental Design.....	144
4.2 Results.....	147
4.2.1 Experiment 1: Sand vs. Gravel.....	147
4.2.2 Experiment 2: Sand vs. Gravel-Sand Mixture .....	155

4.2.3 Experiment 3: Painted Concrete, White vs. Black.....	162
4.3 Discussion .....	168
5. Streambed Heating Model.....	170
5.1 Development .....	170
5.1.1 Cartesian Model .....	170
5.1.2 Cylindrical Model .....	177
5.2 Calibration.....	183
5.2.1 Cartesian Model .....	183
5.2.2 Cylindrical Model .....	207
5.2.3 Summary .....	220
5.3 Model Verification.....	221
5.3.1 Grid Sensitivity .....	222
5.3.2 Comparison with Analytical Solution, Simple Case.....	226
5.3.3 Comparison with Analytical Model, Bedrock.....	235
5.3.4 Comparison with 1-D Model, Bedrock.....	241
5.3.5 Summary .....	247
5.4 Implementation in CE-QUAL-W2.....	248
5.5 Sensitivity Analysis.....	252
5.5.1 Sensitivity to Flow Rates.....	253
5.5.2 Sensitivity to Substrate Types .....	265
5.5.3 Sensitivity to Dynamic Shading.....	272
5.5.4 Dynamic Streambed Heating Guidelines .....	274

6. Auxiliary Model Algorithms.....	277
6.1 Dynamic Shading Algorithm .....	277
6.1.1 Data Requirements .....	278
6.1.2 Shade Algorithm .....	279
6.1.3 Shade Algorithm Testing .....	282
6.2 Effective Solar Radiation Formulation .....	291
6.2.1 Model Formulations .....	291
6.2.2 Solar Radiation Data .....	309
6.2.3 Solar Altitude Comparison.....	310
6.2.4 Model Calibration and Testing.....	313
6.2.5 Sensitivity of Simulation Year .....	322
6.2.6 Sensitivity of Dew Point Temperature Data .....	324
6.2.7 Summary and Discussion.....	325
6.2.8 Conclusion.....	327
7. Summary and Recommendations.....	328
7.1 Summary and Conclusions.....	328
7.2 Recommendations for Future Work.....	331
8. References .....	334
9. Appendix A: Shade File Format .....	345
10. Appendix B: Statistics Calculations.....	349
11. Appendix C: Thermophysical Properties of Matter .....	350
12. Appendix D: Temperature Probe Quality Assurance and Control.....	360

12.1 Suspect and Erroneous Data .....	360
12.1.1 Field Monitoring .....	360
12.1.2 Experimental Lab Work .....	364
12.2 Quality Assurance and Control .....	369
12.2.1 Temperature Probe 4 .....	371
12.2.2 Temperature Probe 5 .....	377
13. Appendix E: Secondary Light Extinction Analysis .....	383

## List of Figures

Figure 1: Bull Run Watershed in NW Oregon.....	3
Figure 2: Bull Run River-Reservoir system.....	3
Figure 3: Schematic of short-wave solar penetration to the streambed and conductive transfer from bed to water and vice-versa .....	5
Figure 4: Components of surface heat transfer .....	6
Figure 5: Declination angle, models and data.....	28
Figure 6: Comparison of equation of time models and tabulated values from List, 1958.....	32
Figure 7: Difference between equation of time models and tabulated values from List, 1958.....	32
Figure 8: Solar Azimuth calculated by three methods for July 3.....	35
Figure 9: Solar azimuth angle differences, model – tabulated data (Cugle, 1943) for three days.....	36
Figure 10: Solar Altitude and Azimuth.....	37
Figure 11: Solar azimuth data on July 3 <sup>rd</sup> .....	39
Figure 12: Solar azimuth angle over daylight for July 3.....	40
Figure 13: Bull Run Watershed.....	63
Figure 14: Lower Bull Run River field study area.....	64
Figure 15: Bathymetric river cross-section locations.....	65

Figure 16: Combined data set for developing the river channel bathymetry .....	66
Figure 17: SURFER elevation contour of the river channel .....	67
Figure 18: Model grid plan view with segment numbers .....	68
Figure 19: Volume-elevation curve comparing data and the CE-QUAL-W2 model grid .....	68
Figure 20: Surface area-elevation curve comparing data and the CE-QUAL-W2 model grid .....	69
Figure 21: Stream temperature monitoring sites.....	70
Figure 22: Stream temperature data, Lower Bull Run River .....	71
Figure 23: Streambed temperature monitoring sites .....	72
Figure 24: Streambed temperature probes, probes in the cobble went to a depth of 0.5 m below the sediment-water interface, probes in the bedrock went down to depth of 1 m. ....	74
Figure 25: Streambed temperature Probe 1, cobble substrate near bank, shaded .....	77
Figure 26: Streambed temperature Probe 2, cobble substrate closer to center, sunny. ....	78
Figure 27: Streambed Probe 1 (near bank, shaded) and Probe 2 (closer to center, sunny) temperature comparison .....	80
Figure 28: Difference between streambed temperature Probe 2 (closer to center, sunny)and Probe 1 (near bank, shaded) .....	81
Figure 29: Streambed temperature Probe 3, cobble substrate, near bank downstream of Probe 1.....	83

Figure 30: Streambed Probe 1 (near bank, shaded) and Probe 3 (near bank downstream) temperature comparison .....	84
Figure 31: Difference between streambed temperature Probe 3 (near bank shade, downstream of Probe 1) and Probe 1 (near bank, shaded).....	85
Figure 32: Streambed temperature Probe 4, bedrock substrate near bank, shaded .....	87
Figure 33: Streambed temperature Probe 5, bedrock substrate, near opposite bank to Probe 4, sunny .....	88
Figure 34: Streambed Probe 4 (near bank, shaded) and Probe 5 (near opposite bank to Probe 4, sunny) temperature comparison.....	90
Figure 35: Difference between streambed temperature Probe 4 (near bank shade,) and Probe 5 (near bank, opposite side, sunny).....	91
Figure 36: Streambed substrate for the field site .....	93
Figure 37: Sample of bedrock material from drilling in Reach 3. ....	97
Figure 38: Exposed bedrock in Reach 2, Columbia River Basalt.....	97
Figure 39: Bedrock in pool reach (Reach 3) covered with brown periphyton.....	98
Figure 40: Substrate surface boulders and large cobbles .....	99
Figure 41: Cross section of mineral substrates found in Reach 1. ....	100
Figure 42: Ground Penetrating Radar survey transect locations.....	101
Figure 43: Ground Penetrating Radar Results .....	103
Figure 44: Meteorological sites in the Lower Bull Run River.....	104
Figure 45: Air temperature, C in the Lower Bull Run River .....	106
Figure 46: Percentage Relative Humidity in the Lower Bull Run River .....	106

Figure 47: Calculated dew point temperature, C in the Lower Bull Run River.....	107
Figure 48: Wind speed, m/s in the Lower Bull Run River.....	107
Figure 49: Wind direction, degrees in the Lower Bull Run River.....	108
Figure 50: Calculated cloud cover using solar radiation data in the Lower Bull Run River and Headworks.....	108
Figure 51: Global Solar Radiation, W/m <sup>2</sup> in the Lower Bull Run River.....	109
Figure 52: Light attenuation measurement sites in the Lower Bull Run River. ....	110
Figure 53: Calculated light extinction coefficients with depth, based on data, Bull Run River, OR.....	120
Figure 54: Calculated light extinction coefficients with depth separated by date of collection, based on data, Bull Run River, OR.....	121
Figure 55: Calculated light extinction coefficients with depth separated by river reach (See Figure 52) , based on data, Bull Run River, OR.....	122
Figure 56: Fraction of incident radiation hitting the river bottom, September 20, 2002 .....	125
Figure 57: Fraction of radiation reflecting off the river bottom, September 20, 2002 .....	125
Figure 58: Sketch of Potential Hyporheic flow in Study Reach.....	126
Figure 59: Dye study probe.....	128
Figure 60: Dye study monitoring sites.....	128
Figure 61: Flow measurement sites.....	132
Figure 62: Cross-section data at RM 4.956, upstream flow measurement.....	134

Figure 63: Cross-section data at RM 4.925, downstream flow measurement .....	135
Figure 64: Flow measurements in the Lower Bull Run River .....	135
Figure 65: Vegetation top elevation, m.....	140
Figure 66: River centerline to controlling vegetation distance, m .....	141
Figure 67: Vegetation density in the Lower Bull Run River .....	142
Figure 68: Topographic Slices along the Lower Bull Run River.....	143
Figure 69: Experimental lab design .....	145
Figure 70: Experimental lab design setup.....	147
Figure 71: Sand and gravel experimental lab setup .....	148
Figure 72: Gravel substrate and water temperature .....	149
Figure 73: Sand substrate and water temperature .....	150
Figure 74: Experiment 1 side boundary condition temperatures .....	151
Figure 75: Experiment 1 bottom boundary condition temperatures .....	152
Figure 76: Gravel and Sand substrate temperatures at 1 cm depth.....	152
Figure 77: Gravel and Sand substrate temperature at 6 cm depth.....	153
Figure 78: Gravel and Sand substrate temperature at 11 cm depth.....	153
Figure 79: Air temperature and radiation for Experiment 1 .....	154
Figure 80: Water and air temperature for Experiment 1 .....	155
Figure 81: Sand and gravel-sand mixture experimental lab setup .....	156
Figure 82: Gravel-sand mixture substrate and water temperature .....	157
Figure 83: Sand substrate and water temperature .....	158
Figure 84: Experiment 2 side boundary condition temperatures .....	159

Figure 85: Experiment 2 bottom boundary condition temperatures .....	160
Figure 86: Gravel-sand mixture and Sand substrate temperatures at 6 cm depth.....	160
Figure 87: Experiment 2 air temperature and radiation .....	161
Figure 88: Water and air temperature for Experiment 2 .....	162
Figure 89: White and black concrete experimental lab setup .....	163
Figure 90: Black painted concrete substrate and water temperature.....	164
Figure 91: White painted concrete substrate and water temperature .....	165
Figure 92: Experiment 3 side boundary condition temperatures .....	166
Figure 93: Experiment 3 bottom boundary condition temperatures .....	166
Figure 94: Experiment 3 air temperature and radiation .....	167
Figure 95: Water and air temperature for Experiment 3 .....	168
Figure 96: Cartesian coordinate system numerical grid, x direction. ....	171
Figure 97: Surface Boundary Condition, Cartesian and cylindrical coordinate systems. .....	174
Figure 98: Cylindrical Coordinates .....	178
Figure 99: Model-data bedrock streambed temperature comparison, Probe 4, September 5 <sup>th</sup> to 13 <sup>th</sup> , 2002.....	186
Figure 100: Model-data bedrock streambed temperature comparison, Probe 4, September 13 <sup>th</sup> to 21 <sup>st</sup> , 2002.....	187
Figure 101: Model-data bedrock streambed temperature comparison, Probe 5, September 5 <sup>th</sup> to 13 <sup>th</sup> , 2002, depths 0 to 0.4 m.....	189

Figure 102: Model-data bedrock streambed temperature comparison, Probe 5, September 5 <sup>th</sup> to 13 <sup>th</sup> , 2002, depths 0.4 to 1.0 m.....	190
Figure 103: Model-data bedrock streambed temperature comparison, Probe 5, September 13 <sup>th</sup> to 21 <sup>st</sup> 2002, depths 0 to 0.4 m. ....	191
Figure 104: Model-data bedrock streambed temperature comparison, Probe 5, September 13 <sup>th</sup> to 21 <sup>st</sup> 2002, depths 0.4 to 1.0 m. ....	192
Figure 105: Model-data cobble streambed temperature comparison, Probe 1 site, using only thermophysical properties of substrate.....	195
Figure 106: Model-data cobble streambed temperature comparison, Probe 1 site, August 7 <sup>th</sup> to 15 <sup>th</sup> , 2002. ....	197
Figure 107: Model-data cobble streambed temperature comparison, Probe 1 site, August 15 <sup>th</sup> to 24 <sup>th</sup> , 2002. ....	198
Figure 108: Model-data cobble streambed temperature comparison, Probe 1 site, August 30 <sup>th</sup> to September 5 <sup>th</sup> , 2002.....	199
Figure 109: Model-data cobble streambed temperature comparison, Probe 2 site, August 7 <sup>th</sup> to 15 <sup>th</sup> , 2002.....	201
Figure 110: Model-data cobble streambed temperature comparison, Probe 2 site, August 15 <sup>th</sup> to 24 <sup>th</sup> , 2002.....	202
Figure 111: Model-data cobble streambed temperature comparison, Probe 3 site, August 23 <sup>rd</sup> to 30 <sup>th</sup> , 2002.....	205
Figure 112: Model-data cobble streambed temperature comparison, Probe 3 site, August 30 <sup>th</sup> to September 5 <sup>th</sup> , 2002.....	206

Figure 113: Experiment 1, Sand Substrate, November 17 <sup>th</sup> to 22 <sup>nd</sup> , 2002.....	210
Figure 114: Experiment 1, Sand Substrate, November 17 <sup>th</sup> to 22 <sup>nd</sup> , 2002.....	212
Figure 115: Experiment 2, Gravel and Sand Substrate, November 22 <sup>nd</sup> to 28 <sup>th</sup> , 2002. .....	214
Figure 116: Experiment 2, Sand Substrate, November 22 <sup>nd</sup> to 28 <sup>th</sup> , 2002.....	216
Figure 117: Experiment 3, Black painted concrete, December 15 <sup>th</sup> to 21 <sup>st</sup> , 2002.....	218
Figure 118: Experiment 3, White painted concrete, December 15 <sup>th</sup> to 21 <sup>st</sup> , 2002.....	220
Figure 119: Streambed vertical grid resolution comparison, part 1.....	223
Figure 120: Streambed vertical grid resolution comparison, part 2.....	223
Figure 121: Streambed vertical grid resolution comparison, near surface.....	224
Figure 122: Streambed horizontal grid resolution comparison.....	225
Figure 123: Streambed bottom boundary condition depth.....	226
Figure 124: 3-D Model and Analytical Model solutions for Cartesian coordinate system, 100% rock .....	228
Figure 125: 3-D Model and Analytical Model solutions for Cartesian coordinate system, 50% rock and 50% water .....	230
Figure 126: 3-D Model and Analytical Model solutions for Cartesian coordinate system, 100% water.....	231
Figure 127: 3-D Model and Analytical Model solutions for cylindrical coordinate system, 100% rock. ....	232
Figure 128: 3-D Model and Analytical Model solutions for cylindrical coordinate system, 50% rock and 50% water. ....	234

Figure 129: 3-D Model and Analytical Model solutions for cylindrical coordinate system, 100% water.....	235
Figure 130: 3-D Model, Data, and Analytical Model temperature comparison, bedrock streambed, Probe 5, September 5 <sup>th</sup> to 13 <sup>th</sup> 2002, depths 0 to 0.4 m. ....	238
Figure 131: 3-D Model, Data, and Analytical Model temperature comparison, bedrock streambed, Probe 5, September 5 <sup>th</sup> to 13 <sup>th</sup> 2002, depths 0.8 to 1.0 m. ....	239
Figure 132: 3-D Model, Data, and Analytical Model temperature comparison, bedrock streambed, Probe 5, September 13 <sup>th</sup> to 21 <sup>st</sup> 2002, depths 0 to 0.4 m. ....	240
Figure 133: 3-D Model, Data, and Analytical Model temperature comparison, bedrock streambed, Probe 5, September 13 <sup>th</sup> to 21 <sup>st</sup> 2002, depths 0.8 to 1.0 m. ....	241
Figure 134: 3-D Model, Data, and 1-D Model temperature comparison, bedrock streambed, Probe 5, September 5 <sup>th</sup> to 13 <sup>th</sup> 2002, depths 0 to 0.4 m. ....	244
Figure 135: 3-D Model, Data, and 1-D Model temperature comparison, bedrock streambed, Probe 5, September 5 <sup>th</sup> to 13 <sup>th</sup> 2002, depths 0.8 to 1.0 m. ....	245
Figure 136: 3-D Model, Data, and 1-D Model temperature comparison, bedrock streambed, Probe 5, September 13 <sup>th</sup> to 21 <sup>st</sup> 2002, depths 0 to 0.4 m. ....	246
Figure 137: 3-D Model, Data, and 1-D Model temperature comparison, bedrock streambed, Probe 5, September 13 <sup>th</sup> to 21 <sup>st</sup> 2002, depths 0.8 to 1.0 m. ....	247
Figure 138: Streambed model grid with CE-QUAL-W2 model grid, looking downstream .....	252

Figure 139: Continuous water temperatures at RM 4.88, comparing model results at a constant flow of 0.85 m<sup>3</sup>/s (30 cfs) with and without a streambed heating model. .... 256

Figure 140: Daily minimum and maximum water temperatures at RM 4.88, comparing model results at a constant flow of 0.85 m<sup>3</sup>/s (30 cfs) with and without a streambed heating model..... 256

Figure 141: Continuous water temperatures at RM 0.33, comparing model results at a constant flow of 0.85 m<sup>3</sup>/s (30 cfs) with and without a streambed heating model. .... 257

Figure 142: Daily minimum and maximum water temperatures at RM 0.33, comparing model results at a constant flow of 0.85 m<sup>3</sup>/s (30 cfs) with and without a streambed heating model..... 257

Figure 143: Continuous water temperatures at RM 4.88, comparing model results at a constant flow of 0.57 m<sup>3</sup>/s (20 cfs) with and without a streambed heating model. .... 259

Figure 144: Daily minimum and maximum water temperatures at RM 4.88, comparing model results at a constant flow of 0.57 m<sup>3</sup>/s (20 cfs) with and without a streambed heating model..... 259

Figure 145: Continuous water temperatures at RM 0.33, comparing model results at a constant flow of 0.57 m<sup>3</sup>/s (20 cfs) with and without a streambed heating model. .... 260

Figure 146: Daily minimum and maximum water temperatures at RM 0.33, comparing model results at a constant flow of 0.57 m<sup>3</sup>/s (20 cfs) with and without a streambed heating model..... 260

Figure 147: Continuous water temperatures at RM 4.88, comparing model results at a constant flow of 0.28 m<sup>3</sup>/s (10 cfs) with and without a streambed heating model. .... 262

Figure 148: Daily minimum and maximum water temperatures at RM 4.88, comparing model results at a constant flow of 0.28 m<sup>3</sup>/s (10 cfs) with and without a streambed heating model..... 263

Figure 149: Continuous water temperatures at RM 4.88, comparing model results at a constant flow of 0.28 m<sup>3</sup>/s (10 cfs) with and without a streambed heating model. .... 263

Figure 150: Daily minimum and maximum water temperatures at RM 0.33, comparing model results at a constant flow of 0.28 m<sup>3</sup>/s (10 cfs) with and without a streambed heating model..... 264

Figure 151: Continuous water temperatures at RM 4.88, comparing model results at constant flow rates with and without a streambed heating model..... 264

Figure 152: Daily minimum and maximum water temperatures at RM 4.88, comparing model results at a constant flow of 0.28 m<sup>3</sup>/s (10 cfs) and different types of substrate with and without a streambed heating model..... 268

Figure 153: Daily minimum and maximum water temperatures at RM 0.33, comparing model results at a constant flow of 0.28 m<sup>3</sup>/s (10 cfs) and different types of substrate with and without a streambed heating model..... 268

Figure 154: Daily minimum and maximum water temperatures at RM 4.88, comparing model results at a constant flow of 0.28 m<sup>3</sup>/s (10 cfs) incorporating vegetative and topographic shading with and without a streambed heating model. .... 274

Figure 155: Topographic and Vegetative shading, solar altitude and vegetation height affect the shadow length..... 278

Figure 156: Schematic showing azimuth angle and stream orientation and shadow length..... 282

Figure 157: East Mountain topographic testing ..... 284

Figure 158: South Mountain topographic testing..... 285

Figure 159: West Mountain topographic testing..... 286

Figure 160: North Mountain topographic testing..... 287

Figure 161: Shade from varying tree height, distance between controlling vegetation: 30.5 m (100 ft). Orientation angle is the angle of the model segment relative to North..... 289

Figure 162: Shade from varying tree height, distance between controlling vegetation: 61.0 m (200 ft). Orientation angle is the angle of the model segment relative to North..... 289

Figure 163: Shade from varying distance between controlling vegetation, tree height  
10 m (32.8 ft). Orientation angle is the angle of the model segment relative to  
North..... 290

Figure 164: Shade from varying distance between controlling vegetation, tree height  
35 m (115 ft). Orientation angle is the angle of the model segment relative to  
North..... 290

Figure 165: Solar radiation sites monitored around the United States and data used to  
compare with model results..... 309

Figure 166: Solar radiation results for the Meeus (1999) and Bird and Hulstrom (1981)  
model and the EPA (1971) model ..... 313

## List of Tables

Table 1: Modeling approaches for streambed heating. ....	12
Table 2: Streambed heating model parameters from literature .....	14
Table 3: Streambed study characteristics .....	17
Table 4: Heat budget components.....	21
Table 5: Streambed monitoring studies.....	23
Table 6: Error statistics between equation of time models and tabulated values.....	33
Table 7: Solar azimuth error ranges between model and data .....	36
Table 8: Azimuth angle model-data error statistics for July 3 .....	40
Table 9: Atmospheric refraction correction for solar altitude, NOAA (2004).....	41
Table 10: Solar Constant values from literature .....	42
Table 11: Extraterrestrial solar irradiance from satellite data (NASA, 2004). ....	43
Table 12: Empirical values for precipitable water content .....	46
Table 13: Empirical values for atmospheric ozone.....	48
Table 14: Ozone model parameters based on location (Van Heuklon, 1979) .....	48
Table 15: Empirical values for atmospheric turbidity.....	49
Table 16: Empirical values of the aerosol absorptance coefficient, Bird and Hulstrom (1981) .....	50
Table 17: Empirical values for the ratio of forward scatter irradiance to the total irradiance.....	51

Table 18: Empirical values of the fraction of dust in the atmosphere .....	52
Table 19: Atmospheric transmission empirical values .....	54
Table 20: Empirical values for albedo or reflectivity .....	55
Table 21: Water surface reflectivity for varying solar altitude, (Lee, 1978) .....	55
Table 22: Reflectivity equation coefficients based on cloud cover (Anderson, 1954) .....	55
Table 23: Summary table of thermophysical properties of matter.....	60
Table 24: Lower Bull Run River model grid layout .....	69
Table 25: Thermistor depths in Streambed Temperature Probes for cobble and bedrock media .....	74
Table 26: Columbia River Basalt stratigraphy, from Swanson (1978).....	96
Table 27: Substrate classification by particle size, Cummins (1962).....	99
Table 28: Light attenuation data collected on July 25, 2002 in Reach 3 .....	110
Table 29: Light attenuation data collected on August 23, 2002 in Reaches 1 and 2 .	111
Table 30: Light attenuation data collected on August 30, 2002 in Reaches 1 and 2 .	111
Table 31: Light attenuation data collected on September 20, 2002 in Reaches 1, 2 and 3 .....	111
Table 32: Percentage of Total Irradiance (300 - 2,500 nm) from Sun and Sky (Jerlov, 1968).....	114
Table 33: Fraction of radiation absorbed in the surface layer and downward irradiance formularization.....	115
Table 34: Fraction of radiation absorbed in the surface layer and downward irradiance formularization (Wunderlich, 1972) .....	117

Table 35: Light extinction coefficients from literature .....	118
Table 36: Calculated light extinction coefficients from field data, Bull Run River, OR, 2002.....	119
Table 37: Calculated light extinction coefficient and reflection in three reaches of the Bull Run River, September 20, 2002 .....	124
Table 38: Dye study monitoring sites .....	127
Table 39: Dye sample fluorescence readings.....	130
Table 40: Water level measurements, Reach 1 .....	131
Table 41: Vegetation characteristics collected in the field .....	136
Table 42: Experimental design thermistor locations.....	146
Table 43: Annual mean air temperature in the Lower Bull Run River .....	176
Table 44: Model-data streambed temperature error statistics for Probe 4 .....	185
Table 45: Model-data streambed temperature error statistics for Probe 5. ....	188
Table 46: Thermophysical characteristics of the cobble substrate and water .....	194
Table 47: Thermophysical characteristics used to calibrate the streambed heating model in the cobble reach for the Probe 1 to 3 sites. ....	195
Table 48: Fraction of water temperature used to calibrate the streambed temperature predictions at the Probe 1 and Probe 2 sites.....	196
Table 49: Model-data streambed temperature error statistics for the Probe 1 site.....	196
Table 50: Model-data streambed temperature error statistics for the Probe 2 site.....	200
Table 51: Fraction of water temperature used to calibrate the streambed temperature predictions at the Probe 3 site. ....	203

Table 52: Model-data streambed temperature error statistics for the Probe 3 site.....	204
Table 53: Thermophysical characteristics of the gravel substrate and plastic bucket	209
Table 54: Model-data streambed temperature error statistics for the gravel substrate. .....	209
Table 55: Thermophysical characteristics of the sand substrate and plastic bucket ..	211
Table 56: Model-data streambed temperature error statistics for the sand substrate.	211
Table 57: Thermophysical characteristics of the gravel and sand substrate and plastic bucket .....	214
Table 58: Model-data streambed temperature error statistics for the gravel and sand substrate.....	214
Table 59: Thermophysical characteristics of the sand substrate and plastic bucket ..	215
Table 60: Model-data streambed temperature error statistics for the sand substrate.	216
Table 61: Thermophysical characteristics of the black painted concrete and plastic bucket. ....	217
Table 62: Model-data streambed temperature error statistics for the black painted concrete. ....	218
Table 63: Thermophysical characteristics of the white painted concrete and plastic bucket. ....	219
Table 64: Model-data streambed temperature error statistics for the white painted concrete. ....	219
Table 65: Thermal diffusivity values for the simple case model application substrate. .....	228

Table 66: 3-D Model-Analytical Model streambed temperature difference statistics for Cartesian coordinate system, 100% rock. ....	228
Table 67: 3-D Model-Analytical Model streambed temperature difference statistics for Cartesian coordinate system, 50% rock and 50% water. ....	229
Table 68: 3-D Model-Analytical Model streambed temperature difference statistics for Cartesian coordinate system, 100% water.....	231
Table 69: 3-D Model-Analytical Model streambed temperature difference statistics for cylindrical coordinate system, 100% rock. ....	232
Table 70: 3-D Model-Analytical Model streambed temperature difference statistics for cylindrical coordinate system, 50% rock and 50% water. ....	233
Table 71: 3-D Model-Analytical Model streambed temperature difference statistics for cylindrical coordinate system, 100% water.....	235
Table 72: Analytical Model-data streambed temperature error statistics for Probe 5, bedrock. ....	237
Table 73: Thermophysical characteristics of the bedrock substrate for 1-D and 3-D models .....	243
Table 74: 1-D Model-data streambed temperature error statistics for Probe 5, bedrock. ....	243
Table 75: Vertical and Lateral temperature gradients in the bedrock streambed.....	249
Table 76: Vertical and Lateral temperature gradients in the cobble streambed.....	249
Table 77: Vertical and Lateral temperature gradients in the bedrock streambed model. ....	250

Table 78: Volume-weighted water temperatures at RM 4.88 over the model simulation period with and without a streambed heating model.....	254
Table 79: Daily minimum and maximum water temperature model results for various constant flows with and without a streambed heating model.....	255
Table 80: Daily minimum and maximum water temperature model results for various constant flows and varying substrates with and without a streambed heating model.....	267
Table 81: Temporal averages of daily streambed heat fluxes for different substrates and flow rates. ....	271
Table 82: Daily minimum and maximum water temperature model results for various constant flows and effective shade with and without a streambed heating model. ....	273
Table 83: Criteria for determining sunward bank.....	280
Table 84: Equation references for solar radiation models compared.....	308
Table 85: Site locations and details for the seventeen monitoring sites and their data sources.....	310
Table 86: EPA (1971) – Meeus (1999) and Bird and Hulstrom (1981) solar altitude and radiation comparisons.....	312
Table 87: Empirical coefficients which provided the smallest model-data error statistics.....	314
Table 88: Model-data error statistics for 2,726 clear-sky days at 17 sites.....	315

Table 89: Model-data error statistics for 17 sites in the U.S. with 2,726 clear-sky days. .....	316
Table 90: Empirical coefficients which provided the smallest model-data mean error statistics for 16 sites in April.....	318
Table 91: Model-data error statistics for 16 sites calibrated in April and applied to all the data .....	318
Table 92: Empirical coefficients which provided the smallest model-data mean error statistics for 15 sites in 2001.....	320
Table 93: Model-data error statistics for 15 sites calibrated in 2001 and applied to 2002.....	320
Table 94: Empirical coefficients which provided the smallest model-data mean error statistics for clear-sky days in April at Aurora, Oregon.....	321
Table 95: Model-data error statistics for April and September at Aurora, Oregon ...	322
Table 96: Meeus (1999) and Bird and Hulstrom (1981) model input year sensitivity analysis results.....	323
Table 97: Klein (1948) model and Meeus (1999) and Bird and Hulstrom (1981) model input dew point temperature annual sensitivity.....	325

## Notation

### Solar Formulation

$\varphi_s$	clear-sky solar radiation (direct and diffuse) at the ground surface, $\text{W/m}^2$ .
$A_o$	solar altitude (uncorrected), degrees.
$\psi$	latitude, degrees.
$\delta$	solar declination angle, radians.
$H$	local hour angle, radians.
$h_l$	local hour, hours.
$\gamma$	standard meridian, degrees
$\gamma_l$	longitude, degrees.
$h_e$	equation of time, hours.
$Jday$	Julian day as a floating-point value on a scale of 1 to 365 days for a year (366 for a leap year), days.
$h_{TZ}$	time zone relative to Greenwich Mean Time, hours.
$\tau_d$	angular fraction of the year, radians.
$\varphi_{ext}$	extraterrestrial solar radiation, $\text{W/m}^2$ .
$a'$	mean atmospheric transmission coefficient for a cloudless, dust-free, moist air after scattering, dimensionless.
$a''$	mean atmospheric transmission coefficient for cloudless, dust-free, moist air after scattering and absorption, dimensionless.
$d$	atmospheric dust, dimensionless.
$R_g$	ground surface reflectivity (or albedo), dimensionless.
$\varphi_o$	solar constant, $\text{W/m}^2$ .
$E_o$	eccentricity correction, dimensionless.
$r_o$	average distance between the Earth and the sun, 1 AU, Astronomical Unit.
$r$	distance between the Earth and the sun at any given time, AU.
$m_p$	relative optical air mass, dimensionless.
$w$	precipitable water content in the atmosphere, cm.
$z$	elevation, meters.

$T_{dpt}$	dew point temperature, degrees Celsius.
$d_s$	atmospheric dust scattering of solar radiation, dimensionless.
$d_a$	atmospheric dust absorption of solar radiation, dimensionless.
$\alpha_1$	coefficient dependent on the fraction of cloud cover, dimensionless.
$\beta_1$	coefficient dependent on the fraction of cloud cover, dimensionless.
$a_h$	hourly average atmospheric transmission coefficient, dimensionless.
$a_t$	daily atmospheric transmission coefficient, dimensionless.
$\varphi_d$	direct solar radiation on a horizontal ground surface, $W/m^2$
$\varphi_l$	scattered solar radiation on a horizontal ground surface, $W/m^2$
$r_s$	atmospheric albedo, dimensionless.
$T_A$	transmittance of aerosol absorptance and scattering, dimensionless.
$T_w$	transmittance of water vapor, dimensionless.
$T_{UM}$	transmittance of uniformly mixed gases, dimensionless.
$T_o$	transmittance of ozone content, dimensionless.
$T_R$	transmittance of Rayleigh scattering in the atmosphere, dimensionless.
$B_a$	ratio of forward-scattered irradiance to the total scattered irradiance due to aerosols, dimensionless.
$T_{AA}$	transmittance of aerosol absorptance, dimensionless.
$K_1$	empirical absorptance coefficient, dimensionless.
$\tau_A$	overall atmospheric turbidity, dimensionless.
$\tau_{A0.38\mu m}$	aerosol optical depth from the surface in a vertical path at 380 nm wavelength (no molecular absorption), dimensionless.
$\tau_{A0.5\mu m}$	aerosol optical depth from the surface in a vertical path at 500 nm wavelength (ozone absorption), dimensionless.
$X_o$	amount of ozone in a slanted path, cm.
$U_o$	ozone content in the atmosphere, cm.
$A'$	empirical coefficient for calculating the ozone content in the atmosphere, atm-cm.
$C'$	empirical coefficient for calculating the ozone content in the atmosphere, atm-cm.
$F'$	empirical coefficient for calculating the ozone content in the atmosphere, days.
$H'$	empirical coefficient for calculating the ozone content in the atmosphere, dimensionless.
$P'$	empirical coefficient for calculating the ozone content in the atmosphere, degrees.
$B'$	empirical coefficient for calculating the ozone content in the atmosphere, dimensionless.

$X_w$	precipitable water content in a slanted path, cm
$A_{0-corrected}$	corrected solar altitude to account for light bending when hitting the atmosphere, degrees.
$RC$	atmospheric refraction correction, degrees.
$e$	eccentricity of earth's orbit, dimensionless.
$v$	true anomaly of the sun, degrees.
$M$	geometric mean anomaly of the sun, degrees.
$c$	center for the sun, degrees.
$h_{ist}$	true solar time, minutes
$\theta_{LO}$	geometric mean longitude of the sun, degrees.
$\varepsilon_p$	corrected obliquity of the ecliptic, degrees.
$\chi$	ecliptical (celestial) latitude
$t$	Julian centuries since the epoch 2000
$\lambda$	apparent longitude of the sun, degrees.
$\varepsilon_0$	mean obliquity of the ecliptic, degrees.
$\theta_{TLO}$	true longitude of the sun, degrees.
$JD$	Julian Ephemeris Day (based on a continuous count of days since the beginning of the year -4712)
$t_{yr}$	year based on the Gregorian calendar.
$t_{mn}$	month based on the Gregorian calendar.
$t_{dd}$	decimal day for the day and fraction of the day, days.
$t_{day}$	integer day of the month from the Gregorian calendar, days.
$S$	sensitivity of solar radiation, dimensionless.
$A_z$	solar azimuth angle, degrees
$\varphi_c$	solar radiation considering the effects of cloud cover
$C$	cloud cover, scale of 1 to 10

### Dynamic Shade Algorithm

$\phi_0$	river segment (model segment) orientation angle, degrees
$H_v$	vegetation height, meters
$S_v$	vegetation shadow length, meters
$S_w$	the length of the shadow cast over the water, meters
$D_{vw}$	distance from vegetation to edge of water, meters
$S_p$	shadow length perpendicular to the edge of the water, meters

$S_{RF}$	shade reduction factor, a function of vegetation density and extent along length of river (or model) segment, dimensionless
$S_{fact}$	the fraction of water surface that is covered by shade, dimensionless
$B_w$	the wetted river channel width, meters
$\varphi_{effective}$	effective solar radiation striking the water surface after shading

### Streambed Heating Algorithm

$\beta$	streambed thermal diffusivity, $m^2/s$
$k$	streambed thermal conductivity, $W/m \text{ } ^\circ C$
$\rho_s$	streambed density, $kg/m^3$
$c_{ps}$	streambed specific heat, $J/kg \text{ } ^\circ C$
$\rho_s c_{ps}$	streambed volumetric heat capacity, $J/m^3 \text{ } ^\circ C$
$T$	streambed temperature, $^\circ C$ (also represented as $T_{i,j,k}^n$ )
$T_w$	bulk water temperature, $^\circ C$
$\tau$	change in time from initial time, days to seconds
$\gamma_{i+1,j,k}$	forward difference weighting of the thermal diffusivity in the x direction (Cartesian coordinate system), 1/seconds
$t$	time, seconds
$\Delta t$	time step for streambed numerical model, seconds
$\varphi_{at}, \varphi_{z_1=0}$	solar radiation attenuated through the water column reaching the water-streambed interface, $W/m^2$
$h$	the heat convection coefficient, $W/m^2 C$
$D_z$	thermal diffusivity of water, $m^2/s$
$\delta_w$	thermal laminar layer thickness above which the water temperature is equal to the bulk water temperature, m
$T_{int}$	streambed temperature at the water-streambed interface
$\Gamma$	Sum of the spatial streambed temperature terms with their respective difference weighting of the thermal diffusivities (Cartesian coordinate system), $^\circ C$
$L$	the maximum depth of the streambed, m
$T_b$	the bottom surface boundary condition temperature, $^\circ C$
$W$	the maximum width of the streambed, m
$x, y, z$	Cartesian coordinate system
$r, \phi, z$	cylindrical coordinate system

$\sigma_{i+1,j,k}$	forward difference weighting of the thermal diffusivity in the radial direction (cylindrical coordinate system), 1/seconds
$\Omega$	Sum of the spatial streambed temperature terms with their respective difference weighting of the thermal diffusivities (cylindrical coordinate system), °C
$R$	the maximum radius of the model grid, m
$T_{b2}$	the side surface boundary condition temperature (cylindrical coordinate system), °C
$T_o$	surface water temperature for analytical solution to simple case, °C
$\alpha$	convection coefficient for the vertical water velocity in the substrate, m/s
$\Delta T_w$	the change in water temperature over an increment in time, °C
$\Delta T$	the change in the streambed temperature for the specific depth over an increment in time, °C
$z_1$	depth below water surface, m
$q$	heat flux, W/m <sup>2</sup>
$\Delta H_1$	change in heat content of streambed over a time period, J/m <sup>2</sup> °C
$H_t$	heat content of streambed at a specific time, J/m <sup>2</sup> °C

### Meteorology

$T_a$	air temperature, °C
$RH$	relative humidity of the air, percentage from 0 to 100

### Light Attenuation

$I_o$	incident solar radiation at the water surface, equivalent to $\phi_c$ , W/m <sup>2</sup>
$I_{z_1}$	solar radiation at depth, $z_1$ , W/m <sup>2</sup>
$\eta_1$	light extinction coefficient, surface water losses, m <sup>-1</sup>
$\eta_2$	light extinction coefficient, deep water losses, m <sup>-1</sup>
$\beta$	fraction of radiation absorbed in the first 0.6 m below the water surface (dimensionless)
$z_o$	depth at the water surface and by definition: $z_o = 0$ , meters

## Flow Measurements

$Q_{total}$	total river flow, m <sup>3</sup> /s
$u_{i,top}$	near surface water velocity measurement from river cross section piece, m/s
$u_{i,bottom}$	near bottom water velocity measurement from river cross section piece, m/s
$b_i$	river cross section piece width, meters
$d_i$	river cross section piece depth, meters
$d_{i-1/2}$	river depths at one-half the distance, between the flow measurements, meters
$d_{i+1/2}$	river depths at one-half the distance, between the flow measurements, meters

## **1. Introduction**

The State of Oregon, Department of Environmental Quality (ODEQ) is developing total maximum daily loads (TMDLs) to address water quality concerns and threatened and endangered species habitat requirements in water bodies throughout Oregon. Approximately 940 water body segments in Oregon are listed as water quality limited for stream temperature (ODEQ, 1998a). The State temperature standards for water quality limited streams were developed to protect the most sensitive beneficial uses of Oregon streams (ODEQ, 1998b). In many cases the most sensitive beneficial use is protecting threatened and endangered salmonid species. The main stem of the Willamette River and its larger tributaries are currently water quality limited for temperature and ODEQ is leading the process to develop a temperature TMDL for 945 river km (ODEQ, 2001).

The State has upgraded its temperature modeling abilities by using the model Heat Source (ODEQ, 1999), a one-dimensional hydrodynamic and temperature model that accounts for the impact of riparian vegetative shading and topographic shading on stream temperature. One important aspect of the modeling effort for stream temperature is how to model the short-wave solar radiation that penetrates the water surface and impacts the streambed substrate. Temperature predictions can be affected significantly under low-flow stream conditions, depending on how the solar radiation is modeled. The purpose of this research is to develop an algorithm based on field data

that accurately accounts for streambed temperature processes and to implement it in the model CE-QUAL-W2 (Cole and Wells, 2000).

The goal of this research is to examine the influence of streambed heating on stream water temperatures and incorporate a dynamic streambed heating algorithm in the CE-QUAL-W2 water quality model.

The Bull Run system provides an opportunity to study streambed heating because the system is already well understood and a preliminary model (Annear et al. 1999) has already been developed for the river under study.

## **1.1 Bull Run**

The Bull Run River-Reservoir system is a 264 km<sup>2</sup> watershed located 41.8 km east of downtown Portland as shown in Figure 1. The watershed consists of two reservoirs, Reservoirs #1 and Reservoir #2, Bull Run Lake and river sections above and below the reservoirs as shown in Figure 2. The reservoirs serve as the primary drinking water source for over 790,000 people in the Portland metropolitan area (Water Bureau, 2002a). In addition to supplying drinking water, both reservoirs are used for generating approximately 88.5 Million kW-h (Water Bureau, 2002b) of hydropower annually.

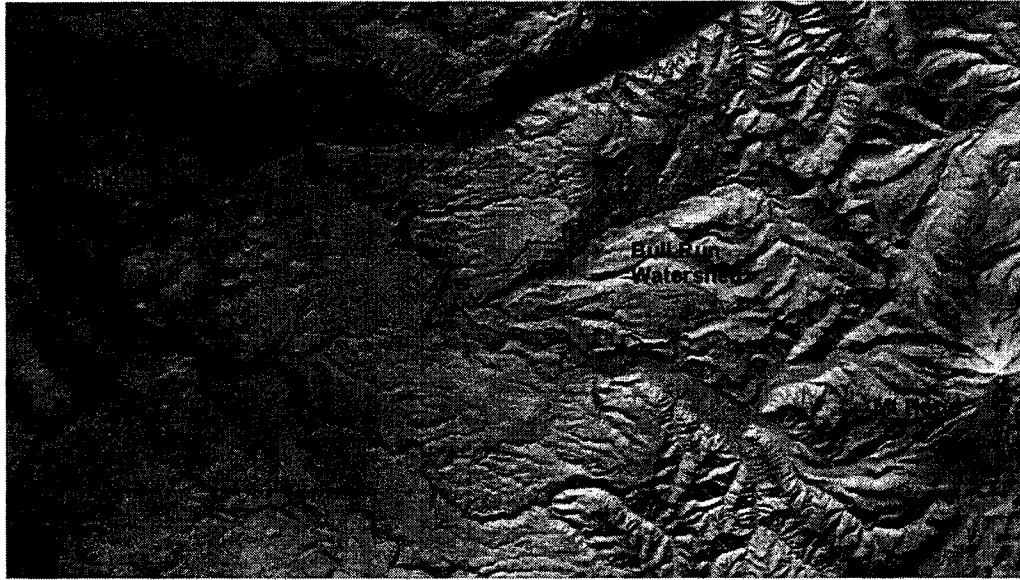


**Figure 1: Bull Run Watershed in NW Oregon**

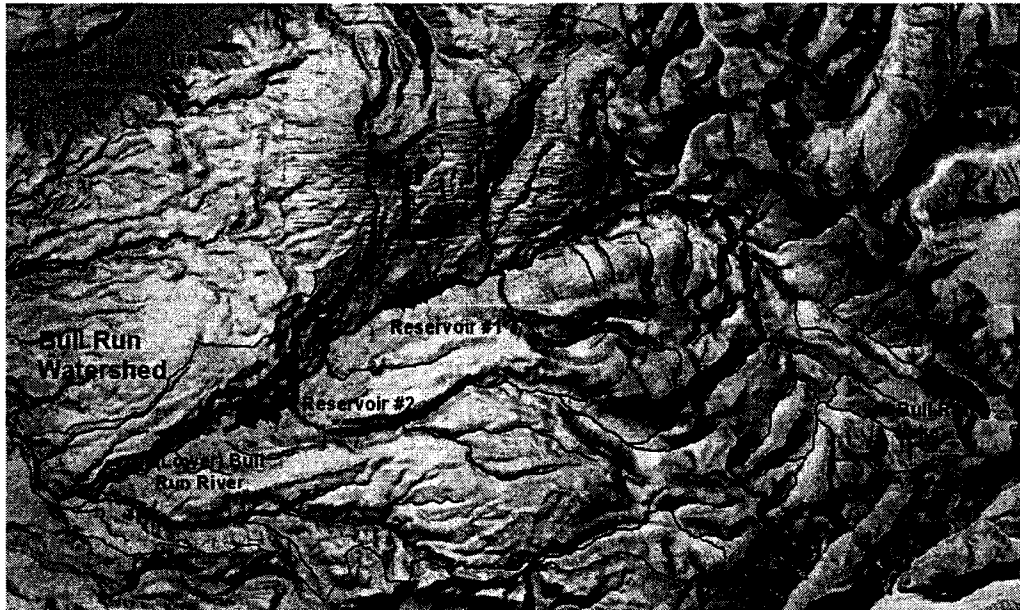


**Figure 2: Bull Run River-Reservoir system**

Historical reservoir operations did not send water downstream from Reservoir #2 to the Lower Bull Run River, resulting in low in-stream flows and temperatures that violated State standards. In March 1998 Steelhead and in March 1999 Spring

Chinook salmon were listed as threatened in the Lower Columbia Evolutionary Significant Unit, which includes the Sandy River Basin and the Bull Run River (National Marine Fisheries Service, Federal Register 1998, 1999). Stream temperatures in the Lower Bull Run River were found to be in violation of the State of Oregon's water quality standard of the seven-day moving average of the daily maximum stream temperature should not exceed 17.8 °C (Oregon Administrative Rules: 340-041). Recent work funded by the City of Portland, Water Bureau investigated modeling the system to develop management strategies to reduce stream temperatures in the summer (Annear and Wells, 2000). The low flows during the summer resulted in a narrower wetted channel but the overall disturbed stream channel would remain wide-open to solar radiation, vegetative and topographic shading, and streambed heating. Streambed heating or cooling is defined as the component of a water body heat budget accounting for conductive heat transfer between the streambed and the overlying water column as shown in Figure 3. During the day there can be conductive heat gains or losses, as well as short-wave solar radiation heating of the streambed. As the sun goes down and stream temperatures cool, the heat stored in the streambed can then be transferred via conduction with the overlying water column.

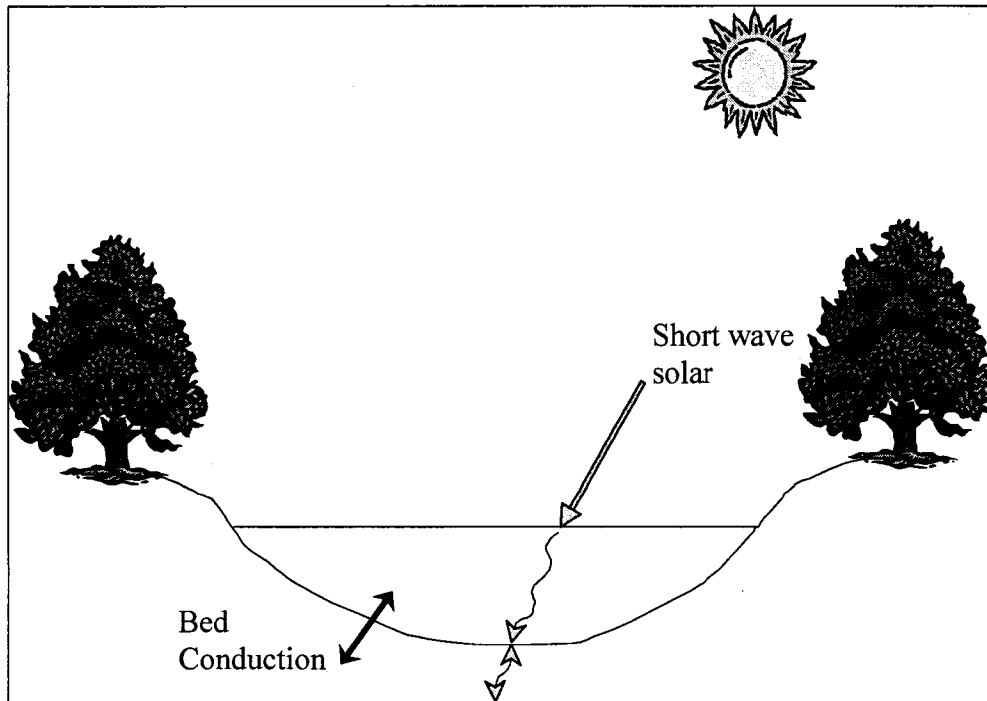


**Figure 3: Schematic of short-wave solar penetration to the streambed and conductive transfer from bed to water and vice-versa.**

Annear and Wells (2000) used the CE-QUAL-W2 Version 3 model to simulate water temperatures in the Lower Bull Run River. Version 3 is an improvement over CE-QUAL-W2 Version 2 (Cole and Buchak, 1995), which allows sloping stream channels to be modeled. CE-QUAL-W2 consists of directly coupled hydrodynamic and water quality transport models and simulates parameters such as temperature, algae concentration, dissolved oxygen concentration, pH, nutrient concentrations and detention time. Figure 4 shows the W2 model surface heat components in the heat balance. The model also includes the effects of shading from vegetation and topography.

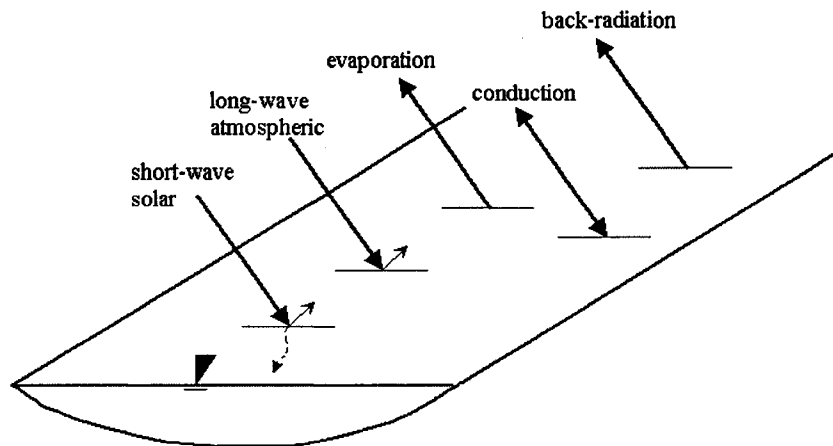


**Figure 4: Components of surface heat transfer**

The current CE-QUAL-W2 V3 (W2) model of the Lower Bull Run River does not account for dynamic streambed heating impacts on stream temperatures. Streambed heating is primarily of concern in shallow, clear streams exposed to abundant solar radiation. Currently, W2 has an algorithm for streambed conductive heating, but it assumes a constant streambed temperature and a constant exchange coefficient. W2 also has an algorithm that handles the short-wave solar radiation reaching the streambed by either immediately re-transmitting the energy back into the water column or is lost to the streambed. The fraction lost to the streambed is also lost to the model system and has no influence on the heat budget. Both aspects of the current W2 streambed heating model approach do not account for dynamic streambed heating, which can diminish temperature maximums and increase temperature minimums.

## 1.2 Research Objectives

The objectives of this research are:

- Monitor streambed temperatures in the Lower Bull Run River to characterize:
  1. Vertical temperature gradients in streambeds with different substrates such as cobble and bedrock;
  2. Longitudinal temperature variability by monitoring one site downstream of another in cobble substrate; and
  3. Lateral temperature variability by monitoring two parallel sites in cobble and bedrock substrates.
- Monitor environmental factors influencing the river heat budget such as:
  1. Meteorological conditions;
  2. Shade characteristics;
  3. Light attenuation characteristics; and
  4. Substrate geologic characteristics.
- Collect bathymetric cross section data to support model development.
- Conduct experimental lab work in a controlled environment to reduce the influence of wind, variable flow, and uncertainties with the substrate material. The experimental work will also be used to demonstrate heating processes expected in the field.
- Develop a streambed heating algorithm for incorporation in the water quality model, CE-QUAL-W2.

- Calibrate the streambed heating model for the time period when field data were collected.
- Run sensitivity analyses with the streambed heating algorithm in CE-QUAL-W2 to determine the relative impact on stream temperatures using a larger spatial scale.
- Use the model to identify any criteria when streambed heating might have a significant role in the heat budget, such as low stream flows.
- Review and compare the solar radiation formulation in the CE-QUAL-W2 with other formulations and identify if other models provide a better formulation when compared with data.

## **2. Literature Review**

The importance of streambed heating has been documented by many researchers evaluating shallow streams. Brown (1969) and Pluhowski (1970) both showed that streambed heating can be important for predicting diurnal temperatures in shallow streams. Jobson (1977) showed that the importance of heat conduction relative to other energy exchange terms increases as the diurnal variation of the stream temperature increases. Sinokrot and Stefan (1994) showed the average daily stream temperature is not sensitive to streambed heat exchange but is important for prediction of hourly stream temperatures or daily maximums. Kim and Chapra (1997) noted the streambed heating term can be important in predicting both the diurnal and the annual variation of stream temperature in streams with depths less than 3 m. Chen et al. (1998) showed that the effect of streambeds is to decrease daily maximums and to increase daily minimums.

In modeling streambed-heating processes, both Sinokrot and Stefan (1993) and Chen et al. (1998) showed that for shallow streams the streambed-heating component is a significant part of the overall heat balance for the stream, being of the same order of magnitude as all the other heat flux components (conduction, evaporation, net long-wave radiation) except solar radiation flux.

Conclusions of recent work in modeling temperatures in shallow streams by Sinokrot and Stefan (1993), Chen et al. (1998), and Kim and Chapra (1997) are that

streambed heating (see Figure 3) is an essential component of shallow-stream modeling and is essential for diurnal temperature prediction.

## 2.1 Modeling Approaches

Temperature modeling approaches including bed conduction have been:

1. A simplified analytical model of the bed temperature distribution where heat is transferred only by conduction from the water to the bed [Jobson (1977), Chen et al. (1998), Silliman et al. (1995)]

This approach has been chosen because of its straightforward and direct computation by Chen et al. (1998) allowing less computational time. The model is limited since it assumes only one uniform sediment temperature over the assumed depth of the bed and does not account for the impact of solar radiation heating up the upper sediment layer.

2. A numerical model of the bed temperature distribution where heat is transferred only by conduction from the water to the bed [Sinokrot and Stefan (1993), Sinokrot and Stefan (1994), Fang and Stefan (1998)]

A numerical solution of the heat balance equation is used to predict the vertical profile of temperature in the bed and the flux between the water and the bed. In this case, the top of the bed is assumed to be the temperature of the water and hence does not account for the impact of solar radiation heating the upper sediment layer directly.

3. A numerical model of the bed temperature distribution where heat is transferred by conduction and by direct solar radiation onto the bed [Kim and Chapra (1997)]

This approach adds the impact of the short-wave solar radiation on the surface of the sediment. A summary of several approaches to sediment heating is shown in Table 1. In most of the streambed models, researchers have used various parameter values from their numerical and analytical model studies. A summary of these model parameters is shown in Table 2.

**Table 1: Modeling approaches for streambed heating.**

Reference	Governing Equation	Solution and boundary conditions
Silliman et al. (1995)	$\frac{\partial T}{\partial t} + \alpha \frac{\partial T}{\partial z} = \beta \frac{\partial^2 T}{\partial z^2}$ <p>where <math>T</math> is the temperature of the sediment, <math>\alpha</math> is an advective term (accounting for groundwater flow), <math>\beta</math> is the thermal diffusivity, <math>t</math> is time, <math>z</math> is elevation</p>	$T = \frac{\Delta T_w}{2} [erfc\left\{\frac{z_1 - \alpha t}{2\sqrt{\beta t}}\right\} + \exp\{\alpha z_1 / \beta\} erfc\left\{\frac{z_1 + \alpha t}{2\sqrt{\beta t}}\right\}]$ <p>where <math>\Delta T_w</math> is the temperature difference in the water over a time <math>\tau</math> from the initial time and initial temperature, and <math>z_1</math> is depth.</p>
Sinokrot and Stefan (1993), (1994); Fang and Stefan (1998)	$\frac{\partial T}{\partial t} = \beta \frac{\partial^2 T}{\partial z^2}$	<p>Finite difference implicit technique, no flux BC at <math>z_1 = L</math> and</p> $T = T_w \text{ at } z_1 = 0; \text{ flux computed from } q = -k \frac{\partial T}{\partial z} \Big _{z_1=0}$
Kim and Chapra (1997)	$\frac{\partial T}{\partial t} = \beta \frac{\partial^2 T}{\partial z^2}$	<p>Finite difference implicit technique, BC at depth <math>L</math> is no flux condition <math>q _{z_1=L} = -k \frac{\partial T}{\partial z} \Big _{z_1=L} = 0</math>, flux computed from</p> $q = -\varphi_{z_1=0} - k \frac{\partial T}{\partial z} \Big _{z_1=0}$ <p>where <math>\varphi_{z_1=0}</math> is the heat flux from solar radiation reaching the top of the streambed</p>

Reference	Governing Equation	Solution and boundary conditions
Jobson (1977)	$\frac{\partial T}{\partial t} = \beta \frac{\partial^2 T}{\partial z^2}$	<p><math>q = \sum \Delta T_w \Delta H_1</math> where <math>q</math> is the heat flux to the water from the bed, <math>\Delta T_w</math> is the change in water temperature over a time period, <math>\Delta H_1</math> is the change in response of the slab over a time period per unit change in water temperature</p> $\Delta H_1 = H_t - H_{t+\Delta t} = \rho c_p L$ $\left( 1 - \frac{8}{\pi^2} \sum_{n=0}^{\infty} \frac{(-1)^n}{(2n+1)^2} \exp\left[ \frac{-\beta(2n+1)^2 \pi^2 t}{4L^2} \right] \sin\left[ \frac{(2n+1)\pi}{2} \right] \right)$ <p><math>\beta</math> is the thermal diffusivity, <math>L</math> is the depth of the slab</p>

**Table 2: Streambed heating model parameters from literature**

Reference	Thermal diffusivity, $\beta: \beta = \frac{k}{\rho_s c_{ps}}$	Thermal conductivity, $k$	Volumetric heat capacity $\rho_s c_{ps}$	Depth at which T is constant, L	Description
Fang and Stefan (1998)	0.035 m <sup>2</sup> /d		2.3E6 J/m <sup>3</sup> /°C	10 m	Lake sediment study, determined by calibration
Fang and Stefan (1998)	0.01-0.11 m <sup>2</sup> /d		1.4E6-3.8E6 J/m <sup>3</sup> /°C		Literature reported range and is a function of sediment composition
Sinokrot and Stefan (1993)				6 m	Did not report calibration values
Silliman et al. (1995)	0.0046 cm <sup>2</sup> /s	0.0023 cal/cm/s/°C	0.5 cal/cm <sup>3</sup> /°C		Taken from Carslaw and Jaeger (1959)
Jobson (1977)	0.01 cm <sup>2</sup> /s (range of 0.006 to 0.2 cm <sup>2</sup> /s were not found to be sensitive to the model results)		0.55 cal/cm <sup>3</sup> /°C	0.25 m (using one slab temperature model)	Concrete lined channel
Jobson (1977)	0.0077 cm <sup>2</sup> /s		0.68 cal/cm <sup>3</sup> /°C		Sand bed, Braslavski et al. (1963)
Chen et al. (1998)	1.18E-6 m <sup>2</sup> /s or 0.0118 cm <sup>2</sup> /s		1.491E6 J/m <sup>3</sup> /°C or 0.356 cal/cm <sup>3</sup> /°C	10.33 m	Homogeneous rock

Reference	Thermal diffusivity, $\beta: \beta = \frac{k}{\rho_s c_{ps}}$	Thermal conductivity, $k$	Volumetric heat capacity $\rho_s c_{ps}$	Depth at which T is constant, L	Description
Kim and Chapra (1997)	3E-7 m <sup>2</sup> /s		795.2 J/kg/°C	0.6 m (chosen since penetration depth of heat was only about 0.25 m for the diurnal case)	Sand – dry, density of dry sand was 1750 kg/m <sup>3</sup>
Kim and Chapra (1997)	9E-7 m <sup>2</sup> /s		799.8 J/kg/°C	0.6 m	Stone density was 2500 kg/m <sup>3</sup>
Pluhowski (1970)		0.00394 cal/cm/s/°C		18.3 m estimated	Water saturated sands and gravel mixtures

15

Note:  $\beta$  is the thermal diffusivity,  $k$  is the thermal conductivity,  $\rho$  is the density, and  $c_p$  is the specific heat of the streambed

## 2.2 Streambed Study Characteristics

Prior streambed studies used predominately 1-dimensional (1-D) longitudinal models for river study lengths ranging from 0.4 km to 48.2 km. The streambed substrates were characterized by mud, sand, gravel, rocks and solid breccia substrates. Flows varied considerably from 0.01 to 351 m<sup>3</sup>/s and water depths varied from 0.2 to 13.0 m. Although the lake studies by Fang and Stefan (1996 and 1998) were year round, many of the studies focused on the summer when stream temperatures were warmer, solar radiation had more influence, and shading from vegetation was present. Table 3 list some of the previous studies and shows some of their limitations.

Table 4 lists the heat budget components covered in the heat transport models. Brown (1969) and Pluhowski (1970) used meteorological data measured on site for each of the stream reaches studied. Other studies used local meteorological data combined with meteorological data from sites outside the study area. Lake studies by Fang and Stefan (1996 and 1998) used ice and snow cover in their heat budgets. The river studies did not consider ice and snow since these were less important in moving water and ice impacts are usually not important for critical temperature conditions for fish. Shading from vegetation was considered in several studies, and a few incorporated shading from man-made structures along the banks, but there was little or no discussion of incorporating topographic shading.

**Table 3: Streambed study characteristics**

Reference	Model Time step	Description	Study Size	Time duration	Substrate	Limitations	Water Depth, m	Flow, m <sup>3</sup> /s
Fang and Stefan (1996)	1 day	Lake sediment study (27), 1-D vertical model, theoretical lake classes	1.7 km <sup>2</sup>	Model: Year round	NA	Daily time step	13, max	Does not apply
Fang and Stefan (1998)	1 day	1-D vertical model, Ryan Lake, Minnesota	0.061 km <sup>2</sup>	Model: Year round Data: Nov to April	Sand to very organic materials	Daily time step	5, ave 11, max	Does not apply
Sinokrot and Stefan (1993)	1 hour	Stream 1-D longitudinal model, Straight, Baptism, Clearwater, Zumbro and Mississippi Rivers in Minnesota	4.4 to 48.2 km	Model: 9 months, Data: September 7 to October 7	Sand, gravel, organic mud and rocks	Daily average meteorological conditions	0.3 - 1	1.5 – 351, daily
Sinokrot and Stefan (1994)	1 day	Stream 1-D longitudinal model, Sensitivity analysis of meteorological conditions and streambed conduction	NA	June-August	NA	Daily average meteorological conditions	NA	NA

Reference	Model Time step	Description	Study Size	Time duration	Substrate	Limitations	Water Depth, m	Flow, m <sup>3</sup> /s
Brown (1969) Brown (1972)	1 hour	3 streams in Oregon (assumed 1 1-D longitudinal model)	396 – 610 m	Model: 1 day, Data: Sept 1, May 20, May 20 - 21	Solid green-breccia, gravel	1-D model only done on discrete 1 days periods	NA	0.01-0.02
Silliman et al. (1995)	NA	Stream 1-D longitudinal model, Juday Creek, Indiana	NA	Data: August 6 - 22	NA	Extent of meteorological data and model time step are unknown	NA	0.3 – 0.71
Jobson (1977)	<Daily	Canal in Southern California	26 km	Model and Data: 141 days	Concrete		3, max	NA
Jobson (1977)	<Daily	Chattahoochee River, GA	28 km	Model: 6 days, October and 4 days in March	Saturated Sand	Meteorological conditions not described	1.0 – 2.9	16 - 230
Jobson and Keefer (1979)	5 min	Stream 1-D longitudinal model, Chattahoochee River, GA	28 km	Model: 6 days, October and 4 days in March	Saturated Sand	Flow, transport and temperature models were run independently	1.1 – 2.2	NA

Reference	Model Time step	Description	Study Size	Time duration	Substrate	Limitations	Water Depth, m	Flow, m <sup>3</sup> /s
Chen et al. (1998)	1 hour	Stream 1-D longitudinal model, Grande Ronde River, OR	15 km	Streambed evaluation: August 6, 1991; Modeled 1991-1992	Homogeneous rock	Assumed all solar radiation absorbed by water		
Kim and Chapra (1997)	2 min	Stream 1-D longitudinal model, Boulder Creek, CO	13.7 km	Model: 24 hours, September 20 - 21	Dry Sand (test) Stone for application	Hydrodynamic and heat transport modules are run independently	0.2 – 0.6 m	0.71
Hondzo and Stefan (1994)	Daily	Stream 1-D longitudinal model, Rum River	NA	Model and Data: September 7 to October 7	Medium sand	Daily values misses diurnal effects	NA	NA
Pluhowski (1970)	8 hour	Stream 1-D longitudinal model, 5 reaches of Connetquot River, Long Island, NY	692 – 885 m	Model and Data: 7-day period in June	Saturated sand and gravel mixtures		NA	0.05 – 0.5

Reference	Model Time step	Description	Study Size	Time duration	Substrate	Limitations	Water Depth, m	Flow, m <sup>3</sup> /s
Comer et al (1975)	NA	Stream 1-D longitudinal model, Spawn Creek in NW Utah	NA	Data: August to May, presented only 6 24 hour snapshots during this period	39% sand, 61% gravel	Considerable groundwater inflow	0.2	0.28

**Table 4: Heat budget components**

Reference	Solar Radiation	Evaporation	Streambed Conduction	Air Temperature	Wind Speed	Relative Humidity	Precipitation	Ice Cover	Shading	Cloud Cover
Fang and Stefan (1996)	Yes	Yes	Yes	Yes	Yes	Yes	Snowfall & rainfall	Yes	No	NA
Fang and Stefan (1998)	Yes	Yes	Yes	Yes	Yes	Yes	Snowfall & rainfall	Yes	No	NA
Sinokrot and Stefan (1993)	Yes	Yes	Yes	Yes	Yes	Yes	No	No	Vegetation	Yes
Sinokrot and Stefan (1994)	Yes	Yes	Yes	Yes	Yes	Yes	No	No	Vegetation	Yes
Brown (1969) Brown (1972)	Yes	Yes	Yes	Yes	Yes	Yes	No	NA	Vegetation and topography (?)	NA
Jobson and Keefer (1979)	Yes	Yes	Yes	Yes	Yes	Yes	Yes	No	Vegetation and man-made structures	NA
Kim and Chapra (1997)	Yes	Yes	Yes	Yes	Yes	Yes	Yes	No	No	NA

Reference	Solar Radiation	Evaporation	Streambed Conduction	Air Temperature	Wind Speed	Relative Humidity	Precipitation	Ice Cover	Shading	Cloud Cover
Silliman et al. (1995), Hondzo and Stefan (1994), and Jobson (1977)	NA	NA	NA	NA	NA	NA	NA	NA	NA	NA
Chen et al. (1998)	Yes	Yes	Yes	Yes	Yes	Yes	Yes	Yes	Yes	Yes
Pluhowski (1970)	Yes	Yes	Yes	Yes	Yes	Yes	No	No	Vegetation and man-made structures	NA
Comer et al. (1975)	Yes	Yes	Yes	Yes	Yes	Yes	NA	NA	NA	Yes
NA: Not available										

### 2.3 Streambed Temperature Monitoring Approaches

Some researchers have monitored streambed temperatures in the field while others have relied on previous studies to utilize existing mathematical relationships to model streambed heating without field studies. Kim and Chapra (1997), Jobson (1977) and Jobson and Keefer (1979) did not collect streambed temperature data. Streambed temperatures were estimated using either annual mean air temperature or historical stream temperature records. Table 5 provides a list of the studies with streambed monitoring and some details of the study methodology.

**Table 5: Streambed monitoring studies**

Reference	Depth of instruments	Number of measurement points	Equipment	Frequency of data collection
Fang and Stefan (1998)	0.5, 1.0 and 1.5 m	3	NA	Every 2 min, ave over 20 min
Sinokrot and Stefan (1993) and Hondzo and Stefan (1994)	0.0 – 1.8 m	9 (Rum River)	NA	Every 2 min, ave over 20 min
Brown (1969) Brown (1972)	Pairs of thermocouples placed every 1 cm within rocks places in stream	NA	Thermocouples placed in gravel or drilled holes in bedrock	10 min,
Silliman et al. (1995)	0.14 m	1	NA	1 hour

Reference	Depth of instruments	Number of measurement points	Equipment	Frequency of data collection
Pluhowski (1970)	0.30 – 2.13 m	7	Wells drilled for each depth and water pumped for 5 minutes before measuring temperature	NA
Comer et al (1975)	0.03, 0.16, 0.40 and 1.0 m	4	Thermistors deployed in a PVC pipe	2 hours

Sinokrot and Stefan (1993) monitored streambed temperature on the Rum River from September to October to calibrate a streambed heating model, and then used the calibrated model on 5 different rivers over wider time ranges. There was no flow, water level or streambed characteristics provided for the Rum River to compare with the other five rivers modeled. The streambed heating algorithm was calibrated using a daily time step over 10-year period. Groundwater was not considered because the reaches were short and inflows were known.

Brown (1969 and 1972) removed large pieces of the streambed and cut into the rock to place the thermistors. He used a rock saw to cut open a piece of the streambed rock and then drilled holes every 1 cm for thermistors. Each hole was then filled with mercury and sealed with silicon. He then put the rock back together and sealed it with epoxy cement. The rock was then put back in the river. When he was monitoring gravel streambeds he simply pushed the instruments into the streambed to depth.

Comer (1975) conducted streambed temperature monitoring by placing a cylindrical probe into the streambed. His approach used thermistors in a PVC pipe

that was filled with silicon. A larger diameter metal pipe (sheath) was then used for inserting into the streambed. The PVC pipe was placed inside the metal pipe in the streambed screwed onto the cap at the bottom. The metal sheath was then unscrewed from the cap and removed from the streambed. This approach assumed the surrounding streambed material (sand and gravel) would collapse around the instrument.

## **2.4 Position of the Sun**

The solar radiation formulation used in the CE-QUAL-W2 model (EPA, 1971) was reviewed to improve the accuracy of the sun's position and the solar radiation impinging on the water surface.

### **2.4.1 Standard Meridian**

CE-QUAL-W2 (EPA, 1971) incorporates a routine that calculates the solar altitude and azimuth. The longitude,  $\gamma_l$ , and latitude,  $\psi$ , of the water body are necessary to eventually compute the solar azimuth. EPA (1971), Wunderlich (1972) and Ryan and Stolzenbach (1972) calculated the standard meridian,  $\gamma$  (degrees), of the time zone using

$$\gamma = 15.0 \left\lfloor \frac{\gamma_l}{15.0} \right\rfloor \quad (1)$$

## 2.4.2 Local Hour and Julian Day

The local hour,  $h_l$  (hours), was calculated using the time during the day (Wunderlich, 1972; Ryan and Stolzenbach, 1972; and Meeus, 1999) as

$$h_l = 24(Jday - \lfloor Jday \rfloor) \quad (2)$$

where  $Jday$  is the Julian day, representing the local day and time since the beginning of the year based on a Julian calendar of 365 days (366 for leap years).

Meeus (1999) calculated the Julian Ephemeris Day,  $JD$ , based on a continuous count of days since the beginning of the year -4712. The Julian Ephemeris Day begins at Greenwich mean noon and was calculated from the Gregorian calendar. Meeus (1999) calculated the Julian Ephemeris Day from the Gregorian calendar using

$$JD = \lfloor 365.25(t_{yr} + 4716.0) \rfloor + \lfloor 30.6001(t_{mn} + 1) \rfloor + t_{dd} + \left(2 - \lfloor t_{yr} / 100.0 \rfloor + \lfloor \lfloor t_{yr} / 100.0 \rfloor / 4.0 \rfloor\right) - 1524.5 \quad (3)$$

where  $t_{yr}$  and  $t_{mn}$  are the year and month based on the Gregorian calendar, and  $t_{dd}$  is decimal day for the day and fraction of the day. Meeus (1999) adjusted the Gregorian calendar month and year to place dates in January and February in the preceding year as the 13<sup>th</sup> and 14<sup>th</sup> months. If the month was less than or equal to 2, then  $t_{yr}$  and  $t_{mn}$  were adjusted as

$$\begin{aligned} t_{yr} &= t_{yr} - 1 \\ t_{mn} &= t_{mn} + 12 \end{aligned} \quad (4)$$

Meeus (1999) calculated the decimal day of the month using

$$t_{dd} = t_{day} + h_l/24 \quad (5)$$

where  $t_{day}$  is the integer day of the month from the Gregorian calendar and  $h_l$  is the local hour.

### 2.4.3 Solar Declination

Wunderlich (1972) and Ryan and Stolzenbach (1972) calculated the solar declination angle,  $\delta$  (degrees), using

$$\delta = 23.45 \frac{\pi}{180} \text{Cos} \left[ \frac{2\pi}{365} (172 - \lfloor Jday \rfloor) \right] \quad (6)$$

where  $Jday$  is the Julian day. The declination angle varies throughout the year but can be considered constant for a day (Ryan and Stolzenbach, 1972). The value 23.45 in Equation (6) corresponds to the obliquity of the ecliptic and is the maximum value of the solar declination. Lee (1978) used 23.5 as the obliquity of the ecliptic.

Spencer (1971) computed the declination angle,  $\delta$  (radians), as

$$\begin{aligned} \delta = & 0.006918 - 0.399912 \text{Cos}(\tau_d) + 0.070257 \text{Sin}(\tau_d) \\ & - 0.006758 \text{Cos}(2\tau_d) + 0.000907 \text{Sin}(2\tau_d) \\ & - 0.002697 \text{Cos}(3\tau_d) + 0.001480 \text{Sin}(3\tau_d) \end{aligned} \quad (7)$$

where  $\tau_d$  (radians) is the angular fraction of the year, which Spencer (1971) calculated as

$$\tau_d = \frac{2\pi(\lfloor Jday \rfloor - 1)}{365} \quad (8)$$

Woolf (1968) used a slightly different equation for the angular fraction of the year,  $\tau_d$  (radians), such as

$$\tau_d = \frac{2\pi(\lfloor Jday \rfloor - 1)}{365.242} \quad (9)$$

Solar declination data were obtained from List (1958) for comparison with the results from Equation (6) and (7). Figure 5 shows the results of Equation (6) and (7) compared to the data from List (1958). Both Equation (6) and (7) accurately follow the trend of the data, but the work of Spencer (1971) more accurately matches declination angle data throughout the year.

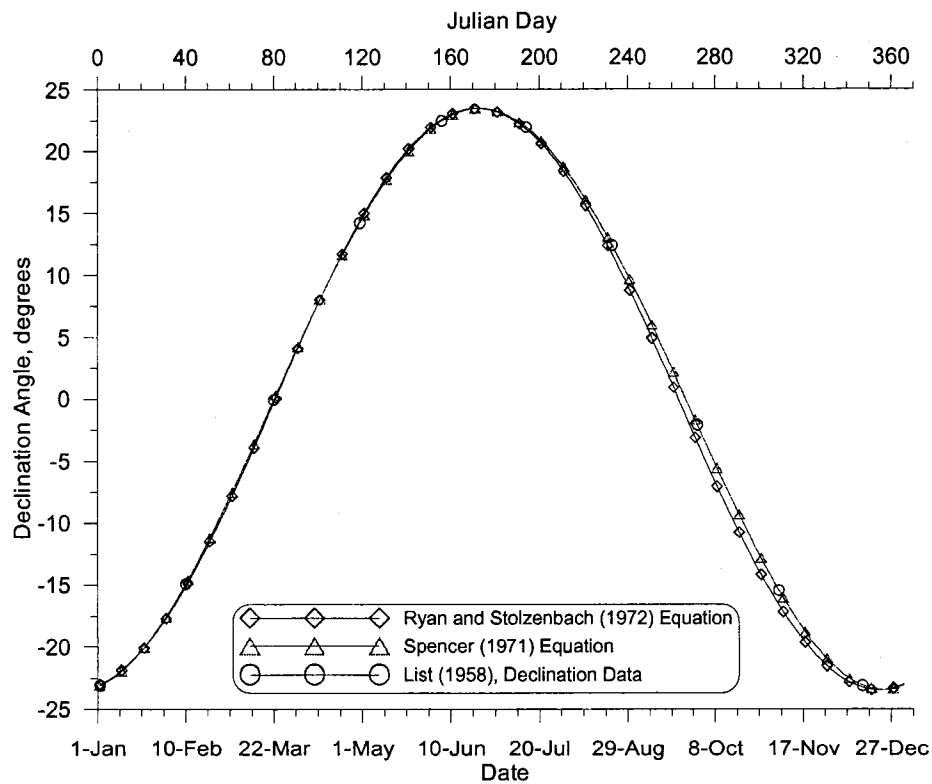


Figure 5: Declination angle, models and data

Meeus (1999) calculated the solar declination angle,  $\delta$  (degrees), using

$$\delta = \text{arcSin}(\text{Sin}(\varepsilon_p)\text{Sin}(\lambda)) \quad (10)$$

where  $\lambda$  is the apparent longitude of the sun and  $\varepsilon_p$  is the corrected obliquity of the ecliptic. Meeus (1999) also presented a more robust version of Equation (10) as

$$\delta = \text{arcSin}(\text{Sin}(\chi)\text{Cos}(\varepsilon_p) + \text{Cos}(\beta)\text{Sin}(\varepsilon_p)\text{Sin}(\lambda)) \quad (11)$$

where  $\chi$  (degrees) is the ecliptical (celestial) latitude, but the difference in solar declination between the two equations was negligible. The corrected obliquity of the ecliptic,  $\varepsilon_p$  (degrees), was calculated (Meeus, 1999) using

$$\varepsilon_p = \varepsilon_0 + 0.00256\text{Cos}(125.04 - 1934.136t) \quad (12)$$

where  $t$  is the Julian centuries and  $\varepsilon_0$  (degrees) is the mean obliquity of the ecliptic and was calculated by Meeus (1999) using

$$\varepsilon_0 = 23.0 + [26.0 + ((21.448 - t\{46.8150 + t(0.00059 - 0.001813t)\})/60)]/60 \quad (13)$$

Meeus (1999) calculated the apparent longitude of the sun,  $\lambda$  (degrees), using

$$\lambda = \theta_{TLO} - 0.00569 - 0.00478\text{Sin}(125.04 - 1934.136t) \quad (14)$$

where  $\theta_{TLO}$  (degrees), is the true longitude of the sun and was calculated as

$$\theta_{TLO} = \theta_{LO} + c \quad (15)$$

Meeus (1999) calculated the center for the sun,  $c$  (degrees), using

$$c = \text{Sin}(M)(1.914602 - t(0.004817 + 0.000014t)) + \text{Sin}(2M)(0.019993 - 0.000101t) + 0.000289\text{Sin}(3M) \quad (16)$$

where the geometric mean anomaly of the sun,  $M$  (degrees), was calculated from Meeus (1999) using

$$M = 357.52911 + t(35999.05029 - 0.0001537t) \quad (17)$$

The geometric mean longitude of the sun,  $\theta_{LO}$  (degrees), was calculated from Meeus (1999) as

$$\theta_{LO} = 280.46646 + t(36000.76983 + 0.0003032t) \quad (18)$$

If  $\theta_{LO}$  has value outside of 0 to 360 degrees then 360 degrees are added or subtracted until  $\theta_{LO}$  is within this range. Meeus (1999) calculated the Julian centuries since the epoch 2000  $t$  using

$$t = \frac{(JD - 2451545.0)}{36525.0} \quad (19)$$

where  $JD$  is the Julian Ephemeris Day.

#### 2.4.4 Equation of Time

The equation of time,  $h_e$  (hours), represents the difference between true solar time and mean solar time due to seasonal variations in the orbital velocity of the earth (Ryan and Stolzenbach, 1972). In CE-QUAL-W2 Version 2, monthly values of EQT

were used and linearly interpolated between. CE-QUAL-W2 Version 3 used 36 values over the course of a year to interpolate more accurately.

Woolf (1968) calculated the equation of time,  $h_e$  as

$$h_e = \begin{pmatrix} 0.004289\text{Cos}(\tau_d) - 0.123570\text{Sin}(\tau_d) \\ -0.060783\text{Cos}(2\tau_d) - 0.153809\text{Sin}(2\tau_d) \end{pmatrix} \quad (20)$$

where  $\tau_d$  the angular fraction of the year from Equation (9). Spencer (1971) calculated the equation of time using

$$h_e = \left( \frac{24}{2\pi} \right) \begin{pmatrix} 0.000075 + 0.001868\text{Cos}(\tau_d) - 0.032077\text{Sin}(\tau_d) \\ -0.014615\text{Cos}(2\tau_d) - 0.040849\text{Sin}(2\tau_d) \end{pmatrix} \quad (21)$$

where  $\tau_d$  the angular fraction of the year from Equation (8). DiLaura (1984) developed an equation for calculating the equation of time,  $h_e$  (hours), as

$$h_e = 0.170\text{Sin}[4\pi(\lfloor Jday \rfloor - 80)/373] - 0.129\text{Sin}[2\pi(\lfloor Jday \rfloor - 8)/355] \quad (22)$$

where  $Jday$  is the Julian day and fraction of the day.

Figure 6 compares the equation of time values throughout the year from Woolf (1968), Spencer (1971), DiLaura (1984), and the previous method in CE-QUAL-W2 (36 values over the year) with the equation of time data from List (1958). The difference between each equation of time model and the tabulated data is shown in Figure 7. Table 6 provides model-data error statistics for each model with the tabulated data from List (1958). Based on the error statistics, the DiLaura (1984) model provided the best estimate of the equation of time throughout the year.

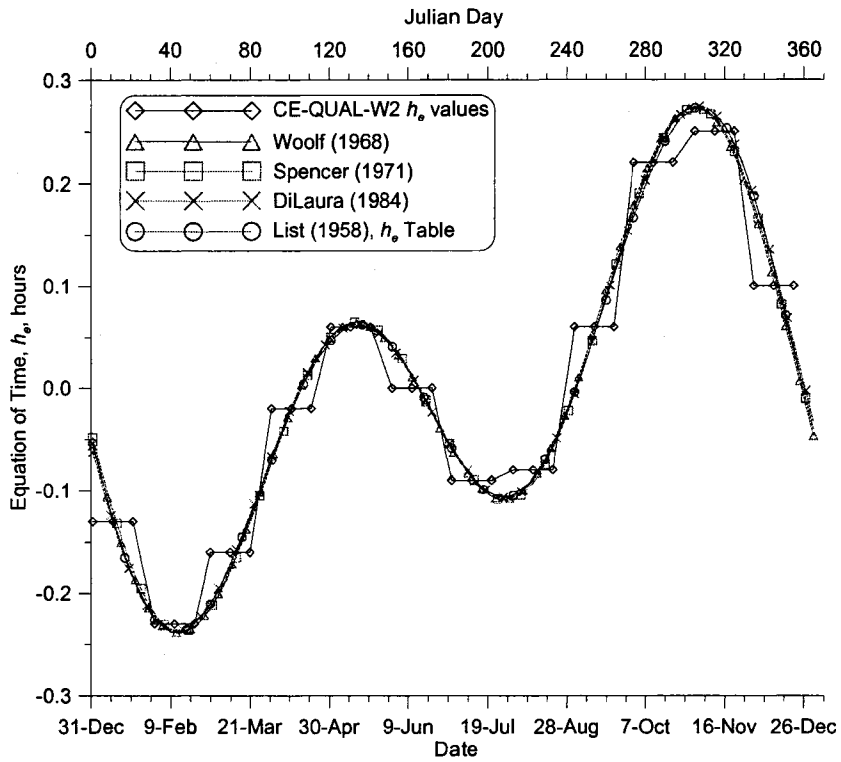


Figure 6: Comparison of equation of time models and tabulated values from List, 1958.

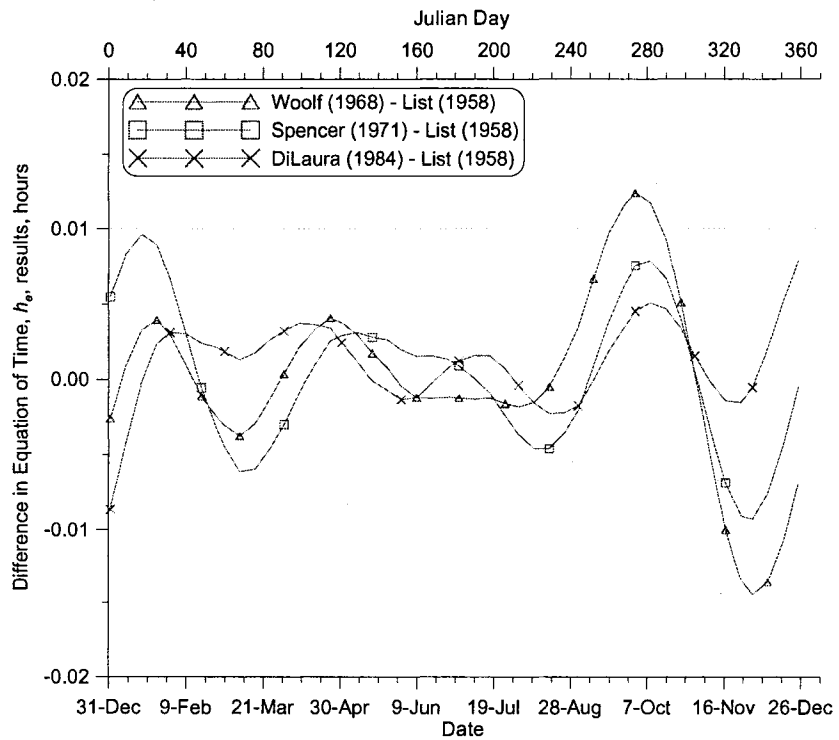


Figure 7: Difference between equation of time models and tabulated values from List, 1958.

**Table 6: Error statistics between equation of time models and tabulated values**

Difference between equation and tabulated values	ME <sup>1</sup> , hrs	AME <sup>1</sup> , hrs	RMS <sup>1</sup> , hrs
Woolf (1968)-List(1958)	-4.53E-5	4.33E-3	5.99E-3
Spencer(1971)-List(1958)	2.10E-4	4.04E-3	4.86E-3
DiLaura(1984)-List(1958)	1.15E-3	2.35E-3	2.97E-3
<sup>1</sup> ME: Mean error; AME: Absolute mean error, RMS: Root mean square error, see Appendix B.			

The equation of time,  $h_e$  (minutes), was calculated by Meeus (1999) using

$$h_e = 4 \left[ \begin{array}{l} y \sin(2\theta_{LO}) - 2e \sin(M) + 4ey \sin(M) \cos(2\theta_{LO}) \\ - 0.5y^2 \sin(4\theta_{LO}) - 1.25e^2 \sin(2M) \end{array} \right] \quad (23)$$

where  $y = (\tan(\varepsilon_p/2))^2$

where  $\theta_{LO}$  is the geometric mean longitude of the sun from Equation (18),  $M$  is the geometric mean anomaly of the sun from Equation (17),  $\varepsilon_p$  is the corrected obliquity of the ecliptic from Equation (12), and  $e$  is the eccentricity of earth's orbit. Meeus (1999) calculated the eccentricity of earth's orbit,  $e$  (dimensionless), using

$$e = 0.016708634 - t(0.000042037 + 0.0000001267t) \quad (24)$$

where  $t$  is the Julian centuries from Equation (19).

#### 2.4.5 Local Hour Angle

The local hour angle,  $H$  (radians), is the angular position of the sun for a given location at a specific time during the day. EPA (1971) and Ryan and Stolzenbach (1972) calculated the local hour angle,  $H$  (radians), using

$$H = \frac{2\pi}{24} \left[ h_l - (\gamma_l - \gamma) \frac{24}{360} + h_e - 12.0 \right] \quad (25)$$

where  $h_l$  is the local hour,  $\gamma$  is standard meridian, and  $\gamma_l$  is the longitude. DiLaura (1984) calculated the local angle using

$$H = \frac{2\pi}{24} \left[ h_l + (\gamma - \gamma_l) \frac{24}{360} + h_e \right] \quad (26)$$

Wunderlich (1972) presented another approach for calculating the local hour angle,  $H$  (radians), using

$$\begin{aligned} &\text{Sun East of Longitude:} \\ H &= \frac{2\pi}{24} \left[ h_l + (\gamma - \gamma_l) \frac{24}{360} + h_e + 12.0 \right] \\ &\text{Sun West of Longitude:} \\ H &= \frac{2\pi}{24} \left[ h_l + (\gamma - \gamma_l) \frac{24}{360} + h_e - 12.0 \right] \end{aligned} \quad (27)$$

where one of two equations is used depending on the position of the sun during the day.

Since there are no local hour angle tabulated data to compare with the results of Equation (25) through (27) the solar azimuth was calculated, using each equation, and then the solar azimuths were compared with tabulated data. Equation (25) and (27) were used with Equations (30) to (32) to calculate the solar azimuth,  $A_z$  (degrees). Equation (26) was used with a method from DiLaura (1984) to calculate the solar azimuth.

Figure 8 shows the three methods resulted in the same solar azimuth angles being calculated for July 3. Since the results of using Equations (25) through (27) are the same for July 3 and throughout the year, only Equation (25) was presented in

Figure 9 for January 2, April 3, and July 3. The calculated azimuth angles from Equation (25) were then compared with tabulated data from Cugle (1943) by subtracting Equation (25) from the data in Cugle (1943).

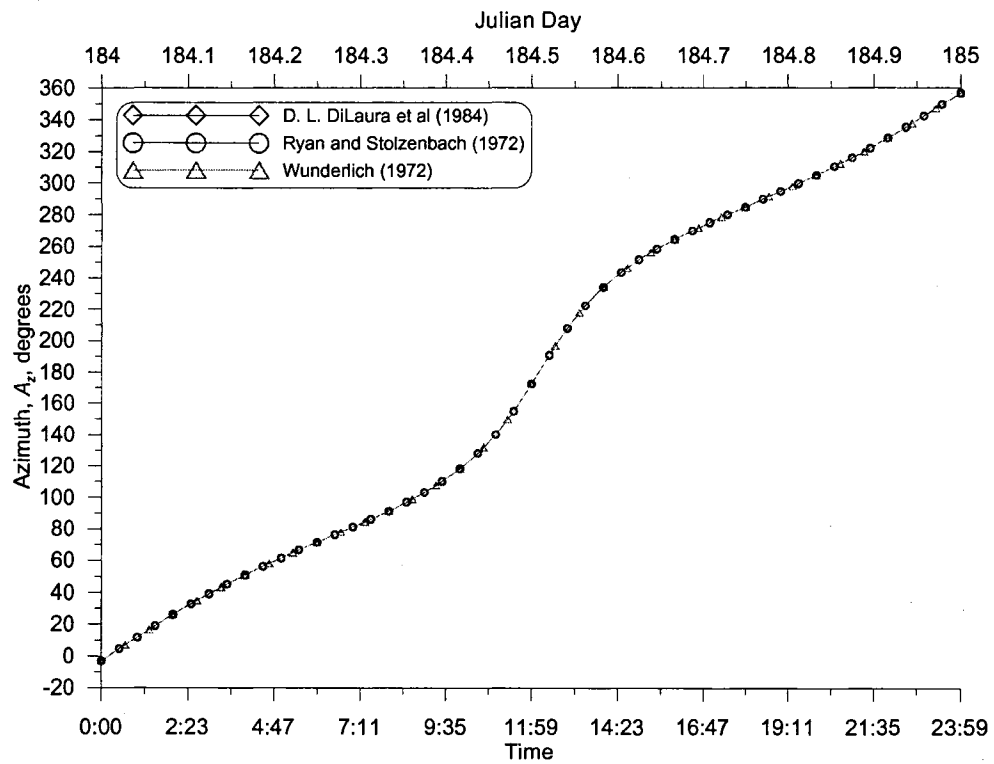


Figure 8: Solar Azimuth calculated by three methods for July 3

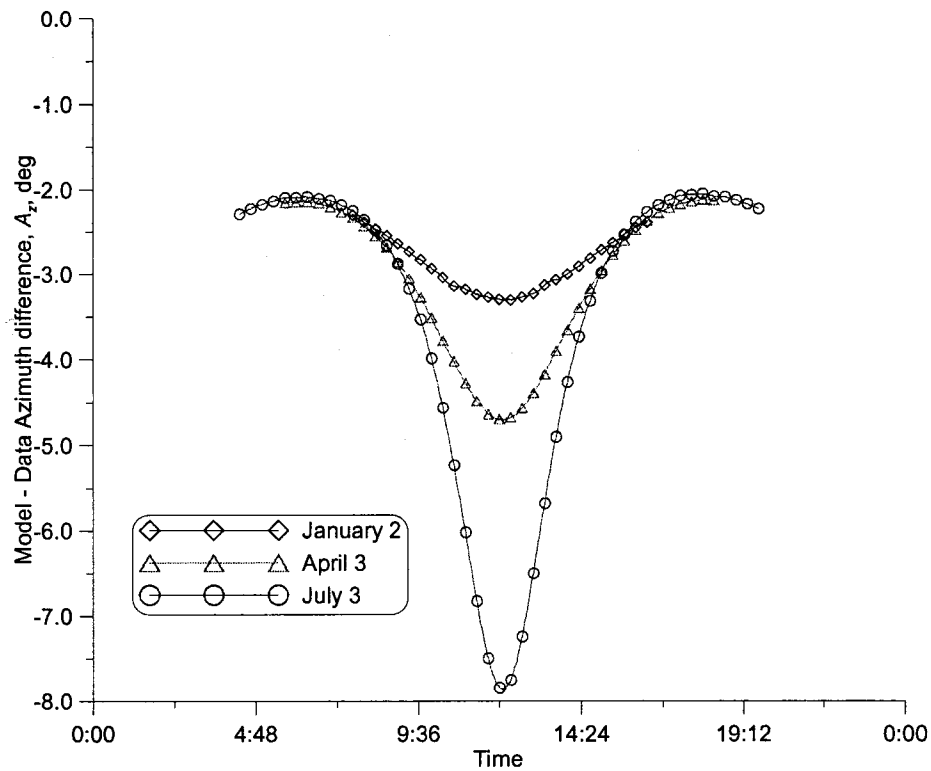


Figure 9: Solar azimuth angle differences, model – tabulated data (Cugle, 1943) for three days

Table 7 shows the solar azimuth angle model-data error ranges for these three days based on Equation (25). Note that the "data" used in these comparisons were derived from calculated tables based on the polar distance and the co-latitude of the location (Cugle, 1943).

Table 7: Solar azimuth error ranges between model and data

Date	Declination Angle, deg	Equation (25) Error Range (Model -Data), deg
January 2	-23.0	-2.31 to -3.31
April 3	+5.0	-2.12 to -4.71
July 3	+23.0	-2.06 to -7.87

Meeus (1999) calculated the local hour angle,  $H$  (degrees), between 0 and 360 degrees, using

$$H = h_{lst} / 4 - 180 \quad (28)$$

where  $h_{lst}$  (minutes) is the true solar time and Meeus (1999) calculated it using

$$h_{lst} = 60h_l + h_e - 4\gamma_l \quad (29)$$

where  $h_l$  is the local hour, and  $h_e$  is the equation of time from Equation (23).

#### 2.4.6 Solar Altitude

The solar altitude is the angle of inclination of the sun relative to the horizon from an observer's perspective as shown in Figure 10.

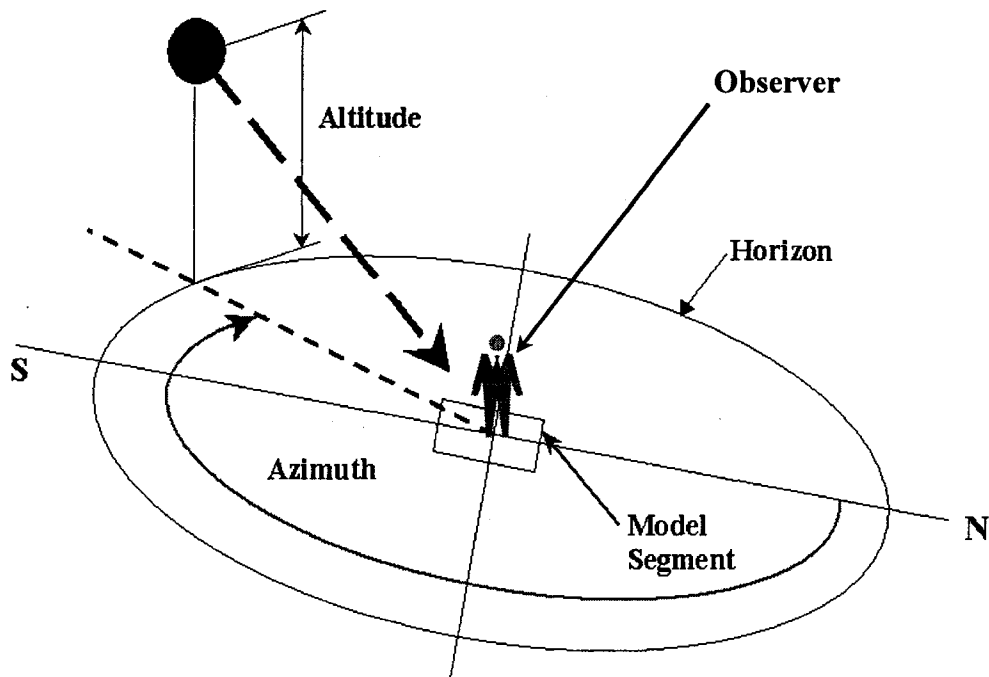


Figure 10: Solar Altitude and Azimuth

Wunderlich (1972) and Meeus (1999) calculated the solar altitude,  $A_o$  (degrees), using

$$A_o = \text{arcSin}[\text{Sin}(\psi)\text{Sin}(\delta) + \text{Cos}(\psi)\text{Cos}(\delta)\text{Cos}(H)] \quad (30)$$

Wunderlich (1972) used Equations (6) and (27) for the solar declination and local hour angle whereas Meeus (1999) used Equations (10) and (28).

#### 2.4.7 Solar Azimuth

The solar azimuth is the direction of the sun with respect to a North-South axis measured clockwise from the North as shown in Figure 10. Lee (1978) calculated the solar azimuth,  $A_z$  (degrees), based on

$$A_z = \text{arcSin}\left(\frac{-\text{Cos}(\delta)\text{Sin}(H)}{\text{Cos}(A_o)}\right) \quad (31)$$

The results of this equation were compared to data obtained from three sources: Cugle (1943), U.S. Navy-Hydrographic Office (1934) and the U.S. Navy-Hydrographic Office (1952). The three sources of data are compared in Figure 11 for July 3<sup>rd</sup>.

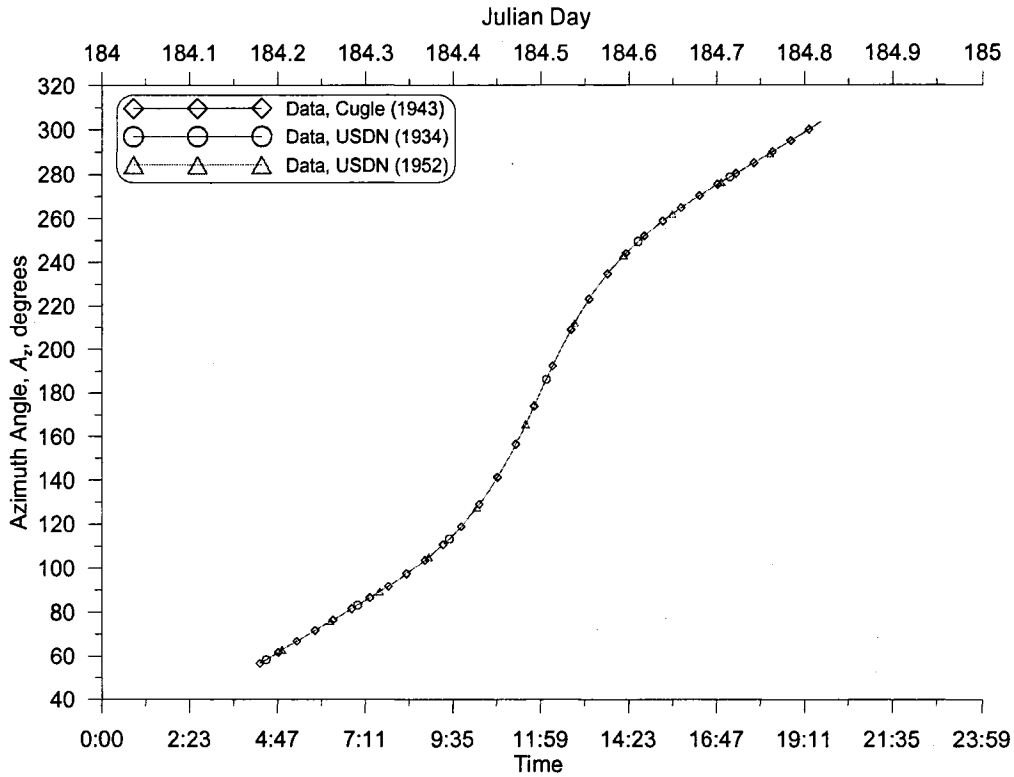


Figure 11: Solar azimuth data on July 3<sup>rd</sup>

U.S. Naval Observatory (2000) presented an additional method for calculating the solar azimuth using

$$\begin{aligned} \text{If } H < 0 \text{ then } A_z &= \text{arcCos}(X) \\ \text{Otherwise } A_z &= (2\pi - \text{arcCos}(X)) \end{aligned} \quad (32)$$

where  $X$  is defined as

$$\begin{aligned} \text{If } X > +1 \text{ Set } X &= +1 \\ \text{If } X < -1 \text{ Set } X &= -1 \end{aligned} \quad (33)$$

once calculated using

$$X = \frac{[\text{Sin}(\delta)\text{Cos}(\psi) - \text{Cos}(\delta)\text{Cos}(H)\text{Sin}(\psi)]}{\text{Cos}(A_o)} \quad (34)$$

Figure 12 compares calculated azimuth angles from Equation (31) and the methodology in Equations (32) to (34) with tabulated data from Cugle (1943). Table 8

provides the error statistics comparing the methodologies with the tabulated data. The figure and error statistics indicates the U.S. Naval Observatory (2000) model resulted in calculated azimuths angles closer to the tabulated data than the Lee (1978) model.

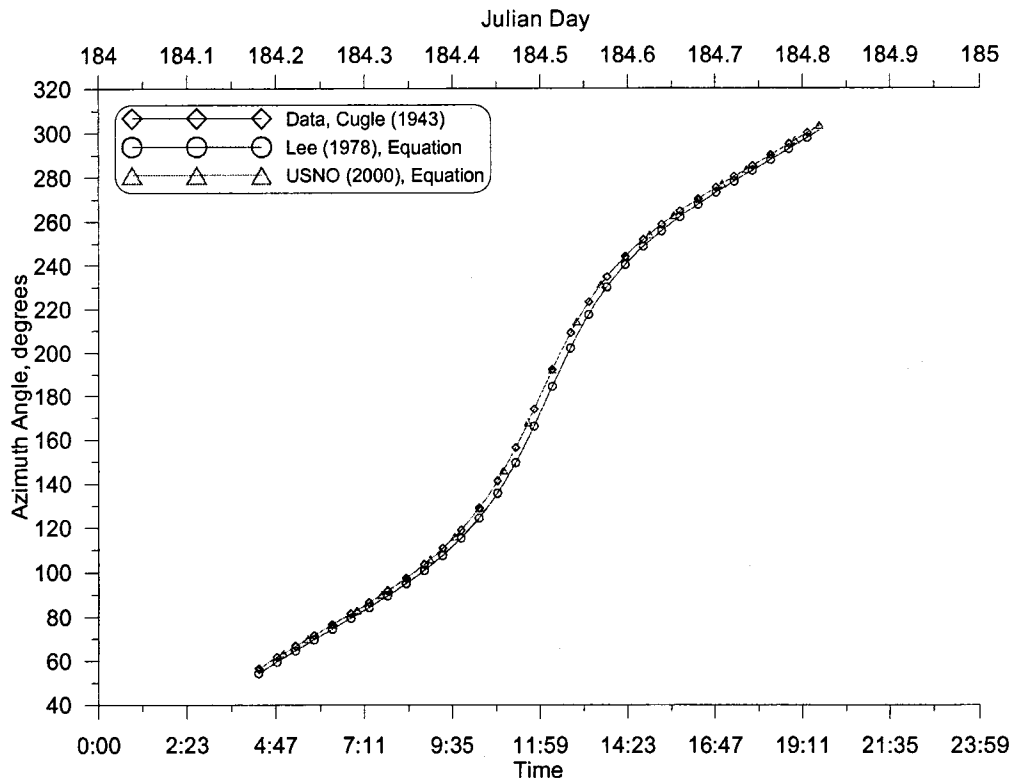


Figure 12: Solar azimuth angle over daylight for July 3

Table 8: Azimuth angle model-data error statistics for July 3

Model	ME <sup>1</sup> , deg	AME <sup>1</sup> , deg	RMS <sup>1</sup> , deg
Lee (1978), Equation (31)	-3.47	3.47	1.86
USNO (2000), Equations (32) to (34)	1.24	1.24	1.40

<sup>1</sup> ME: Mean error; AME: Absolute mean error, RMS: Root mean square error, see Appendix B.

NOAA (2004) also presented an equation for the solar azimuth,  $A_z$  (degrees), using

$$A_z = 180.0 - \text{arcCos} \left[ \frac{\text{Sin}(\psi) \text{Cos}(90.0 - A_o) - \text{Sin}(\delta)}{\text{Cos}(\psi) \text{Sin}(90.0 - A_o)} \right] \quad (35)$$

where  $A_o$  is the solar altitude from Equation (30),  $H$  is the local hour angle from Equation (25), and  $\delta$  is the solar declination from Equation (10).

#### 2.4.8 Atmospheric Refraction

NOAA (2004) presented a correction for the effect of atmospheric refraction on the solar altitude. When sunlight hits the upper atmosphere, the path of the light is bent, which changes the solar altitude. NOAA (2004) calculated the corrected solar altitude,  $A_{o\text{-corrected}}$  (degrees), using

$$A_{o\text{-corrected}} = A_o + RC \quad (36)$$

where  $A_o$  is the solar altitude using Equation (30) and  $RC$  is the atmospheric refraction correction. Table 9 provides the equations for calculating the atmospheric refraction correction as a function of the uncorrected solar altitude,  $A_o$ .

**Table 9: Atmospheric refraction correction for solar altitude, NOAA (2004)**

$A_o$	Approximate Atmospheric Refraction Correction, $RC$
85° to 90°	0.00
5° to 85°	$\frac{1^\circ}{3600''} \left[ \frac{58.1''}{\tan(A_o)} - \frac{0.07''}{\tan^3(A_o)} + \frac{0.000086''}{\tan^5(A_o)} \right]$
-0.575° to 5°	$\frac{1^\circ}{3600''} [1735'' - 518.2'' A_o + 103.4'' A_o^2 - 12.79'' A_o^3 + 0.711'' A_o^4]$

$A_o$	Approximate Atmospheric Refraction Correction, $RC$
$< -0.575$	$\frac{1^\circ}{3600''} \left[ \frac{-20.774''}{\tan(A_o)} \right]$

## 2.5 Extraterrestrial Solar Radiation

### 2.5.1 Solar Constant

The solar constant,  $\phi_o$  ( $\text{W/m}^2$ ), has been covered in the literature extensively. Table 10 lists solar constant values found in the literature. The National Aeronautics and Space Administration started monitoring solar influx in earth orbit in the 1970s (NASA, 2004). Table 11 lists the minimum and maximum values of extraterrestrial solar irradiance recorded from several satellites. The average of all the minimum and maximum values in Table 11 is  $1367.4 \text{ W/m}^2$ .

**Table 10: Solar Constant values from literature**

Solar Constant $\text{W/m}^2$	Reference
1367.00	Pelletier and Chapra (2004)
1367.00	Dingman (2002)
1363.64	Lee (1978)
1352.53	Ryan and Stolzenbach (1972)
1353.06	Wunderlich (1972)
1356.64	Orlob and Selna (1967)
1328.67	Kennedy (1949)
1356.64	Klein (1948)
1356.64	Kimball (1930)
1356.64	Hamon et al. (1954)

**Table 11: Extraterrestrial solar irradiance from satellite data (NASA, 2004).**

Satellite	Minimum Irradiance, W/m <sup>2</sup>	Maximum Irradiance, W/m <sup>2</sup>	Operation Range
Active Cavity Radiometer Irradiance Monitor I	1364.48	1369.71	February 16, 1980 to July 14, 1989
Active Cavity Radiometer Irradiance Monitor II	1363.75	1367.14	October 4, 1991 to December 31, 1997
Nimbus-7 Earth Radiation Budget	1368.50	1374.80	November 16, 1978 to December 13, 1993
Earth Radiation Budget Satellite	1363.10	1367.60	October 25, 1984 to June 19, 1996

### 2.5.2 Incoming Solar Radiation

Wunderlich (1972), Lee (1978), and Bras (1990) calculated the extraterrestrial solar radiation,  $\varphi_{ext}$  (W/m<sup>2</sup>), using

$$\varphi_{ext} = \varphi_o E_o \sin(A_o) \quad (37)$$

where  $E_o$  (dimensionless) is the eccentricity correction and is calculated as

$$E_o = \left( \frac{r_o}{r} \right)^2 \quad (38)$$

where  $r_o$  (AU) is the average distance between the earth and the sun (1 Astronomical Unit), and  $r$  (AU) is the distance between the earth and the sun at any time. Wunderlich (1972), Ryan and Stolzenbach (1972), and Brown and Barnwell (1987) calculated the relative Earth-Sun distance,  $r$  (AU), using

$$r = 1 + 0.017 \cos\left(\frac{2\pi}{365}(186 - \lfloor Jday \rfloor)\right) \quad (39)$$

Spencer (1971) and Dingman (2002) calculated the eccentricity correction,  $E_o$ , as

$$E_o = 1.000110 + 0.034221\text{Cos}(\tau_d) + 0.001280\text{Sin}(\tau_d) \\ + 0.000719\text{Cos}(2\tau_d) + 0.000077\text{Sin}(2\tau_d) \quad (40)$$

where  $\tau_d$  is the angular fraction of the year from Equation (8).

Meeus (1999) calculated the distance between the Earth and the Sun at any given time,  $r$  (AU), as

$$r = (1.000001018\{1 - e^2\}) / (1 + e\text{Cos}\{v\}) \quad (41)$$

where  $e$  is the eccentricity of earth's orbit from Equation (24), and  $v$  (degrees) is the true anomaly of the sun and was calculated using

$$v = M + c \quad (42)$$

where  $c$  is the center of the sun from Equation (16), and  $M$  is the geometric mean anomaly of the sun from Equation (17).

## 2.6 Atmospheric Attenuation

Solar radiation atmospheric attenuation models were reviewed in the literature with several approaches considering only one or two atmospheric influences. One of the most comprehensive atmospheric attenuation models was developed by Bird and Hulstrom (1981) in a report titled "*A Simplified Clear Sky Model for Direct and Diffuse Insolation on Horizontal Surfaces.*"

### 2.6.1 Optical Air Mass and Transmittance

Wunderlich (1972) calculated the relative optical air mass,  $m_p$  (dimensionless), based on the relationship developed by Kasten (1964) and incorporated changes in barometric pressure with altitude from List (1958) as

$$m_p = \frac{\left[ \frac{(288 - 0.0065z)}{288} \right]^{5.256}}{\left[ \sin(A_o) + 0.1500(A_o + 3.885)^{-1.253} \right]} \quad (43)$$

where  $z$  (meters) is the elevation. Bird and Hulstrom (1981) calculated the transmittance of Rayleigh scattering in the atmosphere,  $T_R$  (dimensionless), as

$$T_R = \exp\left(-0.0903m_p^2(1 + m_p - m_p^{1.01})\right) \quad (44)$$

Bird and Hulstrom (1981) also developed an equation for the transmittance of uniformly mixed gases such as carbon dioxide and oxygen,  $T_{UM}$  (dimensionless), as

$$T_{UM} = \exp\left(-0.0127m_p^{0.26}\right) \quad (45)$$

### 2.6.2 Precipitable Water Content

The precipitable water content in the atmosphere is often included in atmospheric attenuation models as an empirical coefficient. Table 12 lists empirical values for precipitable water content found in the literature.

**Table 12: Empirical values for precipitable water content**

$w$ , cm	Description	Reference
2.93	Mid-latitude Summer atmospheric model	Bird and Hulstrom (1981)
1.42	U.S. Standard atmospheric model	Bird and Hulstrom (1981)
1.50	Used in Qual2k model	Pelletier and Chapra (2004)

Researchers have developed equations to calculate the precipitable water content based on the dew point temperature. Wunderlich (1972) calculated the precipitable water content in the air,  $w$  (cm), for a clear day from Reitan (1963) using

$$w = \exp(-0.981 + 0.0341T_{dpt}) \quad (46)$$

where  $T_{dpt}$  ( $^{\circ}\text{F}$ ) is the mean monthly dew point temperature and the coefficients  $-0.981$  and  $0.0341$  are empirical values from Reitan (1963) based on comparing meteorological data at 15 stations around the U.S. Dingman (2002) converted the relationship to

$$w = 1.12 \exp(0.0614T_{dpt}) \quad (47)$$

where  $T_{dpt}$  ( $^{\circ}\text{C}$ ) is the monthly mean dew point temperature. Bolsenga (1965) then used the work from Reitan (1963) and developed an equation for the mean daily precipitable water content,  $w$  (cm), as

$$\begin{aligned} \text{Mean daily, } w &= \exp(-1.249 + 0.0427T_{dpt}), T_{dpt} \text{ (}^{\circ}\text{F)} \\ w &= \exp(0.1174 + 0.07686T_{dpt}), T_{dpt} \text{ (}^{\circ}\text{C)} \end{aligned} \quad (48)$$

where  $T_{dpt}$  is the mean daily dew point temperature. The mean hourly precipitable water content,  $w$  (cm), from Bolsenga (1965) was calculated as

$$\begin{aligned} \text{Mean hourly, } w &= \exp(-1.288 + 0.0384T_{dpt}), T_{dpt} \text{ (}^\circ\text{F)} \\ w &= \exp(-0.0592 + 0.06912T_{dpt}), T_{dpt} \text{ (}^\circ\text{C)} \end{aligned} \quad (49)$$

where  $T_{dpt}$  is the mean hourly dew point temperature. The transmittance of the water vapor,  $T_w$  (dimensionless), was calculated by Bird and Hulstrom (1981) as

$$T_w = 1 - \frac{2.4959X_w}{(1 + 79.034X_w)^{0.6828} + 6.385X_w} \quad (50)$$

where  $X_w$  (cm) is the precipitable water in a slanted path, which was calculated as

$$X_w = wm_p \quad (51)$$

### 2.6.3 Ozone Absorption

The transmittance of the ozone content,  $T_o$  (dimensionless), was calculated by Bird and Hulstrom (1981) as

$$\begin{aligned} T_o &= 1 - 0.1611X_o(1 + 139.48X_o)^{-0.3035} - \\ &0.002715X_o(1 + 0.044X_o + 0.0003X_o^2)^{-1} \end{aligned} \quad (52)$$

where  $X_o$  (cm) is the amount of ozone in a slanted path and was calculated by Bird and Hulstrom (1981) using

$$X_o = U_o m_p \quad (53)$$

where  $U_o$  (cm) is the ozone content in the atmosphere.

The ozone content in the atmosphere is often included in atmospheric attenuation models as an empirical coefficient (Bird and Hulstrom, 1981) which may

be adjusted to calibrate a model to field data. Table 13 lists several empirical values for ozone content found in the literature.

**Table 13: Empirical values for atmospheric ozone**

$U_o$ , cm	Description	Reference
0.31	Mid-latitude Summer atmospheric model	Bird and Hulstrom (1981)
0.34	U.S. Standard atmospheric model	Bird and Hulstrom (1981)
0.3 to 0.4	Average in "literature"	Van Heuklon (1979) (from Elterman (1968) and Halpern et al. (1974))
0.2 to 0.6	Variation in ozone globally and temporal	Van Heuklon (1979)
0.3	Used in Qual2k model	Pelletier and Chapra (2004)

Van Heuklon (1979) developed a model to calculate the amount of ozone in the atmosphere,  $U_o$  (cm), as a function of location and time of year using

$$U_o = \frac{235 + \left[ \frac{A' + C' \sin(0.9856(\lfloor Jday \rfloor + F'))}{20 \sin(H'(\gamma_l + P'))} + \right] \sin^2(B' \psi)}{1000.0} \quad (54)$$

where  $A'$ ,  $B'$ ,  $C'$ ,  $F'$ ,  $H'$ , and  $P'$  are coefficients that are a function of hemisphere and listed in Table 14.

**Table 14: Ozone model parameters based on location (Van Heuklon, 1979)**

Parameter	Northern Hemisphere	Southern Hemisphere
$A'$ , (atm-cm)	150.0	100.0
$C'$ , (atm-cm)	40.0	30.0
$F'$ , (days)	-30.0	152.625
$H'$ , (dimensionless)	3.0	2.0
$P'$ , (degrees)	20.0 if $\gamma_l > 0$ 0.0 if $\gamma_l < 0$	-75.0
$B'$ , (dimensionless)	1.28	1.50

## 2.6.4 Atmospheric Turbidity

Bird and Hulstrom (1981) calculated the transmittance of aerosol absorptance and scattering,  $T_A$  (dimensionless), using

$$T_A = \exp\left[-\tau_A^{0.873}\left(1 + \tau_A - \tau_A^{0.7088}\right)m_p^{0.9108}\right] \quad (55)$$

where  $\tau_A$  (dimensionless) is the overall atmospheric turbidity and defined as the broadband aerosol optical depth from the surface in a vertical path and varies from 0.02 to 0.50 and was calculated by Bird and Hulstrom (1981) as

$$\tau_A = 0.2758\tau_{A0.38} + 0.35\tau_{A0.50} \quad (56)$$

where  $\tau_{A0.38\mu m}$  (dimensionless) is the aerosol optical depth from the surface in a vertical path at 380 nm wavelength (no molecular absorption), and  $\tau_{A0.5\mu m}$  (dimensionless) is the aerosol optical depth at 500 nm wavelength (ozone absorption) (Bird and Hulstrom, 1981 and Muneer et al., 2000). Optical depth values for the two wavelengths may be developed based on data or adjusted during model calibration. Table 15 provides a list of some optical depth values found in the literature.

**Table 15: Empirical values for atmospheric turbidity**

$\tau_{A0.5\mu m}$ (dimensionless)	$\tau_{A0.38\mu m}$ (dimensionless)	Description	Reference
0.163		Mean sea-level, Washington D.C.	Flowers et al. (1969)
0.093		Eastern U.S.,	Elterman (1964)
0.047		Mean sea-level, Washington D.C.	Moon (1940)
0.105		Washington D.C.	Angstrom (1929)

$\tau_{A0.5\mu m}$ (dimensionless)	$\tau_{A0.38\mu m}$ (dimensionless)	Description	Reference
0.020 – 0.030		Minimum value over United States at sea level	Flowers et al. (1969)
0.100	0.05	Mt Vernon in Washington	Pelletier and Chapra (2004)
0.56	0.72	United Kingdom	Muneer (1997)
0.2661	0.3538	U.S. Standard Atmosphere	Muneer (1997)

### 2.6.5 Aerosol Absorptance

The transmittance of aerosol absorptance,  $T_{AA}$  (dimensionless), was calculated by Bird and Hulstrom (1981) using

$$T_{AA} = 1 - K_1(1 - m_p + m_p^{1.06})(1 - T_A) \quad (57)$$

where  $K_1$  is an empirical absorptance coefficient. Bird and Hulstrom (1981) recommended the coefficient be set to 0.1 unless information on aerosols was available. Table 16 lists the aerosol absorptance coefficients discussed in Bird and Hulstrom (1981).

**Table 16: Empirical values of the aerosol absorptance coefficient, Bird and Hulstrom (1981)**

$K_1$	Description
0.0933	rural aerosol
0.385	urban aerosol, contains more carbon
0.1	recommended unless aerosol data available

### 2.6.6 Atmospheric Albedo

Bird and Hulstrom (1981) characterized the scattering of irradiance in the atmosphere by the atmospheric albedo,  $r_s$  (dimensionless), using

$$r_s = 0.0685 + (1 - B_a) \left( 1.0 - \frac{T_A}{T_{AA}} \right) \quad (58)$$

where  $B_a$  (dimensionless) is the ratio of forward-scattered irradiance to the total scattered irradiance due to aerosols is an empirical coefficient. Table 17 lists some empirical values for the ratio found in the literature.

**Table 17: Empirical values for the ratio of forward scatter irradiance to the total irradiance**

$B_a$	Description	Reference
0.84	recommended	Bird and Hulstrom (1981)
0.85		Pelletier and Chapra (2004)
0.82	rural aerosol	Bird and Hulstrom (1981)
0.86	Mid-latitude Summer atmosphere with Haze L aerosol model	Dave (1978)
1.00	all forward scattering	Bird and Hulstrom (1981)
0.50	isotropic scattering	Bird and Hulstrom (1981)
0.00	all backward scattering	Bird and Hulstrom (1981)

### 2.6.7 Atmospheric Dust

Solar radiation atmospheric attenuation models may also consider the affects of atmospheric dust. Klein (1948) divided the influence of dust into two components for the atmospheric dust coefficient,  $d$  (dimensionless), using

$$d = d_s + d_a \quad (59)$$

where  $d_s$  (dimensionless) is coefficient for the affects of scattering, and  $d_a$  (dimensionless) is the coefficient for the affects of absorption. The influence of dust on attenuating solar radiation is a function of the relative optical air mass and time of year, (Kimball, 1930). Klein (1948) and Bolsenga (1964) tabulated the dust attenuation values from Kimball (1930), as shown in Table 18. Both Klein (1948) and Dingman (2002) considered the solar radiation attenuation due to absorption from dust as negligible,  $d_a \approx 0$  resulting in  $d = d_s$ .

**Table 18: Empirical values of the fraction of dust in the atmosphere**

$d$	Description	Reference
0.00 to 0.08	remote sites	Klein (1948) and Bolsenga (1964), from Kimball (1930)
0.03 to 0.10	moderate sized cities	
0.06 to 0.13	larger metropolitan areas	

### 2.6.8 Atmospheric Transmission

While Bird and Hulstrom (1981) characterized several parameters involving aerosols and ozone which affect radiation transmission in the atmosphere. Other researchers (Wunderlich, 1972 and Orlob and Selna, 1967) considered atmospheric transmission predominantly as a function of precipitable water content and optical air mass.

Wunderlich (1972) characterized atmospheric interference in two components: the mean atmospheric transmission coefficient for a cloudless, dust-free, moist air

after scattering only  $a'$ , and the mean atmospheric transmission coefficient for cloudless, dust-free, moist air after scattering and absorption,  $a''$ .

The transmission coefficients  $a'$  and  $a''$ , were originally tabulated by Kimball (1930) and documented in figures, which were developed into equations by Orlob and Selna (1967). The mean atmospheric transmission coefficient for a cloudless, dust-free, moist air after scattering,  $a'$  (dimensionless), was calculated by Orlob and Selna (1967) as

$$a' = \exp\left[-(0.465 + 0.134w)(0.129 + 0.171\exp(-0.880m_p))m_p\right] \quad (60)$$

Dingman (2002) presented a different equation for  $a'$  as

$$a' = \exp\left[-(0.0363 + 0.0084w) - (0.0572 + 0.0173w)m_p\right] \quad (61)$$

where  $m_p$  is the average daily optical air mass from a figure in Kennedy (1940).

Orlob and Selna (1967) calculated the mean atmospheric transmission coefficient for cloudless, dust-free, moist air after scattering and absorption,  $a''$  (dimensionless), as

$$a'' = \exp\left[-(0.465 + 0.134w)(0.179 + 0.421\exp(-0.721m_p))m_p\right] \quad (62)$$

Dingman (2002) presented a similar equation for  $a''$  as

$$a'' = \exp\left[-(0.124 + 0.0207w) - (0.0682 + 0.0248w)m_p\right] \quad (63)$$

where  $m_p$  is the average daily optical air mass from a figure in Kennedy (1940).

Some atmospheric attenuation models simplify modeling the atmospheric attenuation further and characterize all of the atmospheric attenuation variables into one atmospheric transmission coefficient (Kennedy, 1949 and Ryan and Stolzenbach, 1972), which is used to calibrate the model to data.

Kennedy (1949) related the daily atmospheric transmission coefficient,  $a_t$  (dimensionless), to an hourly average transmission coefficient,  $a_h$  (dimensionless), using

$$a_h = 1.49a_t - 0.50 \quad (64)$$

where  $a_t$  (dimensionless) is the daily atmospheric transmission coefficient for a specific location (Ryan and Stolzenbach, 1972). Table 19 lists some daily atmospheric transmission coefficients found in the literature.

**Table 19: Atmospheric transmission empirical values**

$a_t$ , Daily	Description	Reference
0.91	Fit to 248 days of data from Fresno, CA	Kennedy (1949)
0.70	June	Hamon et al. (1954)
0.85	December	Hamon et al. (1954)
0.60 to 0.90	Absence of clouds, throughout year	Lee (1978)

### 2.6.9 Surface Reflectivity

The ground surface reflectivity,  $R_g$  (dimensionless), or albedo represents the fraction of the incident radiation on the ground surface that reflects back to the atmosphere and is dependent on the surface material and the angle of the sun. The

reflectivity of many surfaces has been well documented in the literature. Table 20 lists empirical reflectivity values found in the literature for water.

**Table 20: Empirical values for albedo or reflectivity**

Albedo, $R_g$	Description	Reference
0.03 to 0.40	water	Eagleson (1970)
0.05 to 0.60	water	Lee (1978)
0.03 to 0.10	water surface, sea	Muneer (1997)
0.20	Used in Qual2k model	Pelletier and Chapra (2004)

Lee (1978) provided a table of reflectivity values for a water surface relative to the solar altitude,  $A_o$ , as shown in Table 21.

**Table 21: Water surface reflectivity for varying solar altitude, (Lee, 1978)**

$A_o$ , degrees	$R_g$	$A_o$ , degrees	$R_g$
60	0.05	10	0.35
30	0.10	5	0.60
20	0.15		

Anderson (1954) calculated the total reflectivity of the water surface,  $R_g$  (dimensionless), as

$$R_g = \alpha_1 (A_o)^{\beta_1} \quad (65)$$

where coefficients  $\alpha_1$  and  $\beta_1$  are dependent on the fraction of cloud cover and are listed in Table 22.

**Table 22: Reflectivity equation coefficients based on cloud cover (Anderson, 1954)**

Cloudiness, C	Clear, 0.0	Scattered, 0.1 – 0.5	Broken, 0.6 – 0.9	Overcast, 1.0
$\alpha_1$	1.18	2.20	0.95	0.33
$\beta_1$	-0.77	-0.97	-0.75	-0.45
High Altitude Clouds				
$\alpha_1$		2.20	1.10	0.51

Cloudiness, C	Clear, 0.0	Scattered, 0.1 – 0.5	Broken, 0.6 – 0.9	Overcast, 1.0
$\beta_1$		-0.98	-0.80	-0.58
Low Altitude Clouds				
$\alpha_1$		2.17	0.78	0.20
$\beta_1$		-0.96	-0.68	-0.30

### 2.6.10 Ground-level Clear-Sky Solar Radiation

EPA (1971) calculated the incoming solar radiation at the ground surface based on a least squares fit using a polynomial regression on the solar altitude. This solar radiation formulation model was used in the water quality model CE-QUAL-W2 (Cole and Wells, 2000). The clear-sky solar radiation at the ground surface, was originally computed in BTU/ft<sup>2</sup>day, but was converted to W/m<sup>2</sup> below. The total clear sky solar radiation was calculated using a least squares fit polynomial regression of the solar altitude,  $A_o$  (degrees), and included direct and diffuse radiation and the influence of ground surface reflectivity (albedo):

$$\varphi_s = 24(2.044A_o + 0.1296A_o^2 - 1.941E - 3A_o^3 + 7.591E - 6A_o^4) \quad (66)$$

The solar radiation model by Klein (1948) was used in the water quality model QUAL2E (Brown and Barnwell, 1987) and CE-QUAL-RIV1 (Environmental Laboratory, 1995) and involved calculating the precipitable water content, relative optical air mass, two atmospheric transmission coefficients and dust to calculate the total clear sky radiation. After considering scattering and absorption in a moist and dusty atmosphere and ground surface reflectivity, the total clear sky solar radiation,  $\varphi_s$  (W/m<sup>2</sup>), was calculated from Klein (1948) using

$$\varphi_s = \varphi_{ext} \left[ \frac{a'' - d + 0.5(1 - a' + d)}{1 - 0.5R_g(1 - a' + d)} \right] \quad (67)$$

where  $\varphi_{ext}$  ( $\text{W}/\text{m}^2$ ) is the extraterrestrial solar radiation from Equation (37).

Ryan and Stolzenbach (1972) and Kennedy (1949) calculated the clear-sky solar radiation using

$$\varphi_s = \varphi_{ext} a_t^{m_p} \quad (68)$$

where  $a_t$  is the daily atmospheric transmission coefficient, and  $m_p$  is the optical air mass from Equation (43).

Lee (1978) calculated the clear-sky solar radiation using

$$\varphi_s = \varphi_{ext} a_t^{\frac{1}{\sin(A_o)}} \quad (69)$$

where  $A_o$  is the solar altitude from Equation (30).

The Meeus (1999) and the Bird and Hulstrom (1981) models were used by Pelletier and Chapra (2004) in the water quality model QUAL2kw for calculating the solar position and atmospheric attenuation, respectively. The clear-sky solar radiation,  $\varphi_s$  ( $\text{W}/\text{m}^2$ ), was calculated from Bird and Hulstrom (1981) using

$$\varphi_s = \frac{(\varphi_d + \varphi_l)}{(1 - R_g r_s)} \quad (70)$$

where  $\varphi_d$  is the direct solar radiation,  $\varphi_l$  is the scattered solar radiation, and  $r_s$  is the atmospheric reflectivity (albedo). Bird and Hulstrom (1981) calculated the direct solar radiation,  $\varphi_d$  ( $\text{W}/\text{m}^2$ ), using

$$\varphi_d = 0.9662\varphi_{ext}T_A T_w T_{UM} T_o T_R \quad (71)$$

where  $T_A$  (dimensionless) is the transmittance of aerosol absorptance and scattering,  $T_w$  (dimensionless) is the transmittance of water vapor,  $T_{UM}$  (dimensionless) is the transmittance of uniformly mixed gases,  $T_o$  (dimensionless) is the transmittance of ozone content, and  $T_R$  (dimensionless) is the transmittance of Rayleigh scattering in the atmosphere. The solar radiation from atmospheric scattering,  $\varphi_l$  ( $\text{W/m}^2$ ), was calculated (Bird and Hulstrom, 1981) using

$$\varphi_l = 0.79\varphi_{ext}T_{AA}T_w T_{UM} T_o \left( \frac{0.5(1-T_R) + B_a \left(1 - \frac{T_A}{T_{AA}}\right)}{1 - m_p + m_p^{1.02}} \right) \quad (72)$$

where  $m_p$  is the relative optical air mass and  $T_{AA}$  (dimensionless) is the transmittance of aerosol absorptance.

### 2.6.11 Cloud Cover

Wunderlich (1972) calculated the reduction in solar radiation due to clouds,  $\varphi_c$  ( $\text{W/m}^2$ ), as

$$\varphi_c = \varphi_s (1 - 0.65C^2) \quad (73)$$

where  $\varphi_s$  is the ground surface solar radiation, and  $C$  is the cloud cover. The cloud cover is reported as a fraction from 0 to 1 where 0 represents no cloud cover and 1 presents full cloud cover.

## **2.7 Thermophysical Properties of Matter**

Thermophysical properties of matter were reviewed in the literature to investigate and summarize the range of values for various materials which may characterize a stream or lake sediments. All units were converted to metric to all comparisons between literature sources. Table 23 summarizes the thermal diffusivity, thermal conductivity, density, specific heat and volumetric heat capacity for several potential streambed materials. A more exhaustive list of thermophysical properties is listed in Appendix C.

**Table 23: Summary table of thermophysical properties of matter**

Reference	Thermal Diffusivity, $\beta$ : $m^2/s$	Thermal conductivity, $k$ : $W/m\ ^\circ C$	Volumetric Heat capacity, $\rho c_p$ : $J/m^3\ ^\circ C$	Density, $\rho$ : $kg/m^3$	Specific Heat, $c_p$ : $J/kg\ ^\circ C$	Material
Geiger (1965)	1.10E-07 - 2.80E-07	0.06	3.77E+05			Bog Sediments
Bejan (1993), Grigull and Sander (1984), Cenegal (1997)	1.00E-06	1.28		1450	880	Clay at 20 $^\circ C$
Carslaw and Jaeger (1959)	1.10E-06	2.51		2600	880	Granite
Bejan (1993), Grigull and Sander (1984), Kreith and Bohn (1986)	1.20E-06	2.90		2750	890	Granite at 20 $^\circ C$
Incropera and De Witt (1990) and Cenegal (1997)		2.79		2630	775	Granite, Barre
Carslaw and Jaeger (1959)	7.00E-07	1.68		2500	922	Limestone
Incropera and De Witt (1990) and Cenegal (1997)		2.15		2320	810	Limestone, Salem
Grigull and Sander (1984)	1.30E-6 - 1.40E-6	2.80		2500 - 2700	810	Marble at 20 $^\circ C$
Incropera and De Witt (1990) and Cenegal (1997)	1.20E-06	2.80		2680	830	Marble, Halsten
Geiger (1965) and Chen et al. (1998)	6.00E-07 - 2.30E-06	1.68 - 4.61	1.49E+06 - 2.43E+06	2500 - 2900		Rock
Carslaw and Jaeger (1959) and Chow (1964)	1.18E-06	1.76				Rock, Average
Incropera and De Witt		0.27		1515	800	Sand

Reference	Thermal Diffusivity, $\beta$ : $m^2/s$	Thermal conductivity, $k$ : $W/m\ ^\circ C$	Volumetric Heat capacity, $\rho c_p$ : $J/m^3\ ^\circ C$	Density, $\rho$ : $kg/m^3$	Specific Heat, $c_p$ : $J/kg\ ^\circ C$	Material
(1990) and Cenegal (1997)						
Jobson (1977)	7.70E-07		2.85E+06			Sand
Kim and Chapra (1997)	3.00E-07		1.39E+06	1750	795	Sand
Pluhowski (1970)		1.65				Sand and gravel, saturated with water
Geiger (1965)	3.00E-07 - 5.00E-07	0.17 - 0.29	4.19E+05 - 1.68E+06	1400 - 1700		Sand, dry
Kreith and Bohn (1986) and Bejan (1993)		0.58				Sand, dry at 20 °C
Kreith and Bohn (1986) and Bejan (1993)		1.13		1640		Sand, moist at 20 °C
Geiger (1965)	4.00E-07 - 1.00E-06	0.84 - 2.51	8.38E+05 - 2.51E+06	2600		Sand, wet
Carslaw and Jaeger (1959)	1.10E-06	2.51		2300	964	Sandstone
Grigull and Sander (1984) and Bejan (1993)	1.00E-6 - 1.30E-6	1.6-2.1		2150 - 2300	710	Sandstone at 20 °C
Incropera and De Witt (1990) and Cenegal (1997)		2.90		2150	745	Sandstone, Berea
Likens and Johnson (1969)		0.57				Sediments, center of Tub Lake
Likens and Johnson (1969)		0.46				Sediments, center of Stewart's Dark Lake
Fang and Stefan (1998)	4.05E-07		2.30E+06			Sediments, Lake

Reference	Thermal Diffusivity, $\beta$ : $m^2/s$	Thermal conductivity, $k$ : W/m °C	Volumetric Heat capacity, $\rho c_p$ : J/m <sup>3</sup> °C	Density, $\rho$ : kg/m <sup>3</sup>	Specific Heat, $c_p$ : J/kg °C	Material
Likens and Johnson (1969)		0.59				Sediments, shoreline of Stewart's Dark Lake
Likens and Johnson (1969)		0.57				Sediments, shoreline of Tub Lake
Parker (1967)	1.974E-07	0.43		952	2303	High-density polyethylene, HDPE

### 3. Field Work

The site chosen for field work was the Lower Bull Run River, below Reservoir #2 and part of the Bull Run watershed as shown in Figure 13. The Lower Bull Run River was selected because there are low stream flows in the summer, plenty of opportunities for direct solar radiation on the river channel, and restricted access to the watershed protected field equipment. Previous work by Annear et al (1999) developed a model of the Lower Bull Run River from the Headwork's facility to the rivers confluence with the Sandy River.

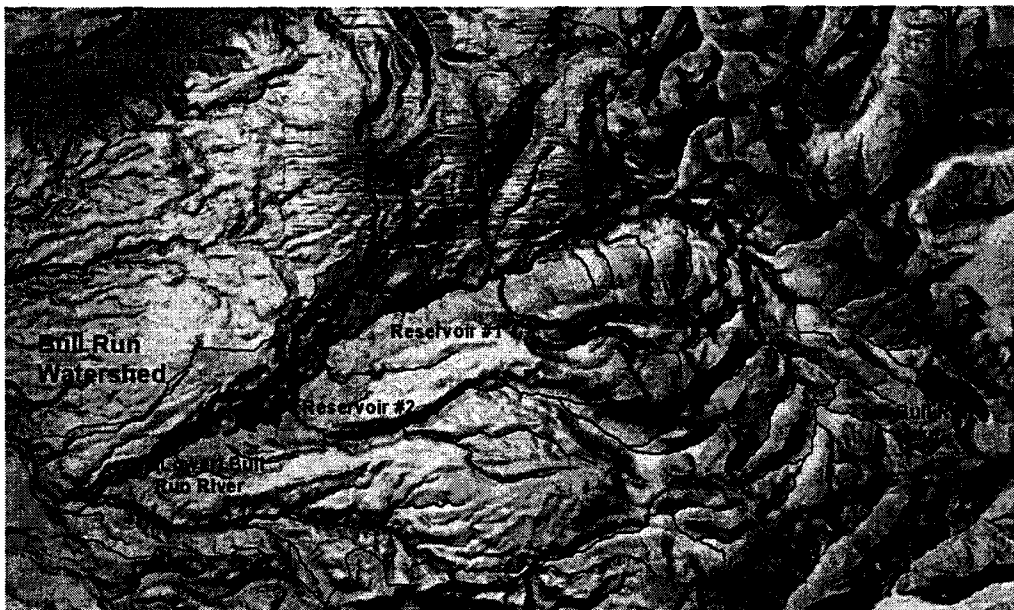
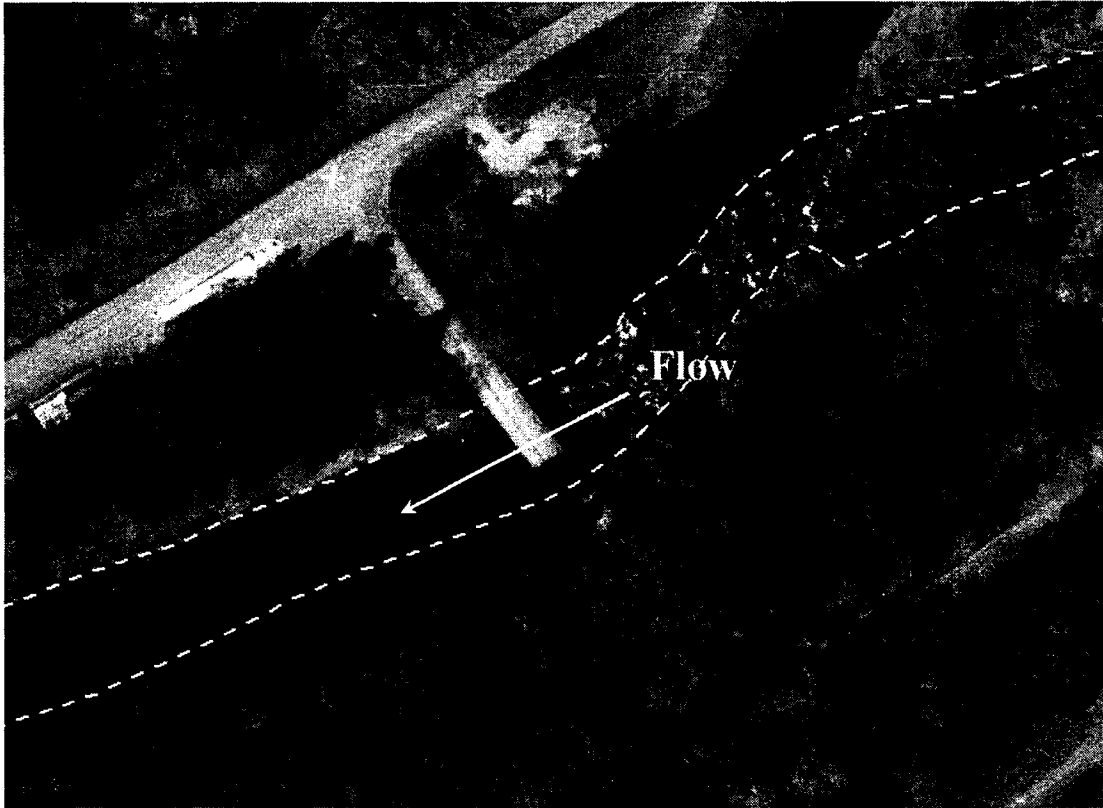


Figure 13: Bull Run Watershed

Fieldwork site was conducted between July 25<sup>th</sup> and September 20<sup>th</sup>, 2002 in the Lower Bull Run River around the Rt. 14 Bridge (RM 4.88) as shown in Figure 14.

The site was located 1.8 miles downstream from the Headwork's facility where water is diverted to the City of Portland.



**Figure 14: Lower Bull Run River field study area**

### **3.1 Bathymetric Data**

Bathymetric cross-sections were collected at nine locations in the field site on July 25<sup>th</sup> and July 26<sup>th</sup> 2002. Figure 15 shows the location of the survey points and cross-sections. Cross-section elevations were tied to a survey benchmark located on the Rt. 14 Bridge.



**Figure 15: Bathymetric river cross-section locations**

The river channel bathymetry also considers river cross-sections between the measured cross-sections. A river channel centerline was developed using a geographic information system (GIS). The centerline was used to create a series of spatial cross-sections, horizontal coordinates only, between the measured cross-sections. The cross-section elevation data was then used with these GIS cross-sections to linearly interpolate elevations. The result was an expanded set of bathymetric cross-sections as shown in Figure 16.

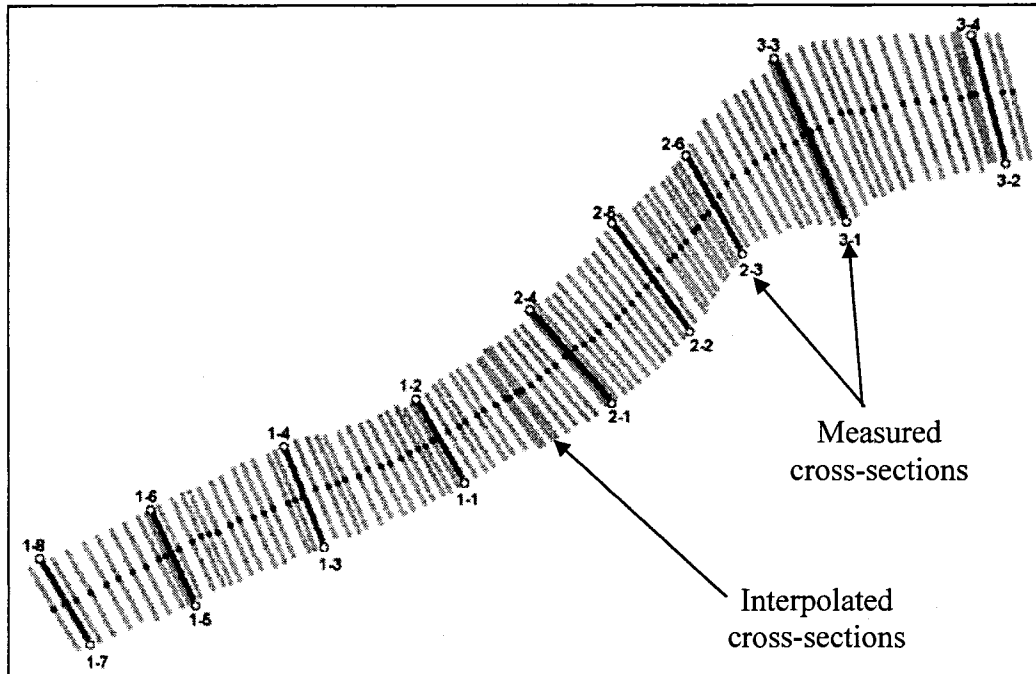


Figure 16: Combined data set for developing the river channel bathymetry

The measured bathymetric cross-sections and the interpolated cross-sections were combined in a contour plotting software, SURFER, to generate a contour plot shown in Figure 17. The contour plot and the river centerline were then used to slice the river bathymetry into 10 pieces to develop the CE-QUAL-W2 model segments. The volume-elevation curves for each segment were calculated and used to develop the model grid. For a given elevation range the contour plot specified a volume. The volume was divided by the model grid layer thickness (the elevation range) and segment length. The resulting channel width was used in the model bathymetry file as the model segment layer width. The model grid can be determined by either preserving volume or the surface area as a function of elevation. The Lower Bull River model grid developed preserved the volume as a function of elevation. Figure 18 shows a plan view of the model grid layout overlaying an aerial photo of the river.

The river was broken into three reaches, which represent different substrates and river channel slopes. A volume-elevation curve from the computed model grid was compared with the SURFER volume-elevation curve in Figure 19. The surface area-elevation curve for the computed model grid and the data from the SURFER plot are compared in Figure 20. The model grid was broken into three water bodies, each with different slopes to represent the three reaches identified in Figure 18. Reach 1 was characterized by large cobble and boulder substrate with a 2.5 % river channel slope. Reach 2 had exposed bedrock with channel constrictions and an overall slope similar to Reach 1. Reach 3 had bedrock substrate with a channel slope close to zero, representing a pool section. Table 24 lists the model grid layout providing branch slopes, segment lengths, and segment layer thicknesses. The length of the river section modeled was 220 m.

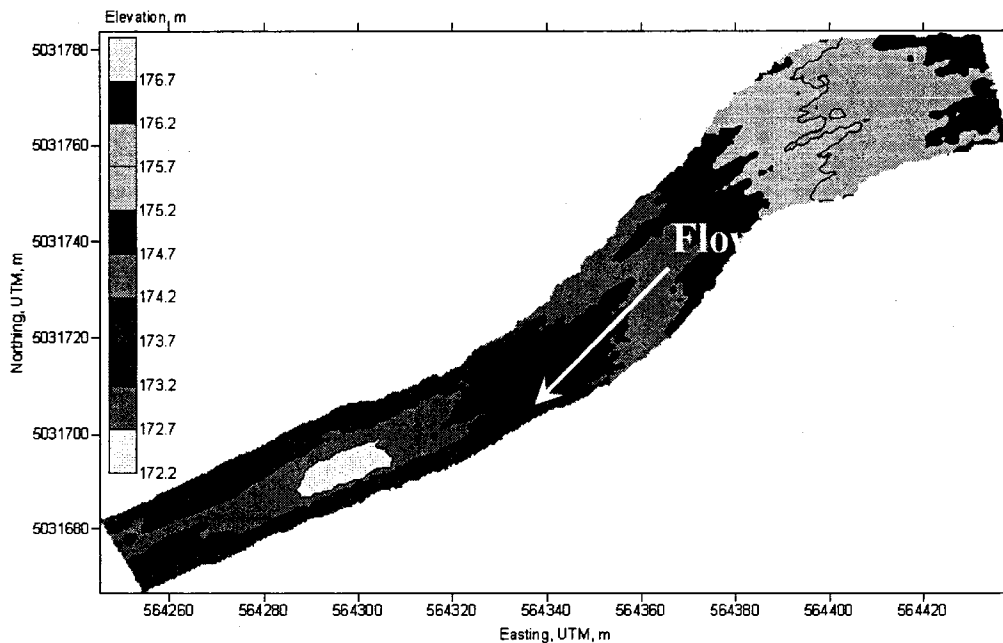


Figure 17: SURFER elevation contour of the river channel

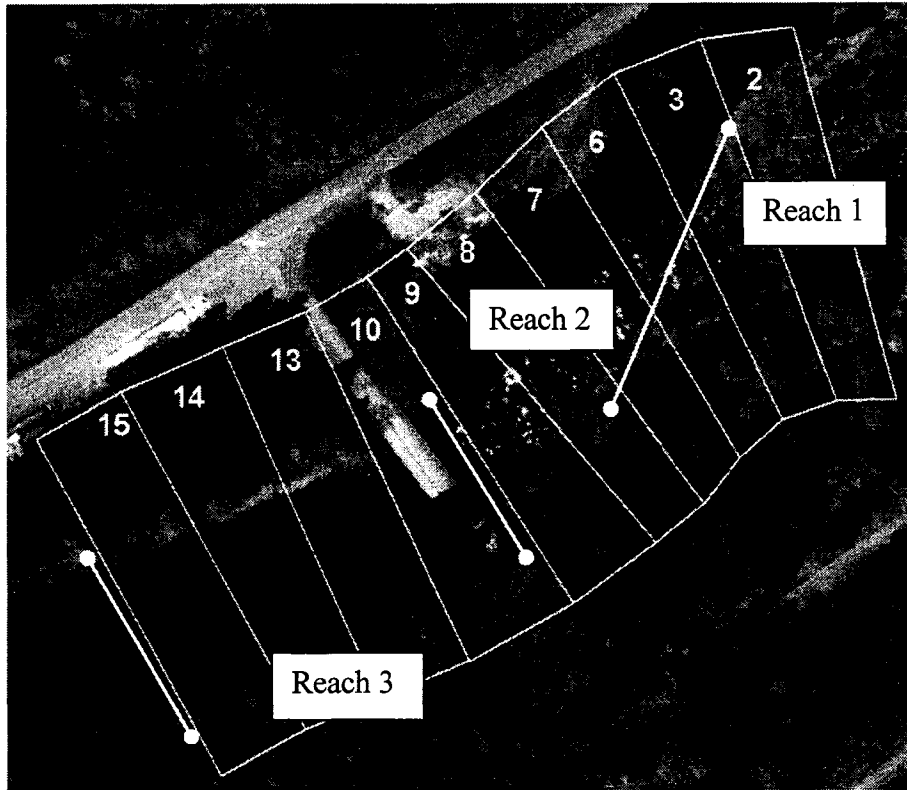


Figure 18: Model grid plan view with segment numbers

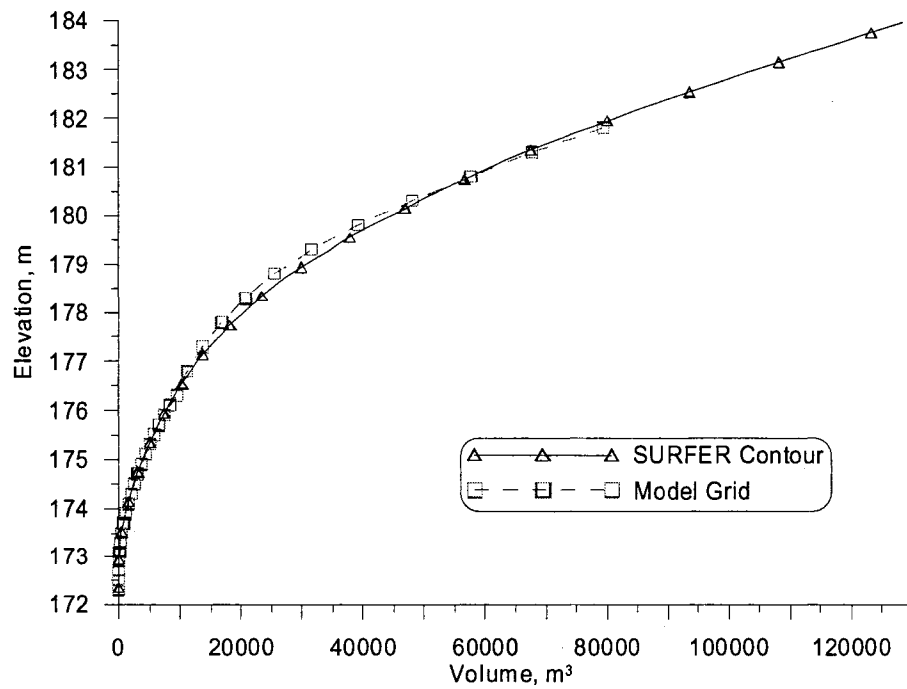


Figure 19: Volume-elevation curve comparing data and the CE-QUAL-W2 model grid

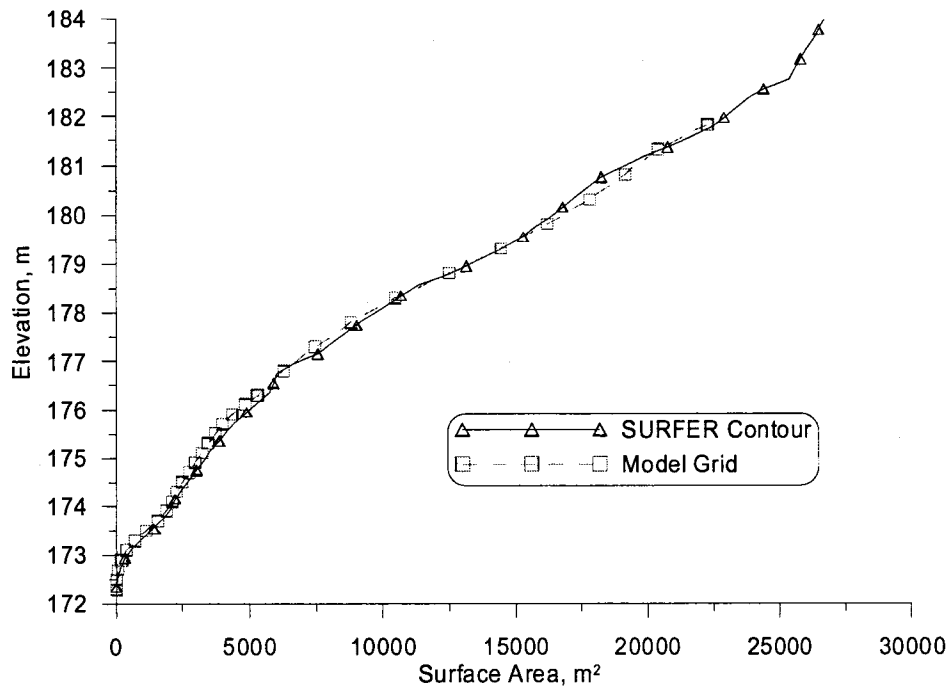


Figure 20: Surface area-elevation curve comparing data and the CE-QUAL-W2 model grid

Table 24: Lower Bull Run River model grid layout

Seg	Water body	Branch	Segment Length, m	River Distance, m	Layer height, m	Orient. angle, deg	Bottom Elev.	Branch Slope
2	1	1	20	210.0	0.2	74.5	175.88	0.0247
3	1	1	20	190.0	0.2	69.1	175.35	
6	2	2	20	170.0	0.2	63.8	174.89	0.0237
7	2	2	20	150.0	0.2	58.8	174.58	
8	2	2	20	130.0	0.2	53.4	173.97	
9	2	2	20	110.0	0.2	49.3	173.44	
10	3	3	25	87.5	0.2	57.3	172.94	0.0030
13	3	3	25	62.5	0.2	64.8	172.34	
14	3	3	25	37.5	0.2	65.9	172.48	
15	3	3	25	12.5	0.2	61.2	172.72	

### 3.2 Stream Temperature Data

Stream temperature data were collected at two locations upstream of the Rt.14 Bridge using OnSite StowAway temperature logger, recording at 10-minute intervals.

The USGS monitored one location downstream of the bridge at 15-minute intervals using a thermocouple. Figure 21 shows the three monitoring site locations. The two upstream monitoring sites upstream included replicate thermistors, which showed consistent temperature measurements at each site. Figure 22 shows the stream temperature recorded at the three locations. The figure also includes several water temperature measurements taken using a thermometer with a resolution of 0.2 °C. The graphs indicate diurnal fluctuations in temperature of about 5 °C due to daily solar heating. The data collected at site 132 were used as the upstream boundary condition for the model. The data collected at site 133 and the USGS gage station (14140000) were used in calibrating the model.

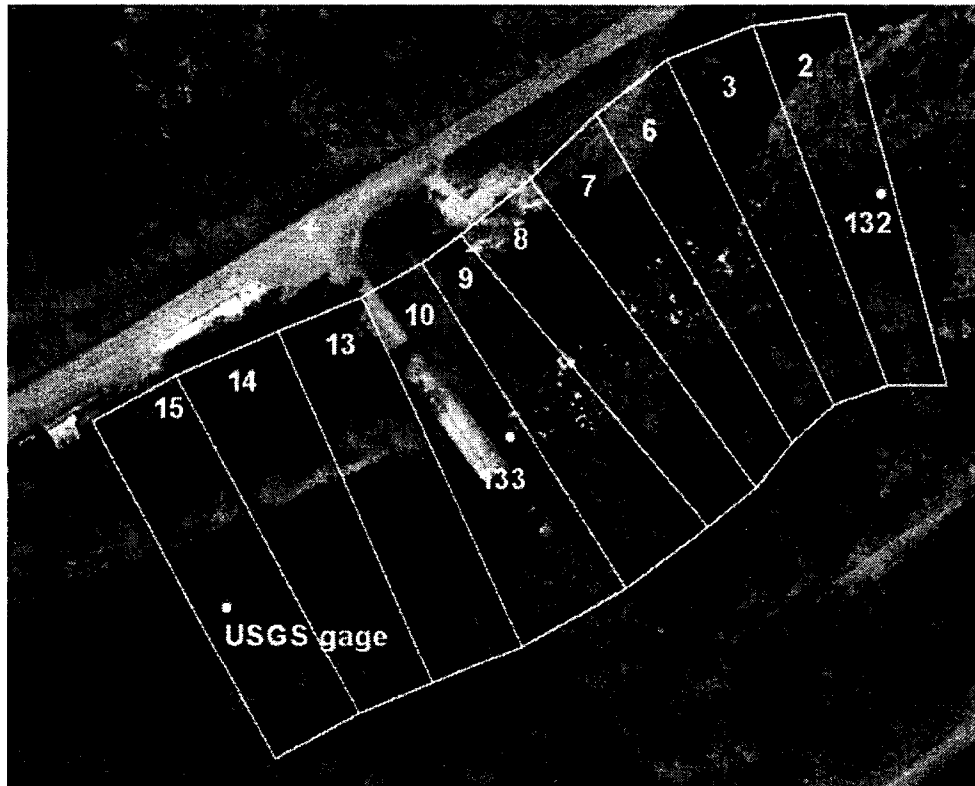


**Figure 21: Stream temperature monitoring sites.**

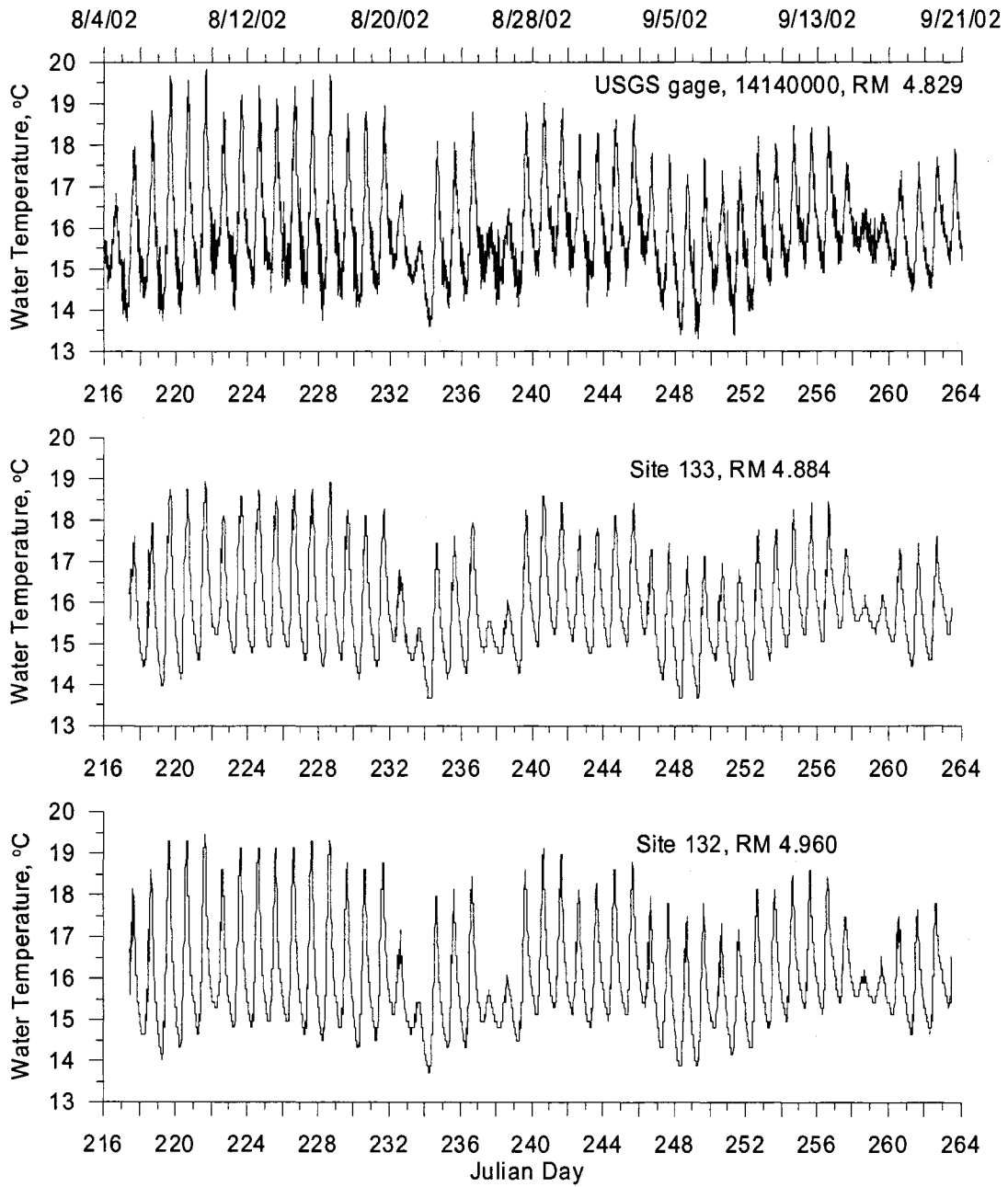


**Figure 22: Stream temperature data, Lower Bull Run River**

### 3.3 Streambed Temperature Data

Streambed temperatures were monitored at five locations as shown in Figure 23. The three locations monitored above the bridge were in cobble substrate (Probes 1

to 3) and the two locations monitored below the bridge were in bedrock substrate (Probes 4 and 5).

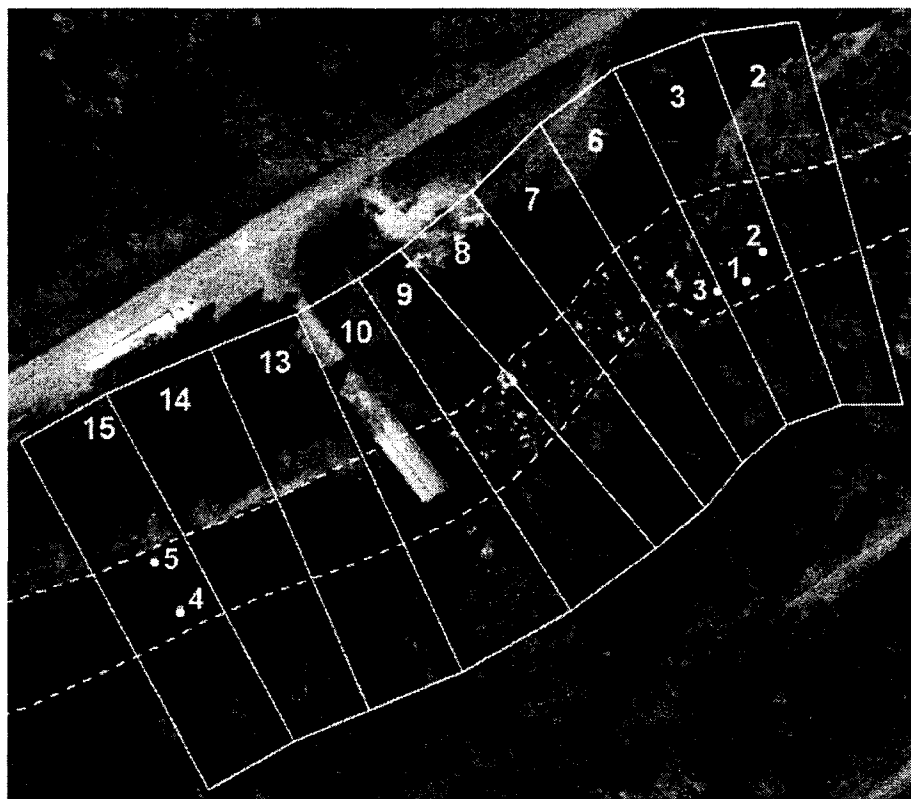


**Figure 23: Streambed temperature monitoring sites**

The temperature probes were constructed using 6.35 mm (0.25 in.) diameter PVC pipe with a length of 1.25 m. The pipe was cut in half longitudinally, 6 holes were drilled in one side of the pipe to fit 6 glass bead thermistors. The glass beads were set in each hole but not allowed to protrude from the outside edge of the pipe. The thermistor beads were held in place by silicone sealant for waterproofing. The thermistors were wired on the inside of the pipe and then filled with silicone sealant. The two pipe halves were joined together and sealed on the outside with more silicone. The cable connection coming out of the top of the probe was also sealed with silicone.

Figure 24 shows one of the completed probes. Three probes were constructed, but only two were used in the field at any one time. The two probes were placed in the field and after a week or more they were moved to a new location.

The probes placed in the cobble reach were placed at a maximum depth of 0.50 m due to the compact nature of the substrate and the inability of equipment to effectively penetrate deeper. The holes were dug by hand while storing the cobble material around the edges of the hole as shown in Figure 24. The probe was placed in the hole, and the substrate replaced in the reverse order that it was removed. Figure 24 shows an image of two probes placed in the streambed after the holes were filled. The substrate was then expected to gradually settle around the probes, which was confirmed when the probes were removed a few weeks later. A probe placement schematic in the cobble substrate is shown in Figure 24 where only the bottom three thermistors were buried in the substrate. The depths of the thermistors for each temperature probe and their recording periods are listed in Table 25.

Two probes, Probes 4 and 5, were placed in bedrock in holes drilled by the City of Portland, Water Bureau staff using a hydraulic drill with a diamond bit drill head. The holes were drilled to depths of 1.05 and 1.0 m with diameters between 25 and 32 mm (1.0 to 1.25 in). These probes were placed in the holes so the top thermistor was just below the substrate – water interface (see Figure 24 and Table 25). The probe was pressed against the side of the drilled hole with a long narrow piece of wood, and then sand was used to fill in the backside of the hole.

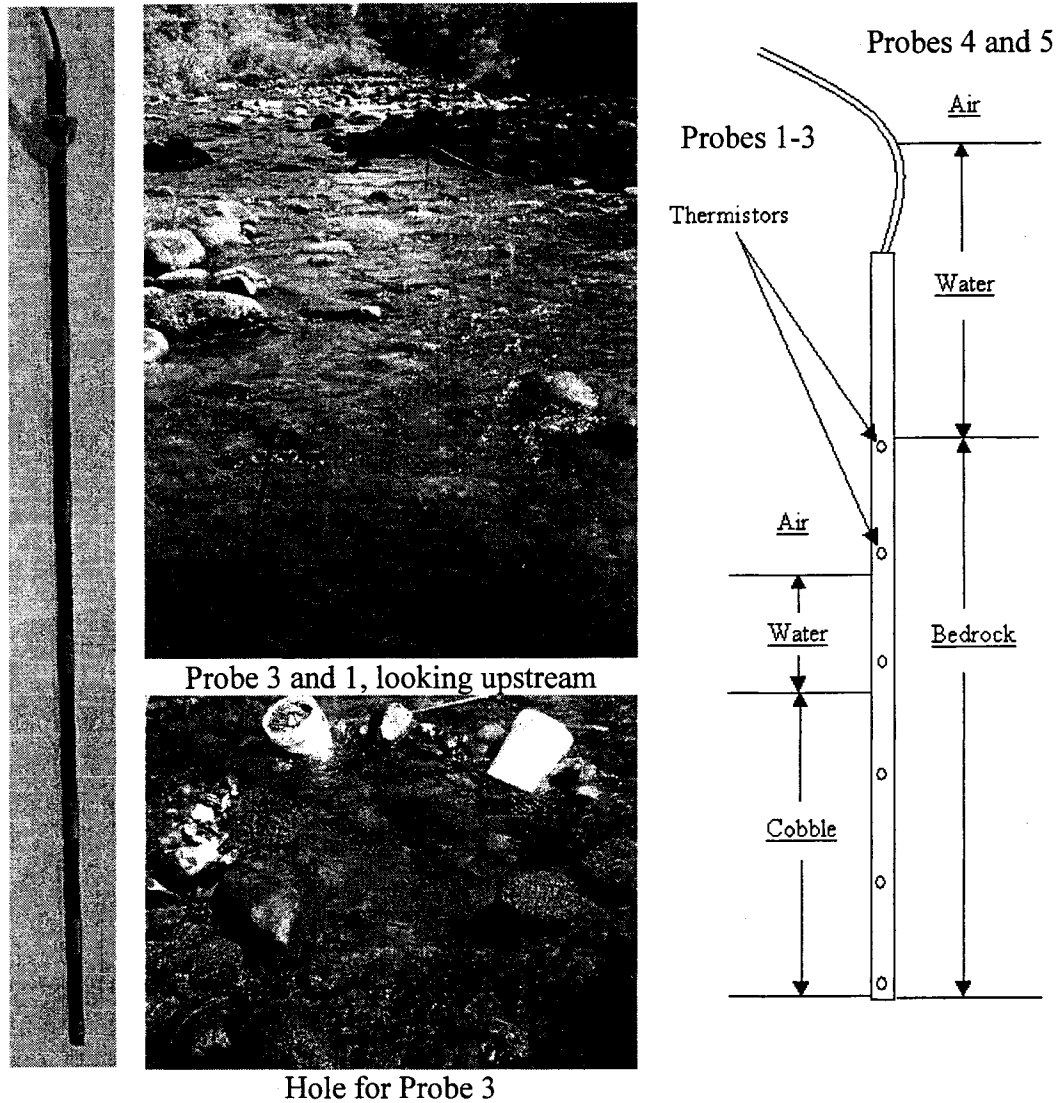


Figure 24: Streambed temperature probes, probes in the cobble went to a depth of 0.5 m below the sediment-water interface, probes in the bedrock went down to depth of 1 m.

Table 25: Thermistor depths in Streambed Temperature Probes for cobble and bedrock media

Probe	1	2	3		4	5
Start Date	08/07/02	08/07/02	08/23/02		09/05/02	09/05/02
End Date	09/05/02	08/23/02	09/05/02		09/20/02	09/20/02
Media	Depth, m	Depth, m	Depth, m	Media	Depth, m	Depth, m
Cobble	0.11	0.07	0.10	Bedrock	0.0	0.0
	0.31	0.27	0.30		0.2	0.2
	0.51	0.47	0.50		0.4	0.4
			0.6		0.6	
			0.8		0.8	
			1.0		1.0	

Probes 1 and 2 were placed in the streambed for two weeks to examine lateral variability on streambed temperatures. Probe 2 was then removed from the substrate and was placed downstream of Probe 1 to investigate longitudinal variability in streambed temperature (re-designated Probe 3). After 2 weeks the two probes were both removed and placed at the two bedrock sites. Probe 3 was then re-designated Probe 4 and Probe 1 was re-designated Probe 5. The third probe built served as a backup in case problems arose with one of the other two probes. Data collected from the temperature probes were examined in the field to determine if any of the data were erroneous before the probes were placed in the bedrock. Some of the temperature measurements in the bedrock substrate were found to be erroneous. See Appendix D for further discussion on suspect data.

### **3.3.1 Cobble Streambed Temperature Results**

Figure 25 shows the cobble streambed temperature from August 7, to September 6, 2002. The figure shows streambed temperatures for Probe 1 which was located near the south bank of the Bull Run River and was in the shade for most of the day. Temperature results indicate there were diurnal warming and cooling in the substrate with the largest temperature swings in the water and the lower depths with decreasing daily temperature swings at higher depths. Additionally the daily peak temperatures are also delayed later in time for deeper depths. The figure also shows

the temperature at a depth of 0.5 m does not cool off at night as much as the shallower depths.

Figure 26 shows the temperature results from Probe 2, which was placed more towards the center of the river where there was more sun exposure from August 7 to 23, 2002. The figure shows a similar diurnal pattern as shown in Figure 25 with the exception of the temperature measurements at 0.47 m depth for August 7 to 14, 2002. During this time period the temperature data indicates that it was much warmer than the depths above. This could be due to inter-gravel flow through before the substrate material resettled from putting the probe in the streambed. The temperature results at this depth tend to follow the more expected pattern after August 14, 2002 with night temperatures only slightly higher than the shallower depths.

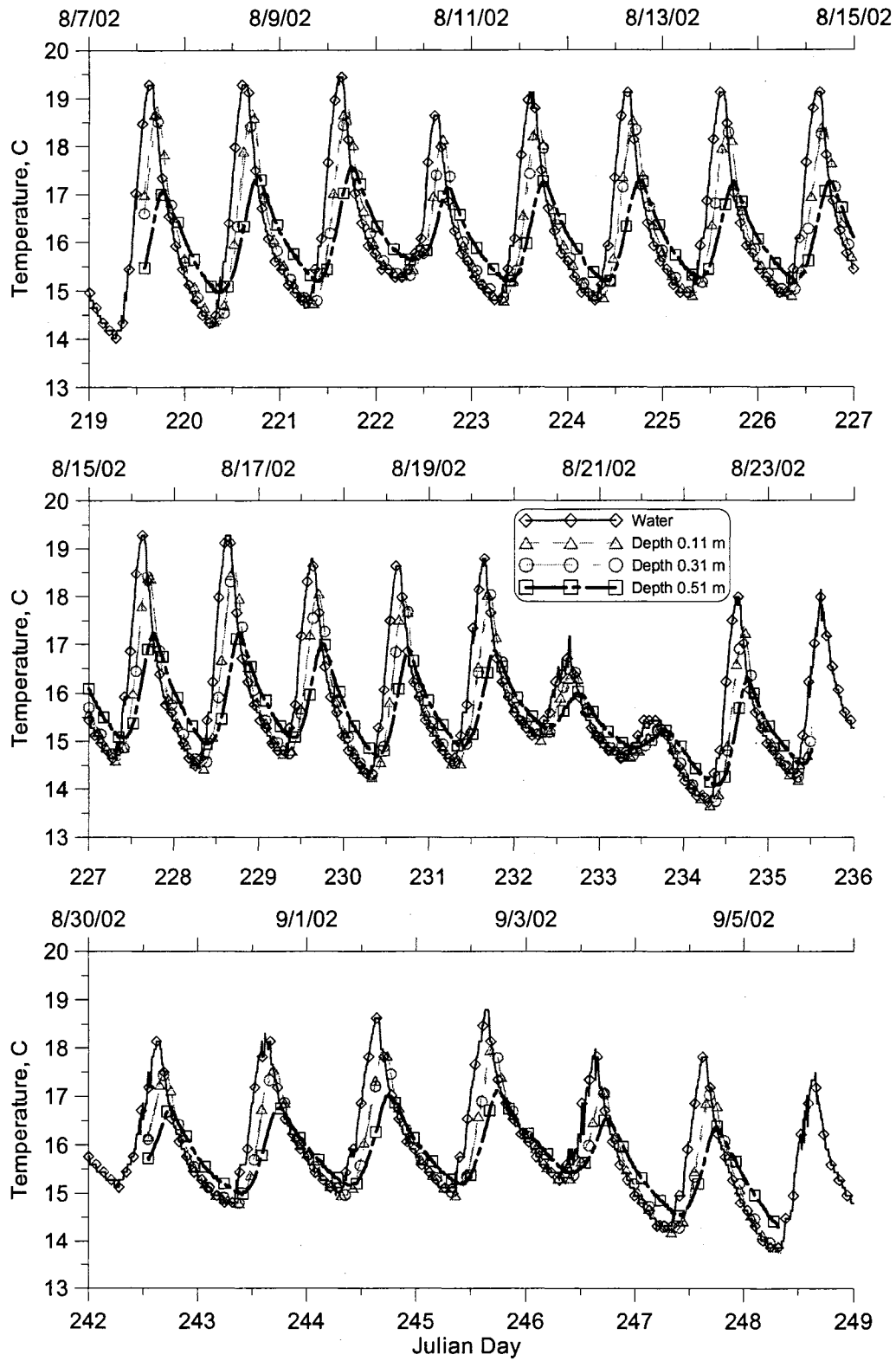


Figure 25: Streambed temperature Probe 1, cobble substrate near bank, shaded

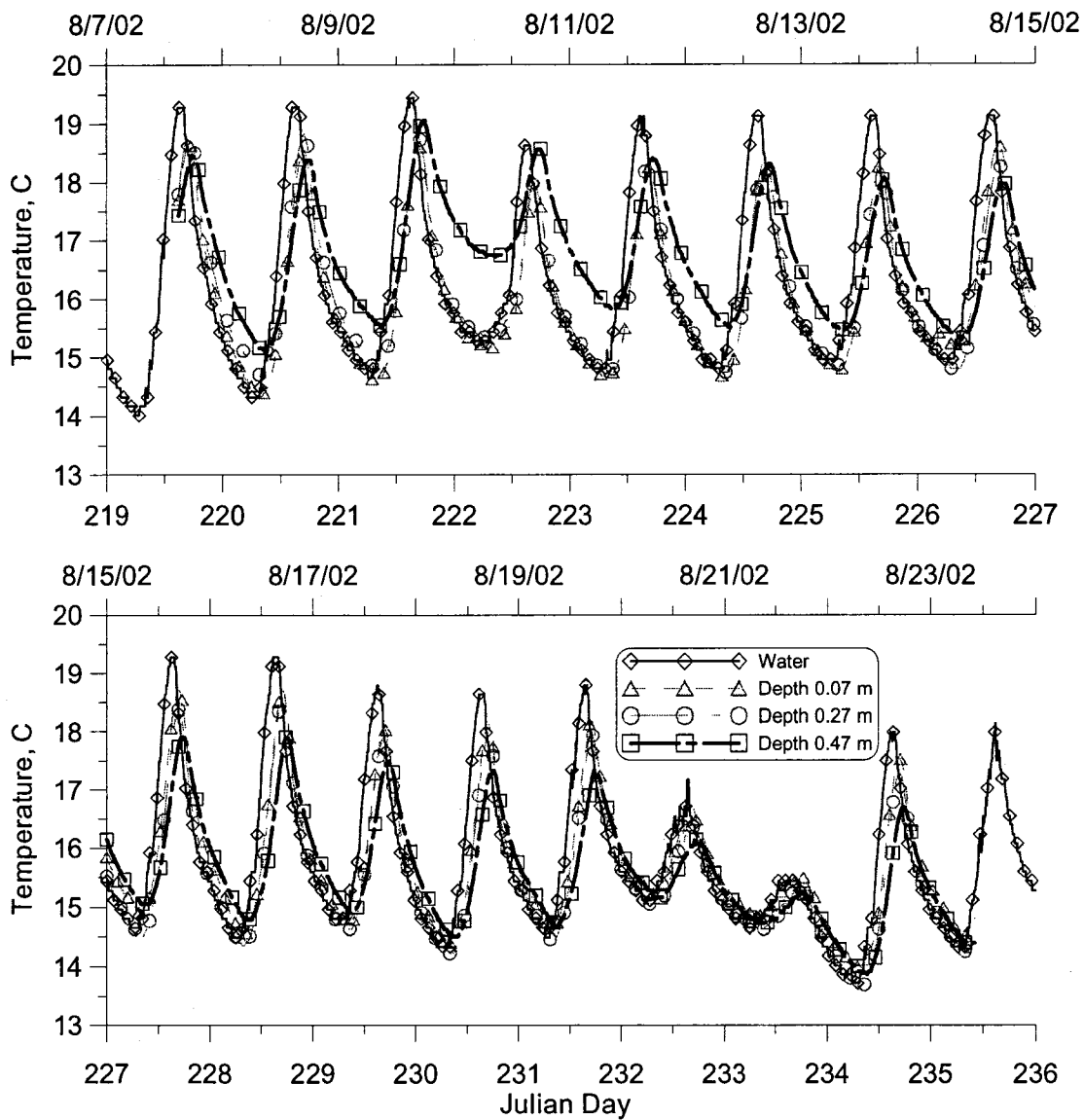


Figure 26: Streambed temperature Probe 2, cobble substrate closer to center, sunny

The substrate temperatures recorded at the shaded site (Probe 1) were then compared, at similar depths, with the substrate temperatures from the site exposed to more solar radiation (Probe 2). Figure 27 compares the substrate temperatures for the two sites. The figures show the temperatures are similar for the first two depths at 0.1 and 0.3 m. There are more significant differences at a depth of 0.5 m. As mentioned

previously, the temperatures measured at 0.50 m depth for Probe 2 for the first 7 days (August 7 to August 14, 2002) may have been influenced by interflow from unsettled streambed material. The figure indicates that even after August 14 the temperatures from the shaded site (Probe 1) reach lower daily peak temperatures compared to the site with more solar radiation exposure. Figure 28 shows the difference between the streambed temperatures in the sun (Probe 2) and the streambed temperatures in the shade (Probe 1) from August 15 to August 23, 2002. The figure indicates the streambed temperature at 0.1 m depth was consistently higher near the middle of the river versus near the bank. At a depth of 0.3 m the daytime peak temperatures were warmer at Probe 2 but during the rest of the diurnal cycle the temperature at Probe 1 appeared to be warmer. At a depth of 0.5 m Probe 2 is warmer by over 0.5 °C over several days but also dipping below zero for brief periods each day, indicating Probe 1 had higher temperatures.

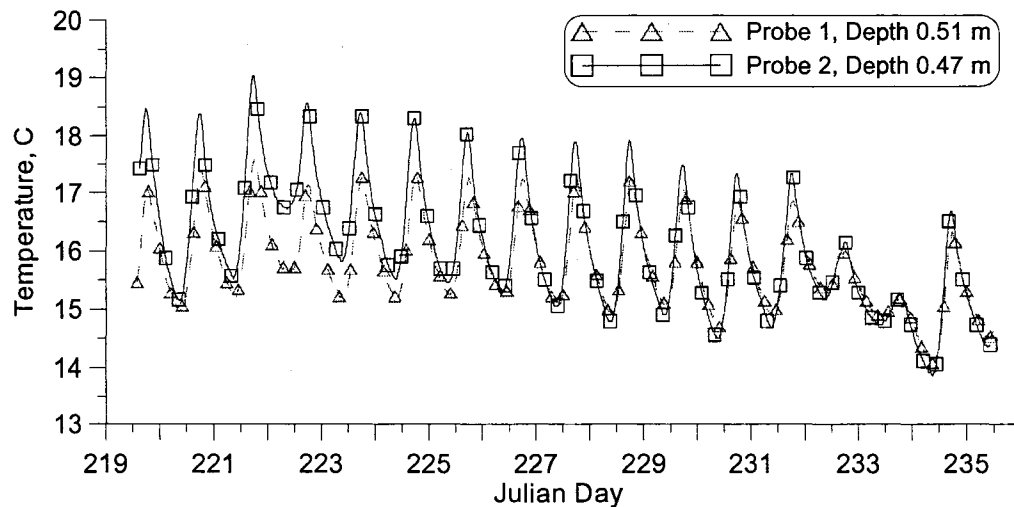
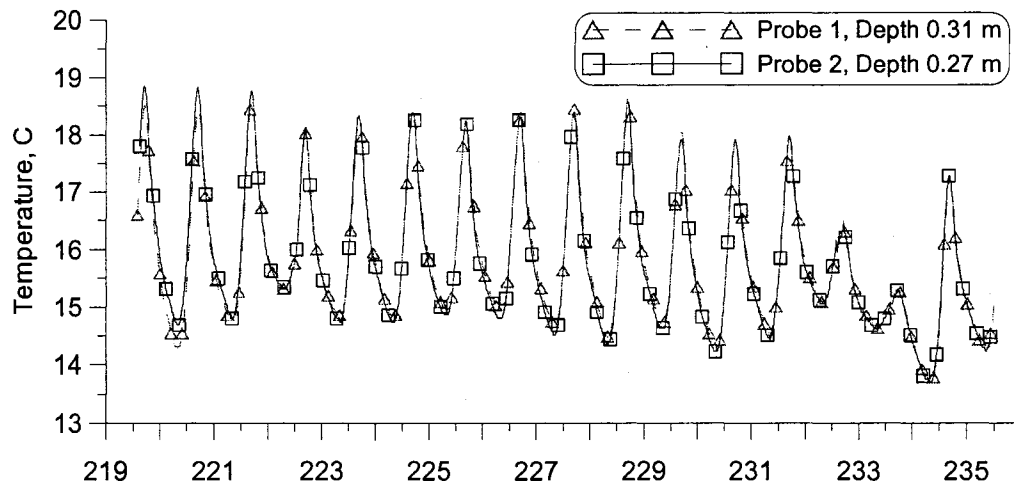
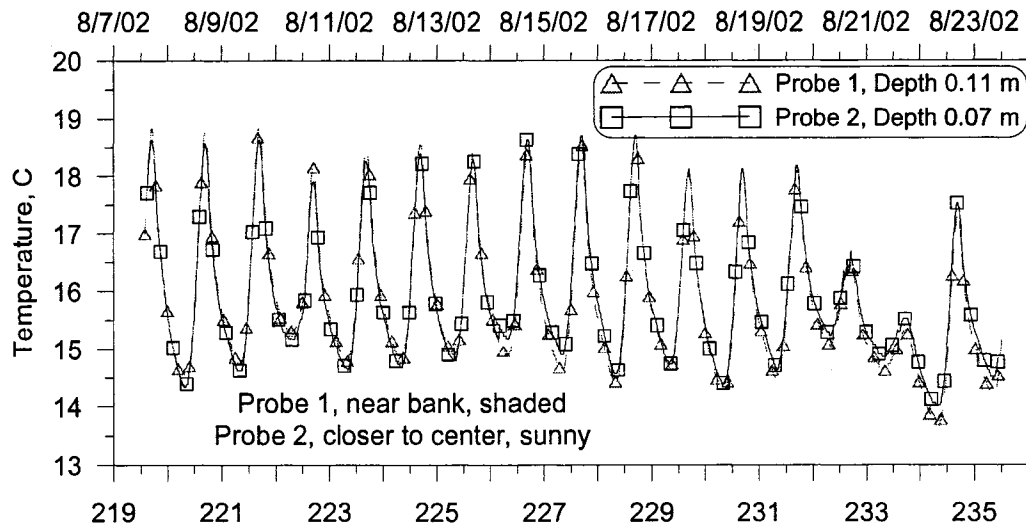


Figure 27: Streambed Probe 1 (near bank, shaded) and Probe 2 (closer to center, sunny) temperature comparison

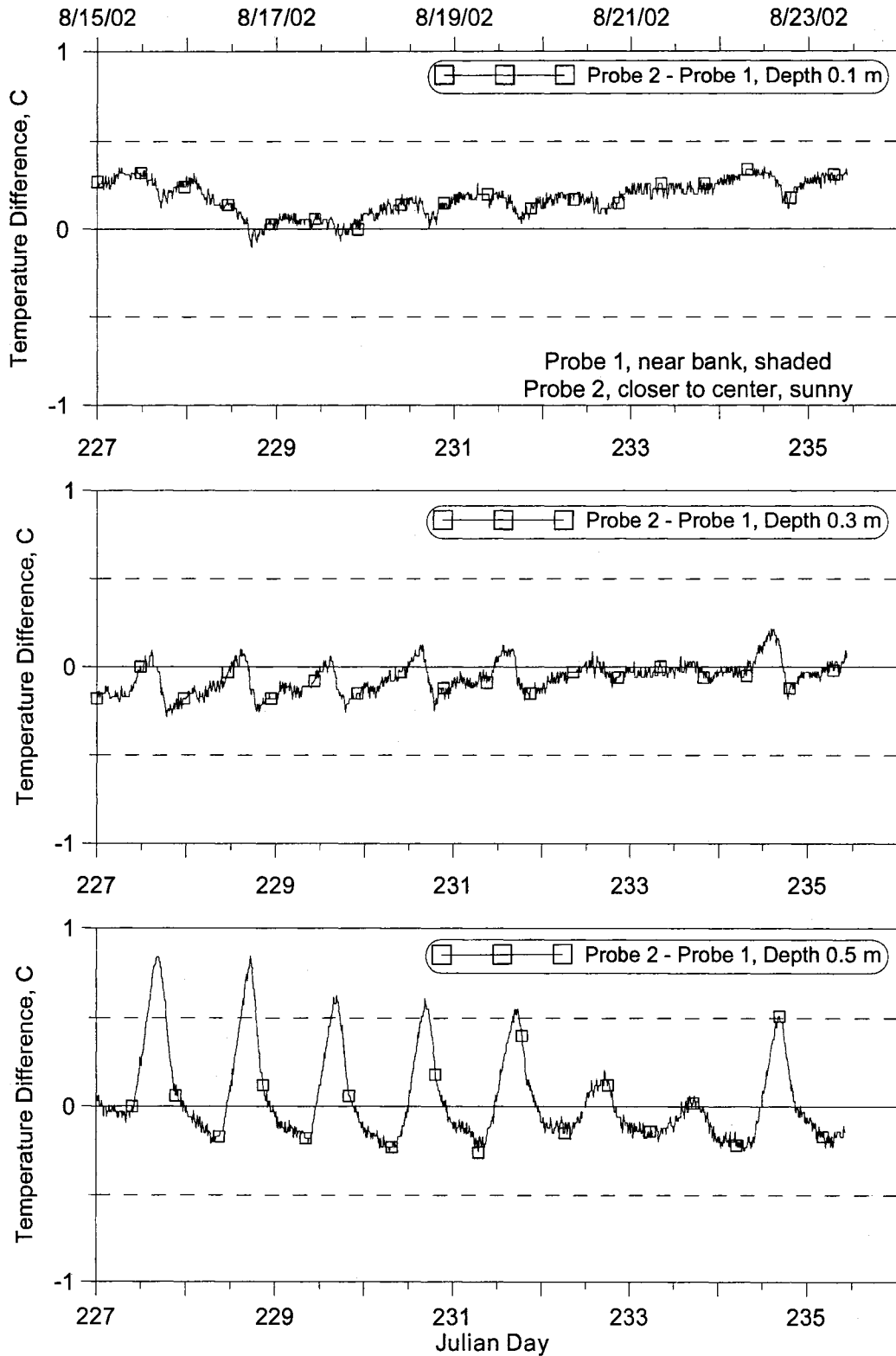


Figure 28: Difference between streambed temperature Probe 2 (closer to center, sunny) and Probe 1 (near bank, shaded)

After Probe 2 was placed in the river for several weeks, it was moved to a location along the south bank of the Bull Run River that was just downstream of Probe 1. Refer to Figure 23 for its location. The temperature thermistor probe was redesignated as Probe 3, and Figure 29 shows a time series of streambed temperatures measured. The figure shows the streambed temperatures following a diurnal pattern of increasing and decreasing temperatures with the temperatures recorded at a depth of 0.5 m showing the smallest temperature swing over a day. Figure 30 shows a comparison plot of streambed temperatures for both probes at their corresponding depths. The figure indicates the streambed temperatures are similar at depths of 0.1 and 0.3 m, and at a depth of 0.5 m the temperatures at Probe 1 are higher throughout the diurnal cycle compared to Probe 3 downstream. Figure 31 shows the difference between the streambed temperature measurements at the two sites between August 30 and September 6. The difference in temperature at depth of 0.1 and 0.3 m shows little difference between the two sites with some diurnal variation at a depth of 0.3 m but still fluctuating around zero. The difference in temperature between the two sites at a depth of 0.5 m shows there is some variation with the temperatures at Probe 3 less than the upstream site, Probe 1. The difference in streambed temperature shows a large diurnal swing than the shallower depths.

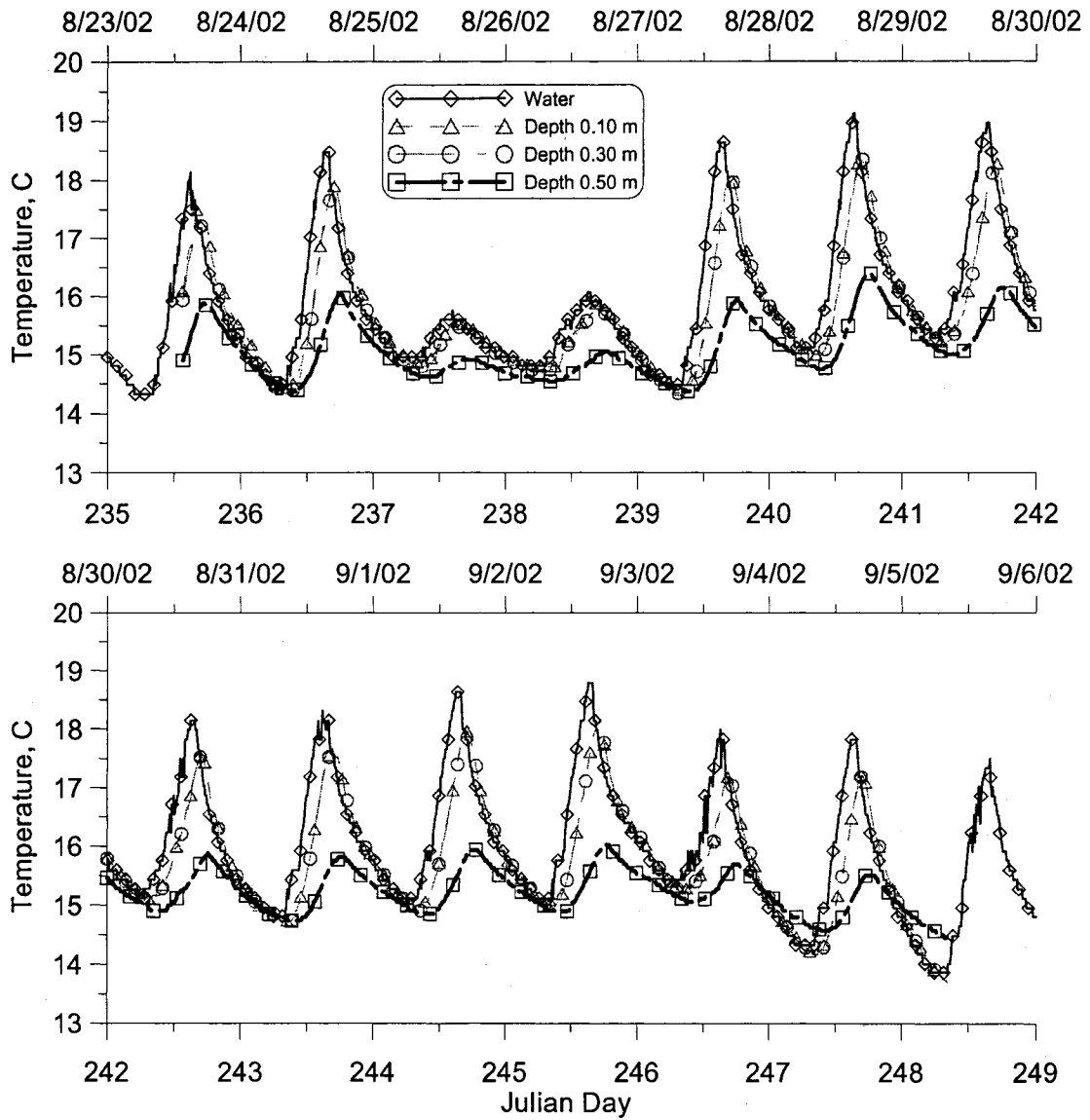


Figure 29: Streambed temperature Probe 3, cobble substrate, near bank downstream of Probe 1

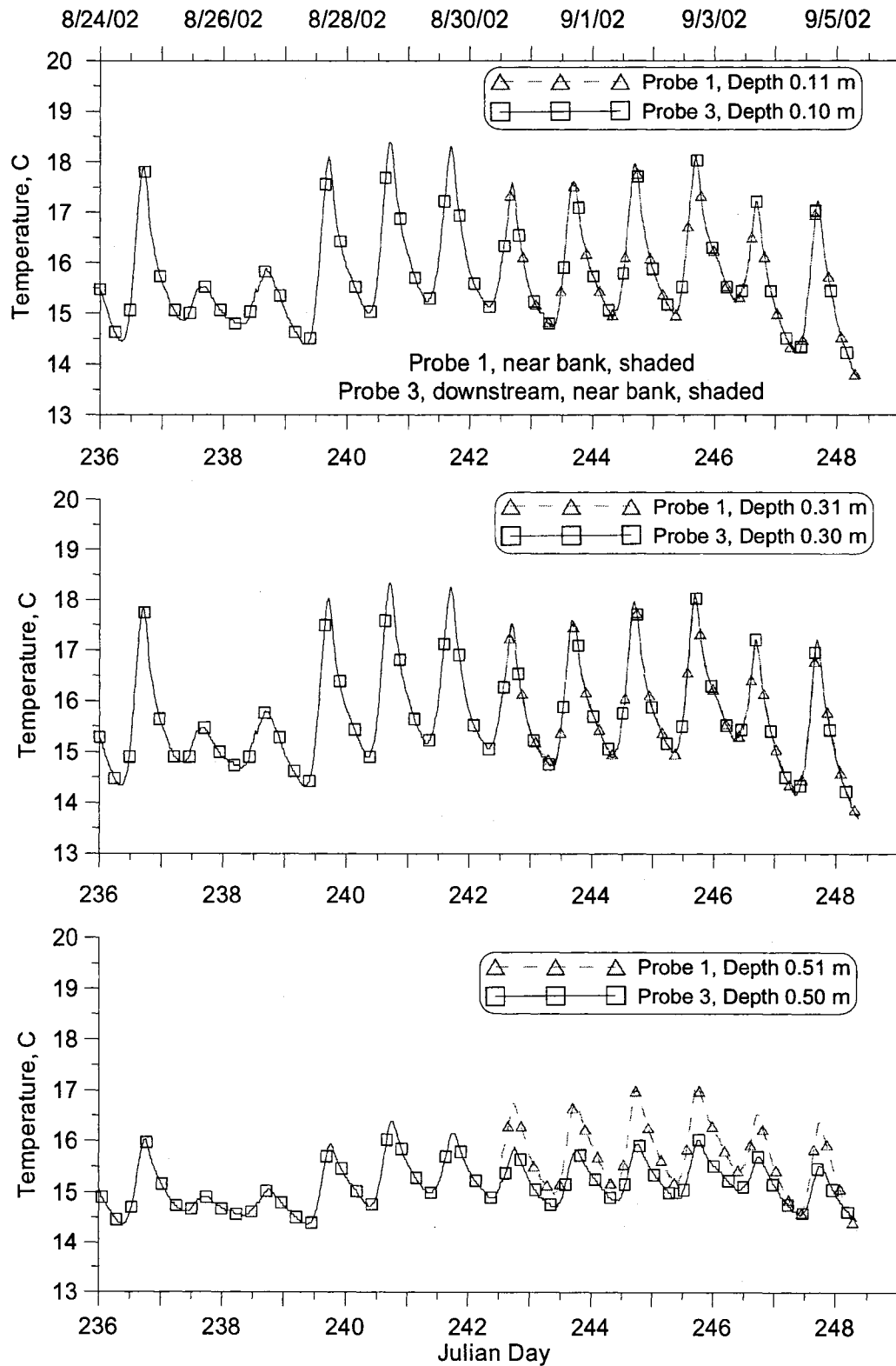
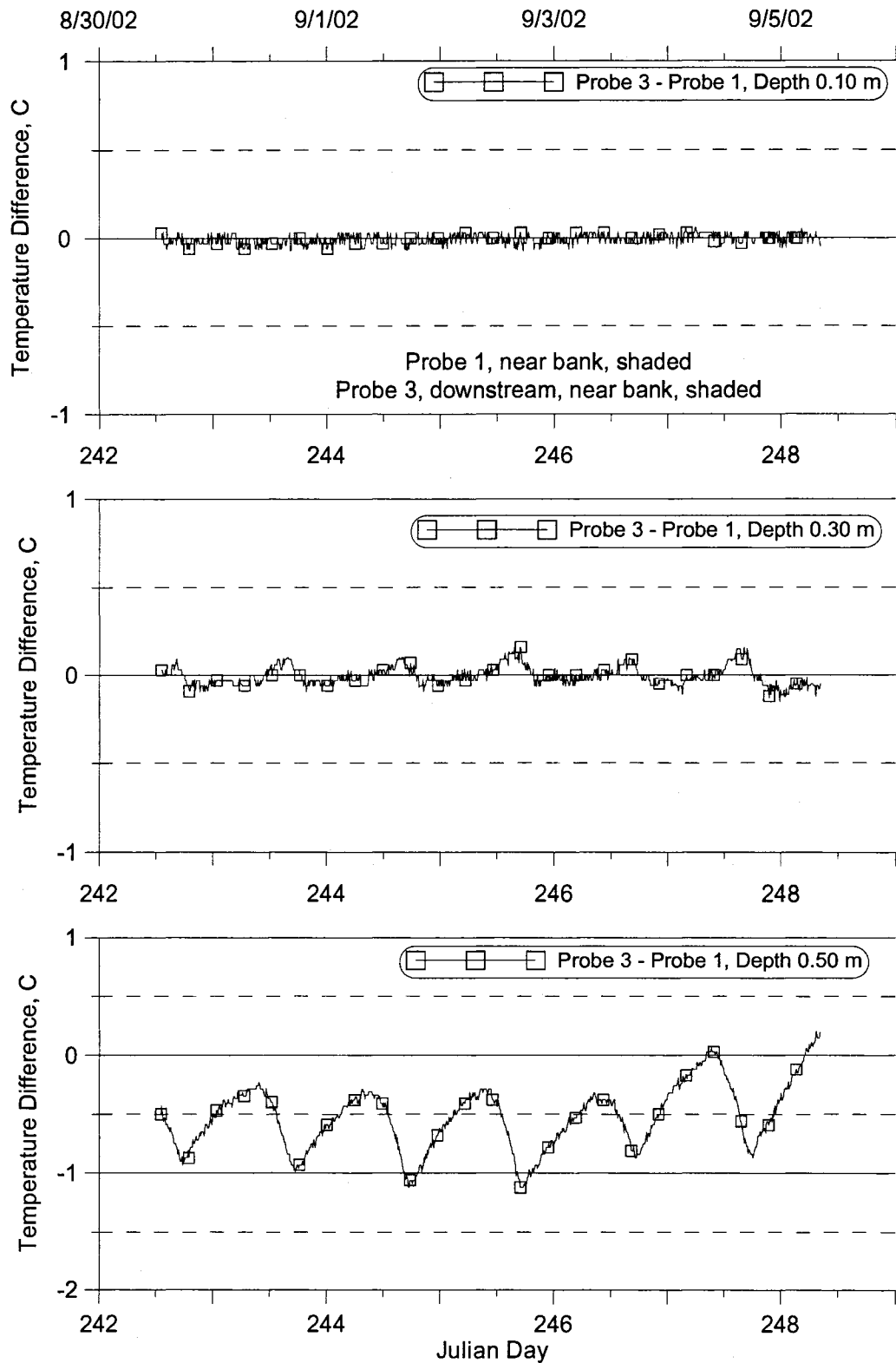


Figure 30: Streambed Probe 1 (near bank, shaded) and Probe 3 (near bank downstream) temperature comparison



**Figure 31: Difference between streambed temperature Probe 3 (near bank shade, downstream of Probe 1) and Probe 1 (near bank, shaded)**

### 3.3.2 Bedrock Streambed Temperature Results

Once the streambed temperature studies were done in the cobble substrate, the bedrock streambed was monitored from September 5 to September 13, 2002. The temperature results from Probe 4 which was placed near the south shore of the Bull River, see Figure 23, indicated the data measurements at depths of 0.0, 0.2 and 0.6 m were erroneous. Temperature measurements for Probe 5 at a depth of 0.6 m were also found to be erroneous. Erroneous data are discussed in Appendix D. Figure 32 shows the temperature measurements from Probe 4, which was located near the river bank and remained in the shade throughout the day. The figure indicates there are large temperature swings in the water temperature data but even at a depth of 0.4 m there is no diurnal temperature swing. The figure also indicates the temperature remains relatively constant at each depth, possibly showing large scale trends in temperature. Temperatures were found to decrease with increasing depth.

Figure 33 shows the temperature measurements from Probe 5, which was located near the opposite river bank to Probe 4, the north bank and remained in the sun throughout most of the day. The figure shows the temperature at a depth of 0.0 m was almost the same to the water temperature, as expected. The figure also shows that even 0.2 m in depth the diurnal fluctuation in the substrate temperature had been considerably dampened. For increasing depths the temperature decreased and was found to be following larger scale temporal trends and remained relatively constant over the time period monitored.

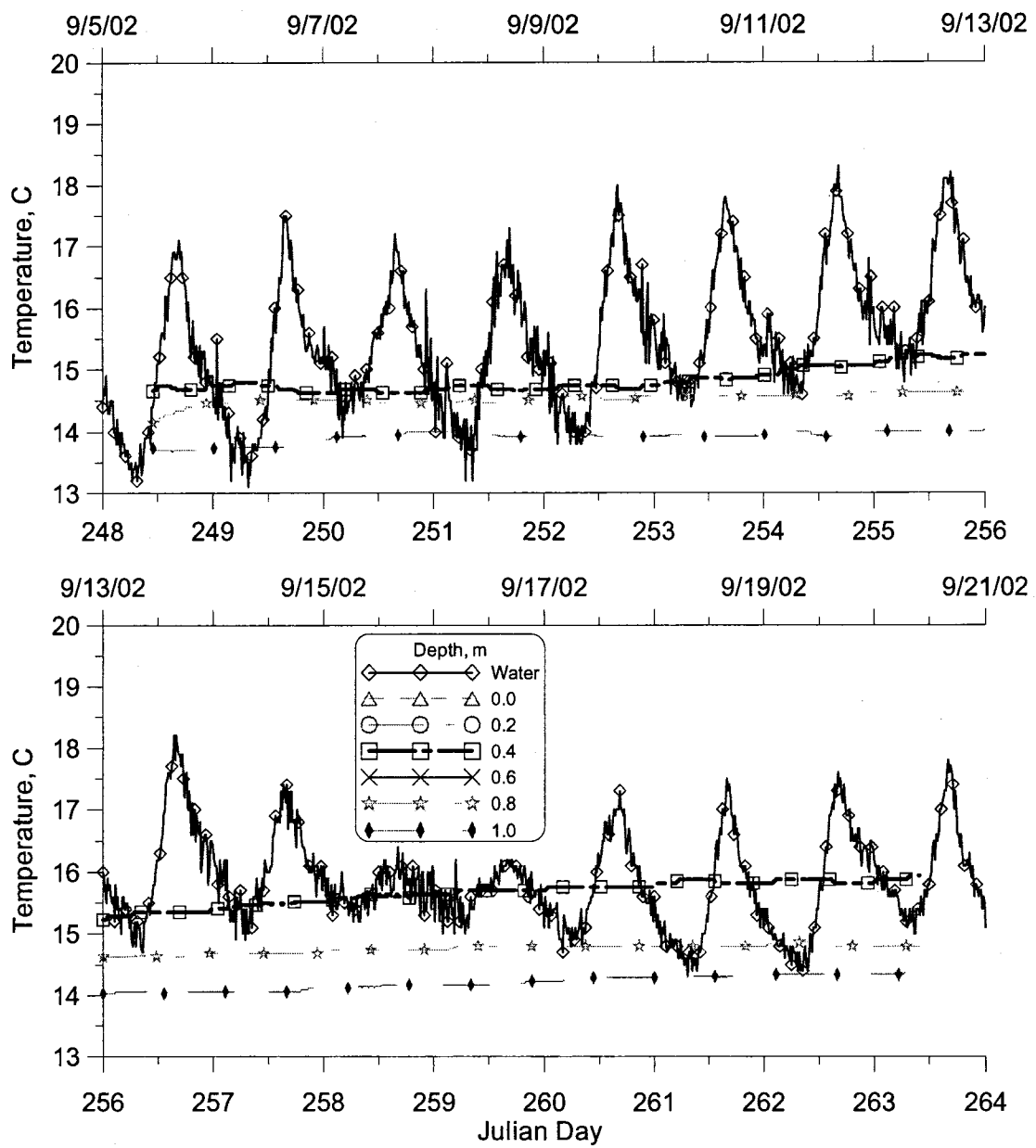


Figure 32: Streambed temperature Probe 4, bedrock substrate near bank, shaded

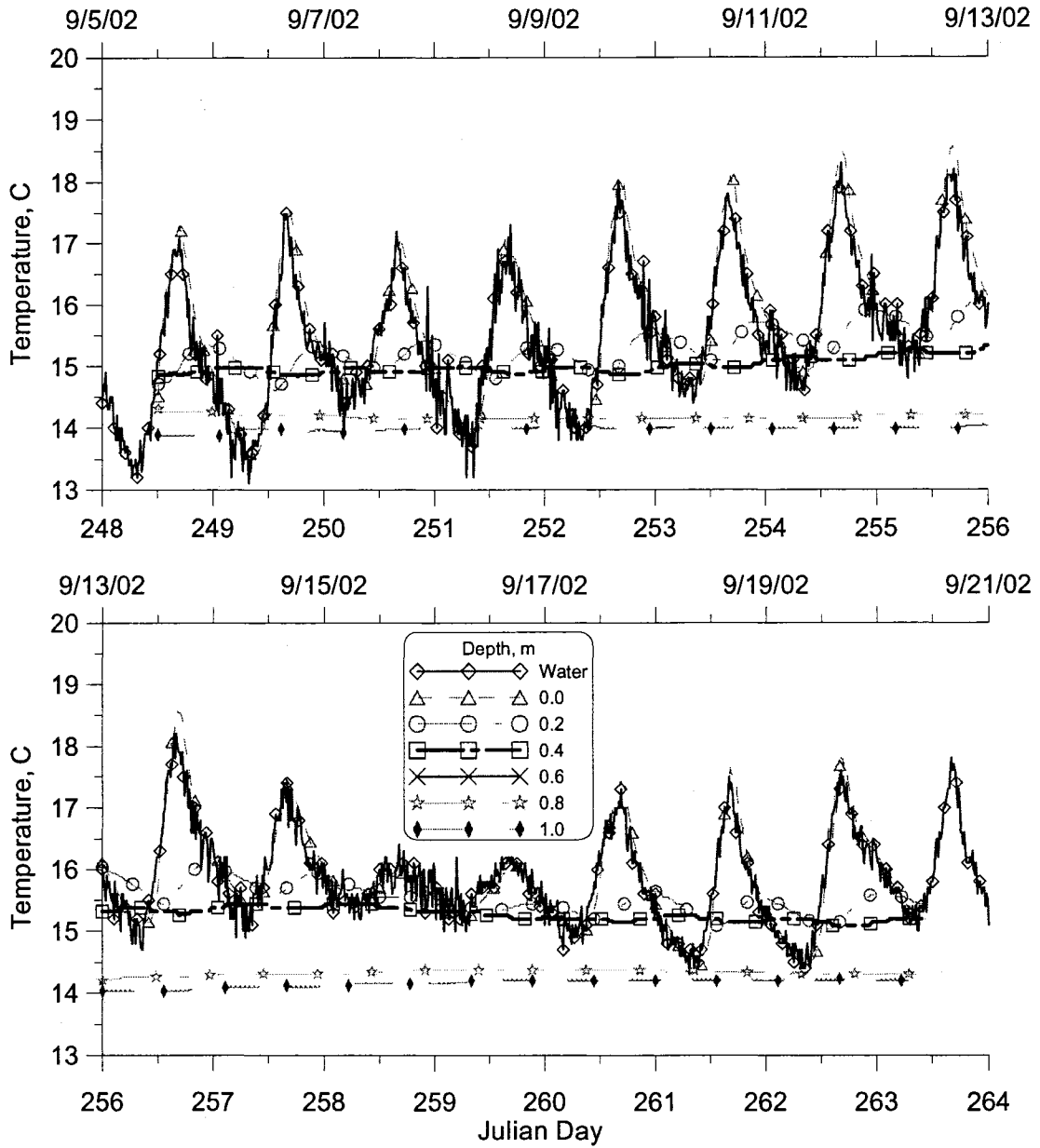


Figure 33: Streambed temperature Probe 5, bedrock substrate, near opposite bank to Probe 4, sunny

Figure 34 shows comparison plots of streambed temperature for both bedrock sites where there were corresponding data. The temperature data at 0.4 m depth indicate the two sites are similar for most of the monitoring period with a temperature deviating between the two sites after September 16, 2002. Both probes show similar

temperatures at a depth 0.8 m with Probe 4 showing slightly higher temperatures. The substrate temperature recorded at 1.0 m depth indicates both sites have similar temperatures. Figure 35 shows the difference between the temperature data at different depths for the two sites. The figure shows there is an increasing difference between the two sites with Probe 4 continuing to warm over the duration of the monitoring period but within 1 °C. The temperature difference at 0.8 m shows a Probe 4 is consistently about 0.5 °C higher than Probe 5. The difference in temperatures at 1.0 m depth indicates there is little difference between the two with the plot fluctuating around zero and falling within a range of -0.3 to 0.2 °C. The difference in temperature at the 1.0 m depth also indicates there is a slight rise in temperature at Probe 4 near the end of the simulation which may be due to heat propagating from above.

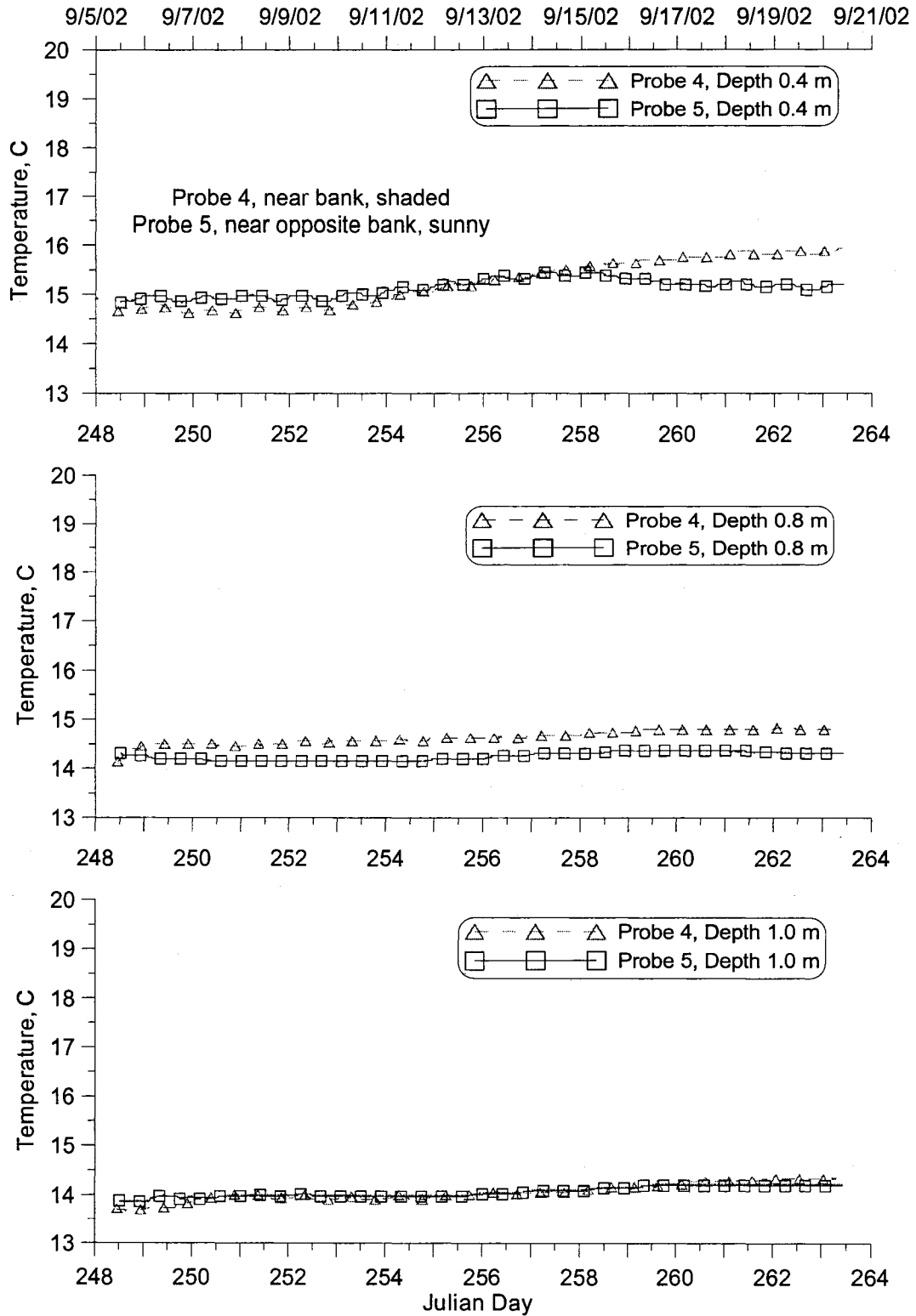


Figure 34: Streambed Probe 4 (near bank, shaded) and Probe 5 (near opposite bank to Probe 4, sunny) temperature comparison

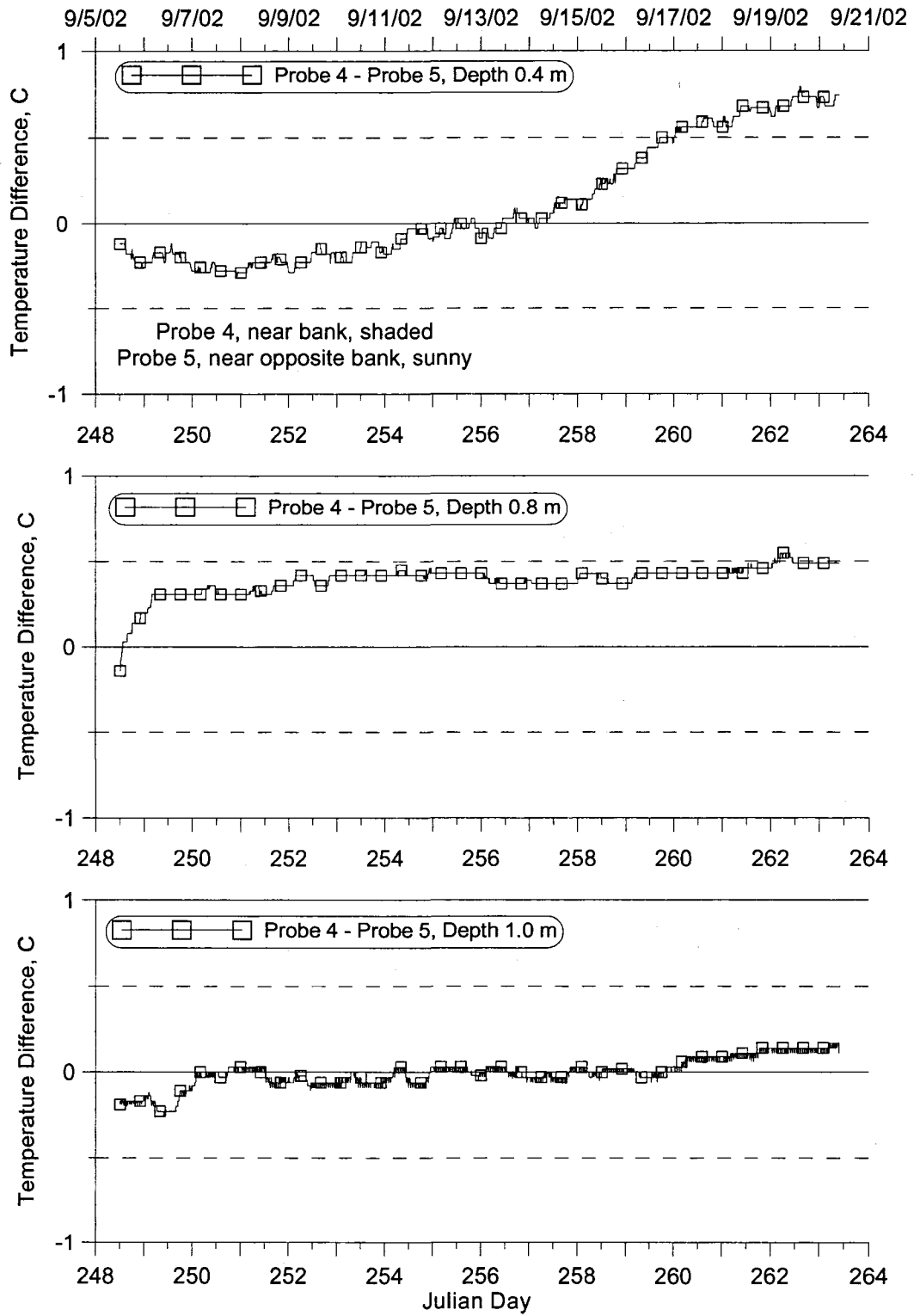


Figure 35: Difference between streambed temperature Probe 4 (near bank shade,) and Probe 5 (near bank, opposite side, sunny)

### **3.4 Streambed Substrate and Geology**

The streambed at the field site transitioned from cobble and boulder substrate at the upstream end to primarily bedrock at the downstream end. The streambed substrate can be characterized by three regions as shown in Figure 36. Reach 1 is characterized primarily by boulders and large cobble and represents the toe end of a plane-bed reach with run characteristics in low flow. Reach 2 substrate is characterized primarily by boulders and bedrock with a very uneven bottom surface capturing some cobble. The reach is a turbulent cascade with a slope of 2.4%. Reach 3 is characterized as a mid-channel pool reach with the deepest parts of the pool closer to head of the reach. The substrate is primarily bedrock with boulders and large cobbles predominately on the sides and banks. The toe of the reach slopes upward and is dominated by large cobble and boulders overlying the bedrock. Downstream of Reach 3 the river has a riffle reach.

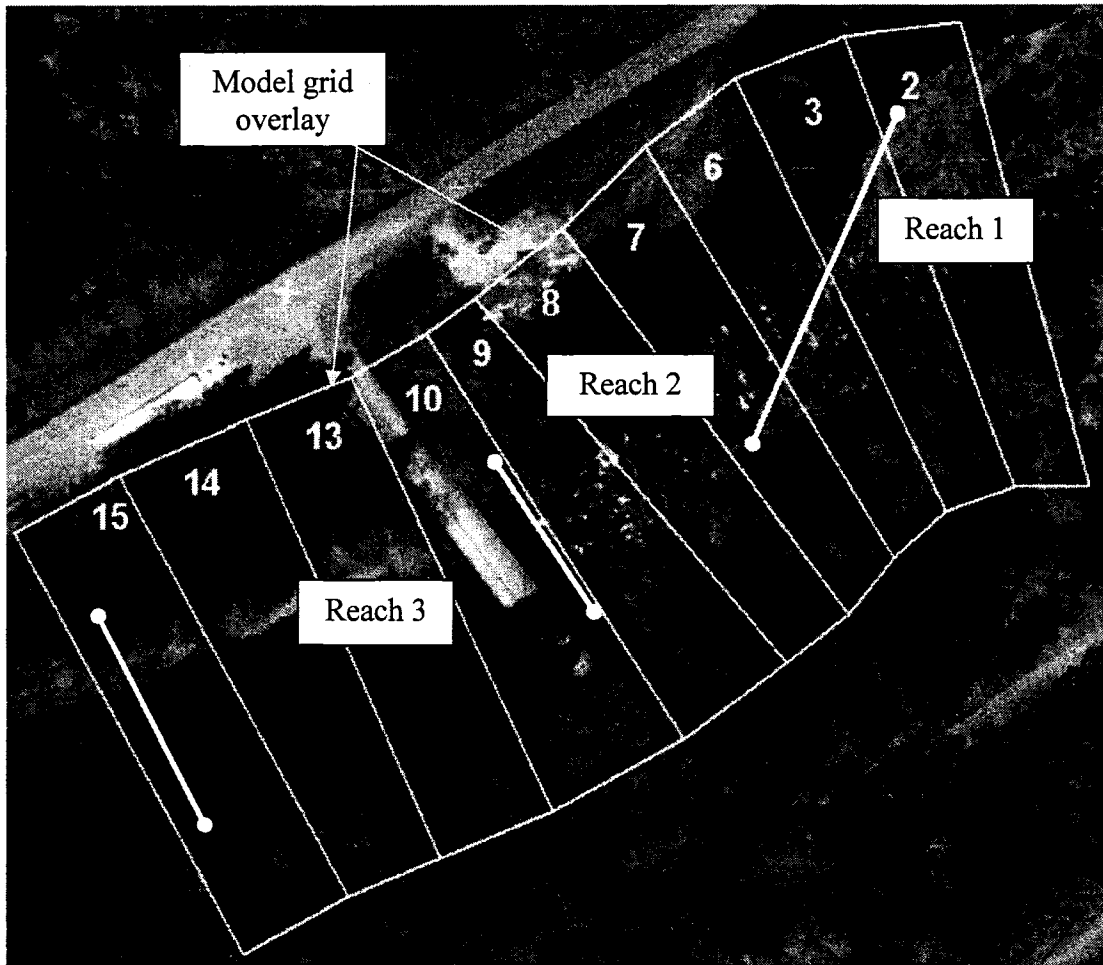


Figure 36: Streambed substrate for the field site

### 3.4.1 Bedrock Substrate

The underlying river channel geology has been discussed by the USGS (1996), Baldwin (1981) and Beeson and Moran (1979). The U.S. Forest Service mapped the river channel geology in 1997 as Columbia River Basalts. The bedrock substrate in the Reaches 1 and 2 (and elsewhere in the basin) are where the Columbia River Basalts have been exposed and remain resistant to fluvial erosion (U.S.F.S., 1997). Baldwin (1981) noted the Columbia River Basalts poured out 14 million years ago

from Eastern Oregon and Washington during the Miocene period. The basalt flows entered Western Oregon through low elevation sections in the lower Cascade Range at the time (Baldwin, 1981; Beeson and Moran, 1979).

The Columbia River Basalts consist primarily of the Wanapum Basalt and Grande Ronde Basalt Formations (Beeson and Moran, 1979; USGS, 1996). Table 26 shows the Columbia River Basalt stratigraphy from Beeson and Moran (1979), based on work by Swanson (1978). The Wanapum Formation in the Bull Run has two members, identified as the Priest Rapids Member on top and the older Frenchman Springs Member underneath (USGS, 1996; Beeson and Moran, 1979). The USGS (1996) characterized both members as fine-grained basalts. Vogt (1981) identified two units of fine-grained basalt in the Grande Ronde Formation based on magnetic polarity. The two formations in the Bull Run are part of the Yakima Basalt Subgroup and Baldwin (1981) characterized the subgroup as a dense, dark-gray fine-grained rock. The Columbia River Basalts were then eventually covered by younger flows and fragmented igneous rocks (Baldwin, 1981).

In Reach 3 the holes were drilled in the bedrock to place two temperature probes as shown in Figure 23. Samples of the bedrock substrate were collected after drilling and are shown in Figure 37. The bedrock particles are dark gray and appear to be fine grained indicating the substrate is likely part of the Columbia River Basalt Formation. Although the substrate extracted from the drilling process was dark gray the bedrock exposed to the water or air varied in color. Figure 38 shows a bedrock outcrop in Reach 2 where the material was exposed to air due to low stream flow. The

exposed bedrock was mostly dark gray with little periphyton growing due to higher velocities. Figure 39 shows the bedrock in Reach 3 covered with brown periphyton. The periphyton were present throughout the reach and influence the substrate's reflectivity.



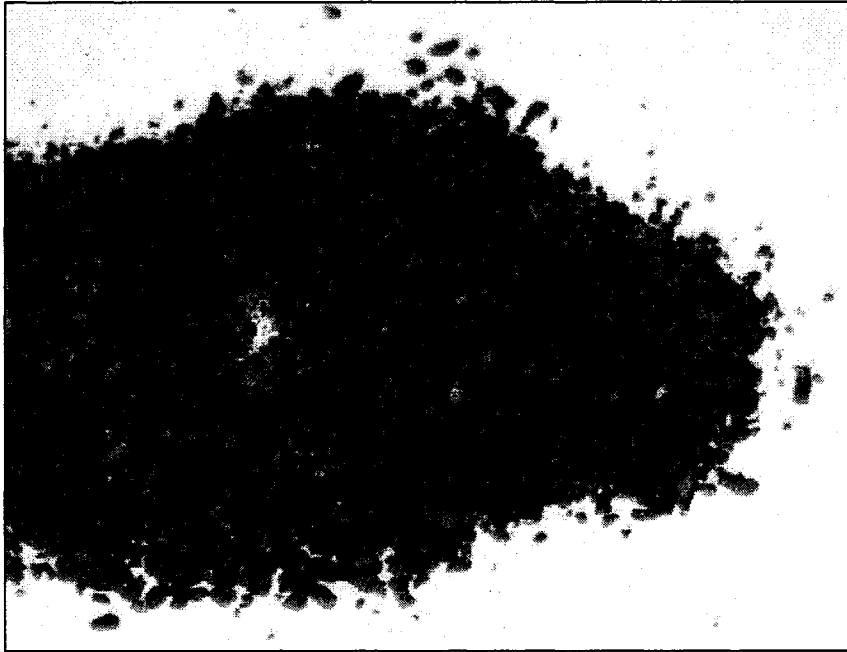


**Figure 37: Sample of bedrock material from drilling in Reach 3.**

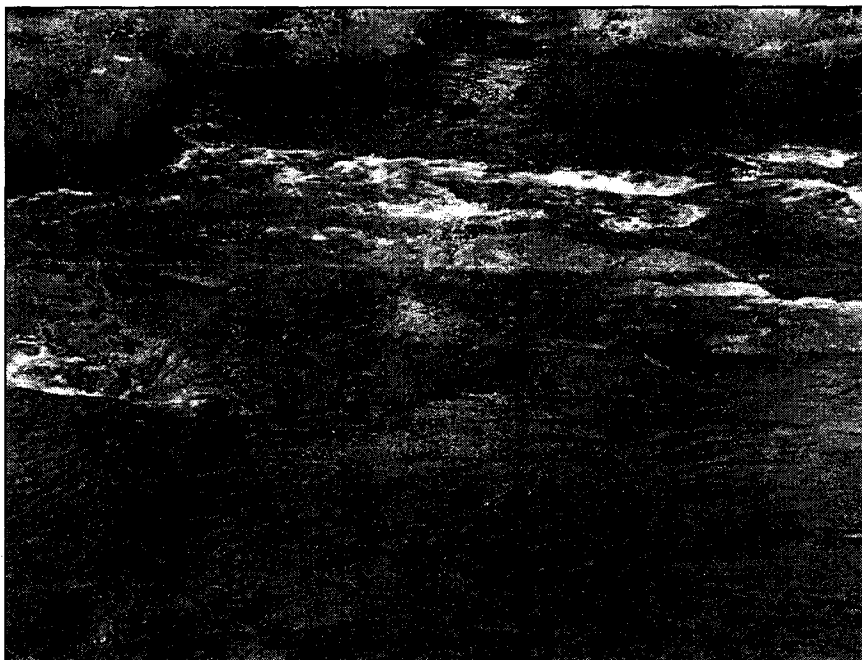


**Figure 38: Exposed bedrock in Reach 2, Columbia River Basalt**



**Figure 39: Bedrock in pool reach (Reach 3) covered with brown periphyton**

### **3.4.2 Boulder/Cobble Substrate**

Three temperature probes were placed in Reach 1 for the first few weeks of the field study. Boulders and large cobble substrate dominated this reach and are believed to be lying over the Columbia River Basalt seen in Reaches 2 and 3.

Figure 40 shows an example of the substrate in Reach 1. When digging the holes to place the temperature probes, the particle size was observed to decrease with depth. Table 27 lists the particle diameters for various size categories, based on work by Cummins (1962). Figure 41 shows a typical cross section of the substrate with photos of the actual grain sizes removed. Periphyton were present throughout the reach as shown in Figure 40 and have an influence on the substrate's reflectivity.

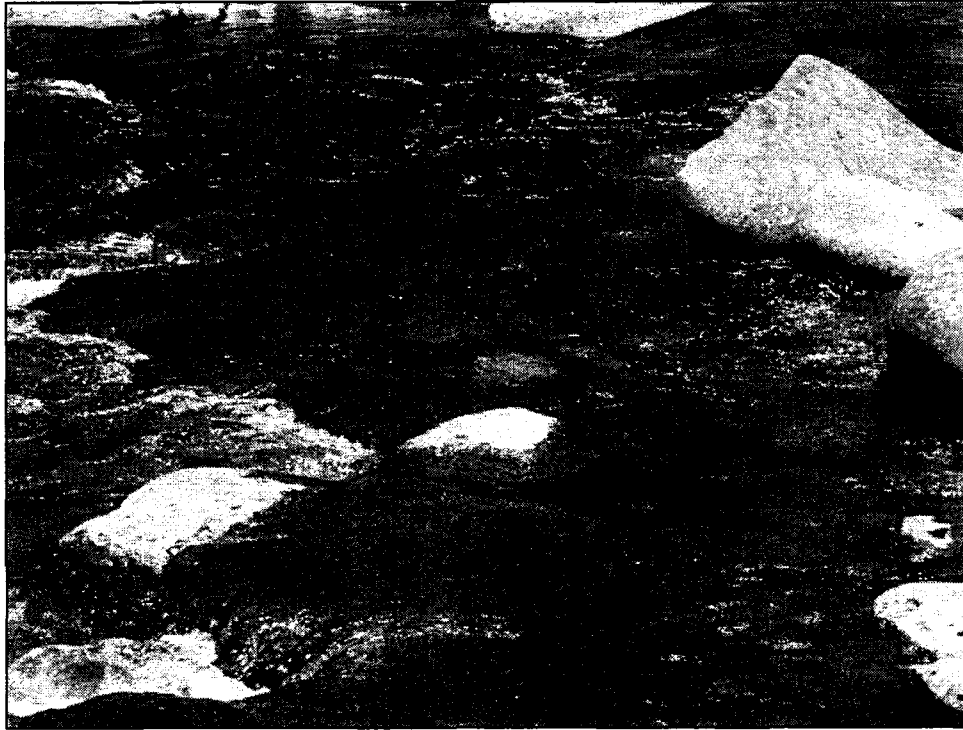


**Figure 40: Substrate surface boulders and large cobbles**

**Table 27: Substrate classification by particle size, Cummins (1962)**

Material	Size Category	Particle Diameter (mm)
Boulder		>256
Cobble	Large	128-256
	Small	64-128
Pebble	Large	32-64
	Small	16-32
Gravel	Coarse	8-16
	Medium	4-8
	Fine	2-4
Sand	Very Coarse	1-2
	Coarse	0.5-1
	Medium	0.25-0.5
	Fine	0.125-0.25
	Very Fine	0.063-0.1256
Silt		<0.063

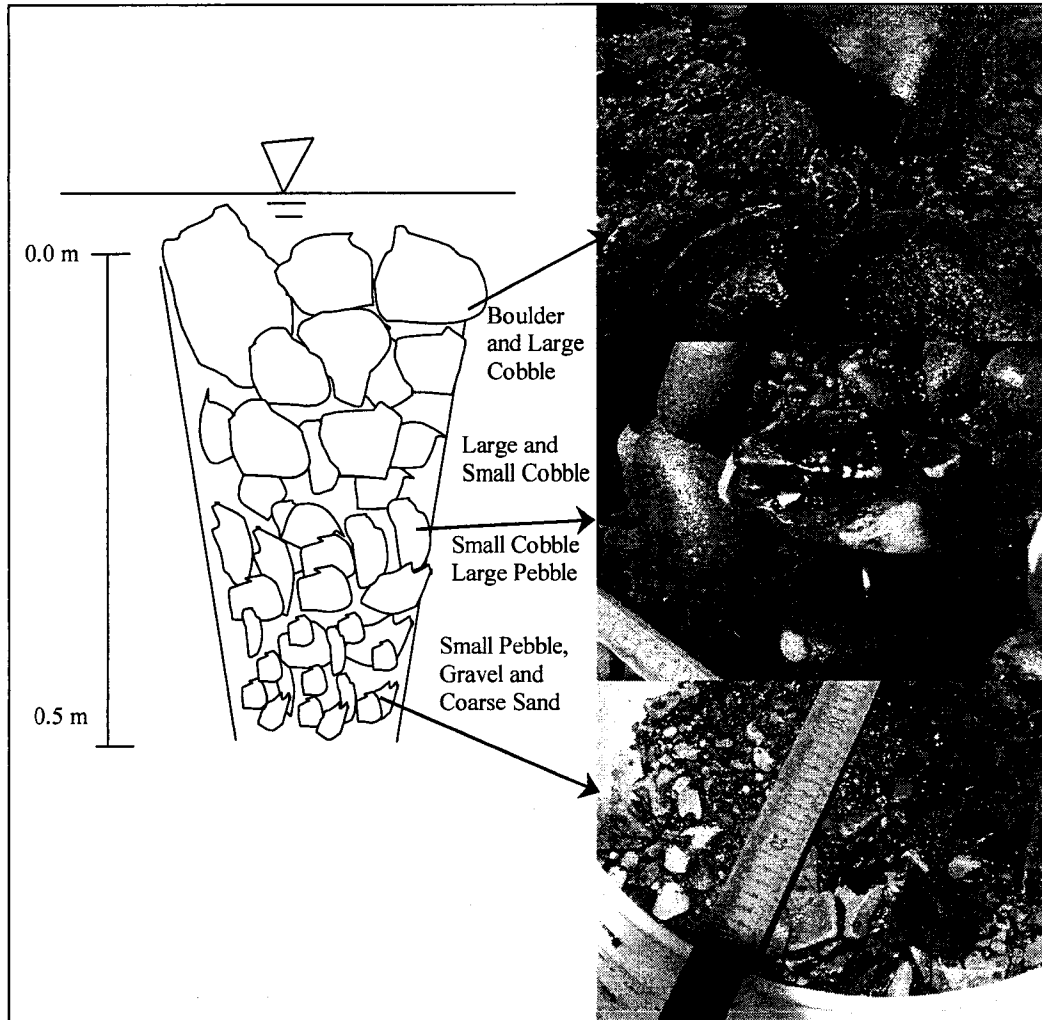


**Figure 41: Cross section of mineral substrates found in Reach 1.**

On August 18, 2002 Ground Penetrating Radar (GPR) was used at two sites to determine the depth of the cobble overlying the bedrock. Figure 42 shows the locations of two GPR survey transects which were conducted by moving radar from the banks of the river out into the wetted river channel using rocks cropping out above the water surface. Figure 43 shows the results of the two GPR survey transects. The two images in Figure 43 show the depth below the surface in meters on the y-axis and longitudinal distance along the x-axis.

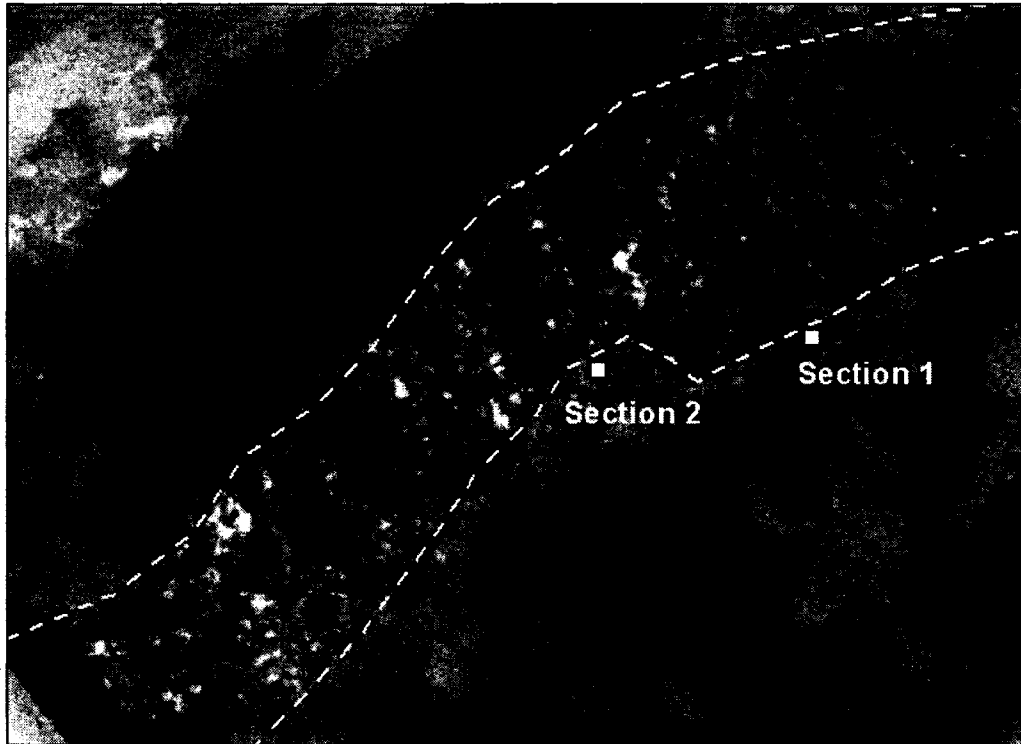


**Figure 42: Ground Penetrating Radar survey transect locations**

The first transect, Section 1, was approximately 25 m upstream from where the cobble layer discontinues over the bedrock. As the left panel of Figure 43 indicates there is a flat reflector layer at about 3.5 to 4.0 m down which may represent the underlying basalt layer. Above this layer there are several disorganized reflectors (series of dark and light areas) which represent the cobble and gravel material overlying the basalt. A transect of the surface topography is illustrated near the top of the panel with the surface sloping down and flattening out after 5 m. The GPR transect after 5 m represents the wetted river channel with a small reflector representing the water surface. Based on this transect the cobble layer in the river channel is roughly 2.5 to 3 m thick. The right panel in Figure 43 represents the second

transect, Section 2, which is just upstream of where the cobble layer discontinues over the basalt layer. The left side of the figure shows the bank and moving to the right, shows the transition to the wetted channel. The figure shows there is a reflector that represents the basalt layer which surfaces on right side end of the transect in the wetted channel. This reflector is approximately 1 m in depth on the left side of the figure and may represent the same basalt layer upstream in Section 1. Below this reflector there appears to be another reflector at a depth of 3 m, which may indicate an older basalt flow formation. The two GPR transect data sets seem to indicate the bedrock from the Columbia Basalt Formation is about 1 to 3 m below the cobble and gravel layer. The upstream site has a thicker layer of cobble overlying the basalt but the downstream site shows a thinner cobble and gravel layer.

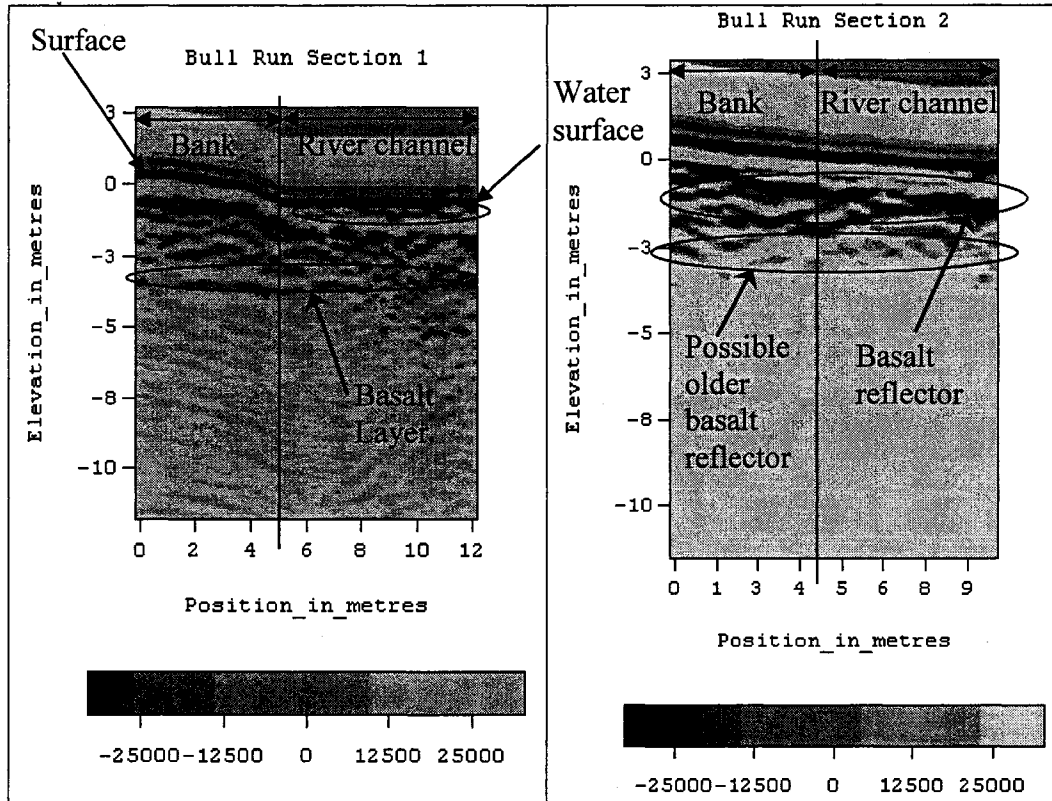
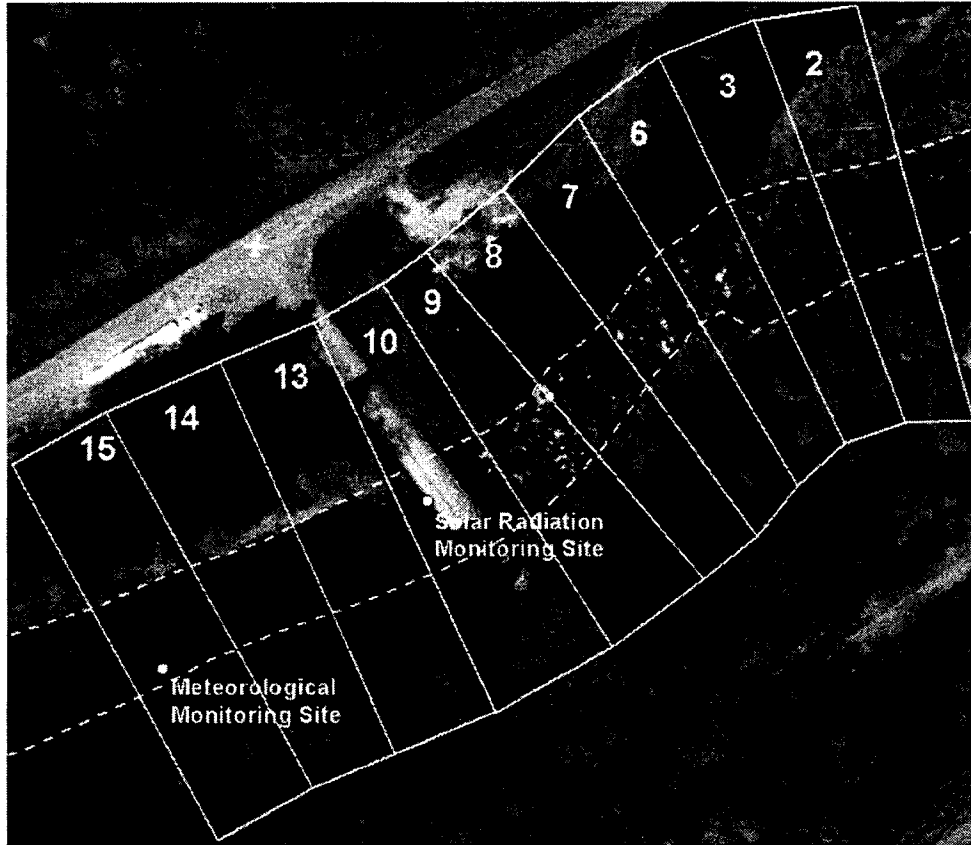


Figure 43: Ground Penetrating Radar Results

### 3.5 Meteorological Data

Meteorological data were collected at two locations in the lower river; at the USGS gage station (14140000) and on the Rt. 14 Bridge, shown in Figure 44. The monitoring site on the bridge measured solar radiation at 10-minute intervals. The monitoring site at the USGS gage station was maintained by the City of Portland, Water Bureau and measured air temperature, relative humidity, wind speed and wind direction at 15-minute intervals. The CE-QUAL-W2 model uses air temperature, dew point temperature, wind speed and direction and solar radiation or cloud cover.



**Figure 44: Meteorological sites in the Lower Bull Run River**

The air temperature recorded in the lower river is shown in Figure 45 and shows regular diurnal temperature swing over the two months of data. The relative humidity shown in Figure 46 shows a diurnal cycle with the humidity increasing each evening as night progresses and decreasing as the day warms. The dew point temperature  $T_{dpt}$  ( $^{\circ}\text{C}$ ) was calculated by rearranging an equation from Singh (1992):

$$RH = \left[ \frac{112 - 0.1T_a + T_{dpt}}{112 + 0.9T_a} \right]^8 \quad (74)$$

where  $T_a$  is the air temperature and  $RH$  is the relative humidity. The resultant dew point temperature is shown in Figure 47. Wind speed and direction are shown in

Figure 48 and Figure 49, respectively. The minimum wind speed measured was 0.18 m/s. The predominant wind direction, 60 to 80 degrees and 260 to 280 degrees, follows the river channel orientation.

The cloud cover in the lower river was calculated by calibrating the theoretical clear-sky solar radiation for the Lower River and Headworks monitoring sites and then using Equation (73) with the solar radiation data. Figure 50 shows the calculated cloud cover for both sites. The solar data monitored at the lower river was found to be similar to the data at the Headworks site but the solar data in the lower river was influenced by shade from vegetation during the middle of the day. As a result the cloud cover estimates for the model and data calculation would be biased during the day. The cloud cover information used for the lower river was therefore obtained from the calculated values at the Headworks site.

Since the solar radiation data in the lower river were influenced by shade the cloud cover data from Headworks were used to calculate the cloudy sky solar radiation in the lower river with the theoretical clear-sky solar radiation in the lower river. The data gaps in the lower river were filled using theoretical clear-sky solar radiation and cloud cover to calculate the cloud sky solar radiation. Figure 51 shows a plot of the calculated lower river cloudy sky solar radiation and the data. The air temperature, calculated dew point temperature, wind speed and direction, cloud cover and solar radiation from the lower river were used in the model developed.

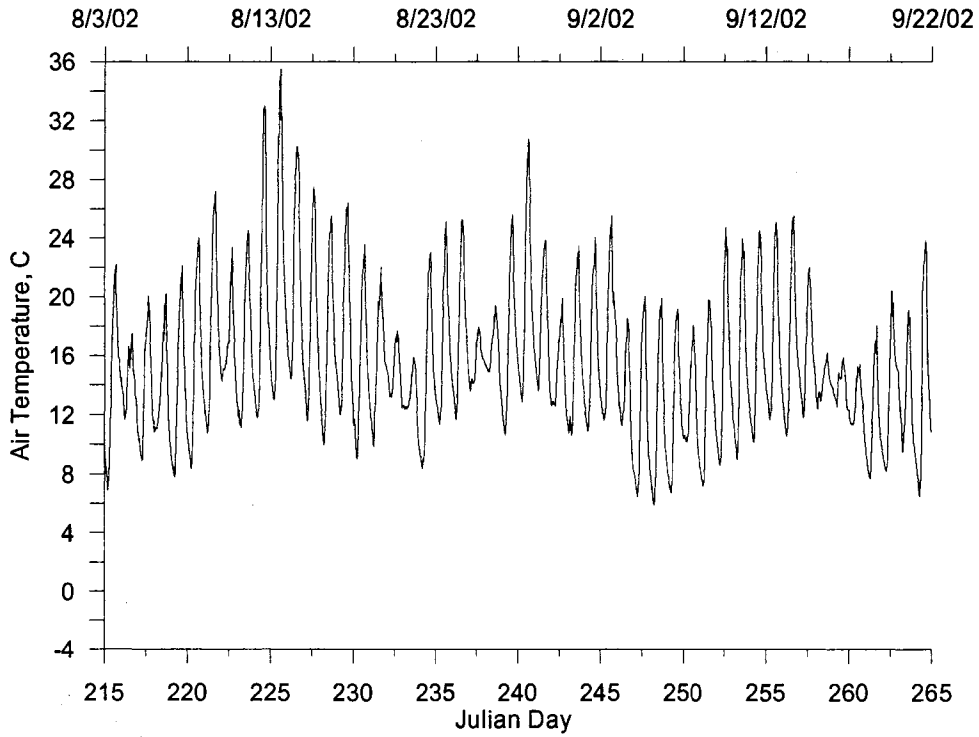


**Figure 45: Air temperature, C in the Lower Bull Run River**

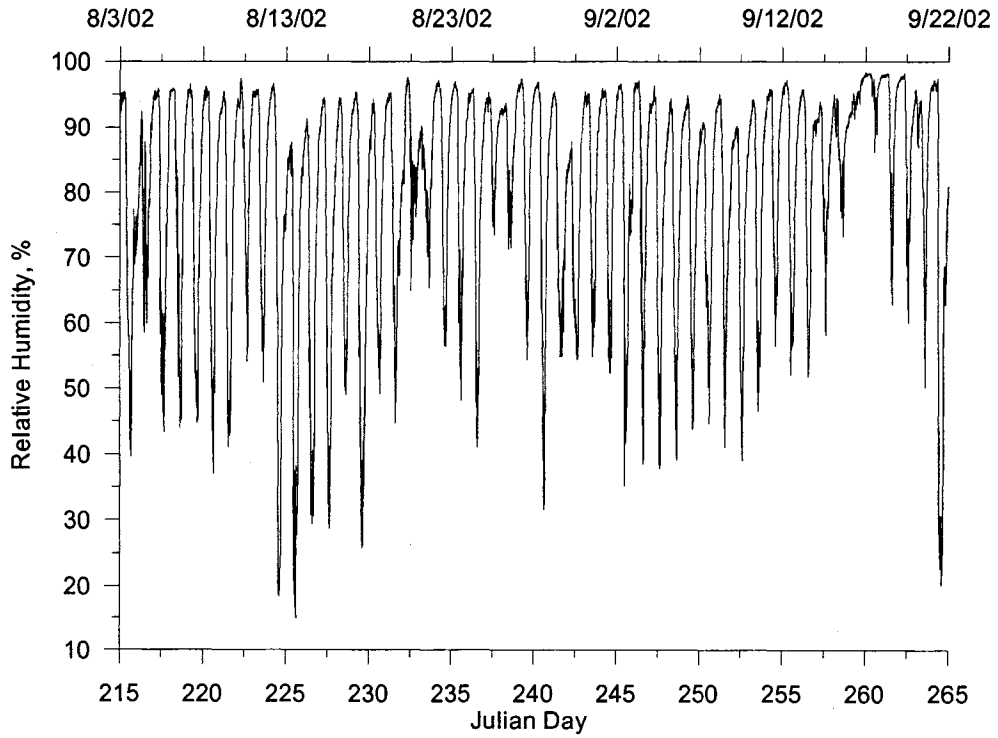


**Figure 46: Percentage Relative Humidity in the Lower Bull Run River**

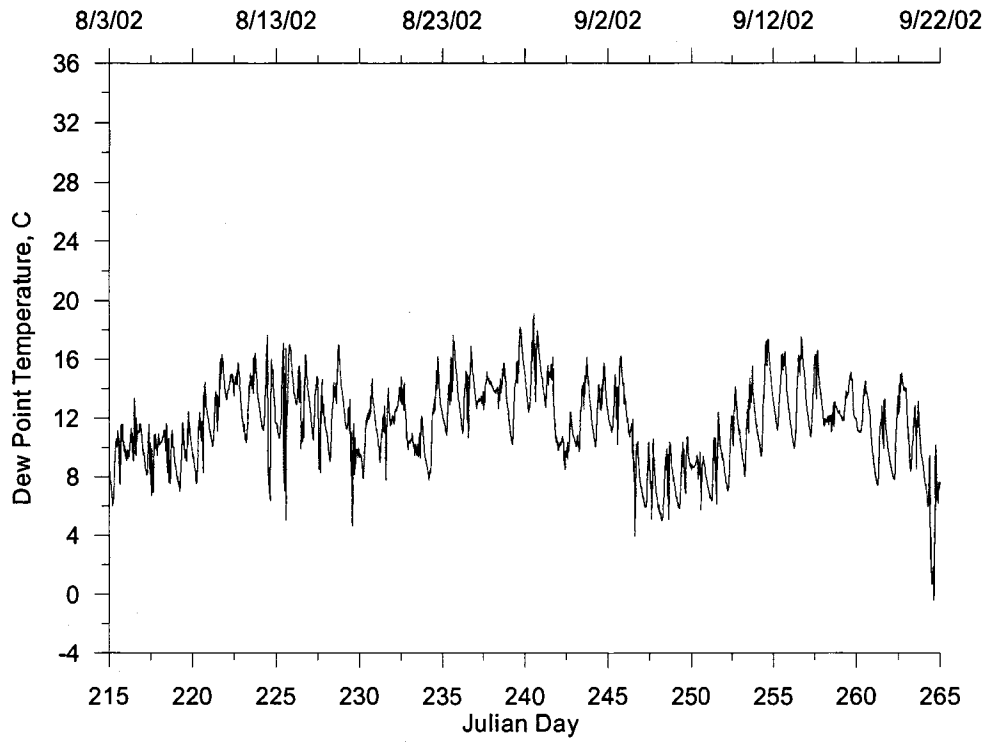


Figure 47: Calculated dew point temperature, C in the Lower Bull Run River

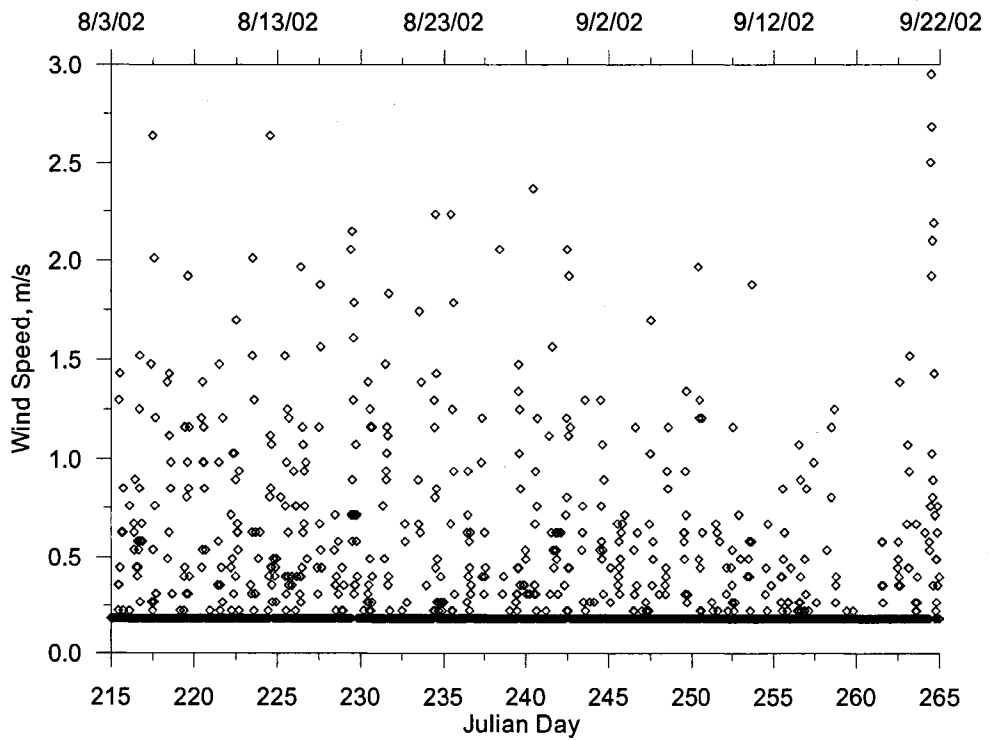


Figure 48: Wind speed, m/s in the Lower Bull Run River

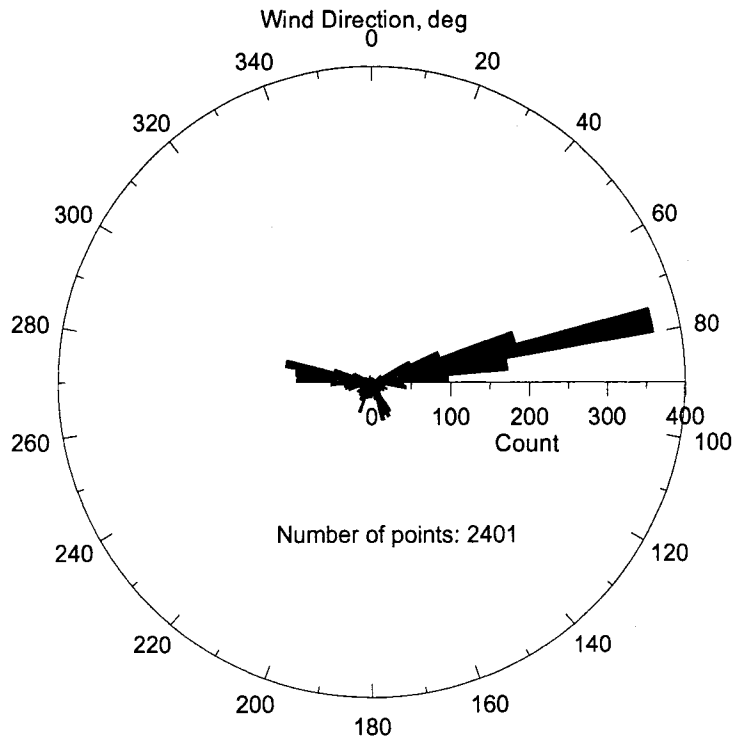


Figure 49: Wind direction, degrees in the Lower Bull Run River

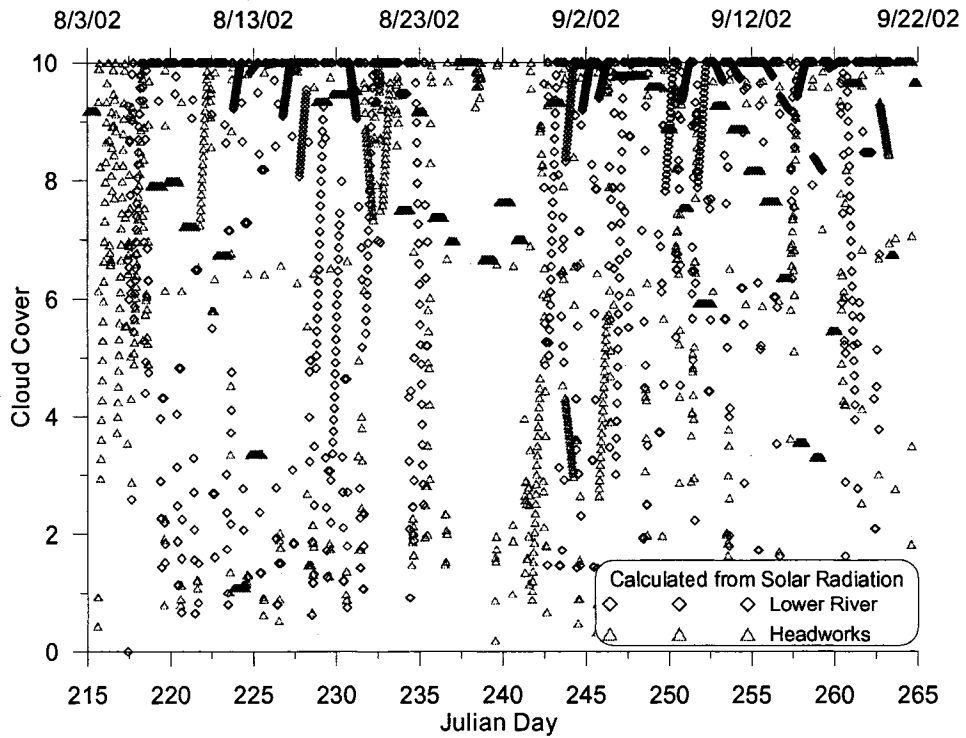


Figure 50: Calculated cloud cover using solar radiation data in the Lower Bull Run River and Headworks

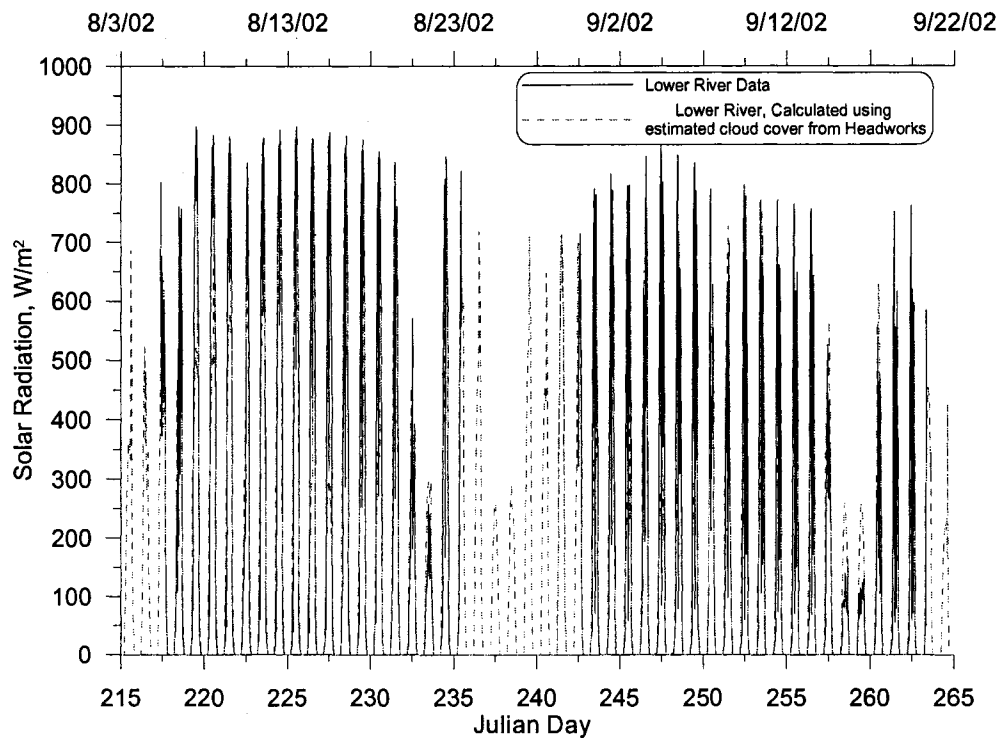


Figure 51: Global Solar Radiation,  $W/m^2$  in the Lower Bull Run River

### 3.6 Light Attenuation Data

Light attenuation data were collected on July 25<sup>th</sup>, August 23<sup>rd</sup>, August 30<sup>th</sup>, and September 20<sup>th</sup>, 2002 at the monitoring sites in Figure 52. The reach designations shown in Figure 36 are the same as the streambed substrate reaches. Table 28 and Table 29 list the data collected on July 25<sup>th</sup> and August 23<sup>rd</sup>, 2002 using a spherical photosynthetic active radiation (PAR) sensor (LI-COR-193SA Spherical Quantum Sensor). Measurements were made above the water surface and then at the bottom of the water column.

Table 30 and Table 31 list the data collected on August 30<sup>th</sup> and September 20<sup>th</sup>, 2002, respectively, using an incident PAR sensor (LI-COR-192SA Quantum

Sensor). On August 30<sup>th</sup> measurements were made above the water surface and then at the bottom of the water column. On September 20<sup>th</sup> measurements were made just below the water surface and at several depths below the surface and the incident sensor was also inverted to measure radiation reflecting off the substrate. When the incident sensor was completely covered the radiation measured was zero.

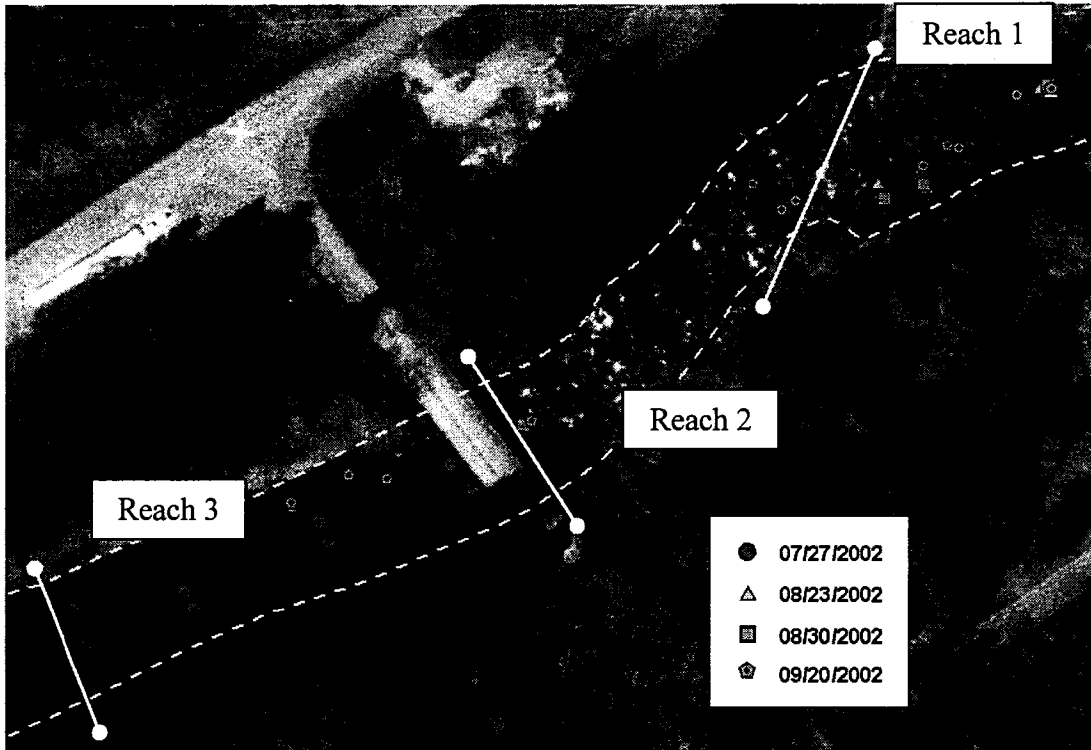


Figure 52: Light attenuation measurement sites in the Lower Bull Run River.

Table 28: Light attenuation data collected on July 25, 2002 in Reach 3

Time	Site	Reach	Radiation, $\mu$ moles/m <sup>2</sup> /s		Depth, m
			Above Water Surface	Below Water Surface	
3:15 PM	1	3	3510	1800	0.29
3:17 PM*	2	3	3625	1795	0.38
3:19 PM	3	3	3720	1575	0.58
3:23 PM	4	3	3640	1540	0.74
3:28 PM*	5	3	3690	1560	0.65
3:33 PM*	6	3	3632	1340	1.02

Time	Site	Reach	Radiation, $\mu$ moles/m <sup>2</sup> /s		Depth, m
			Above Water Surface	Below Water Surface	
3:38 PM*	7	3	3580	1430	0.57
3:43 PM*	8	3	3490	1650	0.37
* time estimated					

**Table 29: Light attenuation data collected on August 23, 2002 in Reaches 1 and 2**

Time	Site	Reach	Radiation, $\mu$ moles/m <sup>2</sup> /s		Depth, m
			Above Water Surface	Below Water Surface	
1:42 PM	1	1	4300	2300	0.19
1:45 PM	2	1	2700	1100	0.26
1:52 PM	3	1	4200	1850	0.29
1:57 PM*	4	1	3800	1780	0.09
2:03 PM*	5	1	3950	1800	0.19
2:08 PM*	6	1	3800	1950	0.13
2:15 PM	7	1	3960	2100	0.16
2:20 PM	8	2	3800	1800	0.35
* time estimated					

**Table 30: Light attenuation data collected on August 30, 2002 in Reaches 1 and 2**

Time	Site	Reach	Radiation, $\mu$ moles/m <sup>2</sup> /s		Depth, m
			Above Water Surface	Below Water Surface	
1:47 PM	1	1	1300	900	0.20
1:53 PM	2	1	1630	610	0.07
1:59 PM	3	1	1110	840	0.12
2:03 PM	4	1	1080	610	0.14
2:15 PM	5	2	442	242	0.22
* time estimated					

**Table 31: Light attenuation data collected on September 20, 2002 in Reaches 1, 2 and 3**

Time	Site	Reach	Inverted Sensor	Radiation Below Water Surface, $\mu$ moles/m <sup>2</sup> /s	Depth, m	Measurement Number
2:10 PM	1	1		1275	0.01	1
2:11 PM*	1	1		1160	0.07	2
2:12 PM*	1	1		1070	0.20	3

Time	Site	Reach	Inverted Sensor	Radiation Below Water Surface, $\mu$ moles/m <sup>2</sup> /s	Depth, m	Measurement Number
2:14 PM*	1	1	Inverted	19.9	0.22	
2:20 PM	2	1		1290	0.04	1
2:21 PM*	2	1		1150	0.13	2
2:22 PM*	2	1		1060	0.26	3
2:24 PM*	2	1	Inverted	5.0	0.35	
2:27 PM	3	1		1060	0.01	1
2:28 PM*	3	1		900	0.06	2
2:30 PM*	3	1	Inverted	7.0	0.08	
2:35 PM	4	1		1130	0.01	1
2:37 PM	4	1		1020	0.10	2
2:38 PM	4	1		950	0.21	3
2:40 PM	4	1	Inverted	12.9	0.20	
2:41 PM	5	1		1275	0.01	1
2:42 PM	5	1		1045	0.20	2
2:43 PM	5	1	Inverted	18.2	0.20	
2:49 PM	6	2		1270	0.01	1
2:50 PM	6	2		960	0.20	2
2:51 PM	6	2	Inverted	14.2	0.23	
2:53 PM	7	2		1160	0.01	1
2:54 PM	7	2		1020	0.26	2
2:54 PM	7	2	Inverted	21.4	0.29	
3:02 PM	8	2		1180	0.01	1
3:03 PM	8	2		900	0.20	2
3:04 PM	8	2	Inverted	17.8	0.28	
3:08 AM	9	2		1275	0.01	1
3:09 AM	9	2		850	0.34	2
3:10 AM	9	2	Inverted	19.8	0.44	
3:22 PM	10	3		1080	0.01	1
3:23 PM	10	3		540	1.02	2
3:24 PM	10	3	Inverted	11.2	0.59	
3:30 PM	11	3		1095	0.01	1
3:31 PM	11	3		610	0.76	2
3:32 PM	11	3	Inverted	17.2	0.80	
3:36 PM	12	3		997	0.01	1
3:39 PM	12	3		530	1.36	2
3:42 PM	13	3		995	0.01	1
3:43 PM	13	3		644	0.50	2
3:44 PM	13	3	Inverted	10.0	0.49	

\* time estimated

The data were originally used to calculate the extinction coefficient using Beer-Lambert Law from Cole and Wells (2000) (See Appendix E):

$$I_{z_1} = (1 - \beta') I_o e^{-\eta_2 z_1} \quad (75)$$

where the  $I_o$  ( $\text{W}/\text{m}^2$ ) is the incident solar radiation at the water surface (equivalent to  $\varphi_c$ ),  $I_{z_1}$  ( $\text{W}/\text{m}^2$ ) is the radiation at depth  $z_1$ ,  $\eta_2$  ( $\text{m}^{-1}$ ) is the light extinction coefficient,  $z$  (meters) is the depth between  $I_o$  and  $I_{z_1}$  ( $z=0$ ), and  $\beta'$  (dimensionless) is the fraction of radiation absorbed in the first 0.6 m below the water surface (Cole and Wells, 2000). The value of  $\beta'$  is determined empirically and a default value of 0.45 was recommended in the CE-QUAL-W2 model (Cole and Wells, 2000). Jerlov's (1968) ocean studies have resulted in estimates of how much radiation is attenuated at depths of 1 m and 10 m as shown in Table 32. Additional values of  $\beta'$  have been developed from ocean studies with results listed in Table 33. The studies focused on surface layers, where  $\beta'$  corresponds to light attenuation to depths of 10 m (ocean) and 0.6 m (Lakes).

**Table 32: Percentage of Total Irradiance (300 - 2,500 nm) from Sun and Sky (Jerlov, 1968).**

Water Type	Percentage of Total Irradiance, Depth 1 m	Percentage of Total Irradiance, Depth 10 m
Ocean water, Type I	44.5	22.2
Ocean water, Type IA	44.1	20.8
Ocean water, Type IB	42.9	16.9
Ocean water, Type II	42.0	14.2
Ocean water, Type III	39.4	7.6
Coastal water, Type 1 ≈ Ocean water, Type III	36.9	5.9
Coastal water, Type 3	33.0	2.7
Coastal water, Type 5	27.8	0.69
Coastal water, Type 7	22.6	0.17
Coastal water, Type 9	17.6	0.052

Table 33: Fraction of radiation absorbed in the surface layer and downward irradiance formularization

Site	$\beta'$	Downward Irradiance Formulization	Reference	$\eta_1, m^{-1}$	$\eta_2, m^{-1}$
Run 1, 800 mi north of Hawaii, open ocean	0.74	$I_{z_1} / I_o = \beta' e^{z_1 \eta_1} + (1 - \beta') e^{z_1 \eta_2}$ $\beta'$ accounts for losses in first 10 m of depth	Paulson and Simpson (1977)	0.59	0.0625
Composite observations (Runs 4, 5, 6, 9 10) 800 mi north of Hawaii, open ocean	0.62		Paulson and Simpson (1977)	0.66	0.20
Based on observations at Crater Lake, OR	0.40	$I_{z_1} / I_o = \beta' e^{z_1 \eta_1} + (1 - \beta') e^{z_1 \eta_2}$	Kraus (1972)	0.20	0.025
Ocean water, Type I, clear water	0.58	$I_{z_1} / I_o = \beta' e^{z_1 \eta_1} + (1 - \beta') e^{z_1 \eta_2}$ $\beta'$ accounts for losses in first 10 m of depth	Paulson and Simpson (1977) Based on data from Jerlov* (1968)	2.86	0.043
Ocean water, Type I (upper 50 m)	0.68			0.83	0.035
Ocean water, Type IA	0.62			1.66	0.050
Ocean water, Type IB	0.67			1.0	0.059
Ocean water, Type II	0.77			0.66	0.071
Ocean water, Type III, dirty water	0.78			0.714	0.127
Ocean water, Type I	0.3963			$I_{z_1} / I_o = e^{z_1 \eta_2} (1 - \beta' \tan^{-1}(z_1 \eta_1))$ $\beta'$ accounts for losses in first 10 m of depth	Zaneveld and Spinrad (1980), based on Data from Jerlov* (1976)
Ocean water, Type IA	0.3981	4.4236	0.0490		
Ocean water, Type IB	0.4103	4.0725	0.0574		
Ocean water, Type II	0.4158	3.9865	0.0670		
Ocean water, Type III	0.4234	3.7062	0.1250		
Coastal water, Type 1 $\approx$ Ocean water, Type III	0.4500	3.3772	0.1360		

Site	$\beta'$	Downward Irradiance Formulation	Reference	$\eta_1, \text{m}^{-1}$	$\eta_2, \text{m}^{-1}$
Coastal water, Type 3	0.4495			3.7049	0.2231
Coastal water, Type 5	0.4626			3.6806	0.3541
Coastal water, Type 7	0.4789			3.7150	0.5028
Coastal water, Type 9	0.5247			3.6026	0.5913
Eastern Tropical Pacific	0.6280			0.4896	0.0637
Eastern Tropical Atlantic	0.3650			0.6580	0.0691
Lake Tahoe, CA	0.251			0.622	0.0680
Lake Tahoe, CA (Clear)	0.40			$I_{z_1} / I_o = (1 - \beta') e^{z_1 \eta_2}$ $\beta'$ accounts for losses in first 0.6 m of depth	Dake and Harleman (1966 and 1969)
Castle Lake, CA (Turbid)	0.40		0.27		
Distilled water, Natural light	0.75		0.0285		
C.J. Brown Lake, OH	0.85	$I_{z_1} / I_o = (1 - \beta') e^{z_1 \eta_2}$ $\beta'$ accounts for losses in first 0.6 m of depth	Williams et al. (1980)		

\*Jerlov (1968) proposed classifying water types based on spectral transmittance at high solar altitudes, Type I is the clearest and Type III is less clear water to Type 9 for the coastal water as the most opaque.

Research by Wunderlich (1972) also applied their downward irradiance formulation to several lakes and oceanic water with varying degrees of influence for  $\beta'$  as shown in Table 34.

**Table 34: Fraction of radiation absorbed in the surface layer and downward irradiance formularization (Wunderlich, 1972)**

Site	$\beta'$	Downward Irradiance Formulization, $I_{z_1} / I_o = (1 - \beta') e^{z_1 \eta_2}$ Equation valid below depth, m	$\eta_2$ , m <sup>-1</sup>
Pure water	0.63	2	0.052
Clear oceanic water	0.64	2	0.081
Average oceanic water	0.68	3	0.122
Average coastal sea water	0.69	2	0.325
Turbid coastal sea water	0.69	2	0.425
Lake Mendota	0.58	1	0.720
Trout Lake	0.50	1	1.400
Big Ridge Lake	0.24	0.5	1.110
Fontana Lake	0.24	0.5	0.930

The data from the four sampling dates listed in Table 28 through Table 31 consisted of 62 measurements below the water surface with 55 of the measurements (89%) at depths less than 0.6 m and 7 measurements at depths between 0.6 and 1.4 m. These data lie within the depth range where  $\beta'$  attenuates the incident water surface radiation. The literature thus far has focused on oceanic and lake studies where the light extinction coefficient was determined at much larger depths than measured in a river system. Instead of using the light extinction relationship identified in Equation (75) where a fraction of the incoming radiation is lost in the surface layer,  $\beta'$  a light extinction equation without  $\beta'$  was used:

$$I_{z_1} = I_o e^{-z_1 \eta_2} \quad (76)$$

Table 35 lists light extinction coefficients from literature using the light extinction formulation in Equation (76). The literature focuses on light extinction coefficients for lakes and lochs.

**Table 35: Light extinction coefficients from literature**

Site	Description	$\eta_2, \text{m}^{-1}$	Reference
Lake Tahoe, Ca	Oligotrophic	0.2	Wetzel (1975)
Crystal Lake, WI	Oligotrophic	0.2	Wetzel (1975)
Crater Lake, OR	Oligotrophic	0.18	Spence (1981)
Lake Borralie, Scotland	Calcareous water	0.34	Spence (1981)
Wintergreen Lake, MI	Eutrophic	0.46-1.68	Wetzel (1975)
Lake Paajarvi, Finland	Brown-stained	0.7	Verduin (1982)
Loch Unagan, Scotland	Brown-stained	1.53	Spence (1981)
Loch Leven, Scotland	Turbid, Eutrophic	2.58	Spence (1981)
Neusiedler See Lake, Austria	Turbid	3.31	Spence (1981)
Highly stained lakes	Average	4.0	Wetzel (1975)
Black Loch, Scotland	Brown-stained, peaty	1.53	Spence (1981)

Equation (76) was rearranged to solve for the light extinction coefficient:

$$\eta_2 = \frac{-\ln\left(\frac{I_{z_1}}{I_o}\right)}{(z_1 - z_o)} \quad (77)$$

where  $z_o$  (meters) is the depth at the water surface and by definition:  $z_o = 0$ .

The data collected in the Bull Run River were then used calculated the light extinction coefficient from Equation (77). Table 36 lists the minimum, maximum, and average light extinction coefficients values for each day when data was collected. The table also provides the standard deviation, weather conditions, and the instrument used. Figure 53 shows a plot of the calculated light extinction coefficients versus

depth for all of the data collected in the Bull Run River. The figure shows there is a loose trend with plenty of scatter in the results.

The calculated light extinction coefficients from data were then separated by the field date when the data was collected and plotted with depth in Figure 54. The figure indicates there are tighter relationships between the depth and the calculated light extinction from data collected on July 25<sup>th</sup> and August 23<sup>rd</sup>. This better relationship may be due to using the spherical sensor rather than the incident sensor or the location of the measurements. The calculated light extinction coefficients were then separated based on their location in specific river reaches (Figure 52). Figure 55 shows calculated light extinction coefficients versus depth for reaches 1 through 3 and indicates there is no good relationship between depth and the light extinction coefficient in the first two reaches. Reach 3 though seems to have a better relationship which may be due to data being available over a wider depth range.

**Table 36: Calculated light extinction coefficients from field data, Bull Run River, OR, 2002**

Instrument Used	Spherical Sensor	Spherical Sensor	Incident Sensor	Incident Sensor
Weather Conditions	Clear Skies	Partly Cloudy	Partly Sunny	Clear Skies
Date	7/25/2002	8/23/2002	8/30/2002	9/20/2002
Light extinction, $\eta_2$ , $m^{-1}$				
Pairs of Measurements	8	8	5	16
Minimum	0.98	2.16	1.85	0.47
Maximum	2.34	8.36	13.30	3.58
Average	1.60	4.13	4.85	1.14
Standard Deviation	0.45	1.91	4.80	0.74

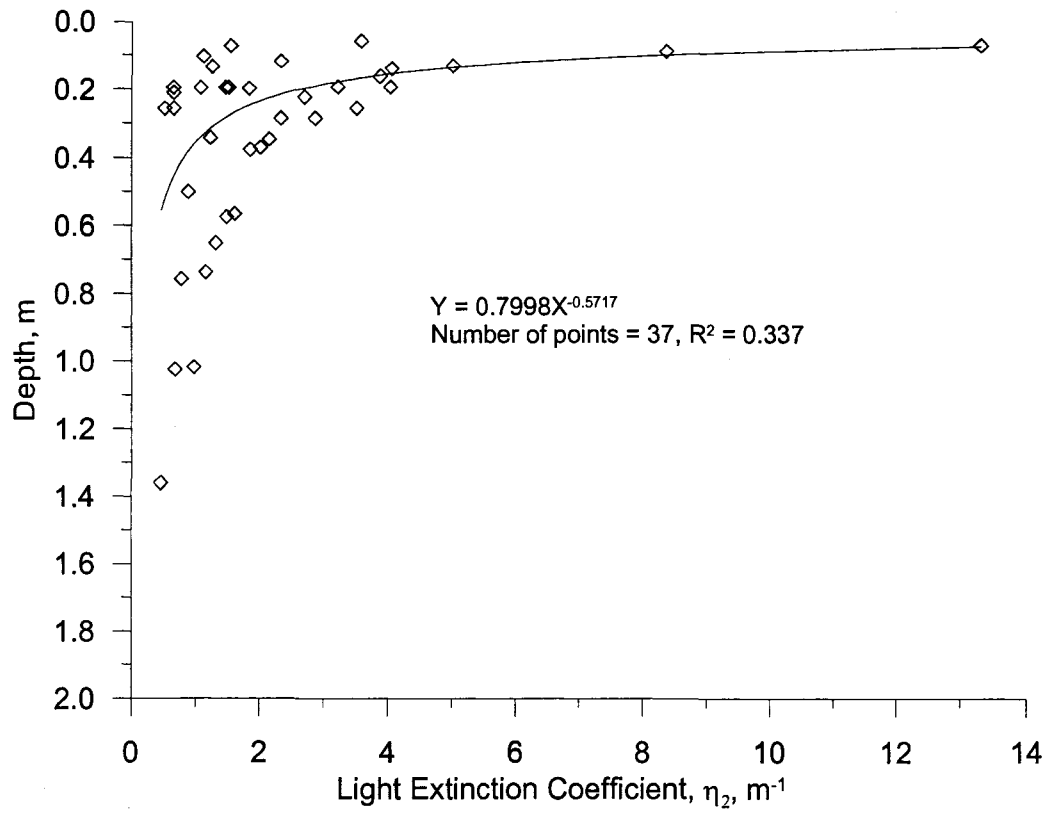
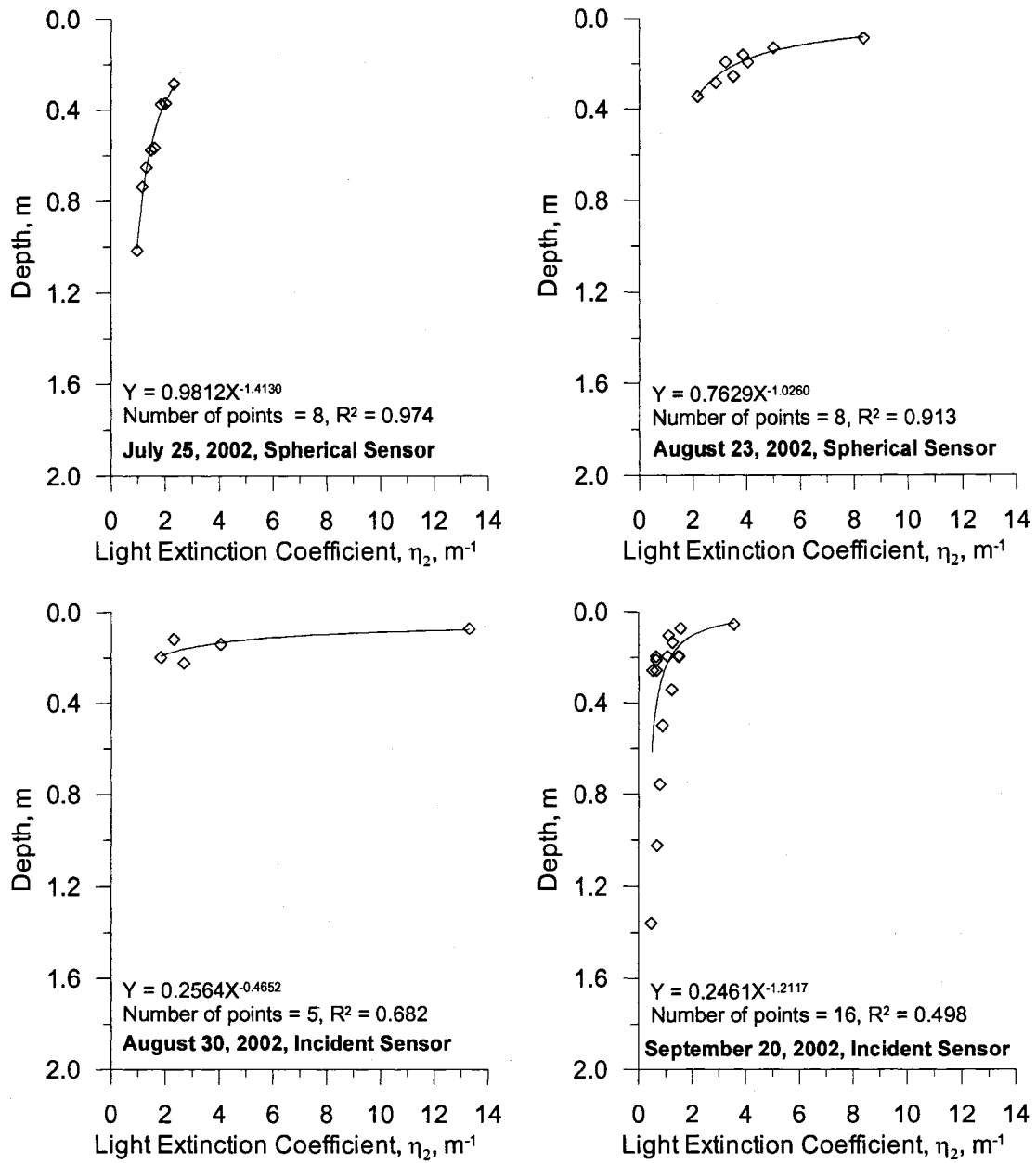
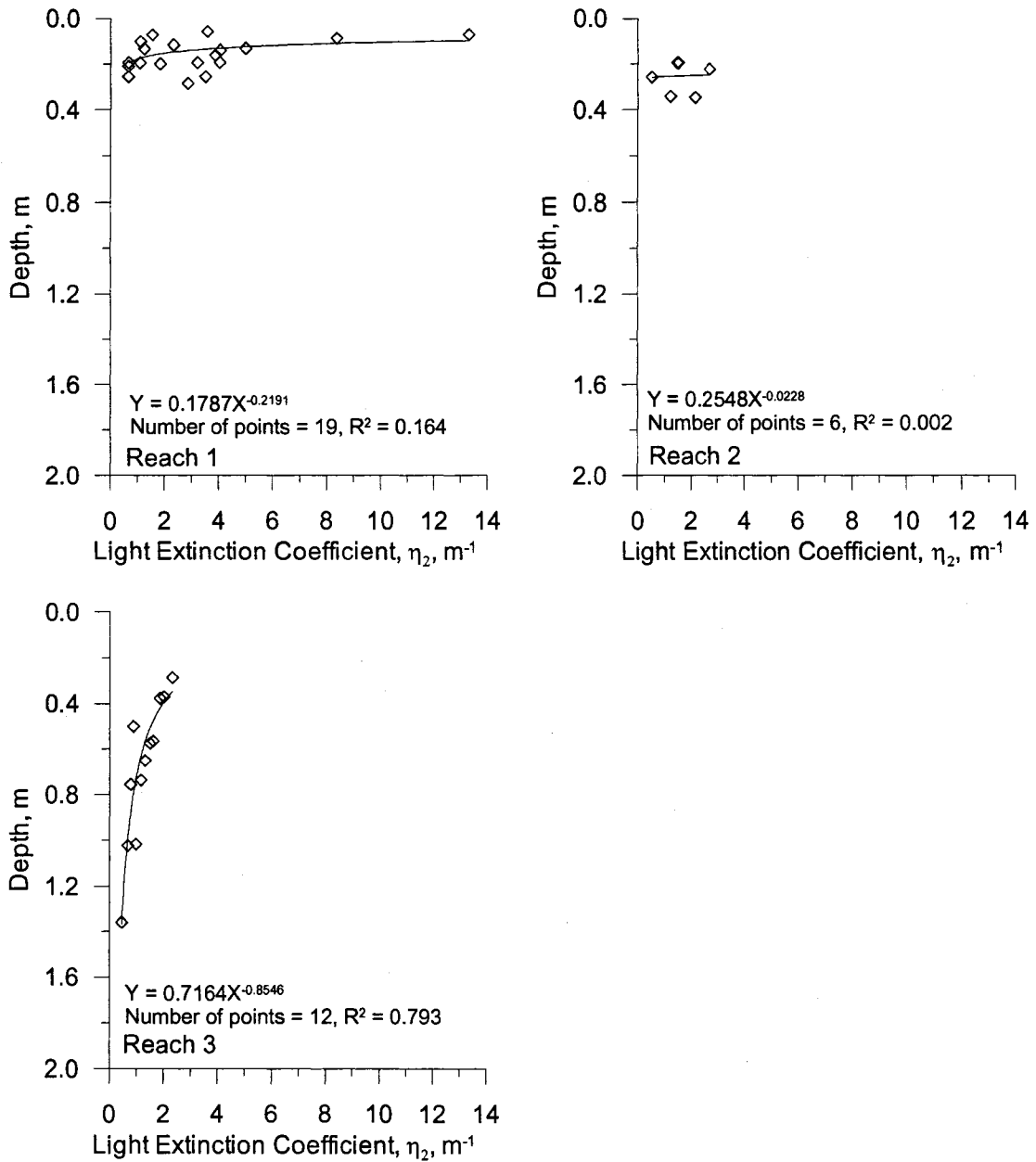


Figure 53: Calculated light extinction coefficients with depth, based on data, Bull Run River, OR



**Figure 54: Calculated light extinction coefficients with depth separated by date of collection, based on data, Bull Run River, OR**



**Figure 55: Calculated light extinction coefficients with depth separated by river reach (See Figure 52), based on data, Bull Run River, OR**

The light extinction data collected on September 20<sup>th</sup> included inverting the incident sensor to measure the reflection off the streambed. The total depth of the river and the calculated light extinction coefficient for each site were used to calculate the fraction of light hitting the streambed using Equation (76). Table 37 lists the

extinction coefficients calculated for each site and the fraction of radiation hitting the streambed. The table also indicates that an average of 66% of the radiation striking the surface hits the streambed. Figure 56 shows a plot of the total river depth and the fraction of radiation hitting the streambed. The figure indicates there is relationship between the two with the fraction of radiation hitting the streambed decreasing as the river depth increases. Using the inverted sensor measurements and the calculated light extinction coefficient for each site the radiation reflected off the streambed at the bottom was calculated using Equation (76). Table 37 lists the fraction of the incident radiation that was reflected off the streambed for each site and lists an average reflection of radiation of 2%. Figure 57 shows a plot of the total river depth versus the fraction of radiation that reflected off the bottom. The figure indicates there is a limited relationship between the two but mostly the figure indicates there is little difference in reflected radiation between the sites.

The light extinction data collection analysis reveals that previous models for characterizing light extinction in lakes and the ocean are not as applicable in river systems because many models incorporate an attenuation factor,  $\beta'$ , for addressing light attenuation in the first 0.6 to 10 m, when river depths in the summer fall less than 0.6 m. The analysis also indicated that a large proportion (66%) of the radiation hitting the water surface penetrates to the streambed and that only a small fraction (2%) reflects back into the water column.

**Table 37: Calculated light extinction coefficient and reflection in three reaches of the Bull Run River, September 20, 2002**

Date	Time	Reach	$\eta_2$ , $m^{-1}$	Total Depth, m	Fraction of Incident Reaching Bottom	Fraction Reflected	Substrate
9/20/2002	2:12 PM	1	0.662	0.28	79.2%	2.1%	Cobble with considerable periphyton
9/20/2002	2:22 PM	1	0.668	0.34	77.5%	0.5%	
9/20/2002	2:28 PM	1	3.579	0.15	62.0%	1.3%	
9/20/2002	2:38 PM	1	0.666	0.30	79.3%	1.5%	
9/20/2002	2:42 PM	1	1.088	0.28	74.5%	2.1%	
9/20/2002	2:50 PM	2	1.530	0.28	66.1%	1.8%	Bedrock, little periphyton, faster water
9/20/2002	2:54 PM	2	0.527	0.34	83.9%	2.3%	
9/20/2002	3:03 PM	2	1.481	0.28	67.0%	2.3%	
9/20/2002	3:09 PM	2	1.232	0.43	59.8%	2.6%	
9/20/2002	3:23 PM	3	0.685	1.11	47.1%	3.2%	Bedrock, deep water, some periphyton
9/20/2002	3:31 PM	3	0.787	0.84	52.0%	3.1%	
9/20/2002	3:39 PM	3	0.469	1.45	51.0%	NA	
9/20/2002	3:43 PM	3	0.892	0.59	59.8%	1.8%	
					66.1%	2.0%	Average

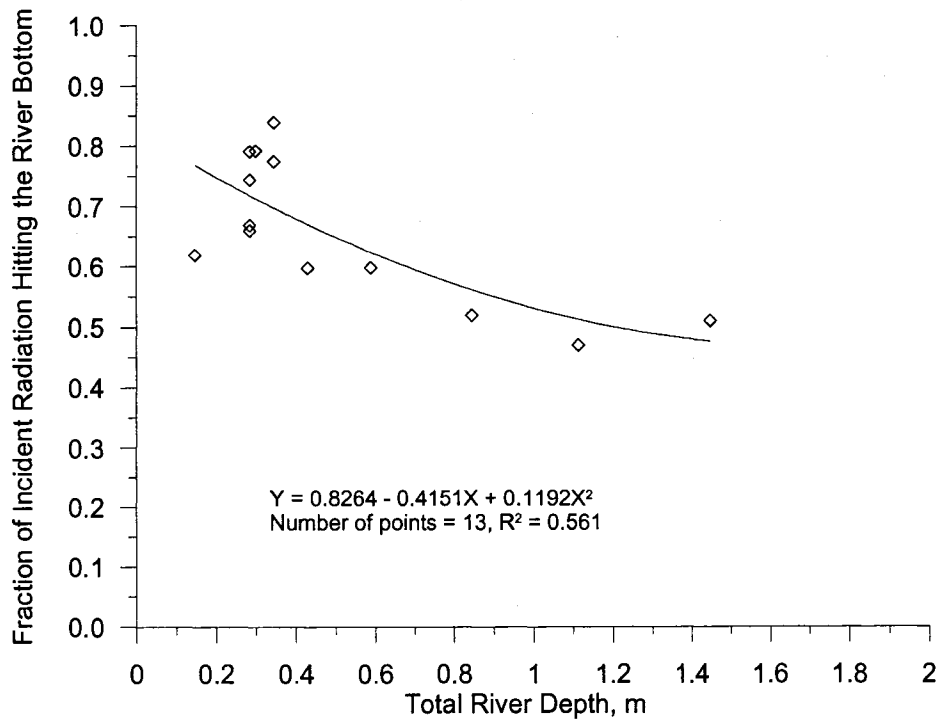


Figure 56: Fraction of incident radiation hitting the river bottom, September 20, 2002

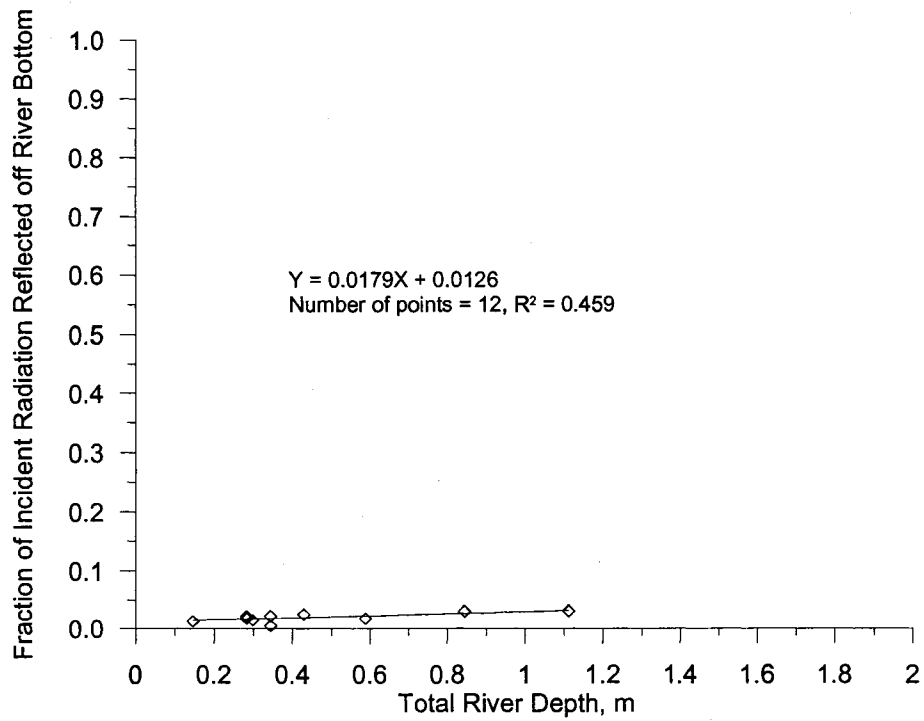


Figure 57: Fraction of radiation reflecting off the river bottom, September 20, 2002

### 3.7 Flow and Dye Study Data

The large cobbles and boulders characterizing Reach 1 indicate there is the possibility of hyporheic flow. If hyporheic flow exists, then it was assumed that the flow in the cobble streambed would emerge at the end of Reach 1 and surfacing in Reach 2 which has a bedrock bottom. Figure 58 illustrates a sketch transition from Reach 1 and Reach 2 and the emergence of any potential hyporheic flow.

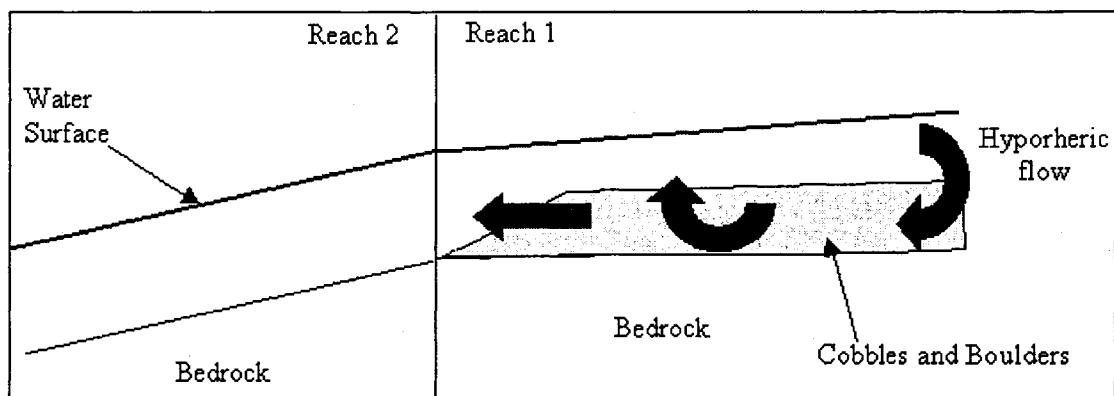


Figure 58: Sketch of Potential Hyporheic flow in Study Reach

Data were collected in several areas to investigate this issue. In order to assess whether groundwater flow was important through the cobble reach, three tests were performed: a dye study, surface water and groundwater levels were measured, and flow measurements were taken.

#### 3.7.1 Dye study

A dye study was conducted in the substrate material to investigate hyporheic flow in the substrate material. A dye injection probe was placed in the streambed by

digging a hole similar to the holes used for the streambed temperature probes. The substrate was removed and stored around the edges of the hole. The probe was placed in the streambed, and the hole was filled. Figure 59 shows the dye injection probe in the streambed. The probe consisted of a 1.27 cm (0.5 in) diameter PVC with a hole drilled one cm from the bottom where a small tube with inner diameter of 3 mm was inserted and run on the inside of the PVC pipe to the top and as shown in Figure 59. The probe was placed in the streambed on August 30, 2002, and air was injected in the tube to ensure that it was not blocked at the buried end. The injection probe was not used until September 5<sup>th</sup> to allow the substrate surrounding it to settle before the dye test was actually conducted. Based on field measurements the injection tube depth was 0.47 m below the surface of the substrate, similar to the deepest thermistors buried in the streambed. 48 ml of Rhodamine WT dye was injected in the tube at 8:15 am and then flushed with 20 ml of water. Based on visual observations in and around the tube, there was no red dye present after flushing. Water samples were then taken downstream of the dye injection point at the three locations listed in Table 38 and shown in Figure 60. Site B was selected because the location is just downstream of where the cobbles overlying the bedrock stop. If the dye was to be transported downstream in the substrate, then it would emerge near this monitoring site.

**Table 38: Dye study monitoring sites**

Dye monitoring site	Distance downstream of dye release, m
A	7.6
B	32.9
C	0.3



Figure 59: Dye study probe

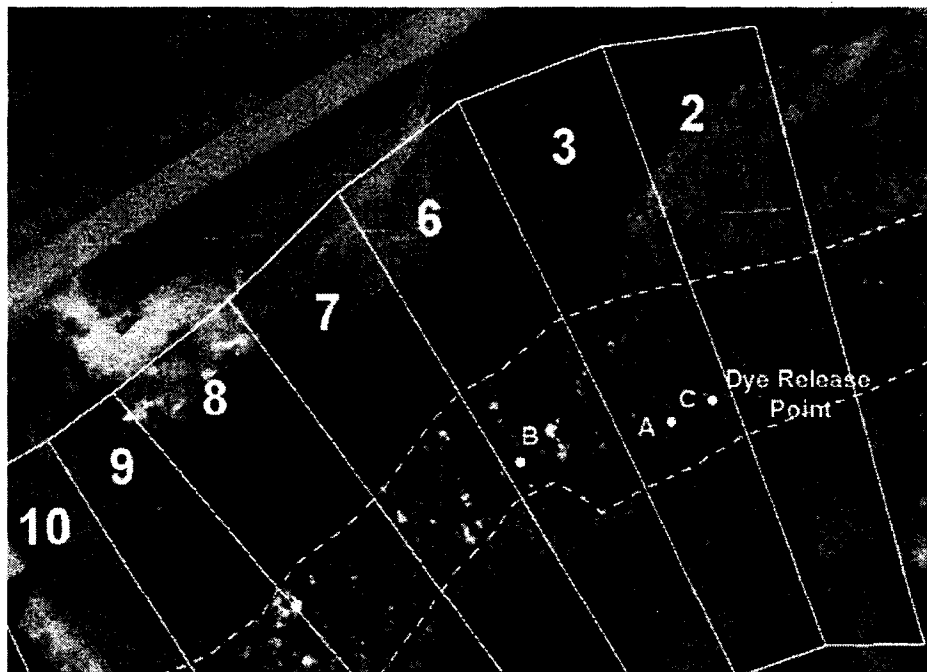


Figure 60: Dye study monitoring sites

The purpose of the dye study was to determine if any dye could be detected downstream of the release. There was no effort to generate a rating curve between fluorescence and dye mass concentration. Samples were tested only to detect the absence or presence of dye. Samples were collected every half hour starting 15 minutes after the dye was released. The area around the dye injection site was also examined visually to determine if any dye began surfacing.

Dye samples were analyzed using a Turner Digital Fluorometer (Model 112). A blanking rod, which came with the fluorometer and consisted of solid black plastic was used between samples analyzed to ensure the fluorometer returned to zero fluorescence between samples. This also ensured there was no drift in the instrument returning to zero. The sample fluorescence readings were similar to the reading from the blanking rod used between each sample indicating the readings fell within the +/- 2 fluorescence units of precision for the instrument. A sample of distilled water was also tested in the fluorometer and resulted in a fluorescence reading within the +/- 2 fluorescence units of precision for the instrument. Table 39 shows the fluorescence readings recorded for all samples. The fluorescence results indicated there was no dye present. This indicates that if there was hyporheic flow present in the reach it was not very large since no dye surfaced after 9 hours of sampling. If a low hyporheic flow rate was present in the cobble substrate, it may have taken more than 9 hours to cause the dye to resurface.

**Table 39: Dye sample fluorescence readings**

Time	Site A		Site B		Site C	
	Sample	Blanking rod	Sample	Blanking rod	Sample	Blanking rod
8:15 AM	48 ml of dye injected					
8:30 AM	0.7	1.1	0.2	0.3		
9:00 AM	-0.2	-0.3	0.1	0.4		
9:30 AM	0.2	-0.3	0.1	0.3		
10:00 AM	1.0	1.1	-0.1	0.1		
10:30 AM	0.6	0.3	-0.3	0.4		
11:00 AM	0.0	0.0	1.0	1.3		
11:30 AM	0.1	0.0	0.0	0.0		
12:00 PM	0.0	0.0	0.4	0.1		
12:30 PM	-0.3	0.2	0.0	-0.2		
1:00 PM	0.0	0.4	1.0	1.0		
1:30 PM	0.6	1.1	0.3	0.1		
2:00 PM	0.1	0.0	0.2	0.1		
2:30 PM	0.3	-0.1	0.3	0.0		
3:00 PM	0.1	-0.1	0.4	-0.1		
3:30 PM	0.0	0.5	1.3	1.0		
4:00 PM	0.4	0.0	0.5	0.3		
4:30 PM	-0.4	0.0	0.2	0.2	0.1	0.2
5:00 PM	0.1	-0.6	0.4	0.1	0.3	0.1
Distilled water fluorescence reading, 1.1 and blanking rod 1.0						

### 3.7.2 Water Level Measurements

The dye injection probe was used before and after the dye study to measure the water level in the substrate and the river water level to determine if there was a gradient between them. The dye injection PVC pipe had a large enough diameter to place a wooden measuring rod in the pipe and measure the water level relative the top of the PVC pipe. The river water level on the outside of the PVC pipe was also measured relative to the top of the pipe on the downstream side to ensure water hitting

the pipe and raising the water level on the upstream side did not bias the measurements. The dye injection probe was placed in the streambed on August 30<sup>th</sup> at 10:45 AM. Water level measurements revealed there was a negligible difference between the substrate and surface water levels. Water level differences were small enough that they could be attributed to measurement error or viscous attachment to the measurement rod placed in the PVC pipe. Also, the velocity of the stream hitting the probe will cause the water to rise in the probe. Table 40 lists the water level measurements and the calculated water level differences. Since there are negligible differences in the water levels, any subsurface flow or upwelling in the substrate was small.

**Table 40: Water level measurements, Reach 1**

Date	Time	Top of probe to water level inside of pipe, cm	Top of probe to water level outside of pipe, cm	Water level difference, cm <sup>1</sup>	USGS Gage flow, m <sup>3</sup> /s
08/30/2002	10:55:00 AM	47.5	50.5	-3.0	0.90
08/30/2002	1:15:00 PM	49.0	50.5	-1.5	0.90
09/05/2002	8:00:00 AM	54.0	54.0	0.0	0.63
09/05/2002	3:12:00 PM	54.0	54.5	-0.5	0.60
09/18/2002	12:56:00 PM	50.0	50.0	0.0	0.84
<sup>1</sup> Negative water level differences indicate an upward gradient.					

### 3.7.3 Flow Measurements

On September 20<sup>th</sup> depth and velocity measurements were taken at two locations in the Lower Bull Run River as shown in Figure 61. Flows were estimated by measuring the river cross-section, depths and velocities. The cross-sections were broken into equal length pieces; and at the center of each piece, a depth and two

velocity measurements were taken. The velocity measurements were taken at 20% of the depth off the river bottom and below the water surface. The two flow estimation sites are characterized by large outcrops of cobble or bedrock so care was taken in evaluating the cross section data used to calculate the cross sectional area.

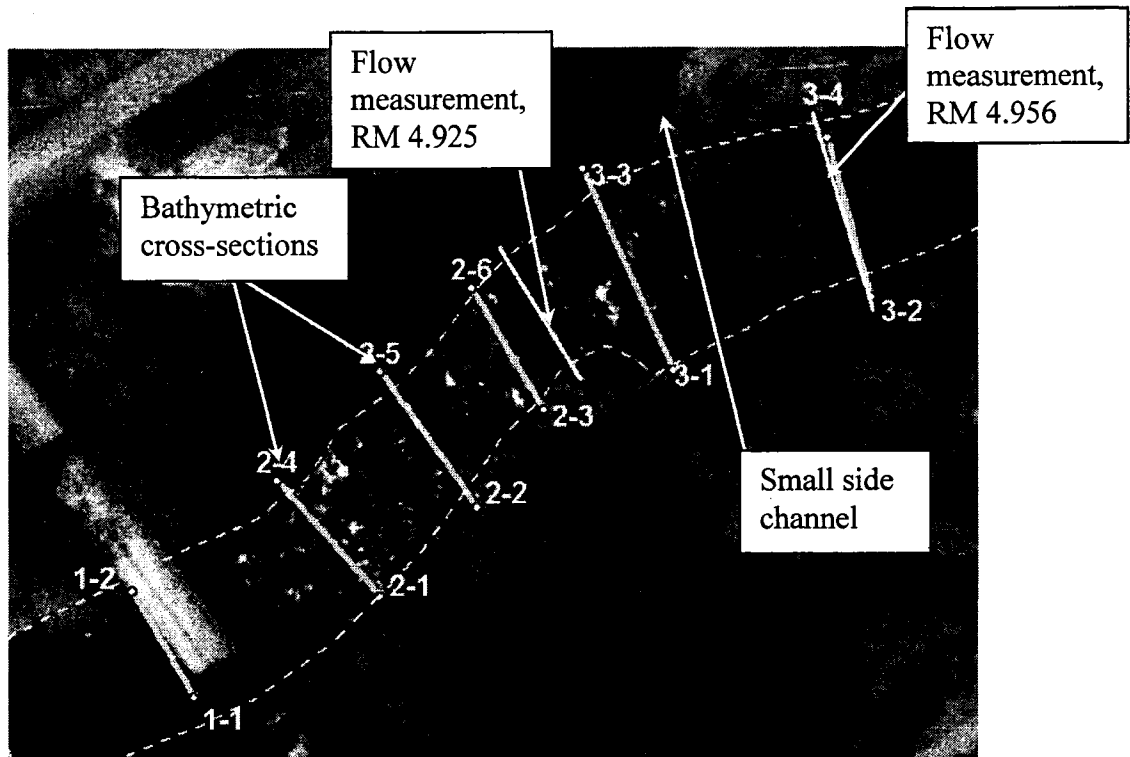


Figure 61: Flow measurement sites

Figure 62 and Figure 63 show the river channel cross-sections and the nearest bathymetric cross sections taken on July 26<sup>th</sup> 2002. The cross sections show the high variability in the channel depths. An equation for calculating the total flow for each piece of the river cross section by French (1985) is

$$Q_{total} = \sum_{i=1}^N b_i d_i \frac{(u_{i,top} + u_{i,bottom})}{2} \quad (78)$$

where  $b_i$  (meters) is the width,  $d_i$  (meters) is the depth,  $u_{i,top}$  (m/s) is near surface velocity and  $u_{i,bottom}$  (m/s) is the near bottom velocity for individual cross-section pieces.  $Q_{total}$  ( $m^3/s$ ) is the total river flow at the cross section location. When considering this approach given the high variability of the cross section data shown in the figures, Equation (78) over-estimates the conveyance cross-sectional area for each piece resulting in a higher flow estimate than seen downstream. Another method for calculating the cross-sectional area utilizes a modified version of the trapezoidal method from French (1985):

$$Q_{total} = \sum_{i=1}^N b_i \frac{(d_{i-1/2} + d_{i+1/2})}{2} \frac{(u_{i,top} + u_{i,bottom})}{2} \quad (79)$$

where  $d_{i-1/2}$  (meters) and  $d_{i+1/2}$  (meters) are river depths at one-half the distance between the flow measurements. If the measured stream depth is used as one value,  $d_{i-1/2}$ , and zero used for the other value,  $d_{i+1/2}$ , representing the range of depths within each piece. Equation (79) was then used in estimating the flow at both locations. The location furthest upstream also included a small flow ( $0.01 m^3/s$ , 0.38 cfs) from a side channel shown in Figure 61. The side channel is at a higher elevation than the main channel. During the summer low flows there was little to no flow seen in the channel, but during the winter when flows are much higher it may serve as part of the active channel. Figure 64 shows the flow data from the USGS gage station (14140000) at RM 4.829, which was measured at 15-minute intervals. The figure also includes the flow estimates at the two upstream locations. The error bars around the

points represent the minimum and maximum flow range for a +/- 10% error in field measurements. The figure indicates the flow in Reach 1 is similar to the flow in Reaches 2 and 3. The flow measurements at the two locations also did not show hyporheic flow effects since the flow differences were within measurement error.

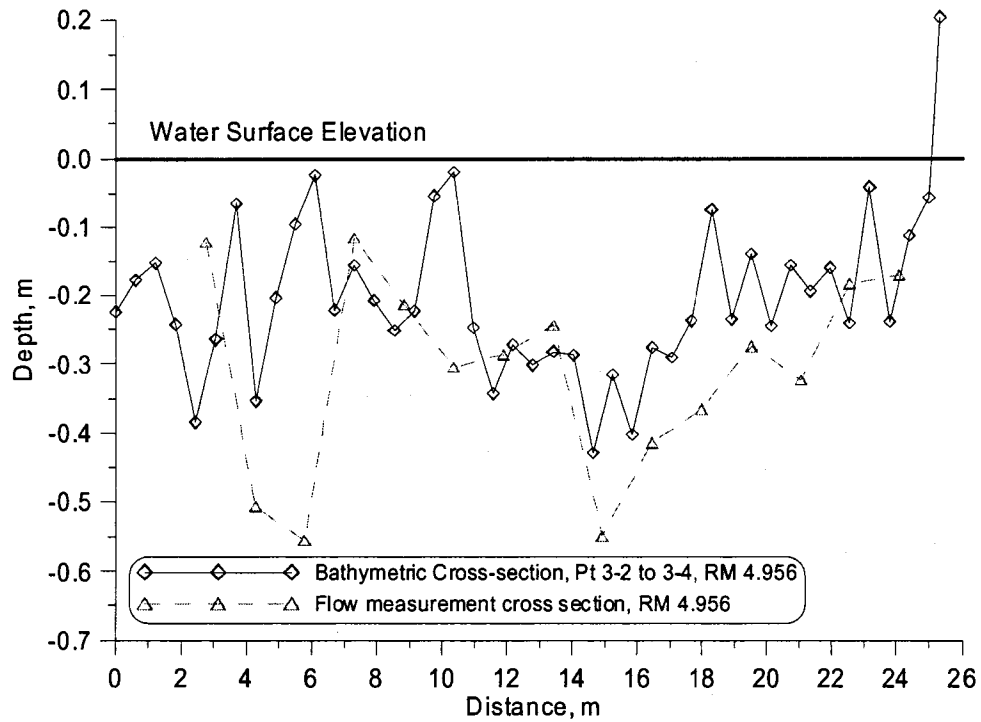


Figure 62: Cross-section data at RM 4.956, upstream flow measurement

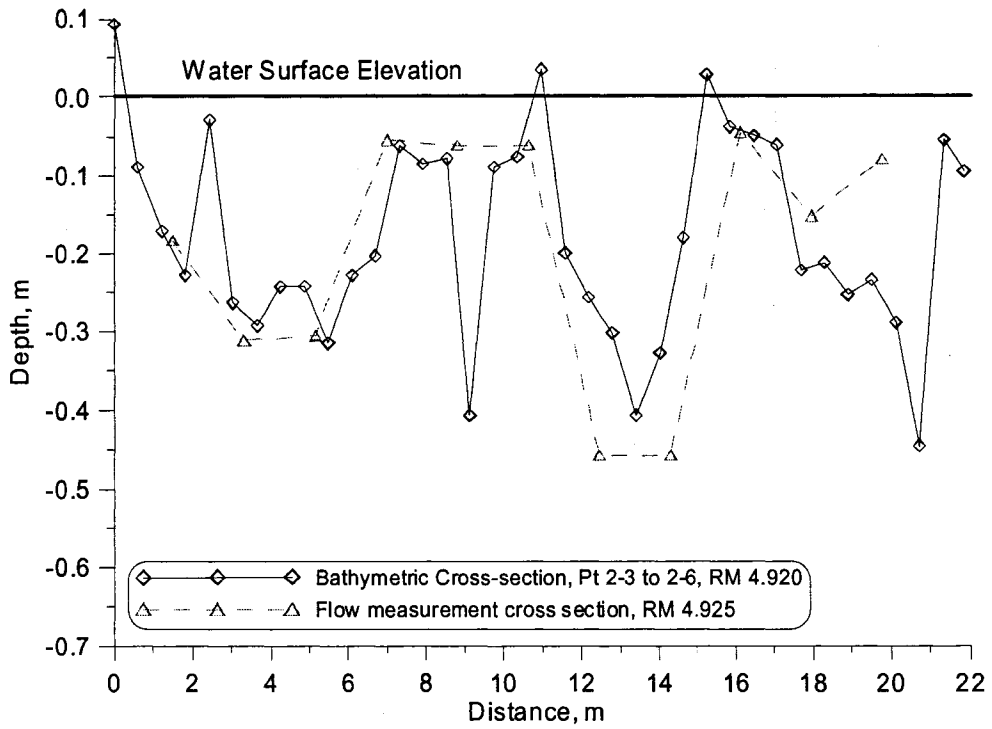


Figure 63: Cross-section data at RM 4.925, downstream flow measurement

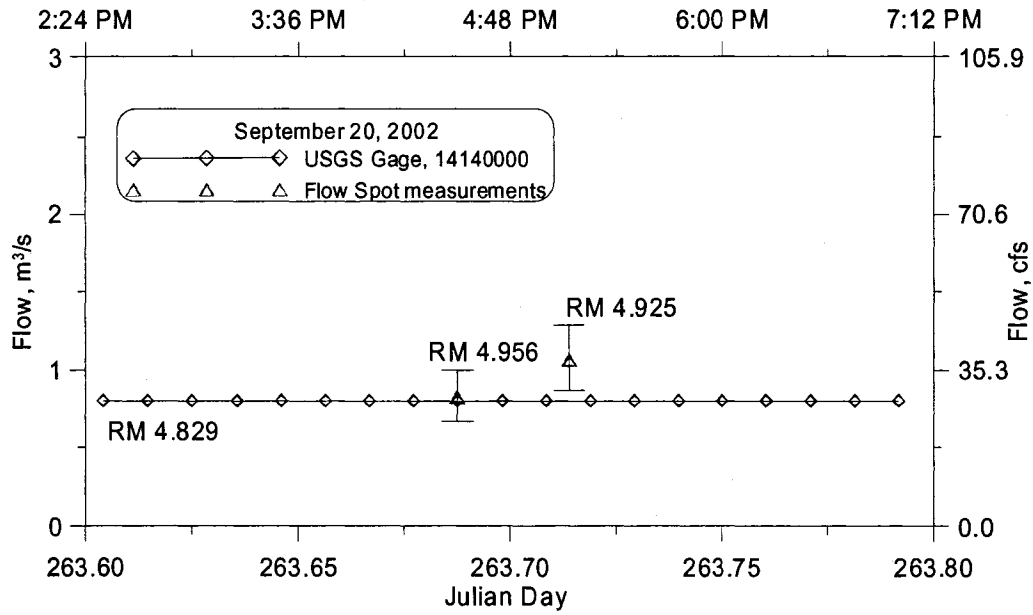


Figure 64: Flow measurements in the Lower Bull Run River

### 3.8 Vegetative and Topographic Shade Data

The CE-QUAL-W2 shade algorithm uses vegetation and topography data to calculate the shade impinging on a model segment's water surface. Vegetation characteristics include: vegetation top elevation, distance from the river centerline to the shade controlling vegetation, and vegetation density. Each model segment also has 18 topographic inclination angles surrounding it.

#### 3.8.1 Vegetation Data

The vegetation data collected in the field consisted of vegetation (tree) heights and the distance from the river centerline to the vegetation. From the approximate middle of the stream channel, a laser range finder was used to measure both tree heights and the vegetation offset distances. Table 41 lists the vegetation heights and offset distances measured in the field.

**Table 41: Vegetation characteristics collected in the field**

River Mile	Left Bank Vegetation Height, m	Left Bank Distance CL to Vegetation, m	Right Bank Vegetation Height, m	Right Bank Distance CL to Vegetation, m
4.826	19.71	15.36	52.80	15.44
4.840	42.72	21.06	36.20	14.01
4.858	40.77	15.06	29.08	19.78
4.876	18.52	40.00	20.98	19.70
4.894	50.74	28.78	44.89	17.61
4.908	20.46	24.36	42.80	16.26
4.920	21.14	21.21	41.97	17.91
4.935	26.55	19.86	62.57	32.34
4.958	28.57	17.09	28.25	23.16

The vegetation heights were converted to vegetation top elevations by adding the bank elevation to the tree heights. The distance from the river centerline to the vegetation for each bank was used directly in developing the model shade file. The model grid resolution was different than the resolution of the data collected. The shade file characteristics were generated by linearly interpolating between the river mile locations where data were collected and the river mile of the model segment center points.

The data collected were compared with similar data collected by the Oregon Department of Environmental Quality (ODEQ) for use in their 1-D temperature model, Heat Source. The ODEQ method for collecting the vegetation shade information involved discretizing the river into 30.5 m (100 ft) pieces. Each piece was characterized by nine vegetation compartments, each 4.6 m (15 ft) wide, for both banks. The vegetation compartments consisted of vegetation height, distance from the river centerline and areal vegetation density. The vegetation height information was defined by a reference table of vegetation characteristics and therefore was standardized for each vegetation type. The ODEQ also conducted field checks to verify the vegetation characteristics. The data used in this analysis was provided by Greg Geist at the ODEQ, who developed the Heat Source model for the Lower Bull Run River.

The ODEQ data were processed to generate the same vegetation characteristics for the CE-QUAL-W2 model. The model uses only one vegetation compartment to describe shade impinging on a model segment. The nine vegetation compartments

provided for each bank were reduced to one compartment for each bank by taking the ratio of the tree height to the distance from the river centerline to the vegetation. The compartment with the highest ratio of height to distance was considered the controlling vegetation. The vegetation density was not used in determining the maximum ratio because the density reflected the areal density in each vegetation compartment, not the density from the perspective of the river. Once the controlling compartment was identified for each bank the vegetation height was added to the stream bank elevation provided in the ODEQ data set, the vegetation offset distance and density were isolated for that compartment. The vegetation density from the one vegetation compartment may under-represent the overall density. The cumulative vegetation density was also calculated for all nine vegetation compartments, which may over-represent the overall vegetation density. The results from the two methods were averaged and associated with the other controlling vegetation characteristics. This method was used successfully in developing a CE-QUAL-W2 application of the Willamette River (Annear et al., 2004). The processed data set consisted of vegetation information every 30.5 m along the river. The model grid resolution was less than 30.5 m so the nearest two vegetation data sets along the river were linearly interpolated using river mile location to obtain the vegetation characteristics for a model segment.

Previous modeling work in the Lower Bull Run River (Annear and Wells, 2002b and Annear et al, 1999) resulted in developing a set of vegetation and topographic shade characteristics. The shade information from this model was

developed on a coarser scale due to longer model segments. The shade characteristics were adjusted to match the resolution of the current model. The older vegetation characteristics, the model developed vegetation information from the ODEQ data and the field data collected in the 2002 summer were compared to examine their variability. Left bank and right bank designation are determined from the perspective of moving downstream. Figure 65 and Figure 66 show the vegetation top elevation and the distance from the river centerline to controlling vegetation for both banks, respectively. Figure 65 shows the ODEQ vegetation top elevations are about 20 m higher than the elevations in the Lower Bull Run River model (Annear et al, 1999). The vegetation top elevation data collected in July 2002 were lower than the ODEQ data for the left bank but higher than the historical model (Annear et al., 1999). The data collected in July varied above and below the ODEQ values for the right bank. The data collected during the field study show higher variability than the ODEQ data because tree height field measurements were used and the ODEQ data used a vegetation height reference table providing a single height for each vegetation type. Figure 66 shows the river centerline to the controlling vegetation distances based on field data from 2002 are larger for the left bank than the ODEQ data set or the historical model. The large deviation in the data collected in July 2002 is based on identifying the active channel from the field data where the ODEQ data and the historical model are based on areal photos. The right bank shows variations between the data collected in July 2002 and the data provided by the ODEQ as well. The

Lower Bull Run River model developed for implementing the dynamic streambed heating algorithm used the vegetation characteristics collected in July 2002.

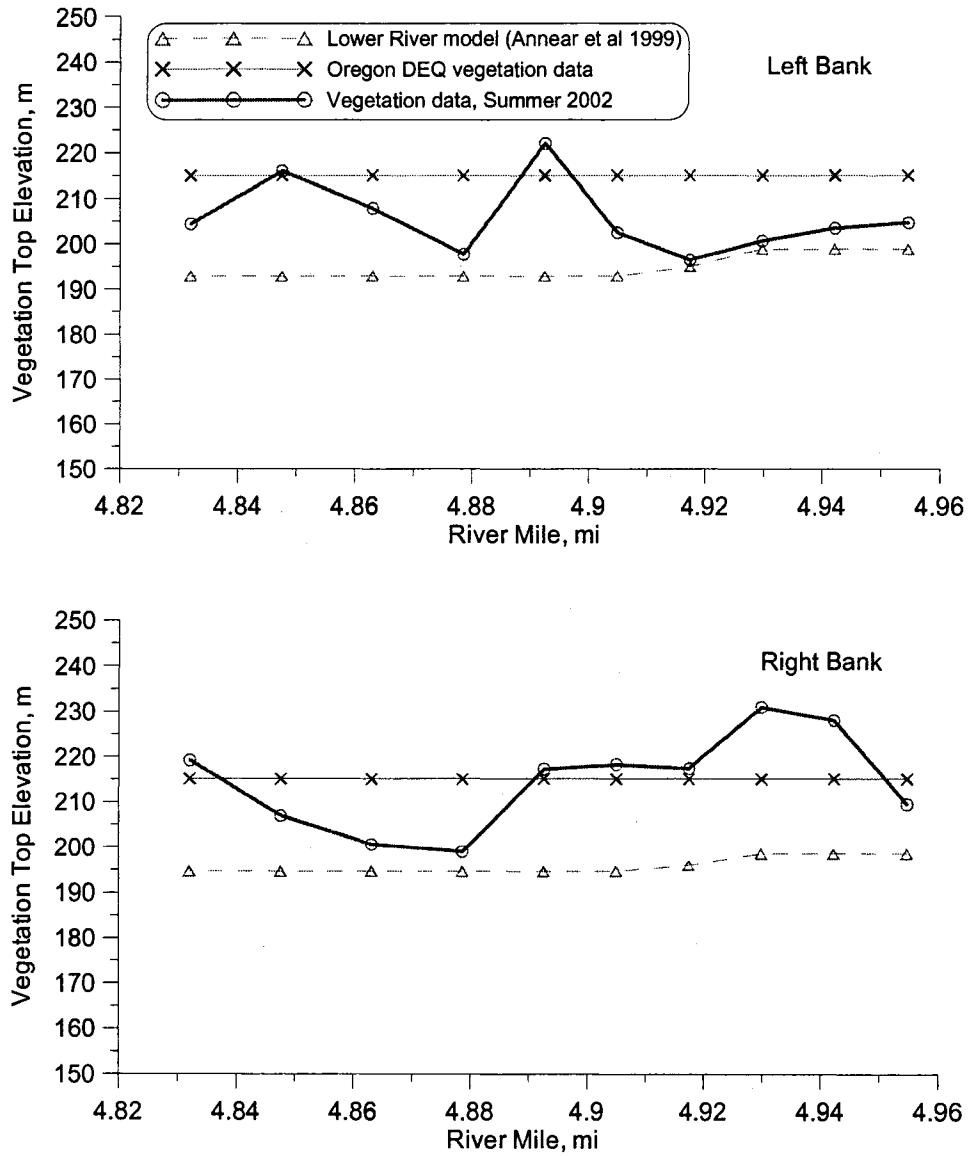


Figure 65: Vegetation top elevation, m

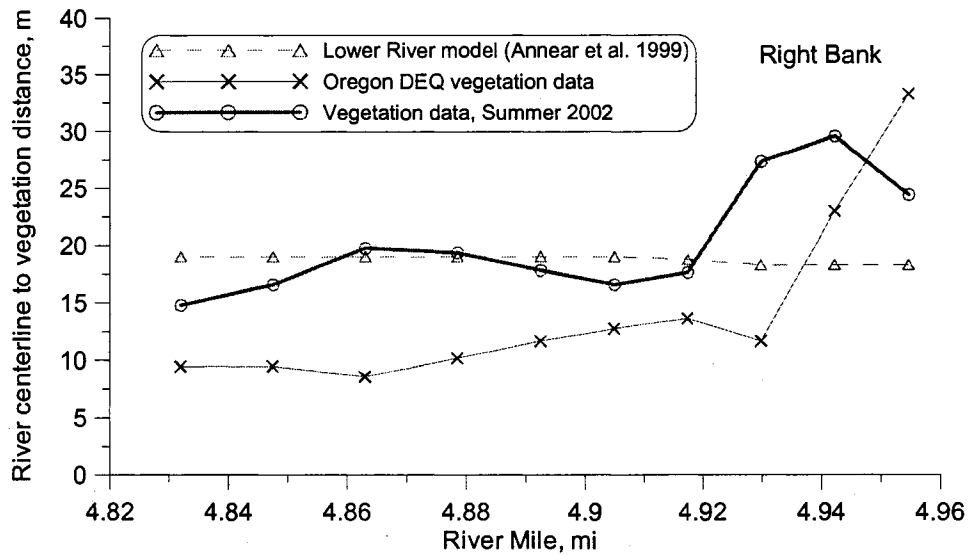
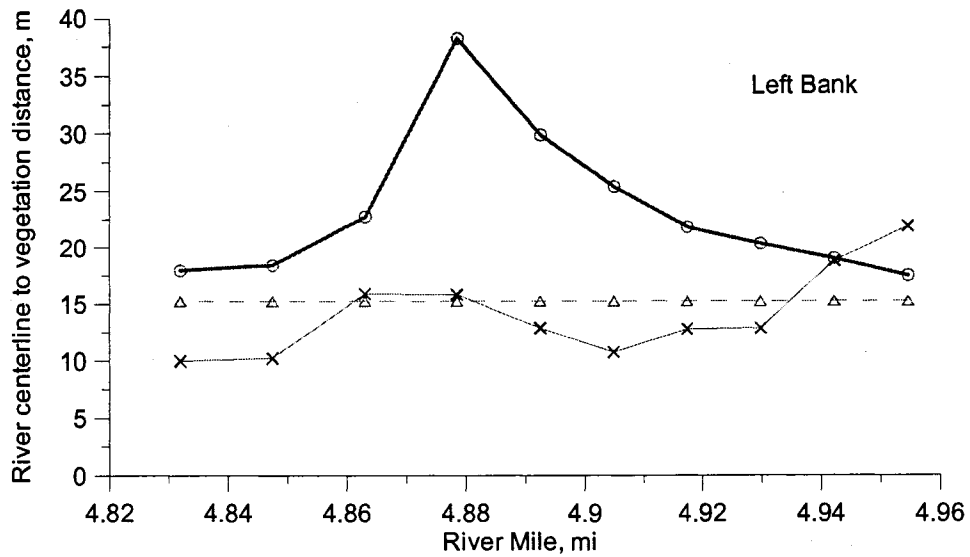


Figure 66: River centerline to controlling vegetation distance, m

There were no vegetation density data collected during the summer of 2002, but the ODEQ vegetation characteristics provided areal vegetation density and the previous Lower Bull Run River model (Annear and Wells, 2002b) used vegetation density data as a calibration tool. Figure 67 shows the two vegetation density data sets and indicates the vegetation densities are similar. The shade file for the Lower Bull

Run River model used an average vegetation density between the two data sets for each model segment.

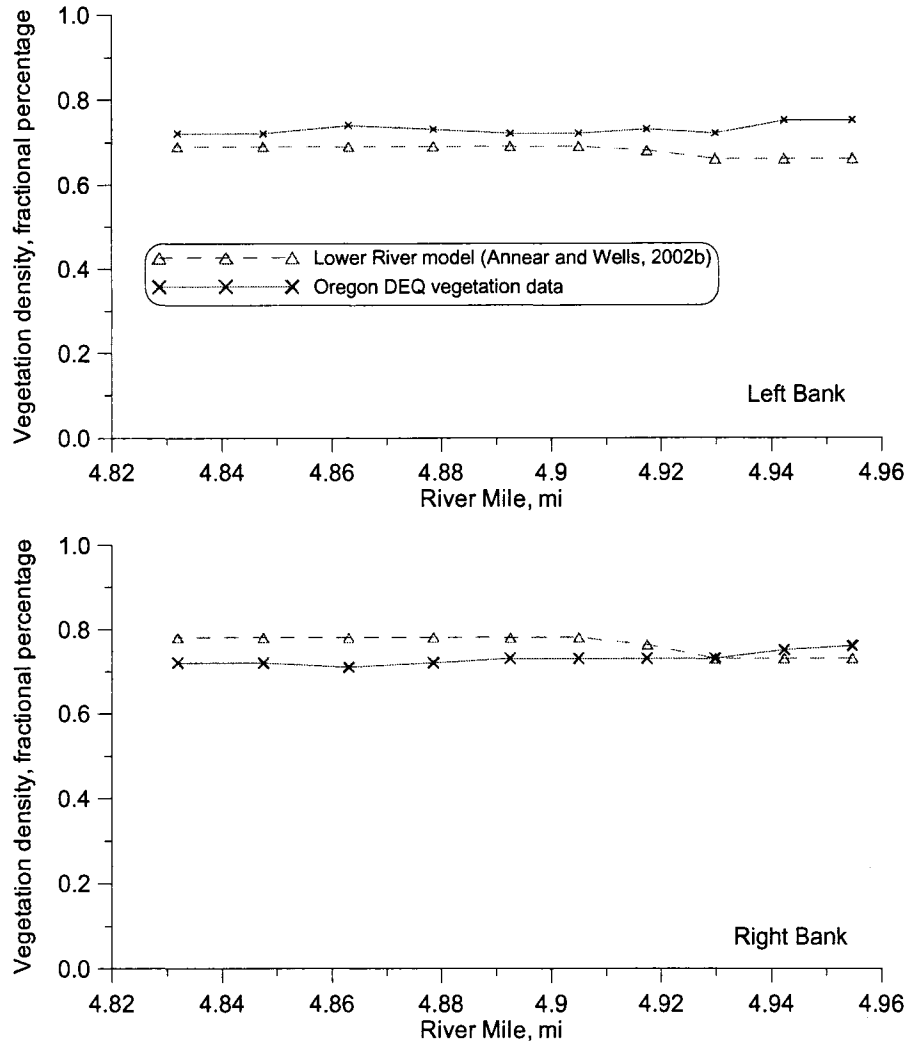
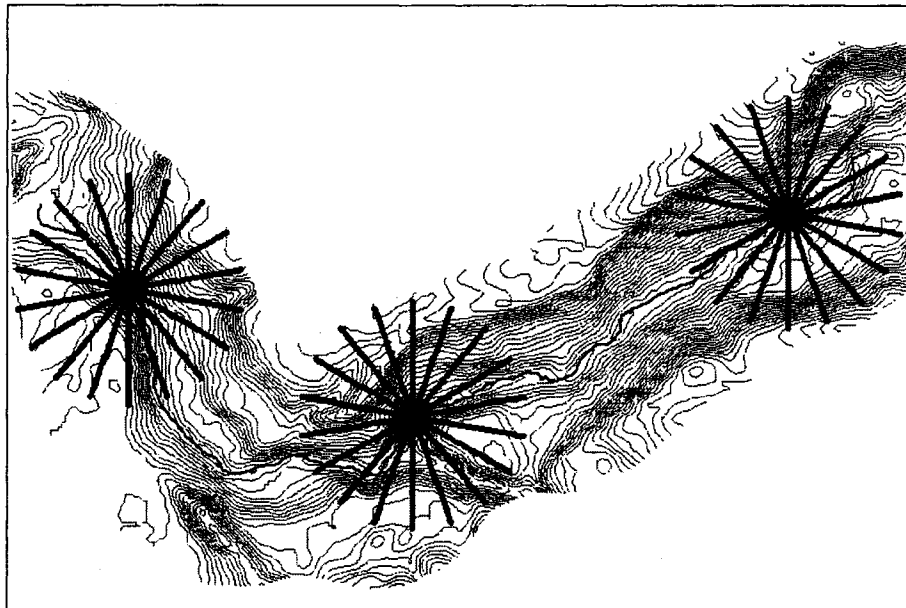


Figure 67: Vegetation density in the Lower Bull Run River

### 3.8.2 Topographic Data

The CE-QUAL-W2 model shade file uses 18 topographic inclination angles surrounding each model segment. The ODEQ shade data provided only three

topographic inclination angles (East, South, and West) at a resolution of 30.5 m (100 ft) along the river. The previous lower river model (Annear et al, 1999) had a coarser grid than the current model grid developed for this research. The inclination angles for the current lower river model were developed using the procedure in Annear et al, 1999. The procedure involved creating 18 horizontal sets of points, characterized by coordinates and an elevation for each point, surrounding the center point of each model segment. Each data set represented a 20 degree increment around the model segment center point. The data points were located out to 1000 m from the model segment center point. Surface elevations were obtained from a contour plot of a USGS DEM as shown in Figure 68. The distances and elevations for each point in a data set were then used to calculate the largest inclination angle for that data set, thereby controlling topographic shading for that 20 degree increment direction around the model segment.



**Figure 68: Topographic Slices along the Lower Bull Run River**

#### **4. Experimental Laboratory Work**

Several lab experiments were conducted to demonstrate streambed heating processes in a more controlled environment, reducing or eliminating the influence of topographic and vegetative stream shading, cloud cover, atmospheric dust and moisture attenuation, wind, and variable stream flow. The results of the experiments were used with the streambed heating algorithm to demonstrate the algorithm's ability to simulate the basic streambed heating processes.

##### **4.1 Experimental Design**

The experiment was designed to monitor the temperature of substrate material in 2 cylinders, each with a volume of  $0.02 \text{ m}^3$  ( $18,930 \text{ cm}^3$ , 5 gallon buckets) with overlying water. The two cylinders had temperature probes embedded in the substrate with 4 thermistors buried in the substrate and 1 in the water above the substrate. The cylinders were placed in a larger box, which was filled with sand to provide a heat sink. The temperature of the outside surface of the cylinders and the air were also monitored with thermistors to better understand the boundary conditions. All thermistors recorded temperature at 5-minute intervals. The radiation source was a narrow spot beam stage light (1000 W), placed 2.3 m above the experimental setup, centered over the two cylinders, producing approximately  $1010 \text{ W/m}^2$ . Radiation was measured with a pyranometer between the two cylinders at 10-minute intervals. The

lamp was turned on for 8.5 hours a day using a timer. Figure 69 shows a drawing of the experimental design with thermistor locations identified and Table 42 provides thermistor location descriptions. Figure 70 shows a photo of the experimental setup.

Each cylinder was filled with substrate material to a depth of 20 cm (volume: 13,550 cm<sup>3</sup>) and then filled with water to a depth of 6 cm (volume: 4,065 cm<sup>3</sup>). Evaporated water from the cylinders was replaced daily with water stored at room temperature.

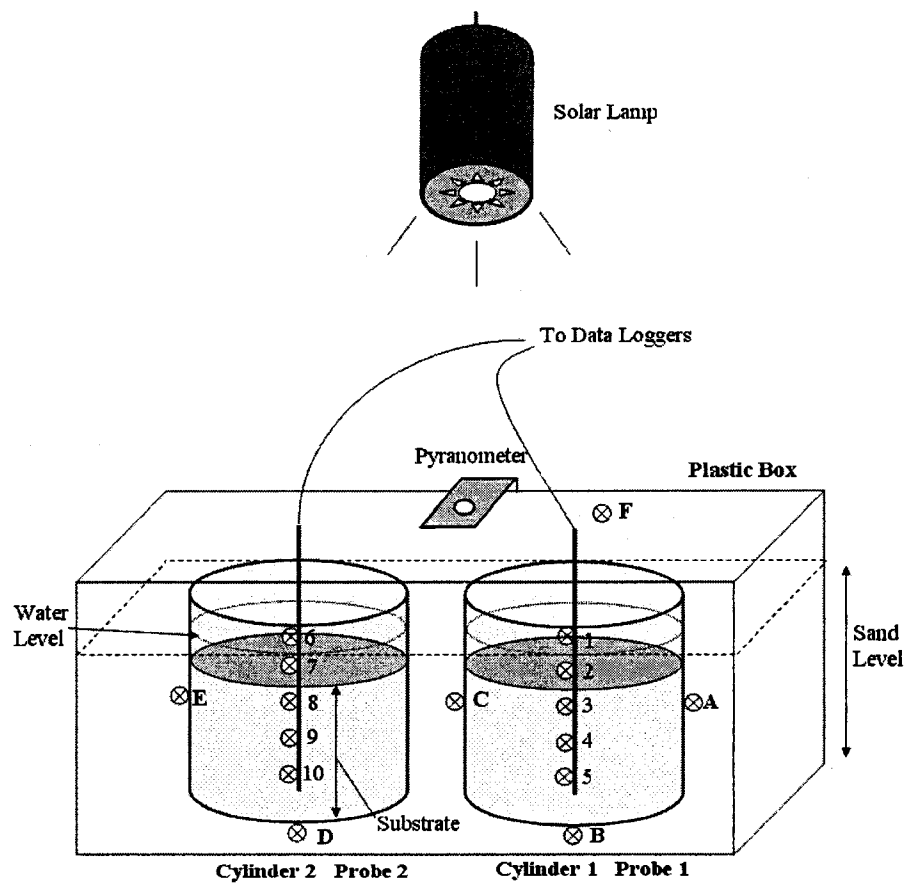
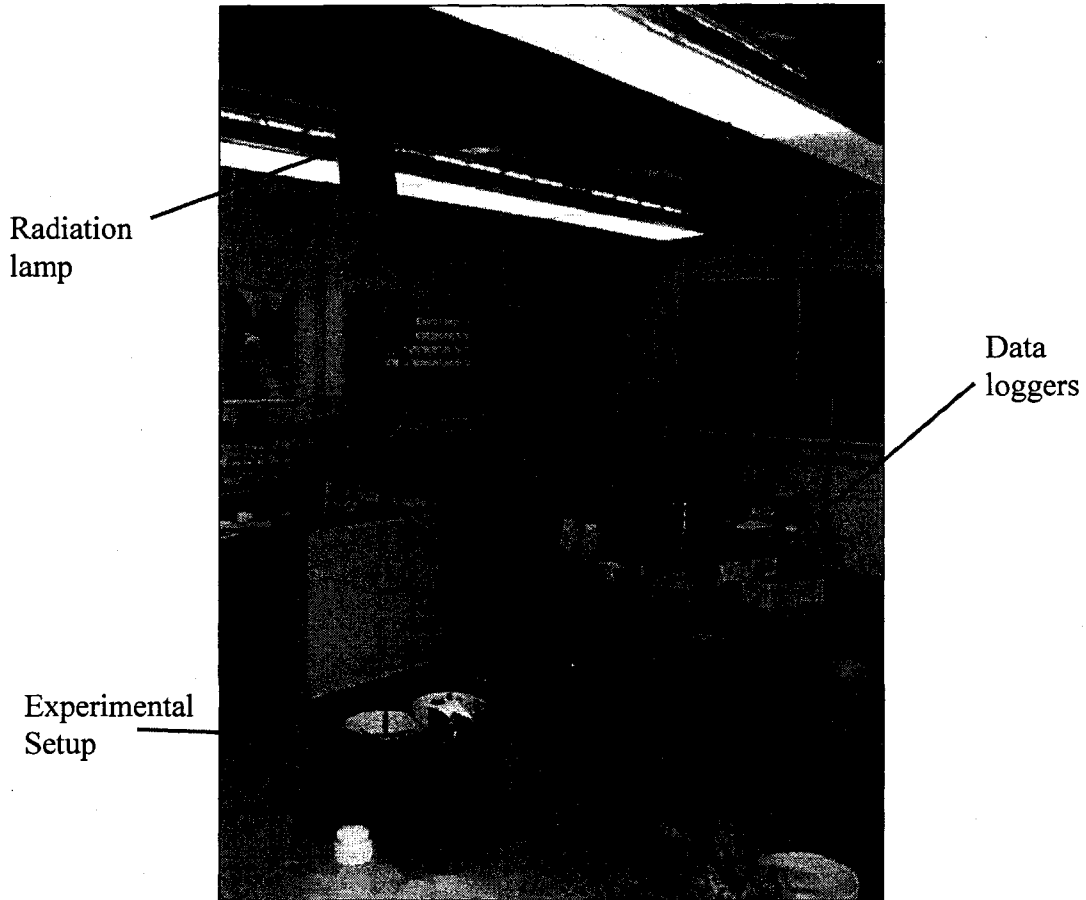


Figure 69: Experimental lab design

**Table 42: Experimental design thermistor locations**

Thermistor Location, T	Description
TA	Cylinder 1 - Right Side
TB	Cylinder 1 - Underside
TC	Cylinder 1 - Left Side
TD	Cylinder 2 - Underside
TE	Cylinder 2 - Left Side
TF	Air Temperature (Outer Wall of Plastic Tub)
T1	Probe 1 – Water
T2	Probe 1– 1 cm depth from surface of substrate
T3	Probe 1– 6 cm depth from surface of substrate
T4	Probe 1– 11 cm depth from surface of substrate
T5	Probe 1– 16 cm depth from surface of substrate
T6	Probe 2 – Water
T7	Probe 2– 1 cm depth from surface of substrate
T8	Probe 2– 6 cm depth from surface of substrate
T9	Probe 2– 11 cm depth from surface of substrate
T10	Probe 2– 16 cm depth from surface of substrate



**Figure 70: Experimental lab design setup**

## **4.2 Results**

### **4.2.1 Experiment 1: Sand vs. Gravel**

The first experiment compared sand and gravel substrates. One cylinder was filled with sand with a limited particle size range and the other cylinder was filled with gravel of similar size. Both cylinders were filled with water to a depth of 6 cm above the top surface of the substrate. The pore space between the gravel and the sand was also filled with water. Figure 71 shows a photo of the experimental lab setup.



**Figure 71: Sand and gravel experimental lab setup**

The experiment was run for 5 days from November 17 to 22, 2002. Temperature measurements recorded during the experiment are presented in Figure 72 to Figure 79. Temperatures measurements recorded at a depth of 16 cm in the Sand substrate cylinder were found to be erroneous. See Appendix D for further discussion on suspect data. Figure 72 shows the water and substrate temperature measurements in the gravel substrate. The figure indicates there are both a time lag in diurnal peaks and a dampening of the temperature swings with increasing depth. The figure also indicates there is a gradual warming trend over the 5 day period for all depths, which may be due to the large radiation source impact on the substrate. Since the large pore space between the gravel was filled with water the 1 cm depth temperature measurements are similar temperatures to the water temperature measurements. Figure 73 shows the water and substrate temperature measurements in the sand

substrate. The figure shows the largest temperature swings in the water with dampening of temperature swings with increasing depth. Due to a smaller amount of pore space filled with water compared to the gravel substrate there is a difference between the water temperature and the substrate temperature at depth of 1 cm.

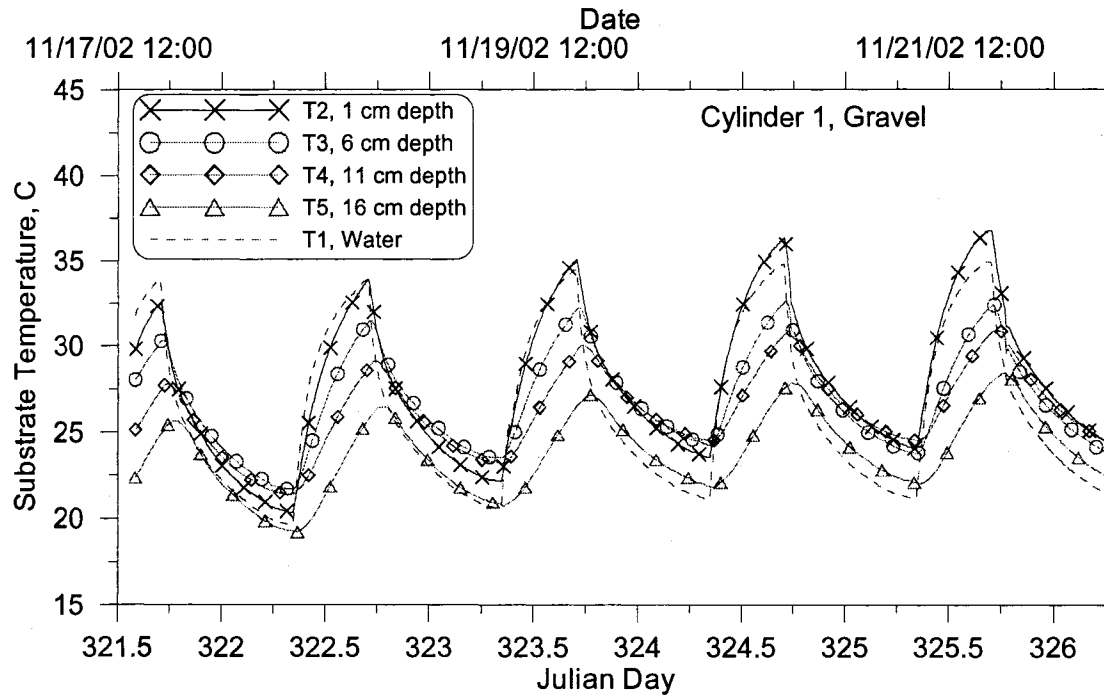


Figure 72: Gravel substrate and water temperature

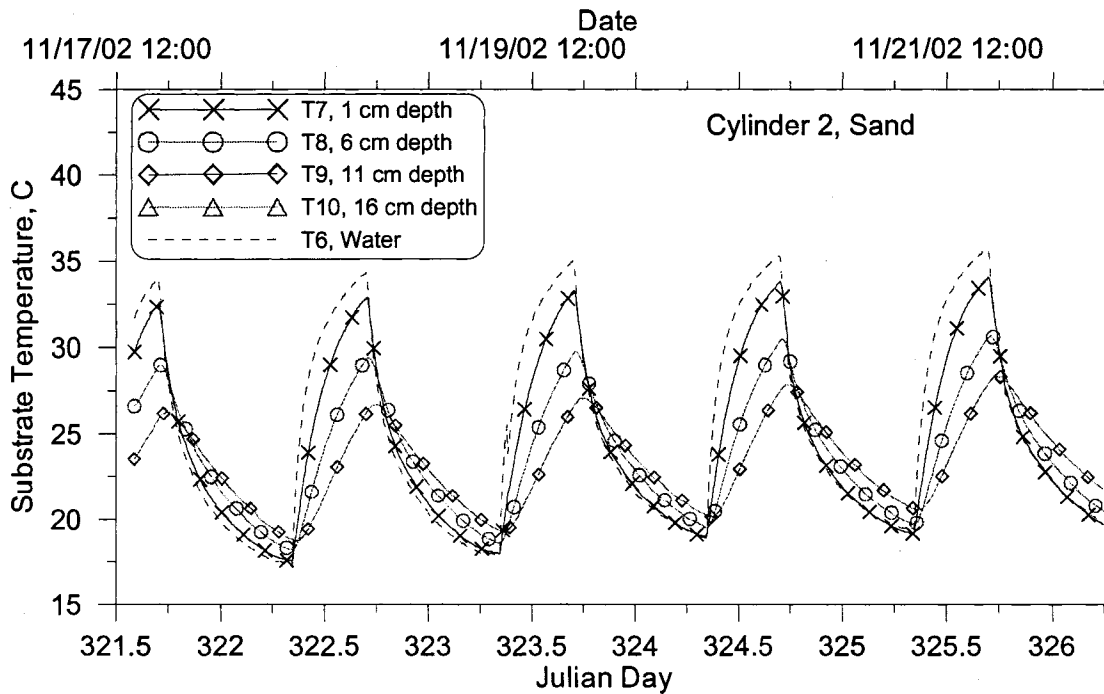


Figure 73: Sand substrate and water temperature

Figure 74 shows the side boundary conditions for the experiment. Three thermistors were attached to the sides of the cylinders as indicated in Figure 69. The temperatures recorded on the outer sides of the cylinders show similar diurnal temperature swings and the thermistor between the cylinders shows higher temperatures due to its placement between the cylinders and directly below the radiation source. Figure 75 shows the temperature of the bottom boundary condition for both cylinders, and indicates they share a similar diurnal temperature pattern. The bottom temperature below the gravel substrate shows higher daily peak and lower nightly temperatures than the bottom temperature below the sand substrate. This difference could be due to the gravel pore space water distributing energy absorbed at the surface more readily.

Figure 76 to Figure 78 show the substrate temperatures from Figure 72 and Figure 73 but compare the temperature between the gravel and sand substrates for the same depth. Figure 76 to Figure 78 show the temperature data recorded in the gravel substrate was consistently higher than the sand substrate. This could be due to the gravel retaining more radiation energy and exchanging it with the surrounding pore space water more effectively than the sand substrate. The figures comparing temperature data at different depths in the substrate all show a gradual warming over the five day run period.

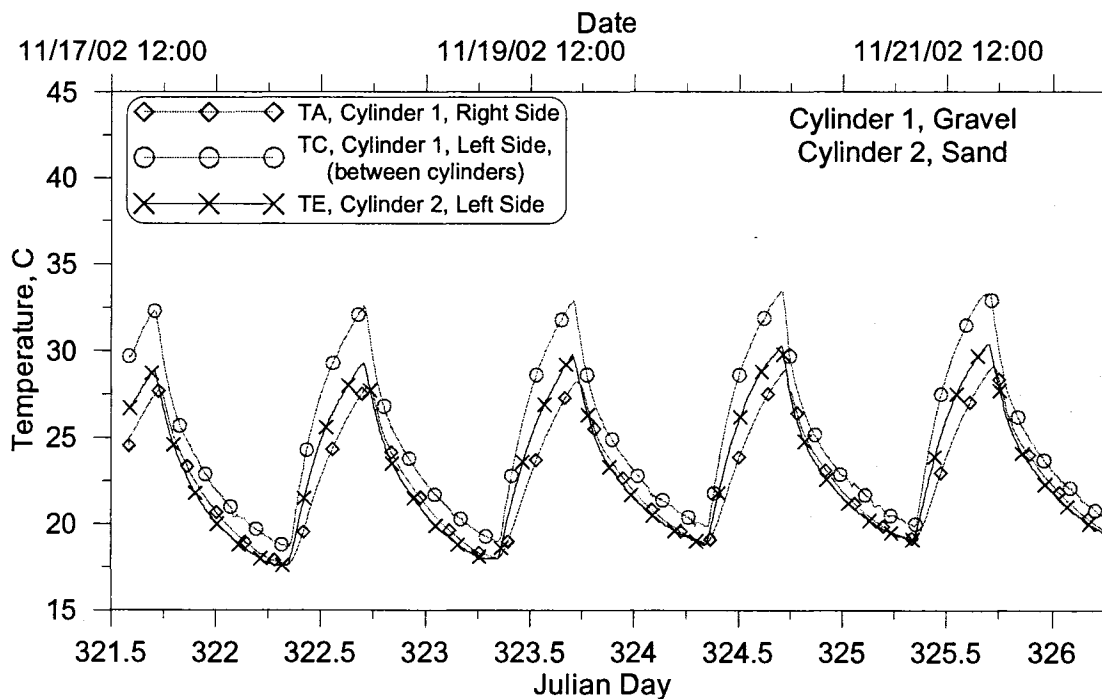


Figure 74: Experiment 1 side boundary condition temperatures

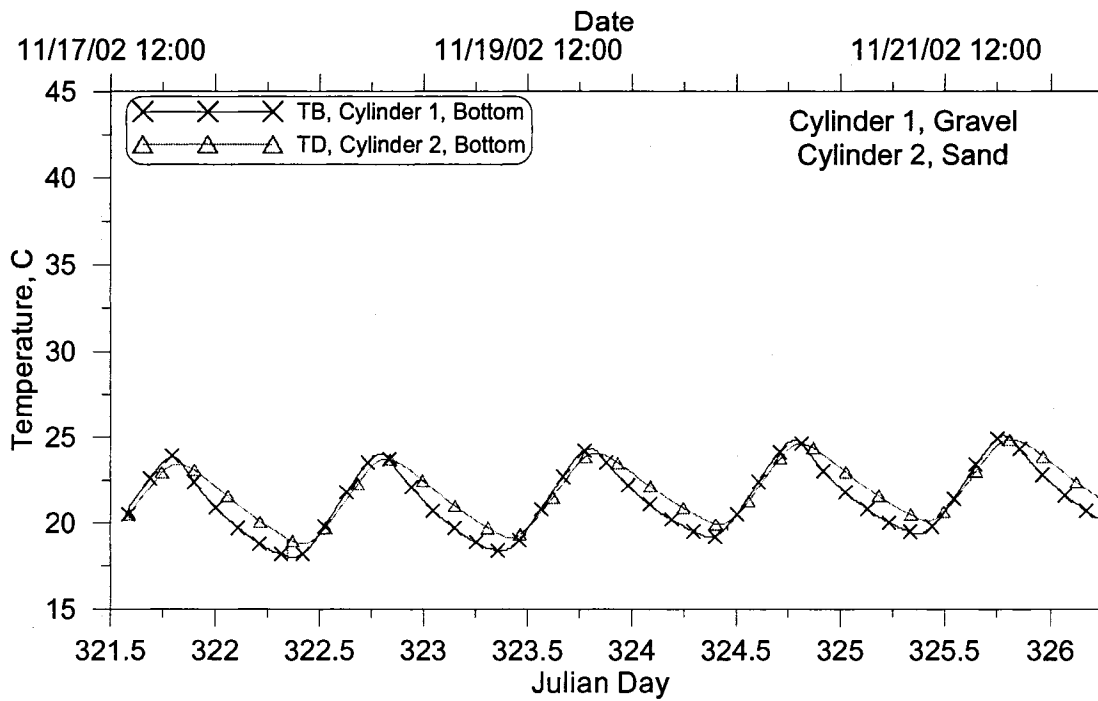


Figure 75: Experiment 1 bottom boundary condition temperatures

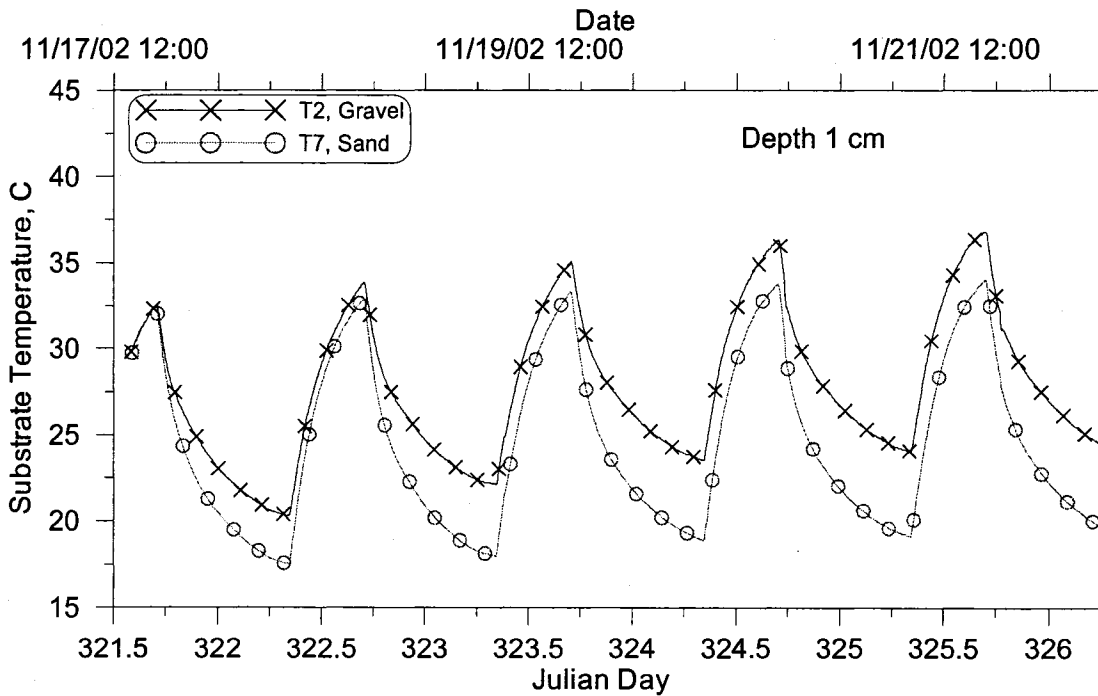


Figure 76: Gravel and Sand substrate temperatures at 1 cm depth

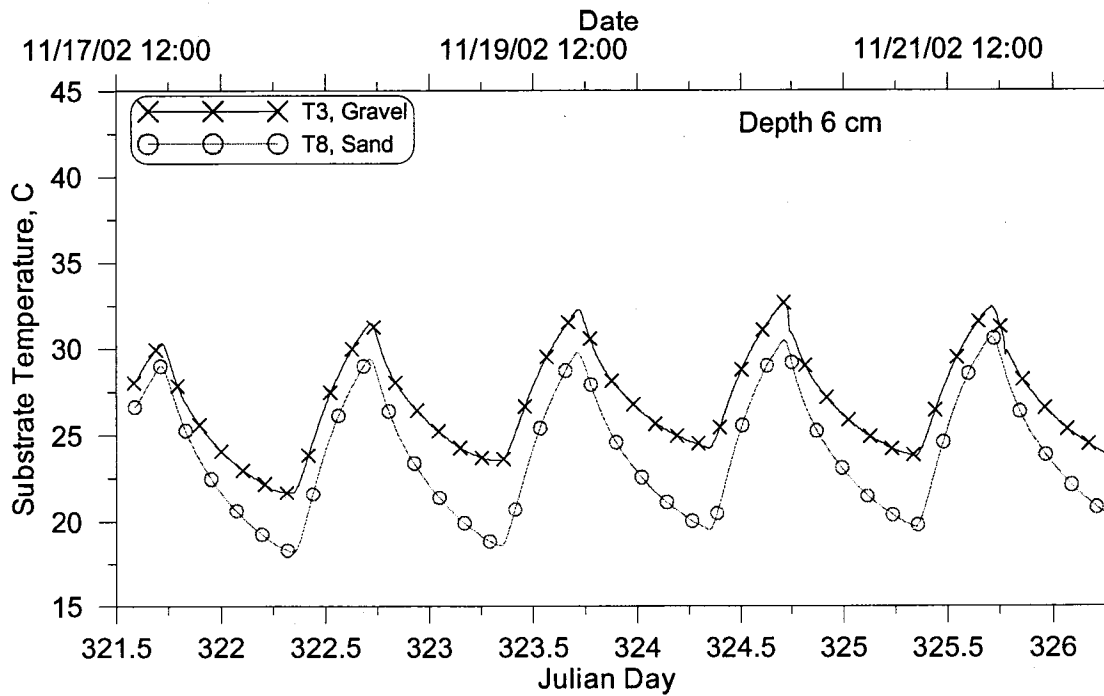


Figure 77: Gravel and Sand substrate temperature at 6 cm depth

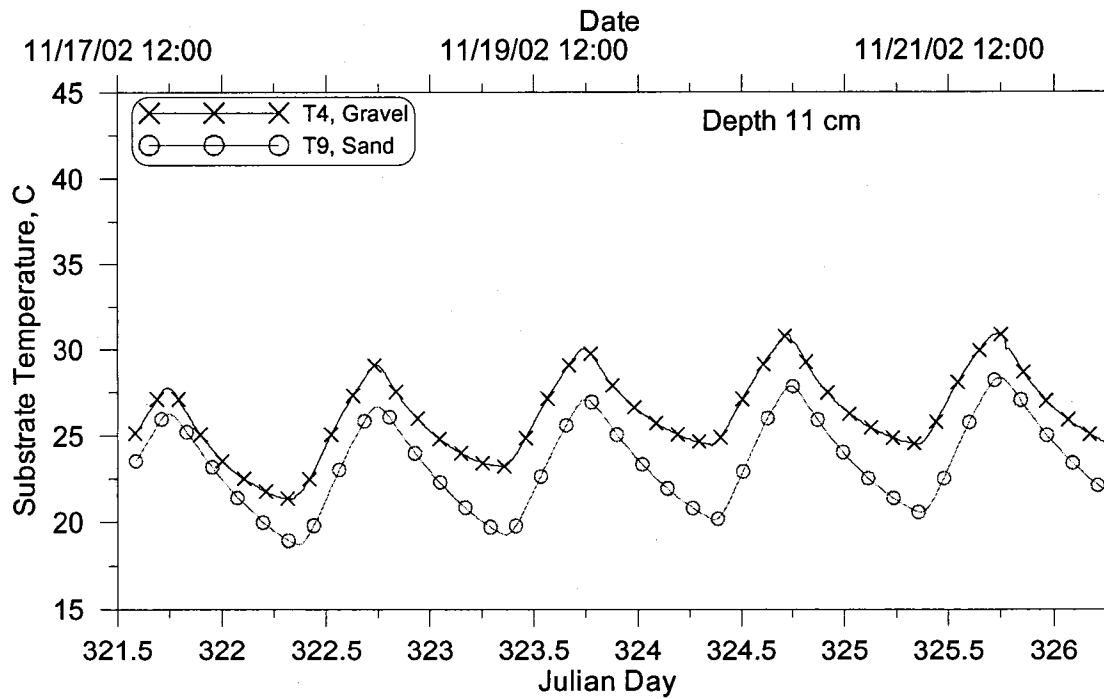


Figure 78: Gravel and Sand substrate temperature at 11 cm depth

Figure 79 shows the air temperature and radiation recorded during the experiment. The figure illustrates the radiation was turned on each day for the same amount of time and remained relatively constant at  $1010 \text{ W/m}^2$ . The air temperature increased considerably once the radiation source was turned on and continued to warm during the day until the source was shut off. The air temperature data also indicates a gradual warming over the period of the experiment.

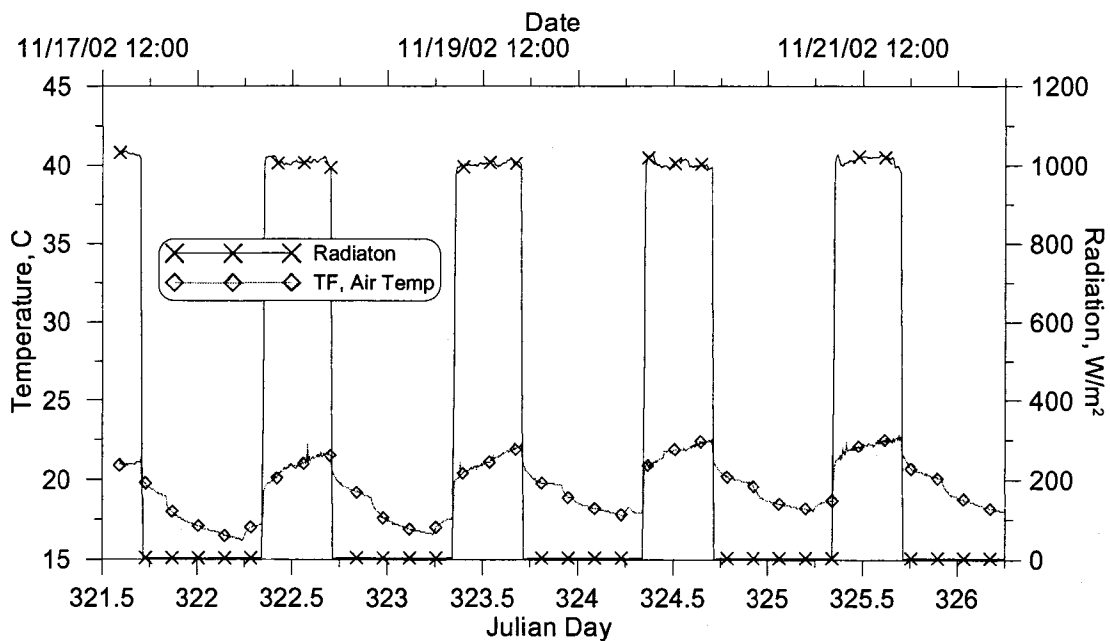


Figure 79: Air temperature and radiation for Experiment 1

Figure 80 shows the water temperature above both substrates and the air temperature. The figure indicates the water above the sand substrate had higher peak temperatures when the radiation source was on, and lower temperatures when it was off than the water above the gravel substrate. Neither substrate returned to room temperature at night, which suggests both substrates are radiating heat back into the water, keeping the water slightly warmer than the surrounding air. This also indicates

there is more heat radiating from the gravel to the water than from the sand to the water. The water above the gravel substrate takes longer to heat up and retains more heat than the water above the sand substrate. This may be due to the gravel having a higher heat capacity than the sand.

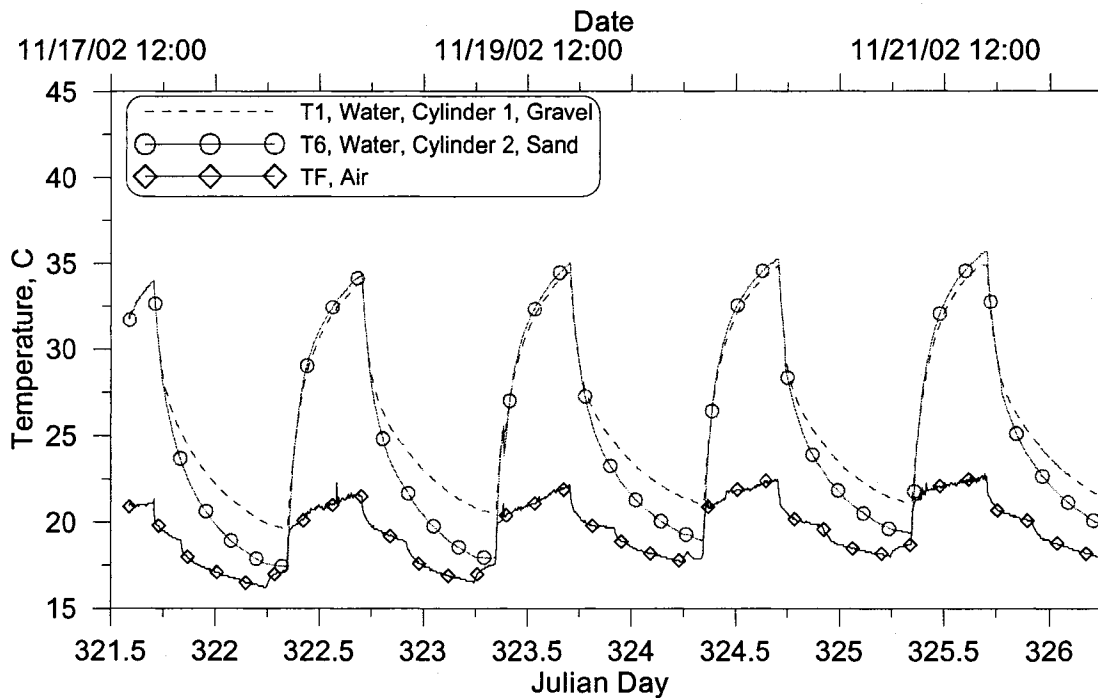
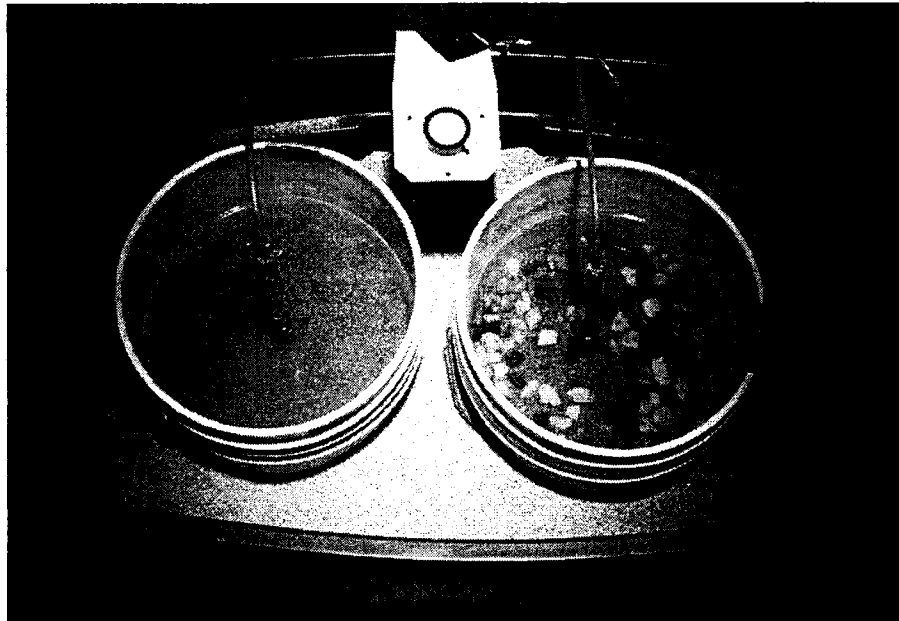


Figure 80: Water and air temperature for Experiment 1

#### 4.2.2 Experiment 2: Sand vs. Gravel-Sand Mixture

The second experiment compared sand substrate and a gravel-sand mixture substrate. One cylinder was filled with sand with a limited particle size range and the other cylinder was filled with gravel and the same type of sand. Both cylinders were then filled with water to a depth of 6 cm above the top surface of the substrate. The

pore space between the gravel-sand mixture and the sand substrates was filled with water. Figure 81 shows a photo of the experimental lab setup.



**Figure 81: Sand and gravel-sand mixture experimental lab setup**

The experiment was run for 6 days from November 22 to 28, 2002. The temperature measurements are presented in Figure 82 to Figure 87. Temperatures measurements recorded at a depth of 16 cm in the sand substrate and at a depth of 1 cm and 11 cm in the gravel-sand mixture substrate were found to be erroneous. Further discussion of erroneous or suspect data can be found in Appendix D.

Figure 82 shows the water and substrate temperature measurements in the gravel-sand mixture substrate. The figure shows there is damped diurnal temperature swing for 16 cm depth compared to 6 cm depth with the water having the largest diurnal temperature change. Similar to the gravel substrate in Experiment 1, the water temperature exhibits larger diurnal temperature swings with lower over night

temperatures than the substrate. Figure 83 shows the water and substrate temperature measurements in the sand substrate. Similar to Experiment 1, the largest temperature swings was in the water with dampening of temperature swings with increasing depth. Both figures show a gradual decrease in peak temperatures over the duration of the experiment.

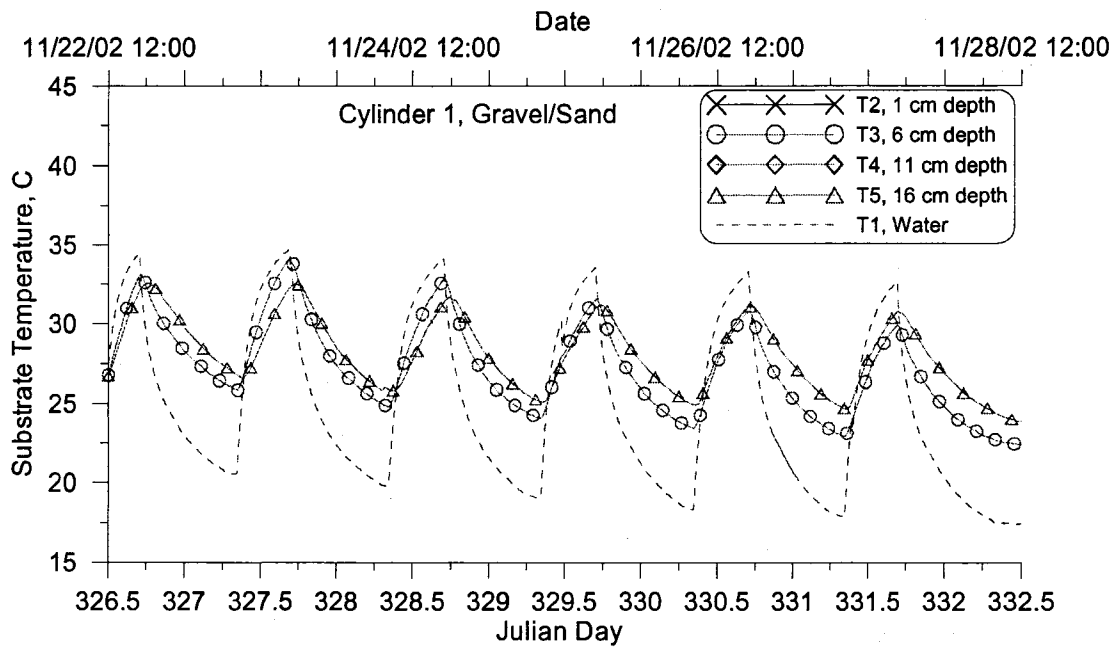
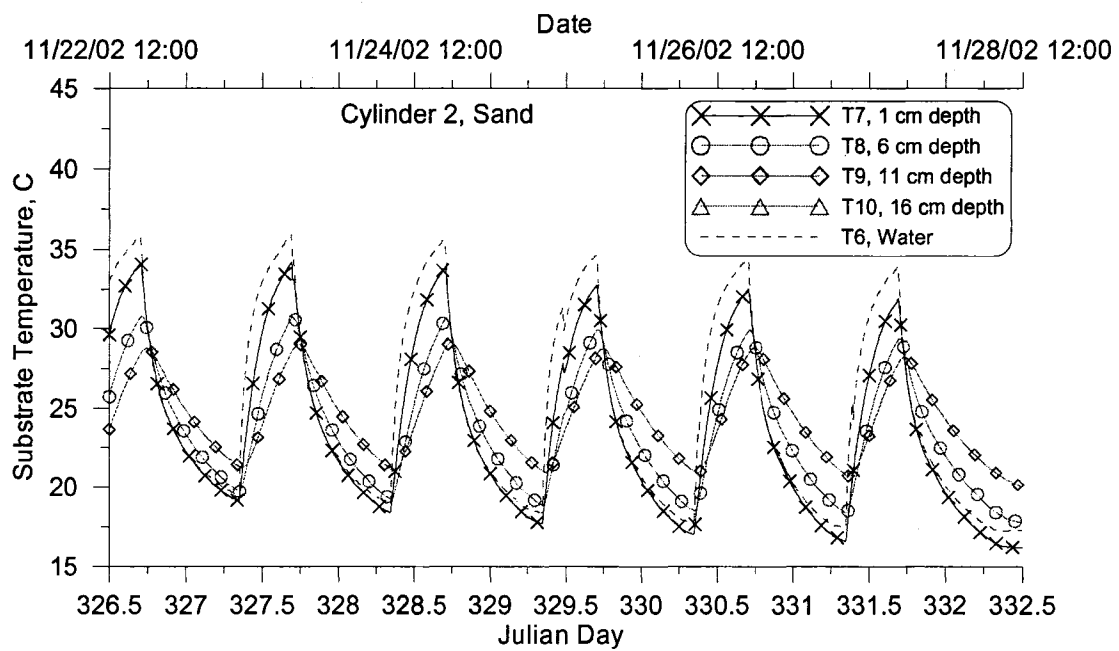


Figure 82: Gravel-sand mixture substrate and water temperature



**Figure 83: Sand substrate and water temperature**

Figure 84 shows the side boundary condition temperature for Experiment 2. The temperatures recorded on the outer sides of the cylinders show similar diurnal temperature swings and the thermistor between the cylinders shows higher temperatures due to its placement between the cylinders and directly below the radiation source. Figure 85 shows the temperature of the bottom boundary condition temperature for both cylinders, and indicates both cylinders show similar diurnal temperature patterns. The bottom temperature below the gravel-sand mixture substrate shows higher daily peak and lower nightly temperatures than the bottom temperature below the sand substrate. The daily bottom temperature peaks and lows also arrive earlier with the overlying gravel-sand mixture substrate than with the sand substrate. This difference could be due to the gravel-sand mixture distributing energy absorbed at the surface more readily.

Similar to Figure 82 and Figure 83, both Figure 84 and Figure 85 show a gradual decrease in peak temperatures over the duration of the experiment. Figure 86 compares the temperatures measured at a depth of 6 cm for both the gravel-sand mixture and sand substrates. The figure indicates the gravel-sand mixture substrate retains more heat than the sand substrate.

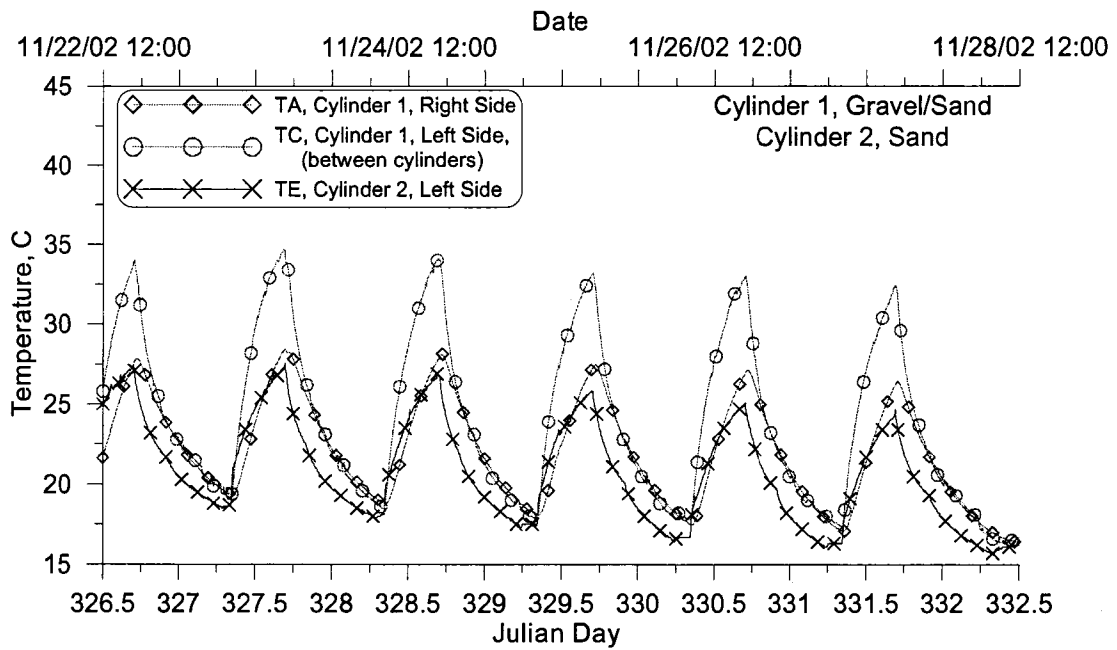


**Figure 84: Experiment 2 side boundary condition temperatures**

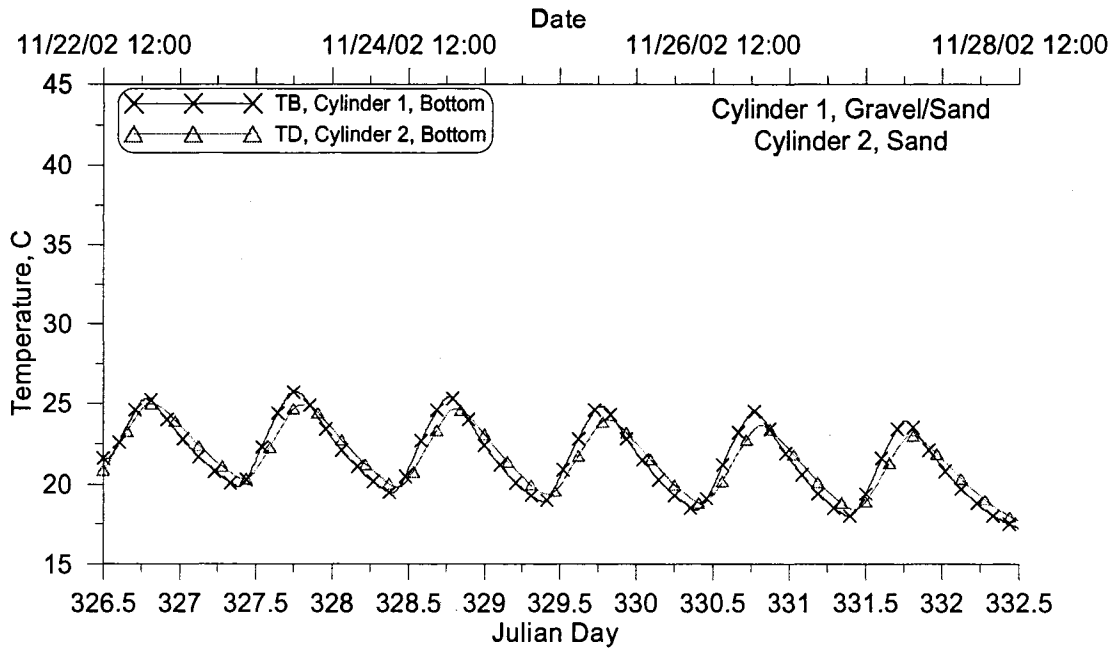


Figure 85: Experiment 2 bottom boundary condition temperatures

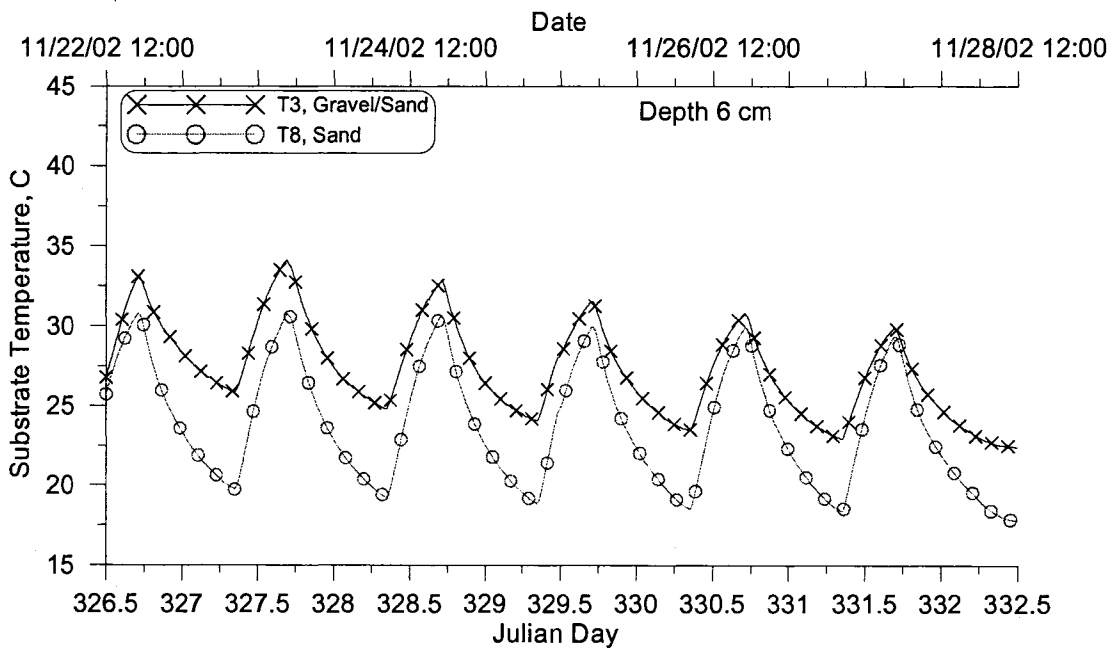


Figure 86: Gravel-sand mixture and Sand substrate temperatures at 6 cm depth

Figure 87 shows a plot of the air temperature and radiation in Experiment 2. The figure shows the radiation source was turned on periodically each day and

remained relatively constant at 1,020 W/m<sup>2</sup>. The air temperature increased considerably once the radiation source was turned on and continued to warm during the day until the source was shut off. The air temperature data also indicate a gradual cooling during the experiment which may explain the cooling trend in daily peak temperature seen in the water and substrate temperature data presented.

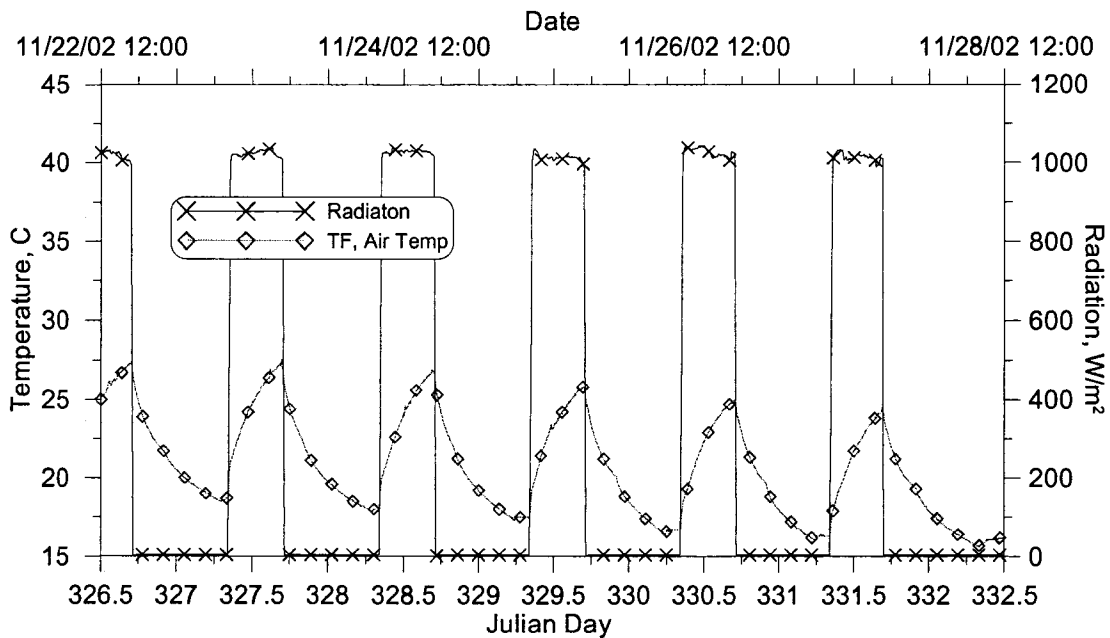


Figure 87: Experiment 2 air temperature and radiation

In Figure 88 the water above the sand substrate reaches slightly higher temperatures each day and slightly lower temperatures during the night than the water above the gravel-sand mixture substrate. Neither substrate returned to room temperature at night, which suggests both substrates are radiating heat back into the water, keeping the water slightly warmer than the surrounding air. In Experiment 2 since the gravel is mixed with sand there is less water heating and cooling and the diurnal change is closer to the water above the sand substrates in Experiment 2 and

Experiment 1. There is more heat radiating from the gravel-sand mixture substrate to the overlying water than the sand substrate but less than with just the gravel substrate from Experiment 1. The water above the gravel-sand mixture substrate takes slightly longer to heat up and retains more heat than the water above the sand substrate.

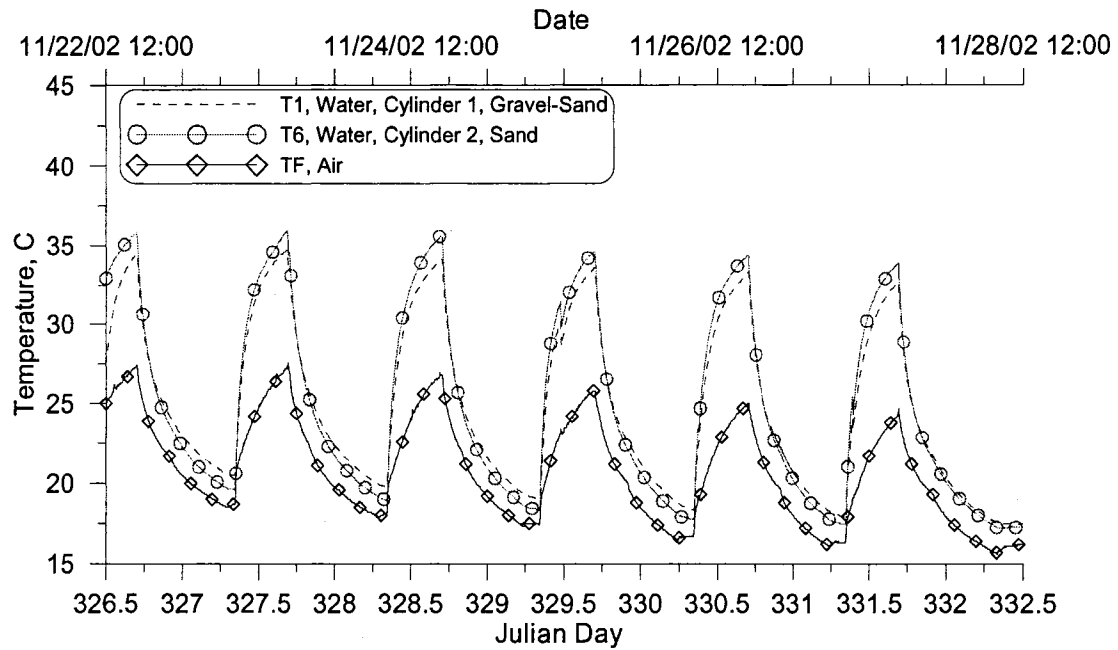
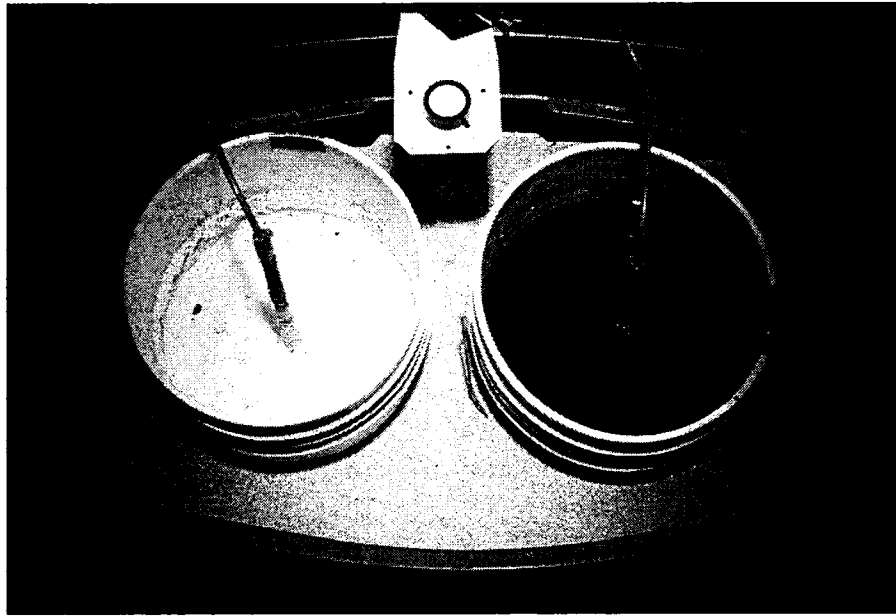


Figure 88: Water and air temperature for Experiment 2

#### 4.2.3 Experiment 3: Painted Concrete, White vs. Black

The third experiment compared 2 cylinders with concrete substrates with one surface painted white and the other painted black. Both cylinders were then filled with water to a depth of 6 cm above the substrate. Figure 89 shows a photo of the experimental setup.



**Figure 89: White and black concrete experimental lab setup**

The experiment was run for 5 days from December 15 to 20, 2002. The temperature measurements are presented in Figure 90 to Figure 93. Temperature measurements recorded at depths of 1, 6 and 11 cm in the concrete with a black painted surface and at a depth of 16 cm in the concrete with a white painted surface were found to be erroneous. Further discussion of erroneous or suspect data can be found in Appendix D.

Figure 90 shows the water and substrate temperature measurements for the black painted concrete substrate cylinder. The figure shows there is a damped diurnal temperature swing at 16 cm depth compared to the water temperatures measured. Figure 91 shows the water and substrate temperature measurements for the white painted concrete substrate cylinder. The figure shows a time lag in the peak temperature and a dampening of the peak temperature with increasing depth. The substrate temperature measured at a depth of 1 cm is similar to the water temperature,

except the water temperature increases earlier than the concrete, as expected, and the concrete temperature at 1 cm depth reaches a higher temperature peak temperature each day.

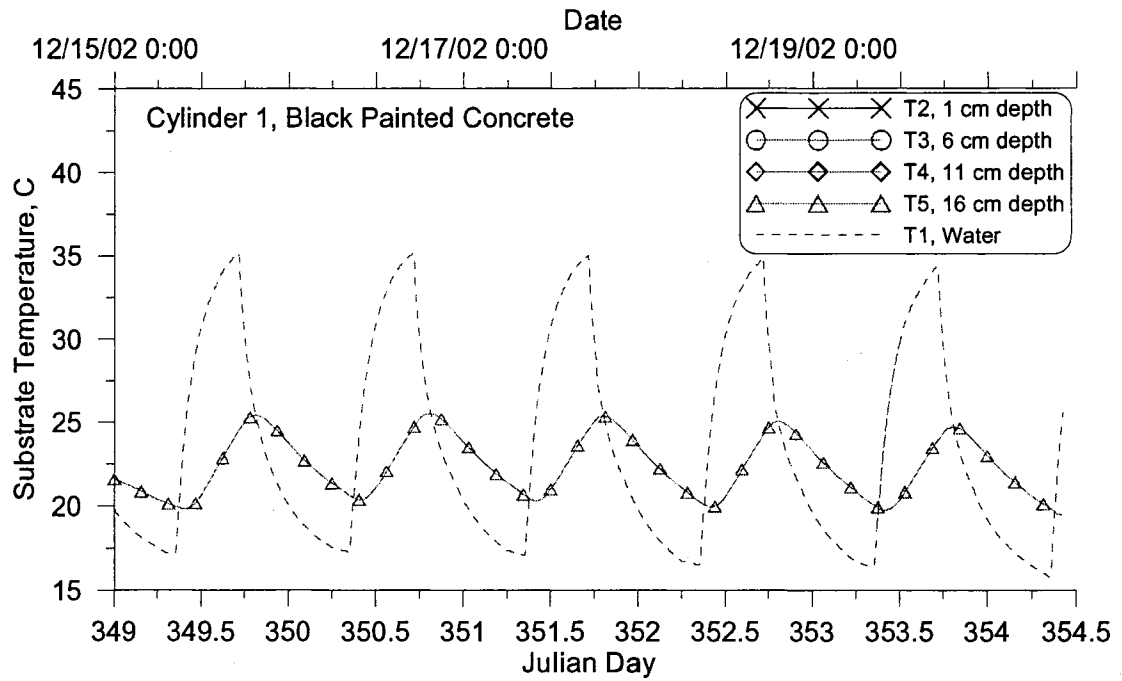


Figure 90: Black painted concrete substrate and water temperature

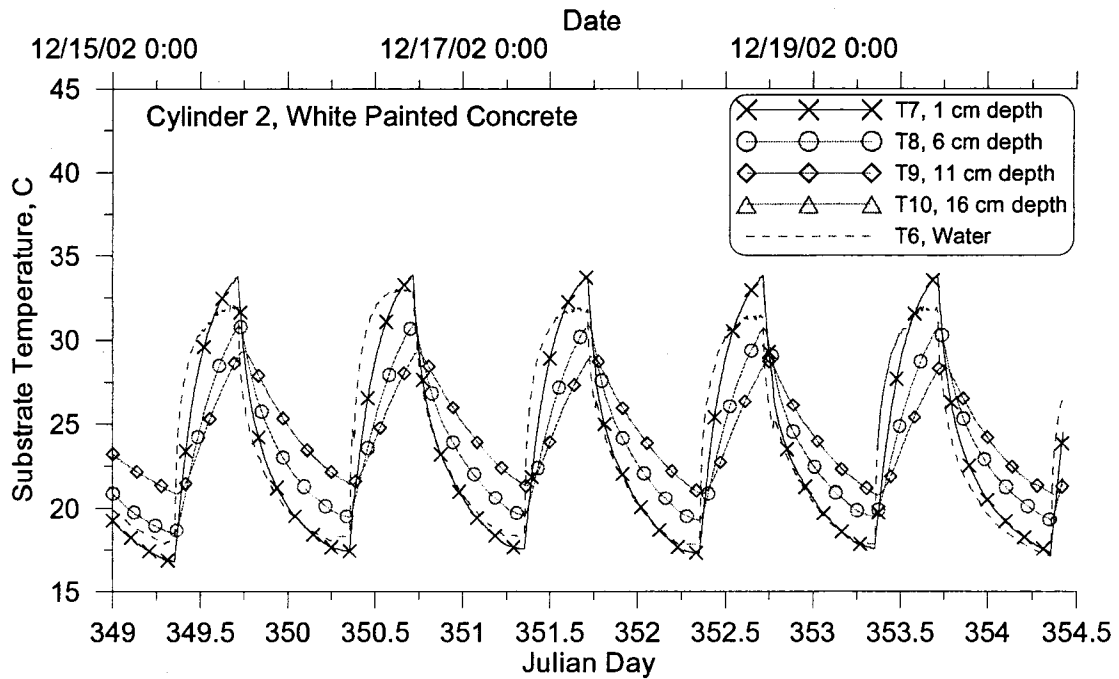


Figure 91: White painted concrete substrate and water temperature

Figure 92 shows the side boundary condition temperature for Experiment 3. The temperatures recorded on the outer sides of the cylinders show similar diurnal temperature swings and the thermistor between the cylinders shows higher temperatures due to its placement between the cylinders and directly below the radiation source. Figure 93 shows the bottom boundary condition temperature for both cylinders, which have a similar diurnal pattern with the bottom temperature below the white concrete slightly lower over the duration of the experiment.

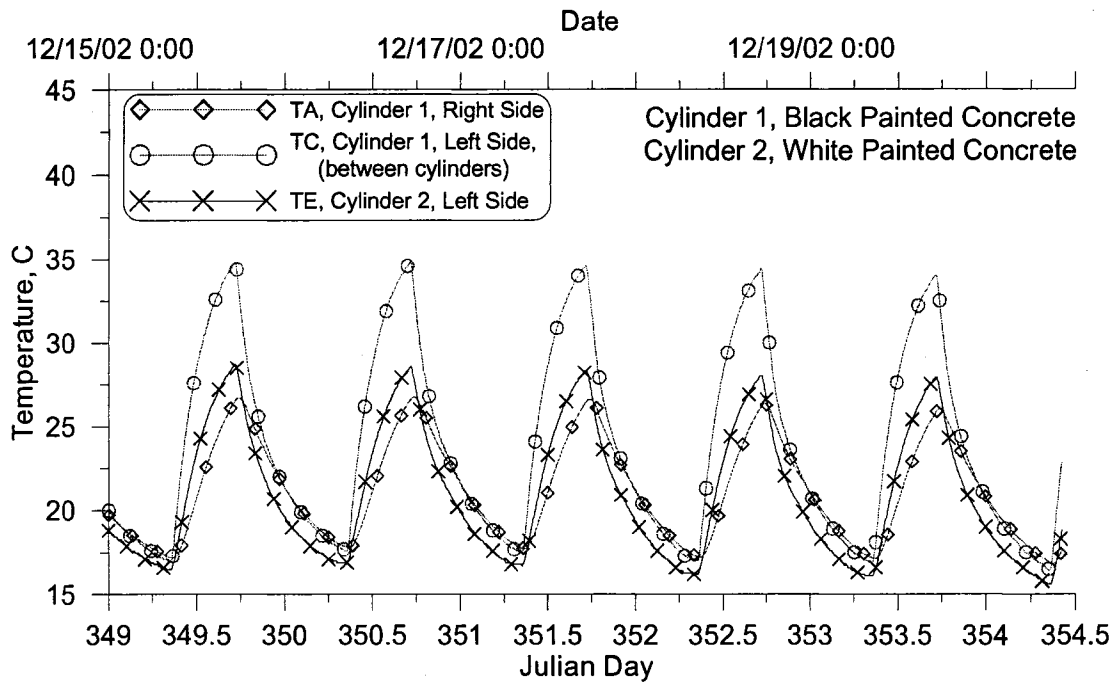


Figure 92: Experiment 3 side boundary condition temperatures

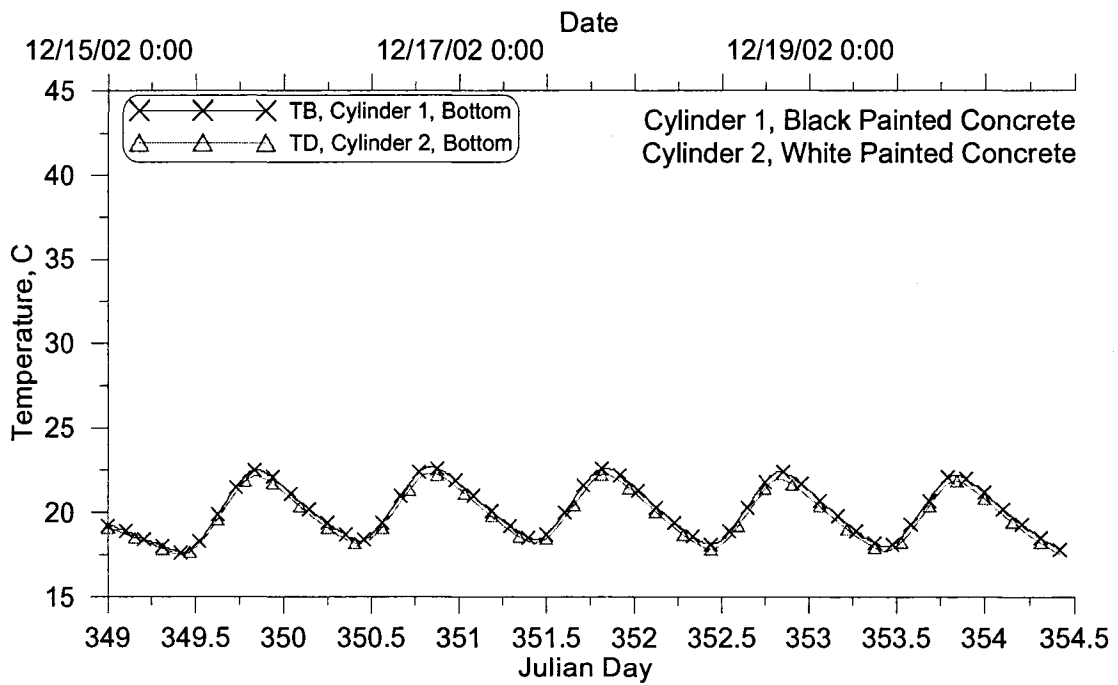


Figure 93: Experiment 3 bottom boundary condition temperatures

Figure 94 shows a plot of the air temperature and radiation in Experiment 3. The figure shows the radiation was turned on periodically each day and remained relatively constant at  $1045 \text{ W/m}^2$ . The air temperature increased considerably once the radiation source was turned on and continued to increase during the day until the radiation source was shut off.

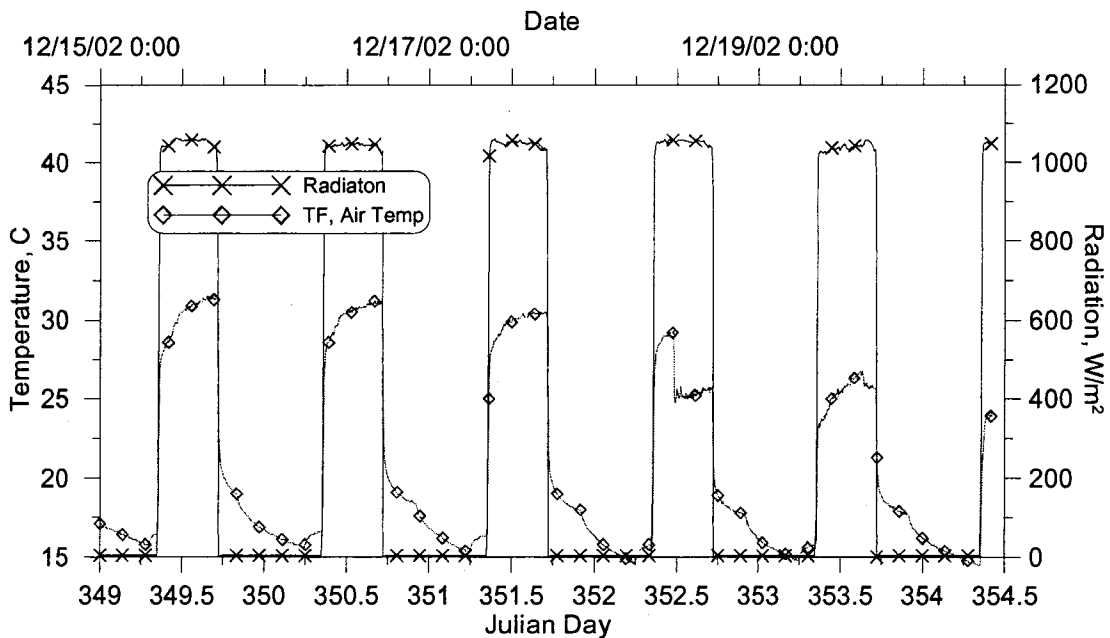


Figure 94: Experiment 3 air temperature and radiation

In Figure 95 the water temperature above the black painted concrete substrate reaches higher temperatures each day and lower temperatures during the night than the water above the white painted concrete. Neither substrate returned to room temperature at night, suggesting both substrates are radiating heat back into the water, keeping it slightly warmer than the surrounding air. The larger temperature change for the black painted concrete was due to more radiation being absorbed by the black surface and reradiated as heat back into the water column than the white painted

concrete. The white painted concrete was reflecting more radiation back into the water and can be shown as the water temperature increased earlier than the water above the black concrete each day.

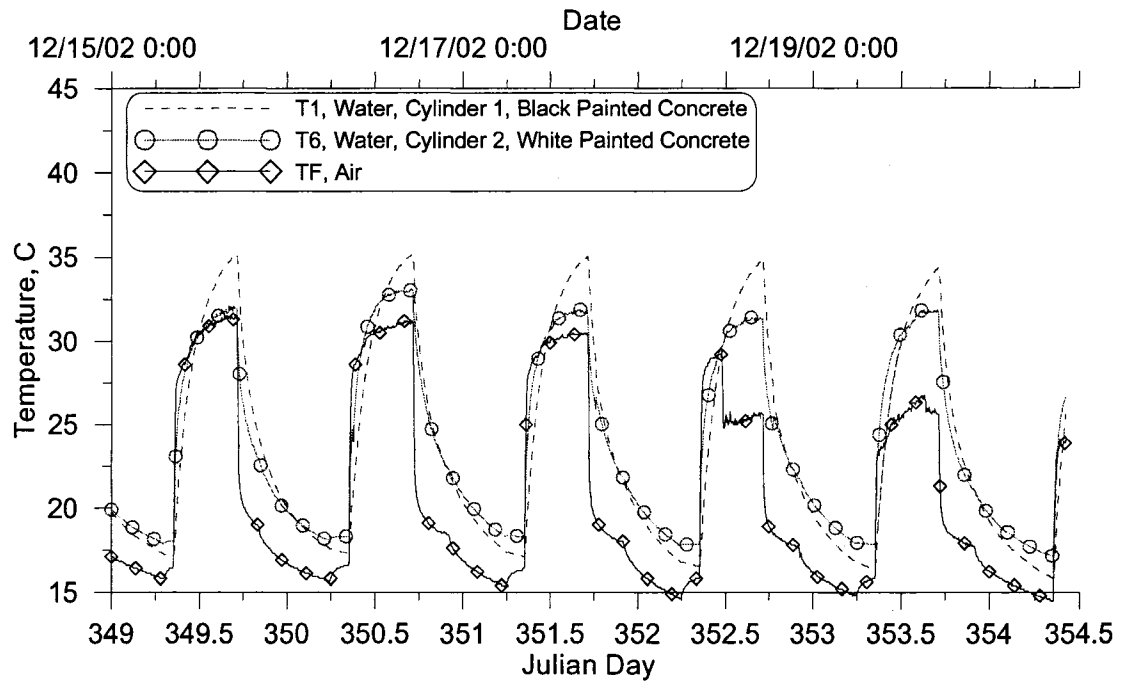


Figure 95: Water and air temperature for Experiment 3

#### 4.3 Discussion

The three experiments demonstrated the influence of substrate media and substrate color on the overlying water column temperature when exposed to a radiation source during the day. Experiment 1 showed the gravel substrate stored more heat than the sand substrate. The gravel substrate also resulted in warmer water temperatures during the night than the water overlying the sand substrate. Experiment 2 showed the same process with the gravel-sand mixture substrate but less dramatic

with overlying water temperatures during the night only slightly warmer than the water above the sand substrate. Experiment 3 showed the black painted concrete stored more heat than the white painted concrete and exchanged it with the water above resulting in higher temperatures during the night.

The three experiments also showed the black painted concrete retained the most heat, followed by the gravel, gravel-sand mixture, sand, and the white painted concrete substrates.

## 5. Streambed Heating Model

### 5.1 Development

The streambed heating algorithm was developed as a three dimensional model in two coordinate systems: Cartesian for the calibrating with the field data and implementation with CE-QUAL-W2, and cylindrical for calibrating with the lab experiment data.

#### 5.1.1 Cartesian Model

##### 5.1.1.1 Governing Equation

The three-dimensional partial differential equation for heat transfer in the streambed (Incropera and De Witt, 1990) is

$$\frac{\partial T}{\partial t} = \frac{\partial}{\partial x} \left( \beta_x \left( \frac{\partial T}{\partial x} \right) \right) + \frac{\partial}{\partial y} \left( \beta_y \left( \frac{\partial T}{\partial y} \right) \right) + \frac{\partial}{\partial z} \left( \beta_z \left( \frac{\partial T}{\partial z} \right) \right) \quad (80)$$

where  $T$  ( $^{\circ}\text{C}$ ) is the streambed temperature,  $t$  (seconds) is time, and  $\beta_x, \beta_y, \beta_z$  ( $\text{m}^2/\text{s}$ ) are the streambed thermal diffusivity coefficients in the  $x$ ,  $y$ , and  $z$  directions and may vary in space. The partial differential equation was converted to an explicit finite central difference numerical scheme for solving. Figure 96 shows a schematic of the numerical grid scheme in the  $x$  direction where  $\Delta x$  is the longitudinal grid spacing

and  $i$  enumerates the numerical grid location. Similarly,  $j$  and  $k$  are used to enumerate the grid location in the  $y$ , and  $z$  directions.

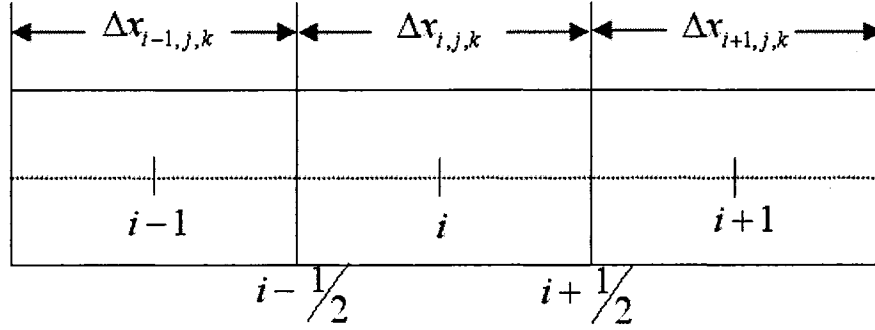


Figure 96: Cartesian coordinate system numerical grid, x direction.

The finite difference approach resulted in a series of coefficients representing the weighted averages of the thermal diffusivity and their spatial rate of change. Given the location  $i$  in the  $x$  direction, the forward difference weighting of the thermal diffusivity,  $\gamma_{i+1,j,k}$  (1/seconds), was expressed as

$$\gamma_{i+1,j,k} = \frac{\beta_{i+1,j,k} \left( \frac{\Delta x_{i+1,j,k}}{2} \right) + \beta_{i,j,k} \left( \frac{\Delta x_{i,j,k}}{2} \right)}{\Delta x_{i,j,k} \left( \frac{\Delta x_{i+1,j,k}}{2} + \frac{\Delta x_{i,j,k}}{2} \right)^2} \quad (81)$$

When considering the backward difference weighting and the  $y$ , and  $z$  directions six spatial difference weighted thermal diffusivity terms were developed and summed,  $\gamma_{i,j,k}$  (1/seconds), as

$$\gamma_{i,j,k} = \gamma_{i+1,j,k} + \gamma_{i-1,j,k} + \gamma_{i,j+1,k} + \gamma_{i,j-1,k} + \gamma_{i,j,k+1} + \gamma_{i,j,k-1} \quad (82)$$

Given the present time as  $n$ , the streambed temperature at location  $i$ ,  $j$ ,  $k$  was solved for the next time step,  $n+1$  ( $t + \Delta t$ ), with the equation:

$$\begin{aligned}
T_{i,j,k}^{n+1} = & \Delta t \gamma_{i+1,j,k} T_{i+1,j,k}^n + \Delta t \gamma_{i-1,j,k} T_{i-1,j,k}^n + \Delta t \gamma_{i,j+1,k} T_{i,j+1,k}^n + \\
& \Delta t \gamma_{i,j-1,k} T_{i,j-1,k}^n + \Delta t \gamma_{i,j,k+1} T_{i,j,k+1}^n + \Delta t \gamma_{i,j,k-1} T_{i,j,k-1}^n \\
& + (1 - \Delta t \gamma_{i,j,k}) T_{i,j,k}^n
\end{aligned} \tag{83}$$

using the present temperature in the streambed at  $i$ ,  $j$ ,  $k$  and the surrounding grid cells. The application of Equation (83) consisted of solving the equation for all grid cells for the first time step using the initial conditions and the incrementing to the next time step and resolving for all the grid cells.

### 5.1.1.2 Internal Stability Criteria

The model formulation consisted of using an explicit finite central difference scheme. In order to ensure the solution is stable and does not result in incorrect temperature predictions a stability criterion must be satisfied. The internal stability criteria is a function of the sum of the spatial difference weighted thermal diffusivity terms,  $\gamma_{i,j,k}$ , and was developed as

$$1 - \Delta t \gamma_{i,j,k} \geq 0 \tag{84}$$

The equation can be rearranged to set the instability criteria for the time step,  $\Delta t$ , as

$$\Delta t \leq \frac{1}{\gamma_{i,j,k}} \tag{85}$$

As long as the solution time step is less than the inverse of the sum of the spatial difference weighted thermal diffusivity terms then the solutions would be stable.

### 5.1.1.3 Surface Boundary Condition

The streambed surface boundary condition consists of heat fluxes from the water, solar radiation striking the water-streambed interface and heat transfer in the streambed. The general equation for the surface boundary condition can be written as

$$h \frac{\partial T}{\partial z} \Big|_{z=0} - \beta \frac{\partial T}{\partial z} \Big|_{z=0} = \frac{\varphi_{at}}{\rho_s c_{ps}} - D_z \frac{\partial T}{\partial z} \Big|_{z=0} \quad (86)$$

where  $h$  (W/m<sup>2</sup>C) is the heat convection coefficient,  $\varphi_{at}$  (W/m<sup>2</sup>) is the solar radiation attenuated through the water column,  $\rho_s$  is the density of the streambed material,  $c_{ps}$  is the specific heat of the streambed material and  $D_z$  is the thermal diffusivity of water. In Equation (86) the first term is the heat flux due to water convection in the streambed, the second term is the heat flux in the streambed due to conduction, the third term is the heat flux from the solar radiation penetrating the water column, and the fourth term is the heat conduction from the water in contact with the streambed. The model developed assumed there was no heat convection from bulk water flowing through the streambed. This assumption resulted in modifying Equation (86) as

$$- \beta \frac{\partial T}{\partial z} \Big|_{z=0} = \frac{\varphi_{at}}{\rho_s c_p} - D_z \frac{\partial T}{\partial z} \Big|_{z=0} \quad (87)$$

The partial differential equation was converted to an explicit finite difference numerical scheme as

$$\frac{2\beta}{\Delta z} (T_{int} - T_{i,j,k}) = \frac{\varphi_{at}}{\rho_s c_{ps}} + \frac{D_z}{\delta_w} (T_w - T_{int}) \quad (88)$$

where  $T_w$  ( $^{\circ}\text{C}$ ) is the bulk water temperature,  $T_{\text{int}}$  ( $^{\circ}\text{C}$ ) is the water-streambed interface temperature,  $\Delta z_{i,j,k}$  (m) is the vertical grid spacing at location at  $i, j, k$ , and  $\delta_w$  (m) is the thermal laminar layer where the water temperature above the streambed is equal to the bulk water temperature,  $T_w$ . Figure 97 shows a schematic of the surface boundary condition and the numerical scheme in the  $z$  direction.

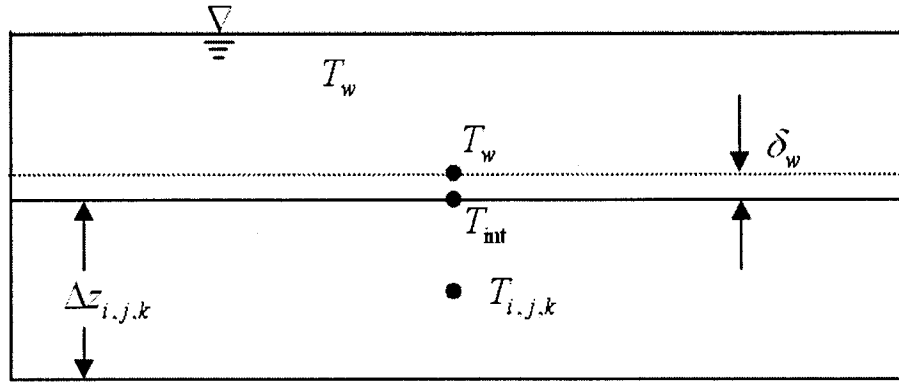


Figure 97: Surface Boundary Condition, Cartesian and cylindrical coordinate systems.

Equation (88) was rearranged to calculate the water-streambed interface temperature,  $T_{\text{int}}$ , as

$$T_{\text{int}} = \frac{\frac{\varphi_{at}}{\rho_s c_{ps}} + \frac{D_z}{\delta_w} T_w + \frac{2\beta_{i,j,k}}{\Delta z_{i,j,k}} T_{i,j,k}}{\frac{2\beta_{i,j,k}}{\Delta z_{i,j,k}} + \frac{D_z}{\delta_w}} \quad (89)$$

The streambed temperature at the surface,  $T_{i,j,k}^{n+1}$ , was calculated using Equation (83)

where

$$T_{i,j,k-1}^n = T_{\text{int}} \quad (90)$$

and the backward difference weighting of the thermal diffusivity was calculated differently for the boundary condition as

$$\gamma_{i,j,k-1} = \frac{2\beta_{i,j,k}}{\Delta z_{i,j,k}^2} \quad (91)$$

Substituting Equations (90) and (91) into Equation (83) yields:

$$T_{i,j,k}^{n+1} = \Gamma + \Delta t \gamma_{i,j,k-1} \left( \frac{\frac{\varphi}{\rho_s c_{ps}} + \frac{D_z}{\delta_w} T_w + \frac{2\beta_{i,j,k}}{\Delta z_{i,j,k}} T_{i,j,k}}{\frac{2\beta_{i,j,k}}{\Delta z_{i,j,k}} + \frac{D_z}{\delta_w}} \right) + (1 - \Delta t \gamma_{i,j,k}) T_{i,j,k}^n \quad (92)$$

where  $\Gamma$  is a sum of the spatial terms in the streambed:

$$\begin{aligned} \Gamma = & \Delta t \gamma_{i+1,j,k} T_{i+1,j,k}^n + \Delta t \gamma_{i-1,j,k} T_{i-1,j,k}^n + \\ & \Delta t \gamma_{i,j+1,k} T_{i,j+1,k}^n + \Delta t \gamma_{i,j-1,k} T_{i,j-1,k}^n + \Delta t \gamma_{i,j,k+1} T_{i,j,k+1}^n \end{aligned} \quad (93)$$

#### 5.1.1.4 Surface Boundary Condition Stability Criteria

The model formulation consisted of using an explicit finite central difference scheme. In order to ensure the solution is stable, a stability criterion must be satisfied at the surface boundary. The surface boundary condition stability criteria is a function of the sum of the spatial difference weighted thermal diffusivity terms,  $\gamma_{i,j,k}$ , the spatial difference weighted thermal diffusivity term at the surface,  $\gamma_{i,j,k-1}$ , and the surface boundary conditions. The surface boundary condition stability criteria for the time step,  $\Delta t$ , was developed from Equation (92) as

$$\Delta t \leq \frac{1}{\gamma_{i,j,k} - \left( \frac{\gamma_{i,j,k-1}}{1 + \frac{\Delta z_{i,j,k} D_z}{2\beta_{i,j,k} \delta_w}} \right)} \quad (94)$$

As long as the numerical time step is less than the inverse of the sum of the spatial difference weighted thermal diffusivity terms minus the influence of the surface boundary condition fluxes, then the solutions would be stable. The criterion on the time step is more stringent than the internal stability criteria.

#### 5.1.1.5 Bottom Boundary Condition

The bottom boundary condition for the streambed model grid was established by a constant surface temperature as

$$T(x, y, L, t) = T_b \quad (95)$$

where  $L$  (m) is the maximum depth of the streambed model grid, and  $T_b$  is the bottom surface boundary condition temperature, and estimated using the annual mean air temperature. Table 43 lists the annual mean air temperature in the Lower Bull Run River from 1999 to 2004.

**Table 43: Annual mean air temperature in the Lower Bull Run River**

Year	Annual mean Air Temp., C	Year	Annual mean Air Temp., C
1999	10.33	2002	10.33
2000	10.39	2003	10.86
2001	10.65	2004	11.42

### 5.1.1.6 Side Boundary Conditions

The side boundary conditions for the streambed model grid were established using the same method as the bottom boundary condition by a constant surface temperature as

$$T(x,0,z,t) = T_b, \quad T(x,W,z,t) = T_b \quad (96)$$

where 0 and  $W$  (m) are the starting and ending distances of the streambed model grid in the lateral direction, and  $T_b$  ( $^{\circ}\text{C}$ ) is the annual mean air temperature.

### 5.1.2 Cylindrical Model

The streambed heating algorithm was developed as a three dimensional model in cylindrical coordinate system to calibrate with the lab experiment data.

#### 5.1.2.1 Governing Equation

The three dimensional partial differential equation for heat transfer in the cylindrical coordinates (Incropera and De Witt, 1990) is

$$\frac{\partial T}{\partial t} = \frac{1}{r} \frac{\partial}{\partial r} \left( r \beta_r \frac{\partial T}{\partial r} \right) + \frac{1}{r^2} \frac{\partial}{\partial \phi} \left( \beta_\phi \frac{\partial T}{\partial \phi} \right) + \frac{\partial}{\partial z} \left( \beta_z \frac{\partial T}{\partial z} \right) \quad (97)$$

where  $T$  ( $^{\circ}\text{C}$ ) is the streambed temperature,  $t$  (seconds) is time, and  $\beta_r, \beta_\phi, \beta_z$  ( $\text{m}^2/\text{s}$ ) are the streambed thermal diffusivity coefficients in the  $r$ ,  $\phi$ , and  $z$  directions and may vary in space. The partial differential equation was converted to an explicit finite central difference numerical scheme for solving. Figure 98 shows a schematic of a

numerical grid cell in the cylindrical coordinate system. In the numerical solution scheme in  $r$  is the radial direction,  $\Delta r$  is the radial grid spacing, and  $i$  enumerates the numerical grid location radially. Similarly,  $j$  and  $k$  are used to enumerate the grid location in the angular,  $\phi$ , and  $z$  directions, respectively.

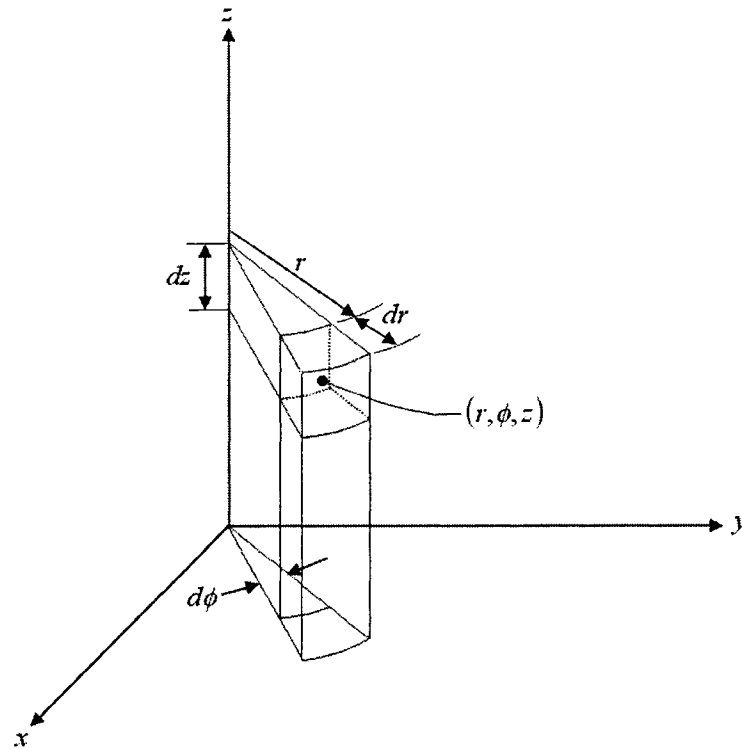


Figure 98: Cylindrical Coordinates

The finite difference approach resulted in a series of coefficients representing the distance weighted averages of the thermal diffusivity and their spatial rate of change. Given the location  $i$  in the  $r$  direction, the forward difference weighting of the thermal diffusivity,  $\sigma_{i+1,j,k}$  (1/seconds), was expressed as

$$\sigma_{i+1,j,k} = \left( \frac{r_i + \frac{\Delta r_i}{2}}{r_i \Delta r_i} \right) \left( \frac{\beta_{i+1,j,k} \left( \frac{\Delta r_{i+1,j,k}}{2} \right) + \beta_{i,j,k} \left( \frac{\Delta r_{i,j,k}}{2} \right)}{\left( \frac{\Delta r_{i+1,j,k}}{2} + \frac{\Delta r_{i,j,k}}{2} \right)^2} \right) \quad (98)$$

In the angular direction the forward difference weighting of the thermal diffusivity,

$\sigma_{i,j+1,k}$  (1/seconds) was expressed as

$$\sigma_{i,j+1,k} = \left( \frac{\beta_{i,j+1,k} \left( \frac{\Delta \phi_{i,j+1,k}}{2} \right) + \beta_{i,j,k} \left( \frac{\Delta \phi_{i,j,k}}{2} \right)}{r_{i,j,k}^2 \Delta \phi_{i,j,k} \left( \frac{\Delta \phi_{i,j+1,k}}{2} + \frac{\Delta \phi_{i,j,k}}{2} \right)^2} \right) \quad (99)$$

and in the  $z$  direction the forward difference weighting of the thermal diffusivity,

$\sigma_{i,j,k+1}$  (1/seconds) was expressed as

$$\sigma_{i,j,k+1} = \frac{\beta_{i,j,k+1} \left( \frac{\Delta z_{i,j,k+1}}{2} \right) + \beta_{i,j,k} \left( \frac{\Delta z_{i,j,k}}{2} \right)}{\Delta z_{i,j,k} \left( \frac{\Delta z_{i,j,k+1}}{2} + \frac{\Delta z_{i,j,k}}{2} \right)^2} \quad (100)$$

When considering the backward difference weighting for the three directions the six spatial difference weighted thermal diffusivity terms were summed,  $\sigma_{i,j,k}$  (1/seconds), as

$$\sigma_{i,j,k} = \sigma_{i+1,j,k} + \sigma_{i-1,j,k} + \sigma_{i,j+1,k} + \sigma_{i,j-1,k} + \sigma_{i,j,k+1} + \sigma_{i,j,k-1} \quad (101)$$

Given the present time as  $n$ , the streambed temperature at location  $i, j, k$  in the cylindrical coordinate system was solved for the next time step,  $n+1$  ( $t + \Delta t$ ), with the equation:

$$\begin{aligned}
T_{i,j,k}^{n+1} = & \Delta t \sigma_{i+1,j,k} T_{i+1,j,k}^n + \Delta t \sigma_{i-1,j,k} T_{i-1,j,k}^n + \Delta t \sigma_{i,j+1,k} T_{i,j+1,k}^n + \\
& \Delta t \sigma_{i,j-1,k} T_{i,j-1,k}^n + \Delta t \sigma_{i,j,k+1} T_{i,j,k+1}^n + \Delta t \sigma_{i,j,k-1} T_{i,j,k-1}^n \\
& + (1 - \Delta t \sigma_{i,j,k}) T_{i,j,k}^n
\end{aligned} \tag{102}$$

using the present temperature in the streambed grid at  $i$ ,  $j$ ,  $k$  and the surrounding grid cells. The application of Equation (102) consisted of solving the equation for all grid cells for the first time step using the initial conditions and the incrementing to the next time step and resolving for all the grid cells.

### 5.1.2.2 Internal Stability Criteria

The model formulation consisted of using an explicit finite central difference scheme. In order to ensure the solution is stable, a stability criterion must be satisfied. In the internal stability criteria is a function of the sum of the spatial difference weighted thermal diffusivity terms,  $\sigma_{i,j,k}$ , and was developed as

$$1 - \Delta t \sigma_{i,j,k} \geq 0 \tag{103}$$

The equation can be rearranged to set the instability criteria for the time step,  $\Delta t$ , as

$$\Delta t \leq \frac{1}{\sigma_{i,j,k}} \tag{104}$$

As long as the solution time step is less than the inverse of the sum of the spatial difference weighted thermal diffusivity terms, then the solution would be stable.

### 5.1.2.3 Surface Boundary Condition

The streambed surface boundary condition consists of heat fluxes from the water, solar radiation striking the water-streambed interface and heat transfer in the streambed. The solution approach for the surface boundary condition in cylindrical coordinates was the same as done in the Cartesian coordinates, as shown in Equations (86) through (90) and in Figure 97. The backward difference weighting of the thermal diffusivity was calculated differently for the boundary condition as

$$\sigma_{i,j,k-1} = \frac{2\beta_{i,j,k}}{\Delta z_{i,j,k}^2} \quad (105)$$

Substituting Equations (90) and (105) into Equation (102) yields:

$$T_{i,j,k}^{n+1} = \Omega + \Delta t \sigma_{i,j,k-1} \left( \frac{\frac{\varphi_{at}}{\rho_s c_{ps}} + \frac{D_z}{\delta_w} T_w + \frac{2\beta_{i,j,k}}{\Delta z_{i,j,k}} T_{i,j,k}}{\frac{2\beta_{i,j,k}}{\Delta z_{i,j,k}} + \frac{D_z}{\delta_w}} \right) + (1 - \Delta t \sigma_{i,j,k}) T_{i,j}^n \quad (106)$$

where  $\Omega$  is a sum of the spatial terms in the streambed:

$$\begin{aligned} \Omega = & \Delta t \sigma_{i+1,j,k} T_{i+1,j,k}^n + \Delta t \sigma_{i-1,j,k} T_{i-1,j,k}^n + \\ & \Delta t \sigma_{i,j+1,k} T_{i,j+1,k}^n + \Delta t \sigma_{i,j-1,k} T_{i,j-1,k}^n + \Delta t \sigma_{i,j,k+1} T_{i,j,k+1}^n \end{aligned} \quad (107)$$

### 5.1.2.4 Surface Boundary Condition Stability Criteria

The explicit finite central difference model formulation required a stability criteria be satisfied at the surface boundary in order to ensure the solution is stable.

Similar to the Cartesian coordinate system solution the surface boundary condition stability criteria is a function of the sum of the spatial difference weighted thermal diffusivity terms,  $\sigma_{i,j,k}$ , the backward difference weighted thermal diffusivity term at the surface,  $\sigma_{i,j,k-1}$ , and the surface boundary conditions. The stability criteria for the time step,  $\Delta t$ , was developed from Equation (106) as

$$\Delta t \leq \frac{1}{\sigma_{i,j,k} - \left( \frac{\sigma_{i,j,k-1}}{1 + \frac{\Delta z_{i,j,k} D_z}{2\beta_{i,j,k} \delta_w}} \right)} \quad (108)$$

As long as the time step is less than the inverse of the sum of the spatial difference weighted thermal diffusivity terms minus the influence of the surface boundary condition fluxes, then the solution would be stable.

### 5.1.2.5 Bottom Boundary Condition

The bottom boundary condition for the streambed model grid was established by a constant surface temperature as

$$T(r, \phi, L, t) = T_b \quad (109)$$

where  $L$  (m) is the maximum depth of the model grid and  $T_b$  is the bottom surface boundary condition temperature. For the lab experiments conducted the bottom boundary condition was monitored with a thermistor.

### 5.1.2.6 Side Boundary Conditions

The side boundary condition for the model grid was established using a constant surface temperature for the outside edge of the cylinder as

$$T(R, \phi, z, t) = T_{b2} \quad (110)$$

where  $R$  (m) is the maximum radius of the model grid and  $T_{b2}$  is the side surface boundary condition temperature. For the lab experiments the side surface boundary conditions were monitored with two thermistors.

## 5.2 Calibration

The Cartesian and cylindrical coordinate system models were calibrated separately using field and lab data respectively.

### 5.2.1 Cartesian Model

The water temperature and solar radiation striking the streambed were monitored in the field and used as input to the model.

The Cartesian model was calibrated to the two substrate types (bedrock and cobble) by adjusting the thermal diffusivity coefficient of the streambed at various depths. The thermal diffusivity coefficients initially used in the model were from Table 23 and Appendix C where a more complete listing of thermophysical properties is provided. The solar radiation striking the streambed surface was calculated by

attenuating the incident solar radiation on the water surface (66% based on field data) and reducing it by the solar radiation reflecting off the streambed (2% based on field data). The bottom boundary condition was set at 20 m below the water-streambed interface.

There were two sites where the bedrock was monitored, one on the south side of the river in the shade, Probe 4 site, and the other on north side of the river in the sun, Probe 5 site. Refer to Figure 23 for the monitoring site locations.

There were three sites where the cobble reach of the Lower Bull Run river was monitored all near the south side of the river closer to the center of the channel with full solar exposure. Figure 23 provides a map of the monitoring sites.

#### **5.2.1.1 Bedrock Substrate, Probe 4**

The Probe 4 temperature data were recorded from September 5<sup>th</sup> to 20<sup>th</sup>, 2002 in the bedrock reach of the Lower Bull Run River. As discussed in Section 3.3 above and in Appendix D the data collected at depths of 0.0, 0.2 and 0.6 m were found to be erroneous and were therefore not compared to model output.

The model calibration consisted of adjusting the thermal diffusivity coefficient vertically for the side of the river near the probe and reducing the amount of effective solar radiation striking the streambed. The thermal diffusivity coefficient,  $\beta$ , was set at  $1.044\text{E-}6 \text{ m}^2/\text{s}$  for depths 0.0 to 0.8 m and  $6.593\text{E-}7 \text{ m}^2/\text{s}$  for depths of 0.8 to 20 m. This represents a decrease of 5% and 40% from the thermal diffusivity of granite ( $1.099\text{E-}6 \text{ m}^2/\text{s}$ ), respectively. The density and specific heat of the streambed were

kept at values representative of granite. The south side of the river was in heavy shade throughout the day so the incident solar radiation was reduced by 70% during the calibration period.

Table 44 shows the model-data error statistics for the streambed temperatures at three depths from Probe 4. Figure 99 and Figure 100 show time series comparisons of data and model results for the three depths over a two week period. The model-data error statistics and figures show there is close agreement between the data and the model streambed temperature predictions.

**Table 44: Model-data streambed temperature error statistics for Probe 4**

Depth, m	Number of Comparisons	ME <sup>1</sup> , °C	AME <sup>1</sup> , °C	RMS <sup>1</sup> , °C
0.40	1,231	0.05	0.09	0.10
0.80	2,155	-0.14	0.15	0.17
1.00	2,155	0.01	0.08	0.12

<sup>1</sup>ME = Mean Error; AME = Absolute Mean Error; RMS = Root Mean Square Error.

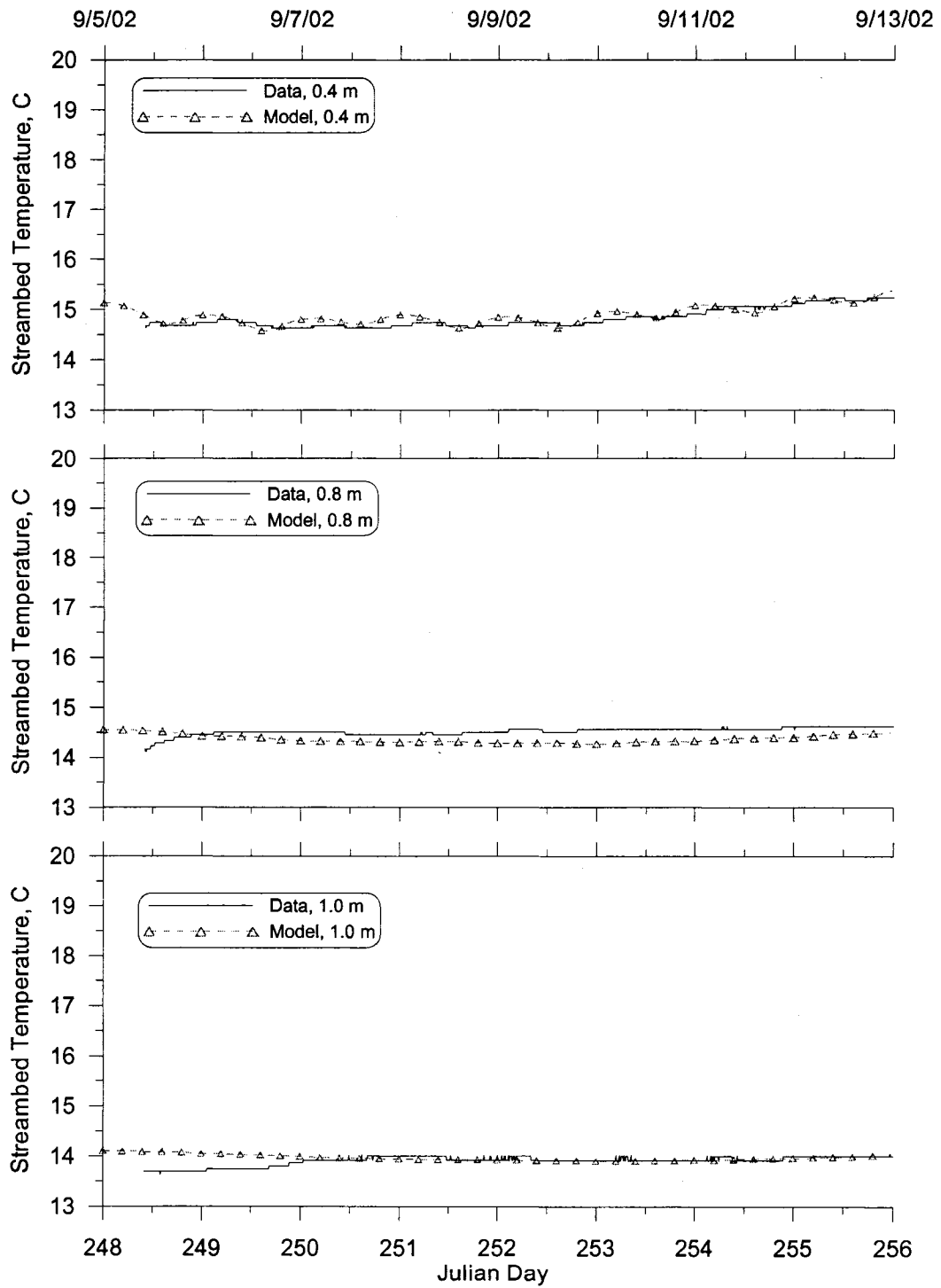


Figure 99: Model-data bedrock streambed temperature comparison, Probe 4, September 5<sup>th</sup> to 13<sup>th</sup>, 2002.

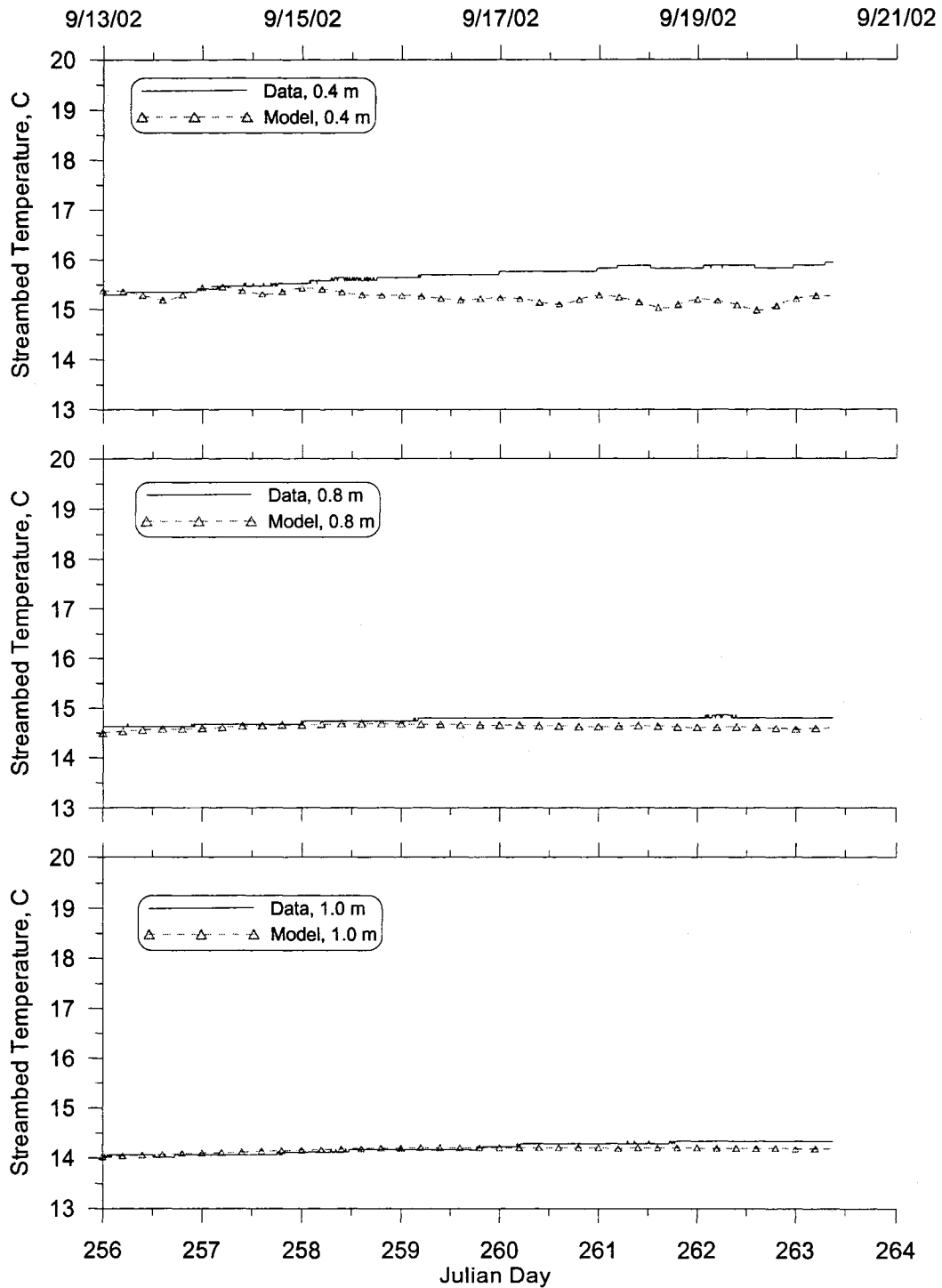


Figure 100: Model-data bedrock streambed temperature comparison, Probe 4, September 13<sup>th</sup> to 21<sup>st</sup>, 2002.

### 5.2.1.2 Bedrock Substrate, Probe 5

The Probe 5 temperature data was recorded from September 5<sup>th</sup> to 20<sup>th</sup>, 2002 in the bedrock reach of the Lower Bull Run River. As discussed in Section 3.3 above and in Appendix D the data collected at depths of 0.6 m were found to be erroneous and were therefore not compared to model output.

The model calibration consisted of adjusting the thermal diffusivity coefficient vertically for the side of the river near the probe. The thermal diffusivity coefficient,  $\beta$ , was set at 1.044E-6 m<sup>2</sup>/s for depths 0.0 to 0.9 m and 6.242E-7 m<sup>2</sup>/s for depths of 0.9 to 20 m. This represents a decrease of 5% and 25% from the thermal diffusivity of granite (1.099E-6 m<sup>2</sup>/s), respectively. The density and specific heat of the streambed were kept at values representative of granite. The north side of the river had no shade and therefore was kept at 100% solar. Table 45 shows the model-data error statistics for the streambed temperatures at three depths from Probe 5. Figure 101 through Figure 104 show time series comparisons of data and model results for the five depths over a two week period. The model-data error statistics and figures show there is close agreement between the data and the model streambed temperature predictions.

**Table 45: Model-data streambed temperature error statistics for Probe 5.**

Depth, m	Number of Comparisons	ME <sup>1</sup> , °C	AME <sup>1</sup> , °C	RMS <sup>1</sup> , °C
0.00	2151	-0.10	0.19	0.31
0.20	2151	-0.06	0.10	0.13
0.40	2151	-0.10	0.11	0.13
0.80	2151	0.18	0.18	0.19
1.00	2151	0.03	0.05	0.07

<sup>1</sup> ME = Mean Error; AME = Absolute Mean Error; RMS = Root Mean Square Error.

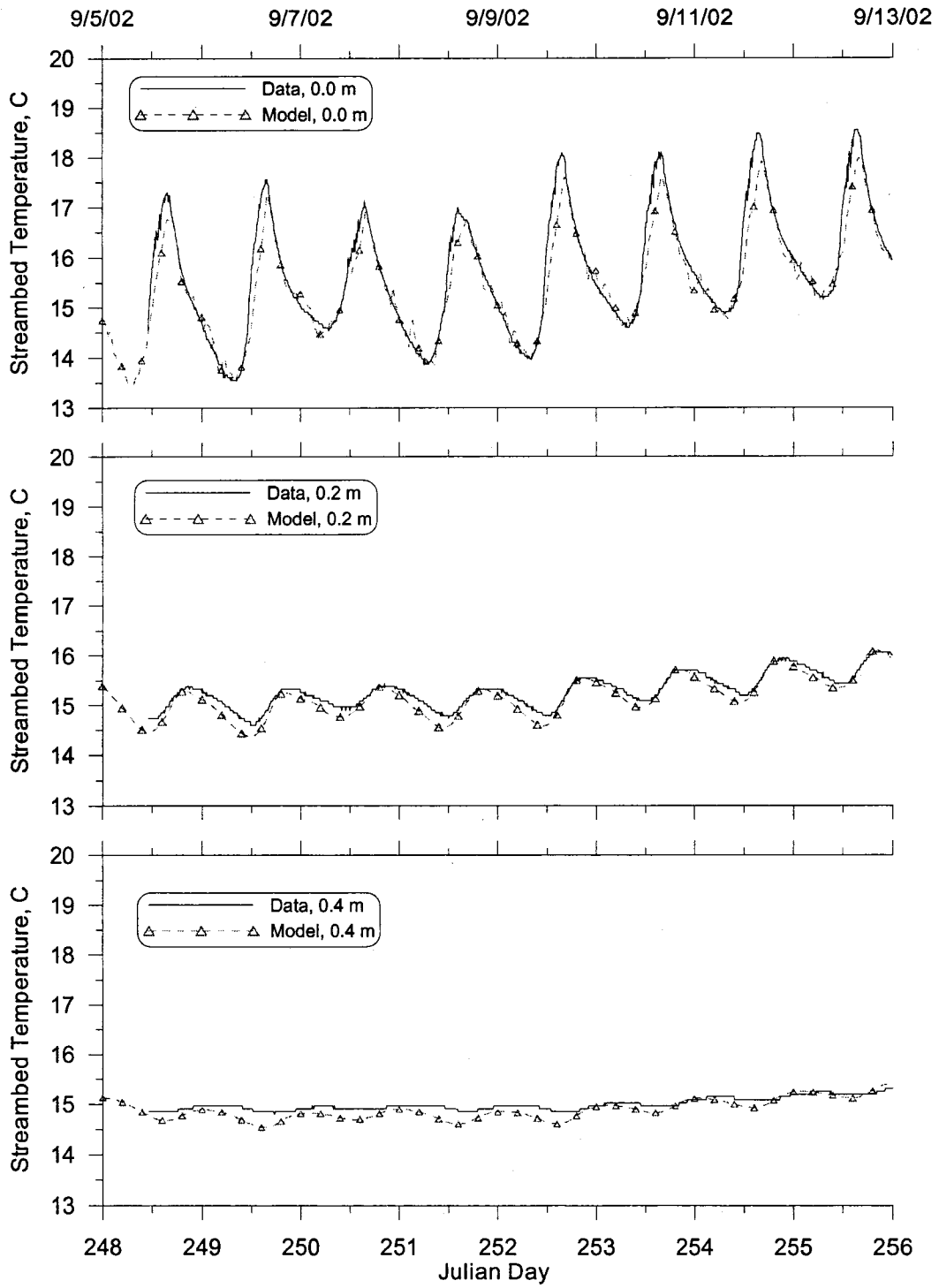


Figure 101: Model-data bedrock streambed temperature comparison, Probe 5, September 5<sup>th</sup> to 13<sup>th</sup>, 2002, depths 0 to 0.4 m.

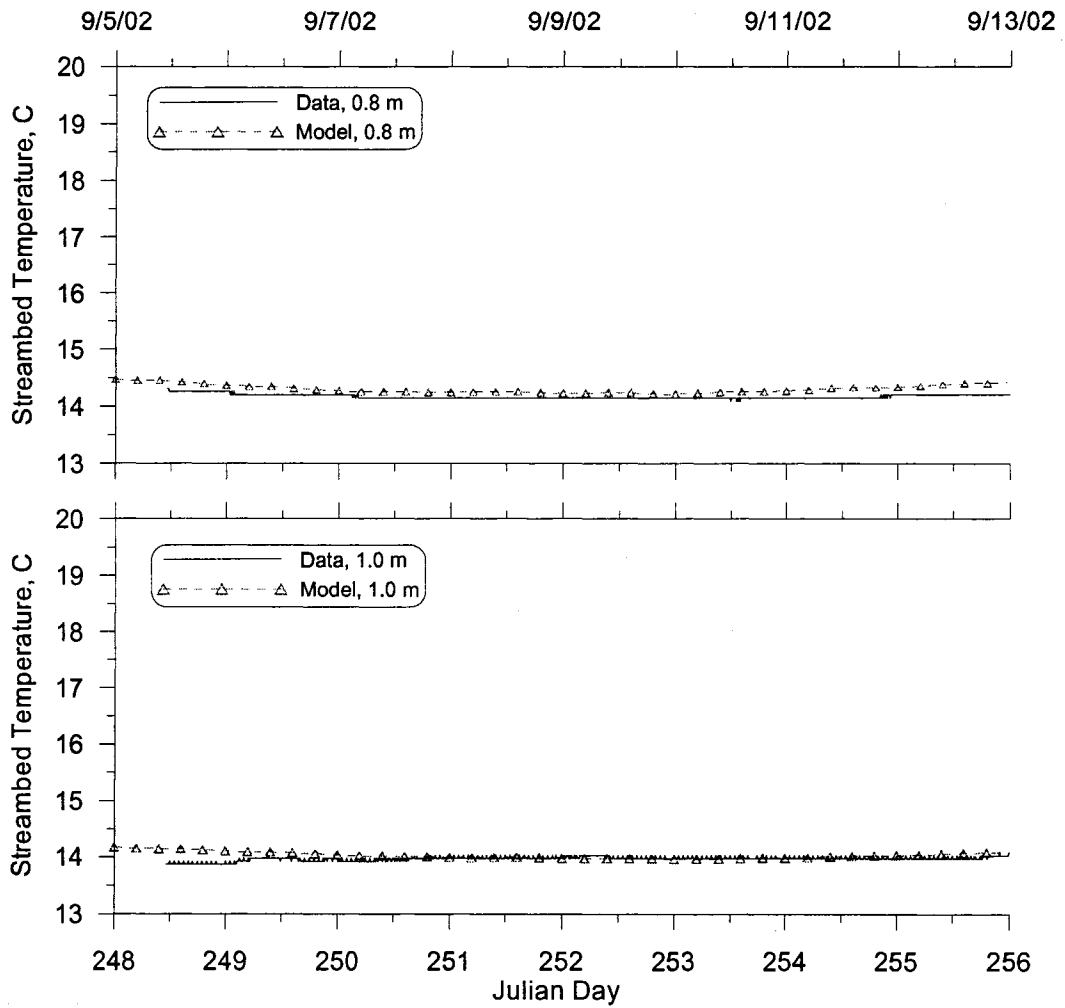


Figure 102: Model-data bedrock streambed temperature comparison, Probe 5, September 5<sup>th</sup> to 13<sup>th</sup>, 2002, depths 0.4 to 1.0 m.

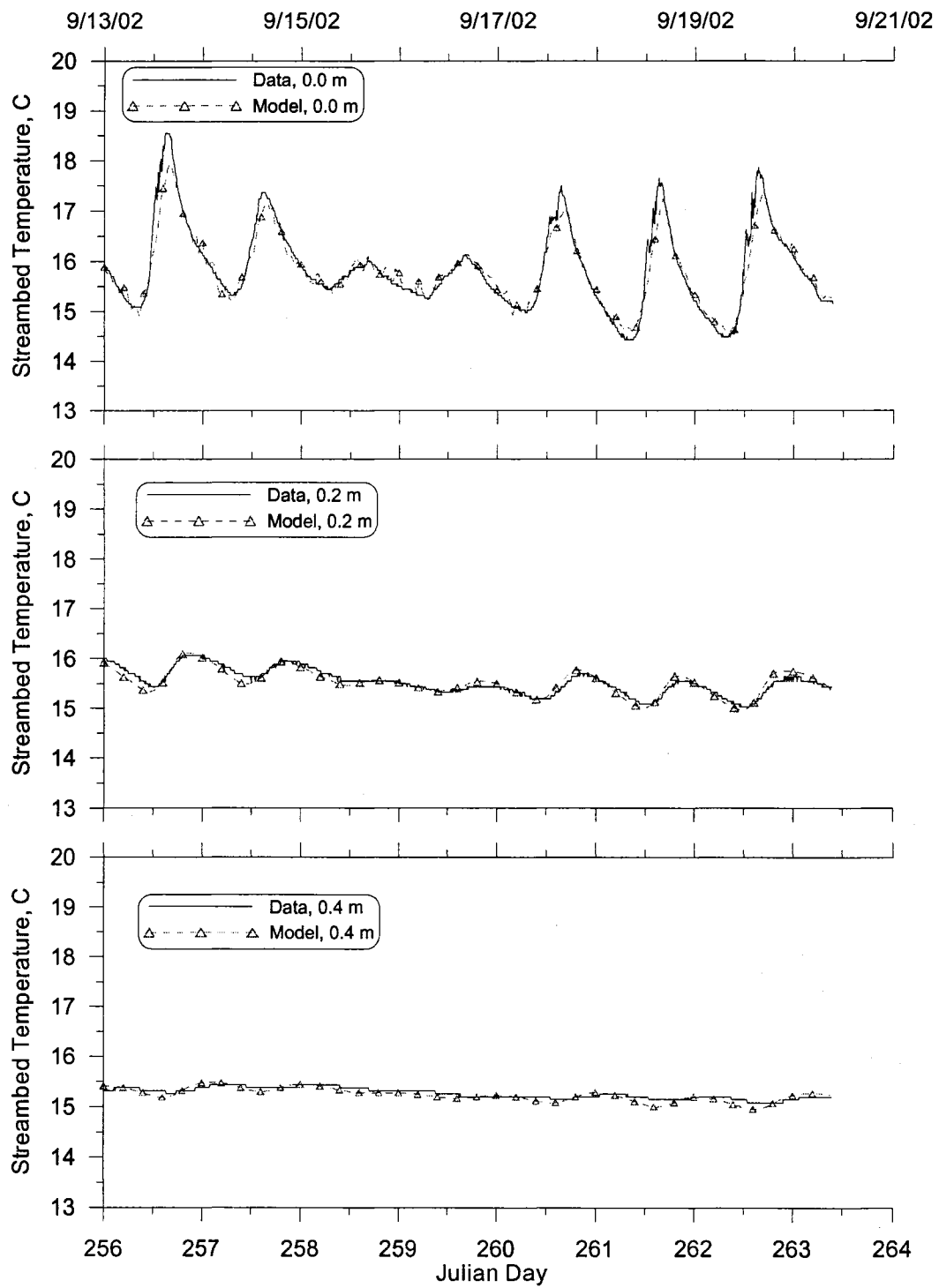


Figure 103: Model-data bedrock streambed temperature comparison, Probe 5, September 13<sup>th</sup> to 21<sup>st</sup> 2002, depths 0 to 0.4 m.

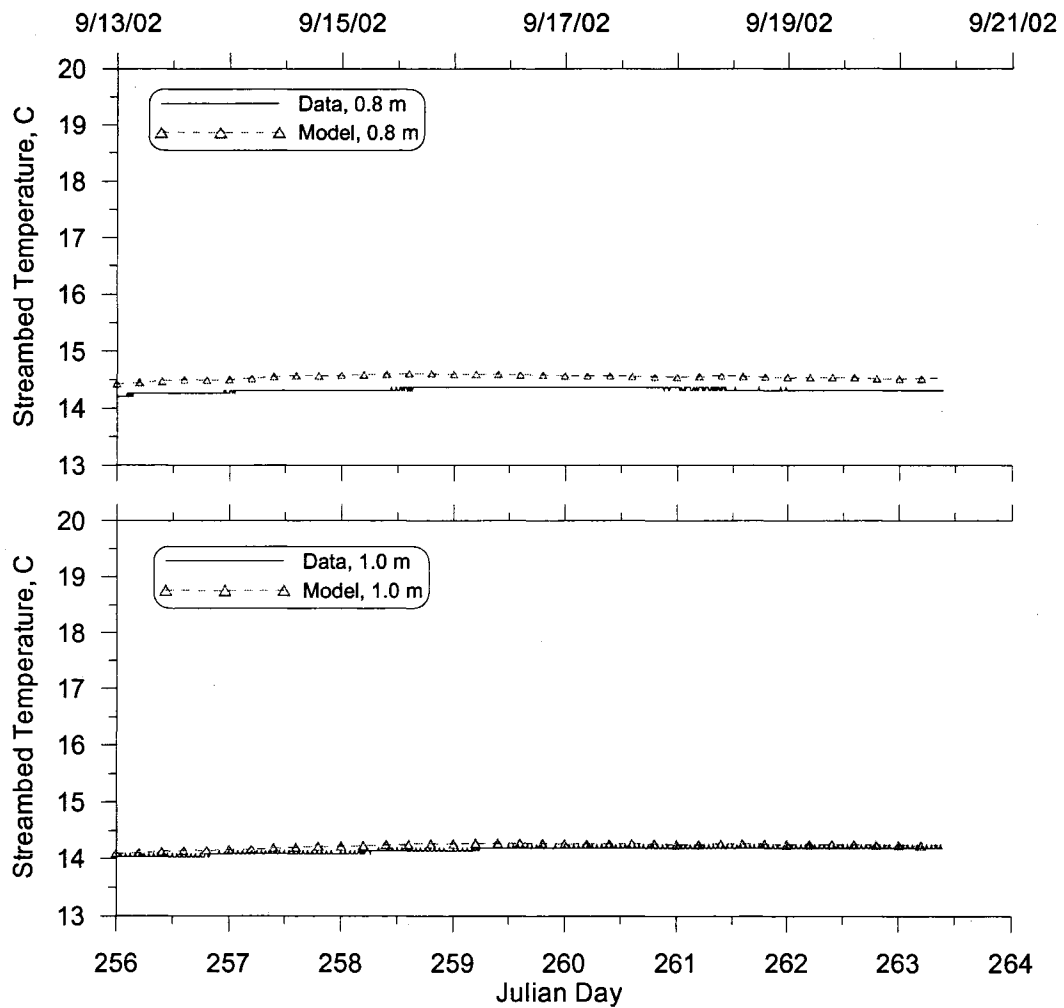


Figure 104: Model-data bedrock streambed temperature comparison, Probe 5, September 13<sup>th</sup> to 21<sup>st</sup> 2002, depths 0.4 to 1.0 m.

### 5.2.1.3 Cobble Substrate, Probe 1

The Probe 1 temperature data were recorded from August 7<sup>th</sup> to September 5<sup>th</sup>, 2002 in the cobble reach of the Lower Bull Run River with a data gap from August 23<sup>rd</sup> to August 30<sup>th</sup>, 2002.

The model calibration consisted of adjusting the thermal diffusivity coefficient vertically. Since the cobble reach consisted of packed rocks, gravel and sand there

was the possibility that the streambed temperatures monitored would be affected by the substrate material and the interstitial water. Table 46 list the density, specific heat and thermal diffusivity of rock and water. The thermophysical characteristics of the rock and water were used in different proportions to characterize the streambed substrate over depth. Near the surface the model calibration required a larger fraction of water as part of the control volume than near the bottom of the model grid, which was dominated by rock. These fractions were adjusted until there was relatively good model data agreement. Table 47 lists the thermophysical characteristics used to calibrate the model. For example at a depth range of 0.0 to 0.23 m the density, specific heat, and thermal diffusivity used consisted of 75% rock and 25% water characteristics. Incorporating the thermophysical characteristics of water in the substrate characteristics was designed to allow the substrate thermal response to represent both the rock and gravel in the river and the influence of the interstitial water. At the deepest layers of the model grid the thermal diffusivity was increased from 5% to 20% above the rock thermal diffusivity value as listed in the last column of Table 47.

During the calibration process the model temperature predictions were found to have excessively dampened diurnal swings compared to the data. Figure 105 shows an example of the model temperature predictions using the calibration values from Table 47. The damped diurnal response from the model indicated that the interstitial water was contributing more to the substrate temperatures recorded at the various depths than currently accounted for by just the thermophysical properties. The

calculated diurnal temperature swing was increased by recalculating the streambed temperature using a fraction of water temperature. Table 48 lists the fraction of water temperature used to recalculate the streambed temperature. The table shows that for depths shallower than 0.52 m the streambed temperature was recalculated with 99.9% streambed temperature and 0.1% water temperature. The water temperature fraction used to recalculate the streambed temperature had a cumulative effect over time on the streambed temperature predictions so only a small fraction was necessary.

While it would have been ideal to collect additional data to identify the temperature of the cobble separate from the temperature of the interstitial water, this approach was reasonable at approximating the interstitial water temperature's impact. The fact that any fraction of water temperature was needed indicated that the cobble substrate temperature monitoring reflected the temperature of the interstitial water and that the interstitial water played a large role in predicting substrate temperatures.

Although the water fraction used was small the model-data comparisons figures (Figure 106 through Figure 108) illustrate it had a large influence on the model calibration.

**Table 46: Thermophysical characteristics of the cobble substrate and water**

Media	Density, $\rho_s$ , kg/m <sup>3</sup>	Specific Heat, $c_{ps}$ , kJ/kg°C	Thermal Diffusivity, $\beta$ , m <sup>2</sup> /s
Water	1000.0	4190.0	1.44E-07
Rock/Stone	2280.0	1471.0	1.18E-06

**Table 47: Thermophysical characteristics used to calibrate the streambed heating model in the cobble reach for the Probe 1 to 3 sites.**

Depth, m	Density, $\rho_s$ , kg/m <sup>3</sup>	Specific Heat, $c_{ps}$ , kJ/kg°C	Thermal Diffusivity, $\beta$ , m <sup>2</sup> /s	Fraction of Rock	Fraction of Water	Fraction increase in $\beta$
0.00 to 0.23	1960.0	2150.8	9.173E-07	75%	25%	0%
0.23 to 0.37	2088.0	1878.9	1.020E-06	85%	15%	0%
0.37 to 0.72	2280.0	1471.0	1.234E-06	100%	0%	5%
0.72 to 20.0	2280.0	1471.0	1.410E-06	100%	0%	20%

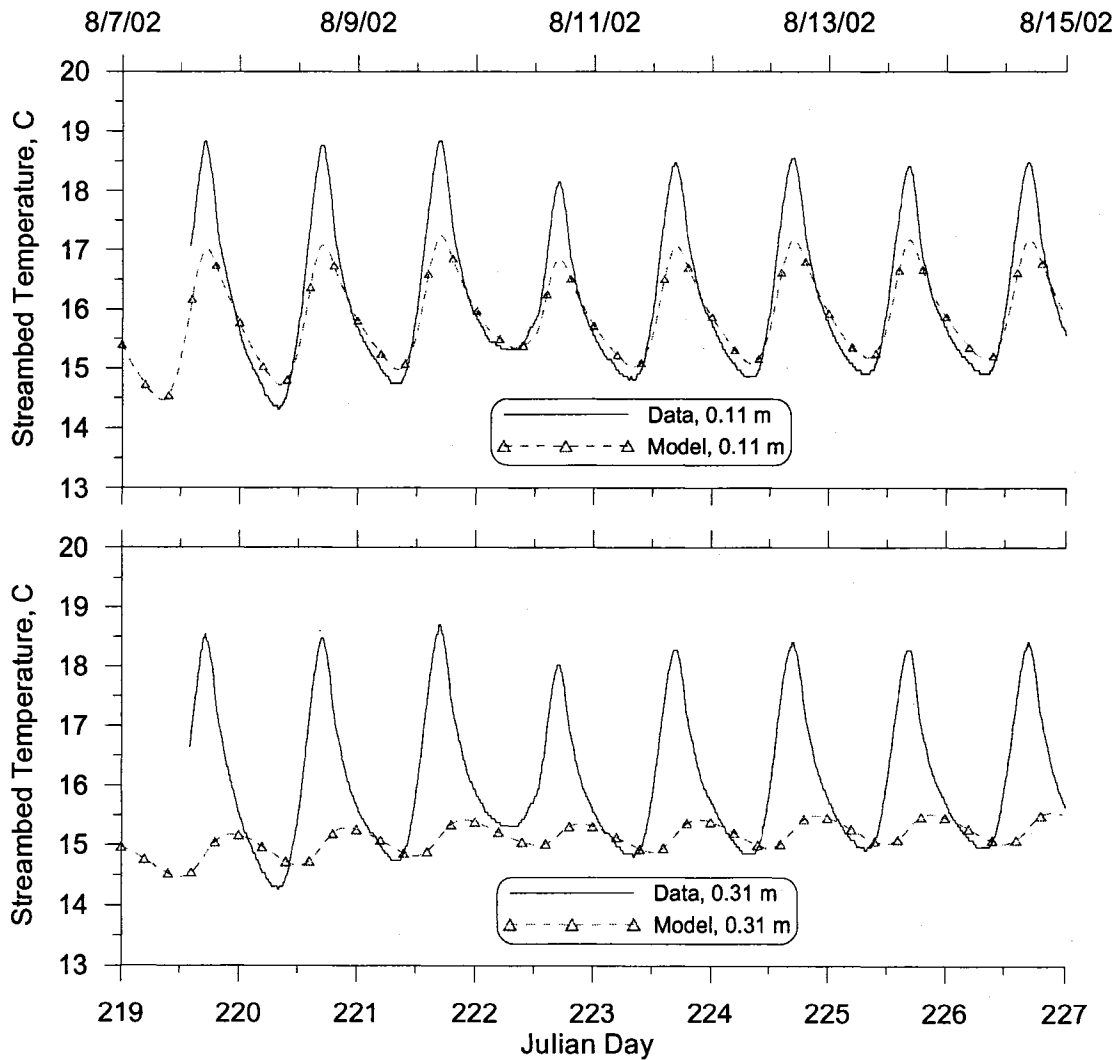


**Figure 105: Model-data cobble streambed temperature comparison, Probe 1 site, using only thermophysical properties of substrate.**

**Table 48: Fraction of water temperature used to calibrate the streambed temperature predictions at the Probe 1 and Probe 2 sites.**

Depth, m	Fraction of water temperature used
0.00 to 0.23	0.1%
0.23 to 0.37	0.1%
0.37 to 0.52	0.1%
0.52 to 0.87	0.0%
0.87 to 20.0	0.0%

Table 49 shows the model-data error statistics for the streambed temperatures at three depths at the Probe 1 site. Figure 106 through Figure 108 show time series comparisons of data and model results for these depths over three weeks. The model-data error statistics and figures show there is close agreement between the data and the model streambed temperature predictions.

**Table 49: Model-data streambed temperature error statistics for the Probe 1 site.**

Depth, m	Number of Comparisons	ME <sup>1</sup> , °C	AME <sup>1</sup> , °C	RMS <sup>1</sup> , °C
0.11	3128	0.23	0.23	0.25
0.31	3128	0.21	0.24	0.27
0.51	3128	0.04	0.14	0.18

<sup>1</sup>ME = Mean Error; AME = Absolute Mean Error; RMS = Root Mean Square Error.

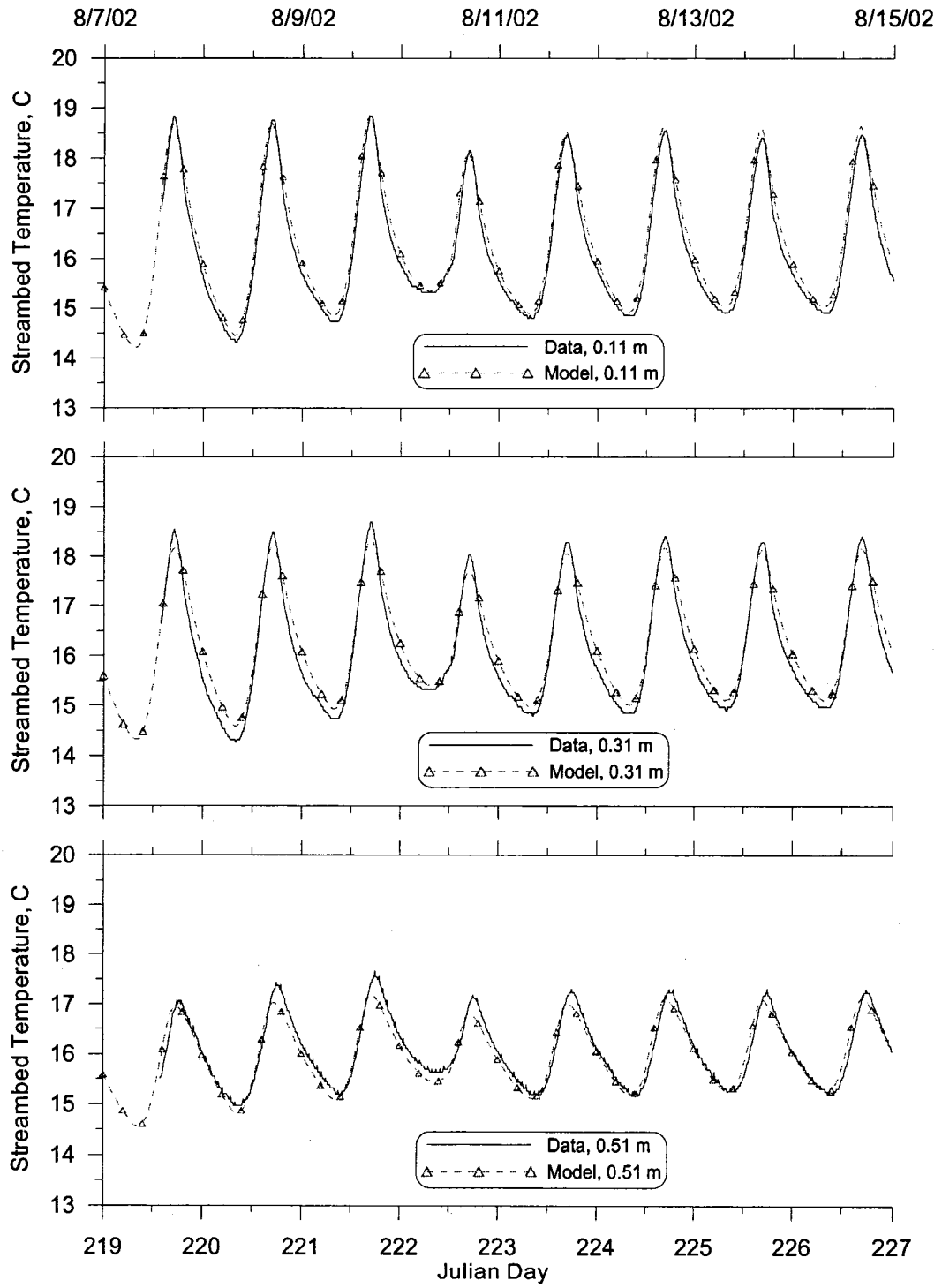


Figure 106: Model-data cobble streambed temperature comparison, Probe 1 site, August 7<sup>th</sup> to 15<sup>th</sup>, 2002.

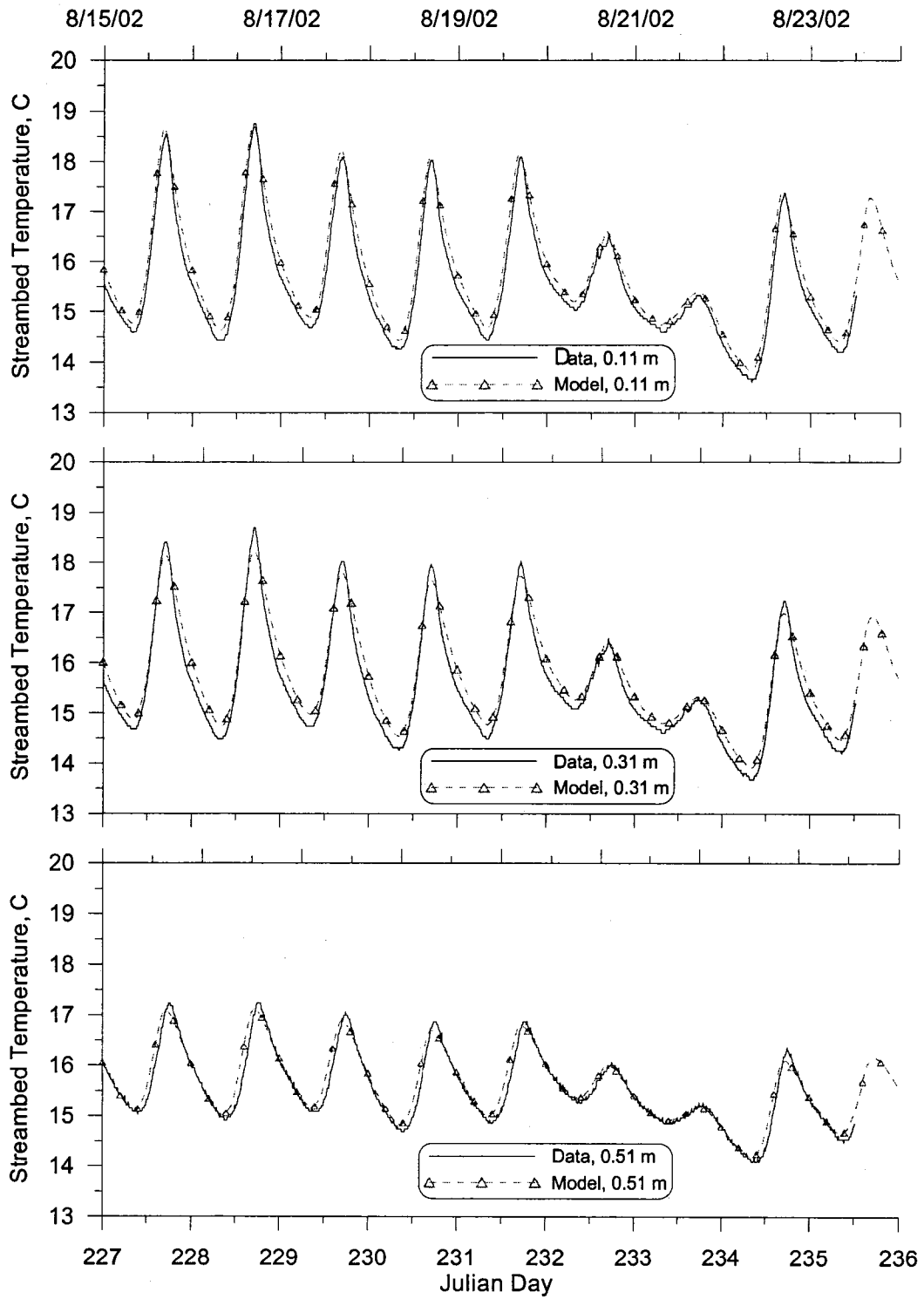


Figure 107: Model-data cobble streambed temperature comparison, Probe 1 site, August 15<sup>th</sup> to 24<sup>th</sup>, 2002.

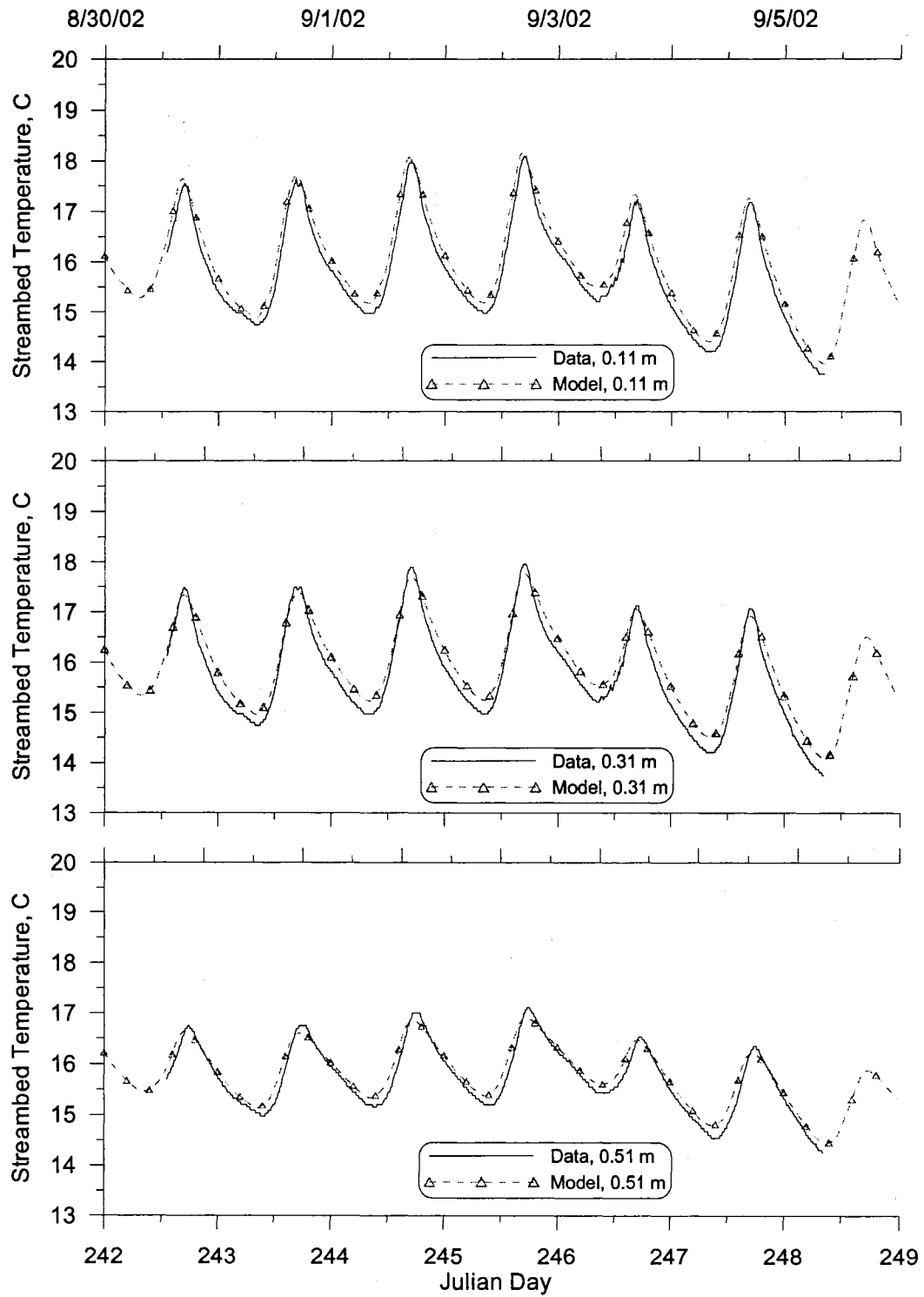


Figure 108: Model-data cobble streambed temperature comparison, Probe 1 site, August 30<sup>th</sup> to September 5<sup>th</sup>, 2002.

#### 5.2.1.4 Cobble Substrate, Probe 2

The Probe 2 temperature data were recorded from August 7<sup>th</sup> to August 23<sup>rd</sup>, 2002 in the cobble reach of the Lower Bull Run River.

The model calibration consisted of adjusting the thermal diffusivity coefficient vertically. The thermophysical properties of the streambed, listed in Table 47, and used to calibrate the model for the Probe 1 site were also used to calibrate the model to Probe 2 site data. The diurnal temperature predictions at the Probe 2 site were also excessively damped compared to data and required the water temperature to recalculate the streambed temperatures. Table 48 above lists the fraction of water temperature used to recalculate the streambed temperature for the Probe 1 site and were also used to calibrate the model to the Probe 2 site data.

Table 50 shows the model-data error statistics for the streambed temperatures at three depths at the Probe 2 site. Figure 109 and Figure 110 show time series comparisons of data and model results for the three depths over two weeks. The model-data error statistics and figures show there is close agreement between the data and the model streambed temperature predictions.

**Table 50: Model-data streambed temperature error statistics for the Probe 2 site.**

Depth, m	Number of Comparisons	ME <sup>1</sup> , °C	AME <sup>1</sup> , °C	RMS <sup>1</sup> , °C
0.07	2277	0.16	0.22	0.29
0.27	2277	0.23	0.28	0.33
0.47	2277	-0.23	0.37	0.51

<sup>1</sup>ME = Mean Error; AME = Absolute Mean Error; RMS = Root Mean Square Error.

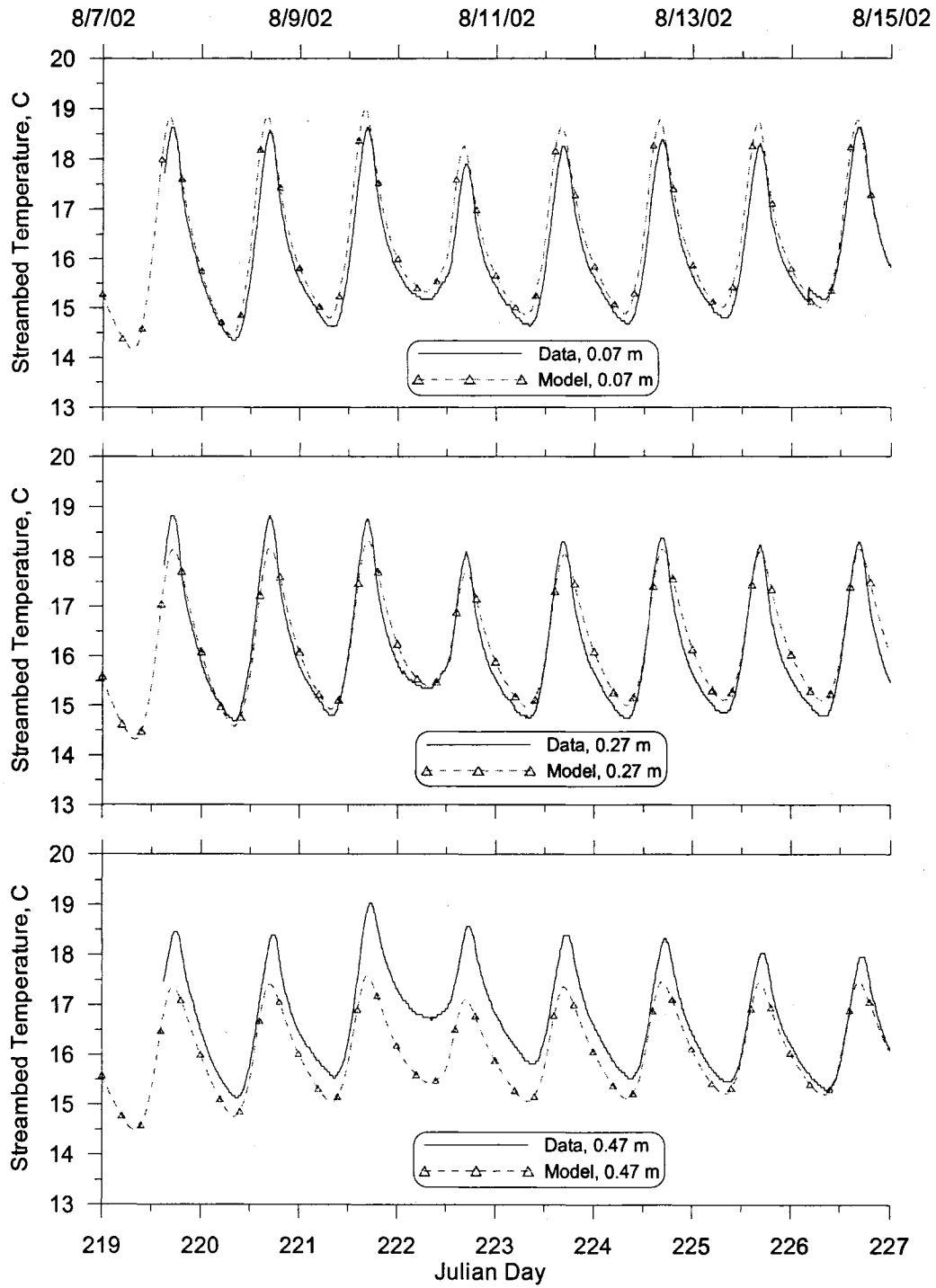


Figure 109: Model-data cobble streambed temperature comparison, Probe 2 site, August 7<sup>th</sup> to 15<sup>th</sup>, 2002.

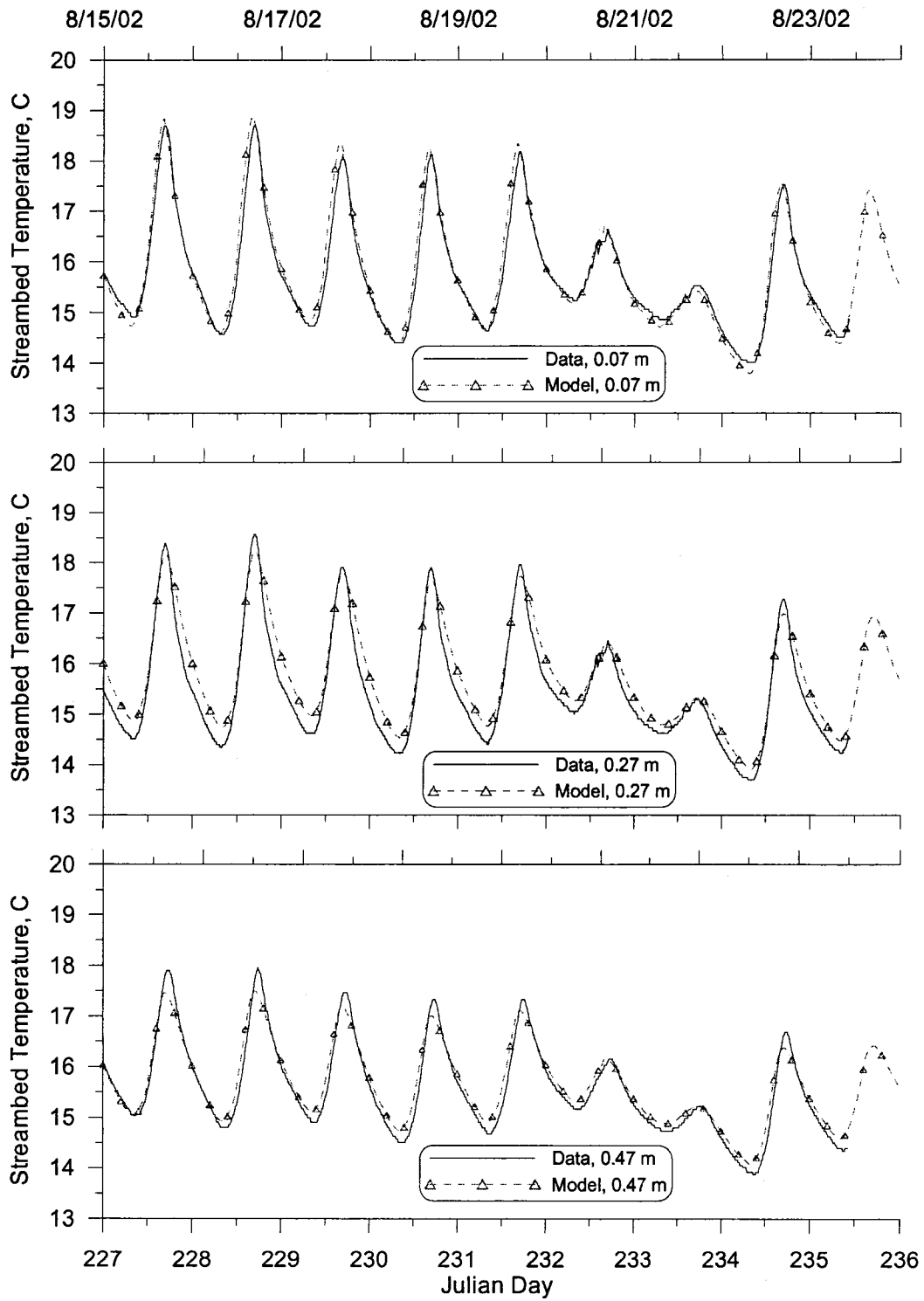


Figure 110: Model-data cobble streambed temperature comparison, Probe 2 site, August 15<sup>th</sup> to 24<sup>th</sup>, 2002.

### 5.2.1.5 Cobble Substrate, Probe 3

The Probe 3 temperature data were recorded from August 23<sup>rd</sup> to September 5<sup>th</sup>, 2002 in the cobble reach of the Lower Bull Run River.

The model calibration consisted of adjusting the thermal diffusivity coefficient vertically. The thermophysical properties of the streambed, listed in Table 47, and used to calibrate the model for the Probe 1 and Probe 2 sites were also used to calibrate the model to data from the Probe 3 site. The diurnal temperature predictions at the Probe 3 site were also excessively damped compared to data and required the water temperature to recalculate the streambed temperatures. Table 51 lists the fraction of water temperature used to recalculate the streambed temperature to calibrate the model to the Probe 3 site data.

Table 52 shows the model-data error statistics for the streambed temperatures at three depths at the Probe 3 site. Figure 111 and Figure 112 show time series comparisons of data and model results for the three depths over two weeks. The model-data error statistics and figures show there is close agreement between the data and the model streambed temperature predictions.

**Table 51: Fraction of water temperature used to calibrate the streambed temperature predictions at the Probe 3 site.**

Depth, m	Fraction of water temperature used
0.00 to 0.23	0.1%
0.23 to 0.37	0.1%
0.37 to 0.52	0.0%
0.52 to 0.87	0.0%
0.87 to 20.0	0.0%

**Table 52: Model-data streambed temperature error statistics for the Probe 3 site.**

Depth, m	Number of Comparisons	ME <sup>1</sup> , °C	AME <sup>1</sup> , °C	RMS <sup>1</sup> , °C
0.10	1842	0.19	0.19	0.22
0.30	1842	0.17	0.21	0.23
0.50	1842	0.35	0.38	0.40

<sup>1</sup>ME = Mean Error; AME = Absolute Mean Error; RMS = Root Mean Square Error.

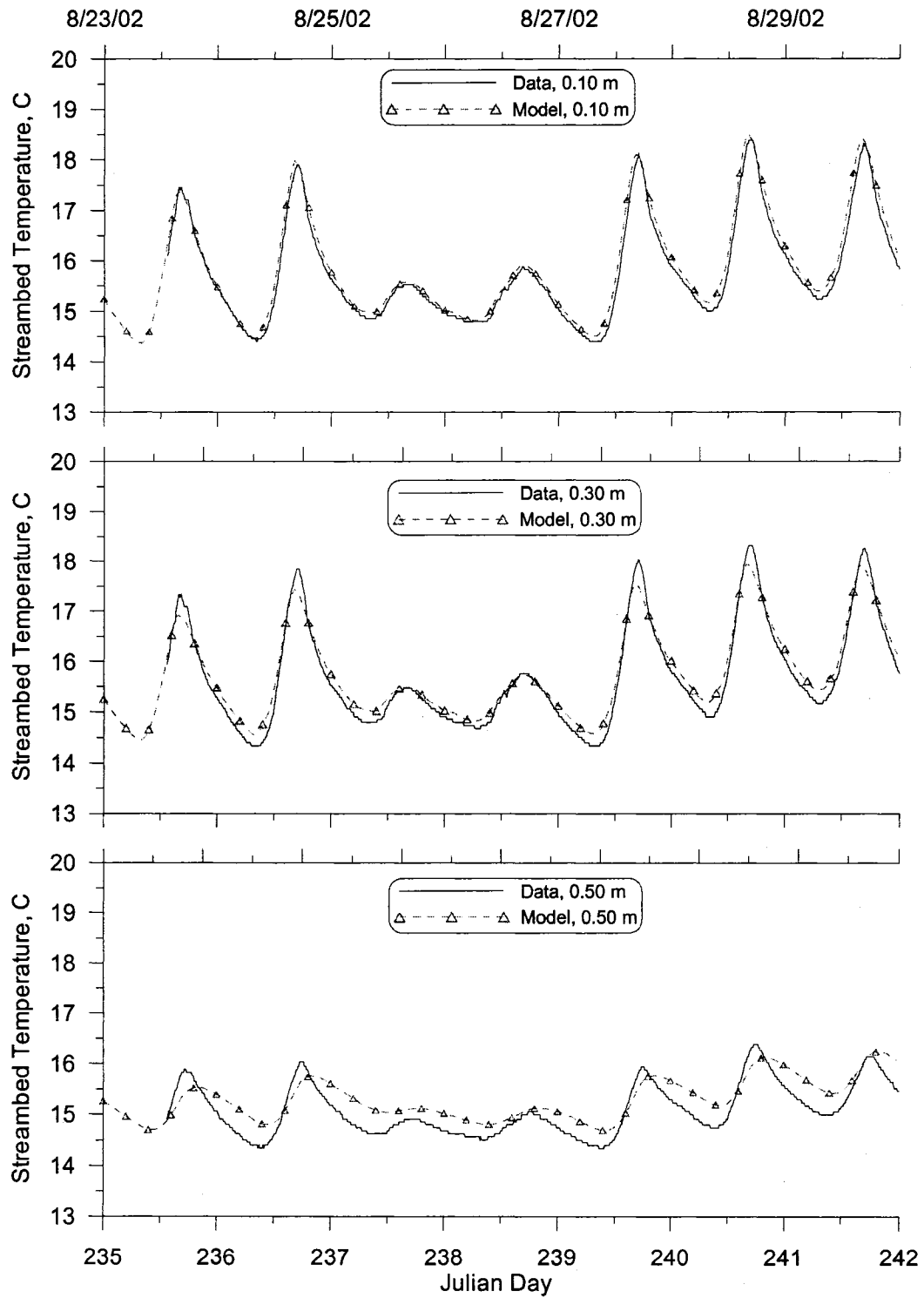
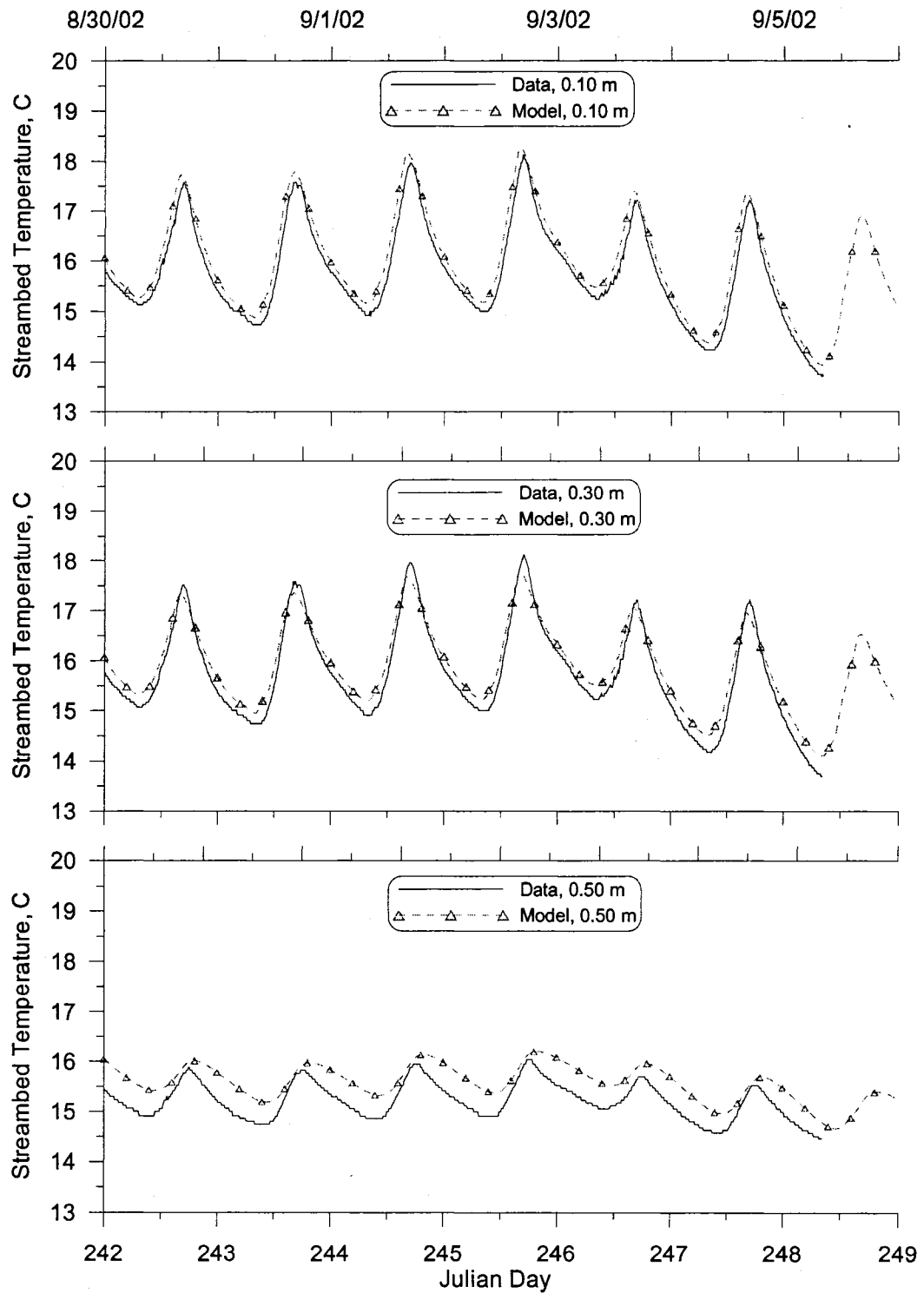


Figure 111: Model-data cobble streambed temperature comparison, Probe 3 site, August 23<sup>rd</sup> to 30<sup>th</sup>, 2002.



**Figure 112: Model-data cobble streambed temperature comparison, Probe 3 site, August 30<sup>th</sup> to September 5<sup>th</sup>, 2002.**

### 5.2.2 Cylindrical Model

The cylindrical coordinate system model was applied to the three experiments conducted in the lab with different media. As discussed above the temperature on the outside of the plastic buckets was monitored in addition to the temperature in the water and media of each bucket. The solar radiation from the lamp was found to be strong with values over  $100 \text{ W/m}^2$ . This resulted in the sand around the buckets absorbing some heat and it became important to not only model the media in the bucket but also the bucket itself. The bucket was made out of high-density polyethylene (HDPE), and was included in the model. The thermophysical characteristics of the plastic bucket were taken from Parker (1967) and included in Table 23. The thermophysical characteristics of the media in the buckets were taken from Table 23 and Appendix C where a more complete listing of thermophysical properties is provided.

The data collected in the lab experiments is discussed in Section 3.3 and in Appendix D. Probe 1 in experiments 1 through 3 had gravel, sand and gravel, and black painted concrete, respectively. A review of the data showed the temperatures recorded at a depth of 0.01 and 0.11 m in experiment 2 were erroneous and for depths of 0.01, 0.06, and 0.11 m in experiment 3. Probe 2 in experiments 1 through 3 had sand, sand, and white painted concrete, respectively. A review of the data showed the temperatures recorded at a depth of 0.16 m in all three experiments were erroneous. The erroneous data were not compared to the model results.

For experiments the side wall and bottom boundary conditions of the model were extended to the outer edge of the model grid and based on the temperature recorded during the experiment. The boundary condition temperatures were interpolated vertically along the sides of the bucket and then around the outer surface of the bucket. The bottom boundary condition was set based on the measure temperature data at the bottom of the bucket. The model grid's outer edge consisted of narrower cells representing the bucket walls and bottom with thermophysical characteristics of plastic.

#### **5.2.2.1 Experiment 1**

##### **Gravel Substrate**

The gravel substrate temperature data were recorded from November 17<sup>th</sup> to 22<sup>nd</sup>, 2002 for experiment 1. The model calibration consisted of adjusting the thermal diffusivity coefficient for the gravel media with water in the pore space and the thermal diffusivity of the plastic bucket. The thermophysical properties of the gravel experiment are listed in Table 53. The thermophysical characteristics of the gravel-water mixture were estimated at 50% rock and 50% water. During the calibration process the model results were found to be too cold compared to the data. In order to increase temperatures throughout the substrate column the thermal diffusivity for the plastic bucket were set at zero, representing a no flux boundary condition. The temperature results for the first three depths had moderate agreement but left the bottom depth too warm compared to data. In later experiments the temperature data at

the first three depths were found to be erroneous and that may be the case with this experiment as well since a no flux boundary condition was needed to match with the model.

Table 54 shows the model-data error statistics for the gravel substrate temperatures at four depths. Figure 113 shows time series comparisons of data and model results for the four depths over one week. The model-data error statistics and figure show there is some moderate agreement between the data and the model at three depths and less agreement with the bottom depth.

**Table 53: Thermophysical characteristics of the gravel substrate and plastic bucket**

Media	Density, $\rho_s$ , kg/m <sup>3</sup>	Specific Heat, $c_{ps}$ , kJ/kg°C	Thermal Diffusivity, $\beta$ , m <sup>2</sup> /s
50% Gravel 50% Water	1640.0	2830.5	6.595E-7
Plastic Bucket	952.0	2303.0	0.0

**Table 54: Model-data streambed temperature error statistics for the gravel substrate.**

Depth, m	Number of Comparisons	ME <sup>1</sup> , °C	AME <sup>1</sup> , °C	RMS <sup>1</sup> , °C
0.01	1383	-1.52	1.63	1.86
0.06	1383	-0.58	0.61	0.73
0.11	1383	0.03	0.69	0.84
0.16	1383	2.38	2.38	2.61

<sup>1</sup>ME = Mean Error; AME = Absolute Mean Error; RMS = Root Mean Square Error.

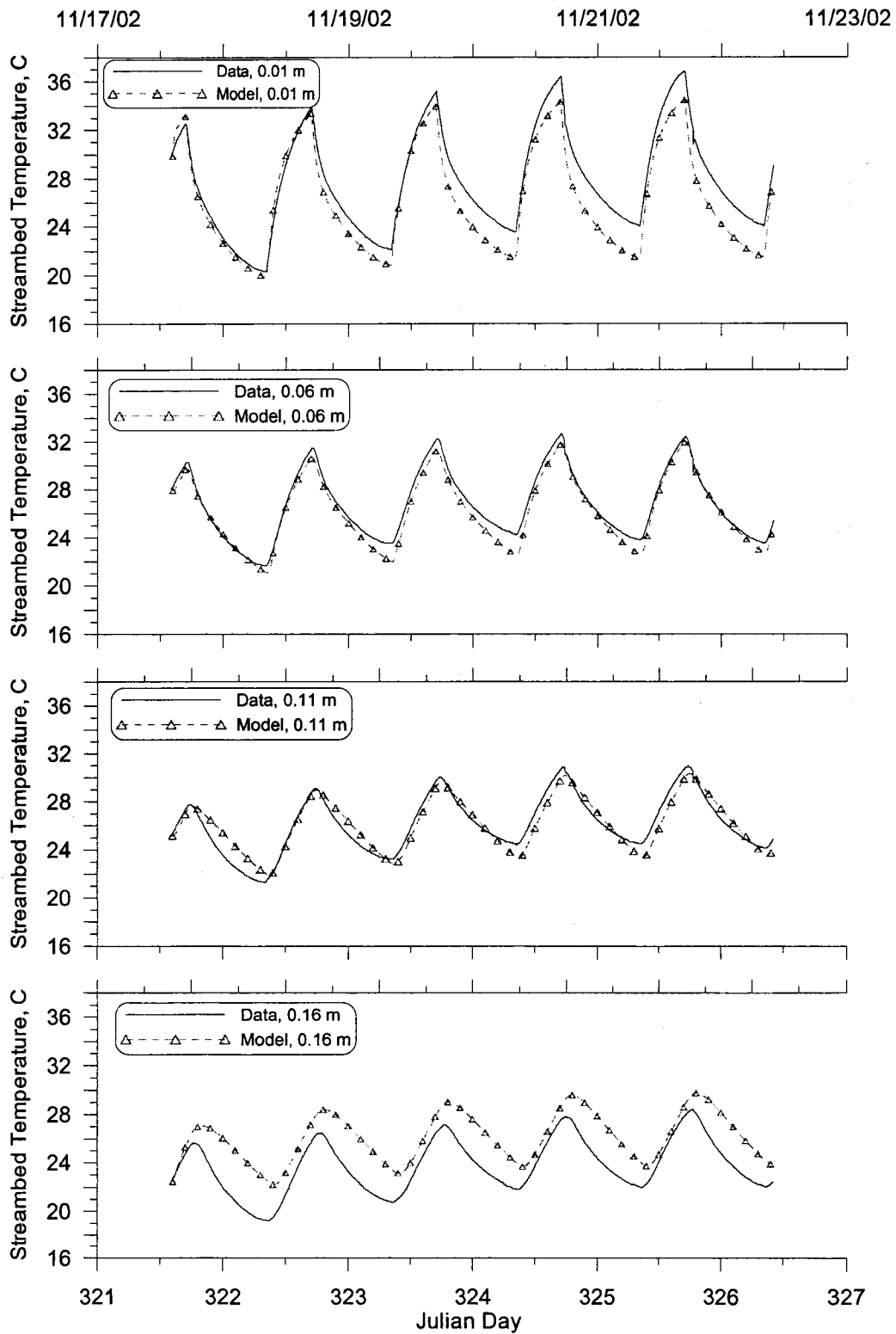


Figure 113: Experiment 1, Sand Substrate, November 17<sup>th</sup> to 22<sup>nd</sup>, 2002.

## Sand Substrate

The sand substrate temperature data were recorded from November 17<sup>th</sup> to 22<sup>nd</sup>, 2002 for experiment 1. The model calibration consisted of adjusting the thermal diffusivity coefficient for the sand media with water in the pore space and the thermal diffusivity of the plastic bucket. The thermophysical properties of the sand experiment are listed in Table 55. The thermophysical characteristics of the sand-water mixture were estimated at 80% sand and 20% water. No adjustments were made to the thermal diffusivity coefficient for the plastic bucket.

Table 56 shows the model-data error statistics for the sand substrate temperatures at three depths. Figure 114 shows time series comparisons of data and model results for the three depths over one week. The model-data error statistics and figure show there is good agreement between the data and the model.

**Table 55: Thermophysical characteristics of the sand substrate and plastic bucket**

Media	Density, $\rho_s$ , kg/m <sup>3</sup>	Specific Heat, $c_{ps}$ , kJ/kg°C	Thermal Diffusivity, $\beta$ , m <sup>2</sup> /s
80% Sand 20% Water	1876.0	1610.0	3.088E-7
Plastic Bucket	952.0	2303.0	1.974E-7

**Table 56: Model-data streambed temperature error statistics for the sand substrate.**

Depth, m	Number of Comparisons	ME <sup>1</sup> , °C	AME <sup>1</sup> , °C	RMS <sup>1</sup> , °C
0.01	1383	0.67	0.67	0.96
0.06	1383	0.53	0.57	0.71
0.11	1383	0.14	0.46	0.52

<sup>1</sup>ME = Mean Error; AME = Absolute Mean Error; RMS = Root Mean Square Error.

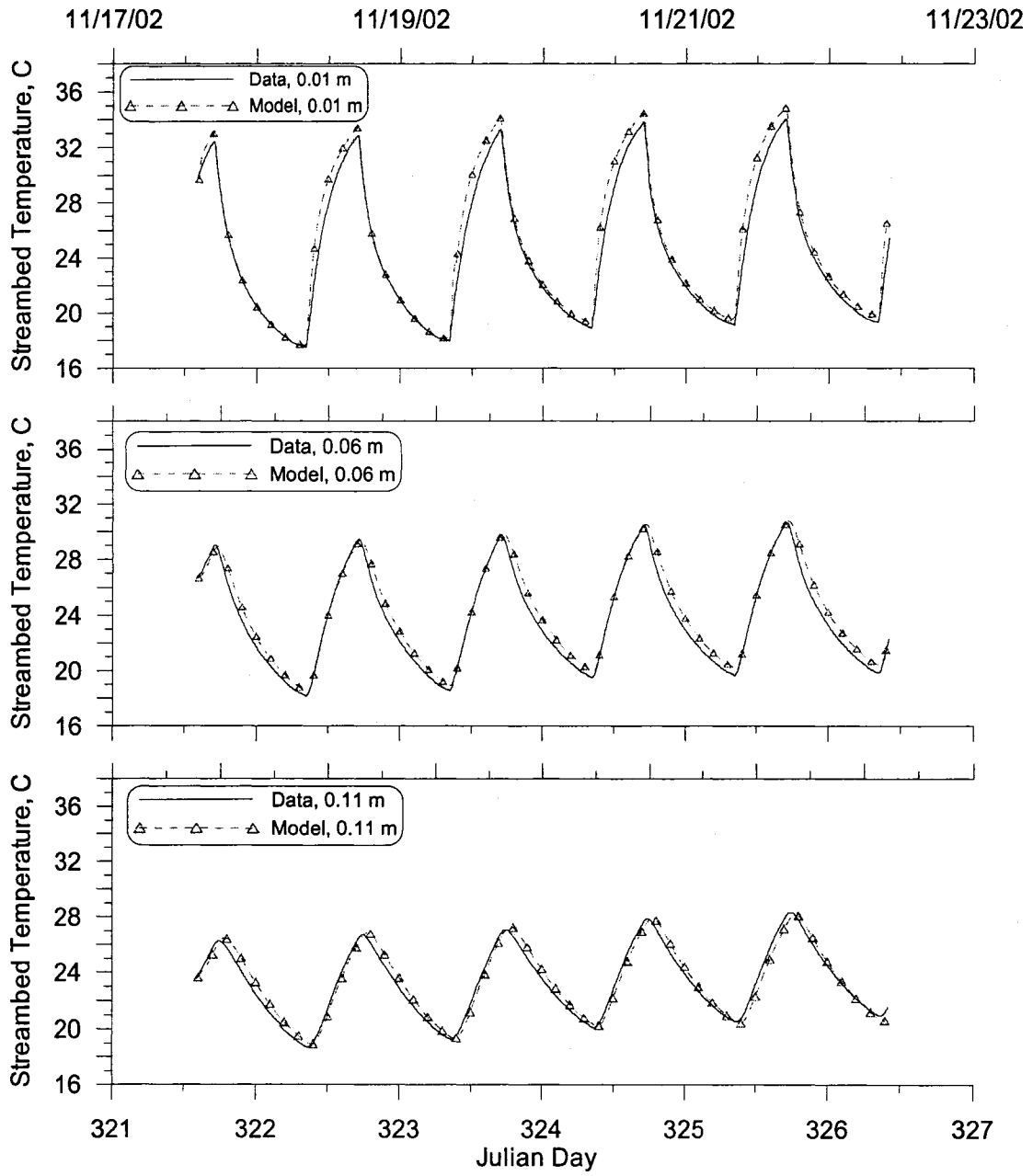


Figure 114: Experiment 1, Sand Substrate, November 17<sup>th</sup> to 22<sup>nd</sup>, 2002.

### 5.2.2.2 Experiment 2

#### Gravel and Sand

The gravel and sand substrate temperature data were recorded from November 22<sup>nd</sup> to 28<sup>th</sup>, 2002 for experiment 2. The model calibration consisted of adjusting the thermal diffusivity coefficient for the mixed media with water in the pore space and the thermal diffusivity of the plastic bucket. The thermophysical properties of the gravel and sand experiment are listed in Table 57. The thermophysical characteristics of the gravel-sand-water mixture were estimated at 45% rock, 45% sand and 10% water. Similar to the gravel media in experiment 1 the thermal diffusivity coefficient for the plastic bucket was set to zero for the sides and bottom to retain enough heat in the media to try to match data. This may indicate the temperature data is suspect. Based on a review of the temperature data at depths of 0.01 and 0.11 m they were found to be erroneous.

Table 58 shows the model-data error statistics for the gravel and sand substrate temperatures at two depths. Figure 115 shows time series comparisons of data and model results for the two depths over one week. The model-data error statistics and figure show there is moderate agreement between the data and the model, but the model is exhibiting too large of a diurnal swing compared to the data.

**Table 57: Thermophysical characteristics of the gravel and sand substrate and plastic bucket**

Media	Density, $\rho_s$ , kg/m <sup>3</sup>	Specific Heat, $c_{ps}$ , kJ/kg°C	Thermal Diffusivity, $\beta$ , m <sup>2</sup> /s
45% Rock/45% Sand, 10% Water	2213.2	1135.4	2.205E-6
Plastic Bucket	952.0	2303.0	0.0

**Table 58: Model-data streambed temperature error statistics for the gravel and sand substrate.**

Depth, m	Number of Comparisons	ME <sup>1</sup> , °C	AME <sup>1</sup> , °C	RMS <sup>1</sup> , °C
0.06	1524	-2.19	2.51	3.02
0.16	1524	-2.90	3.06	3.69

<sup>1</sup> ME = Mean Error; AME = Absolute Mean Error; RMS = Root Mean Square Error.

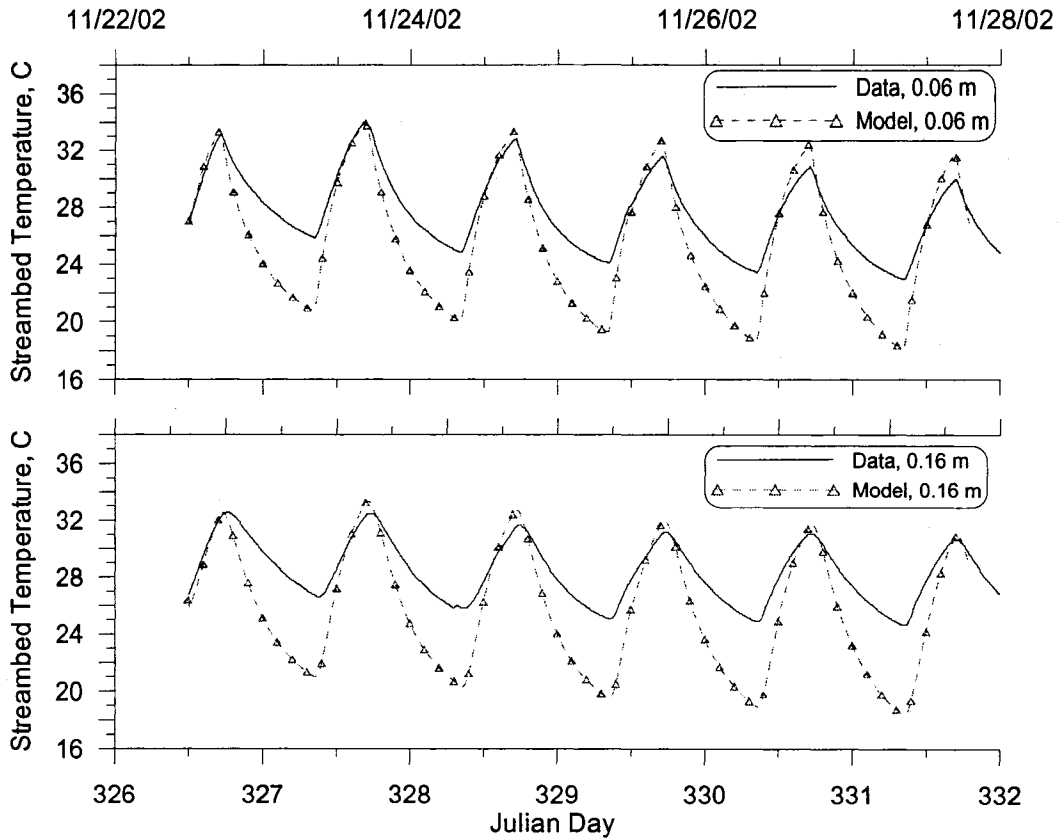


**Figure 115: Experiment 2, Gravel and Sand Substrate, November 22<sup>nd</sup> to 28<sup>th</sup>, 2002.**

## Sand

The sand substrate temperature data were recorded from November 22<sup>nd</sup> to 28<sup>th</sup>, 2002 for experiment 2. The model calibration consisted of adjusting the thermal diffusivity coefficient for the sand media with water in the pore space and the thermal diffusivity of the plastic bucket. The thermophysical properties of the sand experiment are listed in Table 59. The thermophysical characteristics of the sand-water mixture were estimated at 80% sand and 20% water. No adjustments were made to the thermal diffusivity coefficient for the plastic bucket on the side walls. The thermal diffusivity for the plastic bucket on the bottom was set to zero to retain some heat in the bucket to improve model-data agreement.

Table 60 shows the model-data error statistics for the sand substrate temperatures at three depths. Figure 116 shows time series comparisons of data and model results for the three depths over one week. The model-data error statistics and figure show there is moderate agreement between the data and the model, with the model still slightly too cool at a depth of 0.11 m.

**Table 59: Thermophysical characteristics of the sand substrate and plastic bucket**

Media	Density, $\rho_s$ , kg/m <sup>3</sup>	Specific Heat, $c_{ps}$ , kJ/kg°C	Thermal Diffusivity, $\beta$ , m <sup>2</sup> /s
80% Sand 20% Water	1876.0	1610.0	3.088E-7
Plastic Bucket	952.0	2303.0	1.974E-7/0.0

**Table 60: Model-data streambed temperature error statistics for the sand substrate.**

Depth, m	Number of Comparisons	ME <sup>1</sup> , °C	AME <sup>1</sup> , °C	RMS <sup>1</sup> , °C
0.01	1524	1.08	1.09	1.25
0.06	1524	0.33	0.67	0.76
0.11	1524	-1.06	1.17	1.44

<sup>1</sup>ME = Mean Error; AME = Absolute Mean Error; RMS = Root Mean Square Error.

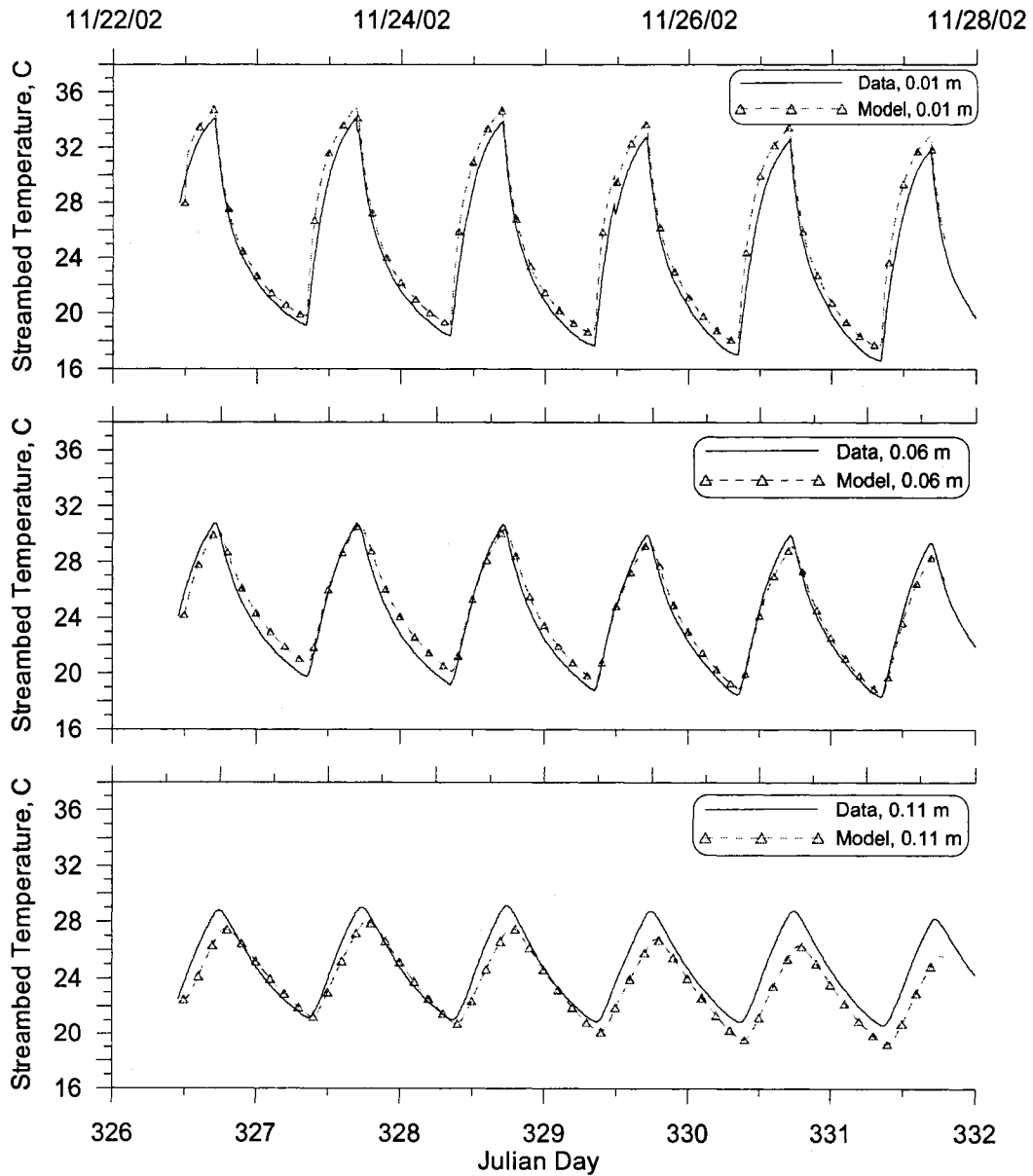


**Figure 116: Experiment 2, Sand Substrate, November 22<sup>nd</sup> to 28<sup>th</sup>, 2002.**

### 5.2.2.3 Experiment 3

#### Black Concrete

The black painted concrete substrate temperature data were recorded from December 15<sup>th</sup> to 21<sup>st</sup>, 2002 for experiment 3. The model calibration consisted of adjusting the thermal diffusivity coefficient of the concrete and the thermal diffusivity of the plastic bucket as listed in Table 63. Similar to the previous two experiments with the thermistor Probe 1 (gravel and gravel-sand substrate) the thermal diffusivity coefficient for the bottom of the plastic bucket was set to zero and for the side walls were set to 3% of the data value to retain enough heat in the media to try to match data. Based on a review of the temperature data at depths of 0.01, 0.06, and 0.11 m they were found to be erroneous and were therefore not compared to the model.

Table 62 shows the model-data temperature error statistics for the black painted concrete substrate at one depth. Figure 117 shows a time series comparison of data and model results for the one depth over one week. The model-data error statistics and figure show there is moderate agreement between the data and the model, but the model is exhibiting a slightly larger of a diurnal swing compared to the data.

**Table 61: Thermophysical characteristics of the black painted concrete and plastic bucket.**

Media	Density, $\rho_s$ , kg/m <sup>3</sup>	Specific Heat, $c_{ps}$ , kJ/kg°C	Thermal Diffusivity, $\beta$ , m <sup>2</sup> /s
100% Concrete	2300.0	964.0	4.159E-7
Plastic Bucket	952.0	2303.0	5.738E-9 /0.0

**Table 62: Model-data streambed temperature error statistics for the black painted concrete.**

Depth, m	Number of Comparisons	ME <sup>1</sup> , °C	AME <sup>1</sup> , °C	RMS <sup>1</sup> , °C
0.165	1501	0.09	0.73	0.83
<sup>1</sup> ME = Mean Error; AME = Absolute Mean Error; RMS = Root Mean Square Error.				

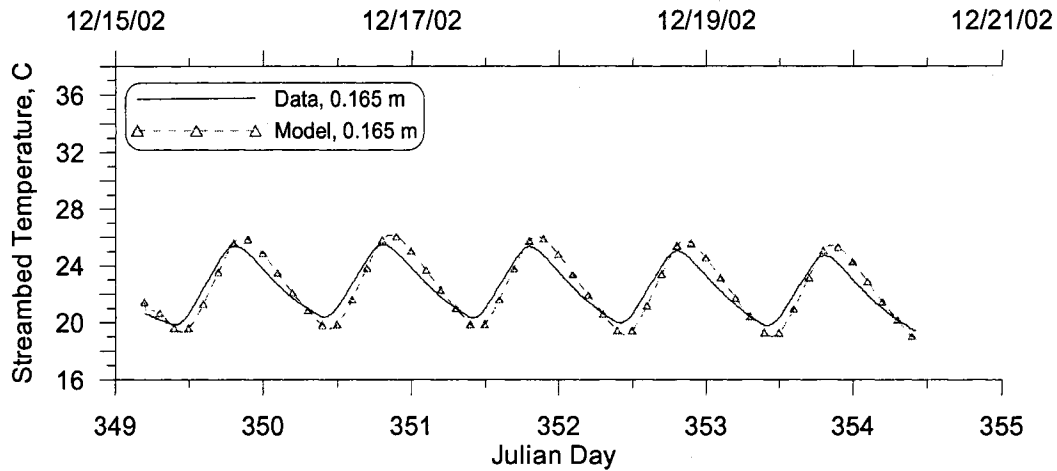


**Figure 117: Experiment 3, Black painted concrete, December 15<sup>th</sup> to 21<sup>st</sup>, 2002.**

#### White Concrete

The white painted concrete substrate temperature data were recorded from December 15<sup>th</sup> to 21<sup>st</sup>, 2002 for experiment 3. The model calibration consisted of adjusting the thermal diffusivity coefficient of the concrete and the thermal diffusivity of the plastic bucket as listed in Table 63. The table shows the thermal diffusivity of the concrete was increased about 50% to provided better model-data agreement. The thermal diffusivity coefficient for the bottom and sides of the plastic bucket were set to zero to retain enough heat in the substrate to try to match data.

Table 64 shows the model-data temperature error statistics for the black painted concrete substrate at one depth. Figure 118 shows a time series comparison of data and model results for the three depths over one week. The model-data error

statistics and figure show there is in good agreement between the data and the model, but the model is exhibiting a slightly larger of a diurnal swing compared to the data at the bottom two depths.

**Table 63: Thermophysical characteristics of the white painted concrete and plastic bucket.**

Media	Density, $\rho_s$ , kg/m <sup>3</sup>	Specific Heat, $c_{ps}$ , kJ/kg°C	Thermal Diffusivity, $\beta$ , m <sup>2</sup> /s
100% Concrete	2300.0	964.0	6.159E-7
Plastic Bucket	952.0	2303.0	0.0

**Table 64: Model-data streambed temperature error statistics for the white painted concrete.**

Depth, m	Number of Comparisons	ME <sup>1</sup> , °C	AME <sup>1</sup> , °C	RMS <sup>1</sup> , °C
0.01	1501	0.28	0.55	0.64
0.06	1501	0.07	0.59	0.70
0.11	1501	-0.51	0.85	1.04

<sup>1</sup>ME = Mean Error; AME = Absolute Mean Error; RMS = Root Mean Square Error.

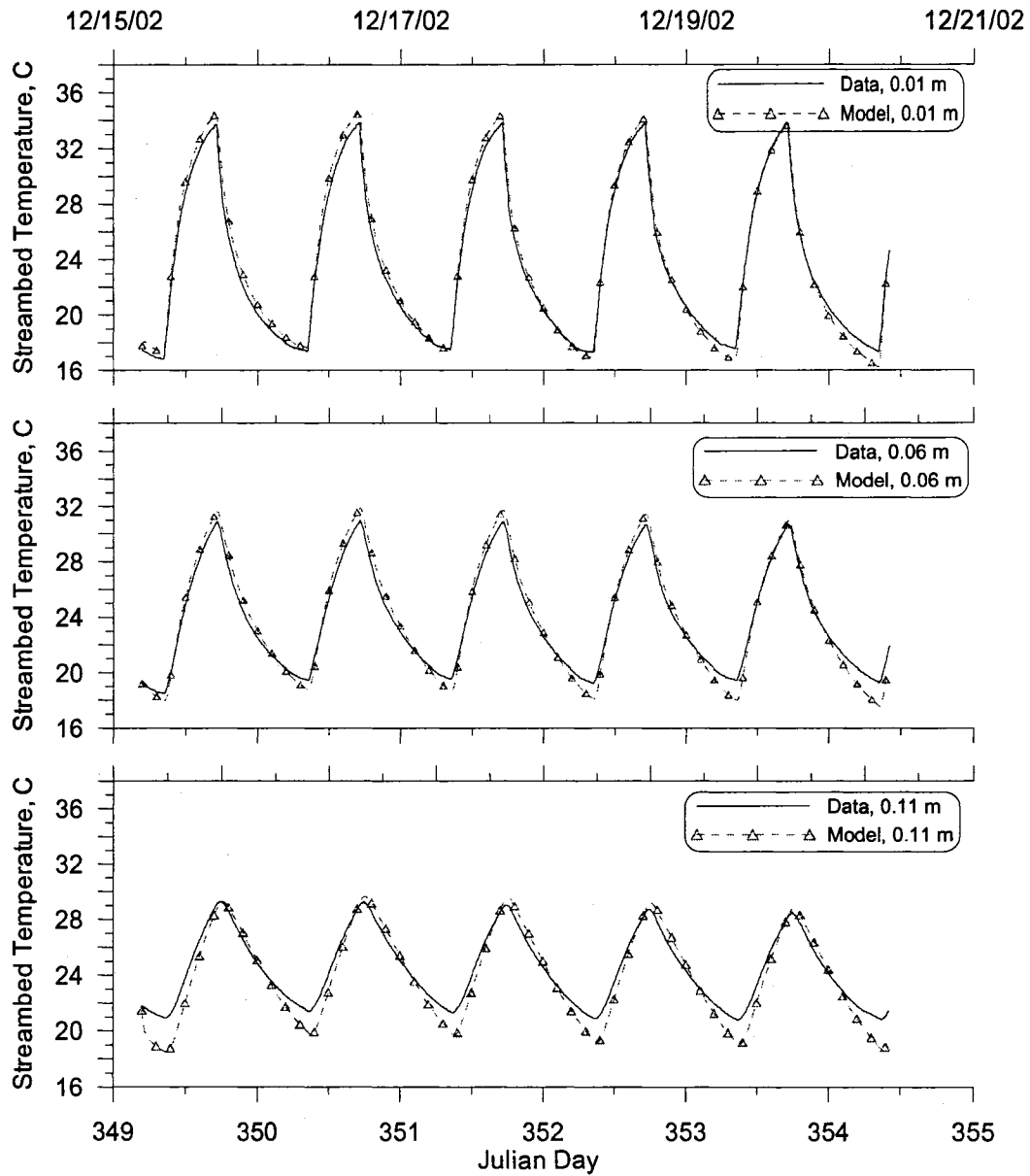


Figure 118: Experiment 3, White painted concrete, December 15<sup>th</sup> to 21<sup>st</sup>, 2002.

### 5.2.3 Summary

Overall the calibration of the model to field data showed there was close agreement between streambed temperature predictions and field data. The model calibrated well for the bedrock substrate reach with the model capturing diurnal

variations near the surface and dampened diurnal temperature variations are deeper locations.

The model calibration of the cobble reach showed the limitation of the data set collected. The interstitial water in the cobble and gravel substrate material played a large role in substrate temperatures. The field monitoring reflected larger diurnal temperature swings than could be accounted for solely adjusting the thermophysical characteristics of the substrate. To calibrate the model in the cobble reach it was necessary to include a small fraction of the water temperature in predicting the streambed temperature. This approach was reasonable at approximating the interstitial water temperature's impact given that there was not enough data to support modeling the cobble and interstitial water distinctly. The experimental design used in the field consisted of burying the thermistors in the cobble substrate which was saturated with water. The thermistors may have been monitoring the interstitial water or the cobble substrate temperatures.

The calibration of the model to the lab data showed there were cases with good model-data agreement and some cases where there was less agreement. Some of the disagreement may have been due to errors with the data collected as discussed in Appendix D and discovered during the calibration process.

### **5.3 Model Verification**

The model verification process consisted of examining the effects of the model grid resolution and the location of the bottom boundary condition on the model

predictions. In addition the 3-D models (Cartesian and Cylindrical) were set up for a simple case scenario and compared to analytical model results for three types of media. The 3-D model results were also compared to the 1-D model results and analytical model results using bedrock substrate.

### **5.3.1 Grid Sensitivity**

#### **5.3.1.1 Vertical Resolution**

The vertical grid resolution was tested to determine if a coarser grid would provide less accurate results. Figure 119 shows vertical temperature profiles at 6:15 pm on September 9<sup>th</sup>, 2002 with different vertical grid resolutions. The horizontal grid resolution was kept constant between the simulations. The figure shows there is a disagreement between the model results in the first 2 meters of depth. The Figure 120 shows a vertical temperature profile plot for just the first 2 meters. The figure indicates the vertical grid resolution of 0.5 m and 1.0 m are too coarse and result in more linear temperature changes than shown with the higher resolution grids. The grid was refined further near the surface as shown in Figure 121 and indicates that in the depth range of 0.0 to 0.5 m a finer grid than 0.1 m grid layers provides more accurate model predictions. The model run results also showed that grid layers of 0.5 m and 1.0 could be used at deeper depths without compromising accuracy.

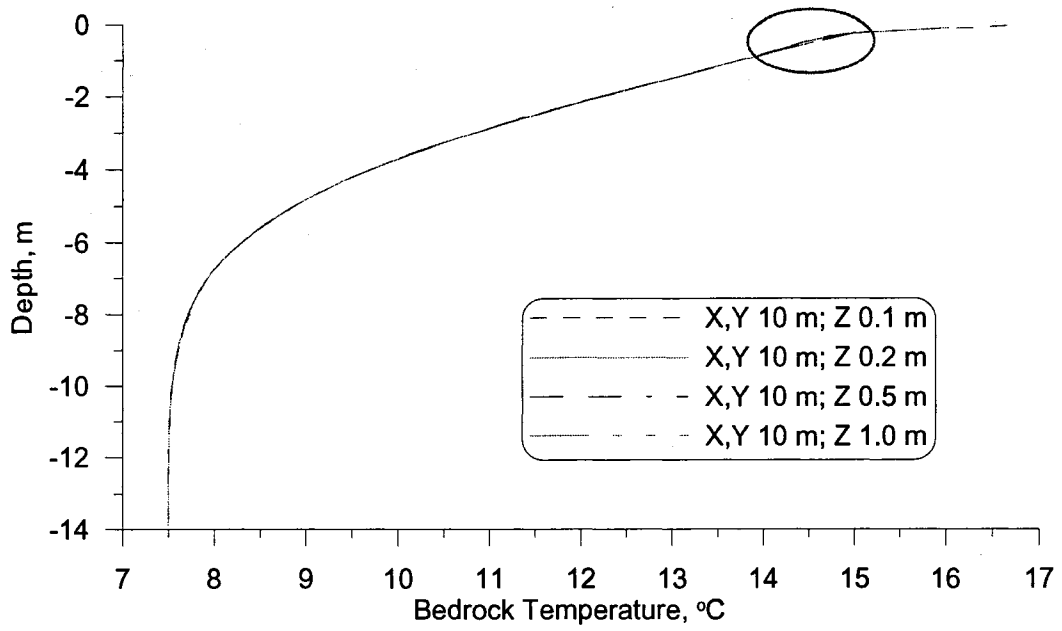


Figure 119: Streambed vertical grid resolution comparison, part 1.

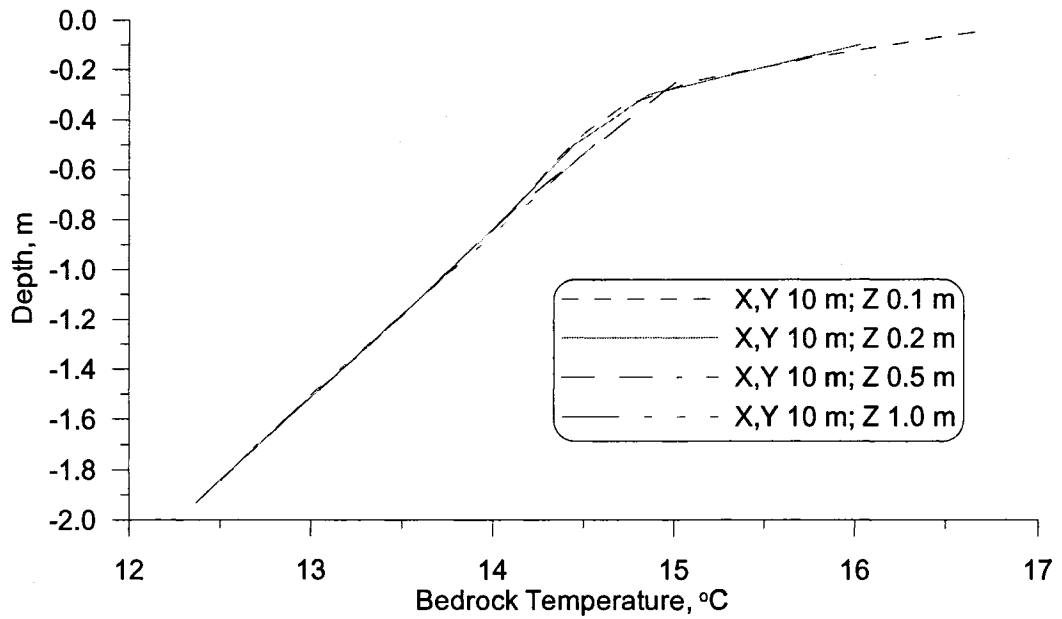


Figure 120: Streambed vertical grid resolution comparison, part 2

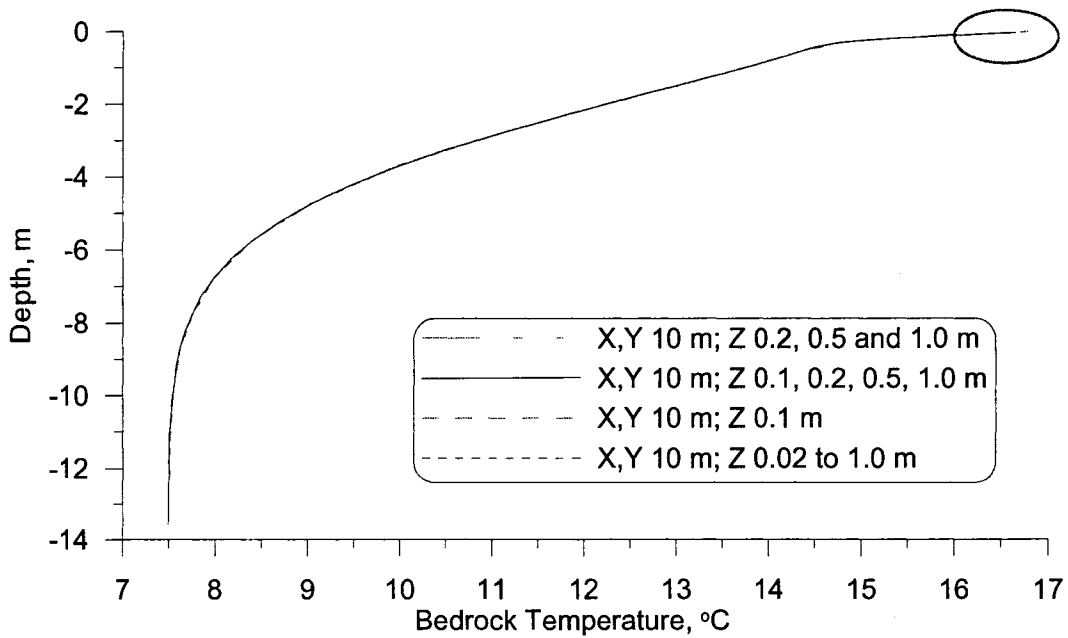
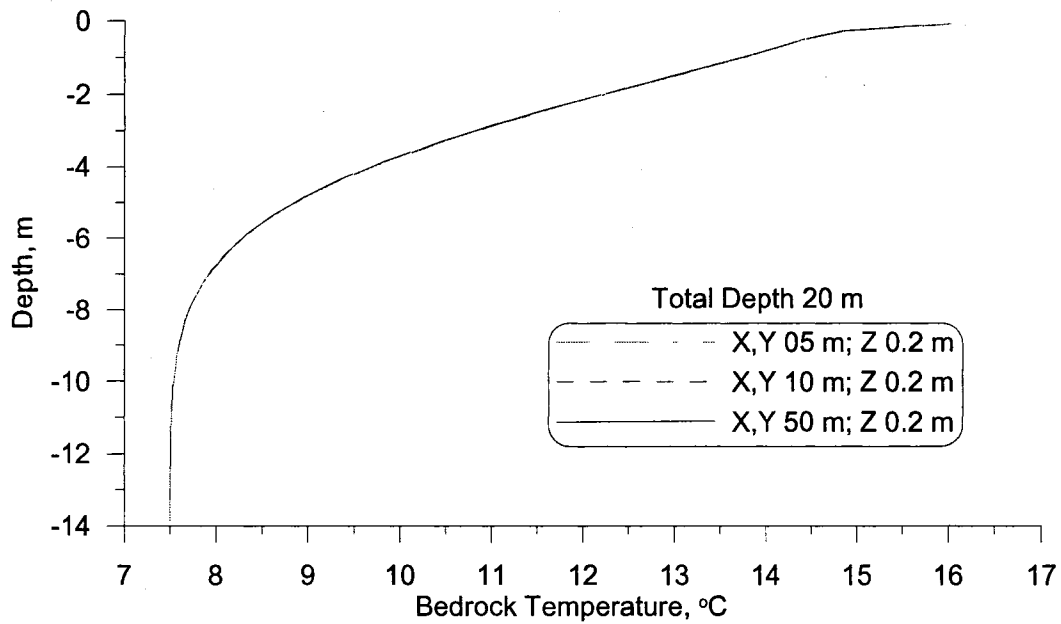


Figure 121: Streambed vertical grid resolution comparison, near surface.

### 5.3.1.2 Horizontal Resolution

The horizontal grid resolution was investigated to determine if a coarser grid would provide less accurate results. Figure 122 shows vertical temperature profiles at 6:15 pm on September 9th, 2002 with different horizontal grid resolutions. The vertical grid resolution was kept constant at 0.2 m. The figure shows there is no difference between the 5 m, 10 m and 50 m grid cell sizes, but this analysis was conducted from the middle of the model grid. If vertical profiles were examined closer to the boundary conditions, then differences might occur with 50 m grid resolution vs. 10 m grid. For the purposes of calibrating the model to field data in the Lower Bull Run River the horizontal grid resolution was varied between 1 and 10 m to ensure the temperature monitoring sites were accurately located in the model.



**Figure 122: Streambed horizontal grid resolution comparison.**

### 5.3.1.3 Bottom Boundary Condition

The location of the bottom boundary condition was also tested to ensure it was sufficiently deep enough to not influence the model results and not too deep to make the computational cost expensive. Figure 123 shows vertical temperature profiles at 6:15 pm on September 9th, 2002 with different depth for the bottom boundary condition. The figure indicates that a total depth of 8 m (or less) is too shallow for the bottom boundary condition to result in accurate model predictions at that depth. The figure also shows that with a bottom boundary condition set at 12 m the model is close to reach the bottom boundary condition temperature of 7.5 °C. The models calibrated to field data used a bottom boundary at a depth of 20 m. Based on Figure 123 a

bottom boundary condition could have been set at 13 m and still resulted in the same model predictions.

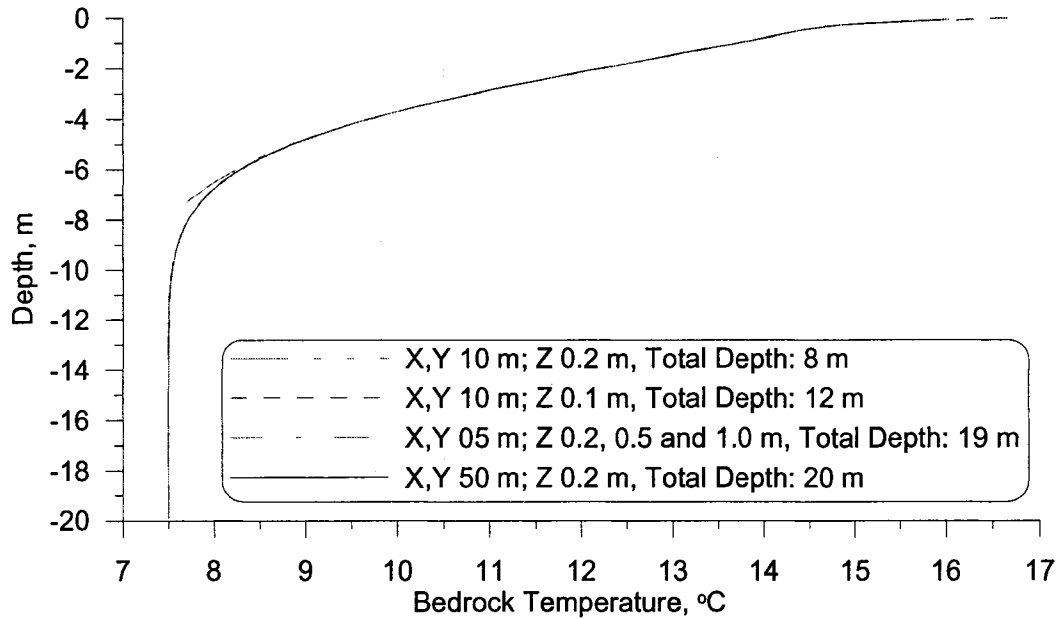


Figure 123: Streambed bottom boundary condition depth.

### 5.3.2 Comparison with Analytical Solution, Simple Case

A simple case model was developed to compare the analytical solution with the 3-dimensional (3-D) Cartesian and cylindrical coordinate system models' results. The simple case consisted of a semi infinite solid with an initial temperature of 0 °C, with boundary conditions fixed at 0 °C, no solar radiation input, and water on the top surface held constant at 10 °C. The one-dimensional (1-D) governing equation for heat transfer in a semi-finite solid from Incropera and De Witt (1990) can be written as

$$\frac{\partial T}{\partial t} = \beta \frac{\partial^2 T}{\partial z^2} \quad (111)$$

where  $\beta$  ( $\text{m}^2/\text{s}$ ) is the thermal diffusivity. Given the conditions for the simple case scenario described above the temperature at a specific depth over time can be calculated (Incropera and De Witt, 1990) as

$$T = T_o \operatorname{erfc}\left(\frac{z}{\sqrt{4\beta t}}\right) \quad (112)$$

where  $T_o$  ( $^{\circ}\text{C}$ ) is the surface water temperature,  $z$  (meters) is the depth, and  $t$  (seconds) is the time. Equation (112) was used to calculate the “streambed” temperature at 4 depths using three types of media with thermophysical characteristics of 100% rock, 100% water and a spilt of 50% water and 50% rock. The analytical model results were then compared to the model output from the 3-D Cartesian and Cylindrical coordinate system models for the same conditions.

### 5.3.2.1 Cartesian Coordinate System Model

The Cartesian coordinate system model consisted of grid cells in the  $x$  and  $y$  directions of 10 m wide with 22 cells (220 m) and 54 vertical layers with a total depth of 20 m. Table 65 lists the thermal diffusivity coefficients of the substrate for three simple case scenarios of rock, rock and water and water media used with the analytical model and the 3-D model. The 3-D model results consisted of time series of temperature predictions at multiple depths from the center of the model grid.

Table 66 shows the 3-D model-analytical model errors statistics for the 100% rock substrate at four depths. Figure 124 shows a time series plot of the 3-D model and analytical model temperature predictions at the four depths. The error statistics

and the figure both show there is close agreement between the 3-D model and the analytical solution.

**Table 65: Thermal diffusivity values for the simple case model application substrate.**

Media	Thermal Diffusivity, $\beta$ , m <sup>2</sup> /s
100% Rock	1.175E-6
50% Rock, 50% Water	6.595E-7
100 Water	1.440E-7

**Table 66: 3-D Model-Analytical Model streambed temperature difference statistics for Cartesian coordinate system, 100% rock.**

Depth, m	Number of Comparisons	ME <sup>1</sup> , °C	AME <sup>1</sup> , °C	RMS <sup>1</sup> , °C
0.05	3733	-0.01	0.01	0.07
0.15	3733	0.00	0.01	0.03
0.55	3733	0.01	0.01	0.01
1.10	3733	0.00	0.01	0.01

<sup>1</sup>ME = Mean Error; AME = Absolute Mean Error; RMS = Root Mean Square Error.

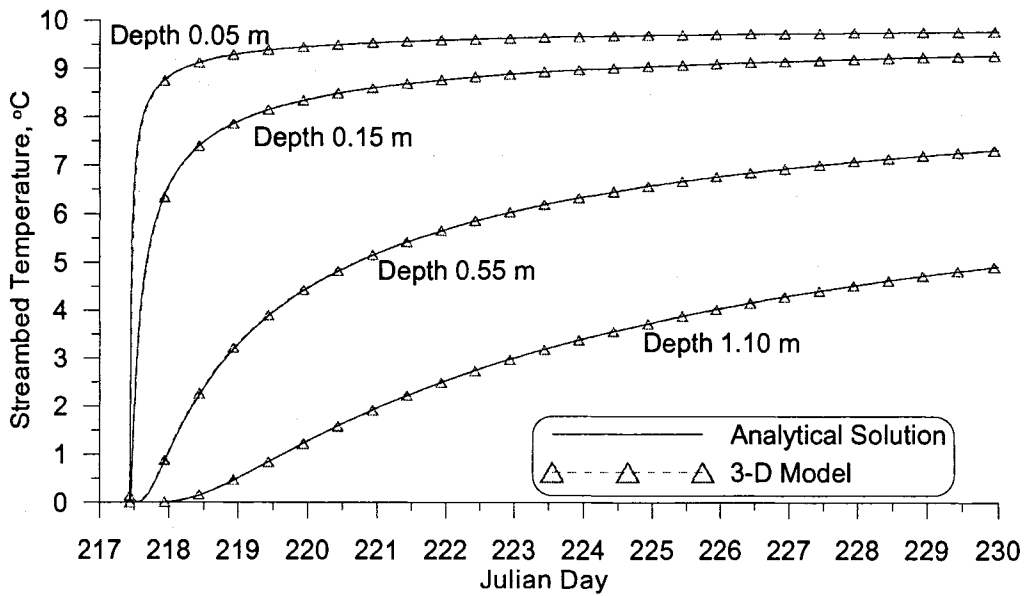


**Figure 124: 3-D Model and Analytical Model solutions for Cartesian coordinate system, 100% rock**

The Cartesian coordinate system model and analytical model were then run with the thermal diffusivity representing a media with 50% rock and 50% water. The results from the 3-D model were then compared to the analytical solution results.

Table 67 shows the 3-D model-analytical model errors statistics for the 50% rock and 50% water substrate at four depths. Figure 125 shows a time series plot of the 3-D model and analytical model temperature predictions at the four depths. The error statistics and the figure both show there is close agreement between the 3-D model and the analytical solution, though not as close as the 100% rock media scenario.

**Table 67: 3-D Model-Analytical Model streambed temperature difference statistics for Cartesian coordinate system, 50% rock and 50% water.**

Depth, m	Number of Comparisons	ME <sup>1</sup> , °C	AME <sup>1</sup> , °C	RMS <sup>1</sup> , °C
0.05	3733	-0.01	0.01	0.09
0.15	3733	-0.01	0.01	0.04
0.55	3733	0.01	0.01	0.01
1.10	3733	-0.01	0.01	0.01

<sup>1</sup>ME = Mean Error; AME = Absolute Mean Error; RMS = Root Mean Square Error.

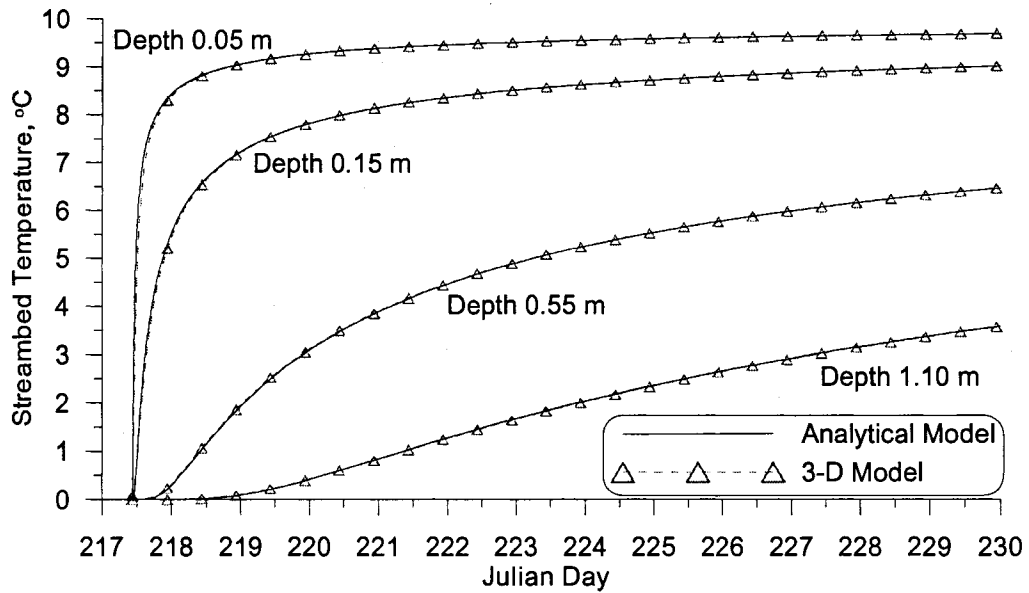


Figure 125: 3-D Model and Analytical Model solutions for Cartesian coordinate system, 50% rock and 50% water

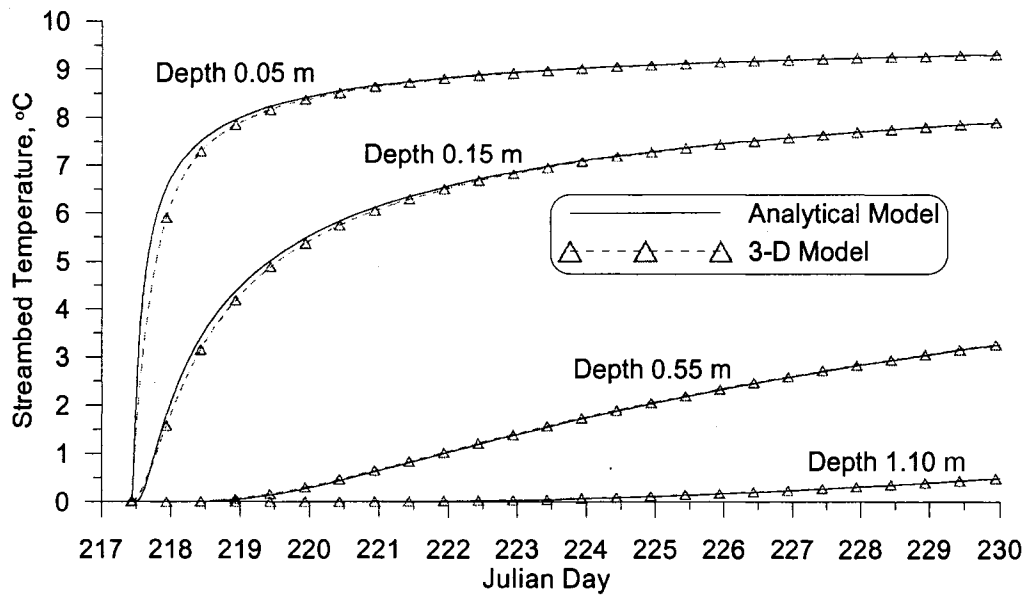
The Cartesian coordinate system model and analytical model were then run with the thermal diffusivity representing a media with 100% water. The results from the 3-D model were then compared to the analytical solution results.

Table 68 shows the 3-D model-analytical model errors statistics for the 100% water substrate at four depths. Figure 126 shows a time series plot of the 3-D model and analytical model temperature predictions at the four depths. The error statistics and the figure both show there is close agreement between the 3-D model and the analytical solution, though not as close as the previous two media scenarios.

**Table 68: 3-D Model-Analytical Model streambed temperature difference statistics for Cartesian coordinate system, 100% water.**

Depth, m	Number of Comparisons	ME <sup>1</sup> , °C	AME <sup>1</sup> , °C	RMS <sup>1</sup> , °C
0.05	3733	-0.07	0.07	0.21
0.15	3733	-0.05	0.05	0.09
0.55	3733	0.02	0.02	0.02
1.10	3733	0.00	0.01	0.01

<sup>1</sup> ME = Mean Error; AME = Absolute Mean Error; RMS = Root Mean Square Error.



**Figure 126: 3-D Model and Analytical Model solutions for Cartesian coordinate system, 100% water.**

### 5.3.2.2 Cylindrical Coordinate System Model

The cylindrical coordinate system model consisted of angular grid cells of 20 degrees and radial grid cells of 10 m out to 130 m maximum radius and 54 vertical layers with a total depth of 20 m. Table 65 above lists the thermal diffusivity coefficients of the substrate for three simple case scenarios of rock, rock and water and water media used with the analytical model and the 3-D model. The 3-D model

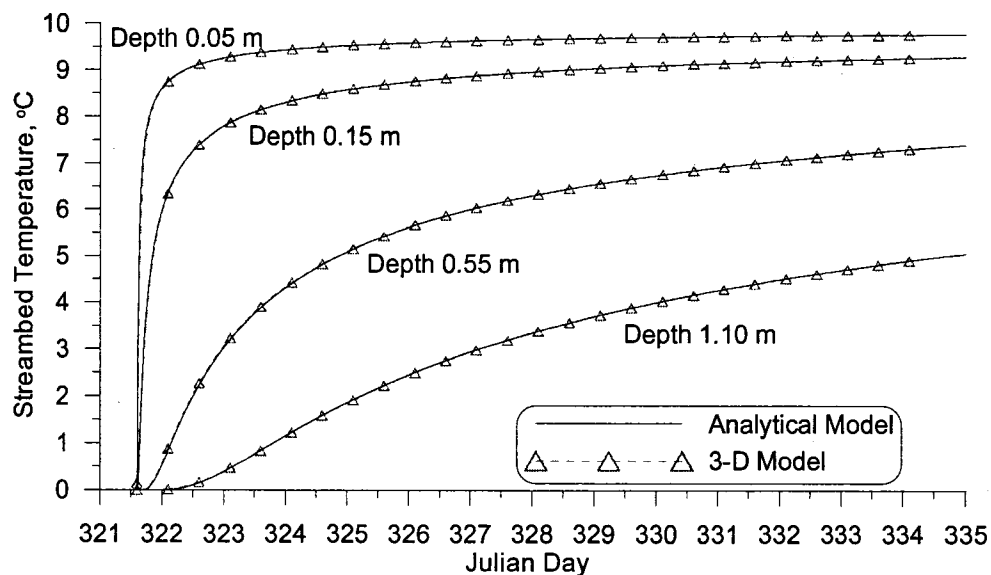
results consisted of time series of temperature predictions at multiple depths from the center of the model grid.

Table 69 shows the 3-D model-analytical model errors statistics for the 100% rock substrate at four depths. Figure 127 shows a time series plot of the 3-D model and analytical model temperature predictions at the four depths. The error statistics and the figure both show there is close agreement between the 3-D model and the analytical solution for the 100% rock substrate.

**Table 69: 3-D Model-Analytical Model streambed temperature difference statistics for cylindrical coordinate system, 100% rock.**

Depth, m	Number of Comparisons	ME <sup>1</sup> , °C	AME <sup>1</sup> , °C	RMS <sup>1</sup> , °C
0.05	3733	-0.01	0.01	0.07
0.15	3733	0.00	0.01	0.03
0.55	3733	0.01	0.01	0.01
1.10	3733	0.00	0.01	0.01

<sup>1</sup>ME = Mean Error; AME = Absolute Mean Error; RMS = Root Mean Square Error.



**Figure 127: 3-D Model and Analytical Model solutions for cylindrical coordinate system, 100% rock.**

The cylindrical coordinate system model and analytical model were then run with the thermal diffusivity representing a media with 50% rock and 50% water. And their results compared.

Table 70 shows the 3-D model-analytical model errors statistics for the 50% rock and 50% water substrate at four depths. Figure 128 shows a time series plot of the 3-D model and analytical model temperature predictions at the four depths. The error statistics and the figure both show there is close agreement between the 3-D cylindrical coordinate system model and the analytical solution, though not as close as the 100% rock media scenario.

**Table 70: 3-D Model-Analytical Model streambed temperature difference statistics for cylindrical coordinate system, 50% rock and 50% water.**

Depth, m	Number of Comparisons	ME <sup>1</sup> , °C	AME <sup>1</sup> , °C	RMS <sup>1</sup> , °C
0.05	3733	-0.01	0.01	0.09
0.15	3733	-0.01	0.01	0.04
0.55	3733	0.01	0.01	0.01
1.10	3733	-0.01	0.01	0.01
<sup>1</sup> ME = Mean Error; AME = Absolute Mean Error; RMS = Root Mean Square Error.				

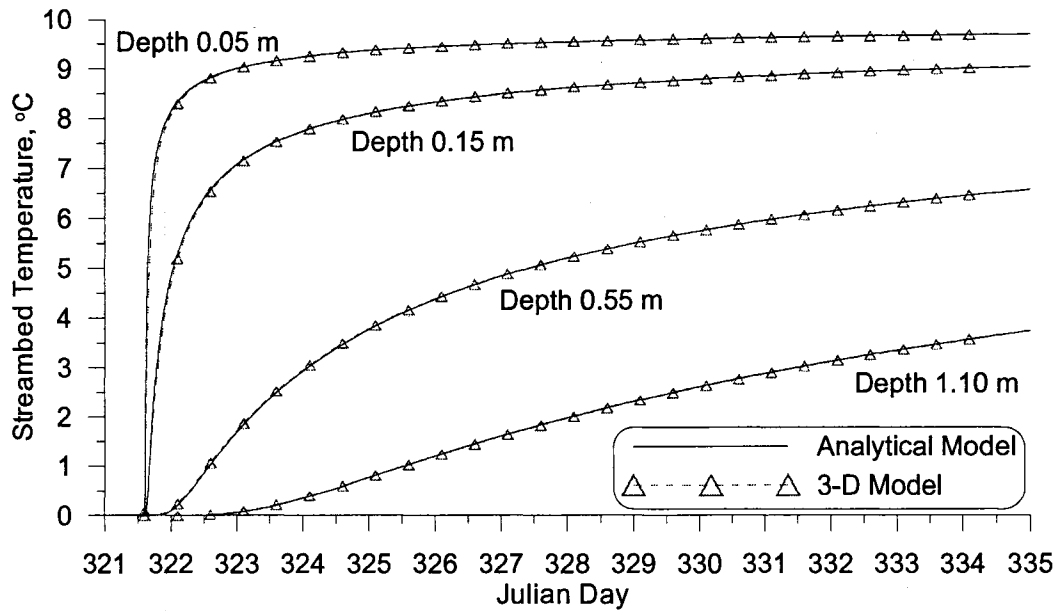


Figure 128: 3-D Model and Analytical Model solutions for cylindrical coordinate system, 50% rock and 50% water.

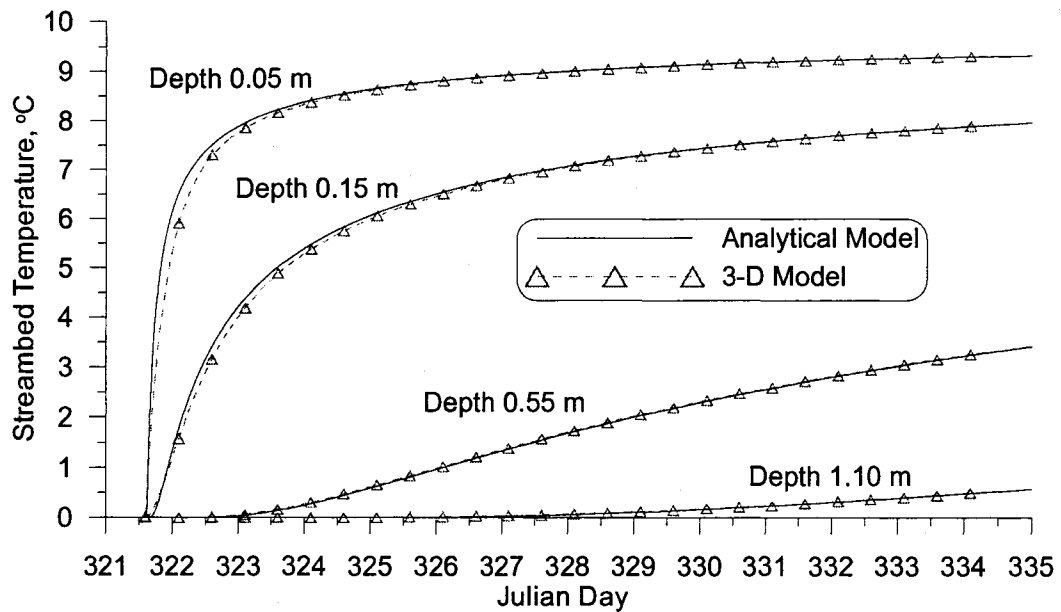
The cylindrical coordinate system model and analytical model were then run with the thermal diffusivity representing a media with 100% water and the results were compared.

Table 71 shows the 3-D model-analytical model errors statistics for the 100% water substrate at four depths. Figure 129 shows a time series plot of the 3-D model and analytical model temperature predictions at the four depths. The error statistics and the figure both show there is close agreement between the 3-D cylindrical coordinate system model and the analytical solution, though not as close as the previous two media scenarios. These results are similar to the Cartesian coordinate system model results.

**Table 71: 3-D Model-Analytical Model streambed temperature difference statistics for cylindrical coordinate system, 100% water.**

Depth, m	Number of Comparisons	ME <sup>1</sup> , °C	AME <sup>1</sup> , °C	RMS <sup>1</sup> , °C
0.05	3733	-0.07	0.07	0.21
0.15	3733	-0.05	0.05	0.09
0.55	3733	0.02	0.02	0.02
1.10	3733	0.00	0.01	0.01

<sup>1</sup> ME = Mean Error; AME = Absolute Mean Error; RMS = Root Mean Square Error.



**Figure 129: 3-D Model and Analytical Model solutions for cylindrical coordinate system, 100% water.**

### 5.3.3 Comparison with Analytical Model, Bedrock

The 3-D Cartesian coordinate system model was also compared to analytical model developed by Silliman et al. (1995). The 1-D heat transfer governing equation discussed in Silliman et al. (1995) can be written as

$$\frac{\partial T}{\partial t} + \alpha \frac{\partial T}{\partial z} = \beta \frac{\partial^2 T}{\partial z^2} \quad (113)$$

where  $\alpha$  (m/s) is convection term which is a function of the vertical water velocity in the substrate. The general solution to the equation can be written (Silliman et al., 1995) as

$$\Delta T = \frac{\Delta T_w}{2} [\operatorname{erfc}\{(z_1 - \alpha t) / 2\sqrt{\beta t}\} + \exp\{\alpha z_1 / \beta\} \operatorname{erfc}\{(z_1 + \alpha t) / 2\sqrt{\beta t}\}] \quad (114)$$

where  $\Delta T_w$  ( $^{\circ}\text{C}$ ) is the change in water temperature over an increment in time and  $\Delta T$  ( $^{\circ}\text{C}$ ) is the change in the streambed temperature for the specific depth,  $z_1$  (m) over an increment in time. In this case there was assumed to be no vertical velocity of the bulk water in the substrate so the convection term equals zero. Equation (114) can be written as

$$\Delta T = \frac{\Delta T_w}{2} [\operatorname{erfc}\{z_1 / 2\sqrt{\beta t}\} + \operatorname{erfc}\{z_1 / 2\sqrt{\beta t}\}] \quad (115)$$

The temperature at a new time step can be determined from the substrate temperature in the previous time step using

$$T_k^{n+1} = (T_w^{n+1} - T_w^n) \operatorname{erfc}\{z_1 / 2\sqrt{\beta t}\} + T_k^n \quad (116)$$

Equation (116) was used with the field data from the bedrock reach of the Lower Bull Run River to calibrate the model to the bedrock streambed temperature data at the Probe 5 site and compared to data and the 3-D calibrated model. The thermal diffusivity used in the analytical model which provided the smallest root mean square error (RMS) was  $5.565\text{E-}6 \text{ m}^2/\text{s}$ . The analytical model from Silliman et al. (1995) did not include the influx of solar radiation.

Table 72 shows the analytical model-data error statistics for five depths in the bedrock reach at the Probe 5 site. The table indicates there is reasonable model-data agreement for all depths and can be compared to the 3-D model-data error statistics in Table 45. Figure 130 through Figure 133 show time series bedrock temperature comparisons of the analytical model results, the data and the 3-D model results for two weeks. The figures show there is close agreement between the two models and the data at the surface but at deeper locations the analytical model has too much diurnal swing compared to the 3-D model results and data.

**Table 72: Analytical Model-data streambed temperature error statistics for Probe 5, bedrock.**

Depth, m	Number of Comparisons	ME <sup>1</sup> , °C	AME <sup>1</sup> , °C	RMS <sup>1</sup> , °C
0.00	2151	-0.11	0.19	0.29
0.20	2151	-0.08	0.69	0.84
0.40	2151	-0.21	0.74	0.90
0.80	2151	-0.02	0.66	0.84
1.00	2151	-0.13	0.67	0.84

<sup>1</sup>ME = Mean Error; AME = Absolute Mean Error; RMS = Root Mean Square Error.

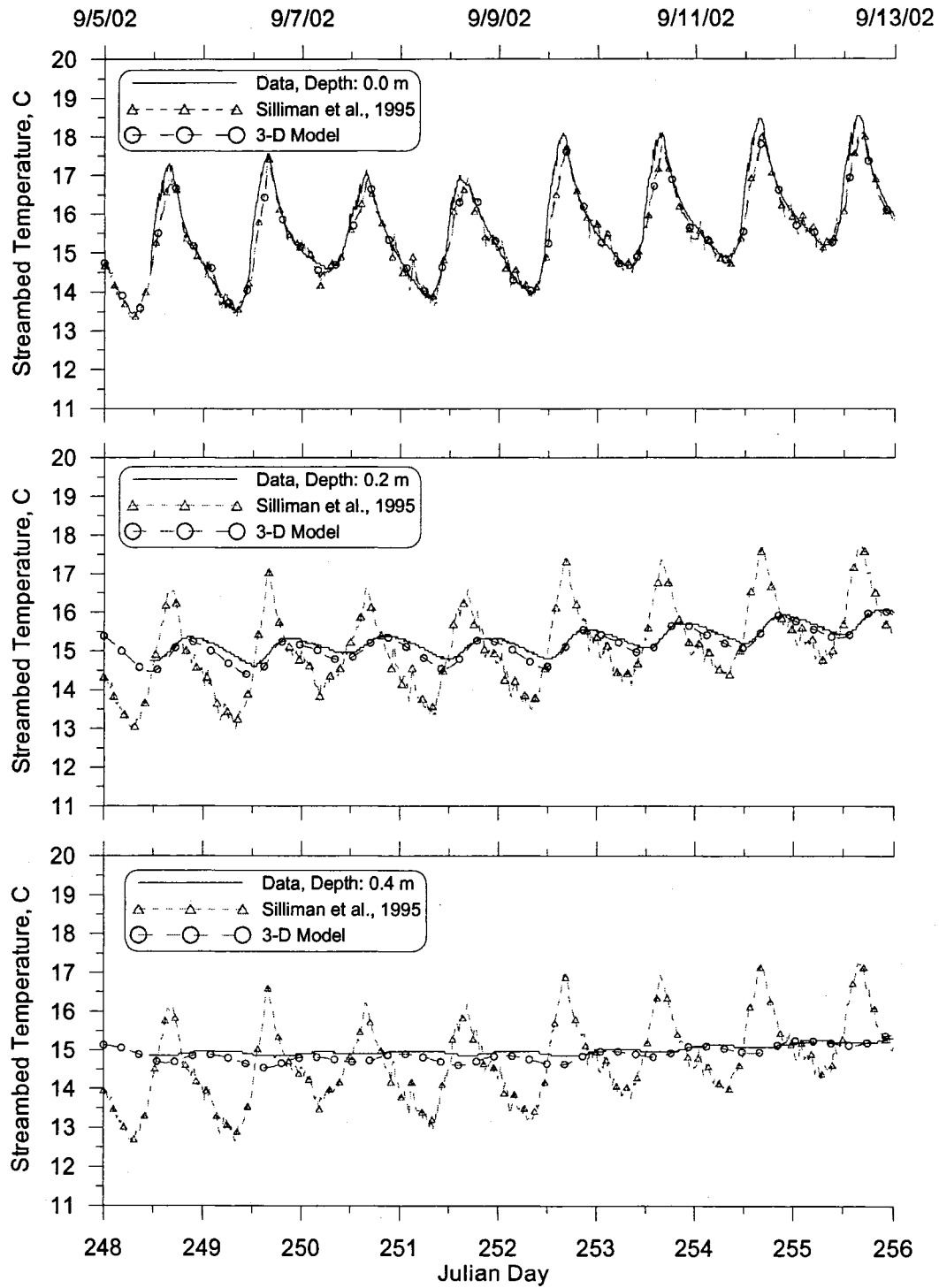
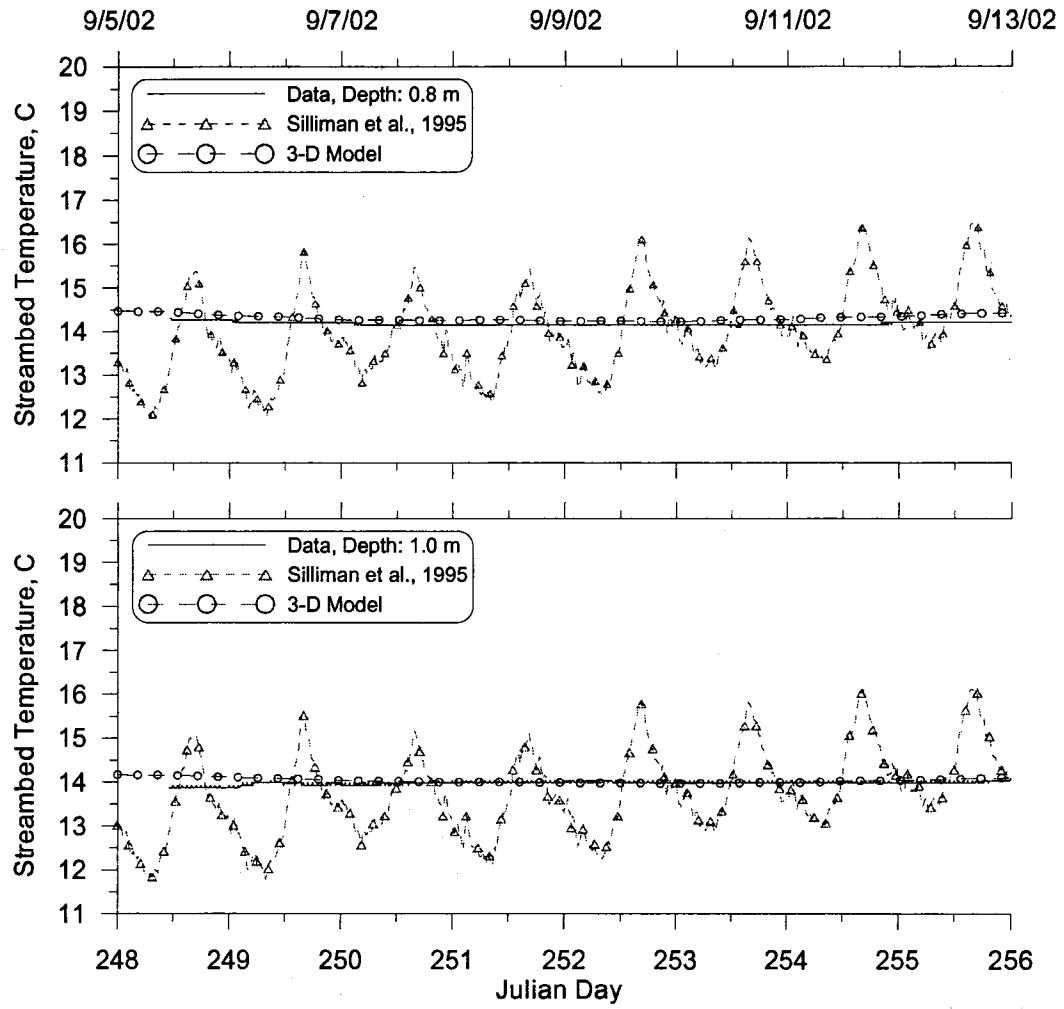
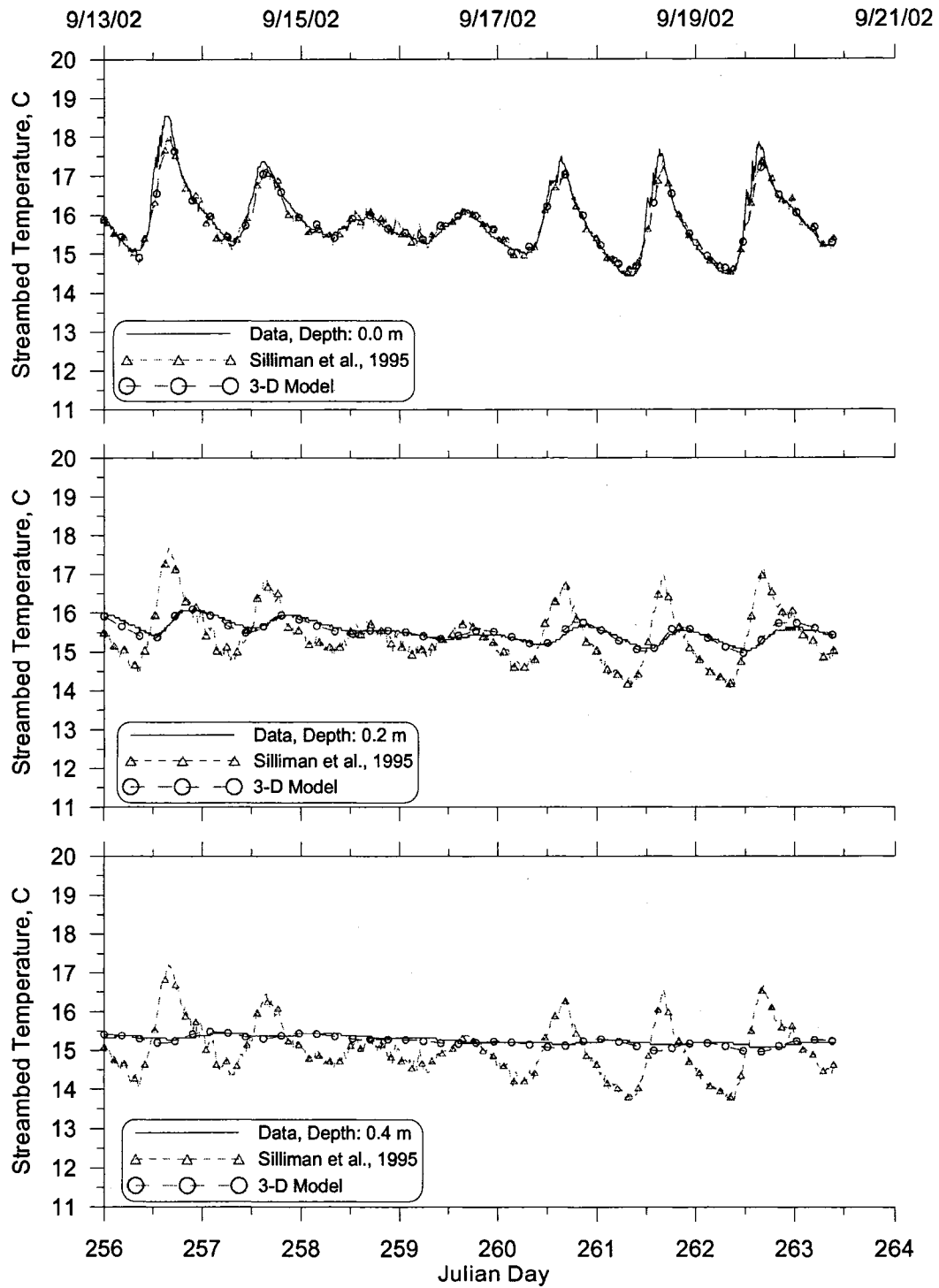


Figure 130: 3-D Model, Data, and Analytical Model temperature comparison, bedrock streambed, Probe 5, September 5<sup>th</sup> to 13<sup>th</sup> 2002, depths 0 to 0.4 m.



**Figure 131: 3-D Model, Data, and Analytical Model temperature comparison, bedrock streambed, Probe 5, September 5<sup>th</sup> to 13<sup>th</sup> 2002, depths 0.8 to 1.0 m.**



**Figure 132: 3-D Model, Data, and Analytical Model temperature comparison, bedrock streambed, Probe 5, September 13<sup>th</sup> to 21<sup>st</sup> 2002, depths 0 to 0.4 m.**

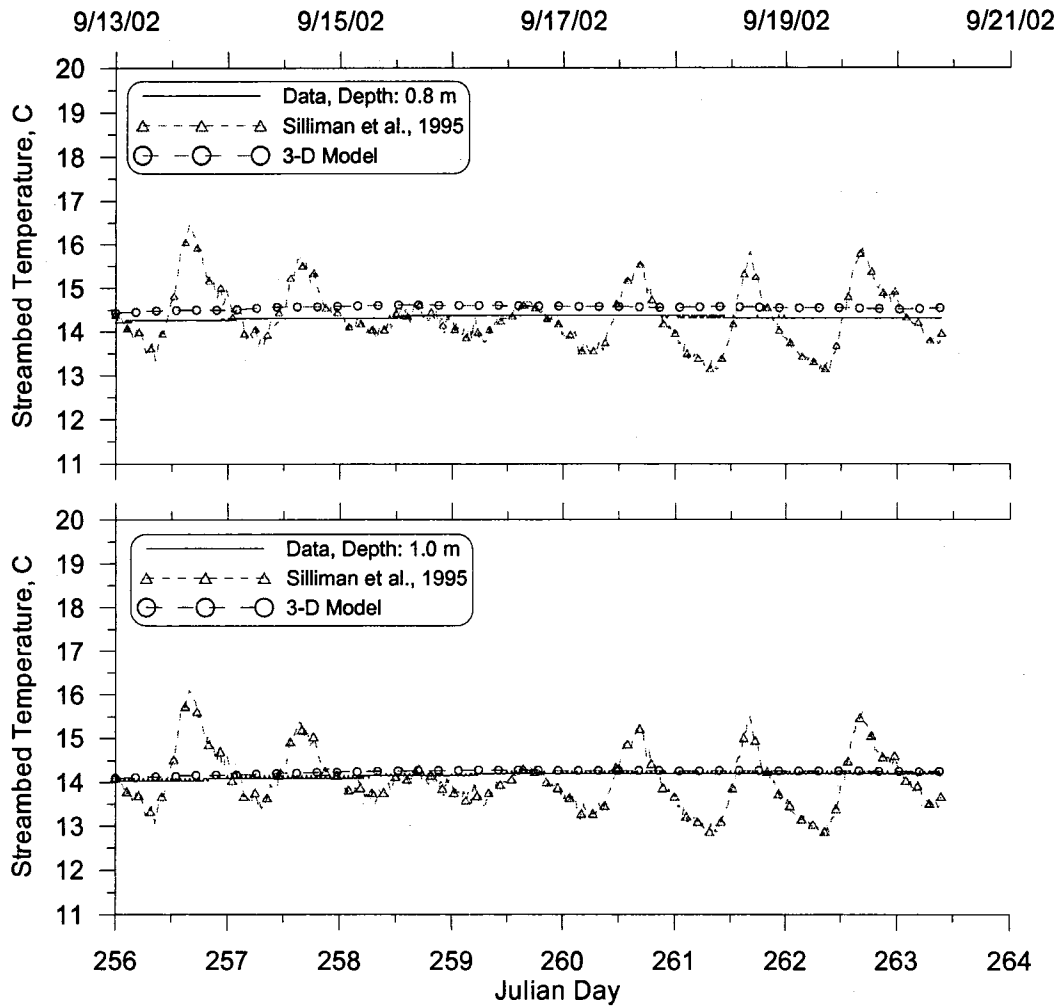


Figure 133: 3-D Model, Data, and Analytical Model temperature comparison, bedrock streambed, Probe 5, September 13<sup>th</sup> to 21<sup>st</sup> 2002, depths 0.8 to 1.0 m.

### 5.3.4 Comparison with 1-D Model, Bedrock

The 3-D Cartesian coordinate system model was compared to a 1-D model developed by Sinokrot and Stefan (1993) which was based on equations from Incropera and De Witt (1990). The 1-D heat transfer governing equation discussed in Sinokrot and Stefan (1993) can be written as

$$\frac{\partial T}{\partial t} = \beta \frac{\partial^2 T}{\partial z^2} \quad (117)$$

The model formulation includes an adiabatic boundary condition at the bottom described as

$$q = -\beta \left. \frac{\partial T}{\partial z} \right|_{z=\text{bottom}} = 0 \quad (118)$$

and the surface boundary condition consists of convection from the overlying water column described as

$$-\beta \left. \frac{\partial T}{\partial z} \right|_{z=0} = h \left. \frac{\partial T}{\partial z} \right|_{z=0} \quad (119)$$

where  $h$  (W/m<sup>2</sup>C) is the convective heat transfer coefficient. The model included no solar radiation input. The series of equations were developed into an implicit finite difference numerical scheme and solved using a tridiagonal matrix algorithm. The model calibration consisted of adjust the bedrock thermal diffusivity and the convection coefficient. Table 73 list the thermophysical characteristics used for the 1-D model and the 3-D model. The thermal diffusivity coefficient used for the 1-D model was 25% higher than the value corresponding to rock from the literature in Table 23 and Appendix C. The convection coefficient used was 6,500 W/m<sup>2</sup>C which provided the smallest root mean square error between the 1-D model and data.

Table 74 shows the 1-D model-data error statistics for five depths in the bedrock reach at the Probe 5 site. The table indicates there is good model-data agreement for all depths and can be compared to the 3-D model-data error statistics in Table 45. Figure 134 through Figure 137 show time series bedrock temperature

comparisons of the 1-D model results, the data and the 3-D model results for two weeks. The figures show there is close agreement between the two models and the data at all depths with the 1-D model slightly cooler than the data and 3-D model at a few depths.

**Table 73: Thermophysical characteristics of the bedrock substrate for 1-D and 3-D models**

Media	Density, $\rho_s$ , kg/m <sup>3</sup>	Specific Heat, $c_{ps}$ , kJ/kg°C	Thermal Diffusivity, $\beta$ , m <sup>2</sup> /s
3-D Model	2600.0	879.9	7.6923E-7 to 1.0989E-6
Sinokrot and Stefan (1993) Model	2600.0	879.9	1.3736E-6

**Table 74: 1-D Model-data streambed temperature error statistics for Probe 5, bedrock.**

Depth, m	Number of Comparisons	ME <sup>1</sup> , °C	AME <sup>1</sup> , °C	RMS <sup>1</sup> , °C
0.00	2151	-0.18	0.21	0.33
0.20	2151	-0.14	0.18	0.22
0.40	2151	-0.18	0.19	0.22
0.80	2151	0.09	0.10	0.13
1.00	2151	-0.03	0.06	0.08
<sup>1</sup> ME = Mean Error; AME = Absolute Mean Error; RMS = Root Mean Square Error.				

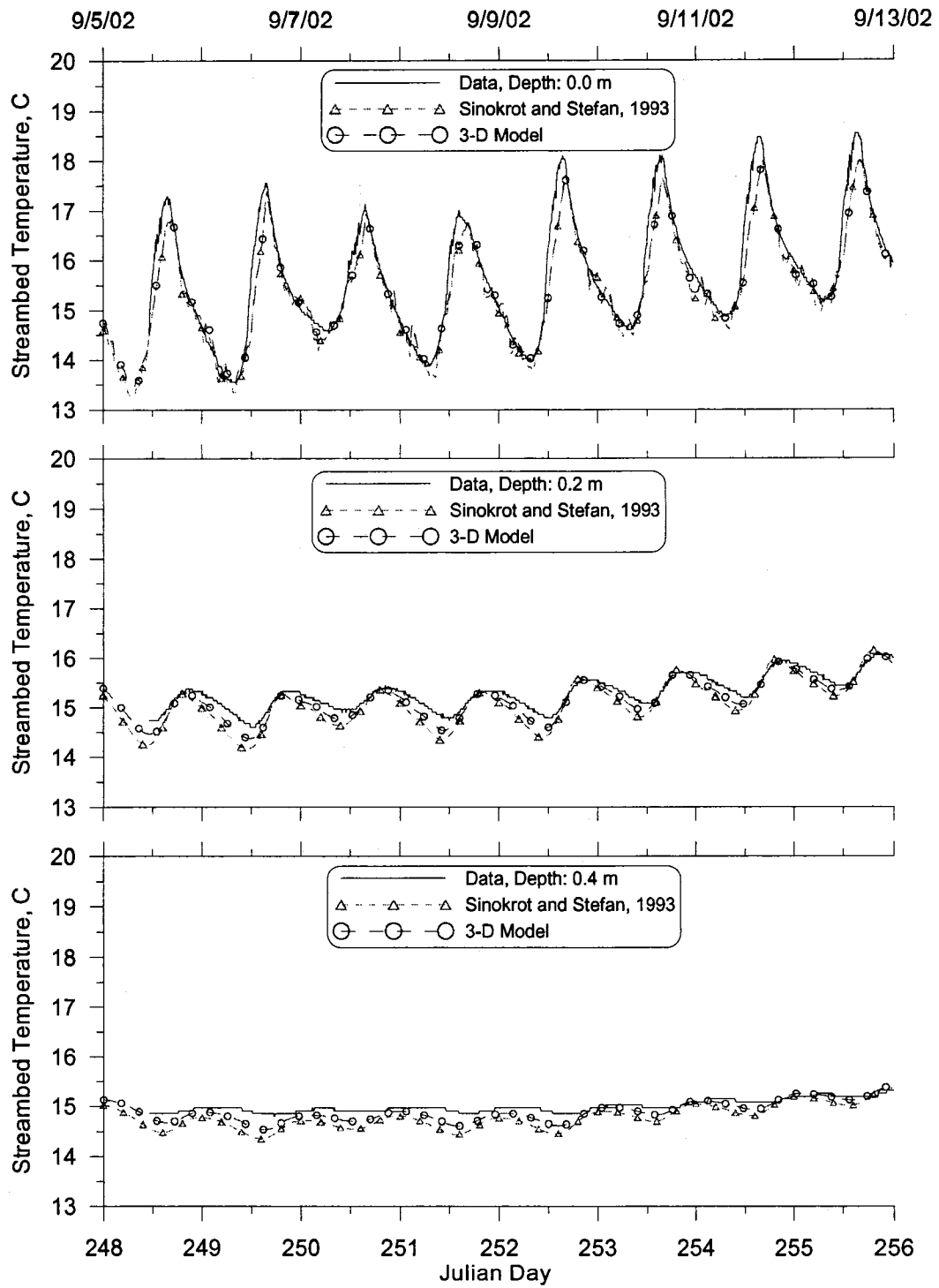


**Figure 134: 3-D Model, Data, and 1-D Model temperature comparison, bedrock streambed, Probe 5, September 5<sup>th</sup> to 13<sup>th</sup> 2002, depths 0 to 0.4 m.**

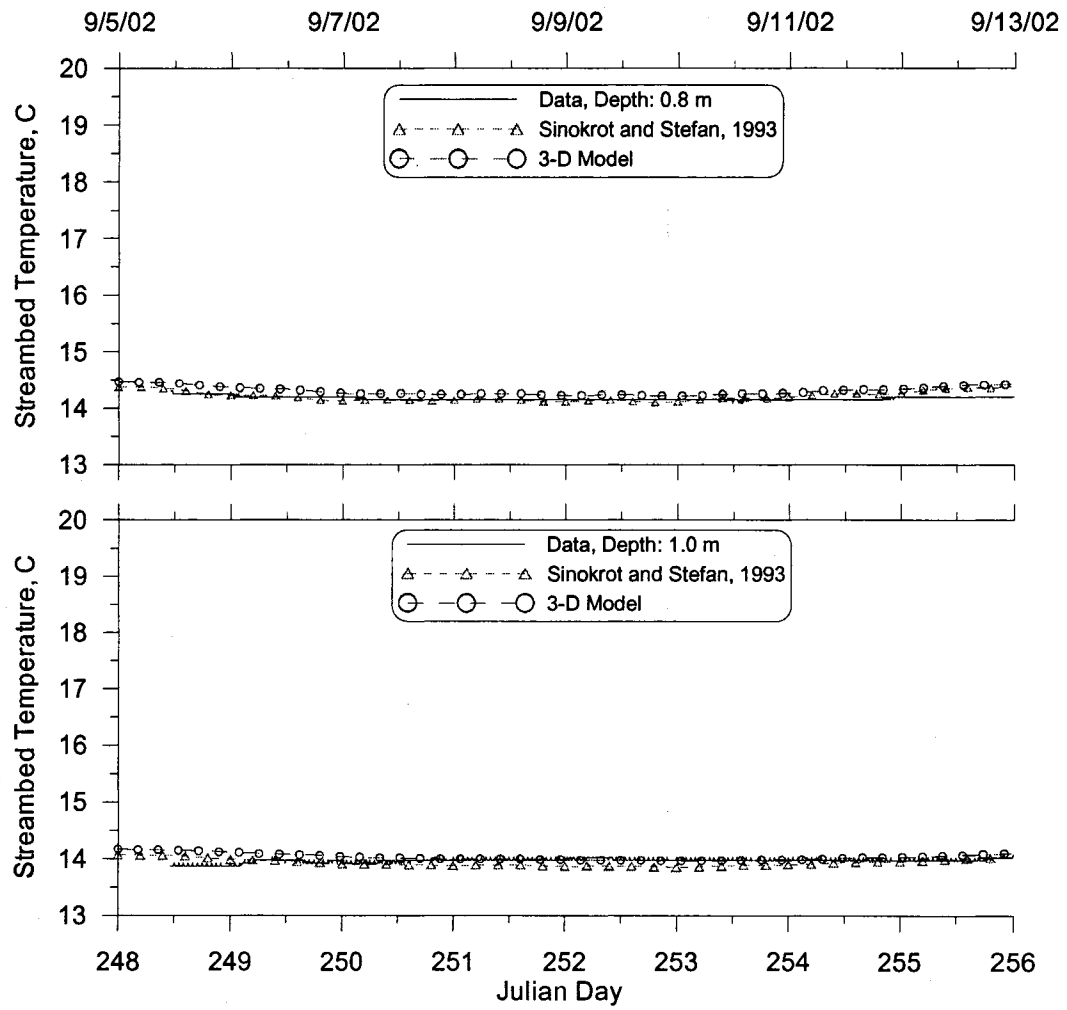


**Figure 135: 3-D Model, Data, and 1-D Model temperature comparison, bedrock streambed, Probe 5, September 5<sup>th</sup> to 13<sup>th</sup> 2002, depths 0.8 to 1.0 m.**

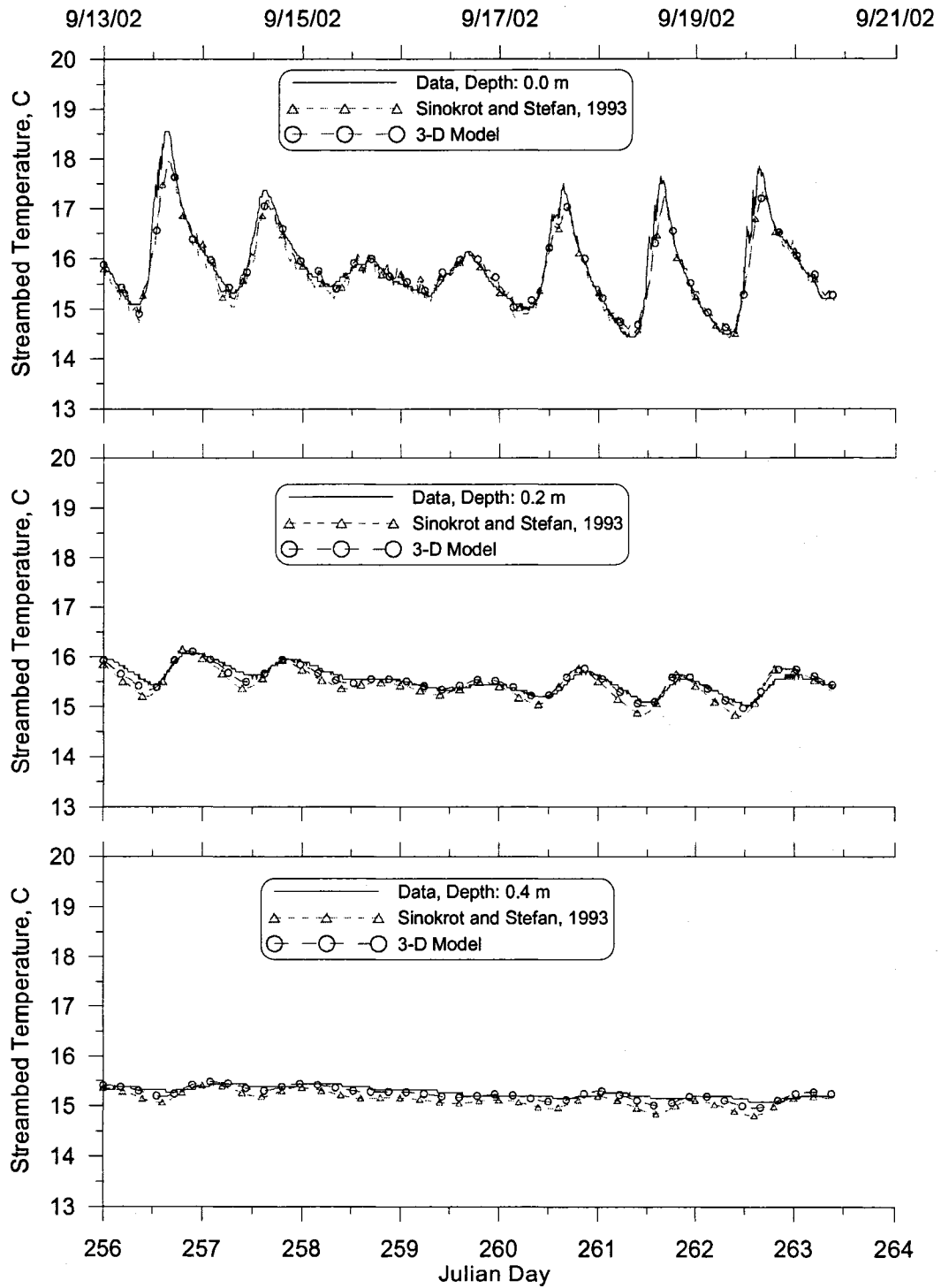


Figure 136: 3-D Model, Data, and 1-D Model temperature comparison, bedrock streambed, Probe 5, September 13<sup>th</sup> to 21<sup>st</sup> 2002, depths 0 to 0.4 m.

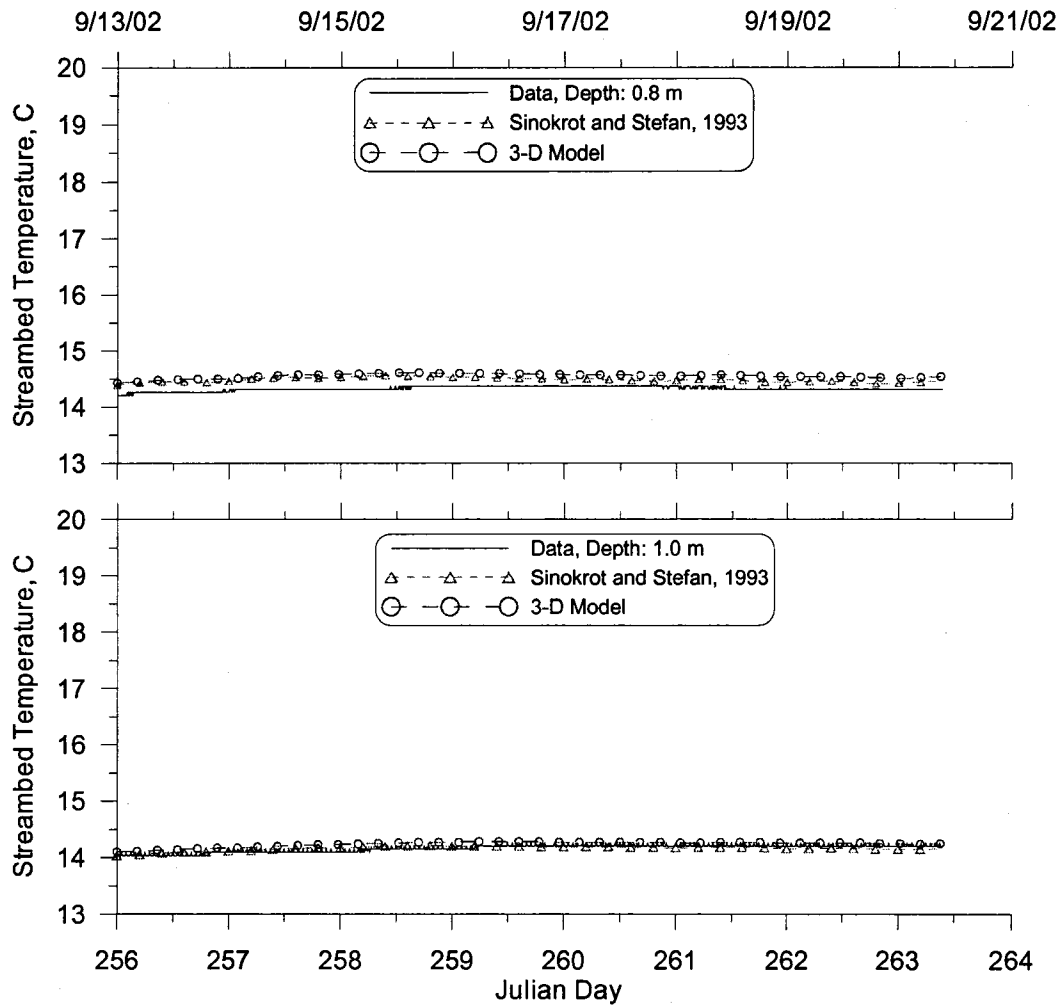


Figure 137: 3-D Model, Data, and 1-D Model temperature comparison, bedrock streambed, Probe 5, September 13<sup>th</sup> to 21<sup>st</sup> 2002, depths 0.8 to 1.0 m.

### 5.3.5 Summary

The model verification process showed the 3-D model compared with the 1-D model and analytical model results for the bedrock substrate. Differences were noted between the thermal diffusivity coefficients used between models which may be due to the analytical model and the 1-D model not incorporating the effects of solar radiation reaching the water-streambed interface. The 3-D model also compared well

with the analytical solution for a simple case scenario with different types of substrate. The grid resolution sensitivity analysis showed that a finer vertical grid resolution was needed near the surface to account for temperature changes accurately but a coarser grid was acceptable at larger depths. The model results were found to be relatively insensitive to changes in the horizontal grid resolution which may be due to the fact that the major heat forcings on the streambed are vertical. The bottom boundary condition was set at a depth of 20 m but could be moved to a depth of 13 m without influencing the model results at that depth. The bottom boundary could be moved to a shallower depth if the bottom model results are less important.

Both the model calibration and verification analyses indicate that the 3-D Cartesian and cylindrical coordinate system models are accurately predicting streambed temperatures over space and time.

#### **5.4 Implementation in CE-QUAL-W2**

The 3-D streambed model was considered for incorporation into CE-QUAL-W2 but the necessity of using a 3-D model instead of a 1-D model was investigated. The streambed temperature data collected in the field was reviewed to quantify the differences between lateral and vertical temperature gradients in the streambed. Table 75 listed the vertical and lateral temperature gradients for the two probe sites in the bedrock reach of the Lower Bull Run River. The table indicates the vertical temperature gradient is two orders of magnitude larger than the lateral temperature gradient.

**Table 75: Vertical and Lateral temperature gradients in the bedrock streambed.**

Start Date	End Date	Vertical Gradient °C/m		Lateral Gradient, °C/m
		Probe 5	Probe 4	Probe 5 to 4
09/05/2002	09/20/2002	-1.72	-2.12	0.01

A similar analysis was conducted with the streambed temperature data collected in the cobble reach. Table 76 lists the vertical, lateral and longitudinal temperature gradient in the cobble reach. The table indicates the vertical temperature gradient is one order of magnitude larger than the lateral or longitudinal temperature gradients. The differential between temperature gradients in the cobble reach is less than in the bedrock reach because the water temperature influences the streambed temperature in the cobble reach more strongly and the measurements were made only to a depth of 0.5 m.

**Table 76: Vertical and Lateral temperature gradients in the cobble streambed.**

Start Date	End Date	Vertical Gradient °C/m		Lateral Gradient, °C/m	Longitudinal Gradient, °C/m
		Probe 1	Probe 2 <sup>1</sup> & 3 <sup>2</sup>	Probe 2 to 1	Probe 3 to 1
08/07/2002	08/23/2002	-0.12	0.04 <sup>1</sup>	-0.04	
08/30/2002	09/05/2002	-0.10	-0.90 <sup>2</sup>		0.03

The streambed heating model of the bedrock reach was then used to investigate the magnitude of the vertical temperature gradient compared to the lateral temperature gradient by changing the model boundary condition temperatures on one river bank. The calibrated streambed model had left and right boundary condition temperatures set at 7.5 °C. Several model scenarios were run with the left boundary condition temperature fixed at 7.5 °C and the right boundary condition temperature increased to

8.5 °C, 10.5 °C, and 15.5 °C. Table 77 lists vertical and lateral temperature gradients from the model results. The table indicates the vertical temperature gradient is two orders of magnitude larger than the lateral temperature gradient.

**Table 77: Vertical and Lateral temperature gradients in the bedrock streambed model.**

Boundary Condition Temperatures, °C	Vertical Gradient °C/m (over 20 m)	Lateral Gradient, °C/m (over 41 m)
Left: 7.5, Right 7.5	0.41	0.005
Left: 7.5, Right 8.5	0.41	0.005
Left: 7.5, Right 10.5	0.41	0.005
Left: 7.5, Right 15.5	0.41	0.005

The review of the streambed monitoring data and the side boundary condition sensitivity model simulations indicate the vertical temperature gradient is much larger than the lateral or longitudinal temperature gradient. This indicates that implementing a 1-D model, ignoring the lateral and longitudinal temperature gradients, into CE-QUAL-W2 would be a good first step in integrating the streambed heating model with the surface water quality model without compromising the accuracy of the model results.

A 1-D version of the streambed heating algorithm was incorporated into the CE-QUAL-W2 model by providing an input file and modifying the model control file and source code model. The input file called "SBed.npt" was created to allow users to input to the model whether the streambed consisted of cobble or bedrock substrate and then provide the density, specific conductivity and thermal diffusivity of the streambed for each model segment. In addition the user specifies the fraction of solar radiation that reflects off the bottom of the streambed back into the water column for each segment. The water quality model control file (w2\_con.npt) was modified to

provide a switch to turn on or off the streambed heating model and provide the initial streambed temperature and boundary condition temperatures.

The 1-D streambed model was incorporated in the water quality model as a separate subroutine which was called when the model loops through the segments to calculate the heat and temperature. The subroutine calculates the heat flux in each layer of the grid which contributes to the wetted grid of the water quality model. The streambed temperature was calculated for all grid layers down to 13 m below the surface water model grid based on the sensitivity analysis of the streambed model grid to the bottom boundary condition. Results of the field data analyses and model calibration were also incorporated into the model such as the calculated light extinction coefficient from field measurements and the calibrated thermophysical properties of the bedrock and cobble substrate reach models. The 3-D model calibration of the cobble substrate model incorporated using 0.1% of the water temperatures to adjust the streambed temperature predictions to better match data. This calibration result, recognizing the importance of the water temperature in the diurnal changes in the cobble streambed temperature, was incorporated in the 1-D model implemented in CE-QUAL-W2.

The governing equations for the streambed heat transfer introduced in the 3-D model development were simplified to a 1-D model and used to model the temperature of the streambed above the water surface, below the water surface and below the water-streambed interface as illustrated in Figure 138.

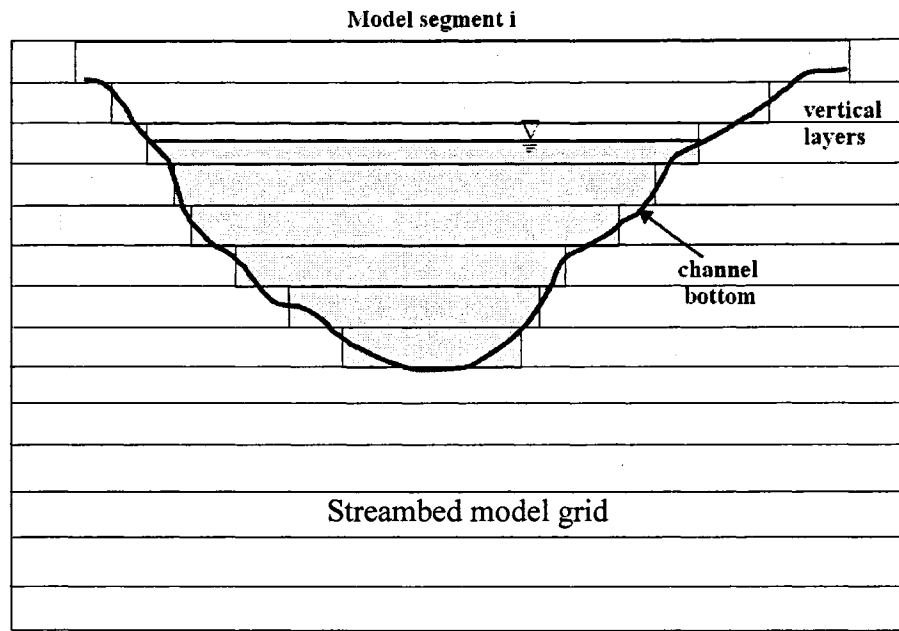


**Figure 138: Streambed model grid with CE-QUAL-W2 model grid, looking downstream**

Streambed temperature model predictions above the water line incorporated the effects of direct solar radiation on the substrate and heat exchange with the air. Below the water line the effects of the attenuated solar radiation and heat exchange with the water were included in calculating the streambed temperatures. Below the water-streambed interface the streambed temperatures were simulated as a simple 1-D model.

### **5.5 Sensitivity Analysis**

A sensitivity analysis was conducted of the streambed heat model in CE-QUAL-W2 using a modified version of the 10.5 km (6.5 mile) Lower Bull Run River developed by Annear et al. (1999). The model was modified to use a reduced channel slope to decrease computation time. The model used meteorological data from 2002

and a light extinction from field data. Most of the sensitivity simulations were run using no vegetative or topographic shade to allow for as much direct solar as possible. Sensitivity simulations were run with vegetative and topographic shade characteristics developed from Annear et al. (1999). The models were run for 46 days from August 5<sup>th</sup> to September 20<sup>th</sup>, 2002 (Julian days 217 to 263) using constant flows of 0.28 to 1.56 m<sup>3</sup>/s (10 to 55 cfs) for each simulation.

### **5.5.1 Sensitivity to Flow Rates**

The first sensitivity analysis examined the effects of different flow rates on the magnitude of streambed heating for the same substrate material. Five simulations were run, each with a different flow rate, no shade, and bedrock substrate with the streambed heating model. The results of these models were compared with the results from five models with no streambed heating at two locations in the Lower Bull Run River (RM 4.88 and RM 0.33). Table 78 lists the volume weighted water temperature at RM 4.88 for simulations with and with the streambed heating model. The last column in the table lists the difference in volume weighted temperatures between the two model simulations for the same flow rate. The results in the table indicate that for lower flows there is slight increase in the volume-weighted temperature when using the streambed heating model and for higher flows there is an even smaller decrease.

**Table 78: Volume-weighted water temperatures at RM 4.88 over the model simulation period with and without a streambed heating model.**

Flow, ft <sup>3</sup> /s	Flow, m <sup>3</sup> /s	Volume-Weighted Water Temperature with No Streambed Heating Model, °C	Volume-Weighted Water Temperature with Streambed Heating Model, °C	Volume-Weighted Water Temperature Difference, °C
55.0	1.56	16.10	16.07	-0.03
40.0	1.13	16.13	16.12	-0.01
30.0	0.85	16.10	16.12	0.03
20.0	0.57	16.09	16.12	0.03
10.0	0.28	15.95	16.02	0.07

The daily minimum and maximum water temperatures were then compared for each pair of simulations (with and without streambed heating model) for the same flow rate. Table 79 shows the average difference between the daily minimum and maximum water temperatures in the river at two locations for the simulation with and without the streambed heating model. The table shows that at RM 4.88 that as flow rate decreases the average difference in the daily minimum temperatures increases. The difference in daily minimum temperatures at RM 0.33 shows no pattern in differences between the daily minimum temperatures at this location. The table also indicates there is a relatively consistent decrease in the daily maximum temperatures at RM 4.88 but at RM 0.33 as the flow decreases the difference in the average daily maximum temperatures increases from -0.19 to 0.24 °C. The different results from the two sites may be due to differences in the channel morphology, travel time and exposure to atmospheric conditions moving downstream.

**Table 79: Daily minimum and maximum water temperature model results for various constant flows with and without a streambed heating model.**

River Substrate	Flow, ft <sup>3</sup> /s	Flow, m <sup>3</sup> /s	RM 4.88		RM 0.33	
			Temporal Average Difference in Water Temperature (WT) with Streambed Heating Model - No Streambed Heating Model			
			Daily Minimum WT, °C	Daily Maximum WT, °C	Daily Minimum WT, °C	Daily Maximum WT, °C
100% Bedrock	55.0	1.56	0.09	-0.24	0.10	-0.19
	40.0	1.13	0.08	-0.13	0.09	-0.12
	30.0	0.85	0.13	-0.17	0.27	-0.06
	20.0	0.57	0.16	-0.14	0.28	0.06
	10.0	0.28	0.24	-0.14	0.03	0.24

Continuous temperatures and daily minimum and maximum temperatures were compared between simulations with and without the streambed heating model. Figure 139 shows a time series plot of the continuous temperature at RM 4.88 when there is a constant flow of 0.85 m<sup>3</sup>/s (30 cfs). The figure indicates there are only small differences between the water temperature results with the streambed heating model (SBH) and without the SBH model. Figure 140 shows a time series of the daily minimum and maximum temperature for the two models at a flow of 0.85 m<sup>3</sup>/s. The figure shows the daily maximum temperatures are consistently lower with the SBH model and the daily minimums are warmer with the SBH model. Figure 141 shows continuous temperature time series plot at RM 0.33 when there is a constant flow of 0.85 m<sup>3</sup>/s. The figure shows there are only minor differences between the two model runs. Figure 142 shows a time series of the daily minimum and maximum temperature for the two models at a flow of 0.85 m<sup>3</sup>/s at RM 0.33. The figure shows the daily minimum temperatures are higher with the SBH model and the daily maximums are slightly less with the SBH model.

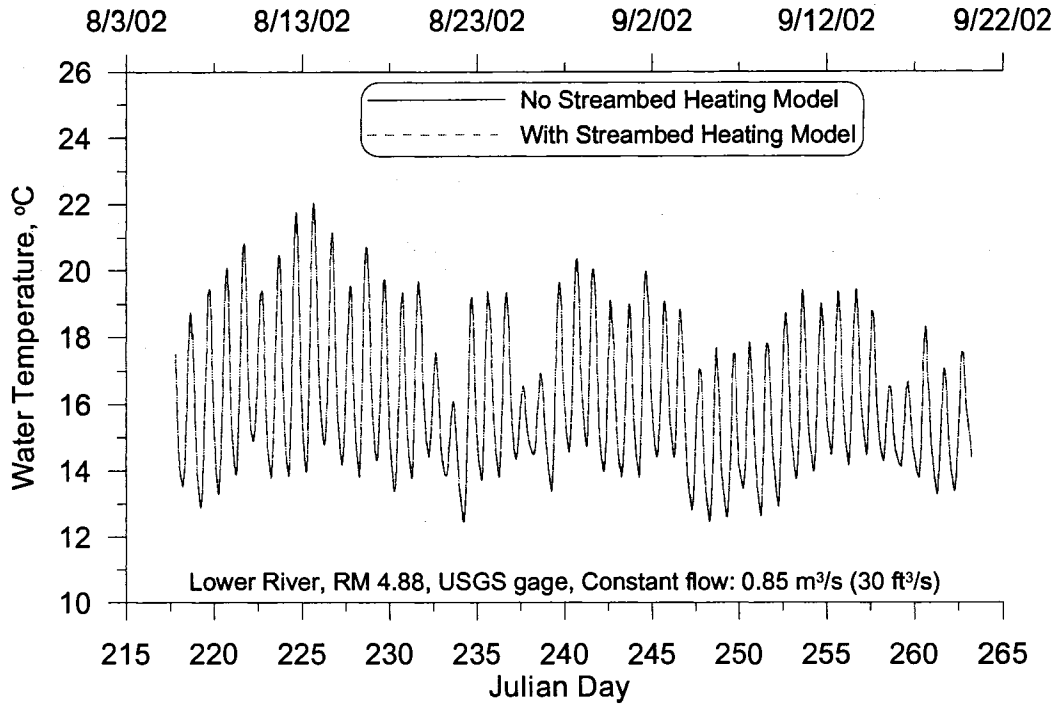


Figure 139: Continuous water temperatures at RM 4.88, comparing model results at a constant flow of 0.85 m<sup>3</sup>/s (30 cfs) with and without a streambed heating model.

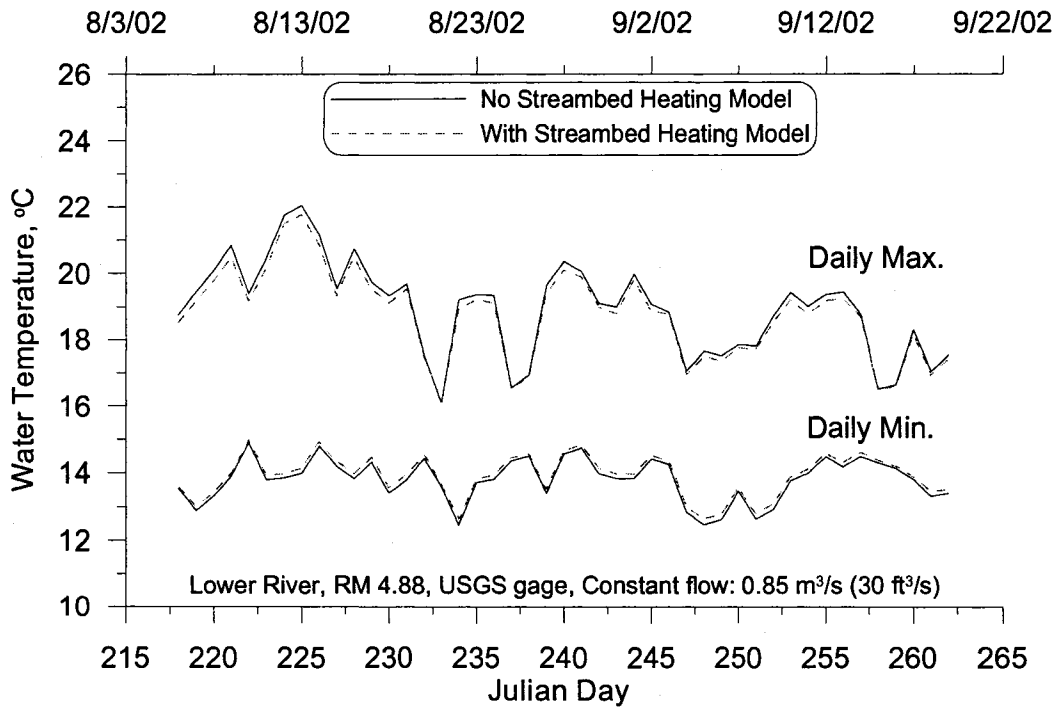


Figure 140: Daily minimum and maximum water temperatures at RM 4.88, comparing model results at a constant flow of 0.85 m<sup>3</sup>/s (30 cfs) with and without a streambed heating model.

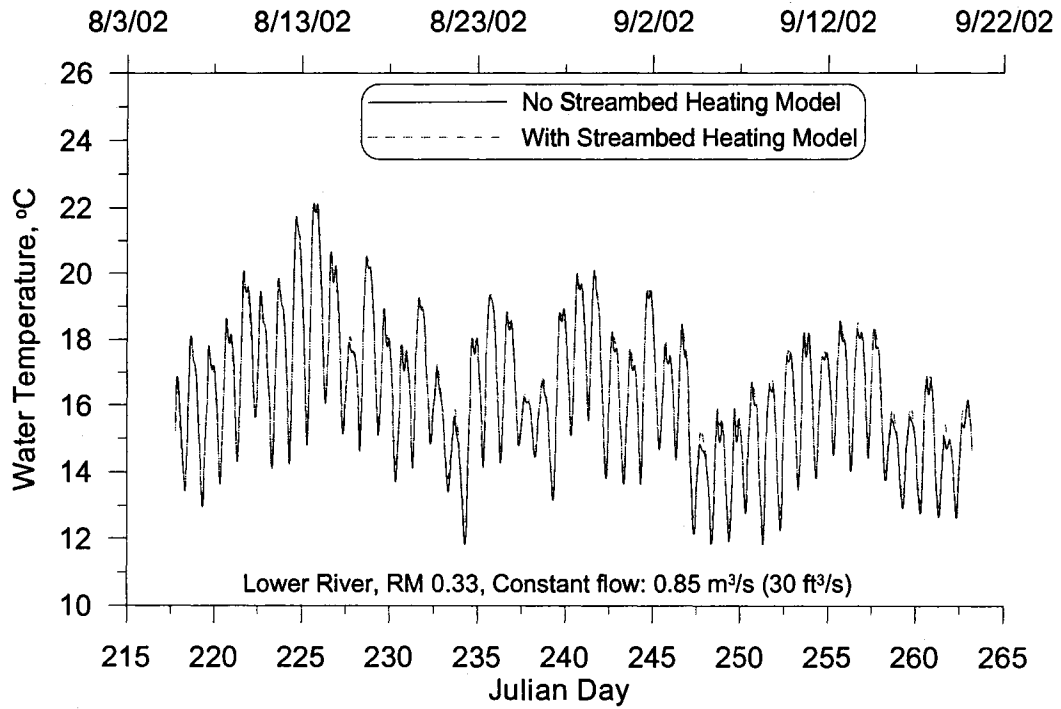


Figure 141: Continuous water temperatures at RM 0.33, comparing model results at a constant flow of 0.85 m<sup>3</sup>/s (30 cfs) with and without a streambed heating model.

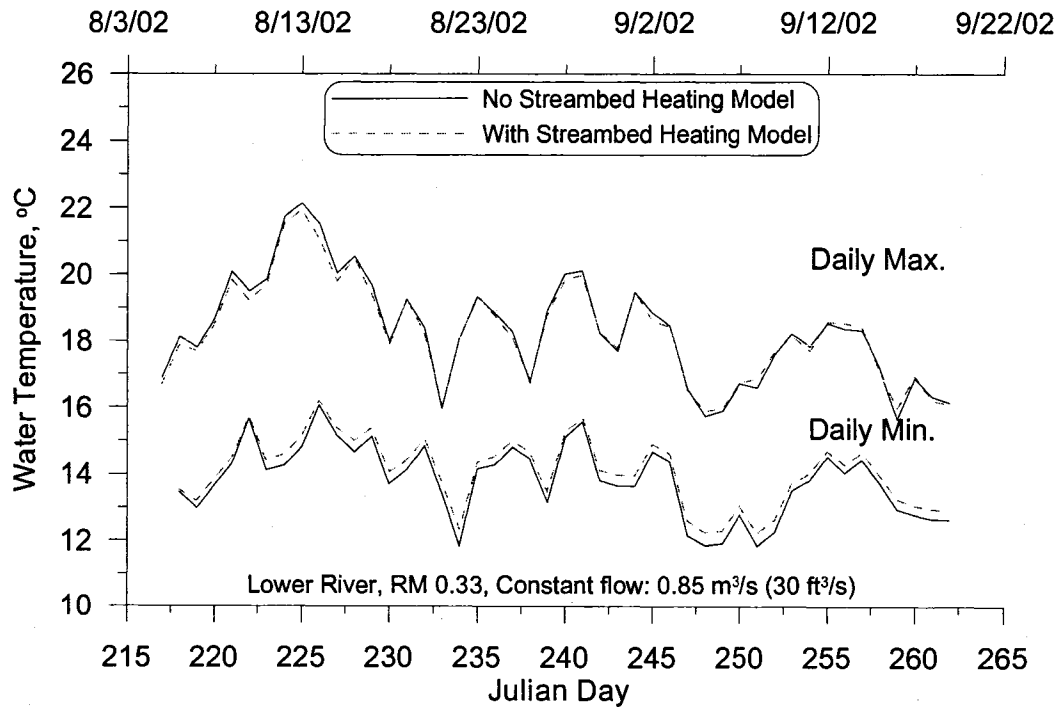


Figure 142: Daily minimum and maximum water temperatures at RM 0.33, comparing model results at a constant flow of 0.85 m<sup>3</sup>/s (30 cfs) with and without a streambed heating model.

Figure 143 shows a time series plot of the continuous temperature at RM 4.88 when there is a constant flow of  $0.57 \text{ m}^3/\text{s}$  (20 cfs). The figure indicates there are small differences between the water temperatures with the SBH model and without the SBH model. The figure also show larger diurnal temperature swings than the model with a flow of  $0.85 \text{ m}^3/\text{s}$  (30 cfs). Figure 144 shows a time series of the daily minimum and maximum temperature for the two models at this lower flow. The figure shows a consistent decrease in daily maximum temperatures and an increase in the daily minimum temperatures with the SBH model. Figure 145 shows continuous temperature time series at RM 0.33 when there is a constant flow of  $0.57 \text{ m}^3/\text{s}$ . The figure shows there are minor differences between the two model runs. Figure 146 shows a time series of the daily minimum and maximum temperature for the two models at RM 0.33 for the lower flow. The figure shows the daily minimum temperatures are higher and the daily maximums are slightly less with the SBH model.

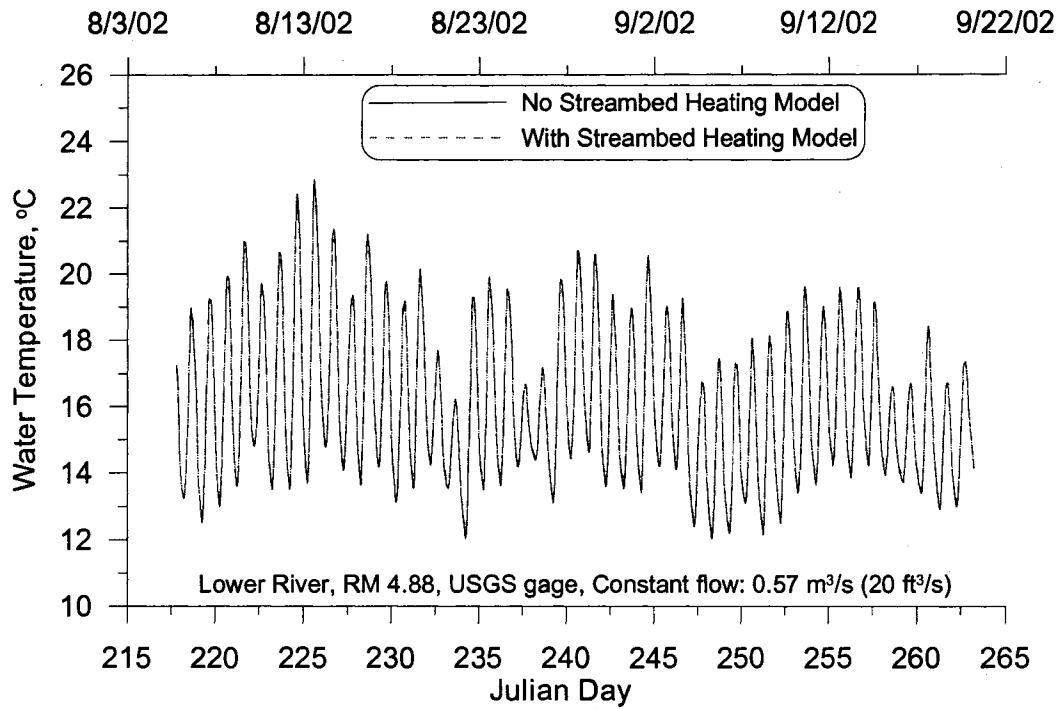


Figure 143: Continuous water temperatures at RM 4.88, comparing model results at a constant flow of 0.57 m<sup>3</sup>/s (20 cfs) with and without a streambed heating model.

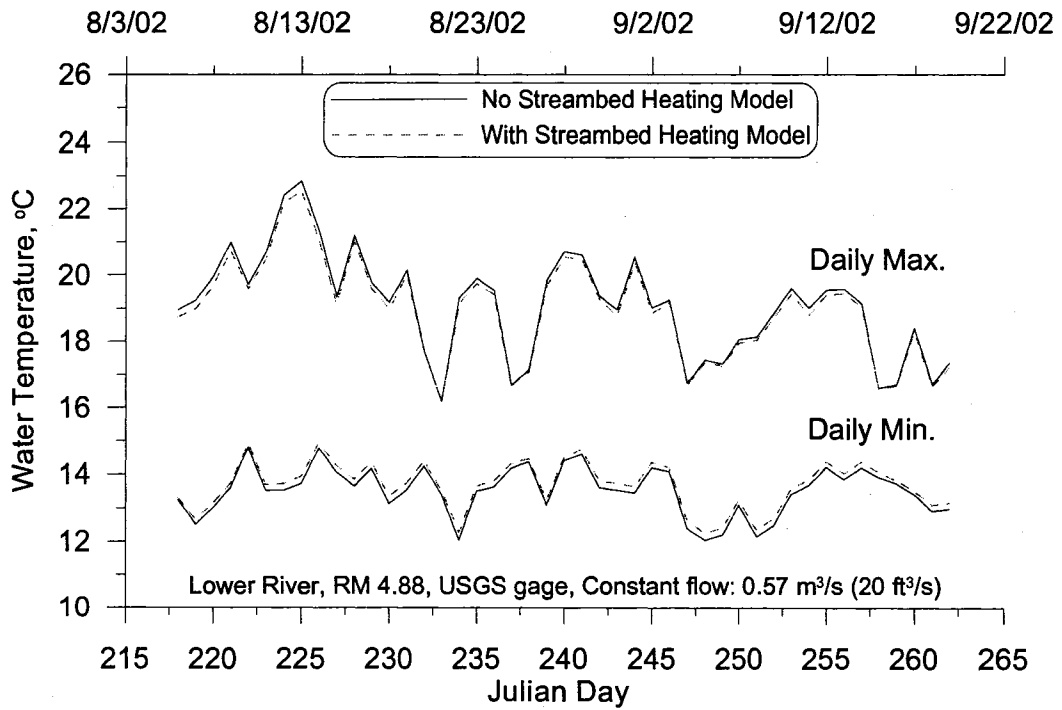
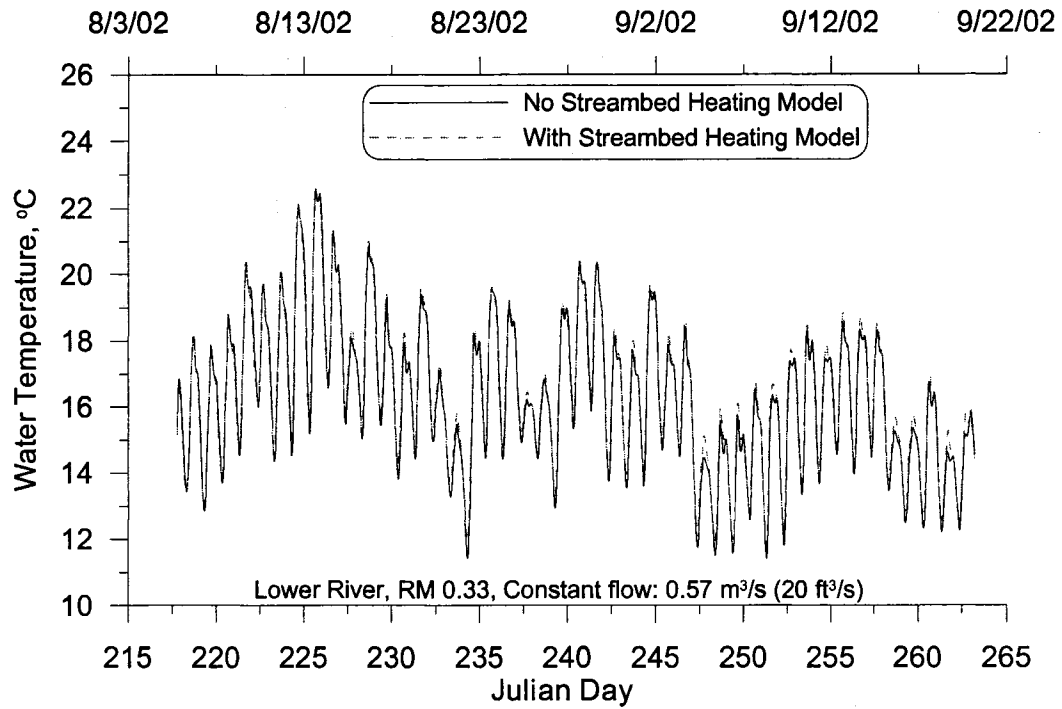
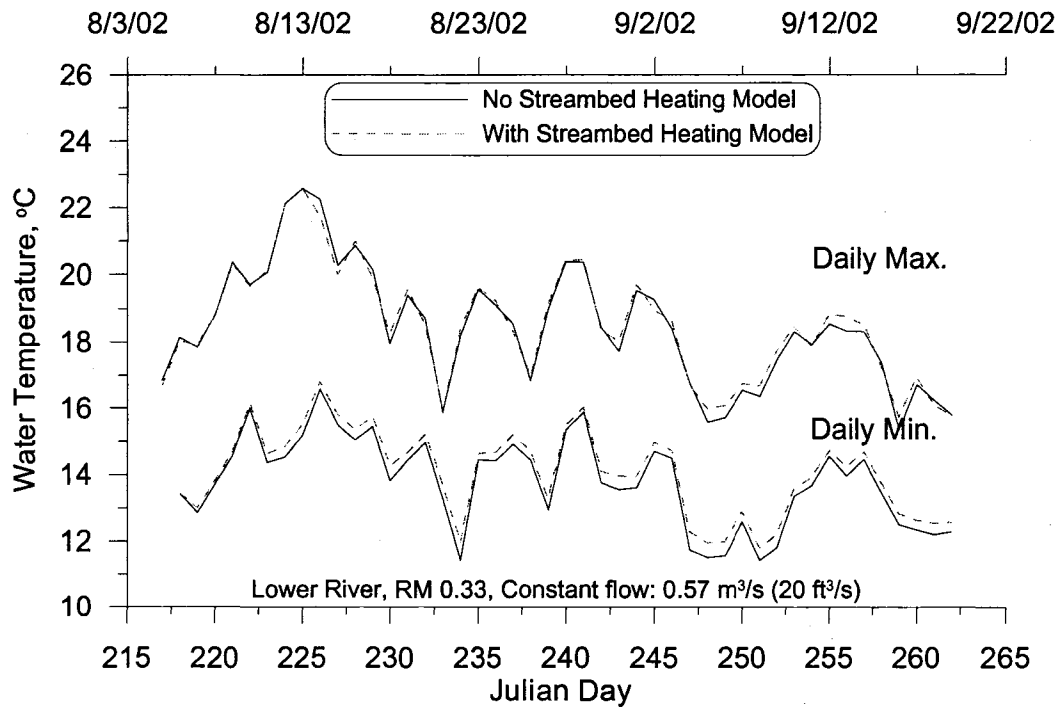


Figure 144: Daily minimum and maximum water temperatures at RM 4.88, comparing model results at a constant flow of 0.57 m<sup>3</sup>/s (20 cfs) with and without a streambed heating model.



**Figure 145: Continuous water temperatures at RM 0.33, comparing model results at a constant flow of 0.57 m<sup>3</sup>/s (20 cfs) with and without a streambed heating model.**



**Figure 146: Daily minimum and maximum water temperatures at RM 0.33, comparing model results at a constant flow of 0.57 m<sup>3</sup>/s (20 cfs) with and without a streambed heating model.**

Figure 147 shows a time series plot of the continuous temperature at RM 4.88 at a constant flow of  $0.28 \text{ m}^3/\text{s}$  (10 cfs). The figure indicates there are small differences between the water temperatures with and without the SBH model. The continuous temperatures show a larger diurnal swings than the model with a flow of  $0.57 \text{ m}^3/\text{s}$  (20 cfs). Figure 148 shows a time series of the daily minimum and maximum temperature for the two models. The figure shows a consistent decrease in daily maximum temperatures and an increase in the daily minimum temperatures with the SBH model. Figure 149 shows continuous temperature time series at RM 0.33 when there is a constant flow of  $0.28 \text{ m}^3/\text{s}$ . The figure shows there are minor differences between the two model runs. Figure 150 shows a time series of the daily minimum and maximum temperature for the two models at RM 0.33. The figure shows the daily minimum temperatures are higher during some of the time and at or slightly below the model results without SBH model. The figures also show there is an increase in the daily maximum temperatures with the SBH model compared without the SBH model. This may be due to the channel morphology and the longer travel time of water at this location, allowing the water to warm up more during the day. The river flow of  $0.28 \text{ m}^3/\text{s}$  results in a wetted river width of 20 m with a water depth of 1.4 m at RM 0.33. The upstream location (RM 4.88) has a much narrower width 2-5 m with a depth of only 0.50 m. This results in a larger surface area at RM 0.33 for incoming solar radiation and slower moving water.

Figure 151 shows the continuous water temperature at RM 4.88 for the three flow rates from September 28<sup>th</sup> to 30<sup>th</sup>, 2002. The figure shows that for decreasing

flows there are larger diurnal temperature swings. The figure also indicates the temperature impacts due to streambed heating are primarily focus on the daily maximum and minimum time periods.

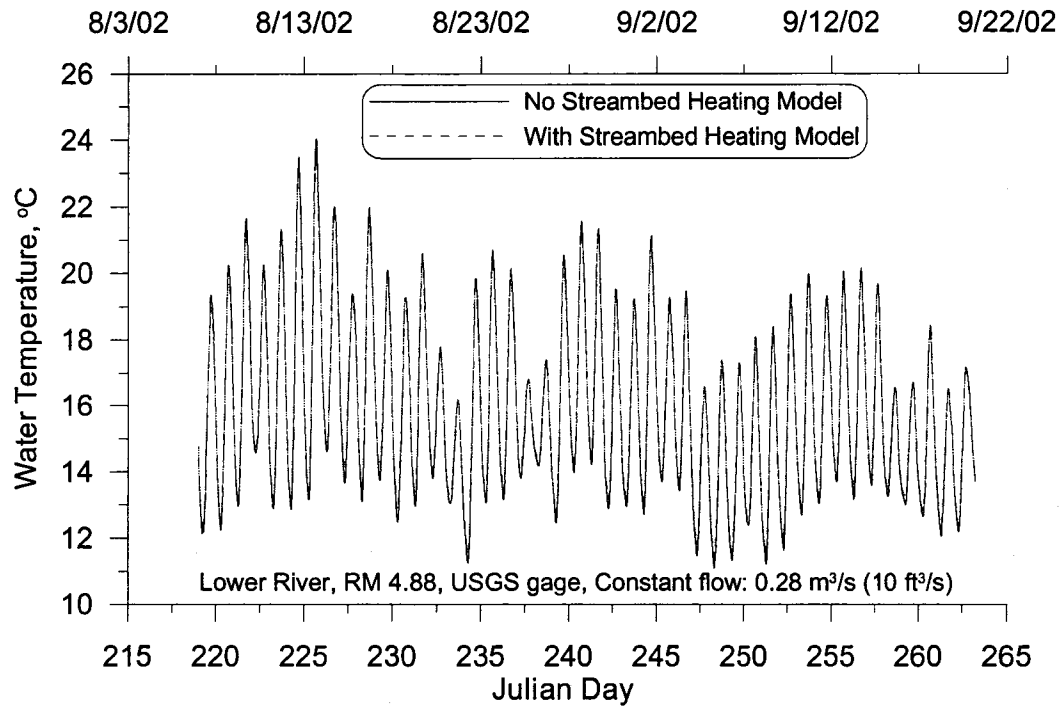


**Figure 147: Continuous water temperatures at RM 4.88, comparing model results at a constant flow of 0.28 m<sup>3</sup>/s (10 cfs) with and without a streambed heating model.**

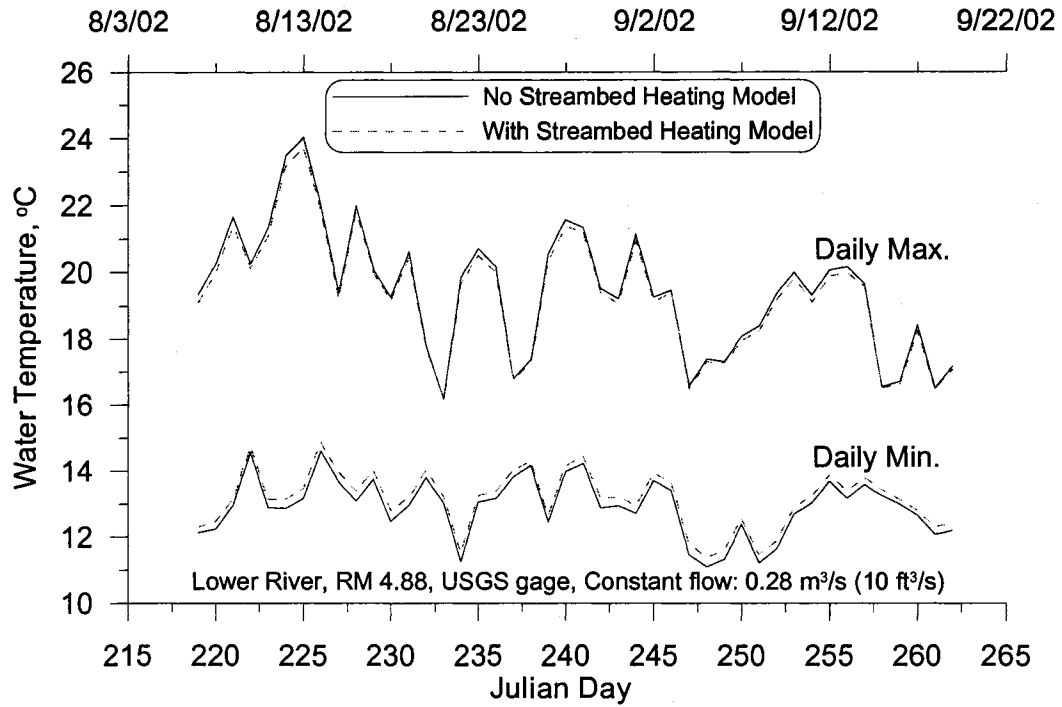


Figure 148: Daily minimum and maximum water temperatures at RM 4.88, comparing model results at a constant flow of 0.28 m<sup>3</sup>/s (10 cfs) with and without a streambed heating model.

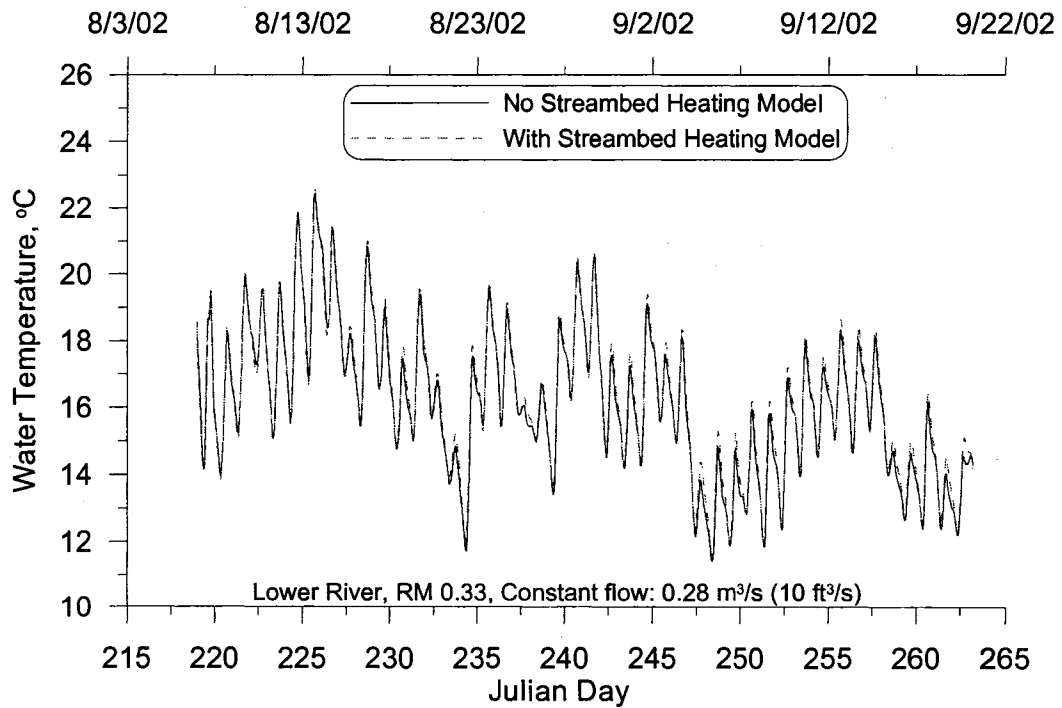
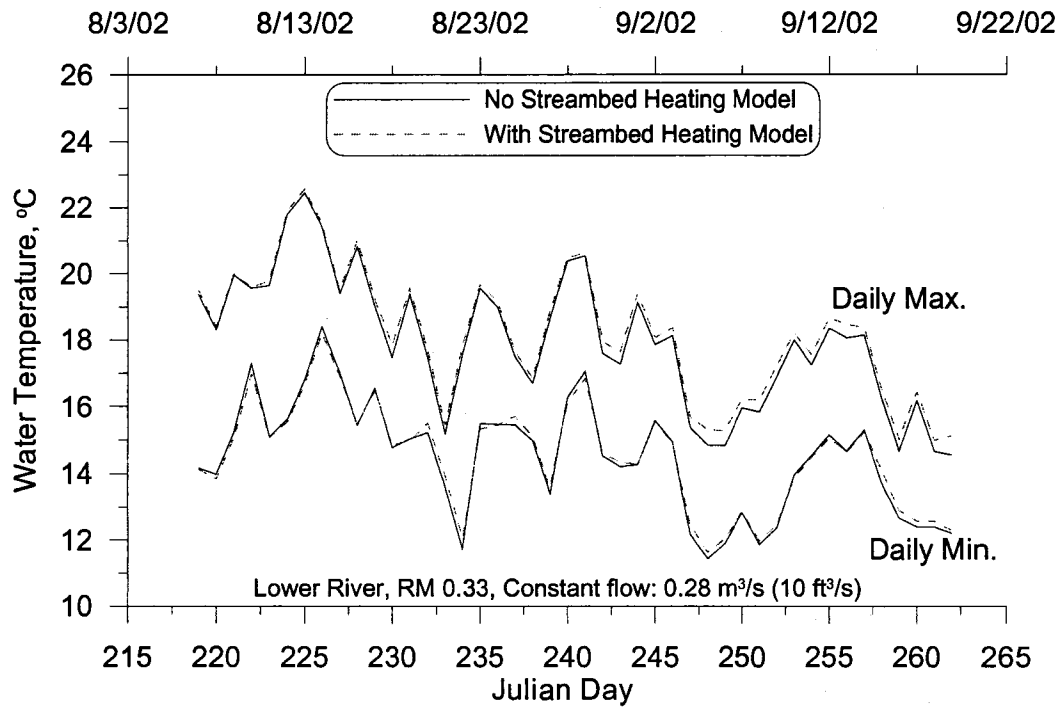
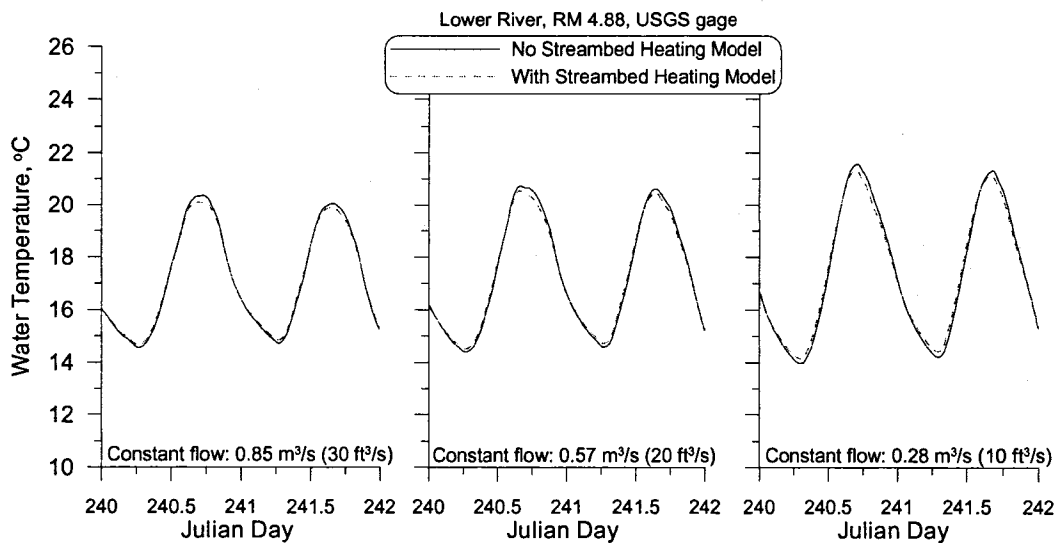


Figure 149: Continuous water temperatures at RM 4.88, comparing model results at a constant flow of 0.28 m<sup>3</sup>/s (10 cfs) with and without a streambed heating model.



**Figure 150: Daily minimum and maximum water temperatures at RM 0.33, comparing model results at a constant flow of 0.28 m<sup>3</sup>/s (10 cfs) with and without a streambed heating model.**



**Figure 151: Continuous water temperatures at RM 4.88, comparing model results at constant flow rates with and without a streambed heating model.**

### 5.5.2 Sensitivity to Substrate Types

The next sensitivity investigated the impacts of different streambed substrates in the streambed heating model. River flows were set constant at 0.85, 0.57 or 0.28 m<sup>3</sup>/s (30, 20 or 10 cfs). Substrate types were varied between 100% bedrock and 100% cobble along the length of the 10.5 km river model. Similar to the previous analysis, the average difference in the daily minimum and maximum water temperatures between the models with and without the SBH model were compared. Table 80 lists the average differences in the daily minimum and maximum water temperature predictions between the two models for the various substrates and flow rates at two locations along the river.

The results in the table indicate that at RM 4.88 there is an increase in the daily minimums and a decrease in the daily maximums for 100% bedrock substrate but for simulations with varying amounts of cobble characterizing the substrate the daily minimums are increased only slightly and the daily maximums are increased as well. This may be due to the way the cobble substrate is modeled by incorporating 0.1% of the water temperature to calculate the streambed temperature diurnal cycle. It should also be noted that RM 4.88 is only 25% of the way downstream from the start of the model. The segments identified with a cobble substrate were spread across the whole model domain so there may be limited impact from the cobble substrate by RM 4.88. The results for the site at RM 0.33 show a similar pattern once cobble is used to characterize the substrate. Both the daily minimum and maximum were warmer for the simulations with 25% to 100% cobble characterizing the streambed. Daily

minimum and maximum temperature for both sites show there is no difference between having 25% cobble or 100% cobble characterizing the streambed. The results also indicate there may be an increasing influences moving downstream when there is cobble substrate. The temperature differences for the daily minimum and maximum water temperatures increases from RM 4.88 to 0.33.

Figure 152 and Figure 153 shows time series of the daily maximum and minimum temperatures for model simulations with 100% bedrock substrate, 100% cobble substrate along the river and no SBH model at RM 4.88 and RM 0.33, respectively. River flows were kept constant at  $0.28 \text{ m}^3/\text{s}$  (10 cfs). Figure 152 indicates the bedrock substrate results in warmer minimum temperatures than the cobble substrate or no SBH model. The daily maximum water temperatures are also lower compared to the other models at RM 4.88. Figure 153 shows there are instances when the daily minimum temperatures at RM 0.33 are warmer with the cobble substrate than the bedrock substrate. There are also instances when the cobble substrate results in cooler daily maximum temperatures than the bedrock substrate.

**Table 80: Daily minimum and maximum water temperature model results for various constant flows and varying substrates with and without a streambed heating model.**

River Substrate	Flow, ft <sup>3</sup> /s	Flow, m <sup>3</sup> /s	RM 4.88: Temporal Average Difference in Water Temperature (WT) with Streambed Heating Model - No Streambed Heating Model			RM 0.33: Temporal Average Difference in Water Temperature (WT) with Streambed Heating Model - No Streambed Heating Model		
			Daily Minimum WT, °C	Daily Maximum WT, °C	Substrate at RM 4.88	Daily Minimum WT, °C	Daily Maximum WT, °C	Substrate at RM 0.33
100% bedrock	30.0	0.85	0.13	-0.17	Bedrock	0.27	-0.06	Bedrock
	20.0	0.57	0.16	-0.14		0.28	0.06	
	10.0	0.28	0.24	-0.14		0.03	0.24	
75% bedrock, 25% cobble	30.0	0.85	0.03	0.02	Bedrock	0.16	0.09	Cobble
	20.0	0.57	0.02	0.05		0.24	0.13	
	10.0	0.28	0.02	0.08		0.17	0.19	
50% bedrock, 50% cobble	30.0	0.85	0.03	0.02	Bedrock	0.16	0.09	Cobble
	20.0	0.57	0.02	0.05		0.24	0.13	
	10.0	0.28	0.02	0.08		0.17	0.19	
25% bedrock, 75% cobble	30.0	0.85	0.03	0.02	Cobble	0.16	0.09	Bedrock
	20.0	0.57	0.02	0.05		0.24	0.13	
	10.0	0.28	0.02	0.08		0.17	0.19	
100% cobble	30.0	0.85	0.03	0.02	Cobble	0.16	0.09	Cobble
	20.0	0.57	0.02	0.05		0.24	0.13	
	10.0	0.28	0.02	0.08		0.17	0.19	

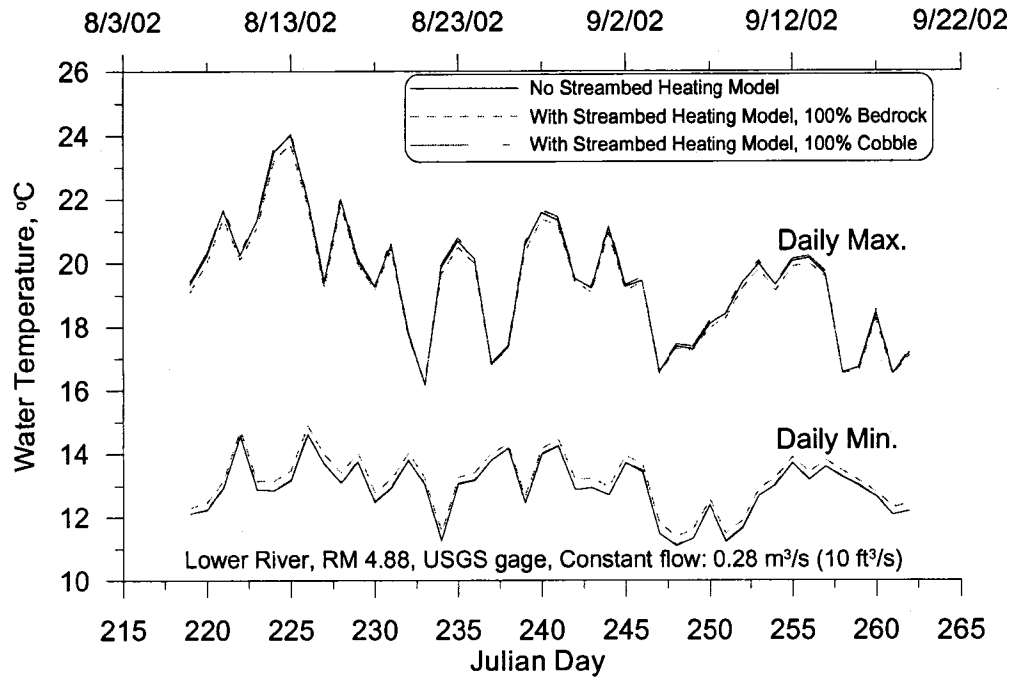


Figure 152: Daily minimum and maximum water temperatures at RM 4.88, comparing model results at a constant flow of 0.28 m<sup>3</sup>/s (10 cfs) and different types of substrate with and without a streambed heating model.

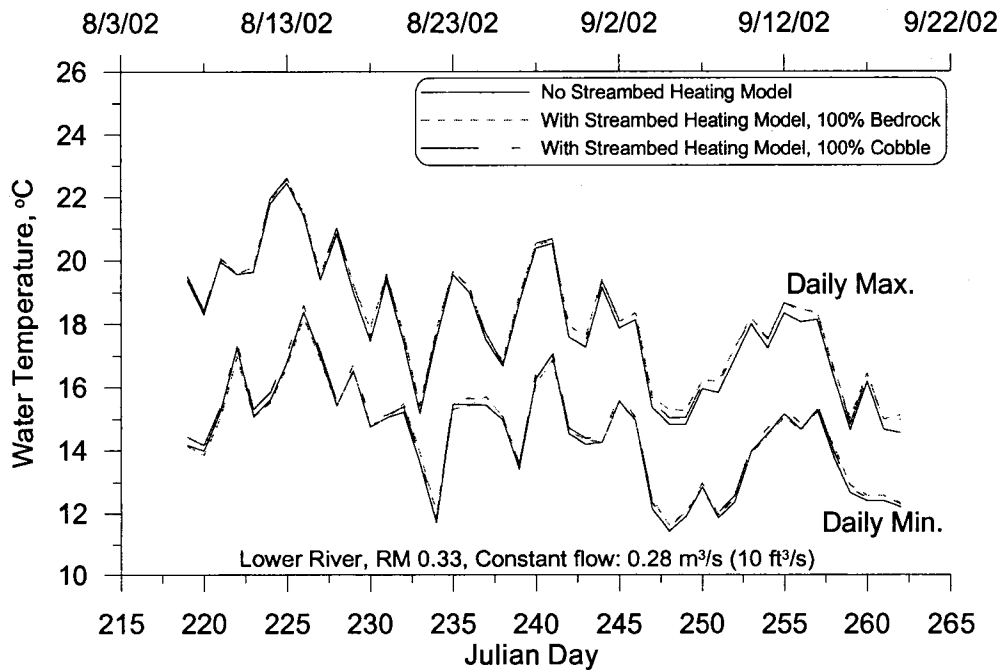


Figure 153: Daily minimum and maximum water temperatures at RM 0.33, comparing model results at a constant flow of 0.28 m<sup>3</sup>/s (10 cfs) and different types of substrate with and without a streambed heating model.

The heat flux between the streambed and water were analyzed for the flows and substrate types presented in Table 80. Table 81 lists the temporal average over the simulation period of the daily average, minimum and maximum streambed heat fluxes for the three flow rates, five substrate types and two sites along the river. A positive heat flux represents heat transfer from the streambed to the water column and a negative heat flux represents heat transfer from the water to the streambed. The daily maximum heat flux corresponds to the time of day when the daily minimum temperatures occur, between 5 and 7 am. The daily minimum heat flux corresponds to the time of day when daily maximum temperatures occur, between 2:30 and 5:30 pm. The table indicates temporal average of the daily average fluxes at RM 4.88 decreases with decreasing river flows across all substrates. A similar relationship holds a RM 0.33 for decreasing flows but the temporal average of daily average streambed heat flux decreases to  $-0.1 \text{ W/m}^2$  and stays constant for different flows. The decrease in heat transfer from the water to the streambed based on the average heat flux may be due to a decrease in surface area between the water and streambed for decreasing river flows. The decrease in heat exchange surface area may also be responsible for decreases in the temporal averages of the daily minimum and maximum streambed heat fluxes for lower flows. Although the model simulations have varied substrate types between 100% bedrock and 100% cobble along the 10.5 km river the model segments specified as having a cobble or bedrock substrate were spread across the river system. As a result although the overall river may have had 50% bedrock and 50% cobble substrate RM 4.88 had had bedrock substrate and RM 0.33 had cobble

substrate as shown in columns 7 and 11 in the table. The substrate type at the river location where the streambed heat fluxes were output from the model is directly responsible for the magnitude of the fluxes. For example, RM 0.33 has bedrock substrate at this site for two sets of simulations (100% bedrock and 25% bedrock for the whole river) which have daily minimum and maximum heat fluxes that are three to twenty times higher than simulations when there is cobble substrate at RM 0.33. The same relationship holds at RM 4.88. If the model scenarios with 100% bedrock and 100% cobble substrates (which ensures the substrates at RM 4.88 and 0.33 are the same) are compared both sites show a decrease in streambed heat fluxes for decreasing flows and when switching from bedrock to cobble substrate. The more conductive solid bedrock material results in larger streambed heat fluxes compared to less conductive and diverse cobble substrate. Although there may be higher streambed heat fluxes at a specific site in the river because the local substrate is bedrock this does not seem to influence the river temperature much at that location. Table 81 indicates there is no difference in daily minimum and maximum water temperatures at either location once cobble substrate is incorporated into the model when comparing the same flow rates.

**Table 81: Temporal averages of daily streambed heat fluxes for different substrates and flow rates.**

River Substrate	Flow, ft <sup>3</sup> /s	Flow, m <sup>3</sup> /s	RM 4.88, Temporal Averages of Streambed Heat Flux				RM 0.33, Temporal Averages of Streambed Heat Flux			
			Daily Ave., W/m <sup>2</sup>	Daily Min., W/m <sup>2</sup>	Daily Max., W/m <sup>2</sup>	Substrate at RM 4.88	Daily Ave., W/m <sup>2</sup>	Daily Min., W/m <sup>2</sup>	Daily Max., W/m <sup>2</sup>	Substrate at RM 0.33
100% bedrock	30.0	0.85	-5.0	-63.0	41.8	Bedrock	-8.7	-43.1	33.9	Bedrock
	20.0	0.57	-4.9	-67.2	47.6		-8.5	-47.0	34.2	
	10.0	0.28	-1.6	-25.5	18.9		-5.2	-39.7	27.5	
75% bedrock, 25% cobble	30.0	0.85	-5.0	-63.9	42.7	Bedrock	-0.1	-15.0	12.3	Cobble
	20.0	0.57	-4.9	-68.5	48.8		-0.1	-5.0	3.1	
	10.0	0.28	-1.6	-26.0	19.4		-0.1	-2.2	1.2	
50% bedrock, 50% cobble	30.0	0.85	-5.1	-64.6	43.3	Bedrock	-0.1	-15.0	12.5	Cobble
	20.0	0.57	-4.9	-69.6	49.8		-0.1	-5.0	3.2	
	10.0	0.28	-1.6	-26.5	19.8		-0.1	-2.2	1.2	
25% bedrock, 75% cobble	30.0	0.85	-0.2	-22.3	19.9	Cobble	-8.8	-43.5	34.7	Bedrock
	20.0	0.57	-0.1	-7.5	5.6		-8.5	-47.1	35.1	
	10.0	0.28	0.0	-1.2	1.0		-5.1	-38.5	25.9	
100% cobble	30.0	0.85	-0.1	-22.6	20.2	Cobble	-0.1	-15.0	13.0	Cobble
	20.0	0.57	-0.1	-7.6	5.9		-0.1	-5.0	3.3	
	10.0	0.28	0.0	-1.3	1.0		-0.1	-2.1	1.1	

### 5.5.3 Sensitivity to Dynamic Shading

Two sets of simulations were conducted to investigate the influence of streamside vegetative and topographic shading on the streambed heating model results. Both vegetative and topographic shade reduced the effective solar radiation striking the water surface, penetrating the water and striking the streambed. The river model was run with all of the substrate characterized by bedrock and the flow was kept constant at three different rates. One set of model simulations compares the effects of full solar (i.e. no shading) on the daily minimum and maximum water temperature with and with the SBH model. The other set used the same flow and substrate characteristics but also used the vegetative and topographic shade used in the calibrated Lower Bull Run River model (Annear et al., 1999). Table 82 lists the model results comparing no shade with vegetative and topographic shade effects on water temperature predictions using the SBH model. The results in the table indicate the shading results in cooler daily minimum and maximum temperatures than without the shading but there is still an influence from the streambed heating at both RM 4.88 and RM 0.33. The daily minimum temperatures at RM 4.88 are still increased with the SBH model and shading just not as much with full solar. The daily maximums are decreased even further with the shading and streambed heating. The RM 0.33 site shows an increase in daily minimum temperatures with full solar and less of an increase or a decrease once shade is introduced. The daily maximum temperatures at RM 0.33 also show less of an increase with shading present. Figure 154 shows a time

series of the daily minimum and maximum temperatures at RM 4.88 for a river flow of 0.28 m<sup>3</sup>/s (10 cfs) with and without the SBH model and both with shade from vegetation and topography. The figure shows similar results with daily minimum temperatures increased and daily maximum temperatures decrease when using the streambed heating model, even with shade.

**Table 82: Daily minimum and maximum water temperature model results for various constant flows and effective shade with and without a streambed heating model.**

Substrate	Vegetative and Topographic Shade	Flow, ft <sup>3</sup> /s	Flow, m <sup>3</sup> /s	RM 4.88		RM 0.33	
				Temporal Average Difference in Water Temperature (WT) with Streambed Heating Model - No Streambed Heating Model			
				Daily Minimum WT, °C	Daily Maximum WT, °C	Daily Minimum WT, °C	Daily Maximum WT, °C
100% Bedrock	No	30.0	0.85	0.13	-0.17	0.27	-0.06
		20.0	0.57	0.16	-0.14	0.28	0.06
		10.0	0.28	0.24	-0.14	0.03	0.24
100% Bedrock	Yes	30.0	0.85	0.10	-0.19	0.10	-0.17
		20.0	0.57	0.12	-0.20	0.01	0.05
		10.0	0.28	0.18	-0.20	-0.03	0.05

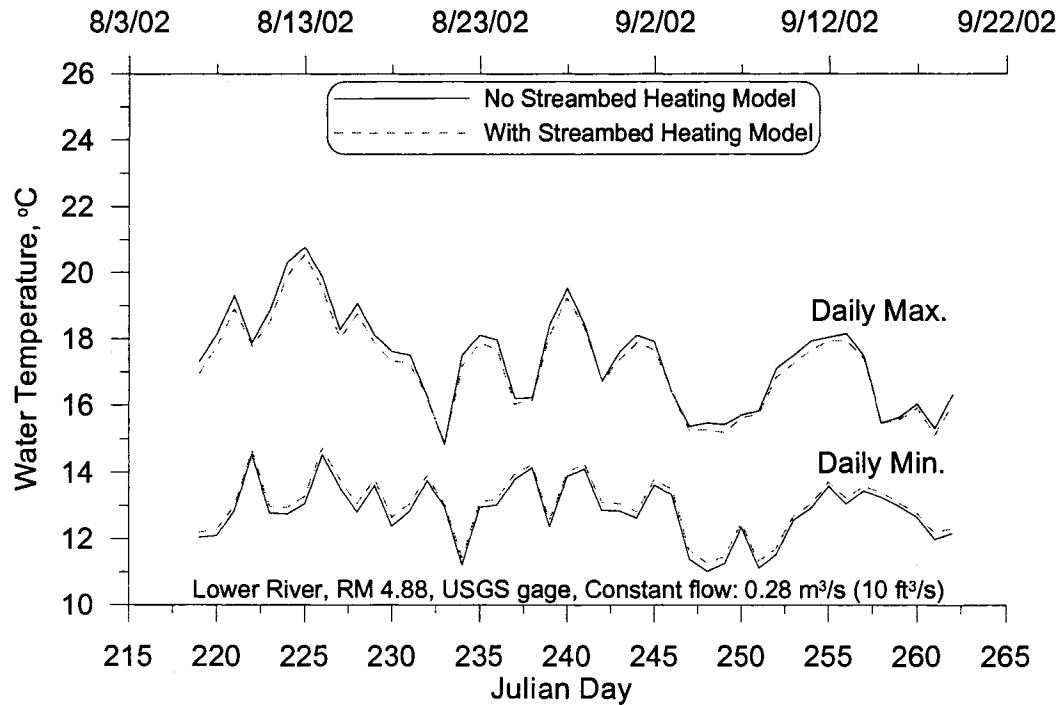


**Figure 154: Daily minimum and maximum water temperatures at RM 4.88, comparing model results at a constant flow of 0.28 m<sup>3</sup>/s (10 cfs) incorporating vegetative and topographic shading with and without a streambed heating model.**

### 5.5.4 Dynamic Streambed Heating Guidelines

The sensitivity analysis showed that lower stream flows resulted in lower streambed heat fluxes but these heat fluxes have more influence on the daily minimum and maximum water temperatures with the largest influence with a bedrock substrate. A streambed with cobble substrate reduced the local streambed heating and reduced the impact on water temperatures across the river. Vegetative and topographic shade decreased the effective solar radiation striking the river and reduced the streambed heating impact on the daily minimum and maximum temperatures.

Developing an overall criterion when streambed heating should be used in a water quality model will depend on several factors. Streambed heating is a function of

the effective solar radiation striking the streambed channel which is a function of shading, channel width, and stream orientation; the channel morphology and flow which will influence the effective water-streambed interface area; light extinction; substrate types and season. When flows increase in a river this usually occurs when there is more rain and hence less solar radiation or the season is cooler such as in autumn or winter. Additionally increased flows are often accompanied by increases in suspended solids or turbidity which increases the light extinction coefficient and hence decreases the solar radiation striking the streambed.

Additional sensitivity analyses would need to be conducted with the streambed heating model on the Lower Bull Run River and other river systems before a dimensionless number or empirical equation could be developed to elucidate when streambed heating is important and should be modeled. This is a complex function of channel shape, flow, shading, and depth. Some guidelines can be developed to assist model users deciding on whether a streambed heating model should be used. A streambed heating model may be important to include when modeling temperature:

- If the river is exposed to a lot of direct sunlight with limited vegetative and topographic shade.
- If the channel morphology and flow rates allow for wide open channels with shallow depths in summer.
- If the water clarity allows solar radiation to penetrate the water column and reach the streambed.

- If the substrate types are dominated by bedrock and consolidated cobble.
- If the low river flow season corresponds to summer periods with a lot of solar radiation and higher air temperatures.

Overall these conditions are typical throughout the Cascade region of Oregon and Washington, but often smaller rivers do not meet all of these criteria. Many smaller rivers may have plenty of vegetation and topography to provide shading. Larger rivers which would have more open channels and more effective solar radiation also have higher flows which may attenuate the effects of streambed heating.

## **6. Auxiliary Model Algorithms**

An important aspect of modeling water temperature and streambed heating is accurately simulating the short-wave solar radiation striking the water surface and the streambed. Two areas of research to improve the calculations of short-wave solar striking the water were inclusion of dynamic streamside shading from vegetation and topography and investigation of additional empirical models for estimating clear-sky solar radiation. Modeling streamside shading in CE-QUAL-W2 can result in better estimates of the effective short-wave solar radiation reaching the water surface. CE-QUAL-W2 currently has the ability to predict clear-sky solar radiation when data are not available. Additional models for estimating clear-sky radiation were developed from literature and compared against the existing model to identify improvements in predicting clear-sky radiation.

### **6.1 Dynamic Shading Algorithm**

The existing algorithms in CE-QUAL-W2 for computing declination angle, solar altitude and azimuth were updated with new equations that improved the model's predictive ability. After computing the solar altitude and azimuth, another model algorithm is used to determine the impact of topographic and vegetative shade on short-wave solar radiation as shown in Figure 155.

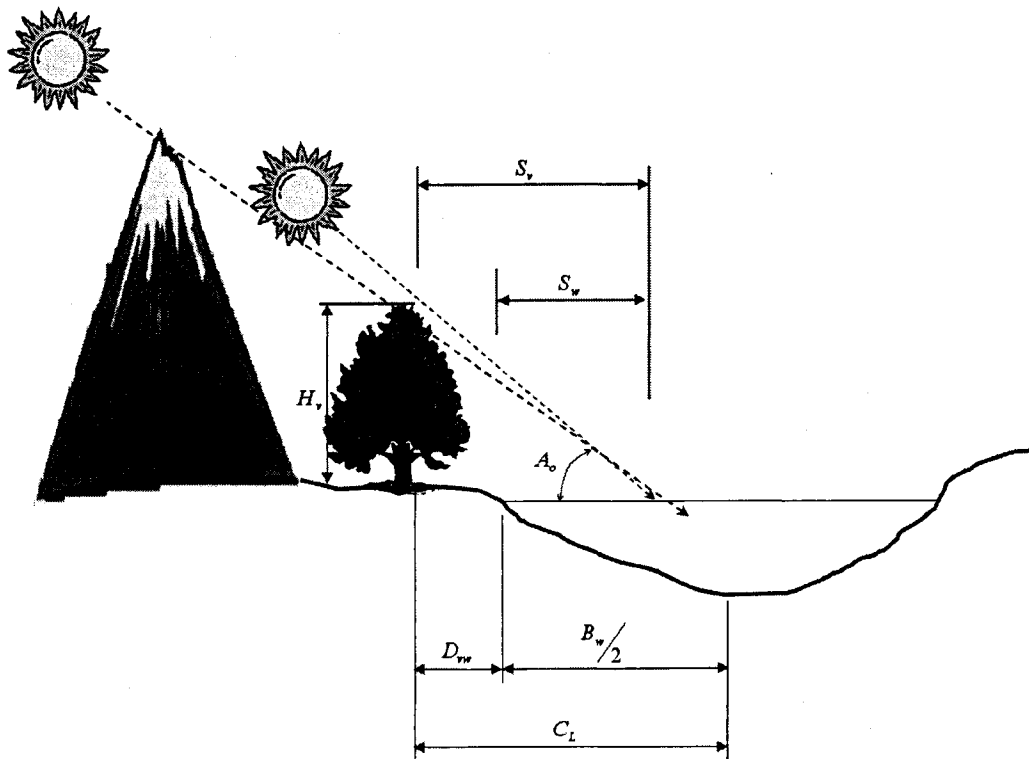


Figure 155: Topographic and Vegetative shading, solar altitude and vegetation height affect the shadow length.

### 6.1.1 Data Requirements

Topography and vegetation data are stored in a file called "shade.npt". An example file "shade.npt" is shown in Appendix A. The file includes tree top elevations for both stream banks. The file also includes the distance from the centerline of the river to the controlling vegetation and the shade reduction factor (SRF) for both stream banks. The shade file has vegetation characteristics recorded by the left and right banks of the stream. The convention used for defining left or right bank is dependent on looking downstream in the system.

The shade model reads in 18 topographic inclination angles surrounding each model segment center-point. The inclination angles can be determined using topographical maps, Digital Elevation Models (DEM), or contour plots. The steepest inclination angle for each of the 18 locations surrounding a segment should be selected since this angle will control the topographic shading. The first inclination angle is taken from the North (orientation angle,  $\phi_0 = 0.0$ ) and moves clockwise to the East with increasing orientation angles around the segment in 20-degree increments. How far away from the river centerline the topography should be analyzed will depend on the system. Wide and flat river systems will utilize longer distances for identifying influencing topography than narrow river canyons. Rather than restricting the algorithm to inclination angles from the southeast through the southwest only, (which is appropriate for the Northern hemisphere), inclination angles from many locations surrounding a segment was used to make the algorithm more general for northern as well as southern hemispheres.

### **6.1.2 Shade Algorithm**

The first step is to use the segment orientation angle  $\phi_0$  (degrees) and the solar azimuth  $A_s$  (degrees) to calculate the stream bank with the sun behind it. The criteria used for determining the bank with the sun behind it was modified from Chen (1996) because the segment orientation angle is determined differently using CE-QUAL-W2. Table 83 shows the criteria used in the model.

**Table 83: Criteria for determining sunward bank**

Sunward Bank	$0^\circ < \phi_0 \leq 180^\circ$	$180^\circ < \phi_0 \leq 360^\circ$
Right	$A_z < \phi_0$ or $A_z > \phi_0 + 180^\circ$	$\phi_0 - 180^\circ < A_z < \phi_0$
Left	$\phi_0 < A_z < \phi_0 + 180^\circ$	$A_z > \phi_0$ or $A_z < \phi_0 - 180^\circ$

Once the data have been read into the model, the algorithm uses the position of the sun to determine which topographic inclination angle coincides with the direction of the incoming solar radiation. The algorithm will determine the closest two inclination angles of the incoming solar radiation and interpolates linearly an inclination angle for the specific direction of the incoming solar radiation. The calculated inclination angle is then used to determine if vegetative or topographic shading dominates. If the solar altitude is below the calculated topographic inclination angle, topographic shading dominates and the short wave solar radiation is reduced by 90% (i.e., full shade). If the solar altitude is above the calculated inclination angle, then vegetative shading dominates.

When vegetative shade dominates, the algorithm calculates shading by determining how far the vegetation shadow extends over the water. Figure 156 show schematics of the azimuth angle, segment orientation and computed shadow lengths.

The vegetation shadow length,  $S_v$  (meters) is calculated as

$$S_v = \frac{H_v}{\tan(A_o)} \quad (120)$$

where  $H_v$  (meters) is the vegetation height, and  $A_o$  is the solar altitude, The length of the shadow cast over the water,  $S_w$  (meters) is then calculated using

$$S_w = S_v - \frac{D_{vw}}{\sin(\phi_0 - A_z)} \quad (121)$$

where  $D_{vw}$  (meters) is the distance between the vegetation and the edge of water. The shadow length perpendicular to the edge of the water,  $S_p$  (meters) is calculated as

$$S_p = S_w \sin(\phi_0 - A_z) \quad (122)$$

Figure 156 shows a diagram with the distances calculated in Equations (120) to (122). These three equations can be simplified as

$$S_p = \frac{H_v \sin(\phi_0 - A_z)}{\tan(A_o)} - D_{vw} \quad (123)$$

A shading reduction factor  $S_{RF}$  (dimensionless) was applied in cases when a model segment has potential shading along only part of its segment length or the vegetation density is less than 100%. If shade-producing vegetation exists along only half the length of a model segment and was 100% opaque, then  $S_{RF} = 0.5$ . If shade-producing vegetation was along only half of the segment with 80% density, then  $S_{RF} = 0.4$ .

The shade factor  $S_{fact}$  (dimensionless) is the fraction of water surface that is covered by shade and is calculated as

$$S_{fact} = S_{RF} \frac{S_p}{B_w} \quad (124)$$

where  $B_w$  is the wetted channel width. The effective solar radiation striking the water surface is then calculated as

$$\varphi_{effective} = \varphi_c (1 - S_{fact}) \quad (54)$$

where  $\varphi_c$  is the incoming solar radiation effected by cloud cover.

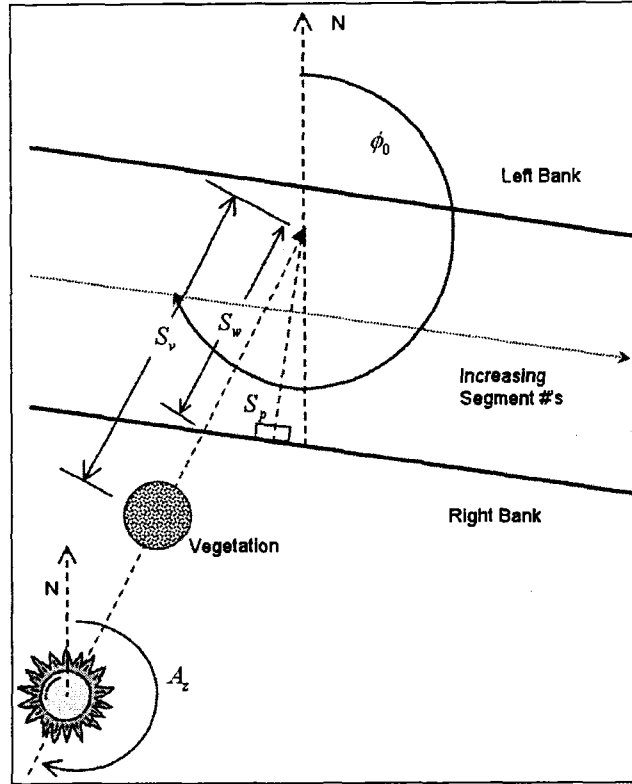


Figure 156: Schematic showing azimuth angle and stream orientation and shadow length.

### 6.1.3 Shade Algorithm Testing

#### 6.1.3.1 Topographic Shading

The shade algorithm was tested to ensure the algorithm correctly utilized the topographic data. Individual simulations were run with no vegetative shade and with mountains located in the East, South, West, and North of each segment in the model. Each mountain had an inclination angle of  $85^\circ$  or 1.4835 radians and for the remaining

orientation angles the inclination angles were 0.0. The simulation was run for July 3<sup>rd</sup> or Julian day 184.

Figure 157 shows the effect on solar radiation from the topographic shading in the east. The effective solar radiation is the same as full solar radiation except between Julian day 184.2 and 184.375. Similar graphs are shown in Figure 158, Figure 159 and Figure 160 for a single mountain in the south, west, and north, respectively.

In Figure 158, the mountain only slightly blocks the sun. For orientation angles from  $160^{\circ}$  to  $180^{\circ}$  and from  $180^{\circ}$  to  $200^{\circ}$  the topographic inclination angles are interpolated between  $85^{\circ}$  and  $0^{\circ}$ . Since the sun is at its highest point when its azimuth is at  $180^{\circ}$ , there is little opportunity for the mountain to generate shade. Figure 159 shows a similar, but reverse, pattern to Figure 157.

Figure 160 shows the influence of a mountain in the North for July 3. The figure shows the mountain has no influence on shading because the solar azimuth would place the sun in the North after the sun went down and no radiation available.

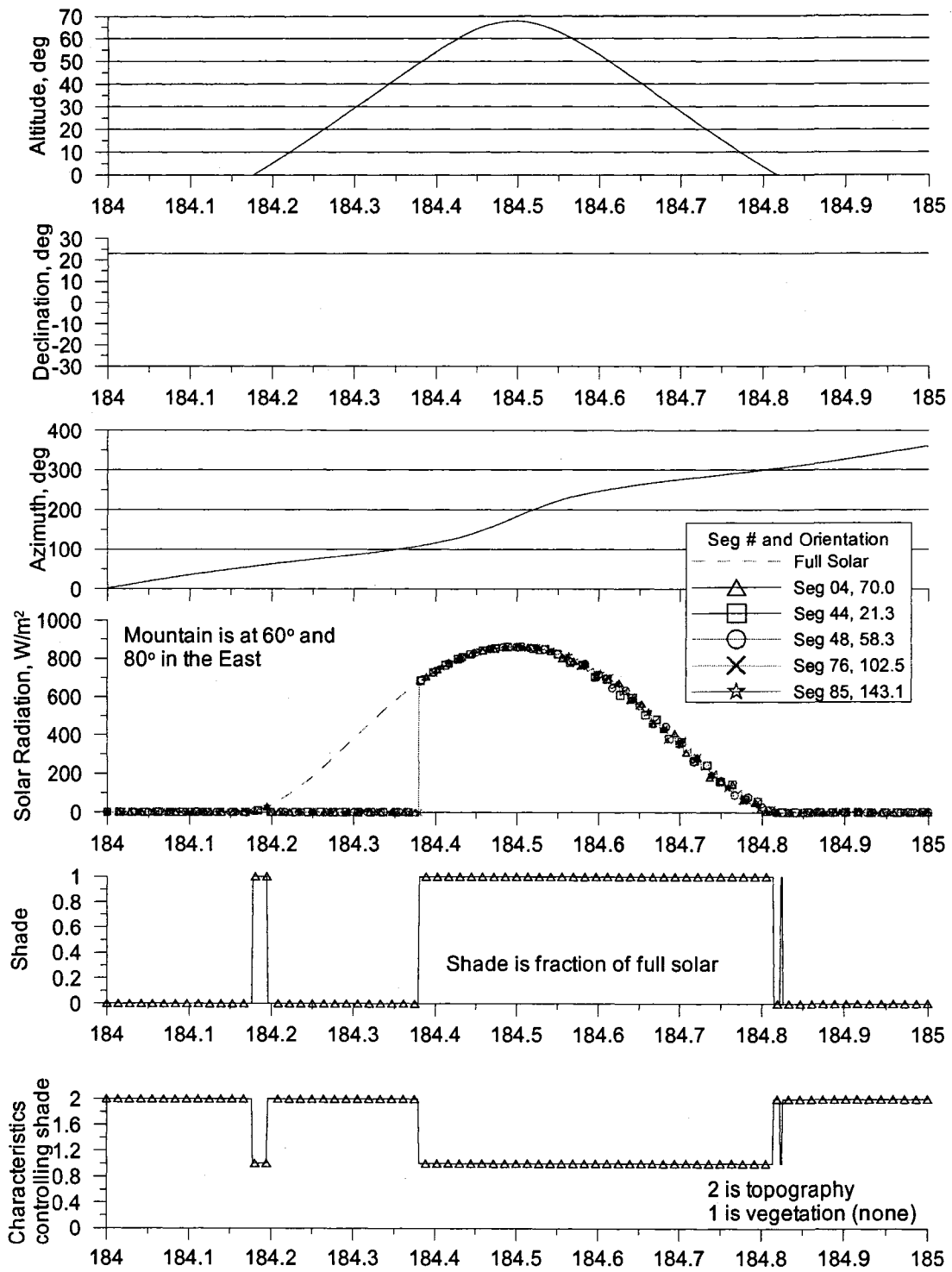


Figure 157: East Mountain topographic testing

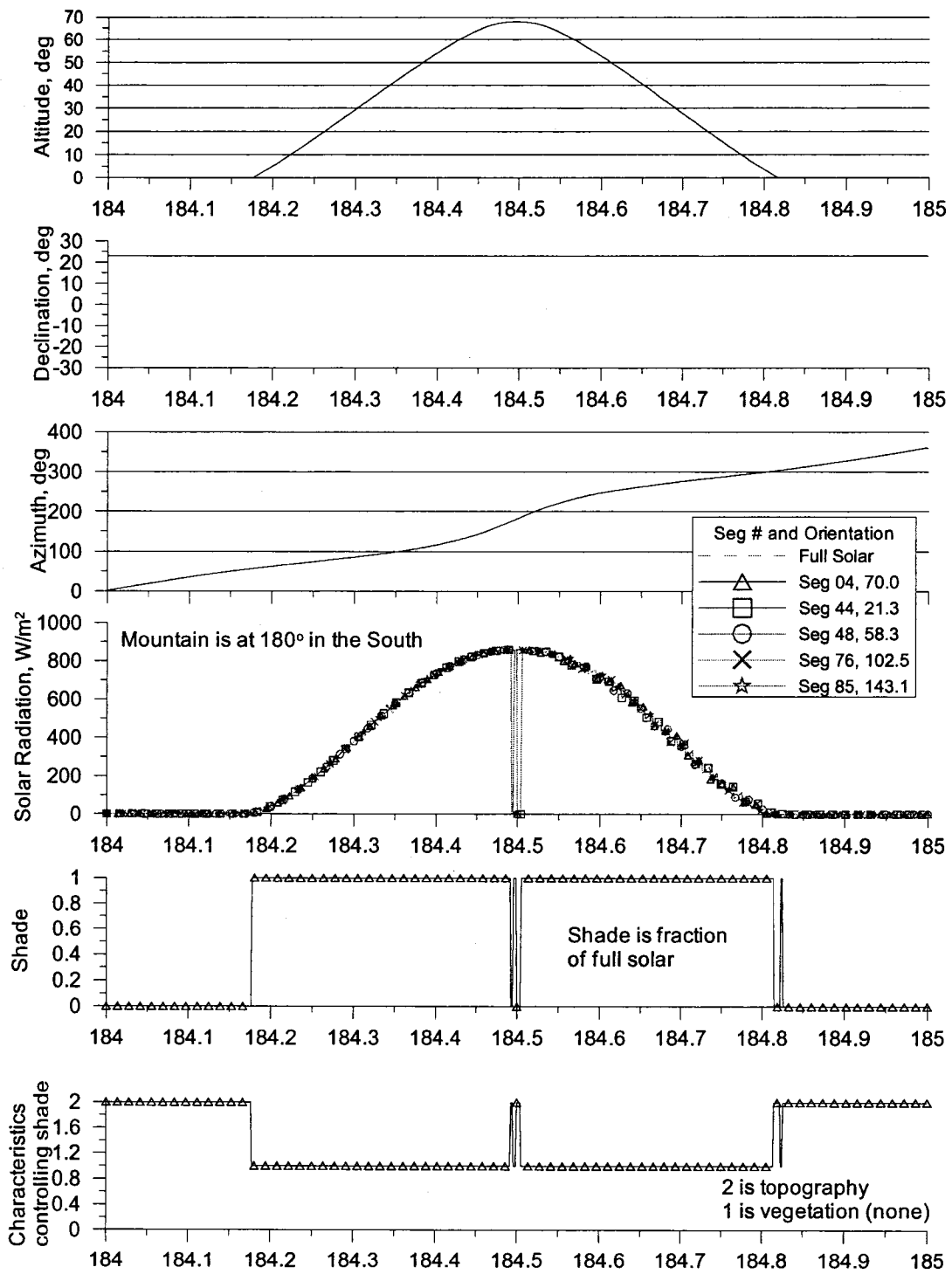


Figure 158: South Mountain topographic testing

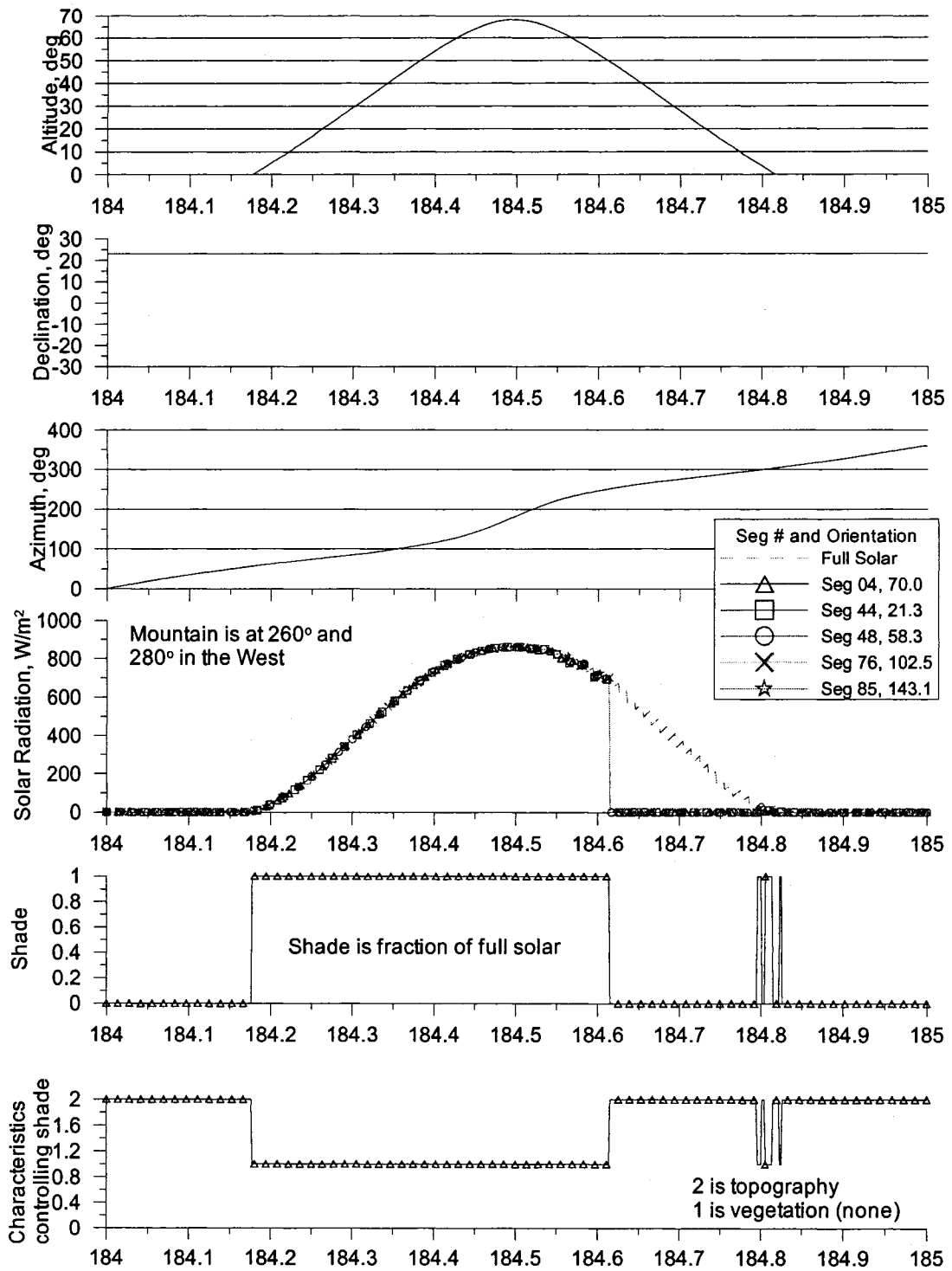


Figure 159: West Mountain topographic testing

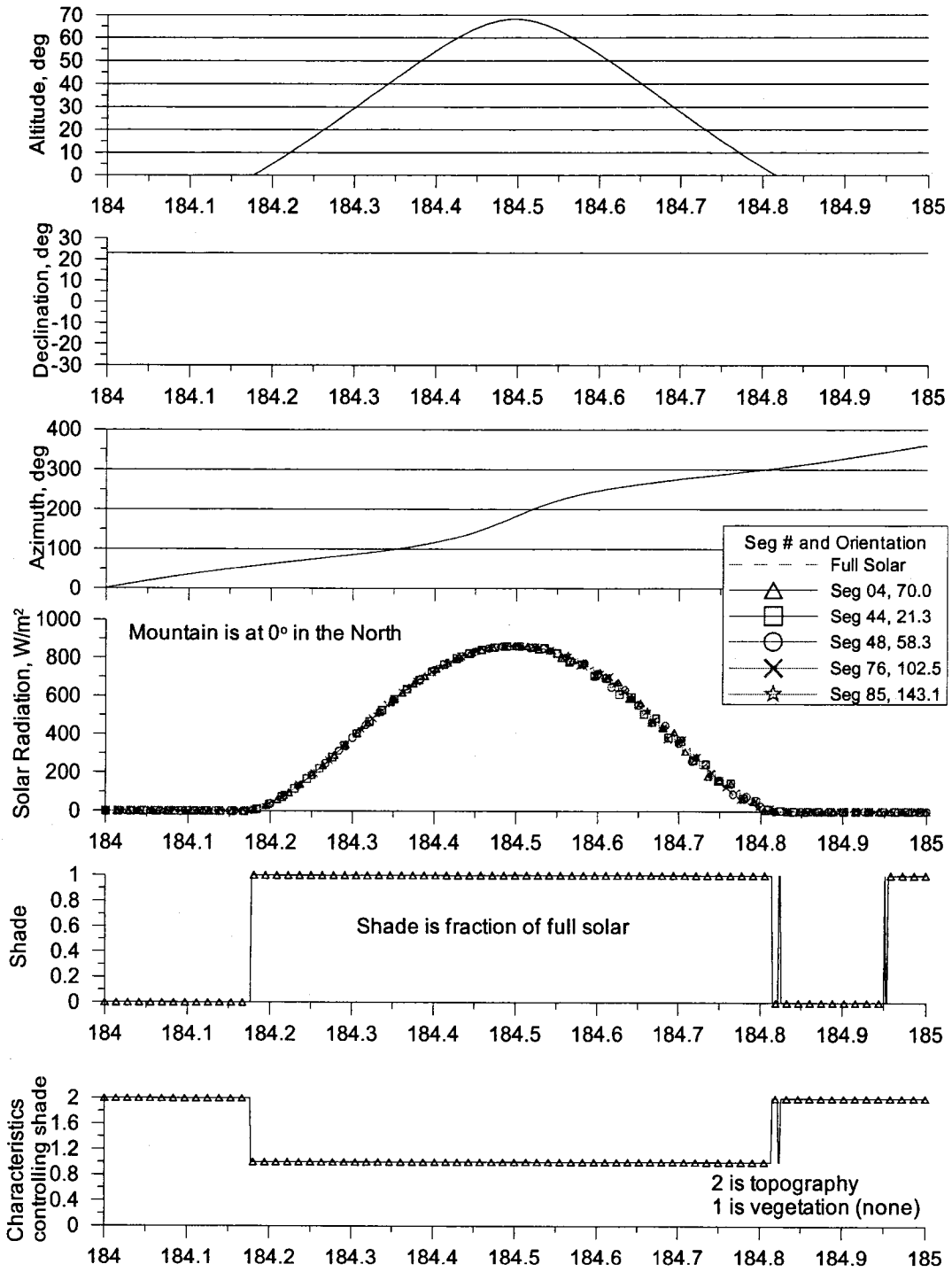


Figure 160: North Mountain topographic testing

### 6.1.3.2 Vegetative Shading

Topographic shading was then neglected in order to test the algorithm's vegetative shading. The Shade Reduction Factor  $S_{RF}$  was set to 1.0, representing full vegetation density and completeness along a segment length. The testing consisted of varying the tree height and varying the distance between controlling vegetation.

Comparisons were made between tree height and the percentage of shade. The tree heights were varied from 0 to 70 m for the vegetation-to-vegetation distances of 30.5 m and 61 m. Figure 161 and Figure 162 show the estimated daily shade (midnight to midnight) by varying the tree heights. The figures show that for increasing tree height the shade increases as expected. As the distances between controlling vegetation become narrower, the increasing tree height has a more immediate effect on shading.

Comparisons were made between vegetation-to-vegetation distance and the percentage of shade. The distance between controlling vegetation was varied from 0 to 100 m for tree heights of 10 m and 35 m. Figure 163 and Figure 164 show the percentage of shade for set tree heights of 10 m and 35 m, respectively. The figures also show that for increasing distance between controlling vegetation the shade decreases as expected.

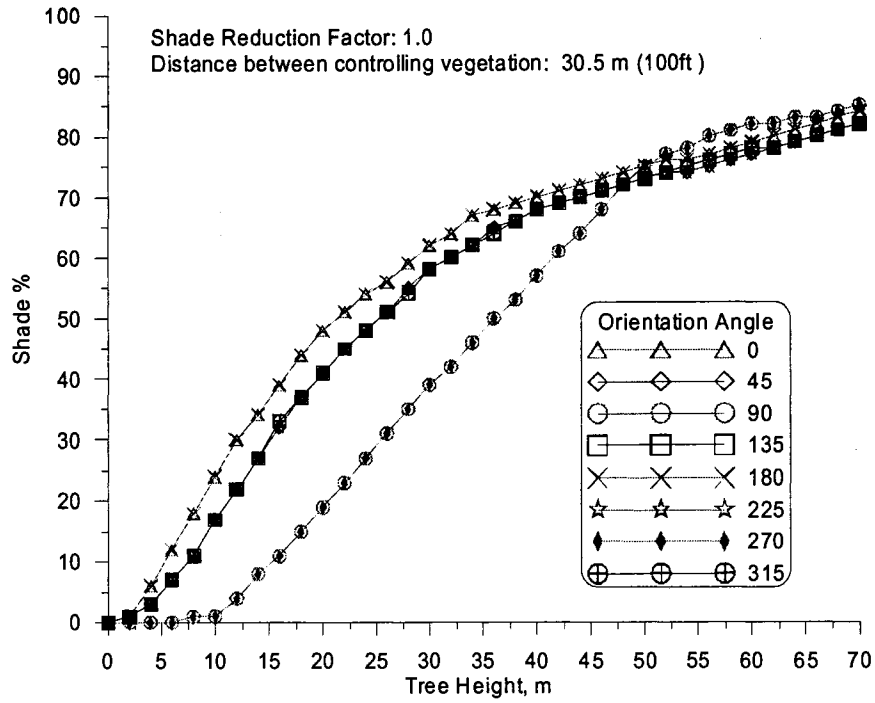


Figure 161: Shade from varying tree height, distance between controlling vegetation: 30.5 m (100 ft). Orientation angle is the angle of the model segment relative to North.

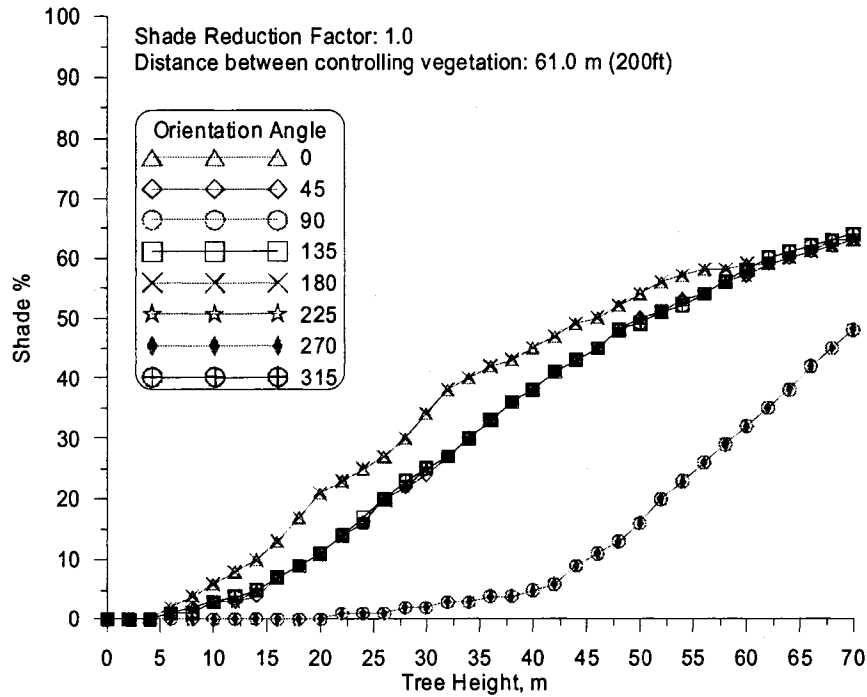


Figure 162: Shade from varying tree height, distance between controlling vegetation: 61.0 m (200 ft). Orientation angle is the angle of the model segment relative to North.

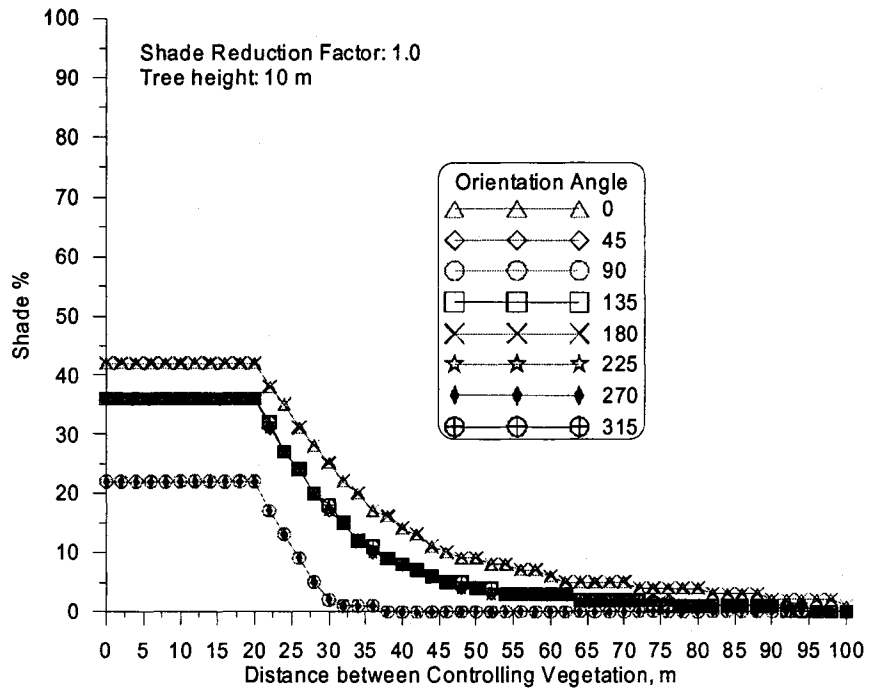


Figure 163: Shade from varying distance between controlling vegetation, tree height 10 m (32.8 ft). Orientation angle is the angle of the model segment relative to North.

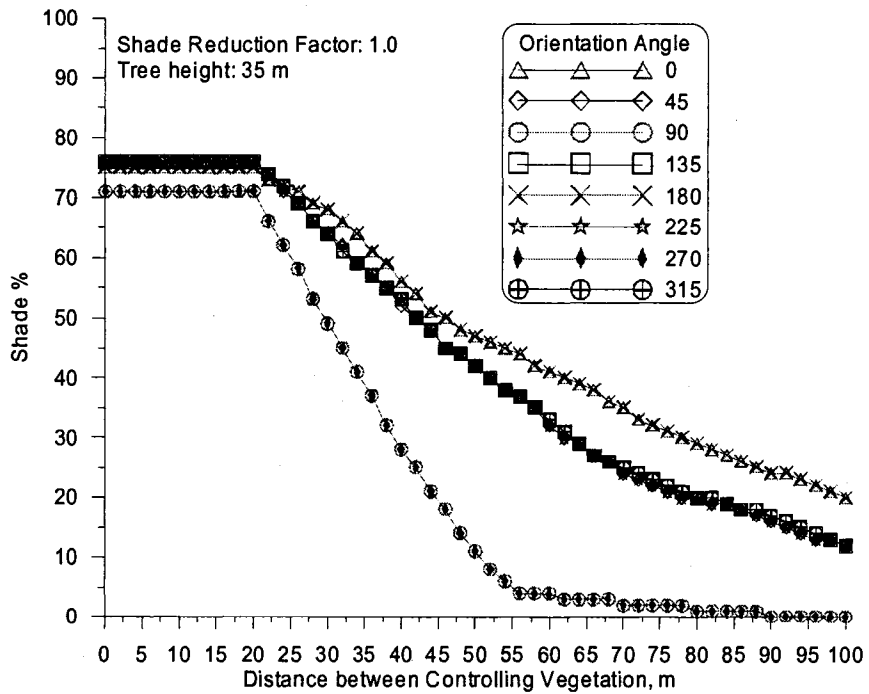


Figure 164: Shade from varying distance between controlling vegetation, tree height 35 m (115 ft). Orientation angle is the angle of the model segment relative to North.

## **6.2 Effective Solar Radiation Formulation**

Different theoretical methods for estimating clear-sky solar radiation were evaluated and recommendations were made on which models to use when solar radiation measurements are not available or limited data allows model calibration. Several solar radiation model formulations were analyzed and calibrated with data at seventeen sites around the United States for clear-sky days. Clear-sky days are days with no clouds to obstruct the monitoring site instrumentation from sunrise to sunset. These models required from zero to five calibration parameters such as atmospheric dust, atmospheric attenuation, and the ratio of forward irradiance scattering, and atmospheric turbidity, elevation, latitude and time of year and GMT or longitude. Input parameters for all the models included latitude, time of year, elevation (except the EPA (1971) model) and time zone relative to GMT or longitude.

### **6.2.1 Model Formulations**

Several models for calculating the position of the sun and atmospheric attenuation of the radiation which are used in current temperature simulation models were reviewed. All of the models for this analysis compared solar radiation data collected on clear-sky days. Additionally the effects of ground surface reflectivity were eliminated from several models since the data collected did not account for reflectivity. A section discussing ground surface reflectivity is included for

completeness and to justify corrections made to several models before comparing model results with data.

#### 6.2.1.1 EPA (1971) Model

This model was used in the water quality model CE-QUAL-W2 (Cole and Wells, 2004). The equations used for calculating the position of the sun have been refined based on updating the original formulation presented in EPA (1971).

The clear-sky solar radiation at the ground surface,  $\phi_s$ , was originally computed in BTU/ft<sup>2</sup>day, but was converted to W/m<sup>2</sup> below. The total clear sky solar radiation was calculated using a least squares fit polynomial regression of the solar altitude,  $A_o$  (degrees), and included direct and diffuse radiation and the influence of ground surface reflectivity (albedo):

$$\phi_s = 24(2.044A_o + 0.1296A_o^2 - 1.941E - 3A_o^3 + 7.591E - 6A_o^4)0.1314 \quad (125)$$

$A_o$  was computed from the angle of inclination of the sun relative to the horizon from an observer's perspective (Wunderlich, 1972; Meeus, 1999) using

$$A_o = \text{arcSin}[\text{Sin}(\psi)\text{Sin}(\delta) + \text{Cos}(\psi)\text{Cos}(\delta)\text{Cos}(H)] \quad (126)$$

where  $\psi$  is the latitude,  $\delta$  is the solar declination, and  $H$  is the local hour angle. The local hour angle,  $H$  (radians), is the angular position of the sun for a given location at a specific time during the day and was calculated from Ryan and Stolzenbach (1972) using

$$H = \frac{2\pi}{24} \left[ h_l - (\gamma_l - \gamma) \frac{24}{360} + h_e - 12.0 \right] \quad (127)$$

where  $h_l$  is the local hour,  $\gamma$  is standard meridian,  $\gamma_l$  is the longitude, and  $h_e$  is the equation of time. The equation of time,  $h_e$  (hours), represents the difference between true solar time and mean solar time due to seasonal variations in the orbital velocity of the earth (Ryan and Stolzenbach, 1972). DiLaura (1984) calculated  $h_e$  as

$$h_e = 0.170 \sin[4\pi(\lfloor Jday \rfloor - 80)/373] - 0.129 \sin[2\pi(\lfloor Jday \rfloor - 8)/355] \quad (128)$$

where  $Jday$  is the Julian day, representing the local day and time since the beginning of the year based on a Julian calendar of 365 days (366 for leap years). The local hour,  $h_l$  (hours), was calculated (Wunderlich, 1972; Ryan and Stolzenbach, 1972; and Meeus, 1999) as

$$h_l = 24(Jday - \lfloor Jday \rfloor) \quad (129)$$

EPA (1971), Wunderlich (1972) and Ryan and Stolzenbach (1972) calculated the standard meridian,  $\gamma$  (degrees), as

$$\gamma = 15.0 \left\lfloor \frac{\gamma_l}{15.0} \right\rfloor \quad (130)$$

The time zones calculate a more appropriate standard meridian than the longitude, so the time zone relative to Greenwich Mean Time (GMT),  $h_{TZ}$  (hours), was used to calculate the standard meridian as

$$\gamma = -15.0 \lfloor h_{TZ} \rfloor \quad (131)$$

The solar declination angle,  $\delta$  (radians), was calculated by Spencer (1971) as:

$$\begin{aligned}
\delta = & 0.006918 - 0.399912\text{Cos}(\tau_d) + 0.070257\text{Sin}(\tau_d) \\
& - 0.006758\text{Cos}(2\tau_d) + 0.000907\text{Sin}(2\tau_d) \\
& - 0.002697\text{Cos}(3\tau_d) + 0.001480\text{Sin}(3\tau_d)
\end{aligned} \tag{132}$$

where  $\tau_d$  (radians) is the angular fraction of the year which Spencer (1971) calculated as

$$\tau_d = \frac{2\pi(\lfloor Jday \rfloor - 1)}{365} \tag{133}$$

### 6.2.1.2 Klein (1948) Model

The model by Klein (1948) was used in the water quality model QUAL2E (Brown and Barnwell, 1987) and CE-QUAL-RIV1 (Environmental Laboratory, 1995) and involved calculating the precipitable water content, relative optical air mass, two atmospheric transmission coefficients and dust to calculate the total clear sky radiation. After considering scattering and absorption in a moist and dusty atmosphere and ground surface reflectivity, the total clear sky solar radiation,  $\varphi_s$  (W/m<sup>2</sup>), was calculated from Klein (1948) using

$$\varphi_s = \varphi_{ext} \left[ \frac{a'' - d + 0.5(1 - a' + d)}{1 - 0.5R_g(1 - a' + d)} \right] \tag{134}$$

where  $\varphi_{ext}$  is the extraterrestrial solar radiation,  $a'$  is the mean atmospheric transmission coefficient for a cloudless, dust-free, moist air after scattering,  $a''$  is the mean atmospheric transmission coefficient for cloudless, dust-free, moist air after scattering and absorption,  $d$  is the atmospheric dust, and  $R_g$  is the ground surface

reflectivity. The extraterrestrial solar radiation,  $\varphi_{ext}$  ( $\text{W}/\text{m}^2$ ), can be calculated from Wunderlich (1972), Lee (1978), and Bras (1990) as

$$\varphi_{ext} = \varphi_o E_o \text{Sin}(A_o) \quad (135)$$

where  $\varphi_o$  ( $\text{W}/\text{m}^2$ ) is the solar constant and  $E_o$  (dimensionless) is the eccentricity correction and is calculated as

$$E_o = \left( \frac{r_o}{r} \right)^2 \quad (136)$$

where  $r_o$  (AU) is the average distance between the earth and the sun (1 Astronomical Unit), and  $r$  (AU) is the distance between the earth and the sun at any time. The solar constant has been presented in the literature extensively and Table 1 lists some of the solar constant values. The National Aeronautics and Space Administration started monitoring solar influx in earth orbit in the 1970s (NASA, 2004). Table 11 lists the minimum and maximum values of extraterrestrial solar irradiance recorded from several satellites. The average of all the minimum and maximum values in Table 11 is  $1367.4 \text{ W}/\text{m}^2$ . The analyses presented in this paper use  $1367 \text{ W}/\text{m}^2$  for the solar constant  $\varphi_o$ .

Spencer (1971) and Dingman (2002) calculated the eccentricity correction,  $E_o$ , as

$$E_o = 1.000110 + 0.034221 \text{Cos}(\tau_d) + 0.001280 \text{Sin}(\tau_d) + 0.000719 \text{Cos}(2\tau_d) + 0.000077 \text{Sin}(2\tau_d) \quad (137)$$

Wunderlich (1972) characterized the atmospheric transmission using the two components:  $a'$ , scattering only and  $a''$ , scattering and absorption. The transmission

coefficients were originally tabulated by Kimball (1930) and documented in figures, which were developed into equations by Orlob and Selna (1967). The mean atmospheric transmission coefficient for a cloudless, dust-free, moist air after scattering,  $a'$  (dimensionless), was calculated from Orlob and Selna (1967) as

$$a' = \exp[-(0.465 + 0.134w)\{0.129 + 0.171\exp(-0.880m_p)\}m_p] \quad (138)$$

where  $m_p$  is the relative optical air mass and  $w$  is the precipitable water content. Orlob and Selna (1967) calculated the mean atmospheric transmission coefficient for cloudless, dust-free, moist air after scattering and absorption,  $a''$  (dimensionless), as

$$a'' = \exp[-(0.465 + 0.134w)\{0.179 + 0.421\exp(-0.721m_p)\}m_p] \quad (139)$$

Wunderlich (1972) calculated the relative optical air mass,  $m_p$  (dimensionless), based on the relationship developed by Kasten (1964) and incorporated changes in barometric pressure with altitude from List (1958), such as

$$m_p = \frac{\left[\frac{(288 - 0.0065z)}{288}\right]^{5.256}}{\left[\sin(A_o) + 0.1500(A_o + 3.885)^{-1.253}\right]} \quad (140)$$

where  $z$  (meters) is the elevation. The precipitable water content in the atmosphere is often included in atmospheric attenuation models as an empirical coefficient. Table 12 lists several empirical values for precipitable water content found in the literature.

Several researchers developed equations to calculate the precipitable water content based on the dew point temperature. Bolsenga (1965) used the work by Reitan

(1963) and developed an equation for the mean hourly precipitable water content,  $w$  (cm), such as

$$w = \exp(-0.0592 + 0.06912T_{dpt}) \quad (141)$$

where  $T_{dpt}$  ( $^{\circ}\text{C}$ ) is the dew point temperature.

Some atmospheric attenuation models consider the affects of atmospheric dust. Klein (1948) divided the influence of dust into two components considering the affects of scattering  $d_s$  (dimensionless) and absorption  $d_a$  (dimensionless) of solar radiation, where the atmospheric dust coefficient  $d$  (dimensionless), was defined as

$$d = d_s + d_a \quad (142)$$

The influence of dust on attenuating solar radiation is a function of the relative optical air mass and time of year, (Kimball, 1930). Klein (1948) and Bolsenga (1964) tabulated the dust attenuation values from Kimball (1930), as shown in Table 18. Both Klein (1948) and Dingman (2002) considered the solar radiation attenuation due to absorption from dust as negligible,  $d_a \approx 0$  resulting in  $d = d_s$ .

The ground surface reflectivity,  $R_g$  (dimensionless), or albedo represents the fraction of the incident radiation on the ground surface that reflects back to the atmosphere and is dependent on the surface material and the angle of the sun. The reflectivity of many surfaces has been documented in the literature. Table 20 lists empirical reflectivity values found in the literature for water.

Lee (1978) provided a table of reflectivity values for a water surface relative to the solar altitude as shown in Table 21.

Anderson (1954) calculated the reflectivity of the water surface,  $R_g$ , as

$$R_g = \alpha_1 (A_o)^{\beta_1} \quad (143)$$

where coefficients  $\alpha_1$  and  $\beta_1$  are dependent on the fraction of cloud cover and listed in Table 22.

### 6.2.1.3 Kennedy (1949) Model

The model from Kennedy (1949) used a more simplified approach including the relative optical air mass and an empirical variable for the atmospheric transmission to calculate the clear-sky solar radiation. The clear-sky solar radiation,  $\varphi_s$  ( $\text{W/m}^2$ ), was calculated using a slightly modified equation to incorporate the hourly (instead of daily) atmospheric transmission coefficient from Kennedy (1940) as

$$\varphi_s = \varphi_{ext} a_h^{m_p} \quad (144)$$

where  $a_h$  (dimensionless) is the hourly average atmospheric transmission coefficient defined by Kennedy (1949) as a function of the daily atmospheric transmission coefficient,  $a_t$  (dimensionless):

$$a_h = 1.49a_t - 0.50 \quad (145)$$

Several atmospheric attenuation models characterize all of the atmospheric attenuation variables into one empirical transmission coefficient (Kennedy, 1949; Ryan and Stolzenbach, 1972). The atmospheric transmission coefficient  $a_t$  was often

used to calibrate their models to data and represented a daily constant for a specific location (Ryan and Stolzenbach, 1972). Table 19 lists some daily atmospheric transmission coefficients found in the literature.

#### 6.2.1.4 Lee (1978) Model

The model from Lee (1978) used an empirical variable for the atmospheric transmission but does not include the relative optical air mass. The clear-sky solar radiation,  $\varphi_s$  ( $\text{W}/\text{m}^2$ ), accounting for direct and diffuse radiation and the influence of reflectivity was calculated using

$$\varphi_s = \varphi_{ext} a_h \frac{1}{\sin(A_o)} \quad (146)$$

This equation represents a modified version of the equation from Lee (1978) where a daily atmospheric transmission coefficient was used. The daily atmospheric transmission coefficient was a calibration parameter for the model.

#### 6.2.1.5 Meeus (1999) and Bird and Hulstrom (1981) Model

The Meeus (1999) and the Bird and Hulstrom (1981) models were used by Pelletier and Chapra (2004) in the water quality model QUAL2kw for calculating the solar position and atmospheric attenuation, respectively. The clear-sky solar radiation,  $\varphi_s$  ( $\text{W}/\text{m}^2$ ), was calculated from Bird and Hulstrom (1981) using

$$\varphi_s = \frac{(\varphi_d + \varphi_l)}{(1 - R_g r_s)} \quad (147)$$

where  $\varphi_d$  is the direct solar radiation,  $\varphi_l$  is the scattered solar radiation, and  $r_s$  is the atmospheric albedo. Bird and Hulstrom (1981) calculated the direct solar radiation,  $\varphi_d$  ( $\text{W/m}^2$ ), using

$$\varphi_d = 0.9662 \varphi_{ext} T_A T_w T_{UM} T_o T_R \quad (148)$$

where  $T_A$  (dimensionless) is the transmittance of aerosol absorptance and scattering,  $T_w$  (dimensionless) is the transmittance of water vapor,  $T_{UM}$  (dimensionless) is the transmittance of uniformly mixed gases,  $T_o$  (dimensionless) is the transmittance of ozone content, and  $T_R$  (dimensionless) is the transmittance of Rayleigh scattering in the atmosphere. The solar radiation from atmospheric scattering,  $\varphi_l$  ( $\text{W/m}^2$ ), was calculated (Bird and Hulstrom, 1981) using

$$\varphi_l = 0.79 \varphi_{ext} T_{AA} T_w T_{UM} T_o \left( \frac{0.5(1 - T_R) + B_a \left( 1 - \frac{T_A}{T_{AA}} \right)}{1 - m_p + m_p^{1.02}} \right) \quad (149)$$

where  $T_{AA}$  (dimensionless) is the transmittance of aerosol absorptance and  $B_a$  (dimensionless) is an empirical ratio of forward-scattered irradiance to the total scattered irradiance due to aerosols. Table 17 lists some empirical values for the ratio found in the literature. The atmospheric albedo,  $r_s$  (dimensionless), was calculated (Bird and Hulstrom, 1981) as

$$r_s = 0.0685 + (1 - B_a) \left( 1.0 - \frac{T_A}{T_{AA}} \right) \quad (150)$$

The transmittance of aerosol absorptance,  $T_{AA}$  (dimensionless), was calculated by Bird and Hulstrom (1981) using

$$T_{AA} = 1 - K_1 (1 - m_p + m_p^{1.06}) (1 - T_A) \quad (151)$$

where  $K_1$  is an empirical absorptance coefficient. Bird and Hulstrom (1981) recommended the coefficient be set to 0.1 unless information on aerosols was available. Table 16 lists the aerosol absorptance coefficients discussed in Bird and Hulstrom (1981).

Bird and Hulstrom (1981) calculated the transmittance of aerosol absorptance and scattering,  $T_A$  (dimensionless), using

$$T_A = \exp \left[ - \tau_A^{0.873} (1 + \tau_A - \tau_A^{0.7088}) m_p^{0.9108} \right] \quad (152)$$

where  $\tau_A$  (dimensionless) is the overall atmospheric turbidity and defined as the broadband aerosol optical depth from the surface in a vertical path. The atmospheric turbidity varies from 0.02 to 0.50 and was calculated by Bird and Hulstrom (1981) as

$$\tau_A = 0.2758 \tau_{A0.38} + 0.35 \tau_{A0.50} \quad (153)$$

where  $\tau_{A0.38\mu m}$  (dimensionless) is the aerosol optical depth from the surface in a vertical path at 380 nm wavelength (no molecular absorption), and  $\tau_{A0.5\mu m}$  (dimensionless) is the aerosol optical depth at 500 nm wavelength (ozone absorption)

(Bird and Hulstrom, 1981 and Muneer et al., 2000). Optical depth values for the two wavelengths may be developed based on data or adjusted during model calibration. Table 15 provides a list of some optical depth values found in the literature.

The transmittance of the ozone content,  $T_o$  (dimensionless), was calculated by Bird and Hulstrom (1981) as

$$T_o = 1 - 0.1611X_o(1 + 139.48X_o)^{-0.3035} - 0.002715X_o(1 + 0.044X_o + 0.0003X_o^2)^{-1} \quad (154)$$

where  $X_o$  (cm) is the amount of ozone in a slanted path, calculated by Bird and Hulstrom (1981) as

$$X_o = U_o m_p \quad (155)$$

where  $U_o$  (cm) is the ozone content in the atmosphere. Bird and Hulstrom (1981) incorporated the ozone content as an empirical coefficient. Table 13 lists some empirical values for ozone content found in the literature.

Van Heuklon (1979) developed a model based on atmospheric monitoring to calculate the amount of ozone in the atmosphere,  $U_o$  (cm), using

$$U_o = \frac{235 + \left[ \frac{A' + C' \sin(0.9856(\lfloor Jday \rfloor + F'))}{20 \sin(H'(\gamma_l + P'))} \right] \sin^2(B'\psi)}{1000.0} \quad (156)$$

where  $A'$ ,  $B'$ ,  $C'$ ,  $F'$ ,  $H'$ , and  $P'$  are coefficients that are a function of hemisphere (see Table 14). The ozone model by Van Heuklon (1979) was used in place of an empirical value in the Bird and Hulstrom (1981) model.

Bird and Hulstrom (1981) calculated the transmittance of the water vapor,  $T_w$  (dimensionless), as

$$T_w = 1 - \frac{2.4959 X_w}{(1 + 79.034 X_w)^{0.6828} + 6.385 X_w} \quad (157)$$

where  $X_w$  (cm) is the precipitable water content in a slanted path, which was calculated by Bird and Hulstrom (1981) using

$$X_w = w m_p \quad (158)$$

Bird and Hulstrom (1981) developed an equation for the transmittance of absorptance of uniformly mixed gases such as carbon dioxide and oxygen,  $T_{UM}$  (dimensionless), such as

$$T_{UM} = \exp(-0.0127 m_p^{0.26}) \quad (159)$$

The transmittance of Rayleigh scattering in the atmosphere,  $T_R$  (dimensionless), was calculated by Bird and Hulstrom (1981), using

$$T_R = \exp(-0.0903 m_p^2 (1 + m_p - m_p^{1.01})) \quad (160)$$

The relative optical air mass,  $m_p$  (dimensionless), was calculated using Equation (140) where the solar altitude was corrected due to atmospheric refraction. The correction for the effect of atmospheric refraction on the solar altitude was presented by NOAA (2004). When sunlight hits the upper atmosphere, the path of the light is bent slightly, changing the solar altitude. The corrected solar altitude,  $A_{o-corrected}$  (degrees), was calculated using

$$A_{o-corrected} = A_o + RC \quad (161)$$

where  $RC$  is the atmospheric refraction correction. Table 9 provides the equations for calculating the atmospheric refraction correction depending on the uncorrected solar altitude.

The uncorrected solar altitude was calculated using Equation (126). The extraterrestrial solar radiation  $\varphi_{ext}$  was calculated using Equation (135) where the eccentricity correction,  $E_o$  was calculated using Equation (136), and an equation from Meeus (1999) to calculate the distance between the Earth and the Sun at any given time,  $r$  (AU), as

$$r = (1.000001018\{1 - e^2\}) / (1 + e\cos\{v\}) \quad (162)$$

where  $e$  is the eccentricity of earth's orbit, and  $v$  is the true anomaly of the sun. Meeus (1999) calculated the true anomaly of the sun,  $v$  (degrees), using

$$v = M + c \quad (163)$$

where  $M$  is the geometric mean anomaly of the sun and  $c$  is the center for the sun. The local hour angle,  $H$  (degrees), was calculated (Meeus, 1999) as

$$H = h_{ist} / 4 - 180 \quad (164)$$

where  $h_{ist}$  (minutes) is the true solar time and was calculated by Meeus (1999) as

$$h_{ist} = 60h_l + h_e - 4\gamma_l \quad (165)$$

If the longitude in Equation (165) is negative, then it is multiplied by -1.0 to adjust the longitude to positive to match the time zone adjustment. The equation of time,  $h_e$  (minutes), was calculated by Meeus (1999) using

$$h_e = 4 \left[ \begin{array}{l} y \sin(2\theta_{LO}) - 2e \sin(M) + 4ey \sin(M) \cos(2\theta_{LO}) \\ - 0.5y^2 \sin(4\theta_{LO}) - 1.25e^2 \sin(2M) \end{array} \right] \quad (166)$$

where  $y = (\tan(\varepsilon_p/2))^2$

where  $\theta_{LO}$  is the geometric mean longitude of the sun, and  $\varepsilon_p$  is the corrected obliquity of the ecliptic. Meeus (1999) calculated the eccentricity of earth's orbit,  $e$  (dimensionless), using

$$e = 0.016708634 - t(0.000042037 + 0.0000001267t) \quad (167)$$

where  $t$  is the Julian centuries. The declination of the sun,  $\delta$ , was calculated by Meeus (1999) using

$$\delta = \text{arcSin}(\sin(\varepsilon_p) \sin(\lambda)) \quad (168)$$

where  $\lambda$  is the apparent longitude of the sun. The corrected obliquity of the ecliptic,  $\varepsilon_p$  (degrees), was calculated (Meeus, 1999) using

$$\varepsilon_p = \varepsilon_0 + 0.00256 \cos(125.04 - 1934.136t) \quad (169)$$

where  $\varepsilon_0$  (degrees) is the mean obliquity of the ecliptic and was calculated by Meeus (1999) using

$$\varepsilon_0 = 23.0 + [26.0 + ((21.448 - t\{46.8150 + t(0.00059 - 0.001813t)\})/60)]/60 \quad (170)$$

Meeus (1999) calculated the apparent longitude of the sun,  $\lambda$  (degrees), using

$$\lambda = \theta_{TLO} - 0.00569 - 0.00478 \sin(125.04 - 1934.136t) \quad (171)$$

where  $\theta_{TLO}$  (degrees) is the true longitude of the sun and was calculated as

$$\theta_{TLO} = \theta_{LO} + c \quad (172)$$

Meeus (1999) calculated the center for the sun,  $c$  (degrees), using

$$c = \sin(M)(1.914602 - t(0.004817 + 0.000014t)) + \sin(2M)(0.019993 - 0.000101t) + 0.000289 \sin(3M) \quad (173)$$

The geometric mean anomaly of the sun,  $M$  (degrees), was calculated from Meeus (1999) using

$$M = 357.52911 + t(35999.05029 - 0.0001537t) \quad (174)$$

The geometric mean longitude of the sun,  $\theta_{LO}$  (degrees), was calculated from Meeus (1999) as

$$\theta_{LO} = 280.46646 + t(36000.76983 + 0.0003032t) \quad (175)$$

If  $\theta_{LO}$  has value outside of 0 to 360 degrees, then 360 degrees are added or subtracted until  $\theta_{LO}$  is within this range. Meeus (1999) calculated the Julian centuries since the epoch 2000  $t$  using

$$t = \frac{(JD - 2451545.0)}{36525.0} \quad (176)$$

where  $JD$  is the Julian Ephemeris Day. Meeus (1999) calculated the Julian Ephemeris Day,  $JD$ , based on a continuous count of days since the beginning of the year -4712. The Julian Ephemeris Day begins at Greenwich mean noon and can be calculated from the Gregorian calendar. Meeus (1999) calculated the Julian Ephemeris Day from the Gregorian calendar using

$$JD = \lfloor 365.25(t_{yr} + 4716.0) \rfloor + \lfloor 30.6001(t_{mn} + 1) \rfloor + t_{dd} + (2 - \lfloor t_{yr} / 100.0 \rfloor + \lfloor \lfloor t_{yr} / 100.0 \rfloor / 4.0 \rfloor) - 1524.5 \quad (177)$$

where  $t_{yr}$  and  $t_{mn}$  are the year and month based on the Gregorian calendar, and  $t_{dd}$  is decimal day for the day and fraction of the day. Meeus (1999) adjusted the Gregorian calendar month and year to place dates in January and February in the preceding year as the 13<sup>th</sup> and 14<sup>th</sup> months. If the month was less than or equal to 2, then  $t_{yr}$  and  $t_{mn}$  were adjusted as

$$\begin{aligned} t_{yr} &= t_{yr} - 1 \\ t_{mn} &= t_{mn} + 12 \end{aligned} \quad (178)$$

Meeus (1999) calculated the decimal day of the month using

$$t_{dd} = t_{day} + h_l / 24 \quad (179)$$

where  $t_{day}$  is the integer day of the month from the Gregorian calendar, and  $h_l$  is the local hour. The day, year, and month, based on the Gregorian calendar, were calculated from the Julian day,  $Jday$ , in the model. The Julian day corresponds to the annual Julian calendar adjusted from the local time zone to GMT using

$$J_{day} = J_{day} - h_{tz} / 24 \quad (180)$$

Meeus (1999) made all solar calculations at Greenwich mean time (GMT) so the model input  $J_{day}$  values were adjusted to GMT for calculations and adjusted back to local standard time (LST) at the end.

### 6.2.1.6 Empirical Coefficients

The solar radiation formulation models, with the exception of the EPA (1971) model, use empirical coefficients which can be adjusted for calibration. Table 84 lists the equation references and the calibration parameters for each model.

**Table 84: Equation references for solar radiation models compared**

Model	Position of the Sun	Atmospheric Attenuation	Adjustable parameters
EPA (1971)	EPA (1971), Spencer (1971), Wunderlich (1972)	EPA (1971)	None
Klein (1948)		Spencer (1971), Kasten (1964), Klein (1948), Bolsenga (1965), Wunderlich (1972)	Dust
Kennedy (1949)		Spencer (1971), Kasten (1964), Kennedy (1949)	Atmospheric Transmission Coefficient
Lee (1978)		Spencer (1971), Kasten (1964), Lee (1978)	Atmospheric Transmission Coefficient
Meeus (1999) and Bird and Hulstrom (1981)	Meeus (1999) and NOAA (2004)	Bird and Hulstrom (1981), Bolsenga (1965), Van Heuklon (1979), Kasten (1964)	Ratio of Forward-Scattered Irradiance to the Total Scattered, Aerosol Absorptance and Atmospheric Turbidity

## 6.2.2 Solar Radiation Data

The five models were used to calculate solar radiation over multiple years and were compared to data collected at seventeen sites in the United States. Figure 165 shows a map of the United States with the seventeen sites where solar radiation data were collected. Table 85 lists the site names, states, elevation, time zone, extent of data, and the data source. Most of the data was obtained from the National Oceanic and Atmospheric Administration program, Integrated Surface Irradiance Study. Data were recorded at intervals of 10, 15, 30, or 60 minutes and compared to model predictions at these same times.

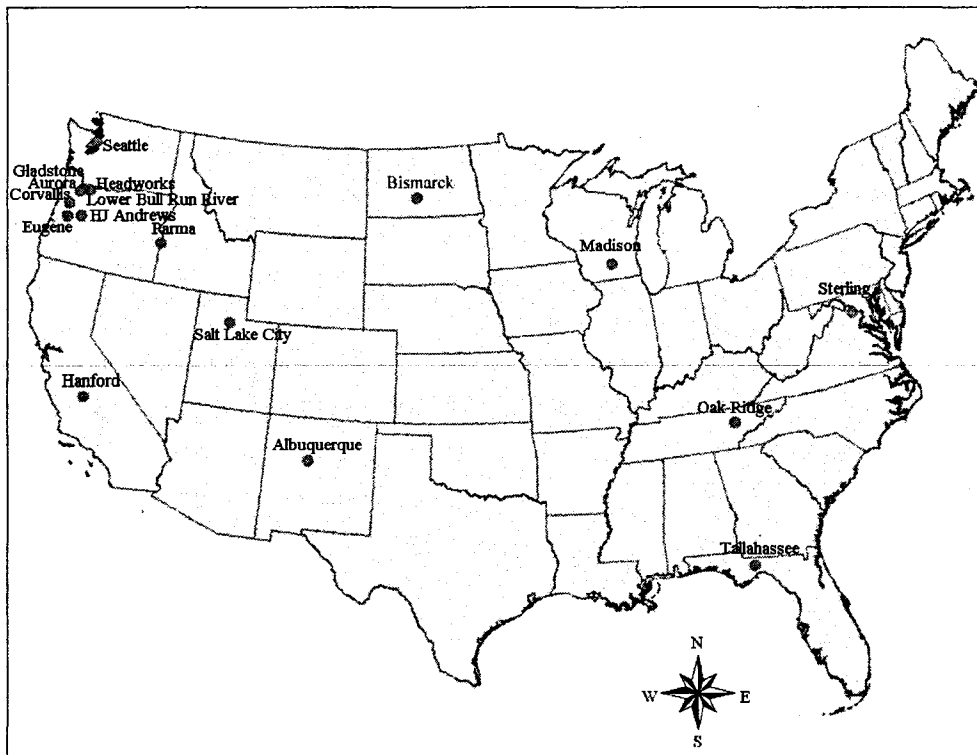


Figure 165: Solar radiation sites monitored around the United States and data used to compare with model results.

**Table 85: Site locations and details for the seventeen monitoring sites and their data sources**

Site	State	Region	Elev., m	Time zone (GMT), hrs	Years of data	Source
Bull Run Headworks	OR	Northwest	263.0	-8	1999-2004	1
Lower Bull Run River	OR	Northwest	181.8	-8	part of 2002	2
Gladstone	OR	Northwest	98.0	-8	1999-2003	3
Aurora	OR	Northwest	43.0	-8	1998-2003	4
Eugene	OR	Northwest	150.0	-8	2001-2003	3
H.J. Andrews	OR	Northwest	430.0	-8	1990-1996	5
Corvallis	OR	Northwest	70.1	-8	2001-2003	4
Parma	ID	Northwest	702.6	-7	1999-2004	4
Seattle	WA	Northwest	20.0	-8	2000-2004	6
Bismarck	ND	Mid-West	503.0	-6	1995-2004	6
Madison	WI	Mid-West	271.0	-6	1996-2004	6
Sterling	VA	East Coast	85.0	-5	1995-2004	6
Oakridge	TN	East Coast	334.0	-5	1995-2004	6
Tallahassee	FL	East Coast	18.0	-5	1995-2002	6
Albuquerque	NM	Southwest	1617.0	-7	1994-2004	6
Salt Lake City	UT	Southwest	1288.0	-7	1995-2004	6
Hanford	CA	Southwest	73.0	-8	1995-2004	6

1. Water Bureau, City of Portland, Oregon (Drinking Water Headworks facility)  
2. Department of Civil and Environmental Engineering, Portland State University (Lower Bull Run River)  
3. University of Oregon Solar Radiation Monitoring Lab  
4. AgriMet, Pacific Northwest Region, Bureau of Reclamation, U.S. Department of Interior  
5. H.J. Andrews Experimental Forest, Oregon State University and the U.S. Forest Service  
6. Integrated Surface Irradiance Study, Atmospheric Turbulence and Diffusion Division, Air Resources Laboratory, National Oceanic and Atmospheric Administration

### 6.2.3 Solar Altitude Comparison

The solar altitude was calculated using the EPA (1971) model (Equations (126) to (133)) and the Meeus (1999) and Bird and Hulstrom (1981) model (Equations (126), (161), (164) and (168)) and compared to investigate the differences between the solar position calculations. Table 86 shows the difference in solar altitude and

resultant radiation between the two models for the seventeen sites in the U.S. The table indicates solar altitude was 2 to 3 percent lower with the EPA (1971) model. Based on this difference in solar altitude, the solar radiation would be 1 to 9 percent lower for the EPA (1971) model. Figure 166 shows the results from the Aurora, Oregon site on April 15 and indicates the Meeus (1999) and Bird and Hulstrom (1981) model has higher solar altitudes after 12:00 pm and only slightly different before 12:00 pm. These results are similar at the other sixteen sites and throughout the year. The solar altitudes from the two models were divided into two groups, before 12:00 pm and after 12:00 pm each day and analyzed separately. The differences between the two models before noon each day indicate the mean difference in solar altitude ranges from -2 to +3 percent across the 17 sites. The differences between the two models after noon each day indicates the mean difference in solar altitude ranges from -3 to -9 percent. The EPA (1971) model consistently calculates a lower solar altitude in the latter half of the day compared to the Meeus (1999) and Bird and Hulstrom (1981) model.

**Table 86: EPA (1971) – Meeus (1999) and Bird and Hulstrom (1981) solar altitude and radiation comparisons**

Location	Solar Altitude, EPA (1971) - Meeus (1999) and Bird and Hulstrom (1981)				Solar Radiation, EPA (1971) - Meeus (1999) and Bird and Hulstrom (1981)
	Mean Difference, Deg	Absolute Mean Difference, Deg	Root Mean Square Difference, Deg	Mean Percentage Difference	Mean Percentage Difference
N = 18,250					
Bull Run Headworks	-0.04	0.12	0.21	-2.6%	-5.4%
Lower Bull Run River	-0.04	0.13	0.21	-3.0%	-4.8%
Gladstone	-0.04	0.18	0.30	-4.3%	-6.4%
Aurora	-0.04	0.21	0.35	-3.4%	-7.3%
Eugene	-0.04	0.12	0.20	-3.1%	-5.0%
H. J. Andrews	-0.04	0.13	0.22	-1.9%	-5.6%
Corvallis	-0.04	0.13	0.21	-2.1%	-5.0%
Parma	-0.03	0.26	0.42	-1.7%	-8.3%
Seattle	-0.04	0.16	0.27	-2.3%	-5.5%
Bismarck	-0.04	0.21	0.35	-2.2%	-6.8%
Madison	-0.03	0.13	0.23	-2.2%	-5.3%
Sterling	-0.03	0.16	0.27	-2.5%	-4.7%
Oakridge	-0.03	0.13	0.22	-3.3%	-4.2%
Tallahassee	-0.03	0.15	0.25	-2.1%	-3.0%
Albuquerque	-0.03	0.21	0.34	-3.0%	-9.4%
Salt Lake City	-0.03	0.29	0.45	-2.1%	-8.3%
Hanford	-0.03	0.21	0.34	-2.5%	-4.4%

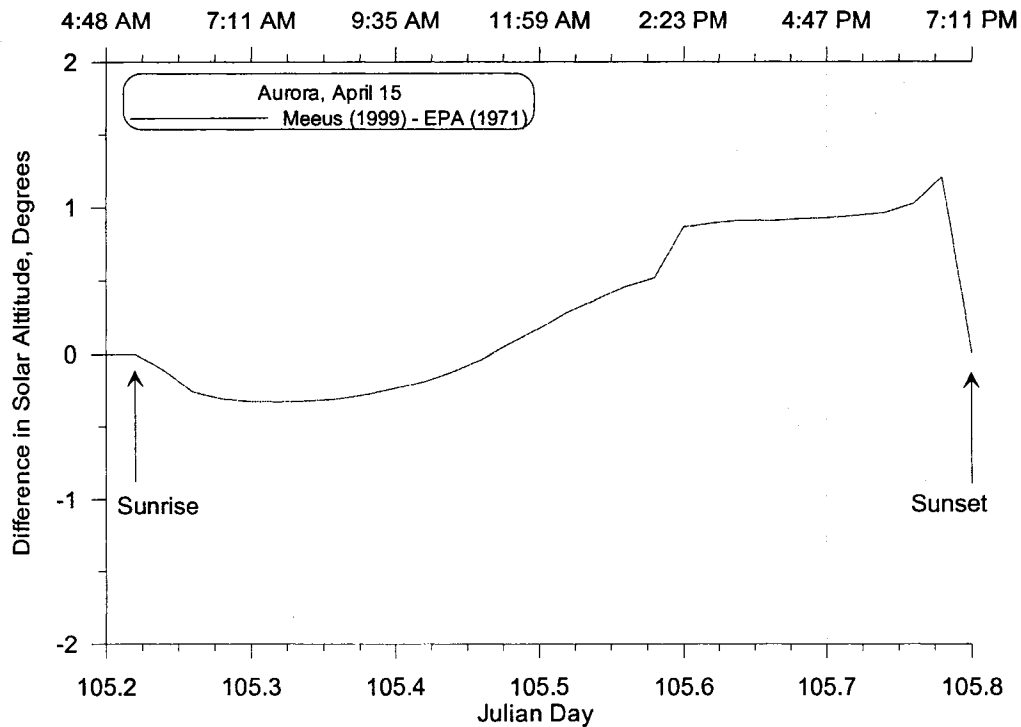


Figure 166: Solar radiation results for the Meeus (1999) and Bird and Hulstrom (1981) model and the EPA (1971) model

## 6.2.4 Model Calibration and Testing

### 6.2.4.1 All Sites and Data

The five models were calibrated with the solar radiation data at the 17 sites. The calibration process consisted of adjusting parameter values which would provide the best model-data comparison results at all of the sites. Anywhere from 10 to 261 clear-sky days were identified throughout the year, using multiple years of data, at each of the 17 sites, resulting in 2,726 clear-sky days for model-data comparisons. The Klein (1948) model results were compared with data which did not include reflectivity so the reflectivity coefficient,  $R_g$ , was set to zero. The EPA (1971),

Kennedy (1949), and Lee (1978) models account for direct and diffuse radiation and the influence of reflectivity, but do not include a reflectivity coefficient explicitly. The calculated solar radiation values for these three models were dynamically corrected for the effects of reflectivity using the using Equation (65) from Anderson (1954) and then compared to the clear-sky solar radiation data.

Table 87 shows the list of model coefficient values which provided the smallest model-data error using the mean error (ME) while trying to minimize the root mean square (RMS) error. Table 88 shows the model-data error statistics for each model. The table shows Meeus (1999) and Bird and Hulstrom (1981) model performs best, with the lowest model-data error statistics, which may be attributable to the model having more empirical coefficients which can be adjusted. The Kennedy (1949) model performed the second best and required one coefficient to be adjusted.

**Table 87: Empirical coefficients which provided the smallest model-data error statistics**

Parameter	EPA (1971)	Klein (1948)	Kennedy (1949)	Lee (1978)	Meeus (1999) and Bird and Hulstrom (1981)
Dust, $d$	No adjustable parameters	0.222			
Atmospheric Attenuation, $a_t$			0.8623	0.8693	
Ratio of Forward Scattering, $B_a$					0.83
Aerosol Absorptance, $K_1$					0.10
Atmospheric Turbidity $\tau_{A0.38}$					0.30
Atmospheric Turbidity $\tau_{A0.50}$					0.20

**Table 88: Model-data error statistics for 2,726 clear-sky days at 17 sites.**

Model/ Solar Radiation	ME <sup>1</sup> , W/m <sup>2</sup>	AME <sup>1</sup> , W/m <sup>2</sup>	RMS <sup>1</sup> , W/m <sup>2</sup>
EPA (1971)	-4.16	21.49	35.53
Klein (1948)	0.00	20.92	35.82
Kennedy (1949)	0.00	20.39	33.71
Lee (1978)	0.00	21.49	35.42
Meeus (1999) and Bird and Hulstrom (1981)	0.00	17.28	29.41
<sup>1</sup> ME = Mean Error; AME = Absolute Mean Error; RMS = Root Mean Square Error.			

Table 89 shows the model-data error statistics for all sites and models. The table indicates there is slight positive bias with the sites located in the Northwestern region of the U.S. while the remaining sites have a negative bias across the five models. The Meeus (1999) and Bird and Hulstrom (1981) model had the lowest model-data RMS error for most of the sites. The smallest model-data mean errors were from the Klein (1948) and Kennedy (1949) models. The EPA (1971) model has relatively consistent model-data errors across the country with no regional patterns in absolute mean error and RMS error. The negative ME for the EPA (1971) model is due the formulation being derived for sea level. Higher altitude sites shown in Table 19 show the under-prediction of the clear-sky solar radiation with increasing elevation with the EPA (1971) model. The Klein (1948) model performs similarly in the Western half of the U.S. and better in the East and Mid-West. The Kennedy (1949), Lee (1978) and the Meeus (1999) and Bird and Hulstrom (1981) models perform better in Southwest, East, and Mid-west than in the Northwest. The data from the Bull Run Headworks and H.J. Andrews solar radiation monitoring sites may have been influenced by vegetative or topographic shade early and late in the day as shown in the poorer model-data errors statistics.

**Table 89: Model-data error statistics for 17 sites in the U.S. with 2,726 clear-sky days.**

Site	Clear-sky days	EPA (1971)			Klein (1948)			Kennedy (1949)			Lee (1978)			Meeus (1999) and Bird and Hulstrom (1981)		
		ME <sup>1</sup> , W/m <sup>2</sup>	AME <sup>1</sup> , W/m <sup>2</sup>	RMS <sup>1</sup> , W/m <sup>2</sup>	ME <sup>1</sup> , W/m <sup>2</sup>	AME <sup>1</sup> , W/m <sup>2</sup>	RMS <sup>1</sup> , W/m <sup>2</sup>	ME <sup>1</sup> , W/m <sup>2</sup>	AME <sup>1</sup> , W/m <sup>2</sup>	RMS <sup>1</sup> , W/m <sup>2</sup>	ME <sup>1</sup> , W/m <sup>2</sup>	AME <sup>1</sup> , W/m <sup>2</sup>	RMS <sup>1</sup> , W/m <sup>2</sup>	ME <sup>1</sup> , W/m <sup>2</sup>	AME <sup>1</sup> , W/m <sup>2</sup>	RMS <sup>1</sup> , W/m <sup>2</sup>
Bull Run Headworks	229	18.6	31.0	52.9	21.5	26.0	53.4	19.3	34.5	55.0	21.0	35.5	56.4	20.8	27.9	51.9
Lower Bull Run River	10	-6.2	14.7	22.8	-9.3	17.5	27.4	-5.8	22.3	34.5	-2.7	23.4	35.7	-8.7	15.9	24.4
Gladstone	144	1.7	11.2	19.0	4.8	14.4	24.4	0.0	13.3	21.6	3.5	14.5	23.2	3.2	9.4	16.5
Aurora	224	-6.4	15.9	25.8	-3.5	13.8	23.1	-8.6	19.3	30.8	-4.6	19.2	30.6	-5.0	11.9	18.8
Eugene	132	-3.9	10.3	16.8	-2.7	16.9	26.8	-3.7	10.4	16.6	-0.6	11.1	17.5	-3.1	10.8	17.8
H.J. Andrews	189	43.5	47.0	80.7	43.1	49.8	89.4	48.4	49.5	82.2	48.3	49.5	82.1	44.5	47.8	85.5
Corvallis	99	5.2	14.8	23.9	7.1	12.8	20.3	4.3	22.1	34.2	8.3	23.9	37.2	6.1	12.6	19.6
Parma	87	-22.3	24.2	40.1	-12.6	18.7	30.4	-17.2	19.3	34.3	-20.2	21.6	37.4	-14.2	15.8	26.2
Seattle	84	1.4	10.8	17.9	3.2	14.3	23.2	-1.9	14.0	22.7	2.7	15.4	24.7	1.5	8.4	14.4
Bismarck	139	-9.7	19.1	30.0	-6.7	20.2	32.2	-6.0	17.8	28.7	-7.0	18.2	29.4	-7.0	15.1	24.0
Madison	172	-11.8	18.1	29.8	-6.0	16.5	27.4	-10.7	18.0	29.6	-9.3	17.9	29.5	-7.5	13.9	22.8
Sterling	186	-13.4	18.7	30.9	-7.9	16.9	28.4	-12.4	18.4	30.2	-8.9	17.5	28.7	-9.0	13.9	23.2
Oakridge	181	-14.1	19.0	31.5	-6.8	16.5	27.8	-8.8	15.7	26.6	-8.0	15.6	26.7	-7.0	13.1	22.0
Tallahassee	166	-7.6	19.9	33.6	-1.2	18.3	33.4	-3.4	17.0	29.5	0.9	17.1	29.6	-1.0	14.9	26.7
Albuquerque	261	-25.5	28.0	45.2	-17.4	23.9	38.6	-6.1	14.9	25.8	-19.2	20.9	35.1	-14.3	17.7	28.5
Salt Lake City	195	-17.6	23.9	38.5	-11.5	23.5	36.9	-3.6	17.8	30.2	-13.3	19.6	34.3	-9.6	16.9	26.7
Hanford	228	-4.3	15.3	24.6	-3.3	19.0	31.3	-1.9	15.1	25.8	2.2	16.2	26.9	-2.3	13.0	21.3

<sup>1</sup>ME = Mean Error; AME = Absolute Mean Error; RMS = Root Mean Square Error.

#### **6.2.4.2 All Sites, April Calibration**

The five models were calibrated to clear-sky solar radiation data at 16 sites in April only, and then used to calculate solar radiation values for the full year. The solar radiation data from the Lower Bull Run River was eliminated from the analysis since there was only data collected during the summer. The calibration process consisted of adjusting parameter values which would provide the lowest model-data mean error. The data set for comparisons consisted of 209 clear-sky days from the 16 sites.

Table 90 shows the list of model coefficient values which provided the smallest model-data error using the mean error while trying to minimize the RMS error. Table 91 shows the model-data error statistics for each model for the April calibration period and the application period of the whole year. The Meeus (1999) and Bird and Hulstrom (1981) model had the lowest RMS errors for both the April calibration period and the all-year application period.

**Table 90: Empirical coefficients which provided the smallest model-data mean error statistics for 16 sites in April.**

Parameter	EPA (1971)	Klein (1948)	Kennedy (1949)	Lee (1978)	Meeus (1999) and Bird and Hulstrom (1981)
Dust, $d$	No adjustable parameters	0.1709			
Atmospheric Attenuation, $a_i$			0.8668	0.8737	
Ratio of Forward Scattering, $B_o$					0.85
Aerosol Absorptance, $K_1$					0.10
Atmospheric Turbidity $\tau_{40,38}$					0.204
Atmospheric Turbidity $\tau_{40,50}$					0.100

**Table 91: Model-data error statistics for 16 sites calibrated in April and applied to all the data**

Model/ Solar Radiation	Calibration April, 209 clear-sky days			Application All data, 2,726 clear-sky days		
	ME <sup>1</sup> , W/m <sup>2</sup>	AME <sup>1</sup> , W/m <sup>2</sup>	RMS <sup>1</sup> , W/m <sup>2</sup>	ME <sup>1</sup> , W/m <sup>2</sup>	AME <sup>1</sup> , W/m <sup>2</sup>	RMS <sup>1</sup> , W/m <sup>2</sup>
EPA (1971)	-12.76	24.79	39.82	-4.16	21.49	35.53
Klein (1948)	0.00	22.42	37.79	8.47	19.84	34.09
Kennedy (1949)	0.00	18.70	31.15	3.27	20.63	33.86
Lee (1978)	0.00	19.97	33.19	3.39	21.73	35.62
Meeus (1999) and Bird and Hulstrom (1981)	0.00	18.32	31.11	6.67	16.85	28.69

<sup>1</sup> ME = Mean Error; AME = Absolute Mean Error; RMS = Root Mean Square Error.

### **6.2.4.3 All Sites, One Year Calibration**

The five models were calibrated with the solar radiation data at 15 sites for clear-sky days in 2001 only, and then used to calculate solar radiation values for 2002 and then compared with data. The solar radiation data from the Lower Bull Run River and H.J. Andrews were eliminated from the analysis since there were no data in 2001 from these two sites. The calibration process consisted of adjusting parameter values which would provide the lowest model-data mean error in 2001. The data set for comparisons consisted of 395 clear-sky days from the 15 sites in 2001.

Table 92 shows the list of model coefficient values which provided the smallest model-data error using the mean error while trying to minimize the RMS error in 2001. Table 93 shows the model-data error statistics for each model for the 2001 calibration period and the application period in 2002. The statistics indicate all of the models had decreased model-data root-mean square errors for 2002 when compared to 2001, but increased mean-errors. The improved RMS statistics may be due to the larger number of clear-sky days in 2002 (442 vs. 395 clear-sky days) than 2001. The Meeus (1999) and Bird and Hulstrom (1981) model had the lowest RMS errors for both years compared to the other models.

**Table 92: Empirical coefficients which provided the smallest model-data mean error statistics for 15 sites in 2001.**

Parameter	EPA (1971)	Klein (1948)	Kennedy (1949)	Lee (1978)	Meeus (1999) and Bird and Hulstrom (1981)
Dust, $d$	No adjustable parameters	0.2156			
Atmospheric Attenuation, $a_i$			0.8633	0.8690	
Ratio of Forward Scattering, $B_a$					0.84
Aerosol Absorptance, $K_1$					0.10
Atmospheric Turbidity $\tau_{A0.38}$					0.287
Atmospheric Turbidity $\tau_{A0.50}$					0.200

**Table 93: Model-data error statistics for 15 sites calibrated in 2001 and applied to 2002.**

Model/ Solar Radiation	Calibration Year 2001, 395 clear-sky days			Application Year 2002, 442 clear-sky days		
	ME <sup>1</sup> , W/m <sup>2</sup>	AME <sup>1</sup> , W/m <sup>2</sup>	RMS <sup>1</sup> , W/m <sup>2</sup>	ME <sup>1</sup> , W/m <sup>2</sup>	AME <sup>1</sup> , W/m <sup>2</sup>	RMS <sup>1</sup> , W/m <sup>2</sup>
EPA (1971)	-3.74	18.70	30.85	-4.86	17.27	28.18
Klein (1948)	0.00	19.01	32.08	-0.40	17.11	29.04
Kennedy (1949)	0.00	18.87	30.73	-2.13	17.31	27.70
Lee (1978)	0.00	20.28	32.92	-1.88	18.70	29.75
Meeus (1999) and Bird and Hulstrom (1981)	0.00	15.05	25.32	-1.17	13.72	23.19

<sup>1</sup>ME = Mean Error; AME = Absolute Mean Error; RMS = Root Mean Square Error.

#### 6.2.4.4 One Site, Spring and Fall

The five models were calibrated for 13 clear-sky days in April (from multiple years) at the Aurora, Oregon site and then the calibrated coefficient values were then applied for 29 clear-sky days in September (from multiple years) to determine how well the models perform with “predicting” another time period. Table 94 shows the list of coefficient values which provided the smallest model-data error using the mean error while trying to minimize the RMS error during April. Table 95 shows the model-data error statistics for each model during both April and September. The Meeus (1999) and Bird and Hulstrom (1981) model had lower RMS errors for both April and September than the other models.

**Table 94: Empirical coefficients which provided the smallest model-data mean error statistics for clear-sky days in April at Aurora, Oregon.**

Parameter	EPA (1971)	Klein (1948)	Kennedy (1949)	Lee (1978)	Meeus (1999) and Bird and Hulstrom (1981)
Dust, $d$	No adjustable parameters	0.1460			
Atmospheric Attenuation, $a_i$			0.8787	0.8800	
Ratio of Forward Scattering, $B_a$					0.85
Aerosol Absorptance, $K_1$					0.10
Atmospheric Turbidity $\tau_{40.38}$					0.07
Atmospheric Turbidity $\tau_{40.50}$					0.07

**Table 95: Model-data error statistics for April and September at Aurora, Oregon**

Model/ Solar Radiation	Calibration April, 13 clear-sky days			Application September, 29 clear-sky days		
	ME <sup>1</sup> , W/m <sup>2</sup>	AME <sup>1</sup> , W/m <sup>2</sup>	RMS <sup>1</sup> , W/m <sup>2</sup>	ME <sup>1</sup> , W/m <sup>2</sup>	AME <sup>1</sup> , W/m <sup>2</sup>	RMS <sup>1</sup> , W/m <sup>2</sup>
EPA (1971)	-16.17	20.84	30.49	-4.47	12.48	19.33
Klein (1948)	0.00	13.47	23.12	11.66	14.22	22.75
Kennedy (1949)	0.00	14.16	22.32	6.97	17.68	29.28
Lee (1978)	0.00	14.61	22.99	6.90	18.17	29.97
Meeus (1999) and Bird and Hulstrom (1981)	0.00	9.00	16.34	9.69	12.06	18.70

<sup>1</sup> ME = Mean Error; AME = Absolute Mean Error; RMS = Root Mean Square Error.

### 6.2.5 Sensitivity of Simulation Year

The first sensitivity analysis involved the Meeus (1999) and Bird and Hulstrom (1981) model which uses a Julian Ephemeris Day dependent on the year rather than a repeating annual Julian calendar. All input variables to the model were kept constant except the simulation year. Solar radiation values calculated for 2001 were compared with 2002 and 2003. The model results were output 50 times a day at the seventeen sites in the U.S.

The model results were used to calculate the daily cumulative solar radiation for each site. The differences between the daily cumulative solar radiation values for 2001 and 2002 and for 2001 and 2003 were calculated. The minimum, maximum, and average statistics of these differences for each site were then calculated for each pair of years and then divided by the average daily cumulative solar radiation in 2001 to calculate a dimensionless sensitivity coefficient. Table 96 shows a list of the

sensitivity coefficients by comparing model results from 2001 with results from 2002 and 2003. The sensitivity coefficients calculated by comparing model results from 2001 with results from 2002 ranged from -0.7% to +0.7% with an average of +0.1% and with results from 2003 ranged from -1.2% to +1.3% with an average of +0.1%. The sensitivity coefficients indicate there are minor differences between the adjacent years when calculating the solar radiation. If comparison years are further apart in time the sensitivity may be different.

**Table 96: Meeus (1999) and Bird and Hulstrom (1981) model input year sensitivity analysis results**

S = Sensitivity	Year 2001 - Year 2002, Daily Cumulative Radiation Difference			Year 2001 - Year 2003, Daily Cumulative Radiation Difference		
	Minimu m S	Average S	Maximu m S	Minimu m S	Average S	Maximu m S
Bull Run Headworks	-0.58%	0.07%	0.62%	-1.09%	0.09%	1.16%
Lower Bull Run River	-0.60%	0.07%	0.63%	-1.16%	0.09%	1.11%
Gladstone	-0.55%	0.08%	0.64%	-1.01%	0.10%	1.18%
Aurora	-0.55%	0.08%	0.65%	-1.00%	0.10%	1.19%
Eugene	-0.52%	0.07%	0.60%	-0.96%	0.09%	1.09%
H.J. Andrews	-0.53%	0.08%	0.63%	-0.96%	0.10%	1.14%
Corvallis	-0.55%	0.08%	0.63%	-1.05%	0.10%	1.14%
Parma	-0.58%	0.08%	0.62%	-1.00%	0.09%	1.13%
Seattle	-0.62%	0.08%	0.69%	-1.12%	0.11%	1.29%
Bismarck	-0.60%	0.09%	0.69%	-1.07%	0.07%	1.26%
Madison	-0.52%	0.08%	0.65%	-0.87%	0.05%	1.16%
Sterling	-0.45%	0.06%	0.60%	-0.78%	0.02%	0.96%
Oakridge	-0.37%	0.06%	0.55%	-0.68%	0.03%	0.91%
Tallahassee	-0.30%	0.05%	0.47%	-0.59%	0.02%	0.77%
Albuquerque	-0.41%	0.06%	0.48%	-0.66%	0.06%	0.86%
Salt Lake City	-0.51%	0.07%	0.55%	-0.86%	0.07%	1.00%
Hanford	-0.41%	0.06%	0.52%	-0.74%	0.07%	0.88%

### 6.2.6 Sensitivity of Dew Point Temperature Data

The second sensitivity analysis conducted evaluated the influence of dew point temperature in the Klein (1948) model and the Meeus (1999) and Bird and Hulstrom (1981) model. Solar radiation was calculated with the two models using dew point temperature data which were adjusted by +/- 10%. The sensitivity of the solar radiation due to changes in dew point temperature was calculated using

$$S = \left( \frac{\varphi_{dataset1} - \varphi_{dataset2}}{\varphi_{dataset1}} \right) \Bigg/ \left( \frac{T_{dpt\ dataset1} - T_{dpt\ dataset2}}{T_{dpt\ dataset1}} \right) \quad (181)$$

expressed as a dimensionless percentage where  $\varphi$  is the calculated clear-sky solar radiation,  $T_{dpt}$  is the dew point temperature data, *dataset1* is the dew point temperature data set used, and *dataset2* corresponds to either +10% or -10% from *dataset1*.

The annual average of the dimensionless sensitivity coefficients was taken at each site. Table 97 shows the sensitivity coefficient for the Klein (1948) model and the Meeus (1999) and Bird and Hulstrom (1981) model. The table indicates the dew point temperature has limited effect on the calculated solar radiation. Sensitivity coefficients were larger for the Klein (1948) model than the Meeus (1999) and Bird and Hulstrom (1981) model.

**Table 97: Klein (1948) model and Meeus (1999) and Bird and Hulstrom (1981) model input dew point temperature annual sensitivity**

Site	10 % Lower Dew Point Temperature		10 % Higher Dew Point Temperature	
	Klein (1948), Sensitivity	Meeus (1999) and Bird and Hulstrom (1981), Sensitivity	Klein (1948), Sensitivity	Meeus (1999) and Bird and Hulstrom (1981), Sensitivity
Bull Run Headworks	0.6%	3.1%	-4.6%	-5.5%
Lower Bull Run River	-0.2%	3.3%	-7.0%	-6.7%
Gladstone	0.4%	3.2%	-5.5%	-5.9%
Aurora	0.2%	3.2%	-6.0%	-6.0%
Eugene	0.4%	3.1%	-5.1%	-5.6%
H.J. Andrews	0.3%	2.7%	-4.9%	-5.2%
Corvallis	0.4%	3.0%	-5.0%	-5.4%
Parma	-0.3%	0.2%	-1.7%	-1.6%
Seattle	0.4%	3.1%	-5.3%	-5.6%
Bismarck	-1.6%	0.1%	-3.8%	-2.0%
Madison	-1.7%	0.5%	-4.6%	-2.8%
Sterling	-2.2%	1.0%	-6.7%	-4.0%
Oakridge	-2.5%	1.3%	-7.7%	-4.7%
Tallahassee	-3.8%	1.9%	-11.2%	-6.3%
Albuquerque	-0.8%	-0.9%	-0.9%	0.0%
Salt Lake City	-0.7%	-0.5%	-1.0%	-0.9%
Hanford	0.0%	3.1%	-5.7%	-5.9%

### 6.2.7 Summary and Discussion

Several empirical models have been developed for calculating the total clear sky solar radiation on the ground surface. Five models were presented, some with modifications, to calculate the position of the sun and the resultant solar radiation. The models used for calculating the position of the sun and solar radiation varied from having no empirical coefficients to four empirical coefficients which had limited

ranges based on the literature. Solar radiation data from 17 sites around the United States were obtained to compare with the model results. The five models were calibrated using the data from the 17 sites in 3 different ways: (1) all sites were calibrated to data from April and then used to predict solar radiation throughout the year, (2) all sites were calibrated for one year and used to predict solar radiation for another year, and (3) one site was calibrated for all data in April and used to predict solar radiation for all of the data in September. The sensitivity of the Klein (1948) and Meeus (1999) and Bird and Hulstrom (1981) models, since they required dew point temperature in their models, were tested for model sensitivity to dew point temperature.

The solar altitude calculated with the EPA (1971) model was 2 to 3 percent lower than calculated with the Meeus (1999) and Bird and Hulstrom (1981) model which resulted in a decrease in solar radiation estimates of 1 to 9 percent. The solar altitude calculated by the Meeus (1999) and Bird and Hulstrom (1981) model is preferred since it is more accurate.

The Meeus (1999) and Bird and Hulstrom (1981) model resulted in the best model calibration with data from the 17 sites around the U.S. When the five models were calibrated to all the clear-sky data at 16 sites in April and the calibrated coefficients were applied to all the data throughout the year the Meeus (1999) and Bird and Hulstrom (1981) model performed best at predicting solar radiation. When all of the models were calibrated to 2001 clear-sky data and then applied and compared with 2002 clear-sky data, all of the models performed better in 2002 than

2001. This may be due to the larger number of clear-sky days available for comparison in 2002 than 2001. For both years the Meeus (1999) and Bird and Hulstrom (1981) model performed best based on mean error and RMS error. When the five models were calibrated to all of the clear-sky data at Aurora, Oregon in April and then applied and compared to data in September, the Meeus (1999) and Bird and Hulstrom (1981) model had the lowest RMS error for both the application periods.

The dew point temperature has limited influence on the calculated solar radiation using the Klein (1948) and the Meeus (1999) and Bird and Hulstrom (1981) models. The Klein (1948) model was found to be slightly more sensitive to changes in dew point temperature than the Meeus (1999) and Bird and Hulstrom (1981) model.

The EPA(1971) model with no calibration parameters did reasonably well in matching field data even though it was developed for solar radiation prediction at sea level and hence under predicted solar radiation at higher altitudes.

### **6.2.8 Conclusion**

The analyses showed that the more complex models for calculating solar radiation are better at estimating incident solar radiation on a water surface but require data to be calibrated for a specific location and time period. If there is on-site clear sky solar radiation data to calibrate a solar radiation model then the Meeus (1999) and Bird and Hulstrom (1981) model should be used. If there is no on-site clear sky solar radiation data available then the modified EPA (1971) should be used to estimate incident solar radiation on the water surface.

## **7. Summary and Recommendations**

### **7.1 Summary and Conclusions**

The field study and laboratory experiments were valuable in documenting vertical and lateral temperature gradients and understanding the impacts of different substrate types. Some of the data collected in the field and laboratory were found to be erroneous which were not used in the model calibration process and illustrated the difficulties in designing and using the temperature probes.

The light extinction data collected in the field revealed 66% of the solar radiation striking the water surface penetrates to the water-streambed interface. Additionally the field data showed 2% of solar radiation reflects off the substrate.

The research resulted in developing a 3-D streambed heating model which was calibrated to field and laboratory data. The model for the cobble substrate calibrated well to the field data but raised questions about the influence of interstitial water temperatures on the cobble substrate temperatures. The streambed heating model calibrated well to data once a small fraction (0.1%) of the water temperature was incorporated in streambed temperature predictions. Additional work in the future should focus on identifying the impact of the interstitial water by monitoring both the cobble substrate and the interstitial water using different field techniques. The impact of the interstitial water should be related to the amount of hyporheic flow in the substrate. The model was calibrated to the data collected in laboratory experiments

but required the model to be expanded to include the container itself and not just the substrate.

A model grid sensitivity analysis was conducted to determine the influence of the boundary conditions and identify if the grid resolution was sufficient to capture temperature gradients in the streambed. The analysis showed that the side boundary conditions had little influence on the temperature results and that setting the bottom boundary condition at 13 m was sufficient to ensure the boundary condition did not influence model results. A refined grid near the surface improved the temperature profiles by capturing sharper temperature gradients. A coarser grid near the bottom boundary had little influence on the model results. The streambed model was compared against an analytical model for a simple case, and an analytical model and 1-D model compared with field data. The 3-D streambed heating model compared well with the other models in all cases.

An extensive sensitivity analysis was conducted with a 1-D streambed heating model incorporated in CE-QUAL-W2 and applied to a reduced slope model application of the Lower Bull Run River. The sensitivity analysis showed there were impacts on the water temperature predictions, primarily increasing the daily minimum temperatures from 0.02 to 0.18 °C and changing the daily maximum temperatures from -0.24 to 0.24 °C for various river flows. Increased flow rates resulted in a decrease in water temperature impacts from streambed heating but larger streambed heat fluxes due to the increased water-streambed interface area. The largest water temperature impacts from streambed heating were found with the river channel

characterized by all bedrock substrate with decreasing impacts once cobble substrate was incorporated into the model simulations. Increased vegetative and topographic shade reduced the effective solar radiation striking the streambed and reduced the impact of streambed heating.

Additional research developed a dynamic streamside shading model in CE-QUAL-W2 to incorporate the effects of shading from vegetation and the surrounding topography. The objective of including this in CE-QUAL-W2 was to more accurately estimate the effective solar radiation reaching the water surface. The shade model included vegetation characteristics such as height, offset from the channel and density with adjustments for leaf out in the spring and leaf cessation in the fall. The model also included the effects of topographic shade by including the inclination angles of the surrounding terrain for each model segment. The shade model was tested with various "mountains" to ensure the effective solar radiation was reduced at the appropriate time based on the sun's position. The vegetative shade was also tested to investigate the effects of vegetation characteristics. The testing showed that increased vegetation density and heights increased the effective shade and increases in the distance between the controlling vegetation and the stream bank decreased the effective shade.

Five empirical models were developed for calculating the clear-sky solar radiation at the ground surface to determine if more accurate models could be used in CE-QUAL-W2 for estimating short-wave solar radiation. Some of the models included modifications from the original author's development. The models were

calibrated to clear-sky solar radiation data from 17 sites around the United States. Multiple tests were conducted with subsets of the data to test the models' abilities to predict clear-sky solar radiation once calibrated to a separate set of data. The analyses showed the Meeus (1999) and Bird and Hulstrom (1981) model calibrated best to the data and had the best predictive abilities in various scenarios, but had the largest number of calibration parameters. The modified EPA(1971) model with no calibration parameters did reasonably well in matching data even though it was developed for solar radiation predictions at sea level and hence under predicted solar radiation at higher altitudes. The analyses showed if there is on-site clear sky solar radiation data available then the Meeus (1999) and Bird and Hulstrom (1981) model should be used and if there is no on-site clear sky solar radiation data then the modified EPA (1971) should be used.

## **7.2 Recommendations for Future Work**

Based on the field work and modeling studies undertaken for this research there are several areas where additional field work and research could be conducted to better understand the impacts of streambed heating on water temperature.

- Although the streambed temperature data was valuable for developing the 3-D model additional data should be collected over longer time periods in multiple substrate types to better understand longer term streambed heat dynamics and their impact on water temperatures. Better field equipment would need to be

developed to allow the instruments to handle the environmental conditions and produce more reliable data. Additional river systems should be studied to better understand the variability between streambeds in river systems.

- Additional field data could be collected to better understand the heat transfer dynamics in the cobble reaches of rivers. Based on the model calibration to field data the interstitial water temperature plays key role in the cobble substrate temperatures which may indicate some hyporheic flow or simply saturated media well connected thermally to water column above. Both the cobble substrate and the interstitial water temperature need to be monitored to better understand the interaction.
- Additional light extinction data should be collected from river systems. The light extinction and reflection data collected in the Lower Bull Run River was limited but illustrated there are some difference with light attenuation in rivers versus lakes or oceans. Additional data from multiple river systems would better identify these differences from lake systems and their implications for river modeling.
- Additional stream channel bathymetry data. The model grid of the Lower Bull Run River was relatively coarse in the vertical direction with vertical layer of 0.5 or 1.0 m. An extensive data set of stream channel bathymetry over several kilometers would allow a more refined model grid and enable the model to be used to investigate the sensitivity of the streambed heating to channel morphology.

- Additional model sensitivity analyses could be conducted on different river systems with larger flows and other substrate types to broaden the scope of streambed heating impacts. Additional sensitivity analyses could also be conducted using the Lower Bull Run River model to refine the impacts vegetative shade, and simulate higher flows. The previous model calibration periods in 1999 could be revisited to investigate the streambed heating impacts during another time period.

## 8. References

- Adams, E. E., Harleman, D.R.F., Jirka, G., Ryan, P.J., and Stolzenbach, K.D. (1981). "Heat Disposal in the Water Environment." R.M. Parson Laboratory, Massachusetts Institute of Technology, Cambridge, MA.
- Anderson, E. R. (1954). "Energy Budget Studies, Water Loss Investigations – Lake Hefner Studies," Technical Report, *Geological Survey Professional Paper 269*, U. S. Geological Survey, Washington, D. C.
- Angstrom, A., (1929). "On the atmospheric transmission of sun radiation and on dust in the air," *Geographic Annals.*, 11, 156-166.
- Annear R. L., Wells, S. A., and Evonuk, D. (1999). "Bull Run River – Reservoir Model: Boundary Conditions and Model Setup." *Technical Report EWR-6-99*, Department of Civil and Environmental Engineering, Portland State University, Portland, OR.
- Annear, R. L., and Wells, S. A. (2000). "Bull Run River – Reservoir Model: Management Strategies to Meet Temperature Guidelines in the Lower Bull Run River." *Technical Report EWR-2-00*, Department of Civil and Environmental Engineering, Portland State University, Portland, OR.
- Annear, R. L., Berger, C., and Wells, S. A. (2001). "CE-QUAL-W2 Version 3.0 Shading Algorithm." *Technical Report EWR-3-01*, Department of Civil and Environmental Engineering, Portland State University, Portland, OR.
- Annear R., and Wells, S. A. (2002a). "Bull Run River – Reservoir Model: Reservoir Model Calibration." *Technical Report EWR-02-02*, Department of Civil and Environmental Engineering, Portland State University, Portland, OR.
- Annear R., and Wells, S. A. (2002b). "Bull Run River – Reservoir Model: River Model Calibration." *Technical Report EWR-03-02*, Department of Civil and Environmental Engineering, Portland State University, Portland, OR.
- Annear, R. L.; McKillip, M. L.; Khan, Sher Jamal; Berger, C. J.; and Wells, S. A. (2004). "Willamette River Basin Temperature TMDL Model: Boundary Conditions and Model Setup," *Technical Report EWR-01-04*, Department of Civil and Environmental Engineering, Portland State University, Portland, OR., 530 pp.
- Baldwin, E. M. (1981). *Geology of Oregon, Third Edition*, Kendall/Hunt Publishing, Dubuque, IA, 170 pp.

- Beak Consultants, Inc. (1998). "Verification of Shading Values in the Lower Bull Run River." prepared for the City of Portland Bureau of Water Works, Portland, OR.
- Beak Consultants, Inc. (2000). "Smolt Production Estimates for the Lower Bull Run River – 1999." prepared for the City of Portland Bureau of Water Works, Portland, OR.
- Beeson, M. H., and Moran, M. R. (1979). "Columbia River Basalt Group stratigraphy in western Oregon." *Oregon Geology*, 41(1), 11-14.
- Berger, C. J., M. L. McKillip, R. L. Annear, S. J. Khan, and S. A. Wells (2004). Willamette River Basin Temperature TMDL Model: Model Calibration, *Technical Report EWR-02-04*, Department of Civil and Environmental Engineering, Portland State University, Portland, OR., 341 pp.
- Bejan, A. (1993). *Heat Transfer*, John Wiley & Sons, Inc., New York, NY, 675 pp.
- Bird, R. E. and R. L. Hulstrom (1981). "A Simplified Clear Sky Model for Direct and Diffuse Insolation on Horizontal Surfaces," Solar Energy Research Institute, *TR-642-761*, Solar Energy Research Institute, Golden, CO., 33 pp
- Bolsenga, S. J. (1964). "Daily Sums of Global Radiation for Cloudless Skies." *Technical Report No. 160*, U.S. Army Material Command, Cold Regions Research and Engineering Laboratory, Hanover, NH, 124 pp.
- Bolsenga, S. J. (1965). "The Relationship Between Total Atmospheric Water Vapor and Surface Dew Point on a Mean Daily and Hourly Basis." *Journal of Applied Meteorology*, 4(3), 430-432.
- Bras, R. L. (1990). *Hydrology: An Introduction to Hydrologic Science*, Addison-Wesley Publishing Company, Reading, MA, 643 pp.
- Brown, G. W. (1969). "Predicting Temperatures of Small Streams." *Water Resources Research*, 5(1), 68-75.
- Brown, G. W. (1972). "An Improved Temperature Prediction Model for Small Streams." Water Resources Research Institute, Oregon State University, Corvallis, OR, 20 pp.
- Brown, L., and Barnwell, T. (1987). "The Enhanced Stream Water Quality Models QUAL2E and QUAL2E-UNCAS: Documentation and User Manual," *EPA/600/3-87/007*, Environmental Research Laboratory, U. S. Environmental Protection Agency, Athens, GA.

Carslaw, H.S., and Jaeger, J.C. (1959). *Conduction of Heat in Solids, Second Edition*, Oxford University, New York, NY, 510 pp.

Cenegal, Y. A. (1997). *Introduction to Thermodynamics and Heat Transfer*, McGraw-Hill Companies, Inc. New York, NY, 922 pp.

Chen, Y. (1996). "Hydrologic and Water Quality Modeling for Aquatic Ecosystem Protection and Restoration in Forest Watersheds: A Case Study of Stream Temperature in the Upper Grande Ronde River, Oregon." PhD dissertation, University of Georgia, Athens, GA, 268 pp.

Chen, Y., Carsel, R., McCuthcheon, S., and Nutter, W. (1998). "Stream Temperature Simulation of Forested Riparian Areas: Watershed-Scale Model Development." *Journal of Environmental Engineering*, 124(4), 304-315.

Chow, V. T. (1964). *Handbook of Applied Hydrology*, McGraw Hill Book Company, Inc., New York, NY, 825 pp.

Cole, T., and E. Buchak (1995). "CE-QUAL-W2: A Two-Dimensional, Laterally Averaged, Hydrodynamic and Water Quality Model, Version 2.0." *Instruction Report EL-95-1*, Waterways Experiment Station, US Army Corps of Engineers, Vicksburg, MS.

Cole, T., and Wells, S. A. (2000). "CE-QUAL-W2: A Two-Dimensional, Laterally Averaged, Hydrodynamic and Water Quality Model, Version 3.0." *Instruction Report EL-00-1*, Waterways Experiments Station, US Army Corps of Engineers, Vicksburg, MS.

Comer, L. E., Bowles, D. S., and Grenney, W. J. (1975). "Field Investigation and Mathematical Model for Heat Transfer Processes in the Bed of a Small Stream." PRWG156(a), Utah Water Research Laboratory, College of Engineering, Utah State University, Logan, UT, 102 pp.

Cugle, C. H. (1943). *Cugle's Two-Minute Azimuths, Volume Two*, E. P. Dutton & Co., Inc., New York, NY, 603 pp.

Cummins, K. W. (1973). "An evaluation of some techniques for the collection and analysis of benthic samples with special emphasis on lotic waters." *The American Midland Naturalist*, 67, 477-504.

Dake, J. M. K., and Harleman, D. R. F. (1966). *An Analytical and Experimental Investigation of Thermal Stratification in Lakes and Ponds*, Cambridge, MA, MIT, Department of Civil Engineering, Hydrodynamics Laboratory Report. 99.

- Dake, J. M. K., and Harleman, D. R. F. (1969). "Thermal Stratification in Lakes: Analytical and Laboratory Studies," *Water Resources Research*, 5(2), 484-495.
- Dave, J. V. (1978). "Extensive Datasets of the Diffuse Radiation in Realistic Atmospheric Models with Aerosols and Common Absorbing Gases," *Solar Energy*, 21, 361-369.
- David Evans and Associates (1991). "Summary Report: Bathymetric and Geophysical Surveying." prepared for the City of Portland Bureau of Water Works, Portland, OR.
- Department of Environmental Quality, State of Oregon (1998a). "Oregon's 1998 303(d) List Water body Segment Summary Report." <<http://www.deq.state.or.us/wq/303dlist/SegmentsSummaryReport.htm>> (December 28, 2002).
- Department of Environmental Quality, State of Oregon (1998b). "Questions and Answers About DEQ's Temperature Standards." <http://www.deq.state.or.us/wq/303dlist/TempFactSheet.htm>> (December 28, 2002).
- Department of Environmental Quality, State of Oregon (1999). "Heat Source Methodology Review." <<http://www.deq.state.or.us/wq/HeatSource/HeatSource.htm>> (December 28, 2002).
- Department of Environmental Quality, State of Oregon (2001). "Recommended modeling options to address Willamette River temperature, aquatic growth, dissolved oxygen, and pH concerns." Watershed Management Section, Department of Environmental Quality, Portland, OR, 20 pp.
- DiLaura, D.L. et al. (1984). "IES Calculation Procedures Committee Recommended practice for the calculation of daylight availability." *Journal of the Illuminating Engineering Society of North America*, 13(4), 381-392.
- Dingman, S. L. (2002). *Physical Hydrology, Second Edition*, Prentice Hall, Upper Saddle River, NJ, 646 pp.
- Eagleson, P. S. (1970). *Dynamic Hydrology*, McGraw-Hill, New York, NY, 462 pp.
- Edinger, J. E., Brady, D.K., and Geyer, J.C. (1974). "Heat Exchange and Transport in the Environment." *Report No.14, Electric Power Res. Inst. Pub. No. EA-74-049-00-3*, Palo Alto, CA, 125 pp.
- Elterman, L. (1964). "Atmospheric Attenuation Model, 1964, in the Ultraviolet, Visible, and Infrared Regions for Altitudes to 50 km," *Environmental Research Paper No 46, AFCRL 64-70*, Air Force Cambridge Research Laboratories, Bedford, MA, 40 pp.

Elterman, L. (1968). "Ultraviolet, Visible and Infrared Attenuation for Altitudes to 50 km," *Technical Report AFCRL 68-0153*, Air Force Cambridge Research Laboratories, Bedford, MA

Environmental Laboratory (1995). "CE-QUAL-RIV1: A Dynamic, One-Dimensional (Longitudinal) Water Quality Model for Streams: User's Manual," *Instruction Report EL-95-2*, Waterways Experiments Station, U. S. Army Corps of Engineers, Vicksburg, MS., 290 pp.

Environmental Protection Agency. (1971) "Effect of Geographical Location on Cooling Pond Requirements and Performance," in *Water Pollution Control Research Series. Report No. 16130 FDQ*, Water Quality Office, U. S. Environmental Protection Agency, Washington, D. C., 160 pp.

Fang, X., and Stefan, H. G. (1996). "Dynamics of heat exchange between sediment and water in a lake." *Water Resources Research*, 32(6), 1719-1727.

Fang, X., and Stefan, H. G. (1998). "Temperature variability in lake streambeds." *Water Resources Research*, 34(4), 717-729.

Flowers, E. C., McCormick, R. A., and Kurfis, K. R. (1969) "Atmospheric Turbidity over the United States, 1961-1966," *Journal of Applied Meteorology*, 8, 955-962.

French, R. H. (1985). *Open-Channel Hydraulics*, McGraw Hill, Inc., New York, NY, 705 pp.

Geiger, R. (1965). *The Climate Near the Ground*, Harvard University Press, Cambridge, MA 611 pp.

Grigull, U. and Sanders, H. (1984). *Heat Conduction*, Hemisphere Publishing Corporation, Washington, DC, 187 pp.

Gulliver, J. S. (1977). "Analysis of Surface Heat Exchange and Longitudinal Dispersion in a Narrow Open Field Channel with Application to Water Temperature Prediction," M.S. Thesis, University of Minnesota, Minneapolis, MN., 187 pp.

Halpern, P., Dave, J. V., Braslev, N. (1974) "Sea level solar radiation in the biologically active spectrum," *Science*, 186, 1204-1208.

Hamon, R. W., Weis, L. L., and Wilson, W. T. (1954). "Insolation as an Empirical Function of Daily Sunshine Duration," *Monthly Weather Review*, 82(6), 141-146.

- Hondzo, M., and Stefan, H. G. (1994). "Riverbed heat conduction prediction." *Water Resources Research*, 30(5), 1503-1513.
- Incropera, F. P., and De Witt, D. P. (1990). *Fundamentals of Heat and Mass Transfer*, John Wiley and Sons, Inc., New York, NY, 967 pp.
- Jerlov, N. G. (1968). *Optical Oceanography*, Elsevier Publishing Co., New York, NY, 194 pp.
- Jerlov, N. G. (1976). *Marine Optics*, Elsevier Publishing Co., New York, NY, 231 pp.
- Jobson, H. E. (1977). "Bed Conduction Computation for Thermal Models." *Journal of Hydraulics*, ASCE, 102(HY10), 1231-1217.
- Jobson, H. E., and Keefer, T. N. (1979). "Modeling Highly Transient Flow, Mass, and Heat Transport in the Chattahoochee River near Atlanta, Georgia." *Geological Survey Professional Paper 1136*, U.S. Geological Survey, 41 pp.
- Kasten, F. (1964). "A New Table and Approximation Formula for the Relative Optical Air Mass," *Technical Report No. 136*, U.S. Army Material Command, Cold Regions Research and Engineering Laboratory, Hanover, NH, 18 pp.
- Kennedy, R. E. (1940). "Average Daily Air Mass." *Monthly Weather Review*, 68(11), 301-303.
- Kennedy, R. E. (1949). "Computation of Daily Insolation Energy." *Bulletin of the American Meteorological Society*, 30(6), 208-213.
- Kim, K., and Chapra, S. (1997). "Temperature Model for Highly Transient Shallow Streams." *Journal of Hydraulic Engineering*, 123(1), 30-39.
- Kimball, H. H. (1930). "Measurements of Solar Radiation Intensity and Determination of its depletion by the Atmosphere," *Monthly Weather Review*, 58(2), 43-52.
- Klein, W. H. (1948). "Calculation of Solar Radiation and the Solar Heat Load on Man," *Journal of Meteorology*, 5(4), 119-129.
- Kraus, E. B. (1972). *Atmosphere-Ocean Interaction*, Clarendon Press, London, England, 275 pp.
- Kreith, F. and Bohn, M. S. (1986). *Principles of Heat Transfer*, Fourth Edition, Harper & Row, New York, NY, 700 pp.

LaHusen, R. G. (1994). "Variations in Turbidity in Streams of the Bull Run Watershed, Oregon, Water years 1989-90." *Water Resources Investigations Reports 93-4045*, U.S. Geological Survey, 33 pp.

Lee, R. (1978). *Forest Microclimatology*, Columbia University Press, New York, NY, 276 pp.

Likens, G.E., and Johnson, N.M. (1969). "Measurements and analysis of the annual heat budget for sediments of two Wisconsin lakes." *Limnol. Oceanogr.*, 14(1):115-135.

List, R. J. (1958). *Smithsonian Meteorological Tables, Sixth Edition*, Smithsonian Institution, Washington, D.C., 575 pp.

Meeus, J. (1999). *Astronomical Algorithms*, Second Edition, Willmann-Bell, Inc., Richmond, VA, 477 pp.

Mills, A. F. (1992). *Heat Transfer*, Irwin, Inc., Homewood, IL, 888 pp.

Moon, P. (1940). "Proposed standard solar radiation curves for engineering use," *Journal of Franklin Institute*, 230, 583-617.

Muneer, T. (1997). *Solar Radiation and Daylight Models for Energy Efficient Design of Buildings*, Architectural Press, New York, NY, 197 pp.

Muneer, T., Gul, M. S., and Kunie, J. (2000). "Models for Estimating Solar Radiation and Illuminance From Meteorological Parameters," *Journal of Solar Energy Engineering*, 122, 146-153.

National Aeronautics and Space Administration (2004). The Goddard Distributed Active Archive Center (DAAC), Climatology Interdisciplinary Data Collection, Total Solar Irradiance [http://daac.gsfc.nasa.gov/CAMPAIGN\\_DOCS/FTP\\_SITE/INT\\_DIS/readmes/sol\\_irrad.html](http://daac.gsfc.nasa.gov/CAMPAIGN_DOCS/FTP_SITE/INT_DIS/readmes/sol_irrad.html) (June, 15 2004)

National Marine Fisheries Service (1998). "Final Rule: Endangered and Threatened Species; Threatened Status for Two ESUs of Steelhead in Washington, Oregon, and California." *Federal Register*, 63(No. 53: March 19, 1998), 13347-13371.

National Marine Fisheries Service (1998). "Final Rule: Endangered and Threatened Species; Threatened Status for Three Chinook Salmon Evolutionarily Significant Units (ESUs) in Washington and Oregon, and Endangered Status for One Chinook Salmon ESU in Washington." *Federal Register*, 64(No 56: March 24, 1999), 14308-14328.

- National Oceanic and Atmospheric Administration (2004). "Solar Calculation Details," Surface Radiation Research Branch, <<http://www.srrb.noaa.gov/highlights/sunrise/calcdetails.html>> (October 8, 2004).
- Nautical Almanac Office (2000). *The Nautical Almanac for the Year 2001*, U.S. Naval Observatory, U.S. Government Printing Office, Washington D.C., 353 pp.
- Oregon Administrative Rules (2001). "Water Pollution Division 41, Statewide water quality management plans; beneficial uses, policies, standards, and treatment criteria for Oregon." *OAR340-041*, 270 pp.
- Orlob, G. T., and Selna (1967). "Prediction of Thermal Energy Distribution in Streams and Reservoirs." Water Resources Engineers, Inc., prepared for the California Department of Fish and Game, Walnut Creek, CA, 90 pp.
- Parker, E. R. (1967). *Materials Data Book fro Engineers and Scientists*, McGraw-Hill Book Co., New York, NY, 398 pp.
- Paulson, C. A., and Simpson, J. J. (1977). "Irradiance Measurements in the Upper Ocean." *Journal of Physical Oceanography*, 7, 952-956.
- Pelletier, G. and Chapra, S. (2004). QUAL2Kw, Documentation and User Manual for a Modeling Framework to Simulate River and Stream Water Quality, *Publication Number 03-03-041*, Washington State Department of Ecology, Olympia, WA, 177 pp.
- Pluhowski, E. J. (1970) "Urbanization and Its Effect on Temperature of the Streams on Long Island, New York," *Geological Survey Professional Paper 627-D*, U.S. Geological Survey, D. C, 110 pp.
- Reda, I. and Adreas, A. (2004) *Solar Position Algorithm for Solar Radiation Applications*, Technical Report NREL/TP-560-34302, Revised, National Renewable Energy Laboratory, Golden, CO, 56 pp.
- Reitan, C. H. (1960). "Distribution of Precipitable Water Vapor Over the Continental United States." *Bulletin of the American Meteorological Society*, 41(2), 79-87.
- Reitan, C. H. (1963). "Surface Dew Point and Water Vapor Aloft," *Journal of Applied Meteorology*, 2(6), 776-779.
- Ryan, P. J., and Stolzenbach, K. D. (1972). "Chapter 1: Environmental Heat Transfer." *Engineering Aspects of Heat Disposal from Power Generation*, D. R. F. Harleman, ed., R. M. Parson Laboratory for Water Resources and Hydrodynamics, Department of Civil Engineering, Massachusetts Institute of Technology, Cambridge, MA.

- Silliman, S. E., Ramirez, J., and McCabe, R. (1995). "Quantifying down-flow through creek sediments using temperature time series: one-dimensional solution incorporating measured surface temperature." *Journal of Hydrology*, 167, 99-119.
- Simpson, J. J., and Dickey, T. D. (1981). "Alternative Parameterizations of Downward Irradiance and Their Dynamical Significance." *Journal of Physical Oceanography*, 11, 876-882.
- Singh, V. (1992). *Elementary Hydrology*, Prentice Hall, New York, NY.
- Sinokrot, B., and Stefan, H. (1993). "Stream Temperature Dynamics: Measurements and Modeling." *Water Resources Research*, 29(7), 2299-2312.
- Sinokrot, B., and Stefan, H. (1994). "Stream Water Temperature Sensitivity to Weather and Bed Parameters." *Journal of Hydraulic Engineering*, 120(6), 722-736.
- Smith, W. (1966). "Note on the relationship between total precipitable water and surface dew point." *Journal of Applied Meteorology*, 5(5), 726-727.
- Spence, D.H.N. (1981) "Light Quality and Plant Responses Underwater", *Plants and the Daylight Spectrum*, H. Smith, ed., Academic Press, New York, NY.
- Spencer, J. W. (1971). "Fourier series representation of the position of the sun," *Search* 2(5), 172.
- Stefan, H. G., Gulliver, J., Hahn, M. G. and Fu, A. Y. (1980). "Water Temperature Dynamics in Experimental Field Channels: Analysis and Modeling," *Project Report No. 193*, St. Anthony Falls Laboratory, University of Minnesota, Minneapolis, MN.
- Swanson, D. A. (1978). "Highlights of the regional Columbia River Basalt mapping program, Basalt Waste Isolation Program: Richland, WA." *Rockwell Hanford Operations RHO-BWI-78-100*, 47.
- Theurer, F. D., Voos, K. A., and Miller, W.J. (1984). "Instream Water Temperature Model, Instream Flow," *Information Paper 16, FWS/OBS-84/15*, U.S. Fish and Wildlife Service, Washington, D.C.
- U.S. Forest Service (1997). *Bull Run Watershed Analysis*, Mt Hood National Forest, Pacific Northwest Region, U.S. Forest Service, Portland, OR, 521 pp.
- U.S. Geological Survey (1996). "Hydrogeological Setting and Preliminary Estimates of Hydrologic Components for the Bull Run Lake and the Bull Run Lake Drainage Basin, Multnomah and Clackamas Counties, Oregon." *Water Resources Investigations*

Report 96-4064, Prepared in Cooperation with City of Portland, Bureau of Water Works, Portland, OR. 47 pp.

U.S. Naval Observatory (2000). *The Astronomical Almanac for the Year 2001*, U.S. Government Printing Office, Washington, D.C., 548 pp.

U.S. Navy Hydrographic Office (1934). *Azimuths of the Sun and Other Celestial Bodies of Declination 0° to 23° for Latitudes Extending to 70° from the Equator, Fifteenth Edition*, H.O. Pub. No. 71, Vol. 5, U.S. Government Printing Office, Washington, D.C., 250 pp.

U.S. Navy Hydrographic Office (1952). *Tables of Computed Altitude and Azimuth: Latitudes 40° - 49°, Inclusive*, H.O. Pub. No. 214, Vol. 5, U.S. Government Printing Office, Washington, D.C., 300 pp.

Van Heuklon, T. K. (1979). "Estimating Atmospheric Ozone for Solar Radiation Models," *Solar Energy*, 22, 63-68.

Verduin, J. (1982). "Components Contributing to Light Extinction in Natural Waters: Methods of Isolation", *Archives of Hydrobiology*, Vol. 93, pp 303-312.

Water Bureau, City of Portland (2002a). "City of Portland, Bureau of Water Works: Introduction." <<http://www.water.ci.portland.or.us/intro.htm>> (Dec. 28, 2002).

Water Bureau, City of Portland (2002b). "City of Portland, Bureau of Water Works: Water System, Dams and Reservoirs." <<http://www.water.ci.portland.or.us/dams.htm>> (Dec. 28, 2002).

Wells, S. A. (1997). "Theoretical basis of the CE-QUAL-W2 river basin model." *Technical Report EWR-6-97*, Department of Civil and Environmental Engineering, Portland State University, Portland, OR.

Wells, S. A., Annear, R., and Berger, C. (1998). "Wetland Benches in the Lower Columbia Slough." *Technical Report EWR-1-98*, Department of Civil and Environmental Engineering, Portland State University, Portland, OR.

Wells, S. A. (1999). "River Basin Modeling Using CE-QUAL-W2." *Proceedings International Water Resources Engineering Conference*, ASCE, CD\_ROM, New York, NY.

Wetzel, R.G. (1975). *Limnology*, W.B. Saunders, Philadelphia, PA.

Williams, D. T., Drummond, G. R., Ford, D. E., and Robey, D. L. 1980. "Determination of Light Extinction Coefficients in Lakes and Reservoirs", in *Surface*

*Water Impoundments, Proceedings of the Symposium on Surface Water Impoundments, Volume II*, American Society of Civil Engineers, H.G. Stefan, ed.

Woolf, H. M. (1968). "On the computation of solar elevation angles and the determination of sunrise and sunset times," NASA technical memorandum, NASA TMX-1646, Washington, DC, 19 pp.

Wunderlich, W. (1972). "Heat and Mass Transfer between a Water Surface and the Atmosphere." *Report No 14, Report Publication No. 0-6803*, Water Resources Research Laboratory, Tennessee Valley Authority, Division of Water Control Planning, Engineering Laboratory, Norris, TN.

Zaneveld, J. R. V., and Spinrad, R. W. (1980). "An Arc Tangent Model of Irradiance in the Sea." *Journal of Geophysical Research*, 85(C9), 4919-4922.

## 9. Appendix A: Shade File Format

The shade file consists of 4 types of vegetation information for each bank of the river and then topographic information as well as specifying the time for leaf-out and for trees to loose their leaves if they are deciduous. The column headings are described in the following table:

Column Heading	Description
Segment	Segment number in the model. Only active segment numbers have shade characteristics.
DYNSh	If between 0 and 1 this is a non-dynamic constant shade reduction similar to that used in Version 3.0. If this number is negative, the rest of the columns to the right will be read and dynamic shading will be implemented.
TTEleLB	Tree top elevation on the left bank (m). The elevation of the left bank plus the height of the tree/vegetation are used to provide the tree top elevation. This is the elevation according to the local datum and is not the height above the stream bank.
TTEleRB	Tree top elevation on the right bank (m).
CIDisLB	Distance from the centerline of the river segment to the shade controlling line of vegetation on the left bank (m).
CIDisRB	Distance from the centerline of the river segment to the shade controlling line of vegetation on the right bank (m).
SRFLB1	Shade reduction factor, left bank. This applies from SRFJD1 to SRFJD2 (and over multiple years for the same time period if the simulation goes over 365 days). Based on the extent of vegetation along the length of the segment and the density of the vegetation (0 to 1).
SRFLB2	Shade reduction factor, left bank. This applies from SRFJD2 to SRFJD1 (and over multiple years for the same time period if the simulation goes over 365 days). Based on the extent of vegetation along the length of the segment and the density of the vegetation (0 to 1).
SRFRB1	Shade reduction factor, right bank. This applies from SRFJD1 to SRFJD2 (and over multiple years for the same time period if the simulation goes over 365 days). Based on the extent of vegetation

Column Heading	Description
	along the length of the segment and the density of the vegetation (0 to 1).
SRFRB2	Shade reduction factor, right bank. This applies from SRFJD2 to SRFJD1 (and over multiple years for the same time period if the simulation goes over 365 days). Based on the extent of vegetation along the length of the segment and the density of the vegetation (0 to 1).
TOPO1 to TOPO18	Topographic inclination angle (radians) for every 20° around a segment starting with TOPO1 at 0° North and moving clockwise.
SRFJD1	Shading reduction factor Julian day for which SRF #1 starts to apply. This is typically thought as “leaf-out” conditions for deciduous trees.
SRFJD2	Shading reduction factor Julian day for which SRF #2 starts to apply. This is typically thought as when deciduous trees loose their leaves.

The two tables below show the shade file characteristics used for the model of the study area in the Lower Bull Run River.

W2 Shading Input File, Vegetation and Topography, calibrated vegetation characteristics and corrected topography

Segment	Dyn Sh	TTEleL B	TTEleR B	CIDisL B	CIDis RB	SRFL B1	SRFL B2	SRFR B1	SRFR B2	TOP O1	TOP O2	TOP O3	TOP O4	TOP O5
1	1.0													
2	-1.0	204.68	209.53	17.46	24.39	0.71	0.52	0.75	0.56	0.286	0.228	0.110	0.021	0.078
3	-1.0	203.47	228.06	19.00	29.50	0.71	0.52	0.74	0.56	0.289	0.231	0.112	0.031	0.079
4	1.0													
5	1.0													
6	-1.0	200.65	231.00	20.33	27.32	0.69	0.51	0.73	0.55	0.291	0.230	0.112	0.063	0.080
7	-1.0	196.44	217.37	21.78	17.61	0.70	0.52	0.75	0.57	0.292	0.231	0.112	0.011	0.075
8	-1.0	202.48	218.31	25.38	16.57	0.71	0.53	0.76	0.58	0.294	0.231	0.113	0.011	0.074
9	-1.0	222.02	217.31	29.86	17.81	0.71	0.53	0.76	0.57	0.297	0.235	0.115	0.011	0.073
10	1.0													
11	1.0													
12	-1.0	197.71	199.05	38.21	19.37	0.71	0.53	0.75	0.57	0.301	0.240	0.117	0.013	0.072
13	-1.0	207.90	200.62	22.73	19.76	0.72	0.53	0.75	0.57	0.304	0.243	0.119	0.022	0.070
14	-1.0	216.05	206.99	18.40	16.57	0.71	0.53	0.75	0.57	0.305	0.243	0.118	0.012	0.071
15	-1.0	204.40	219.19	17.94	14.79	0.71	0.53	0.75	0.57	0.304	0.239	0.116	0.011	0.074
16	1.0													

Table continues on next page

Seg men t	TOPO 6	TOPO 7	TOPO 8	TOPO 9	TOPO 10	TOPO 11	TOPO 12	TOPO 13	TOPO 14	TOPO 15	TOPO 16	TOPO 17	TOPO 18	SRF JDI	SRF JD2
1															
2	0.196	0.238	0.302	0.293	0.222	0.122	0.034	0.065	0.163	0.283	0.340	0.329	0.332	91.	274.
3	0.197	0.227	0.301	0.296	0.227	0.127	0.037	0.061	0.160	0.285	0.329	0.326	0.328	91.	274.
4															
5															
6	0.194	0.223	0.304	0.301	0.232	0.130	0.041	0.057	0.156	0.287	0.319	0.323	0.322	91.	274.
7	0.189	0.225	0.304	0.302	0.238	0.130	0.041	0.050	0.150	0.290	0.309	0.319	0.315	91.	274.
8	0.182	0.228	0.302	0.304	0.243	0.129	0.043	0.048	0.149	0.294	0.306	0.319	0.315	91.	274.
9	0.175	0.229	0.299	0.304	0.242	0.128	0.043	0.048	0.150	0.298	0.306	0.320	0.317	91.	274.
10															
11															
12	0.163	0.230	0.293	0.303	0.240	0.125	0.041	0.048	0.153	0.293	0.305	0.326	0.320	91.	274.
13	0.156	0.231	0.288	0.302	0.242	0.125	0.041	0.047	0.153	0.287	0.303	0.331	0.321	91.	274.
14	0.154	0.234	0.285	0.303	0.245	0.128	0.042	0.045	0.150	0.281	0.299	0.332	0.320	91.	274.
15	0.155	0.238	0.285	0.306	0.249	0.133	0.045	0.041	0.144	0.274	0.293	0.329	0.317	91.	274.
16															

## 10. Appendix B: Statistics Calculations

Model-data error statistics were computed using formulas for the mean error, absolute mean error, and root mean square error. The mean error (ME) was calculated as

$$ME = \frac{\sum_1^n (\text{model} - \text{data})}{n} \quad (182)$$

The absolute mean error was calculated as

$$AME = \frac{\sum_1^n \text{abs}(\text{model} - \text{data})}{n} \quad (183)$$

The root mean square error was calculated as

$$RMS = \sqrt{\frac{\sum_1^n (\text{model} - \text{data})^2}{n}} \quad (184)$$

where  $n$  is the number of observations, model is the model predicted state variable and data is the field data variable.

### 11. Appendix C: Thermophysical Properties of Matter

Reference	Thermal Diffusivity, $\beta$ : $m^2/s$	Thermal conductivity, $k$ : W/m °C	Volumetric Heat capacity, $\rho c_p$ : J/m <sup>3</sup> °C	Density, $\rho$ : kg/m <sup>3</sup>	Specific Heat, $c_p$ : J/kg °C	Material
Air						
Chow (1964)	1.87E-05	0.02		1	1006	Air
Cenegal (1997)	2.21E-05	0.03		1	1005	Air at 25 °C
Mills (1992)		0.03		1	1005	Air at 25 °C
Asphalt						
Incropera and De Witt (1990)		0.06		2115	920	Asphalt
Bejan (1993)	3.60E-07	0.70		2120	920	Asphalt at 20 °C
Grigull and Sander (1984)	3.60E-07	0.70		2120	920	Asphalt at 20 °C
Kreith and Bohn (1986)		0.70		2120		Asphalt at 20 °C
Sediments, Bog						
Geiger (1965)		0.06	3.77E+05			Bog Soil
Geiger (1965)	2.80E-07					Bog, Depth 0-5 cm
Geiger (1965)	1.10E-07					Bog, Depth 5-30 cm
Brick						
Carslaw and Jaeger (1959)	3.80E-07	0.84		2600	838	Brick
Cenegal (1997)	5.20E-07	0.72		1920	835	Brick at 25 °C
Cement						

Reference	Thermal Diffusivity, $\alpha$ : $\text{m}^2/\text{s}$	Thermal conductivity, $k$ : $\text{W}/\text{m}^\circ\text{C}$	Volumetric Heat capacity, $\rho c_p$ : $\text{J}/\text{m}^3^\circ\text{C}$	Density, $\rho$ : $\text{kg}/\text{m}^3$	Specific Heat, $c_p$ : $\text{J}/\text{kg}^\circ\text{C}$	Material
Bejan (1993)	1.30E-07	0.30		3100	750	Cement (Portland, fresh, dry) at 20 °C
Grigull and Sander (1984)	1.30E-07	0.30		3100	750	Cement (Portland, fresh, dry) at 20 °C
Kreith and Bohn (1986)		1.05				Cement, hard at 20 °C
Clay						
Incropera and De Witt (1990)		1.30		1460	880	Clay
Kreith and Bohn (1986)	1.01E-06	1.26		1545	880	Clay (48.7% moisture) at 20 °C
Bejan (1993)	1.00E-06	1.28		1450	880	Clay at 20 °C
Grigull and Sander (1984)	1.00E-06	1.28		1450	880	Clay at 20 °C
Cenegal (1997)		1.30		1460	880	Clay at 25 °C
Geiger (1965)	3.60E-07					Clay, Depth 0-5 cm
Geiger (1965)	2.60E-07					Clay, Depth 5-30 cm
Geiger (1965)	5.00E-08 - 2.00E-07	0.08 - 0.63	4.19E+05 - 1.68E+06	2300 - 2700		Clay, dry
Geiger (1965)	6.00E-07 - 1.60E-06	0.84 - 2.10	1.26E+06 - 1.68E+06	1600 - 2200		Clay, wet
Concrete						
Geiger (1965)	1.00E-06	4.61	2.10E+06	2200 - 2500		Concrete

Reference	Thermal Diffusivity, $\beta$ : $\text{m}^2/\text{s}$	Thermal conductivity, $k$ : $\text{W}/\text{m } ^\circ\text{C}$	Volumetric Heat capacity, $\rho c_p$ : $\text{J}/\text{m}^3 ^\circ\text{C}$	Density, $\rho$ : $\text{kg}/\text{m}^3$	Specific Heat, $c_p$ : $\text{J}/\text{kg } ^\circ\text{C}$	Material
Jobson (1977)	1.00E-06, 6.00E-07 - 2.00E-05		2.30E+06			Concrete
Carslaw and Jaeger (1959)	4.20E-07	0.92		2300	964	Concrete (1:2:4)
Incropera and De Witt (1990)		1.40		2300	880	Concrete (stone mix)
Grigull and Sander (1984)	6.62E-07	1.28		2200	879	Concrete made with gravel, dry at 20 °C
Kreith and Bohn (1986)	4.90E-07	0.13		500	837	Concrete, dry at 20 °C
Mills (1992)	7.50E-07	1.40		2100	880	Concrete, stone 1-2-4 mix at 25 °C
Cenegal (1997)	7.50E-07	1.40		2300	880	Concrete, stone mix at 25 °C
Bejan (1993)	6.60E-07	1.28		2200	880	Concrete, with gravel, dry at 20 °C
Earth						
Bejan (1993)		1.51		1500		Earth, clayey, 28% moisture at 20 °C
Bejan (1993)	1.60E-07	0.59		2040	1840	Earth, coarse-grained at 20 °C
Grigull and Sander (1984)	1.60E-07	0.59		2040	1840	Earth, coarse-grained at 20 °C
Bejan (1993)	3.10E-07	0.13		466	880	Earth, Diatomaceous at 20 °C

Reference	Thermal Diffusivity, $\beta$ : $\text{m}^2/\text{s}$	Thermal conductivity, $k$ : $\text{W}/\text{m}^\circ\text{C}$	Volumetric Heat capacity, $\rho c_p$ : $\text{J}/\text{m}^3^\circ\text{C}$	Density, $\rho$ : $\text{kg}/\text{m}^3$	Specific Heat, $c_p$ : $\text{J}/\text{kg}^\circ\text{C}$	Material
Bejan (1993)		1.05		1500		Earth, Sandy, 8% moisture at 20 °C
Granite						
Carslaw and Jaeger (1959)	1.10E-06	2.51		2600	880	Granite
Bejan (1993)	1.20E-06	2.90		2750	890	Granite at 20 °C
Grigull and Sander (1984)	1.20E-06	2.90		2750	890	Granite at 20 °C
Kreith and Bohn (1986)		3.00		2750		Granite at 20 °C
Incropera and De Witt (1990)		2.79		2630	775	Granite, Barre
Cenegal (1997)		2.79		2630	775	Granite, Barre at 25 °C
Hummus						
Geiger (1965)	2.29E-07					Hummus, Depth 10-20 cm, Mean Summer Values
Geiger (1965)	2.58E-07					Hummus, Depth 2.5-5 cm, Mean Summer Values
Limestone						
Carslaw and Jaeger (1959)	7.00E-07	1.68		2500	922	Limestone
Incropera and De Witt (1990)		2.15		2320	810	Limestone, Salem
Cenegal (1997)		2.15		2320	810	Limestone, Salem at 25 °C
Loam						

Reference	Thermal Diffusivity, $\beta$ : $\text{m}^2/\text{s}$	Thermal conductivity, $k$ : $\text{W}/\text{m } ^\circ\text{C}$	Volumetric Heat capacity, $\rho c_p$ : $\text{J}/\text{m}^3 ^\circ\text{C}$	Density, $\rho$ : $\text{kg}/\text{m}^3$	Specific Heat, $c_p$ : $\text{J}/\text{kg } ^\circ\text{C}$	Material
Geiger (1965)	3.20E-07					Loam, Depth 0-5 cm
Geiger (1965)	2.80E-07					Loam, Depth 5-30 cm
Loess						
Geiger (1965)	6.59E-07					Loess, Depth 10-30 cm, Mean Summer Values
Geiger (1965)	8.60E-07					Loess, Depth 2.5-5 cm, Mean Summer Values
Marble						
Grigull and Sander (1984)	1.30E-6 - 1.40E-6	2.80		2500 - 2700	810	Marble at 20 °C
Cenegal (1997)	1.20E-06					Marble at 25 °C
Incropera and De Witt (1990)		2.80		2680	830	Marble, Halsten
Cenegal (1997)		2.80		2680	830	Marble, Halsten at 25 °C
Paint						
Cenegal (1997)						Paint, Black at 25 °C
Cenegal (1997)						Paint, White at 25 °C
Quartz						
Bejan (1993)	8.00E-07	1.40		2100 - 2500	780	Quartz at 20 °C
Grigull and Sander (1984)	7.20E-7 - 8.50E-7	1.40		2100 - 2500	780	Quartz at 20 °C
Quartzite						
Incropera and De Witt		5.38		2640	1105	Quartzite, Sioux

Reference	Thermal Diffusivity, $\beta$ : $\text{m}^2/\text{s}$	Thermal conductivity, $k$ : $\text{W}/\text{m } ^\circ\text{C}$	Volumetric Heat capacity, $\rho c_p$ : $\text{J}/\text{m}^3 ^\circ\text{C}$	Density, $\rho$ : $\text{kg}/\text{m}^3$	Specific Heat, $c_p$ : $\text{J}/\text{kg } ^\circ\text{C}$	Material
(1990)						
Cenegal (1997)		5.38		2640	1105	Quartzite, Sioux at 25 °C
Rock						
Chen et al. (1998)	1.18E-06		1.49E+06			Rock
Geiger (1965)	6.00E-07 - 2.30E-06	1.68 - 4.19	1.80E+06 - 2.43E+06	2500 - 2900		Rock
Geiger (1965)		4.61	2.18E+06			Rock
Carslaw and Jaeger (1959)	1.18E-06	1.76				Rock, Average
Chow (1964)	1.18E-06	1.76				Rock, Average
Sand						
Incropera and De Witt (1990)		0.27		1515	800	Sand
Jobson (1977)	7.70E-07		2.85E+06			Sand
Kim and Chapra (1997)	3.00E-07		1.39E+06	1750	795	Sand
Pluhowski (1970)		1.65				Sand and gravel, saturated with water
Cenegal (1997)		0.27		1515	800	Sand at 25 °C
Geiger (1965)	2.20E-07					Sand, Depth 0-5 cm
Geiger (1965)	1.15E-06					Sand, Depth 10-20 cm, Mean Summer Values
Geiger (1965)	4.33E-07					Sand, Depth 2.5-5 cm, Mean Summer Values
Geiger (1965)	4.40E-07					Sand, Depth 5-30 cm

Reference	Thermal Diffusivity, $\beta$ : $m^2/s$	Thermal conductivity, $k$ : $W/m\ ^\circ C$	Volumetric Heat capacity, $\rho c_p$ : $J/m^3\ ^\circ C$	Density, $\rho$ : $kg/m^3$	Specific Heat, $c_p$ : $J/kg\ ^\circ C$	Material
Geiger (1965)		0.17	1.17E+06			Sand, dry
Geiger (1965)	3.00E-07 - 5.00E-07	0.17 - 0.29	4.19E+05 - 1.68E+06	1400 - 1700		Sand, dry
Bejan (1993)		0.58				Sand, dry at 20 °C
Kreith and Bohn (1986)		0.58				Sand, dry at 20 °C
Bejan (1993)		1.13		1640		Sand, moist at 20 °C
Kreith and Bohn (1986)		1.13		1640		Sand, moist at 20 °C
Geiger (1965)	4.00E-07 - 1.00E-06	0.84 - 2.51	8.38E+05 - 2.51E+06	2600		Sand, wet
Geiger (1965)		1.68	1.68E+06			Sand, wet
Sandstone						
Carslaw and Jaeger (1959)	1.10E-06	2.51		2300	964	Sandstone
Bejan (1993)	1.00E-6 - 1.30E-6	1.6-2.1		2150 - 2300	710	Sandstone at 20 °C
Grigull and Sander (1984)	1.00E-6 - 1.30E-6	1.60 - 2.10		2150 - 2300	710	Sandstone at 20 °C
Incropera and De Witt (1990)		2.90		2150	745	Sandstone, Berea
Cenegal (1997)		2.90		2150	745	Sandstone, Berea at 25 °C
Bejan (1993)		0.90		1780		Sandy Clay at 20 °C
Sediment, Lake						
Likens and Johnson (1969)		0.57				Sediments, central area of Tub Lake

Reference	Thermal Diffusivity, $\beta$ : $\text{m}^2/\text{s}$	Thermal conductivity, $k$ : $\text{W}/\text{m}^\circ\text{C}$	Volumetric Heat capacity, $\rho c_p$ : $\text{J}/\text{m}^3^\circ\text{C}$	Density, $\rho$ : $\text{kg}/\text{m}^3$	Specific Heat, $c_p$ : $\text{J}/\text{kg}^\circ\text{C}$	Material
Likens and Johnson (1969)		0.46				Sediments, Gelatinous, central area of Stewart's Dark Lake
Fang and Stefan (1998)	4.05E-07		2.30E+06			Sediments, Lake
Likens and Johnson (1969)		0.59				Sediments, shoreline at Stewart's Dark Lake
Likens and Johnson (1969)		0.57				Sediments, shoreline at Tub Lake
Soil						
Incropera and De Witt (1990)		0.52		2050	1840	Soil
Carslaw and Jaeger (1959)	4.60E-07	0.96	2.10E+06	2500	838	Soil (average)
Cenegal (1997)		0.52		2050	1840	Soil at 25 °C
Chow (1964)	4.60E-07	0.96		2500	838	Soil, Average
Bejan (1993)	4.00E-07	1.00		1500	1840	Soil, dry at 20 °C
Kreith and Bohn (1986)	1.38E-07	0.35		1500	1842	Soil, dry at 20 °C
Mills (1992)	3.50E-07	1.00		1500	1900	Soil, dry at 25 °C
Cenegal (1997)	5.20E-07					Soil, dry, heavy at 25 °C
Carslaw and Jaeger (1959)	3.30E-07	0.59		1750	1006	Soil, Sandy with 8% moisture
Chow (1964)	3.30E-07	0.59		1750	1006	Soil, Sandy with 8% moisture

Reference	Thermal Diffusivity, $\beta$ : $\text{m}^2/\text{s}$	Thermal conductivity, $k$ : $\text{W}/\text{m}^\circ\text{C}$	Volumetric Heat capacity, $\rho c_p$ : $\text{J}/\text{m}^3^\circ\text{C}$	Density, $\rho$ : $\text{kg}/\text{m}^3$	Specific Heat, $c_p$ : $\text{J}/\text{kg}^\circ\text{C}$	Material
Geiger (1965)	2.00E-07	0.25	1.26E+06	1500		Soil, Sandy with Water content, 0% volume
Geiger (1965)	6.00E-07	1.01	1.68E+06	1600		Soil, Sandy with Water content, 10% volume
Geiger (1965)	7.20E-07	1.51	2.10E+06	1700		Soil, Sandy with Water content, 20% volume
Geiger (1965)	6.60E-07	1.68	2.51E+06	1800		Soil, Sandy with Water content, 30% volume
Geiger (1965)	6.10E-07	1.80	2.93E+06	1900		Soil, Sandy with Water content, 40% volume
Carslaw and Jaeger (1959)	2.00E-07	0.26		1650	796	Soil, sandy, dry
Chow (1964)	2.00E-07	0.26		1650	796	Soil, sandy, dry
Bejan (1993)		2.00		1930		Soil, wet at 20 °C
Kreith and Bohn (1986)	4.14E-07	2.60		1500		Soil, wet at 20 °C
Mills (1992)	5.00E-07	2.00		1900	2200	Soil, wet at 25 °C
Stone						
Kim and Chapra (1997)	9.00E-07		2.00E+06	2500	800	Stone
Water						
Carslaw and Jaeger (1959)	1.44E-07	0.60		1000	4190	Water
Chow (1964)	1.44E-07	0.60		1000	4190	Water
Geiger (1965)	1.30E-07 - 1.50E-07	0.54 - 0.63	4.19E+06	1000		Water

Reference	Thermal Diffusivity, $\beta$ : $\text{m}^2/\text{s}$	Thermal conductivity, $k$ : $\text{W}/\text{m } ^\circ\text{C}$	Volumetric Heat capacity, $\rho c_p$ : $\text{J}/\text{m}^3 ^\circ\text{C}$	Density, $\rho$ : $\text{kg}/\text{m}^3$	Specific Heat, $c_p$ : $\text{J}/\text{kg } ^\circ\text{C}$	Material
Grigull and Sander (1984)	1.43E-07	0.60		998	4183	Water at 20 °C
Cenegal (1997)	1.40E-07	0.61			4180	Water at 25 °C
Mills (1992)	1.47E-07	0.61		997	4178	Water at 25 °C
Plastic						
Parker (1967)	1.974E-07	0.43		952	2303	High-density polyethylene, HDPE

## **12. Appendix D: Temperature Probe Quality Assurance and Control**

This appendix details some of the temperature data collected in the field and lab which were recognized as being suspect or outright erroneous. A lot of effort was put into designing the temperature probes and conducting the field monitoring and the lab experiments. Even with precautions suspect data was identified. Some possible explanations for the suspect data include: water intrusion into the temperature probes, moisture in the data logger box affecting wire connections, and damage to the temperature thermistors. Additional tests were conducted with a couple of the temperature probes to determine how well they would work in the temperature range from freezing to room temperature.

### **12.1 Suspect and Erroneous Data**

#### **12.1.1 Field Monitoring**

The streambed field monitoring used temperature probes with an array of thermistors in a pipe which was put in the streambed substrate. The first set of data was collected in the cobble substrate and did not require the full length of the monitoring probes to be submerged under water. The data collected during this time period was initially found to be reasonable with no indications of suspect or erroneous data. The temperature probes were then placed in the bedrock substrate using holes drilled by the City of Portland, Water Bureau. The probes were then inserted to a

depth of 1 m which required them to be fully submerged and all of the thermistors on each array to be used. The bedrock monitoring consisted of the temperature probes being placed in the substrate for 1 week. Upon download of the data there were several thermistors that were found to be providing incorrect readings. Due to limits on time left in the field season and increasing river flows, it was not possible to build new temperature probes and have them placed in the bedrock substrate for another few weeks.

Figure 167 shows the temperature data collected by Probe 4, which was placed in the shaded area near the south bank of the Bull Run River. The water temperature presented in this figure was provided by a different instrument maintained at the nearby USGS gage station (14140000, Bull Run River near Bull Run, OR). The figure shows the temperature recorded at a depth of 0.0 m has a diurnal cycle but quickly rises above the temperature of the overlying water. The temperature at a depth of 0.2 m also increases above the overlying water temperature and shows little diurnal change indicating the measurements were inaccurate. The temperature measurements at a depth of 0.6 m were also found to be suspect based on Figure 167, which shows the temperatures initially lower than the temperatures at 0.4 m and 0.8 m depth and then rising above the temperatures at depth 0.4 m. Although the temperature measurements are within a reasonable range their relative position to measurements at 0.4 and 0.8 m depths indicate there were changes at 0.6 m depth temperature that were not seen at other depths.

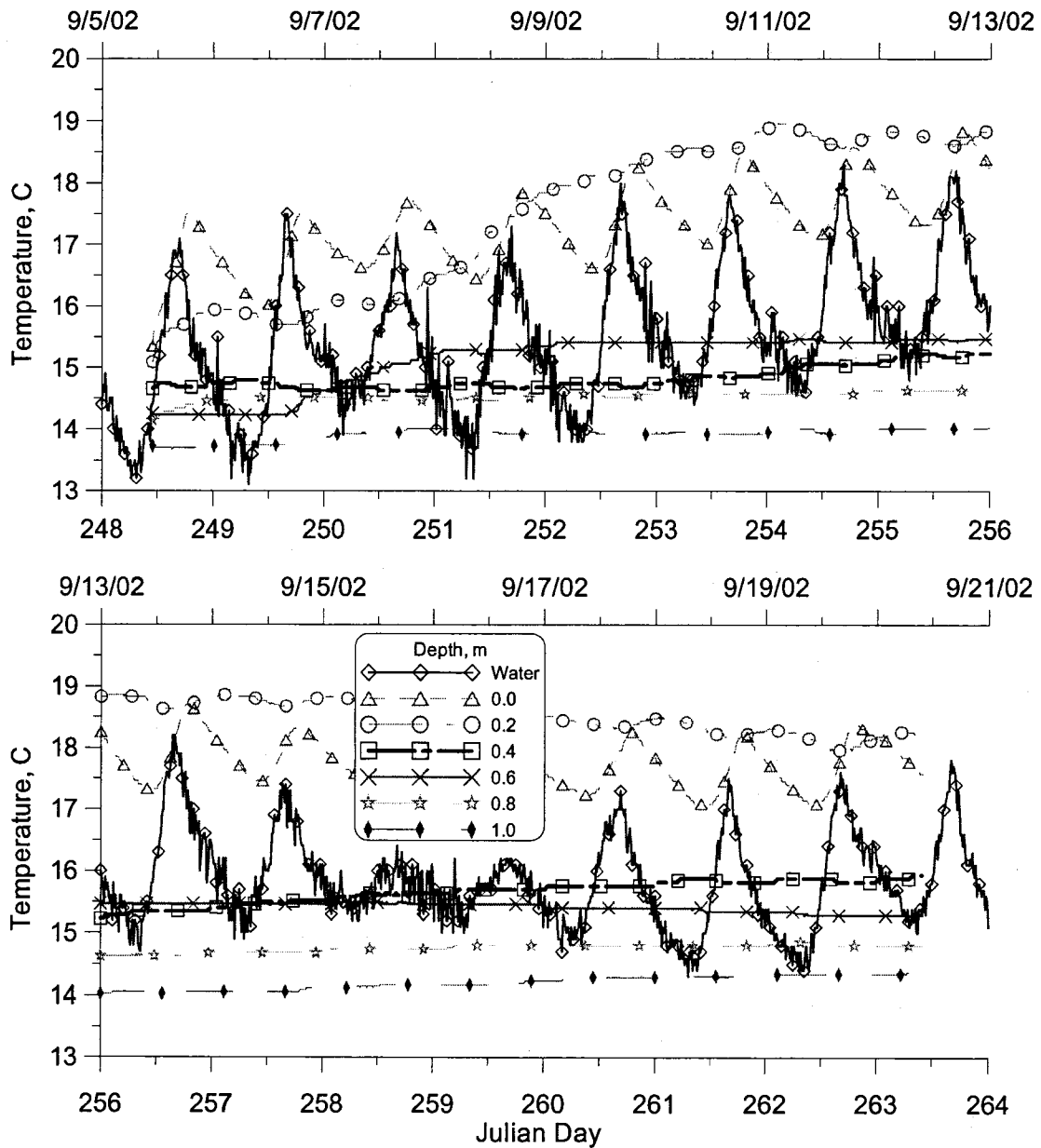


Figure 167: Probe 4 temperature data, placed in bedrock near south bank of Bull Run River, shaded

Figure 168 shows the temperature data collected by Probe 5, which was near the north bank of the Bull Run River with more solar exposure. The water temperature presented in this figure was provided by the USGS gage station nearby. The figure shows the temperatures at 0.6 m depth are fluctuating above and below the

temperature recorded at 0.4 m depth. The temperature measurements at the depth 0.6 m may be reasonable but the deviation above the 0.4 m depth of up to 0.7 °C in the first 5 days was not reasonable.

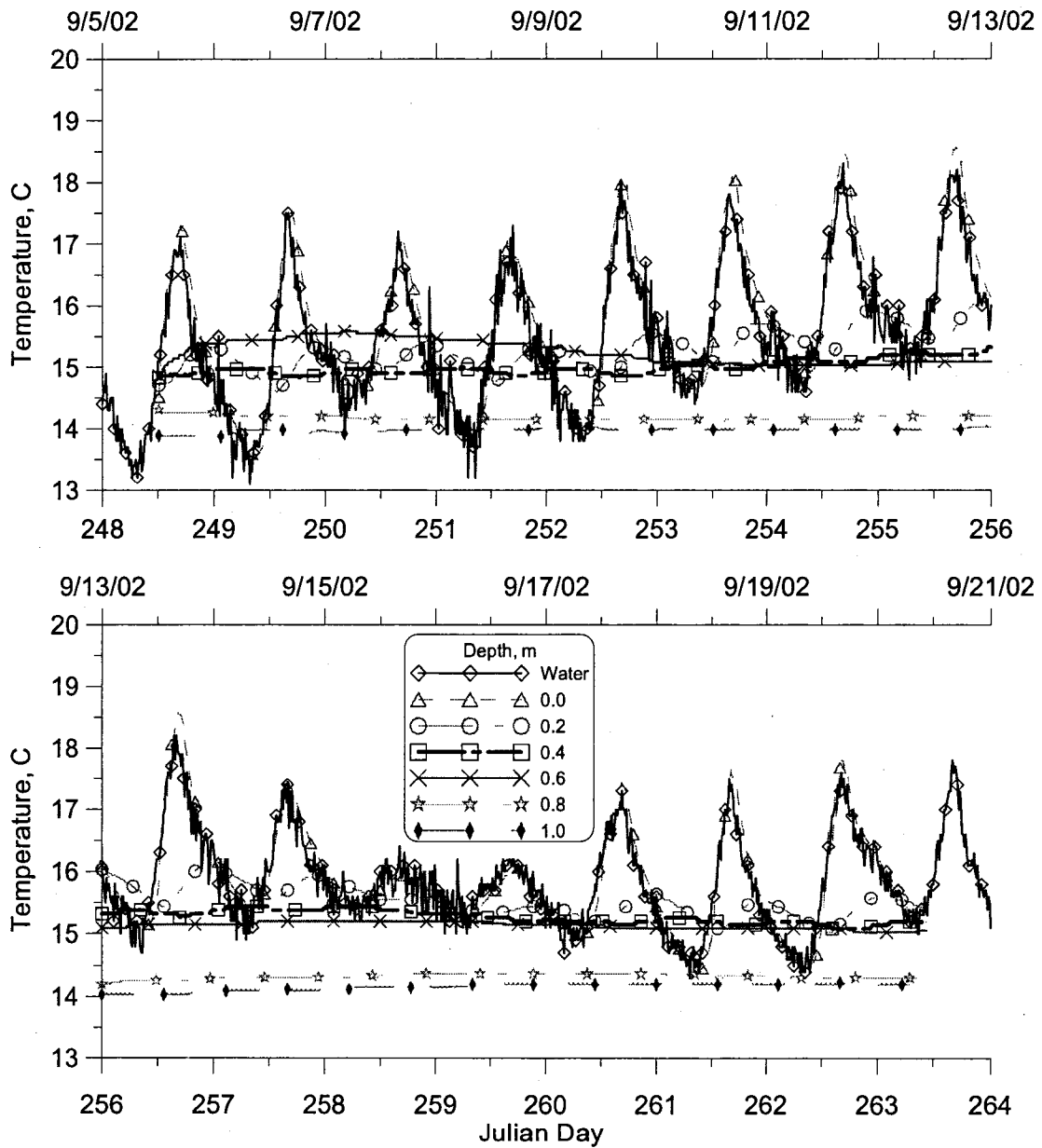


Figure 168: Probe 5 temperature data, placed in bedrock near north bank of Bull Run River, sun exposure

### **12.1.2 Experimental Lab Work**

The experimental lab work was conducted after the field monitoring and new temperature probes were developed using the same design used in the field. Each temperature probe consisted of four thermistors which were buried in the substrate and one in the overlying water column. During the lab experiments some of the thermistors in the substrate were found to record suspect data but the thermistors used to record the media boundary conditions and the air and water temperature were not found to have suspect or erroneous data. This may indicate that abrasions on the thermistors from the media and submersion in the wet substrate may have had an impact on the quality of the data.

#### **12.1.2.1 Experiment 1**

Temperature data from the first lab experiment indicated the temperature measurements recorded in the sand substrate (Cylinder 2, Probe 2, T10, refer to Figure 69 and Table 42) at a depth of 16 cm were erroneous as shown in Figure 169. The figure shows the temperature recorded at the deepest location rising rapidly to exceed the temperatures recorded at all other depths and the water temperature.

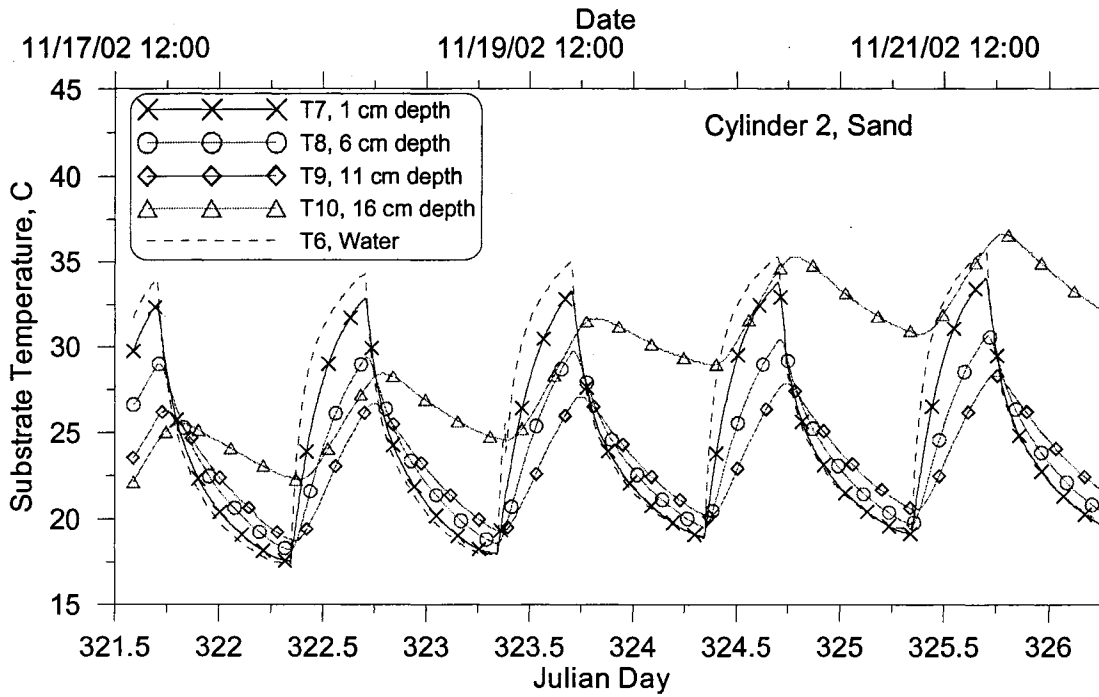
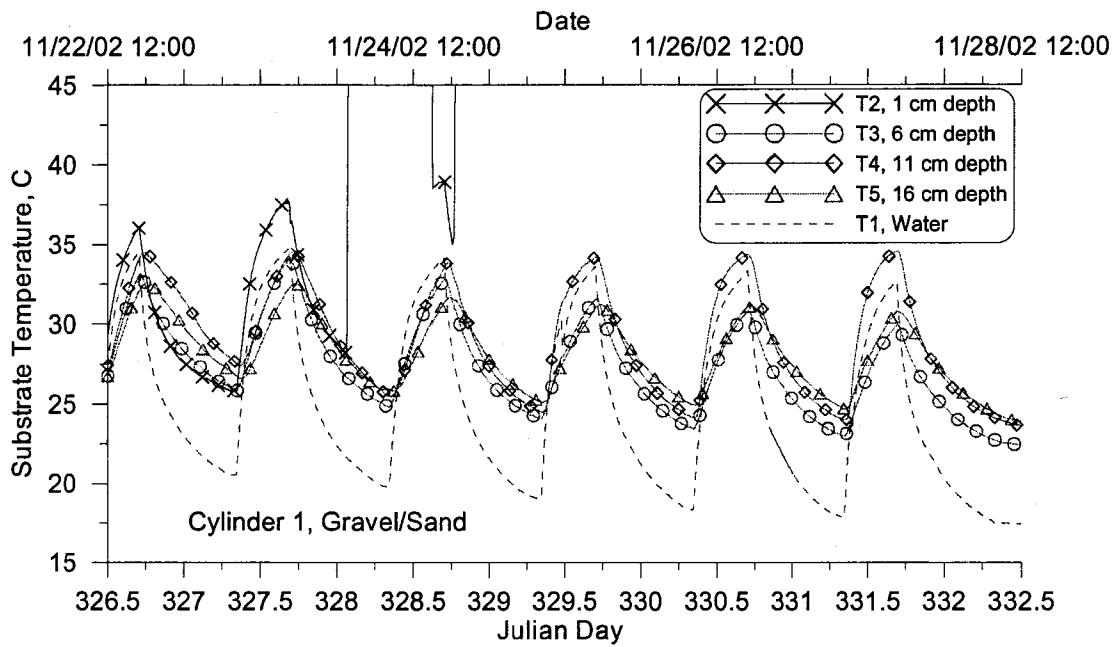


Figure 169: Experiment 1, Probe 2 temperature data recorded in the sand substrate.

### 12.1.2.2 Experiment 2

Figure 170 shows the temperature data recorded in the gravel-sand mixture substrate for experiment 2 (Cylinder 1, Probe 1, refer to Figure 69 and Table 42). The figure indicates the temperature measurements at a depth of 1 cm (T2) and 11 cm (T4) were erroneous. The substrate temperatures recorded at 1 cm depth at the start the lab experiment had reasonable diurnal changes but quickly increased well beyond the temperature range of the experimental setup. Temperatures recorded at 11 cm depth were within reason except the daily peak temperatures increased well above temperatures recorded at other depths.



**Figure 170: Experiment 2, Probe 1 temperature data recorded in the gravel - sand mixture substrate**

The second experiment was an extension of the first experiment so the substrate temperatures recorded in the sand substrate (Cylinder 2, Probe 2, refer to Figure 69 and Table 42) showed erroneous results at a depth of 16 cm (T10) for this experiment as well. Figure 171 shows the temperature data recorded in the sand substrate for the experiment and shows the 16 cm depth temperature was well above all other substrate and water temperature measurements.

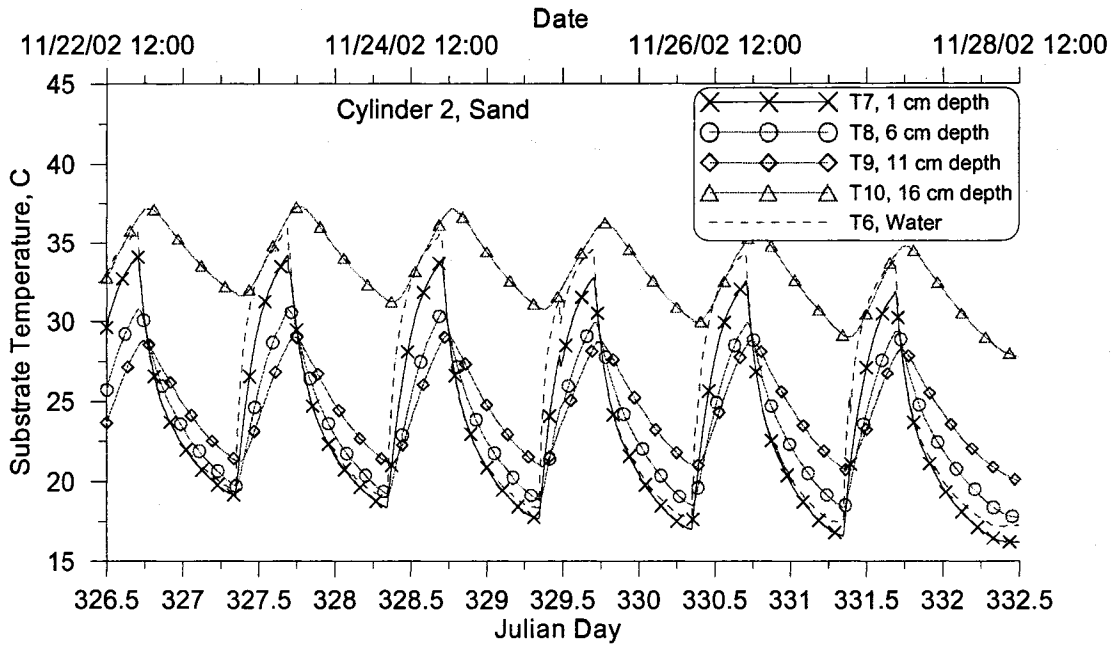


Figure 171: Experiment 2, Probe 2 temperature data recorded in the sand substrate

### 12.1.2.3 Experiment 3

The same probes used in the previous two experiments were then used in monitoring temperature in concrete. Figure 172 shows the temperature data recorded by Probe 1 in the black painted concrete. The figure indicates the erroneous temperature data at depths of 1 cm (T2), 6 cm (T3) and 11 cm (T4) leaving only the data recorded at a depth of 16 cm as reasonable. Figure 173 shows the temperature data recorded by Probe 2 in the white painted concrete where the 16 cm depth temperatures were suspect when compared to the temperatures recorded in substrate at shallower depths.

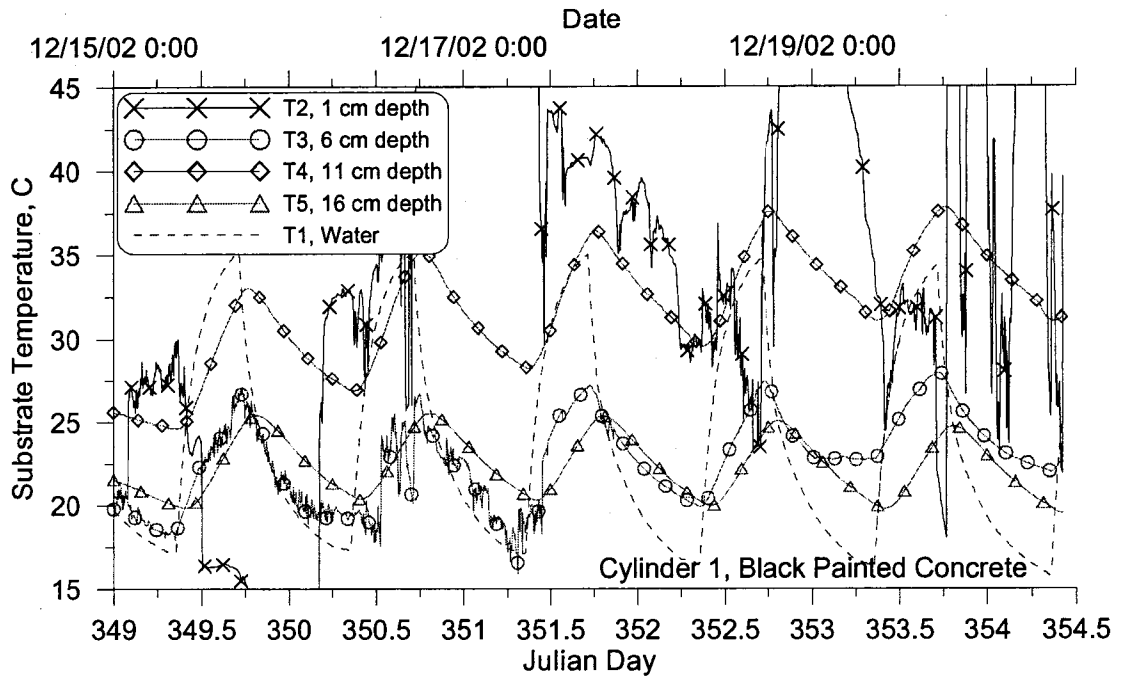


Figure 172: Experiment 3, Probe 1 temperature data recorded in the black painted concrete substrate

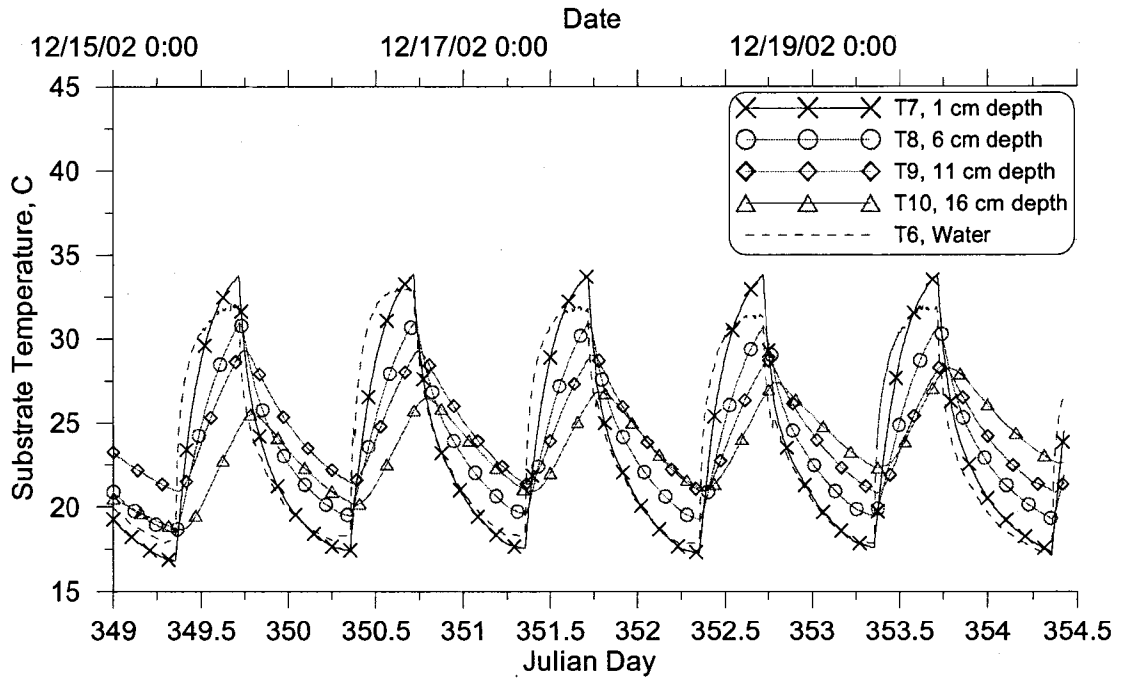


Figure 173: Experiment 3, Probe 2 temperature data recorded in the white painted concrete substrate

## 12.2 Quality Assurance and Control

In order to determine the accuracy of individual thermistors in temperature Probes 4 and 5, each probe was tested under varying conditions and the recorded temperature data was checked for consistency. In experiments 1 and 3 both probes were allowed to sit in a lab for several days and record room temperature. All of the thermistors should record the same temperature readings, and if not it would identify if thermistors were not functioning properly. Experiments 2 and 4 involved immersing each probe in ice water, allowing them to cool to approximately 0 °C, then removing the thermistors from the water and allowing them to return to room temperature. The two experiments provided an opportunity to observe the thermistors' behavior under changing temperature conditions. The four experiments helped isolate malfunctioning thermistors and assist with the interpretation of the field temperature data.

Figure 174 shows a diagram illustrating how the field temperature probes were used and labels the individual thermistors A2 to A7. Table 25 lists the thermistor depth for each of the field probes.

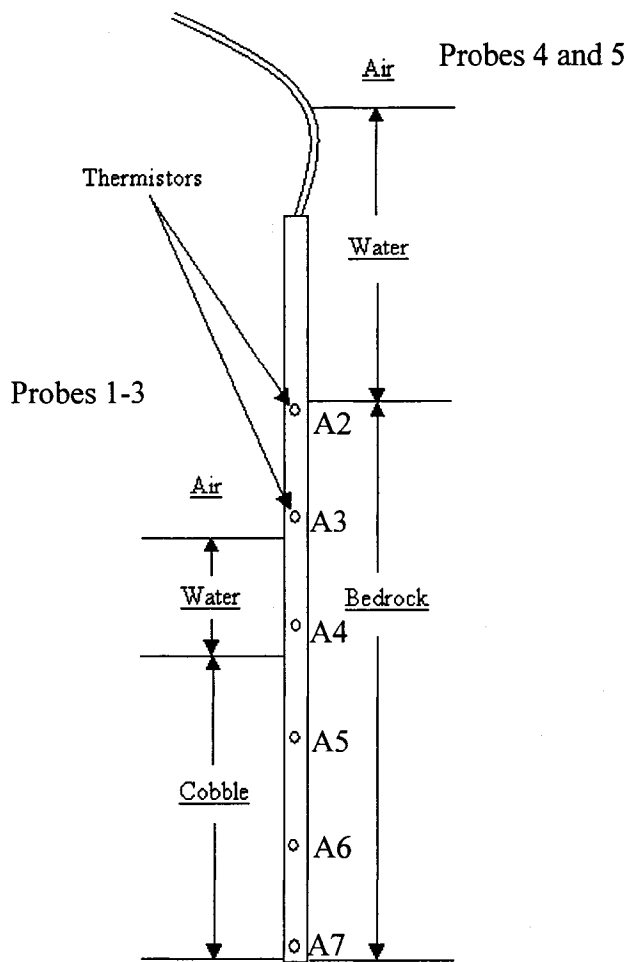


Figure 174: Streambed temperature probes, cobble substrate to a depth of 0.5 m, bedrock substrate to a depth of 1 m.

Table 98: Thermistor depths of streambed temperature Probes for cobble and bedrock

Probe	1	2	3 (also 2)	4 (also 2)	5 (also 1)	Thermistor
Substrate	Cobble	Cobble	Cobble	Bedrock	Bedrock	
	Depth, m	Depth, m	Depth, m	Depth, m	Depth, m	
Relative to the substrate- water interface				0.0	0.0	A2
				0.2	0.2	A3
				0.4	0.4	A4
	0.11	0.07	0.10	0.6	0.6	A5
	0.31	0.27	0.30	0.8	0.8	A6
	0.51	0.47	0.50	1.0	1.0	A7

### **12.2.1 Temperature Probe 4**

Probe 4 was used in monitoring the bedrock streambed temperature near the south bank of the Bull Run River. Prior to monitoring of the bed rock the probe was also used to monitor the cobble substrate temperature (Probe 2 and Probe 3).

#### **12.2.1.1 Experiment 1, Air test**

Probe 4 measured the room air temperature for 6 days. Figure 175 shows the temperature measurements for this experiment and Table 99 lists the results of an analysis of each thermistor's accuracy. At the time of experiment the top thermistor, A2, was accidentally disconnected from the logger so there was no data available. The results indicate there is a bias between the A3 thermistor measurements and the rest of the other thermistor measurements.

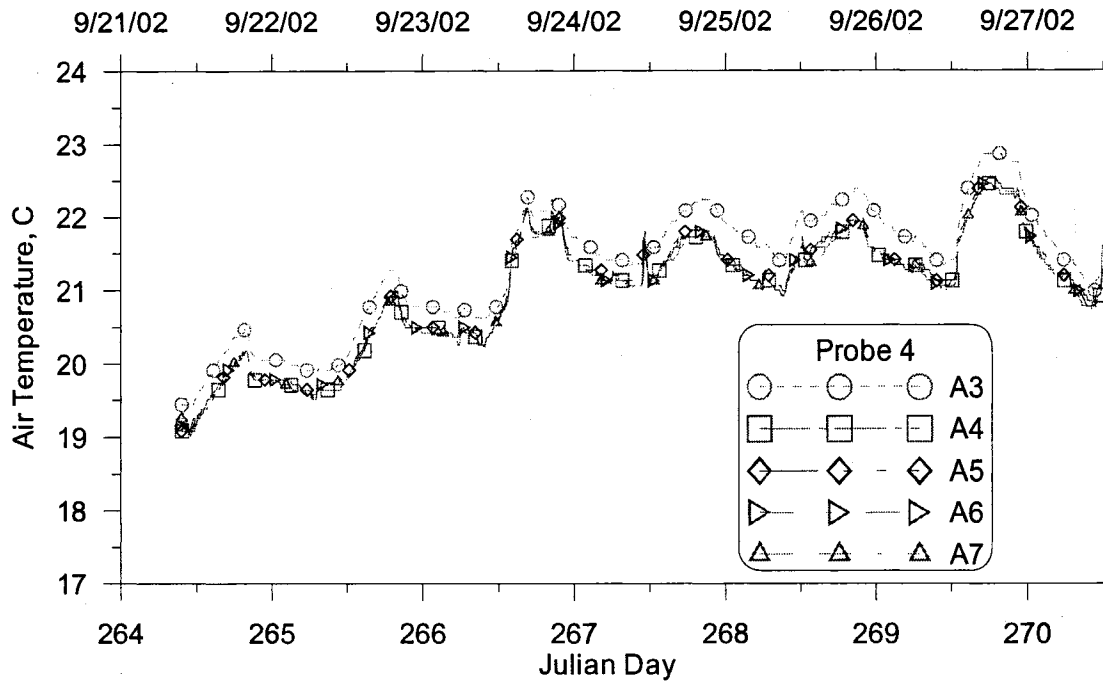


Figure 175: Measured thermistor temperatures in Probe 4, Experiment 1, Air Test.

Table 99: Accuracy of thermistors in Probe 4, Experiment 1, Air Test.

Thermistor	Accuracy
A2	Disconnected from experiment, no data
A3	0.1 to 0.58 °C above average recorded data for thermistors A4-A7
A4	Consistent with average recorded data (A4-A7)
A5	Consistent with average recorded data (A4-A7)
A6	Consistent with average recorded data (A4-A7)
A7	Consistent with average recorded data (A4-A7)

### 12.2.1.2 Experiment 2, Ice test

Probe 4 was immersed in ice water, removed, and allowed to return to room temperature. Figure 176 shows the temperature measurements for this experiment and Table 100 lists the results of an analysis of each thermistor's accuracy. The results are similar to the air test and indicate there is bias with the A3 thermistor compare to the

rest of the thermistors. The results also indicate there was a slight slower recovery to room temperature for thermistors A5 and A7.

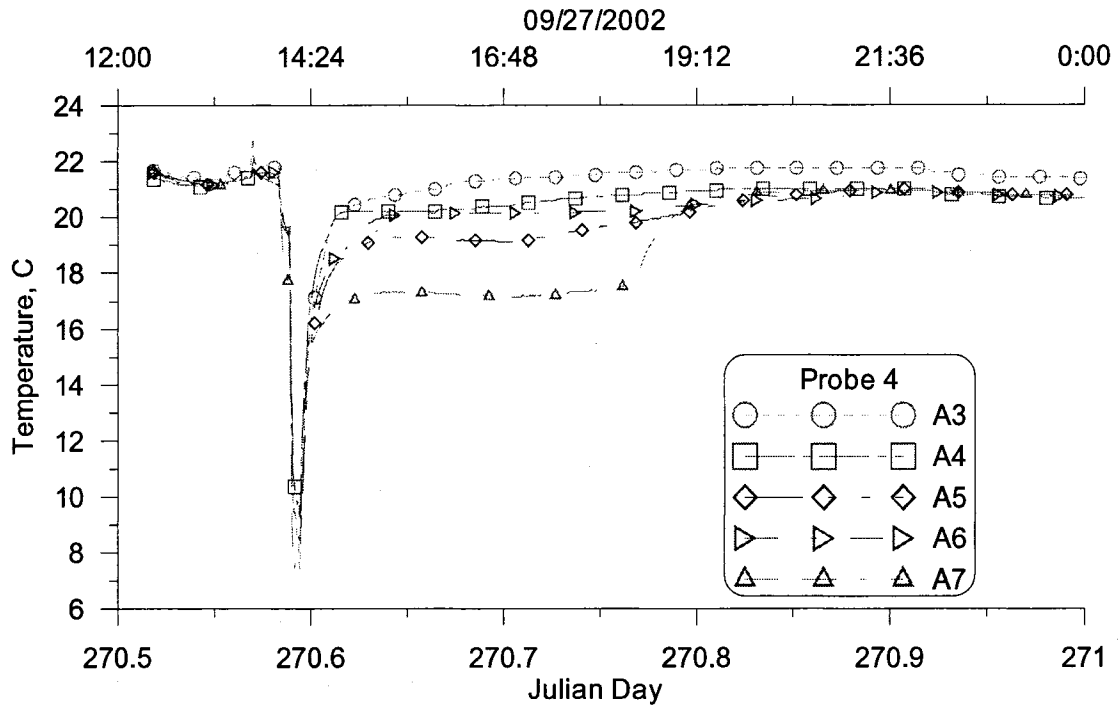


Figure 176: Measured thermistor temperatures in Probe 4, Experiment 2, Ice Test.

Table 100: Accuracy of thermistors in Probe 4, Experiment 2, Ice Test.

Thermistor	Accuracy
A2	Disconnected from experiment, no data
A3	0.54 to 2.18 °C above average recorded data for thermistors A4-A7
A4	Consistent with average recorded data (A4-A7)
A5	Consistent with average recorded data (A4-A7)
A6	Consistent with average recorded data (A4-A7)
A7	Consistent with average recorded data (A4-A7)

### 12.2.1.3 Experiment 3, Second Air test

Probe 4 measured the air temperature of in a laboratory for 8.5 days. Figure 177 shows the temperature measurements for this experiment and Table 101 lists the

results of an analysis of each thermistor's accuracy. Results are similar to the two previous experiments showing the A3 thermistor with a temperature bias compared the remaining thermistors.

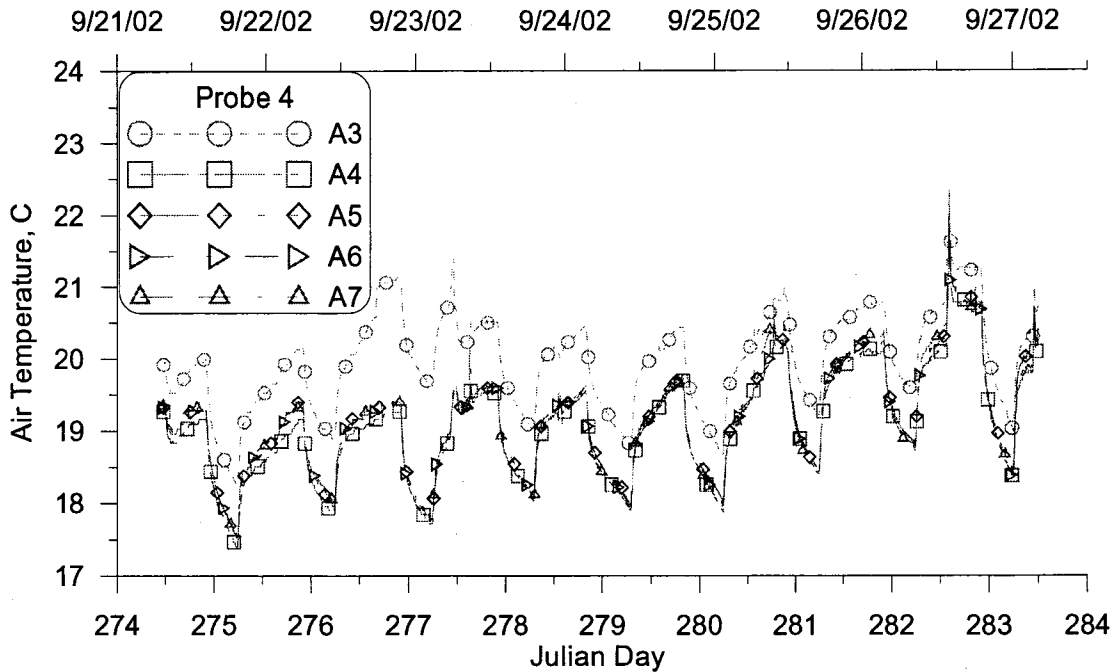


Figure 177: Measured thermistor temperatures in Probe 4, Experiment 3, Air Test.

Table 101: Accuracy of thermistors in Probe 4, Experiment 3, Air Test.

Thermistor	Accuracy
A2	Disconnected from experiment, no data
A3	0.27 to 1.89 °C above average recorded data for thermistors A4-A7
A4	Consistent with average recorded data (A4-A7)
A5	Consistent with average recorded data (A4-A7)
A6	Consistent with average recorded data (A4-A7)
A7	Consistent with average recorded data (A4-A7)

### 12.2.1.4 Experiment 4, Second Ice test

Probe 4 was immersed in ice water until the temperature probes measured 0 °C, removed, and allowed to return to room temperature. Figure 178 shows the temperature measurements for this experiment and Table 102 lists the results of an analysis of each thermistor's accuracy. The disconnection between the A2 thermistor and the logger was corrected for this experiment and allowed the data to be evaluated. The results indicate that only the A3 thermistor was consistent above the remaining thermistors. The experiment also showed a faster recovery to room temperature for the A7 thermistor.

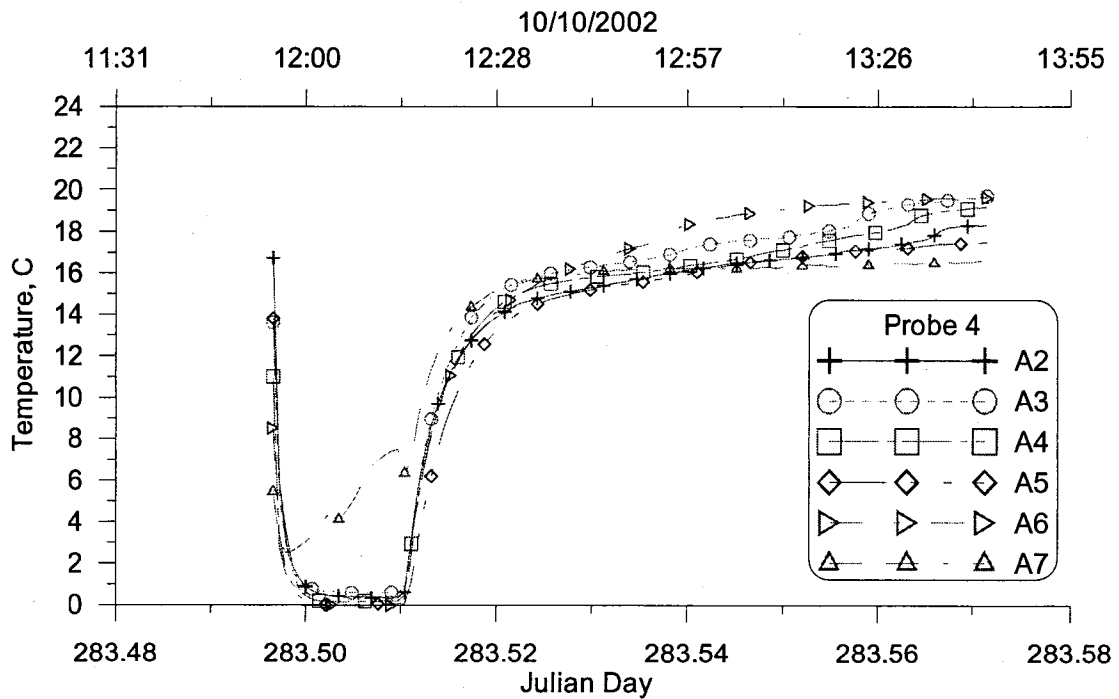


Figure 178: Measured thermistor temperatures in Probe 4, Experiment 4, Second Ice Test.

**Table 102: Accuracy of thermistors in Probe 4, Experiment 4, Second Ice Test.**

<b>Thermistor</b>	<b>Accuracy</b>
A2	Consistent with average recorded data (A2, A4-A7)
A3	0.35 to 1.47 °C above average recorded data for thermistors A2, A4-A)
A4	Consistent with average recorded data (A2, A4-A7)
A5	Consistent with average recorded data (A2, A4-A7)
A6	Consistent with average recorded data (A2, A4-A7)
A7	Consistent with average recorded data (A2, A4-A7)

#### **12.2.1.5 Probe 4, Discussion of Results**

Experiments one through four demonstrate the inaccuracy of thermistor A3 in Probe 4. The temperature measurements were invariably higher than the average of the temperature readings from the other five thermistors. The temperature recorded by thermistor A3 was higher than the average by 0.1 °C (Experiment one) to 2.18 °C (Experiment two).

Thermistors A4, A5, A6, and A7 performed well and recorded temperatures in agreement with the average recorded temperature in all experiments. Thermistor A2, when reconnected in Experiment four, returned results consistent with the average recorded data for thermistors A4-A7 and was considered accurate.

When Probe 4 was used in the field temperature measurements were found to be erroneous for thermistors A2, A3, and A5 (Depths (0.0, 0.2, and 0.6 m, respectively). The combined results may indicate the A3 thermistor was damaged in the field but the A2 and A5 thermistors may have been the result of instrumentation set up error or problems with connectivity to the data logger and not a problem with the thermistors themselves.

### **12.2.2 Temperature Probe 5**

Temperature Probe 5 was used in monitoring the bedrock streambed temperature near the north bank of the Bull Run River. Prior to monitoring of the bedrock the probe was also used to monitor the cobble substrate temperature (Probe 1).

#### **12.2.2.1 Experiment 1, Air test**

Probe 5 has six thermistors (labeled A2 through A7) and was used to measure air temperature in the laboratory for five days. Figure 179 shows the temperature measurements for this experiment and Table 103 lists the results of an analysis of each thermistor's accuracy. The results of experiment indicate the A7 thermistor had a positive bias compared to the other thermistors.

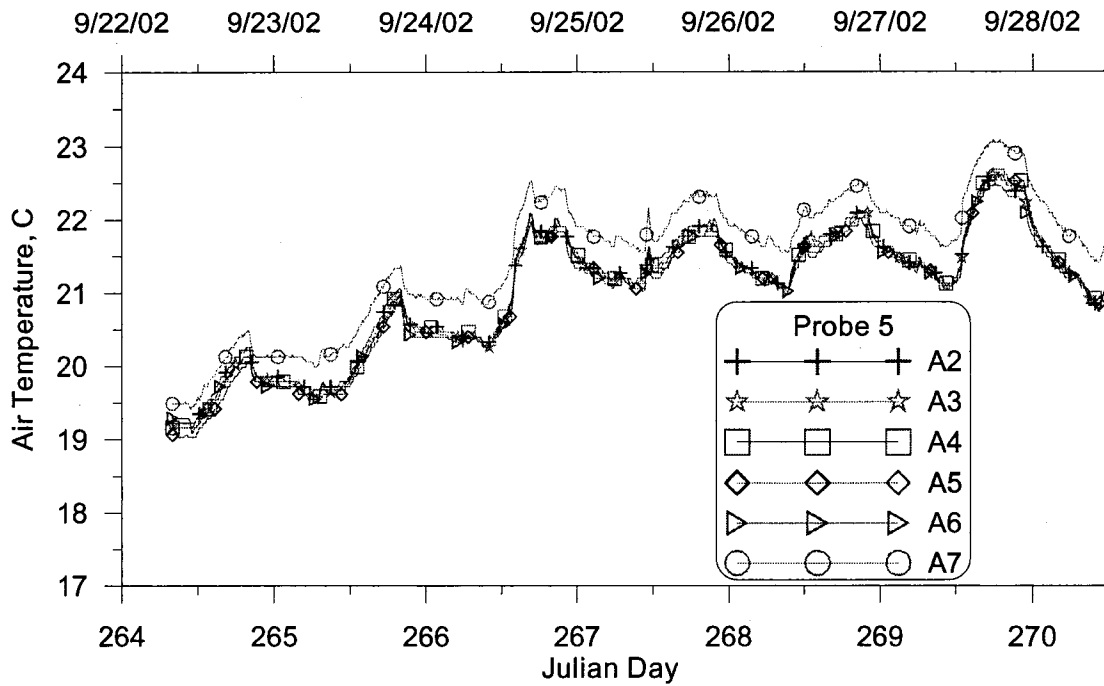


Figure 179: Measured thermistor temperatures in Probe 5, Experiment 1, Air Test.

Table 103: Accuracy of thermistors in Probe 5, Experiment 1, Air Test.

Thermistor	Accuracy
A2	Consistent with average recorded data (A2-A6)
A3	Consistent with average recorded data (A2-A6)
A4	Consistent with average recorded data (A2-A6)
A5	Consistent with average recorded data (A2-A6)
A6	Consistent with average recorded data (A2-A6)
A7	0.23 to 0.65 °C above average recorded data for thermistors A2-A6

#### 12.2.2.2 Experiment 2, Ice test

Probe 5 was immersed in ice water, removed, and allowed to return to room temperature. Figure 180 shows the temperature measurements for this experiment and Table 104 lists the results of an analysis of each thermistor's accuracy. Similar to the first experiment the A7 thermistor has positive bias compared the other thermistors.

The results also indicate there is slower response to room temperature for thermistors A2 and A5.

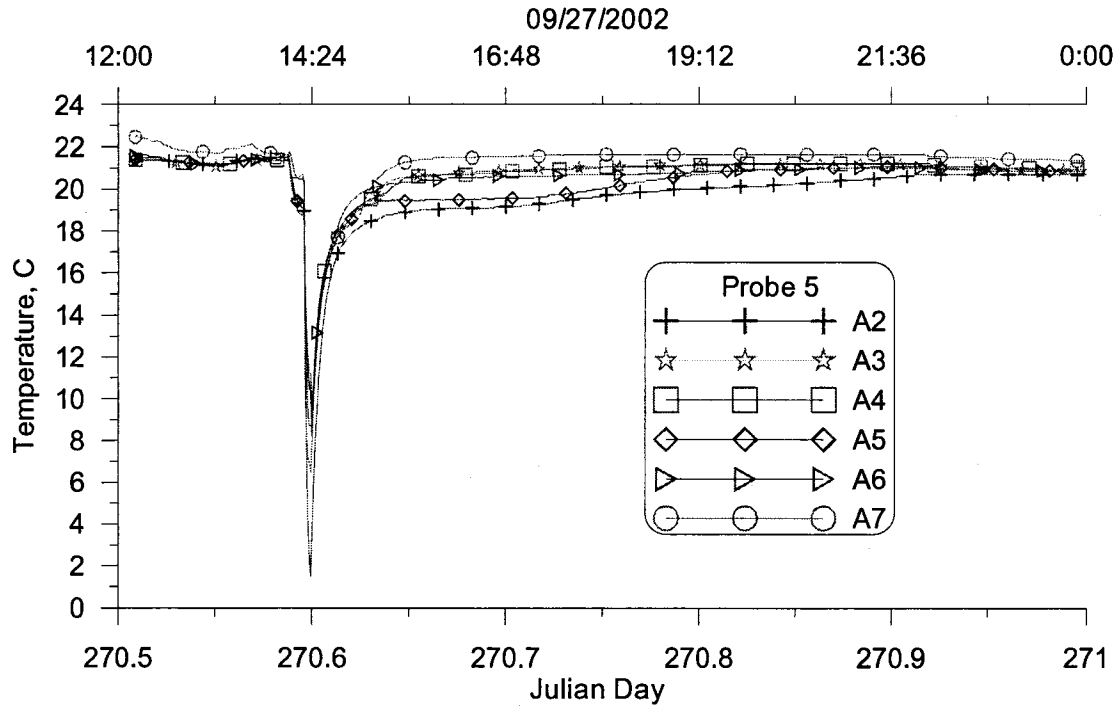


Figure 180: Measured thermistor temperatures in Probe 5, Experiment 2, Ice Test.

Table 104: Accuracy of thermistors in Probe 5, Experiment 2, Ice Test.

Thermistor	Accuracy
A2	Consistent with average recorded data (A2-A6)
A3	Consistent with average recorded data (A2-A6)
A4	Consistent with average recorded data (A2-A6)
A5	Consistent with average recorded data (A2-A6)
A6	Consistent with average recorded data (A2-A6)
A7	0.42 to 1.44 °C above average recorded data for thermistors A2-A6

### 12.2.2.3 Experiment 3, Second Air test

Probe 5 was used to measure the air temperature in the laboratory for 8.5 days.

Figure 181 shows the temperature measurements for this experiment and Table 105

lists the results of an analysis of each thermistor's accuracy. The results are consistent with the previous two experiments with the A7 thermistor showing a bias compared to the rest of the thermistors.

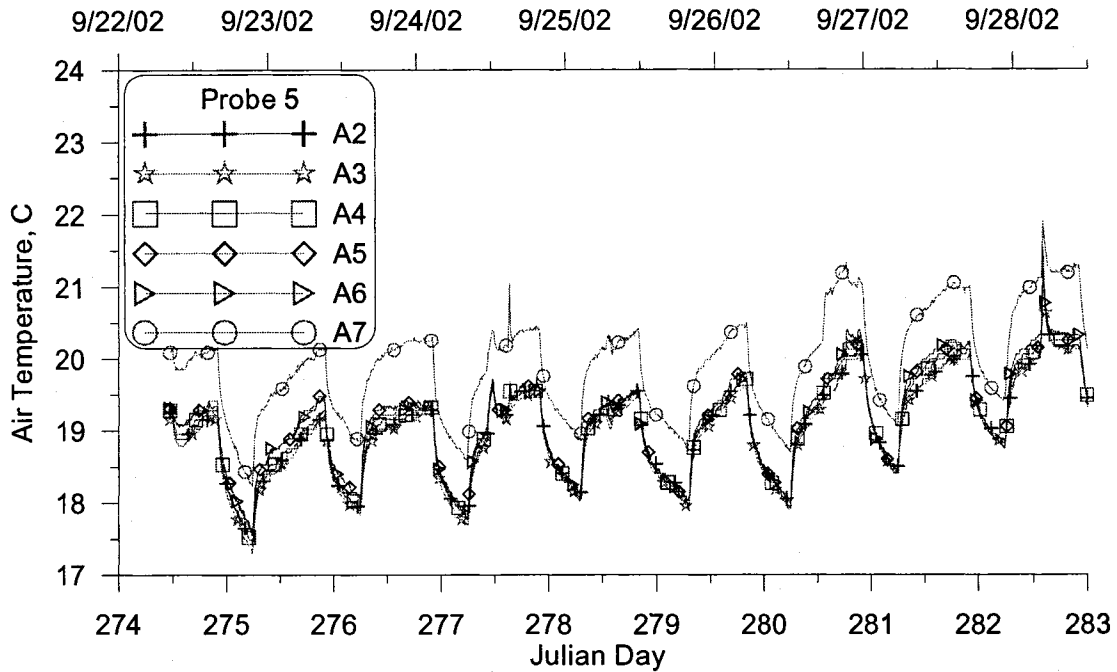


Figure 181: Measured thermistor temperatures in Probe 5, Experiment 3, Second Air Test.

Table 105: Accuracy of thermistors in Probe 5, Experiment 3, Second Air Test.

Thermistor	Accuracy
A2	Consistent with average recorded data (A2-A6)
A3	Consistent with average recorded data (A2-A6)
A4	Consistent with average recorded data (A2-A6)
A5	Consistent with average recorded data (A2-A6)
A6	Consistent with average recorded data (A2-A6)
A7	0.58 to 1.6 °C above average recorded data for thermistors A2-A6

### 12.2.2.4 Experiment 4, Second Ice test

Probe 5 was immersed in ice water, removed, and allowed to return to room temperature. Figure 182 shows the temperature measurements for this experiment and Table 106 lists the results of an analysis of each thermistor's accuracy. The results indicate there were slow responses in recovering to room temperature for several thermistors (A2, A5, and A7). Overall the results show there is a large variation in temperatures measured by the A7 thermistor compared to the rest of the thermistors.

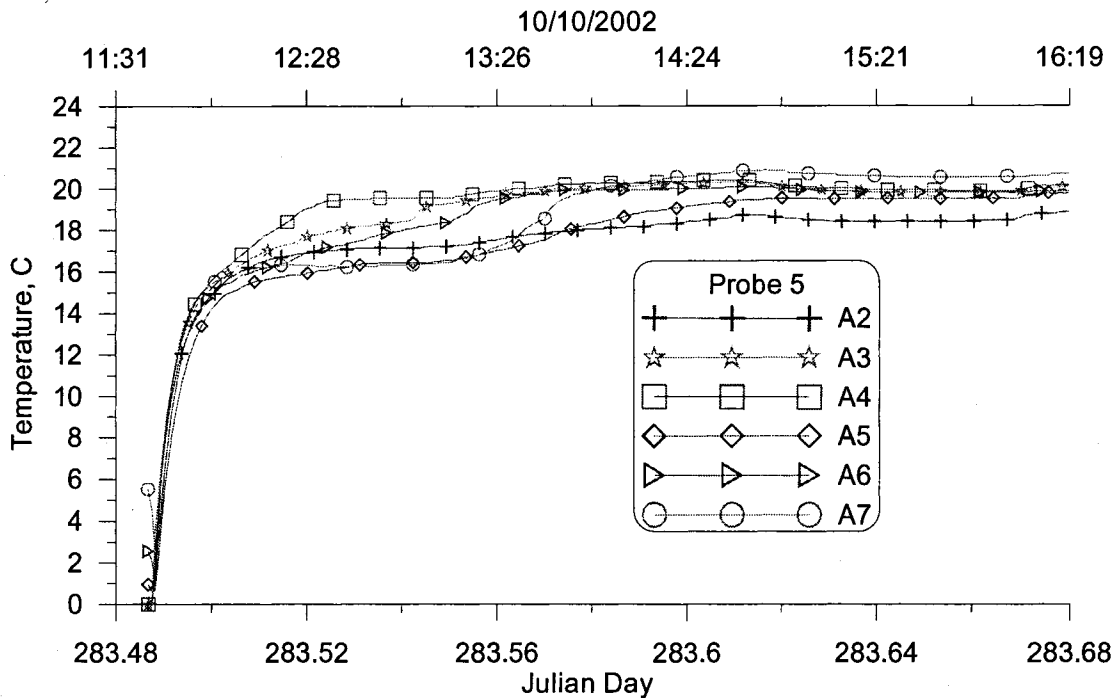


Figure 182: Measured thermistor temperatures in Probe 5, Experiment 4, Second Ice Test.

Table 106: Accuracy of thermistors in Probe 5, Experiment 4, Second Ice Test.

Thermistor	Accuracy
A2	Consistent with average recorded data (A2-A6)
A3	Consistent with average recorded data (A2-A6)
A4	Consistent with average recorded data (A2-A6)

<b>Thermistor</b>	<b>Accuracy</b>
A5	Consistent with average recorded data (A2-A6)
A6	Consistent with average recorded data (A2-A6)
A7	-1.77° to 1.2° C above average recorded data for thermistors A2-A6

#### 12.2.2.5 Probe 5, Discussion of Results

Experiments one through four indicate an inconsistencies with the temperature measurements from thermistor A7 compared to thermistors A2 to A6. The latter thermistors returned consistent results, diverging only briefly in experiments two and four. In contrast, thermistor A7 differed between  $-1.8$  and  $+1.6$  °C from the average temperature data recorded by thermistors A2 to A6. The erroneous data from the A7 thermistor could be due to problems with the instrumentation once removed from the field study. The data collected by the A7 thermistor in the field was consistent and compared well to the rest of the thermistors in Probe 5. The field work indicated the A5 (depth 0.6 m) thermistor was erroneous but this was not indicated in the lab experiments except in the slower response recovering to room temperature in the ice bath experiments. This may indicate the erroneous data in the field was caused by instrumentation set up error or problems with connectivity to the data logger and not a problem with the thermistor itself.

### 13. Appendix E: Secondary Light Extinction Analysis

Light attenuation data were collected on July 25<sup>th</sup> and September 20<sup>th</sup>, 2002 at the monitoring sites in Figure 183. Data collected on August 23<sup>rd</sup> and August 30<sup>th</sup> were not used in this analysis because there were clouds during the measurements. Table 28 and Table 31 list the data collected on July 25<sup>th</sup> and September 20<sup>th</sup>.

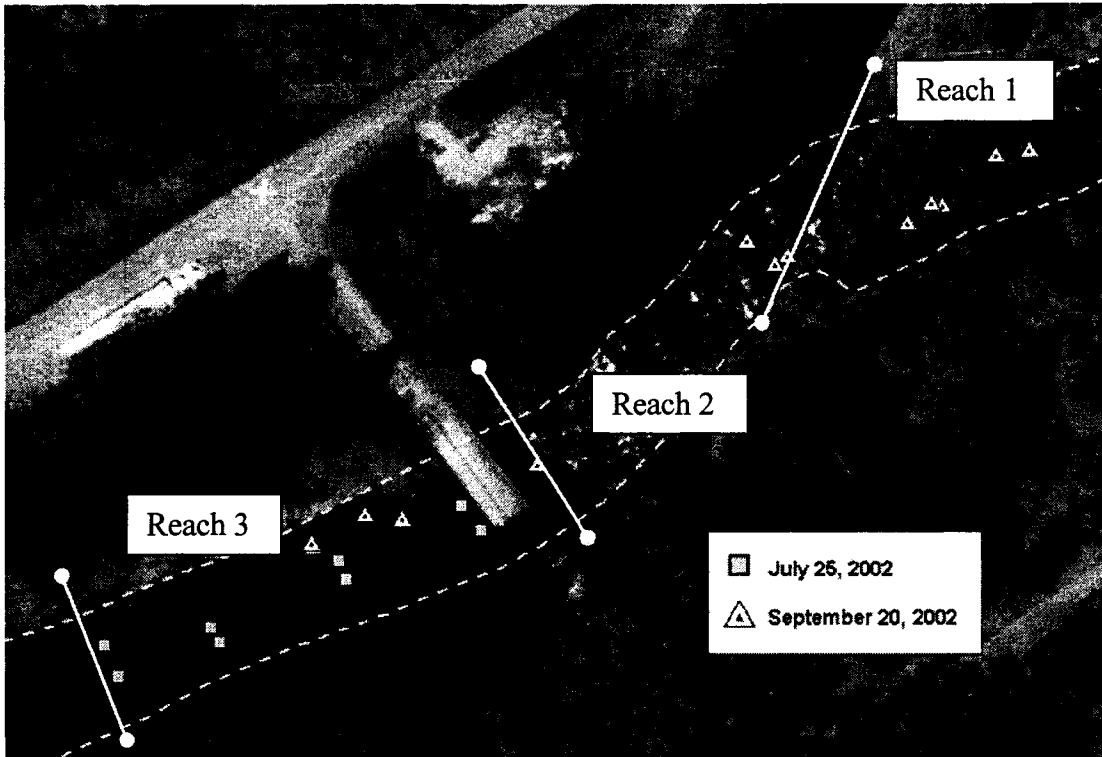


Figure 183: Light attenuation measurement sites in the Lower Bull Run River.

The data were used to calculate the extinction coefficient using Beer-Lambert Law from Cole and Wells, 2000:

$$I_{z_1} = (1 - \beta') I_o e^{-\eta_2(z_1 - z_o)} \quad (185)$$

where the  $I_o$  ( $\text{W}/\text{m}^2$ ) is the incident radiation at the water surface, equivalent to  $\varphi_c$ ,  $I_{z_1}$  ( $\text{W}/\text{m}^2$ ) is the radiation at depth  $z_1$  below the water surface  $z_o = 0$ ,  $\eta_2$  ( $\text{m}^{-1}$ ) is the light extinction coefficient, and  $\beta'$  (dimensionless) is the fraction of radiation absorbed in the first 0.6 m below the water surface (Cole and Wells, 2000). The value of  $\beta'$  is determined empirically and a default value of 0.45 was recommended in the CE-QUAL-W2 model (Cole and Wells, 2000). Additional values of  $\beta'$  have been developed from ocean studies with results listed in Table 33 and Table 34. An effort was made to use the data collected in the Bull Run River to try to calculate both  $\beta'$  and  $\eta_2$  and assumes that  $\beta'$  may be applied to shallower depths.

Three sites monitored on September 20<sup>th</sup> were examined first since there were three measurements taken over the river depth. The first measurement was made near the water surface and included the radiation fraction lost in the surface layer,  $\beta'$ . Equation (185) was rearranged and used to calculate the extinction coefficient as

$$\eta_2 = \frac{-\ln\left(\frac{I_{z_1}}{(1-\beta')I_o}\right)}{(z_1 - z_o)} \quad (186)$$

When calculating the extinction coefficient at each site between the first and second measurements near the surface and then second and third measurements, closer to the bottom, Equation (186) was first used with  $\beta'$  set to zero. Table 107 shows the light extinction coefficient was different between each site's pair of measurements. The table shows the light extinction coefficient calculated using measurements 1 and 2

were higher than the light extinction coefficients calculated using measurements 2 and 3. This may be due to the light attenuation near the surface, usually characterized by  $\beta'$ . So measurement 1 was used with Equation (186) and measurements 2 and 3 independently to estimate a value of  $\beta'$  by calibrating the measurements 1 and 2 and 1 and 3 to get an extinction coefficient similar to the one calculated using measurements 2 and 3 only. The last three columns of Table 107 show the results of “calibrating”  $\beta'$ . The table shows that using a  $\beta'$  of 0.041 to 0.052 (average: 0.049) when comparing the near surface light measurements (Measurement 1) with the measurements at deeper locations (Measurements 2 and 3) results in light extinction coefficients very similar to when light measurements between Measurements 2 and 3 are compared directly where  $\beta'$  was set to zero. The average depth of Measurement 1 between the three sites was 0.023 m and the average depth of Measurement 2 was 0.104 m. The results in Table 107 indicate an average  $\beta'$  of 0.049 applies when comparing measurements near the surface (0.023 m) to deeper locations in the river. When comparing light measurements at depths of 0.104 m and below a  $\beta'$  of 0.0 applies.

The other sites monitored on September 20<sup>th</sup> include only two measurements over depth, one near the surface and one near the bottom. Equation (186) was used with an average  $\beta'$  of 0.049 to calculate the light extinction coefficient for the sites with only two measurements. Table 108 lists the calculated light extinction

coefficients and indicates when incorporating the remaining sites from September 20<sup>th</sup> there is more variability in the light extinction coefficients.

Table 107: Calculated Light Extinction Coefficient at three sites in Reach 1, September 20, 2002

Time	Site	Measurement Number	Radiation below water, $\mu$ moles/m <sup>2</sup> /s	Depth, m	Measurements used in calculating, $\eta_2$ where $\beta' = 0$	$\eta_2$ , m <sup>-1</sup> where $\beta' = 0$	Measurements used in calculating $\eta_2$ where $\beta' > 0$	$\eta_2$ , m <sup>-1</sup> where $\beta' > 0$	$\beta'$
2:10 PM	1	1	1275	0.01					
2:11 PM	1	2	1160	0.07	1 & 2	1.551	1 & 2	0.662	0.053
2:12 PM	1	3	1070	0.20	2 & 3	0.662	1 & 3	0.662	
2:20 PM	2	1	1290	0.04					
2:21 PM	2	2	1150	0.13	1 & 2	1.256	1 & 2	0.668	0.052
2:22 PM	2	3	1060	0.26	2 & 3	0.668	1 & 3	0.668	
2:35 PM	4	1	1130	0.01					
2:37 PM	4	2	1020	0.10	1 & 2	1.120	1 & 2	0.666	0.041
2:38 PM	4	3	950	0.21	2 & 3	0.666	1 & 3	0.666	

**Table 108: Calculated light extinction coefficient, September 20, 2002**

Site	Reach	Extinction Coefficient, $\eta_2, \text{m}^{-1}$	Site	Reach	Extinction Coefficient, $\eta_2, \text{m}^{-1}$
1	1	0.662	8	2	1.209
2	1	0.668	9	2	1.081
3	1	2.490	10	3	0.636
4	1	0.666	11	3	0.720
5	1	0.816	12	3	0.432
6	2	1.258	13	3	0.790
7	2	0.323			
Overall Average					0.904
Reach 3 Average					0.644

Light attenuation data collected on July 25<sup>th</sup> consisted of one measurement above the water surface and one measurement near the river bottom for sites in Reach 3 as shown in Table 28. The calculated fraction of radiation lost in surface layer from the September 20<sup>th</sup> data set utilized radiation measurements just below the water surface (0.023 m). Assuming an overall  $\beta'$  of 0.40 and a  $\beta'$  value of 0.049 was calculated for depths below 0.023 m then the remaining fraction of  $\beta'$  above 0.023 m would be 0.0351. The radiation measurements above the water from July 25, 2003 were used with Equation (185), a  $\beta'$  of 0.351, and a light extinction coefficient based on the average light extinction coefficient from Reach 3 on September 20<sup>th</sup> (0.644  $\text{m}^{-1}$ ) to calculate the radiation in the water at a depth of 0.023 m.

The radiation calculated at a depth of 0.023 m and the measured radiation at the bottom of the river were used with Equation (186) and a  $\beta'$  of 0.049 to calculate the light extinction coefficient for the rest of the water column. Table 109 lists the calculated light extinction coefficients.

**Table 109: Calculated light extinction coefficient, July 25, 2002**

Site	Reach	Measured Radiation above water, $\mu$ moles/m <sup>2</sup> /s	Measured Radiation below water, $\mu$ moles/m <sup>2</sup> /s	Calculated Radiation below water, $\mu$ moles/m <sup>2</sup> /s	Depth, m	$\eta_2$ , m <sup>-1</sup>
1	3	3510		2243	0.02	
1	3		1800		0.29	0.648
2	3	3625		2316	0.02	
2	3		1795		0.38	0.579
3	3	3720		2377	0.02	
3	3		1575		0.58	0.655
4	3	3640		2326	0.02	
4	3		1540		0.74	0.508
5	3	3690		2358	0.02	
5	3		1560		0.65	0.578
6	3	3632		2321	0.02	
6	3		1340		1.02	0.502
7	3	3580		2288	0.02	
7	3		1430		0.57	0.773
8	3	3490		2230	0.02	
8	3		1650		0.37	0.723
Average						0.621
Standard Deviation						0.097

The average light extinction coefficients for Reaches 1 and 2 based on the September 20<sup>th</sup> data set were 0.926 and 0.901, respectively. The average light extinction coefficient for Reach 3 was 0.644, based on the September 20<sup>th</sup> data set, and 0.621, based on the July 25<sup>th</sup> data set. The similarity between calculated light extinction coefficients in Reach 3 between the two dates indicates there may be a better discern the light extinction and the fraction of radiation lost in the surface by collecting more robust data sets.